Search for single top-quark production via flavour-changing neutral currents in strong interactions using $\sqrt{s} = 8$ TeV ATLAS data

D I S S E R T A T I O N

zur Erlangung des akademischen Grades

d o c t o r r e r u m n a t u r a l i u m

(Dr. rer. nat.)

im Fach Physik

eingereicht an der
Mathematisch-Naturwissenschaftlichen Fakultät I
Humboldt-Universität zu Berlin

von

Dipl.-Phys. Conrad Friedrich

Präsident der Humboldt-Universität zu Berlin:
Prof. Dr. Jan-Hendrik Olbertz

Dekan der Mathematisch-Naturwissenschaftlichen Fakultät I:
Prof. Stefan Hecht, Ph.D.

Gutachter:
1. Prof. Dr. Ulrich Husemann
2. Prof. Dr. Heiko Lacker
3. Jun.-Prof. Dr. Arno Straessner

Tag der mündlichen Prüfung: 27.11.2014

Abstract

This thesis presents results of a search for single top-quark production via flavour-changing neutral currents (FCNCs) in strong interactions using data recorded with the ATLAS experiment at the Large Hadron Collider in 2012. A dataset from proton-proton collisions at a centre-of-mass energy of $\sqrt{s} = 8\,\text{TeV}$ and corresponding to an integrated luminosity of $\mathcal{L}_{\text{int}} = 14.1\,\text{fb}^{-1}$ is used. It is searched for FCNC events in which a light quark (u or c) interacts with a gluon to produce a single top quark, either with or without the associated production of another light quark or gluon. Candidate events of leptonically decaying top-quarks are selected by requiring a single electron or muon, a substantial amount of missing transverse energy, and exactly one or two jets of which exactly one has to fulfil a b-tagging criterion. Multivariate techniques are employed in order to distinguish between signal- and background-like events by making use of artificial neural networks that combine multiple kinematic variables into a single classifier output. A Bayesian statistical analysis is performed on the classifier outputs in order to quantify potential signs of FCNC single top-quark production. No excess in signal events is observed and the results are in agreement with the theory predictions. Consequently a new upper limit is set on the FCNC single top-quark production cross-section multiplied by the $t \to Wb$ branching fraction. The observed 95% C.L. limit is found at $\sigma_{qg\to t} \times \mathcal{B}(t \to Wb) < 2.5\,\text{pb}$. Using theory calculations within a model-independent effective theory framework, this limit is converted into upper limits on the coupling constants of the FCNC interactions $\kappa_{ugt}/\Lambda < 5.1 \cdot 10^{-3}\ \text{TeV}^{-1}$ and $\kappa_{cgt}/\Lambda < 1.1 \cdot 10^{-2}\ \text{TeV}^{-1}$, as well as into respective upper limits on the branching fractions $\mathcal{B}(t \to ug) < 3.1 \cdot 10^{-5}$ and $\mathcal{B}(t \to cg) < 1.6 \cdot 10^{-4}$.

Zusammenfassung

In dieser Dissertation werden Resultate einer Suche nach der Produktion von Einzel-Top-Quarks über flavour-verletzende neutrale Ströme (FCNCs) in starken Welchselwirkungen vorgestellt. Hierfür werden Daten aus Proton-Proton-Kollisionen am Large Hadron Collider bei einer Schwerpunktsenergie von $\sqrt{s} = 8\,\text{TeV}$ verwendet. Die Daten wurden mit dem ATLAS-Experiment im Jahr 2012 aufgenommen und entsprechen einer integrierten Luminosität von $\mathcal{L}_{\text{int}} = 14.1\,\text{fb}^{-1}$. In der Analyse werden FCNC-Ereignisse selektiert, in denen ein leichtes Quark (u oder c) mit einem Gluon wechselwirkt, und ein einzelnes Top-Quark und potentiell ein weiterer einzelner Jet produziert wird. Mittels der Forderung nach genau einem Myon oder Elektron, großer fehlender Transversalenergie und exakt einem Bottom-Quark-Jet und eventuellem zusätzlichen Jet im Endzustand werden Kandidaten der gesuchten Ereignisse im leptonischen Zerfallskanal des Top-Quarks selektiert. Zur Unterscheidung zwischen Signal- und Untergrundereignissen werden multivariate Methoden herangezogen. Künstliche neuronale Netze werden verwendet, um diverse kinematische Variablen zu einem einzelnen Klassifikator zu kombinieren. Um die potentielle Produktion von Top-Quarks über FCNCs zu quantifizieren, werden die Ausgaben der neuronalen Netze einer Bayes'schen statistischen Analyse unterzogen. Da kein Überschuss an Signalereignissen festgestellt werden kann und die Ergebnisse den Erwartungen der theoretischen Vorhersagen entsprechen, werden neue obere Schranken auf den FCNC-Produktionswirkungsquerschnitt von Einzel-Top-Quarks ermittelt. Die erhaltene beobachtete obere Schranke bei 95% Vertrauensniveau liegt bei $\sigma_{qg\to t} \times \mathcal{B}(t \to Wb) < 2.5$ pb. Aus dieser werden unter Verwendung von modellunabhängigen theoretischen Berechnungen neue obere Schranken auf die Kopplungskonstanten $\kappa_{ugt}/\Lambda < 5.1 \cdot 10^{-3}\ \text{TeV}^{-1}$ und $\kappa_{cgt}/\Lambda < 1.1 \cdot 10^{-2}\ \text{TeV}^{-1}$, sowie auf die Verzweigungsverhältnisse $\mathcal{B}(t \to ug) < 3.1 \cdot 10^{-5}$ und $\mathcal{B}(t \to cg) < 1.6 \cdot 10^{-4}$ ermittelt.

Contents

1. Introduction

Over the past decades particle physics has brought profound insights into the constituents of matter and their fundamental interactions. The present understanding of their nature has coalesced in the Standard Model of Particle Physics (SM). Within that framework the currently known fundamental particles (twelve fermions, leptons and quarks of three families) and their interactions via three of the four known fundamental forces in nature, the electromagnetic, weak and strong force (mediated via gauge bosons), are described with unprecedented accuracy. The SM therefore represents one of the most successful theoretical models in physics history whose predictions have been experimentally verified at continuously increasing precision and energy scales. With the discovery of the top quark in 1995 at Fermilab [1, 2], the last missing fermion in the third quark family was found. Only the discovery of the Higgs boson was still outstanding to confirm the SM in its entirety – a scalar particle introduced into the theory as a consequence of the Higgs mechanism that describes the mass generation process of elementary particles. Nonetheless it is widely believed that the SM is only a part or an effective approximation of a more fundamental and complete theory, since it suffers from several shortcomings. These include theoretical deficiencies, such as the lack of an inclusion of the gravitational force or solutions to the unification problem, but also is challenged by experimental observations, e.g. of neutrino oscillations, baryon asymmetry, or astrophysical indications for the existence of Dark Matter and Dark Energy. The latter are expected to contribute with approximately 96% to the total matter/energy in the universe, whereas the SM merely provides a theoretical description of the remaining (known) 4% of baryonic matter.

In order to test the Standard Model at even higher energy scales and to confirm or exclude the existence of the last fundamental particle predicted by the theory (the Higgs boson), the Large Hadron Collider (LHC) has been built at CERN and was successfully in operation since 2010. The most outstanding result of the first years of data-taking was the announcement of first evidence for a Higgs-like boson candidate in November 2011 by two of the main LHC experiments, ATLAS and CMS [3–5], and the independent discovery of the new particle in early July of 2012 [6–9]. Later, in March 2013, the zero spin and positive parity of the boson were tentatively confirmed [10–13], thereby validating that the new particle is some kind of Higgs boson and the first elementary scalar particle discovered in history. In addition to the search for the Higgs boson the LHC was built to answer several other open key questions in particle physics and to probe for the existence of new heavy particles and/or interactions described by a variety of extensions to the SM or entirely new physics theories.

The heaviest particle described within the SM, the top quark, has a (pole) mass of $m_t = 173.1 \pm 0.9$ GeV [14] which is close to the electroweak symmetry breaking scale

($v/\sqrt{2} \approx 246$ GeV) set by the vacuum expectation value of the Higgs field (cf. Section 2.1). It therefore plays a key role for testing the SM predictions and probing for physics beyond the Standard Model. In the SM top quarks are produced either in the form of quark/anti-quark pairs via the strong, or singly via the electroweak interaction. The single top-quark production and its decay are almost exclusively mediated via the Wtb vertex. Consequently, top quarks predominantly decay into a W boson and a bottom quark. Decays via the other neutral gauge bosons in so-called Flavour-Changing Neutral Current (FCNC) interactions in the Ztq, γtq or qgt vertices are forbidden at tree level in the SM and may only occur in higher order loop diagrams involving W bosons. Moreover, the rates of the latter processes are highly suppressed and hence only contribute with vanishing branching fractions at the order of $10^{-15} - 10^{-12}$ to the top-quark decay. However, several new physics models exist, which allow for significantly enhanced rates of FCNC processes involving top quarks. Many theories beyond the SM permit FCNC interactions already at tree level or by introducing new particles in higher order loop diagrams. For certain models and parameter spaces this results in predicted branching fractions of up to $\mathcal{O}(10^{-5} - 10^{-3})$, which is in reach of the expected sensitivity of experiments at the LHC [15–18]. Therefore any observation of such processes would be a strong indicator for new physics.

FCNC interactions in the top-quark sector are either studied in the decay channel or in single top-quark production. At hadron colliders, the latter is the method of choice for studies of flavour-changing strong interactions, since the final state signatures of the $t \to qg$ decay mode are largely overwhelmed by multijets production in QCD processes. In this thesis an analysis is presented, which searches for the above type of FCNC interactions in single top-quark production. The analysis uses data from proton-proton (p-p) collisions at the LHC at a centre-of-mass energy of $\sqrt{s} = 8$ TeV that has been recorded with the ATLAS detector in 2012. The dataset corresponds to an integrated luminosity of $\mathcal{L}_{\text{int}} = 14.1\,\text{fb}^{-1}$ and is searched for FCNC events in which a light quark (u or c) interacts with a gluon to produce a single top quark, either with or without the associated production of another light quark or gluon.

The single top quarks are assumed to decay exclusively via the predominant $t \to Wb$ process in the SM. Candidate events with a leptonic W boson decay ($t \to Wb \to \ell\nu b$) are selected in two exclusive categories with exactly one or exactly two jets in the final state. The potential FCNC signal events are expected to be produced at very small rates in comparison to the various SM background processes. Therefore the selected event sample is separated into signal- and background-like events using artificial neural networks that combine multiple kinematic variables into a single output classifier.

In order to measure or calculate limits on the rate of the FCNC signal processes of interest, a Bayesian statistical analysis is performed, applying a binned maximum likelihood method to the neural network output distributions. No significant FCNC signal is observed in both jet categories and new upper limits are set on the cross-section times $t \to Wb$ branching fraction of FCNC single top-quark production in strong interactions. Lastly, the more stringent of both limits is converted into upper limits on the branching fractions and coupling strengths of the involved FCNC processes using NLO theory calculations.

The thesis is organised in ten chapters. A description of the SM theory framework will be given in Chapter 2, followed by a more detailed summary on its present shortcomings and examples of new physics theories beyond the SM that could resolve parts of these deficiencies in Chapter 3. Chapter 3 also provides an overview of past searches for FCNCs in top-quark interactions and describes the reasons for enhanced FCNC rates and their predicted values in different new physics models. In Chapter 4 the reader is introduced to the experimental setup, the LHC accelerator complex and the ATLAS detector in particular, followed by details on the data sample used for the analysis and the Monte Carlo (MC) techniques and samples employed for the simulation of the FCNC signal and SM background processes in Chapter 5. The definition and reconstruction of physics objects from the ATLAS detector information as well as the final event selection and the estimation of the QCD multijet background are detailed in Chapter 6 and 7, respectively. The event classification and details on the neural network analysis techniques are given in Chapter 8 and the sources of systematic uncertainties are summarised in Chapter 9. In Chapter 10 the Bayesian statistical analysis method is introduced and results on the estimated expected and observed upper limits on the cross-section as well as on the coupling constants and branching fractions of the investigated FCNC processes are given. Lastly, a discussion of the results is given in Chapter 11, including a comparison with previous results and theory predictions, as well as prospects for future LHC runs.

An additional topic of this PhD work consists in contributions to the research and development towards an upgrade of the present ATLAS silicon microstrip detector (SCT) for its operation at the so-called High-Luminosity LHC (HL-LHC). The project aims for an extension of the operation of the LHC and its experiments at an approximately five-fold instantaneous luminosity for another ten years beyond 2023/24. An overview of the different steps currently planned for the upgrades of the LHC and ATLAS detector and the technical demands connected to these are given in Appendix F. Also presented are updated performance studies on the different powering concepts for the future detector elements. A large part of the contributions consist in the installation of infrastructure, measurement setups and the prototyping and testing of future ATLAS microstrip detector elements. Appendix F.3 therefore provides an overview of the design of components, the technical implementation and assembly of the future ATLAS microstrip detector modules, as well as on the experiences gained in their prototyping and the optimisation of the tools and techniques employed for their construction.

2. The Standard Model of Particle Physics

Within the last 50 years the Standard Model of Particle Physics [19–22] gave a precise description of fundamental particles physics from the atomic scale down to the shortest length scales accessible to physics experiments today. It therefore has been one of the most successful fundamental physics theories in history and has been tested with unprecedented accuracy by experiments in astrophysics and collider experiments over the past decades, without any major inconsistencies having been found so far. However, there exist unexplained phenomena which cannot be described within the framework of the SM alone, see Section 3 for a detailed discussion.

The SM provides a unified relativistic, quantum field-theoretical descriptions of elementary point-like particles, interacting via electromagnetic and weak forces, together with the strong interaction within a single theoretical framework derived from general mathematical principles. The forces described within the SM are mediated via the exchange of 12 spin-1 particles, so-called gauge bosons. Eight massless gluons (g) mediate the strong force, one massless photon (γ) the electromagnetic force and three massive gauge bosons ($W^{\pm}$,Z^0) the weak force, see Table 2.1. The latter four arise as two different aspects of a unified description of the same electroweak (EW) force by means of spontaneous symmetry breaking, see Section 2.1 for details. The fourth fundamental force, gravitation, is not described within the SM. A unified quantum field-theoretical description of gravitation, together with the other three fundamental forces, still has to be found. The forces described in the SM act on 12 spin-½ fermions, point-like

Table 2.1.: Values of mass, charge and decay width of all spin-1 gauge bosons described in the SM mediating the strong (g), (electro)weak ($W^{\pm}$, Z^0) and the electromagnetic (electroweak) force (γ) [14]. Theory values are marked with *.

Gauge boson	Force	Mass m [GeV]	El. charge Q [e]
gluon (g)	strong	0^*	0^*
photon (γ)	EM (EW)	0^*	0^*
W boson ($W^{\pm}$)	weak (EW)	80.385 ± 0.015	$\pm 1^*$
Z boson (Z^0)		91.1876 ± 0.0021	0^*

matter particles divided into two classes consisting of six quarks and six leptons, plus their corresponding antiparticles of same mass, see Table 2.2. While leptons are either electrically charged ($\pm 1\,e$) or neutral (neutrinos), quarks carry fractional charges of either $-1/3\,e$ or $+2/3\,e$, see Section 2.2. Within the field-theoretical framework of the SM, the interaction of the matter particles (or fields) are described through the local

Table 2.2.: Fundamental spin-½ fermions in the SM. The corresponding antiparticles with opposite quantum numbers for all fermions are not shown. [14]

	Particle	Mass m [GeV]	El. charge Q [e]
Leptons	electron (e^-)	0.5110×10^{-3}	-1
	electr. neutrino (ν_e)	$< 0.002 \times 10^{-3}$	0
	muon (μ^-)	0.1057	-1
	muon neutrino (ν_μ)	$< 0.19 \times 10^{-3}$	0
	tau (τ^-)	1.7768	-1
	tau neutrino (ν_τ)	$< 18.2 \times 10^{-3}$	0
Quarks	up quark (u)	$2.3^{-0.5}_{+0.7} \times 10^{-3}$	$+2/3$
	down quark (d)	$4.8^{-0.3}_{+0.5} \times 10^{-3}$	$-1/3$
	charm quark (c)	1.275 ± 0.02 ($\overline{\text{MS}}$)	$+2/3$
	strange quark (s)	$95 \pm 5 \times 10^{-3}$	$-1/3$
	top quark (t)	173.07 ± 0.89 (pole)	$+2/3$
	bottom quark (b)	4.18 ± 0.03 ($\overline{\text{MS}}$)	$-1/3$

$\text{SU}(3)_C \times \text{SU}(2)_L \times \text{U}(1)_Y$ gauge symmetry[1], where $\text{SU}(3)_C$ represents the gauge group of the Quantum ChromoDynamics (QCD) sector that describes interactions between quarks and gluons carrying a colour charge C, and the electroweak sector is represented by the $\text{SU}(2)_L \times \text{U}(1)_Y$ symmetry group where the corresponding charges are the weak isospin T and weak hypercharge Y_W. The subscript L refers to the parity-violating character of the weak force which is only acting on left-handed fermions. Both, the electroweak and strong (QCD) sector of the SM will be described in more detail in the following two sections.

2.1. Electroweak Theory and Higgs Mechanism

Within the electroweak theory [19–21], also referred to as the Glashow-Weinberg-Salam model, the electromagnetic and weak forces are unified into a more fundamental electroweak force, incorporating the Higgs mechanism to provide a mechanism of spontaneous symmetry breaking which gives elementary particles their mass. Following the common method of constructing most field theories, a set of symmetries is postulated, here the $\text{SU}(2)_L \times \text{U}(1)_Y$ symmetry group, and a renormalisable Lagrangian is derived to describe the kinematics of its field content (particles) which is required to be invariant under local phase transformations of the $\text{SU}(2)_L$ and $\text{U}(1)_Y$ groups:

$$\Psi_L(x) \to \Psi'_L(x) = e^{\frac{1}{2} i g \tau_j \omega_j(x)} \Psi_L(x)\,, \tag{2.1}$$

$$\Psi_L(x) \to \Psi'_L(x) = e^{i g' Y f(x)} \Psi_L(x)\,, \tag{2.2}$$

[1] As generally postulated for most relativistic quantum field theories, the global Poincaré symmetry (translational, rotational and inertial reference frame invariance) is always implied.

where g and $g\prime$ are real (coupling) constants, $\omega_j(x)$ with j= 1,2,3 and $f(x)$ are real differentiable functions of x, Y_W is the weak hypercharge and generator of the $\mathrm{U}(1)_Y$ group and the τ_i are the Pauli matrices and respective generators of the $\mathrm{SU}(2)_L$ group:

$$\tau_1 = \begin{pmatrix} 0 & 1 \\ 1 & 0 \end{pmatrix}, \quad \tau_2 = \begin{pmatrix} 0 & -i \\ i & 0 \end{pmatrix}, \quad \tau_3 = \begin{pmatrix} 1 & 0 \\ 0 & -1 \end{pmatrix}.$$

Further, particles are described in terms of massless Dirac spinor fields $\Psi(x)$ which are subdivided into their left- and right-handed contents to account for the observation that the weak interaction only affects left-handed fermions:

$$\Psi_{R,L} = \frac{1}{2}(1 \pm \gamma^5)\Psi\,.$$

Herein γ^5 stands for the product of the four Dirac γ matrices, defines as $\gamma^5 = i\gamma^0\gamma^1\gamma^2\gamma^3$, see e.g. Section 3.2 in [23]. Following Noether's theorem [24], the (global) invariance of the Lagrangian implies conserved quantities which can be identified as the weak isospin charges T_i $(i = 1, 2, 3)$ and the weak hypercharge $Y_W = 2(Q - T_3)$, where Q is the electric charge given in units of e. Hence, the weak hypercharge Y_W is linked to the electric charge and the third component of the weak isospin T_3. Left-handed fermions (of negative chirality) have $T_3 = \pm 1/2$ and consequently are arranged into three weak isospin ($\mathrm{SU}(2)_L$) doublets, which behave the same way in weak interactions. On the other hand, right-handed fields with $T_3 = 0$ are grouped into weak isospin singlets which are defined to be invariant under $\mathrm{SU}(2)_L$ transformations

$$\Psi_L = \begin{pmatrix} \psi_L^{\nu} \\ \psi_L^{\ell} \end{pmatrix}, \begin{pmatrix} \psi_L^{\mathcal{U}} \\ \psi_L^{\mathcal{D}} \end{pmatrix} \qquad \Psi_R = \psi_R^{\ell},\ \psi_R^{\mathcal{U}},\ \psi_R^{\mathcal{D}}\,,$$

where ν and ℓ stand for the charged (e, μ, τ) and neutral (ν_e, ν_μ, ν_τ) leptons and $\mathcal{U}$ and $\mathcal{D}$ stand for the up-type (u, c, t) and down-type (d, s, b) quarks, respectively. The left-handed fermions consequently are arranged into pairs of three generations or families as shown in Table 2.3. Fermions of different generations are identical in all quantum numbers and only differ in their so-called flavour, i.e. in their fermion type, and in their mass, which increases with higher generations. For each of these, corresponding antiparticles with opposite quantum numbers exist.

To ensure the Lagrangian is invariant under the gauge transformations given in 2.1 and 2.2, additional (massless) gauge vector fields have to be introduced, one weak isospin singlet $B_\mu(x)$ and a weak isospin triplet $W_\mu^i(x)$ $(i = 1, 2, 3)$, where $B_\mu(x)$ is invariant under $\mathrm{SU}(2)_L$ transformations and the $W_\mu^i(x)$ are invariant under $\mathrm{U}(1)_Y$ gauge transformations, respectively. The Lagrangian density that describes the fermion interactions $\mathcal{L}_{\mathrm{int}}^{\mathrm{EW}}$ consequently is invariant under both transformations and usually is referred to as $\mathrm{SU}(2)_L \times \mathrm{U}(1)_Y$ gauge-invariant

$$\mathcal{L}_{\mathrm{int}}^{\mathrm{EW}} = i\left[\bar{\Psi}_L(x)\not{D}\Psi_L(x) + \bar{\psi}_R^{\ell}(x)\not{D}\psi_R^{\ell}(x) + \bar{\psi}_R^{\nu}(x)\not{D}\psi_R^{\ell}(x)\right], \tag{2.3}$$

Table 2.3.: Fermions within the SM arranged into three generations of left-handed isospin doublets and right-handed isospin singlets. Also shown are their respective electric charge Q and third component of the weak isospin T_3. The corresponding anti-particles with opposite quantum numbers are always implied.

	1st Generation	2nd Generation	3rd Generation	Q	T_3
Leptons	$\begin{pmatrix}\nu_e\\ e^-\end{pmatrix}_L$	$\begin{pmatrix}\nu_\mu\\ \mu^-\end{pmatrix}_L$	$\begin{pmatrix}\nu_\tau\\ \tau^-\end{pmatrix}_L$	0 -1	$+1/2$ $-1/2$
	e^-_R	μ^-_R	τ^-_R	-1	0
Quarks	$\begin{pmatrix}u\\ d\end{pmatrix}_L$	$\begin{pmatrix}c\\ s\end{pmatrix}_L$	$\begin{pmatrix}t\\ b\end{pmatrix}_L$	$2/3$ $-1/3$	$+1/2$ $-1/2$
	u_R, d_R	c_R, s_R	t_R, b_R	$2/3, -1/3$	0

where similar terms for the quark fields are always implied and $\not{D}$ is the covariant derivative introduced to assure gauge invariance:

$$D^\mu \Psi_L(x) = \left[\partial^\mu + \frac{1}{2} i g \tau_j W_j^\mu(x) - \frac{1}{2} i g' B^\mu(x)\right] \Psi_L(x)\,, \tag{2.4}$$

$$D^\mu \psi_R^\ell(x) = \left[\partial^\mu - i g' B^\mu(x)\right] \psi_R^\ell(x)\,, \tag{2.5}$$

$$D^\mu \psi_R^\nu(x) = \partial^\mu \psi_R^\nu(x)\,. \tag{2.6}$$

After identifying the corresponding conserved charged and neutral currents, four physical gauge fields can be identified as linear combinations of the $W_\mu^i(x)$ and the $B_\mu(x)$ vector fields:

$$W_\mu^\pm(x) = \frac{1}{\sqrt{2}}(W_\mu^1(x) \mp i W_\mu^2(x))\,, \tag{2.7}$$

$$\begin{pmatrix}A_\mu(x)\\ Z_\mu(x)\end{pmatrix} = \begin{pmatrix}\cos\Theta_W & \sin\Theta_W\\ -\sin\Theta_W & \cos\Theta_W\end{pmatrix}\begin{pmatrix}B_\mu(x)\\ W_\mu^3(x)\end{pmatrix}\,, \tag{2.8}$$

where Θ_W is called the weak mixing angle[2], the $W_\mu^\pm(x)$ are interpreted as the charged physical (a priori massless) $W^\pm$ bosons and the $A_\mu(x)$ and $Z_\mu(x)$ fields as the photon (γ) and Z^0 boson.

The basic interactions between fermions and the gauge bosons mediated by the terms in Equation 2.3 are depicted in Figure 2.1 for the leptonic sector and at leading order in perturbation theory. Perturbation theory in quantum field theoretical calculations is

[2] Θ_W describes the mixing of weak and electromagnetic interactions and has been measured to be $\Theta_W \sim 30°$ and hence to be non-zero (weak and EM interactions are not decoupled). The currently most precise effective value (including contributions from quantum loop corrections) is $\sin^2\Theta_W^{eff} = 0.23116 \pm 0.00059$ [14].

directly related to the generic mathematical concept of perturbation series and hence describes an approximation scheme to problems that are very difficult or impossible to solve exactly. Instead of finding the exact solution to a problem it is approximated in terms of a power series in a small parameter around the exact solution of a related (usually simpler), but solvable problem. In full analogy, the calculation of observables of particle interactions (such as in the electroweak processes described above) can be approximated using a fixed number of terms of a perturbative expansion in orders of the gauge coupling constant (e.g. g, g') as long as the latter stay small (e.g. at high energy / short distance scales). The respective Feynman diagrams, sorted in powers of the coupling constants of the underlying interaction, are then referred to as leading-order (LO) diagrams, i.e. the "tree-level" diagram of the exactly solvable problem; next-to-leading order (NLO) diagrams, i.e. including the first order deviation from the exact solution to the solvable problem; next-to-next-to-leading order (NNLO) diagrams, and so on. More details on the methodology will be discussed within the scope of QCD perturbative expansions in Section 2.2. The same form of interactions as depicted in Figure 2.1 applies

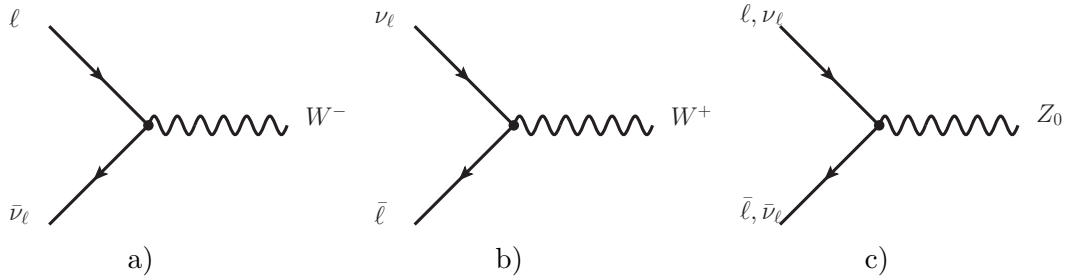

Figure 2.1.: Feynman graphs of fermion interactions at leading order in perturbation theory as occurring in the electroweak theory within the SM.

to quarks with the neutrino/lepton replaced by up-/down-type quarks, with the only difference being the flavour mixing of quark generations discussed later in this section. The full EW Lagrangian can be written as:

$$\mathcal{L}^{\text{EW}}_{\text{gauge}} = -\frac{1}{4} B_{\mu\nu}(x) B^{\mu\nu}(x) - \frac{1}{4} G_{i,\mu\nu}(x) G_i^{\mu\nu}(x)\,, \tag{2.9}$$

where $G_i^{\mu\nu}$ $(i = 1, 2, 3)$ and $B^{\mu\nu}$ are the field strength tensors

$$B^{\mu\nu}(x) = \partial^\nu B^\mu(x) - \partial^\mu B^\nu(x)\,, \tag{2.10}$$

$$G_i^{\mu\nu}(x) = \partial^\nu W_i^\mu(x) - \partial^\mu W_i^\nu(x) + g\,\epsilon_{ijk} W_j^\mu(x) W_k^\nu(x)\,, \tag{2.11}$$

The last term in Equation 2.11 describes self-interactions between gauge bosons which occur due to the non-abelian nature[3] of the gauge group and are depicted in Figure 2.2.

[3] Gauge groups that contain non-commutative transformations for at least a subset of its elements are called non-abelian or non-commutative. This applies in particular to the generators t^a of the group,

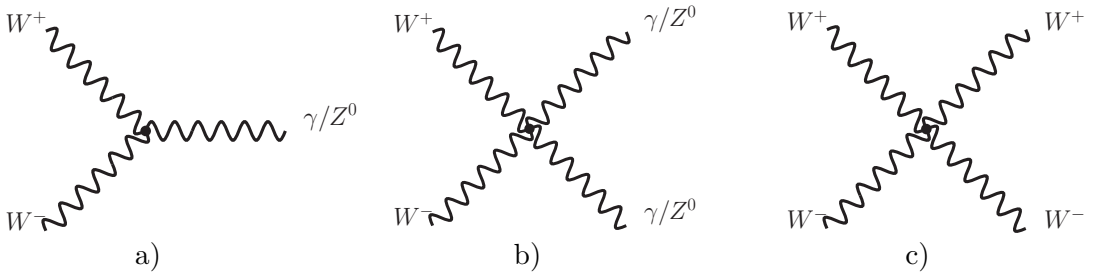

Figure 2.2.: Feynman graphs of gauge boson self-interactions at leading order in perturbation theory as occurring in the electroweak theory within the SM.

Both, fermions as well as the newly introduced gauge bosons are described as massless fields so far, which obviously contradicts observations. However, the straight forward addition of simple mass terms of the form $m^2\bar{\psi}(x)\psi(x)$, $m^2 B_{\mu\nu}(x)B^{\mu\nu}(x)$, etc. in the Lagrangian density results in a non-renormalisable theory and in the gauge invariance being destroyed. Therefore an alternative mass-generation mechanism, the Higgs mechanism [25–28] was introduced, which generates masses for fermions and the $W^{\pm}, Z^0$ gauge bosons via the mechanism of spontaneous symmetry breaking. It involves a new weak isospin (Higgs) doublet of two complex scalar fields, $\Phi = (\phi^+, \phi^0)^T$, to be introduced and an additional scalar potential to be added to the electroweak Lagrangian density:

$$\mathcal{L}_{\text{Higgs}} = \left(D^\mu \Phi(x)\right)^\dagger \left(D_\mu \Phi(x)\right) - V\left(\Phi^\dagger(x)\,\Phi(x)\right)\,, \tag{2.12}$$

$$\text{with}\quad V\left(\Phi^\dagger(x)\,\Phi(x)\right) = \mu^2\,\Phi^\dagger(x)\,\Phi(x) + \lambda\left(\Phi^\dagger(x)\,\Phi(x)\right)^2\,, \tag{2.13}$$

where D^μ is the corresponding covariant derivative

$$D^\mu \Phi(x) = \left[\partial^\mu + \frac{1}{2} i g \tau_j W_j^\mu(x) + i g' Y B^\mu(x)\right]\Phi(x)\,.$$

For $\lambda > 0$ and $\mu^2 < 0$ the potential V exhibits a degenerate, non-zero vacuum state and therefore is usually referred to as the "mexican hat" potential, see Figure 2.3. While the newly introduced Higgs doublet is invariant under the SM gauge transformations, choosing a particular vacuum expectation value (VEV)

$$\Phi_0 = \begin{pmatrix} 0 \\ v/\sqrt{2} \end{pmatrix}\,, \text{with } v = \sqrt{\frac{-\mu^2}{\lambda}}\,,$$

allows to rewrite the Lagrangian $\mathcal{L}_{\text{Higgs}}$ in terms of a perturbative series of Φ around that explicitly chosen ground state, the latter which does not obey the original symmetry of

which obey a commutation rule of the form $\left[t^a, t^b\right] = f^c_{ab} t^c$ with a non-vanishing structure constants f^{abc}. Since the matter fields are constituting representations of the gauge group they are subject to the same non-commutativity when transforming among themselves.

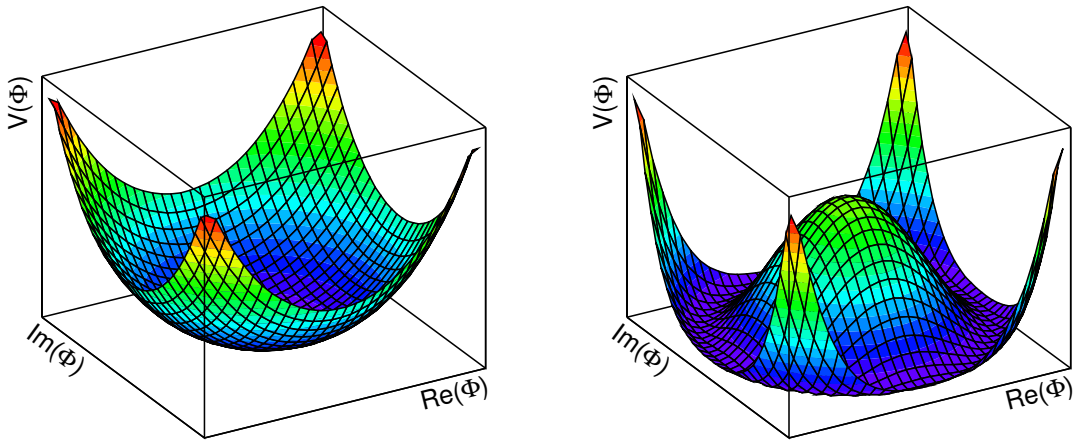

Figure 2.3.: Illustration of the Higgs potential in the complex plane for values of $\mu^2 > 0$ and $\lambda > 0$ (left) or $\mu^2 < 0$ and $\lambda > 0$ (right).

the $\mathrm{SU}(2)_L \times \mathrm{U}(1)_Y$ group any more. The electroweak gauge group is said to be spontaneously broken down to the subgroup of quantum electrodynamics (QED) $\mathrm{SU}(2)_L \times \mathrm{U}(1)_Y \rightarrow \mathrm{U}(1)_Q$ at the characteristic ElectroWeak Symmetry Breaking (EWSB) scale set by the VEV of the Higgs field. It is by this mechanism that masses for the three weak gauge bosons $W^{\pm}, Z^0$ are generated, while the photon stays massless since the U(1) invariance is still obeyed. The perturbative expansion of the Higgs doublet Φ can be rewritten in terms of four new real fields $\sigma(x)$ and $\eta_i(x)$ $(i = 1, 2, 3)$, which represent the deviations from the vacuum ground state Φ_0:

$$\Phi = \frac{1}{\sqrt{2}} \begin{pmatrix} \eta_1(x) + i\eta_2(x) \\ v + \sigma(x) + i\eta_3(x) \end{pmatrix} . \tag{2.14}$$

Three of the four degrees of freedom thereby represent the $n-1$ massless scalar Goldstone bosons predicted for each spontaneously broken symmetry with n degrees of freedom as postulated by the Nambu-Goldstone theorem [29–31]. Via a unitary gauge transformation Φ can be rewritten as

$$\Phi = \frac{1}{\sqrt{2}} \begin{pmatrix} 0 \\ v + \sigma(x) \end{pmatrix} ,$$

making the (unphysical) Goldstone bosons vanish and leading to mass terms for the $W^{\pm}$ and Z^0 gauge bosons in the Lagrangian density after applying the same transformation to the full Lagrangian:

$$M_{W^{\pm}} = \frac{1}{2} v g \ , \qquad M_{Z^0} = \frac{1}{2} v \sqrt{g^2 + g'^2} \, .$$

This implies a value for the VEV of the Higgs field of $v/\sqrt{2} \approx 246$ GeV from measurements of the gauge boson masses. It further provides an explanation for the observed mass difference of the $W^{\pm}$ and Z^0 bosons, which can be expressed via the weak mixing angle Θ_W as

$$M_{Z^0} = \frac{M_{W^{\pm}}}{\cos\theta_W}\,.$$

The remaining fourth real field $\sigma(x)$ on the other hand represents a physical, massive and electrically neutral scalar particle, the Higgs boson.

Following the same principle of spontaneous symmetry breaking, leptons obtain masses through interactions with the Higgs field by adding additional gauge-invariant terms, so-called Yukawa coupling terms [32], to the Lagrangian:

$$\mathcal{L}_{\mathrm{Y}}^{\mathrm{lepton}} = g_{ij}^{\ell}\bar{\Psi}_{i,L}\Phi(x)\Psi_{j,R} \xrightarrow{\Phi=\frac{1}{\sqrt{2}}\begin{pmatrix}0\\ v+\sigma\end{pmatrix}} \frac{v\,g_{ij}^{\ell}}{\sqrt{2}}\,\bar{\psi}_{i,L}^{\ell}\psi_{j,R}^{\ell} + \frac{g_{ij}^{\ell}}{\sqrt{2}}\,\bar{\psi}_{i,L}^{\ell}\psi_{j,R}^{\ell}\,\sigma\,. \tag{2.15}$$

The indices $i, j = 1, 2, 3$ denote the involved fermion generation and g_{ij}^{ℓ} hence represents a 3×3 matrix. It defines the Yukawa coupling strength of fermions with the Higgs field. For the left (mass) terms a new mass matrix can be defined and diagonalised as follows

$$M^{\ell} = \frac{v\,g_{ij}^{\ell}}{\sqrt{2}}\,; \quad M_d^{\ell} = S^{\dagger}M^{\ell}T\,, \tag{2.16}$$

where S and T are unitary matrices. This yields mass terms $\bar{\psi}'_L M^{\ell}\psi'_R = \bar{\psi}_L M_d^{\ell}\psi_R$ with $\psi'_L = S\psi_L$ and $\psi'_R = T\psi_R$ defining the mass eigenstates of the fields. The masses of the leptons are proportional to the strength of the couplings of fermions with the Higgs field, which are a-priori unknown and hence free parameters within the SM. Moreover neutrinos implicitly stay massless when the Higgs field is replaced by its VEV.

Similarly, Yukawa couplings can be defined to give masses to the quarks. However, to obtain masses for up and down quarks simultaneously, the conjugate Higgs field, $\tilde{\Phi} = \left((\phi^0)^*, -(\phi^+)^*\right)^T$ has to be introduced:

$$\mathcal{L}_{\mathrm{Y}}^{\mathrm{quark}} = g_{ij}^{\mathcal{U}}\,\bar{\Psi}_{i,L}\tilde{\Phi}\,\Psi_{j,R} + g_{ij}^{\mathcal{D}}\,\bar{\Psi}_{i,L}\Phi\,\Psi_{j,R} + h.c.\,,$$

where $g_{ij}^{\mathcal{U},\mathcal{D}}$ again are (a-priori non-diagonal) 3×3 matrices reflecting the Yukawa coupling strengths, $\bar{\Psi}_{i,L}$ denote the left-handed SU(2) doublets of the quark fields and $\Psi_{j,R}$ the respective right-handed singlets. Here, the interaction terms with the Higgs boson have been omitted. The indices $i, j = 1, 2, 3$ again indicate the involved fermion generation. Similarly to the lepton case, mass matrices can be defined and diagonalised by unitary transformations:

$$M^{\mathcal{U},\mathcal{D}} = 1/\sqrt{2}\cdot v\,g_{ij}^{\mathcal{U},\mathcal{D}}\,, \quad M_d^{\mathcal{U},\mathcal{D}} = (S^{\mathcal{U},\mathcal{D}})^{\dagger}M^{\mathcal{U},\mathcal{D}}\,T^{\mathcal{U},\mathcal{D}}\,,$$

to change from weak to the mass (or flavour) eigenstates. Expressing the charged

current in terms of the mass eigenstates of the fields results in terms of the form $\bar{\psi}^{\mathcal{U}\prime}_{i,L}\gamma_\mu(S^{\mathcal{U}})^{-1}S^{\mathcal{D}}\psi^{\mathcal{D}\prime}_{j,L}$ to arise. Different to the lepton case where the same expression is diagonal in the mass and weak eigenbases simultaneously, in the quark case this results in a mixing among the different quark flavours in charged current interactions. By convention, the weak and mass eigenstates for the up-type quarks are chosen to be simultaneously diagonal as for the leptons, whereas they are rotated for the down-type quarks when transforming from the weak to the mass eigenbasis. The probability of transitions between different quark generations in charged current interactions is expressed by the unitary Cabibbo-Kobayashi-Maskawa-Matrix [33] $V_{\mathrm{CKM}} = (S^{\mathcal{U}})^{-1}S^{\mathcal{D}}$, which translates between the eigenstates in both bases:

$$\begin{pmatrix} d' \\ s' \\ b' \end{pmatrix} = V_{\mathrm{CKM}} \cdot \begin{pmatrix} d \\ s \\ b \end{pmatrix} = \begin{pmatrix} V_{ud} & V_{us} & V_{ub} \\ V_{cd} & V_{cs} & V_{cb} \\ V_{td} & V_{ts} & V_{tb} \end{pmatrix} \begin{pmatrix} d \\ s \\ b \end{pmatrix} ,$$

$$\text{with} \quad \begin{pmatrix} |V_{ud}| & |V_{us}| & |V_{ub}| \\ |V_{cd}| & |V_{cs}| & |V_{cb}| \\ |V_{td}| & |V_{ts}| & |V_{tb}| \end{pmatrix} \approx \begin{pmatrix} 0.974 & 0.225 & 0.003 \\ 0.225 & 0.973 & 0.041 \\ 0.009 & 0.040 & 0.999 \end{pmatrix} , \tag{2.17}$$

where d, s, b denote the mass eigenstates and d', s', b' the respective weak eigenstates. The V_{CKM} matrix thereby expresses how the quark changes flavour in charged current interactions involving the $W^{\pm}$ bosons, with the transition from flavour i to j given by the matrix element $|V_{ij}|^2$. From the large values [14] given in Equation 2.17 it can be seen that the largest probabilities occur for transitions between quarks of the same generation, while the off-diagonal elements are suppressed.

The electroweak theory became a large success in elementary particle physics, when its renormalisability could be proven by 't Hooft and Veltman in 1971 [34, 35] and its predictions first could be confirmed in 1973 by observations of weak neutral current interactions with the Gargamelle bubble chamber at CERN [36], followed by the discovery of the W and Z bosons in 1983 at the Super Proton Antiproton Synchrotron (Sp$\bar{\mathrm{p}}$S) by the UA1 and the UA2 collaborations [37–40].

2.2. Quantum Chromodynamics

The theory of Quantum ChromoDynamics (QCD) describes the interaction of quarks via the strong coupling through the exchange of eight massless gauge bosons, called gluons. In the 1950s a vast number of new particles (hadrons) have been observed which in 1963 led to the assumption that these could not be fundamental particles but rather have to be composed of point-like particles (quarks) arising in three different variants [22, 41]. In 1965 an additional quantum number, the colour charge, was proposed [42] to explain the existence of the observed Ω^- hadron, composed of three strange quarks with parallel spins, which otherwise would contradict the Pauli principle. Consequently, in the SM known today three versions of each quark exist which differ in their colour charge $C =$

(r, g, b) (and the respective anti-colours) and are grouped into SU(3) triplets of the form

$$\psi_q = \begin{pmatrix} \psi_{q_r} \\ \psi_{q_g} \\ \psi_{q_b} \end{pmatrix} ,$$

with $q \in [u, d, c, s, t, b]$. Following the recipe of constructing the EW theory, an invariance under a symmetry group is postulated, here the invariance of the Lagrangian under local transformations of the non-abelian $SU(3)_C$ gauge group. The number of gauge boson is equal to the number of generators for the group, which in $SU(3)_C$ are represented by eight 3×3 Gell-Mann matrices λ^a $(a = 1, \ldots, 8)$

$$\psi_q(x) \to \psi\prime_q(x) = e^{\frac{1}{2} i g_s \alpha^a(x) \lambda^a} \psi_q(x) ,$$

where g_s is a real (coupling) constant, and $\alpha_a(x)$ $(a = 1 \ldots 8)$ are real differentiable functions of x. The local $SU(3)_C$ gauge group hence implies the existence of eight physical gauge fields, the gluons, which mediate the colour charge interactions between quarks. The QCD Lagrangian can be written as:

$$\mathcal{L}^{\mathrm{QCD}} = i\bar{\psi}_q \not{D} \psi_q - m\bar{\psi}_q \psi_q - \frac{1}{4} G^a_{\mu\nu} G^{\mu\nu,a} , \tag{2.18}$$

with the covariant derivative $\not{D}$ and the field strength tensor $G^{\mu\nu,a}$:

$$D^\mu \psi_q(x) = \left(\partial^\mu + \frac{1}{2} i g_s \lambda^a G^{\mu,a}(x) \right) \psi_q(x) , \tag{2.19}$$

$$G^{\mu\nu,a}(x) = \partial^\nu G^{\mu,a}(x) - \partial^\mu G^{\nu,a}(x) + g_s f^{abc} G^{\mu,b}(x) G^{\nu,c}(x) , \tag{2.20}$$

where f^{abc} are the structure constants of the SU(3) and antisymmetric in all indices. Due to the non-abelian behaviour of the SU(3) group, the gluons themselves carry a colour charge which results in self-interactions of up to four gluons, see Figure 2.4. Leptons on the other hand, are not subject to interactions with gluons since they do not carry any colour charge. The non-observation of free quarks or gluons led to the postulate

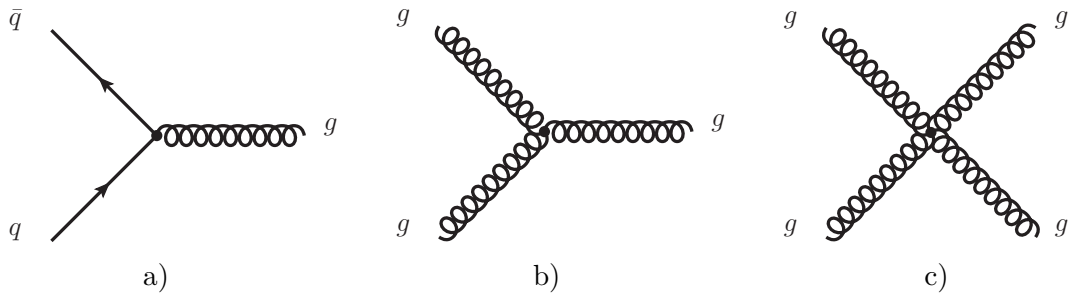

Figure 2.4.: Feynman graphs of quark-gluon and gauge boson self-interactions at leading order in perturbation theory as occurring in the QCD sector of the SM.

that quarks in nature only occur in the form of composite colour-less bound states, so-called hadrons. Albeit not proven analytically, in numerical theory calculations it can be shown that the effective potential between a quark and an anti-quark of opposite colour charge at the distance r contains a term $\propto r$, which is identified as another consequence of the non-abelian nature of the SU(3) group and the triple and quartic gluon self-interactions resulting herefrom. Consequently, the force between quarks constituting hadrons increases at large distances and thereby leads to the observed "confinement" inside mesons (quark/anti-quark pairs) and baryons (triplets of quarks with different colour charges) at typical radii of $\mathcal{O}(1\,\mathrm{fm})$.

Another property of QCD is "asymptotic freedom", which describes the opposite phenomenon to confinement at very high energy scales. At small length scales the strong force diminishes (coupling decreases logarithmically) such that quarks and gluons can be described as quasi-free particles. The principle of asymptotic freedom was first presented in 1973 [43, 44] and allowed for explaining observations in deep-inelastic scattering experiments by precise calculations using perturbation theory. Perturbative QCD describes techniques to make approximate calculations and predictions of observables of processes involving large momentum transfer QCD interactions by making use of the small value of the strong coupling constant α_s at high energy or short distance scales. Within the regime of high momentum transfers, observables can be calculated approximately using a fixed number of terms of a perturbative expansion in orders of the coupling constant α_s, each calculated using the common Feynman diagram formalism. When performing perturbative QCD calculations of observables (such as cross-sections), usually higher order Feynman (loop) integrals from higher order terms of the perturbative expansion have to be included. These in general suffer from two types of divergences: so-called ultra-violet (UV) divergences, and collinear or soft divergences, also referred to as infra-red (or IR) divergences. UV divergences are an result of loop integrals where the momenta of particles circulating the loops go to infinity. They can be circumvented by dimensional regularisation (e.g. in the minimal subtraction scheme [45]) and a renormalisation mechanism by means of which divergences are absorbed through a redefinition of fields, coupling constants and masses using renormalisation constants. This introduces additional Feynman diagrams and additional divergences that can be chosen such that they cancel the former divergences order by order in α_s and at a certain energy scale μ_r (renormalisation scale). By introducing this additional arbitrary energy scale μ_r, the perturbation expansion of the strong coupling constant at a characteristic momentum transfer Q itself becomes dependent on μ_r and can be expressed e.g. at first order as:

$$\frac{1}{\alpha_s(Q^2)} = \frac{1}{\alpha_s(\mu_r^2)} + b\,\ln\left(\frac{Q^2}{\mu_r^2}\right) = b\,\ln\left(\frac{Q^2}{\Lambda^2}\right), \tag{2.21}$$

i.e. in terms of the coupling constant at the reference scale, $\alpha_s(\mu_r^2)$, or alternatively by introducing the non-perturbative scale Λ, a constant of integration that defines the (Landau) pole at which the perturbative expression of α_s diverges and with approaching of which the perturbation theory breaks down with α_s reaching values of $\mathcal{O}(1)$ or higher. The constant b in Equation 2.21 is related to the β-function which encodes the scale

dependence of the coupling and itself can be expanded in orders of α_s as follows

$$\frac{\partial\left(\alpha_s\left(Q^2\right)\right)}{\partial\left(\ln\frac{Q^2}{\mu_r^2}\right)} = \alpha_s^2\left(b + \alpha_s\, b' + \alpha_s^2\, b'' + \ldots\right) . \tag{2.22}$$

Perturbative QCD can only describe the variation of the strong coupling constant with the scale, thereby actually leading to the phenomenon of asymptotic freedom, but not the absolute value of it, i.e. $\alpha_s(\mu_r)$. The latter therefore are obtained from experiments probing α_s at different energy scales which then can be renormalised to a particular energy scale (usually at the mass of the Z_0 boson) using the β-function which is currently known to the fourth order in α_s in theory. The actual observable ($O(\alpha_s)$) of interest must stay independent of the choice of μ_r when holding the bare coupling fixed, and hence may only depend on the renormalised coupling in Eq. 2.21 itself or the ratio of the scales Q^2/μ_r^2 [4]. The whole scale dependence of O thus is absorbed in the renormalised running coupling constant. A more comprehensive description of the formalisms of perturbation theory can be found in e.g. [46, 47].

IR divergences, on the other hand, are the result of the perturbative approach breaking down at low energy scales where either the angular distance $\Omega_{a,b}$ between real emissions of final state particles (a,b) or the energy of the emitted particles E_a, E_b approaches zero. When calculating the cross-section via perturbative expansion, logarithmic terms of the form $\ln\frac{Q^2}{\mu_r^2}$ occur in the coefficients of the expansion in α_s. Since $Q^2 \propto E_a\, E_b\,(1-\cos(\Omega_{a,b}))$, the logarithmic terms become large in these cases, as well as the gluon propagator which at first order is proportional to $1/Q^2$. By rearranging the terms in the expansion by orders in the logarithms $\ln\frac{Q^2}{\mu_r^2}$ (resummation) instead of fixed orders in α_s, the expression can be improved subsequently by only including logarithmic terms up to a certain order, avoiding higher order divergences to spoil the perturbation series. Depending on the order of terms included, the result is referred to be calculated at leading logarithm (LL), next-to-leading logarithm (NLL) approximation, and so on. Resummation thus provides a complementary approach to an fixed order expansion in α_s, usually referred to as leading order (LO), next-to-leading order (NLO) approximation, etc.

Although perturbative QCD by definition is limited to calculations for a finite range in energy scale, it has provided the most precise predictions of QCD available so far. In 1979 the success of QCD continued with the discovery of gluons in three-jet events at PETRA [48, 49]. Over time, new accelerators and experiments became available, like at the Large Electron Positron (LEP) collider at CERN [50], which allowed to further probe the predictions of perturbative QCD up to the level of a few percent. However it took until 1995 to discover the last missing quark of the third generation within the Standard Model, the top quark, at the Tevatron (Fermilab) by the CDF and DØ collaborations [1, 2]. Its discovery enabled physicists to study a whole new and comprehensive field of physics opened by its unique properties.

[4] In mathematical terms the dimensionless observable has to fulfil the renormalisation group equations, see e.g. [46] for a detailed description of the formalism.

2.3. Top-Quark Physics

With a mass of 173.07 ± 0.89 GeV [14] the top quark is the heaviest elementary particle known so far. It features a very short lifetime $\mathcal{O}(10^{-25}\,\mathrm{s})$ which makes it the only quark which decays before the onset of hadronisation processes and hence before its potential confinement in bound states of hadrons. Therefore it is of particular use for studies of the properties of bare quarks and represents a unique probe for various predictions and parameters of the SM.

2.3.1. Top-Quark Production and Decay in the Standard Model

At the LHC top quarks are primarily produced in pairs of a quark and antiquark ($t\bar{t}$) via the strong interaction. At the former proton/antiproton collider Tevatron [51] $t\bar{t}$ pairs were dominantly produced via quark-antiquark annihilation (∼85%), creating a high-energetic gluon which subsequently decays into a top quark and top antiquark, cf. Figure 2.5 (b). At the LHC however, the dominant production channels are gluon fusion processes (∼ 90%), where two gluons in the initial state interact and produce a $t\bar{t}$ pair, either by creating an intermediate high-energetic gluon that subsequently decays as before, or via the exchange of a virtual space-like top quark, see Figure 2.5 (a) for examples of both. The predicted cross-section for $t\bar{t}$ production at the LHC, at a centre-of-mass energy of $\sqrt{s} = 8$ TeV and assuming a top-quark mass of 172.5 GeV, is $\sigma = 253^{+13}_{-15}$ pb, calculated at (exact) NNLO in QCD and including resummation of next-to-next-to-leading logarithmic (NNLL) terms [52–57]. The uncertainty reflects the PDF and α_S uncertainties added in quadrature to the scale uncertainty. The PDF uncertainty was calculated following the PDF4LHC prescription [58], using the MSTW2008 68% CL NNLO [59, 60], CT10 NNLO [61, 62] and NNPDF2.3 5f FFN [63] PDF sets.

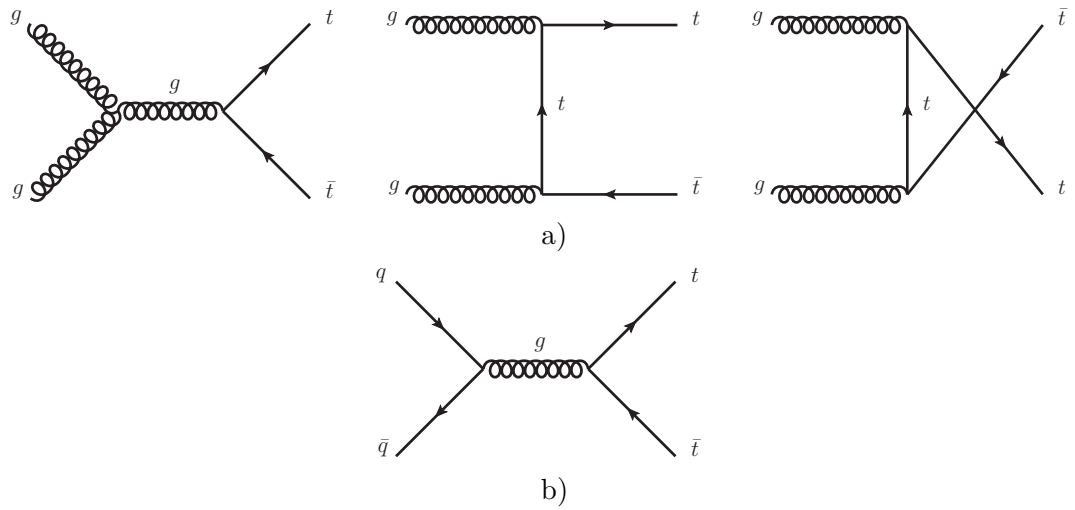

Figure 2.5.: Leading-order Feynman diagrams of SM top quark/antiquark pair production via: a) gluon fusion and b) via quark-antiquark annihilation.

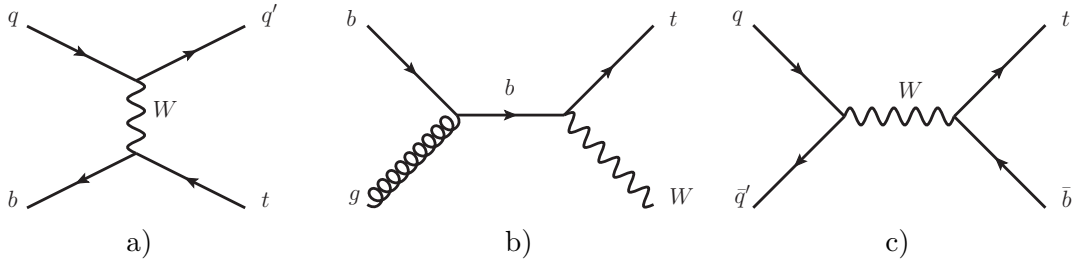

Figure 2.6.: Feynman diagrams of the three SM single top-quark production channels: a) t-channel, b) Wt-channel and c) s-channel.

In addition to the predominant $t\bar{t}$ production, single top quarks are produced via the weak interaction in association with other particles in three different sub-processes:

- the t-channel as the dominant production process, which involves the exchange of a space-like W boson between two incoming quarks (or antiquarks), of which one is being converted into a top quark,
- the Wt-channel, which denotes the associated production of a top quark and a real W boson,
- and the s-channel process which involves the production of a time-like W boson subsequently decaying into a top quark and bottom antiquark.

Figure 2.6 shows the corresponding lowest order Feynman diagrams of all three processes. The predicted t-, Wt and s-channel production cross-sections, calculated at "approximate" NNLO (NNLL accuracy) for a centre-of-mass energy of $\sqrt{s} = 8$ TeV and assuming a top-quark mass of 172.5GeV, are $87.8^{+3.4}_{-1.9}$ pb [64], 22.4±1.5 pb [65] and 5.6±0.2 pb [66]. The uncertainty reflects the scale and PDF uncertainties added in quadrature, the latter of which are calculated using the MSTW2008 90% C.L. NNLO [59, 60] PDF set. In 2009 the first observation of single top-quark production was made by the CDF [67] and DØ [68] collaborations using a combined search of the t-channel and s-channel production processes. Later in 2010, the top quark was rediscovered at the LHC at CERN [69, 70]. The observation of the t-channel single-top production mode alone has first been reported in 2011 by the DØ collaboration [71], shortly followed by the ATLAS collaboration at the LHC the same year [72]. First evidence for Wt-channel production was reported in 2012 by the ATLAS collaboration [73] and first observation in 2013 by the CMS collaboration [74]. Due to the low cross-section and irreducible backgrounds only upper limits could be set on the s-channel production cross-section at the LHC experiments, while just recently the DØ collaboration reported first evidence for observing the last of the three single-top production processes [75] predicted in the SM.

The top quark predominantly decays in weak interactions into a W boson and a bottom quark with a predicted branching fraction of $\mathcal{B}(t \to Wb) \sim 0.998$ [14], see Figure 2.7. This is a consequence of the large value of the CKM matrix element V_{tb} close to unity.

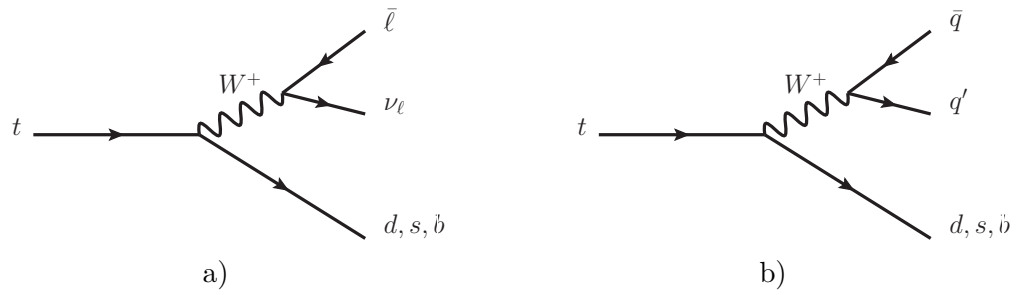

Figure 2.7.: Feynman diagrams of the top-quark decay via $t \to Wb$, divided into channels with subsequent leptonic W decay (a) and hadronic W decay (b).

Due to its large mass close to the EWSB scale, the top quark does not only provide a unique probe for testing the SM parameters, but also is seen as a key to search for physics beyond the SM since it is expected to play a key role in the EW symmetry breaking mechanism. For example, the measurement of the single top-quark production cross-sections allow for the determination of the matrix element $|V_{tb}|$ and hence for testing the unitarity of the CKM matrix. If deviations are observed, these provide a strong indicator for "new physics", e.g. extra quark models or heavy gauge boson production such as W'. Measurements of the top-quark mass were putting large constraints on the Higgs mass before its discovery and in many new physics models additional particles are introduced which the top quark could be a decay product of or could couple to. Effects of the latter could be perceived through deviations from the predicted SM top-quark properties, or in the observation of anomalous couplings of top quarks to the known SM particles such as flavour-changing neutral currents (FCNC).

2.3.2. Flavour-Changing Neutral Currents in SM Top-Quark Physics

In the Standard Model of particle physics single top quarks are almost exclusively produced via charged current interactions of a down-type quark (d,s,b) with a W boson and predominantly decay via the $t \to bW$ channel. Flavour-changing transitions between fermions mediated by neutral gauge bosons, so-called Flavour-Changing Neutral Currents (FCNC), are forbidden at tree level in the SM. No vertex exists which directly couples the neutral gauge bosons (g, Z, γ, H) to fermions of different generations since the neutral currents are diagonal in flavour space, and remain so even after the EWSB. In Figure 2.8 the forbidden tree-level FCNC decays involving a photon, Z boson or gluon are illustrated. Although in the SM flavour-changing neutral currents may occur in higher order loop diagrams involving W bosons, they are highly suppressed due to the Glashow-Iliopoulos-Maiani (GIM) suppression mechanism. The GIM mechanism [76] was originally introduced in 1970 to explain the very small branching ratio of the neutral kaon decay into an muon/anti-muon pair ($\Gamma(K_L^0 \to \mu^+\mu^-)/\Gamma_{\text{tot}}(K_L^0) \simeq 10^{-7}$) and led to the prediction of the charm quark. The K_L^0 decay takes place in a box diagram via the exchange of two W bosons as shown in Figure 2.9 (a). In 1970 only the up, down and strange quark have been observed and Cabibbo postulated [77] that the weak and the

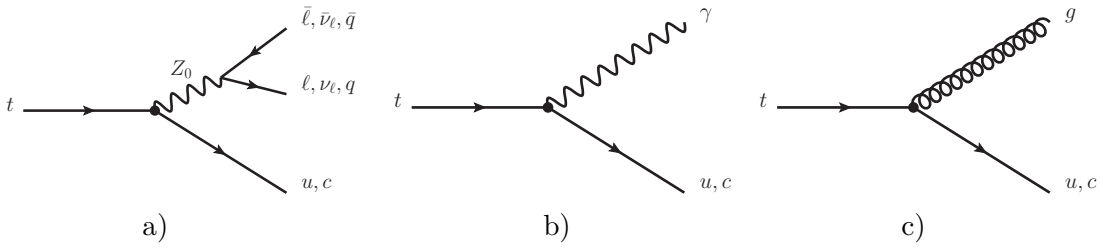

Figure 2.8.: Top quark tree-level FCNC decay channels forbidden in the SM: a) $t \to qZ$ (including the subsequent Z decay), b) $t \to q\gamma$ and c) $t \to qg$, with $q = u, c$. The FCNC vertices are represented by black circles.

mass (or flavour) eigenstates are mixed, such that in charged current interactions the up quark is coupled to a certain linear combination d' of the down and strange-quark mass eigenstates with $d' = \cos\Theta_C\, d + \sin\Theta_C\, s$. Here Θ_C is the so-called Cabibbo angle that reflects the mismatch between the mass eigenstate and the weak eigenstate vector spaces. This alone however could not account for the large suppression observed. This lead to the GIM mechanism by which an additional quark flavour was introduced such that the weak eigenstates are arranged into SU(2) doublets as follows:

$$\begin{pmatrix} u \\ d' \end{pmatrix}, \begin{pmatrix} c \\ s' \end{pmatrix}, \quad \text{with} \quad \begin{pmatrix} d' \\ s' \end{pmatrix} = \begin{pmatrix} \cos\Theta_C & \sin\Theta_C \\ -\sin\Theta_C & \cos\Theta_C \end{pmatrix} \begin{pmatrix} d \\ s \end{pmatrix},$$

where u, d, c, s denote the mass or flavour eigenstates and u', d', c', s' the respective weak eigenstates. By introducing the charm quark an additional decay channel was enabled which is indistinguishable to, and interferes destructively with, the former process, see Figure 2.9 (b). In the limit of exact flavour symmetry and degenerate fermion masses the two diagrams would cancel exactly. However, since this symmetry is broken and mass differences between the quarks occur, the sum of both diagrams becomes $\propto (m_c^2 - m_u^2)/m_W^2$ which is in very good agreement with the observed rates. This mechanism of

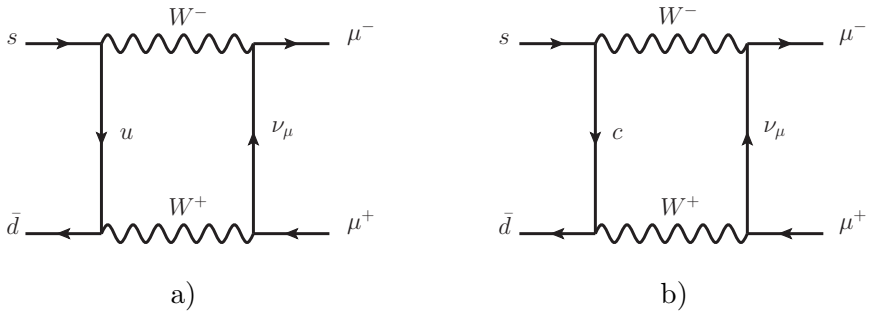

Figure 2.9.: Feynman diagrams of one-loop contribution to the K_L^0 decay into a muon/anti-muon pair, assuming the existence of u, d, s only (a) and the contribution arising when including the additional c quark.

destructive interference of different decay channels (in addition to the loop suppression) in general is referred to as GIM suppression and can also be applied to calculate the amplitude of top-quark FCNC decay processes at loop-level. Considering all possible loop diagrams, the FCNC decay amplitude is subject to large GIM suppressions due to the large top-quark mass m_t and all down-type quarks in the loops having comparatively small masses. Figure 2.10 shows examples of FCNC top-quark decays into a gluon, Z boson or photon plus a u or c quark, mediated by so-called penguin diagrams in the SM at the one-loop level in perturbation theory. The resulting decay branching ratios are extremely suppressed and only reach values at the order of $10^{-15} - 10^{-12}$ [15].

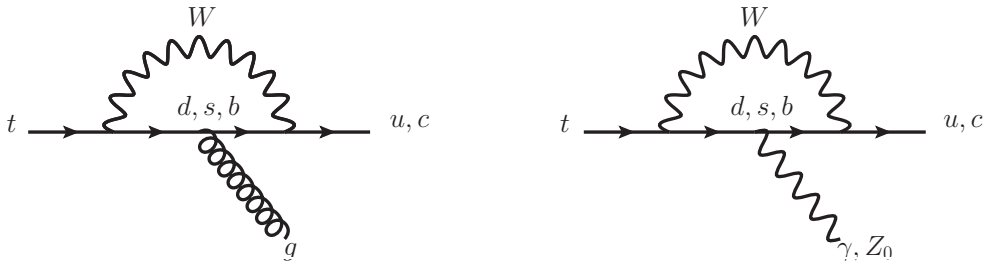

Figure 2.10.: Examples of loop-level Feynman diagrams contributing to the $t \to qg$, $t \to qZ$ and $t \to q\gamma$ decay amplitudes in the Standard Model.

3. Physics Beyond the Standard Model

Experiments at particle accelerators, such as the LEP Collider at CERN, the Stanford Linear Collider (SLC) at SLAC or the Tevatron at Fermilab, could confirm most of the SM predictions, e.g. about the existence of quarks, leptons and gauge bosons and their interactions. The predicted properties of the discovered particles and free parameters of the SM were measured repeatedly with increasing accuracy. With the Large Hadron Collider (LHC) at CERN becoming fully operational in late 2009 it became feasible to probe the SM at even higher scales and precision than ever reached before and to continue the search for one of the remaining key predictions of the SM, the Higgs boson in kinematic regions beyond the reach of former searches with experiments at the LEP or Tevatron accelerators. A discovery would confirm the existence of the Higgs field and hence the mechanism which explains how particle acquire mass within the SM. In July 2012 the ATLAS and CMS collaborations first announced the discovery of a new Higgs-like scalar particle [6–9], which later in March 2013 was confirmed to meet several criteria of a Higgs boson consistent with the Standard Model [10–13]. In addition to further studies of the Higgs candidate properties, the LHC and its experiments were designed to provide answers to several other open questions in physics. It is well known that the Standard Model does not provide a complete description of nature since it does not explain several phenomena and discrepancies in particle- and astrophysics:

- While the SM unifies the electromagnetic and weak forces and describes them together with the strong force it does not include a quantum field theory for the last fundamental force, gravitation. Although the gravitational force is by orders of magnitude weaker at small scales and hence negligible in common particle physics, it becomes significant at the order of the Planck scale, $\mathcal{O}(\sim 10^{19}$ GeV), at which the SM is unable to describe physics.

- The running coupling constants of the three forces and associated gauge groups of the SM are thought to converge at a scale of $\mathcal{O}(\infty^{\prime\infty/}$GeV), possibly including even gravity at the Planck scale. However precision measurements from LEP [78] show that this is not the case within the SM (unification problem).

- Although it is very likely that the discovery of a Higgs boson at CERN is consistent with the SM, the SM does not predict the precise form of the Higgs potential and strength of particle interactions with the Higgs field by means of which they obtain their mass. Rather, the Higgs field and potential are introduced without any fundamental justification.

- A-priori the Higgs boson is predicted to have a very high mass at the order of the GUT scale, $\sim \mathcal{O}(10^{16}$ GeV), due to higher order loop corrections. The observed Higgs-like

boson, however, has a mass of approximately $125 - 127$ GeV [8, 9] which can only be explained from theory by fine-tuning of the SM parameters which is commonly considered unnatural (fine-tuning problem).

- The SM describes neutrinos as massless particles. However experiments with solar and atmospheric neutrinos have proven that neutrino oscillations exist, hence neutrinos from different generations mix with each other, see e.g. [79] for a detailed review. This is only possible if the mixing neutrinos have a finite, non-zero mass.
- The particles predicted by the SM have masses covering a large range from a few (m)eV, such as neutrinos, up to $\mathcal{O}(100$ GeV), e.g. the top quark or Higgs boson. The SM does not explain the mass values of the particles nor their hierarchy.
- Within the SM three particle generations have been observed by experiments so far. The SM does not provide a mechanism to predict or constrain this number.
- With the big bang and the expansion of the universe, matter and antimatter are expected to have been created in equal parts. However, the strength of CP violation in the SM is not sufficient to explain the baryon asymmetry observed in the visible universe [80].
- From observations of the rotational speed of the visible matter in galaxies, e.g. [81], distance measurements of supernovae [82] and large-scale structures (e.g. galaxies and clusters) [83] and their associated redshifts, and observations of the cosmic microwave background [84, 85] it is known that the visible (baryonic) matter accounts for only approximately 4.9% of the matter in the universe. The remaining 95.1% consist of so-called Dark Matter (26.8%) and Dark Energy (68.3%) that does not, or does only very weakly, interact with the visible matter and via the forces described in the SM. From cosmological observations the presently most favoured hypothetical composition of Dark Matter is from non-relativistic (cold) constituents with small free-streaming lengths[1], commonly is referred to as Cold Dark Matter (CDM).
- It was found that the universe is subject to an accelerated expansion, see e.g. [86, 87], while it was thought that the attraction of matter in the universe should lead to an decreased acceleration. The mechanisms or forces causing this acceleration are not described within the SM and are still unknown. A widespread model to explain the observations is to assume the existence of some form of Dark Energy that is distributed rather homogeneously in the universe and drives the accelerated expansion, e.g. caused by a cosmological constant (cf. Lambda-CDM model, see e.g. [88]) that is associated with a constant vacuum energy of negative pressure.

Given the list of open issues above, new physics theories beyond the Standard Model (BSM) are continuously explored to provide a more comprehensive description of nature

[1] The damping of density perturbations plays a key role in the evolution theory of the early universe. A bottom-up scenario of structure formation requires density perturbations to form early at small length scales. The damping of density fluctuations via gravitation is limited to length scales above the so-called free streaming length. Perturbations and hence clustering can only occur at larger scales. CDM particles are assumed to early become non-relativistic from red-shifting their momenta and thus obey a small free streaming length which in turn allows for small scale density perturbations.

in the future. Many new theories resolve parts of the mentioned shortcomings of the SM by either introducing new symmetries, such as in Supersymmetry (SUSY) theories or by introducing new particles, e.g. extra heavy gauge bosons (W', Z') or additional Higgs doublets. Other theories rely on extending the four-dimensional space-time by extra dimensions or take completely different approaches far beyond classical field theories, such as string theories. One of the main goals of the LHC is to search for new physics phenomena, some of which may be described by these BSM theories. Although many of these models predict new physics at scales too high to be probed at the LHC, they may manifest themselves indirectly in different SM observables. The top quark represents a natural candidate to probe these new physics models. Since it has the largest mass among all fundamental particles described in the SM, it often is of particular importance in BSM theories. Due to its large mass close to the EWSB scale, it is expected to play a key role in the symmetry breaking mechanism and in the generation of masses. Therefore it is of particular interest to study any deviations from the SM predictions in top-quark interactions, as well as its production and decay properties.

3.1. FCNC Interactions in BSM Top-Quark Physics

One aspect investigated at the LHC and former accelerators are anomalous FCNC couplings of the top quark to gauge bosons. The SM predictions on the branching fractions of FCNC top-quark decays are too small to be observed in current experiments. However, many new physics models predict much higher branching fractions of FCNC top-quark decays. If such couplings exist in nature they would affect the top-quark production and decay properties and hence could possibly be measured at collider experiments and provide strong evidence of new physics. In most of the new physics models contributing to these interactions, the enhancements in the rates of FCNC processes and hence in their branching fractions ($\mathcal{B}$) are a result of permitting FCNC interactions already at tree level, or are a consequence of introducing new particles in higher order loop diagrams. Such extensions to the SM, amongst others not discussed here, are models with extra (exotic) quarks [89–93] such as the Quark-Singlet (QS) model, Two-Higgs Doublet Models with (2HDM II), or without flavour-conservation (2HDM III) [94–99], the Minimal Supersymmetric Model (MSSM) [100–106] or SUSY models with R-parity violation ($\not{R}$ SUSY) [107, 108]. Further, the Topcolour-assisted Technicolour model (TC2) [109] may contribute to enhanced anomalous FCNC top-quark interaction rates. Reviews are given in [15] or [110] which also provide an overview of the predicted top-quark FCNC decay branching fractions ($\mathcal{B}$) compared to those expected in the SM, see Table 3.1. In the following sections some of these theories will be discussed in detail in the context of their contribution to FCNC interactions involving top-quarks.

3.1.1. Quark-Singlet Model

Extensions of the Standard Model involving additional (exotic) quark singlets (or doublets/triplets) represent one group of theories known to introduce large flavour-changing

Table 3.1.: Theoretical values for the branching fractions of FCNC top-quark decays as predicted by the SM, the quark-singlet model (QS), two-Higgs doublet model with (2HDM II) or without flavour-conservation (2HDM III), the minimal supersymmetric model (MSSM), SUSY models with R-parity violation ($\not{R}$ SUSY) and the Topcolour-assisted Technicolour model (TC2) [15, 110].

Model	$t \to u\gamma$	$t \to uZ$	$t \to ug$	$t \to c\gamma$	$t \to cZ$	$t \to cg$
SM	$4 \cdot 10^{-16}$	$8 \cdot 10^{-17}$	$4 \cdot 10^{-14}$	$5 \cdot 10^{-14}$	$\sim 10^{-14}$	$5 \cdot 10^{-12}$
QS	$\sim 10^{-8}$	$\sim 10^{-4}$	$\sim 10^{-7}$	$\sim 10^{-8}$	$\sim 10^{-4}$	$\sim 10^{-7}$
2HDM II	—	—	—	$\sim 10^{-7}$	$\sim 10^{-8}$	$\sim 10^{-5}$
2HDM III	—	—	—	$\sim 10^{-7}$	$\sim 10^{-6}$	$\sim 10^{-4}$
MSSM	$2 \cdot 10^{-6}$	$2 \cdot 10^{-6}$	$8 \cdot 10^{-5}$	$2 \cdot 10^{-6}$	$2 \cdot 10^{-6}$	$8 \cdot 10^{-5}$
$\not{R}$ SUSY	$1 \cdot 10^{-6}$	$3 \cdot 10^{-5}$	$2 \cdot 10^{-4}$	$1 \cdot 10^{-6}$	$3 \cdot 10^{-5}$	$2 \cdot 10^{-4}$
TC2	—	—	—	$\sim 10^{-7}$	$\sim 10^{-5}$	$\sim 10^{-5}$

neutral couplings between the established fermion generations [111]. The minimal extension represents the addition of a vector-like[2] up- or down-quark singlet (QS), usually denoted as T or B, which results in the unitarity of the CKM matrix being broken and the GIM suppression being partially removed. As a consequence the rates for FCNC top-quark decays via strong interactions, i.e. $t \to cg$ and $t \to ug$, are highly enhanced with respect to the SM predictions. In addition in the QS models the anomalous strong couplings to the u quark can reach the same magnitude as the coupling to a c quark, in contrast to the SM where the former are suppressed by the ratio $|V_{ub}/V_{cb}|^2$. Figure 3.1 shows exemplary Feynman diagrams contributing to the $t \to ug$ and $t \to cg$ couplings, where u_i and d_i denote the different up-type and down-type quarks in the loops, including the newly introduced quark singlet. While the left diagram also exists in the SM and the d_i hence would represent the three known families of down-type quarks, in the QS model the extra heavy down quark enters in the loops.

[2]Vector-like quarks are hypothetical (non-chiral) spin-½ fermions whose left- and right-handed components transform in the same way under the $\mathrm{SU(3)}_C \times \mathrm{SU(2)}_L \times \mathrm{U(1)}_Y$ gauge group and which may couple to SM quarks in the form of seven gauge-covariant multiplets (singlets, doublets, triplets) [111].

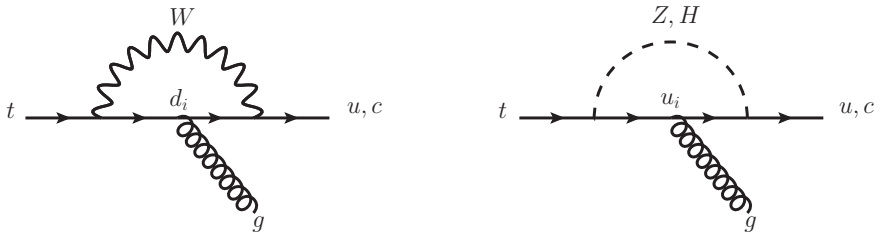

Figure 3.1.: Examples of Feynman diagrams contributing to the $t \to ug$ and $t \to cg$ decay amplitudes in the QS model. The u_i/d_i denote the three known families of up/down-type quarks plus the introduced extra heavy up/down quark T/B.

However, obeying the current experimental limits e.g. from direct searches for exotic quarks, the maximum branching fractions of strong anomalous FCNC top-quark decays derived in theory calculations are predicted to be of the order of $\sim 10^{-7}$. Therefore the present experimental sensitivity at the LHC is not sufficient to observe FCNC single top-quark production via strong interactions by these models [89]. However, FCN couplings in the tqZ vertex can be sizeable with branching fractions of up to $\mathcal{B}(t \to qZ) = 6 \times 10^{-4}$, and effects of couplings to extra heavy quarks could be perceived in K and B physics observables [91].

3.1.2. Two-Higgs Doublet Model

One of the most elementary extensions to the SM is the introduction of an extra complex scalar Higgs doublet to the SU(2)×U(1) sector, usually referred to as Two Higgs Doublet Models (2HDM) [112]. Under the commonly made assumption of CP conservation in the Higgs sector and obeying the SU(2)× U(1) symmetry, the most general form of the Lagrangian for Yukawa couplings to fermions in the 2HDM is given by

$$\begin{aligned}\mathcal{L}_Y = {} & g_{ij}^{\mathcal{U}} \bar{\Psi}_{i,L} \tilde{\Phi}_1 \Psi_{j,R} + g_{ij}^{\mathcal{D}} \bar{\Psi}_{i,L} \Phi_1 \Psi_{j,R} \\ & + f_{ij}^{\mathcal{U}} \bar{\Psi}_{i,L} \tilde{\Phi}_2 \Psi_{j,R} + f_{ij}^{\mathcal{D}} \bar{\Psi}_{i,L} \Phi_2 \Psi_{j,R} + h.c. \ ,\end{aligned} \tag{3.1}$$

(see e.g. [113]) where Φ_1 and Φ_2 are the two scalar Higgs doublets, f_{ij} and g_{ij} are the non-diagonal Yukawa coupling matrices, $\bar{\Psi}_{i,L}$ the left-handed SU(2) doublets of the fermion fields and $\Psi_{j,R}$ the respective right-handed singlets. The indices $i, j = 1, 2, 3$ denote the fermion generation. The two SU(2) Higgs doublets lead to eight fields of which three reflect the Goldstone bosons $\eta_k(x)\,, k \in [1, 2, 3]$ (cf. Eq. 2.14) giving mass to the W and Z gauge bosons. The remaining five degrees of freedom can be associated to five physical Higgs bosons: two charged scalars $H^{\pm}$, two neutral scalars h and H (CP-even), and a pseudoscalar A (CP-odd). Usually the two Higgs doublets are denoted in a basis such that the g_{ij} couplings exclusively generate the fermion masses and the f_{ij} give rise to the new FCNC interactions.

Apart from new physics theories such as Supersymmetry or models with spontaneous CP violation, where an extended Higgs sector is naturally included, three generic prototype 2HD models exist which reflect different forms of Yukawa couplings to the fermion sector [94–99]. The simplest extension to the Higgs sector is described by Equation 3.1 above. It introduces FCNCs at tree level and is usually denoted as the 2HDM III. However, models allowing for tree level FCNC interactions are subject to large constraints from experimental results [98], e.g. from limits on $\Delta F = 2$ mixing processes such as $K_0 - \bar{K}_0$ mixing. To maintain consistency with the observed lack of FCNCs in the light quark sector, several assumptions on the a-priori free parameters for the couplings f_{ij} are applied. One common ansatz [94] to account for constrains from phenomenology is to require the FCN couplings to affect the third generation of quarks only by making

use of the broad mass hierarchy among the quark generations:

$$f_{ij}^{\mathcal{U},\mathcal{D}} = \lambda_{ij}\frac{\sqrt{m_i m_j}}{v}$$

where λ_{ij} are free, real parameters and $m_{i,j}$ the masses of the fermions involved in the interaction. Other proposals [112] are based on symmetry arguments which avoid tree-level FCNC through natural flavour-conservation by imposing additional ad-hoc discrete symmetries, e.g. $\mathbb{Z}_2$ symmetries of the Higgs, or Higgs and down-type (right-handed) quark fields:

$$\begin{aligned} &\Phi_1 \to -\Phi_1 && && \text{(I)} \\ &\Phi_1 \to -\Phi_1 && \text{and} \qquad \Psi_{j,R}^{\mathcal{D}} \to -\Psi_{j,R}^{\mathcal{D}} && \text{(II)}\,, \end{aligned}$$

through which the 2HDM I or 2HDM II are obtained [114]. In these either only one of the Higgs doublets couples to fermions and the other one does not at all (model I) or one Higgs doublet exclusively couples to up-type quarks and the other to down-type quarks only (model II). Note that, while in generic 2HDM the latter Yukawa coupling pattern has to be introduced ad-hoc, they are automatically realised in supersymmetric models through continuous symmetries, e.g. in the MSSM (see Section 3.1.3). In contrast to the SM, in the 2HDM III the Yukawa couplings η_{ij} and ξ_{ij} can not be simultaneously diagonalised by the diagonalisation of the up-type and down-type mass matrices. As a consequence, the Yukawa couplings are not flavour diagonal and hence give rise to tree level flavour-changing couplings through e.g. the neutral scalar and pseudoscalar Higgs bosons H and A.

In 2HD models, the FCNC decay modes $t \to cg$ and $t \to ug$ however are produced at the one-loop level via the exchange of virtual H, A and $H^{\pm}$ bosons, see Figure 3.2. The branching fractions for top-quark FCNC interactions from theory calculations are

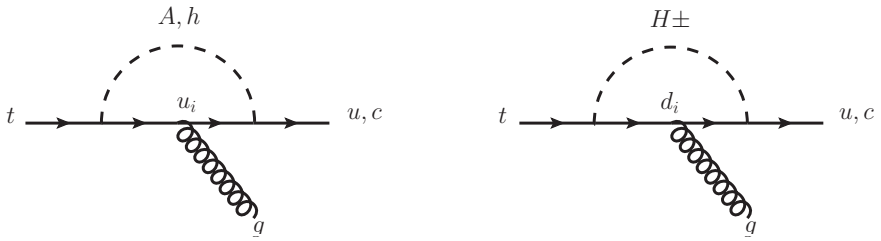

Figure 3.2.: Examples of Feynman diagrams contributing to the $t \to ug$ and $t \to cg$ decay amplitudes in the Two Higgs Doublet Model.

predicted to reach orders of up to $\sim 10^{-4}$ for the cgt coupling and hence values which can be probed by experiments at the LHC. In the 2HDM I and 2HDM II the FCNC decay modes involving strong interactions are dominated by the one-loop exchange of a virtual charged Higgs boson $H^{\pm}$, cf. Figure 3.2 (right). The respective branching fractions are at most enhanced to orders of $\sim 10^{-5}$, which nonetheless is still large enough to be examined at the LHC.

3.1.3. Supersymmetric Models

Models of supersymmetry (SUSY) currently are some of the most investigated candidates for theories beyond the SM. In particular, they allow for new sources of CP violation to explain the observed baryon asymmetry in the universe, offer a solution to the hierarchy problem and in some extensions provide for possible Dark Matter candidates. In supersymmetric models every SM particle is related to a superpartner (sparticle) of same mass but a spin different by ½. This establishes a symmetry between the fermionic and scalar sectors by means of which every SM fermion is related to a bosonic superpartner via a SUSY transformation, and vice versa. A-priori the masses of the new sparticles would have the same spectrum as the known SM particles. Since these have not been observed, SUSY must be a broken symmetry. By the same mechanism SUSY models provide an elegant solution to the hierarchy problem. The chiral symmetries which protect the fermion masses from radiative loop corrections also protect the scalar (i.e. Higgs boson) masses from quadratic divergences occurring in the SM. In SUSY these are cancelled by the new sparticles which avoids the necessity of extensive fine-tuning to circumvent the very high Higgs masses usually found at the order of the highest scale described in the theory. Although SUSY must be broken at some scale and the problematic terms do not cancel exactly, occurring divergences are logarithmic at most and are usually unproblematic when constraining the theory to energy scales of a few TeV. In the so-called Minimal Supersymmetric Standard Model (MSSM) the breaking of the supersymmetry is mediated by a set of generic, so-called soft breaking terms $\mathcal{L}_{\text{soft}}$ in the effective MSSM Lagrangian at the electroweak scale:

$$\mathcal{L}_{\text{MSSM}} = \mathcal{L}_{\text{gauge}} + \mathcal{L}_{\text{matter}} + \mathcal{L}_{\text{D}} + \mathcal{L}_{\text{F}} + \mathcal{L}_{\text{soft}} \,,$$

where $\mathcal{L}_{\text{gauge}}$ and $\mathcal{L}_{\text{matter}}$ describe the kinetics of the gauge bosons and their fermionic superpartners (gauginos), and the kinetics and interactions of the matter fields (fermions and sfermions). $\mathcal{L}_{\text{D}}$ and $\mathcal{L}_{\text{F}}$ denote the so-called D- and F-terms which describe e.g. the Higgs self-interactions, scalar-fermion interactions and contribute to the Higgs masses. For a detailed review of the full MSSM Lagrangian, see e.g. [115].

The superpotential of the MSSM Lagrangian [110] is usually written as follows and describes the R-parity [3] conserving supersymmetric extension of the Yukawa interactions of fermions and Higgs bosons in the SM:

$$\tilde{W} = \lambda^{L}_{i,j}\Phi_1 L_i \bar{E}_j + \lambda^{D}_{i,j}\Phi_1 Q_i \bar{D}_j + \lambda^{U}_{i,j}\Phi_2 Q_i \bar{U}_j + \mu\Phi_1\Phi_2$$

where L_i and Q_i are the left-handed SU(2) doublets of the fermion superfields for leptons and quarks, and $\bar{E}_j$, $\bar{D}_j$ and $\bar{U}_j$ the respective lepton, up- and down-type quark singlets. Again, the indices $i, j = 1, 2, 3$ denote the involved fermion generation and Φ_1 and Φ_2 the two scalar SU(2) Higgs doublets with opposite hypercharge -1 and $+1$. The Yukawa coupling matrices are represented by $\lambda^{L,D,U}_{i,j}$. The MSSM contains two Higgs doublets

[3] R-parity is a symmetry imposed in many supersymmetric models and is defined as $R = (-1)^{3B+L+2S}$, with spin S, baryon number B, and lepton number L. It is introduced to prevent interactions in the theory that violate baryon and lepton number conservation, which have been verified experimentally to high precision. In supersymmetric models SM particles are defined to have an R-parity of $+1$, while their supersymmetric partners are given an R-parity of -1.

causing the same Yukawa couplings as in the 2HDM II. The existence of two doublets in supersymmetric theories is motivated by the arrangement of the scalars into chiral multiplets, paired with chiral fermions. Their complex conjugates belong to multiplets of the opposite chirality which do not couple in the Lagrangian. Hence, the mechanism of simply taking the complex conjugates of a single Higgs doublet to give mass to up- and down-type quarks simultaneously, as is done the SM, is not applicable in SUSY models since this would lead to a non-analytic superpotential $\tilde{W}$. Further, to prevent chiral anomalies[4] which could break the gauge symmetry and spoil the renormalisability of the theory, the sum of hypercharges needs to cancel to zero for each generation of fermions making two Higgs doublets with opposite hypercharge indispensable.

In the MSSM, flavour-changing interactions occur mainly due to the fermion and sfermion mass matrices, which in general are not diagonalisable simultaneously due to the soft breaking terms introduced. Consequently, gluino-quark-squark and neutralino-fermion-sfermion interactions may occur, in with the quarks and squarks have different flavours. These interactions provide the most important contributions to top-quark FCNC processes, examples of which are shown in Figure 3.3. FCNC top-quark

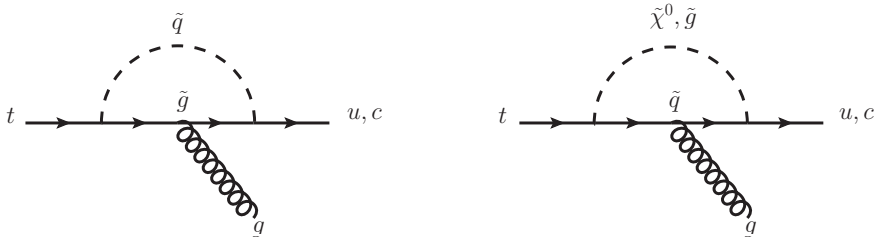

Figure 3.3.: Examples of Feynman diagrams contributing to the $t \to ug$ and $t \to cg$ decay amplitudes in the Minimal Supersymmetric Standard Model.

interactions in the MSSM, including $t \to cg$ decays, have been studied extensively e.g. in [100–103, 117] and the resulting branching fractions for top-quark FCNC decay modes involving strong interactions are estimated to reach values as high as $\sim 10^{-5}$. Certain MSSM models exist in which R-parity violation ($\not{R}$ SUSY) [107, 108] is introduced by additional terms in the superpotential

$$W_{\not{R}} = \lambda^{'}_{i,j,k} L_i L_j \bar{F}_k + \lambda^{''}_{i,j,k} L_i Q_j \bar{D}_k + \lambda^{'''}_{i,j,k} \bar{U}_i D_j \bar{D}_k \ .$$

These give rise to additional sources of flavour-violating interactions and allow for FCNC top-quark decay branching fractions as high as $\sim 10^{-4}$, under some assumptions even up to the order of $\sim 10^{-3}$ [107]. However measurements of the proton decay and precision measurements of FCNC interactions in the low-energy regime impose strong constraints

[4] So-called "harmful" triangular chiral anomalies, in particular, break the classical chiral symmetry in triangular fermionic loop graphs at first perturbative order in the renormalised quantum field theory leading to a non-conservation of the axial vector part of the chiral current in couplings of fermions to the gauge fields. However, in the SM model these are circumvented by the cancellation of contributions from left- and right-handed fermions in their triplet representation in the QCD part, and of contributions from leptons and quarks in the EW theory due to the symmetry between the fermion families and quantum numbers under the $\mathrm{SU}(2)_L \times \mathrm{U}(1)_Y$ group, see e.g. [116] for details.

on the R-parity violating couplings λ_{ijk} [118]. In addition, current experimental limits from searches at the LHC already reach values at a comparable order of precision, see Section 3.2.

3.1.4. Technicolor Models

Technicolor (TC) theories were originally introduced in the 1970's [119] as an extension to the SM in which the mass generation of the W and Z bosons is not caused by elementary scalar Higgs bosons, but through the dynamics of newly introduced strong gauge interactions at the TeV scale. The new couplings are strong and confining at the electroweak scale and become asymptotically weak at high energies (cf. QCD) which imposes a dynamic electroweak symmetry breaking mechanism. Since in TC models fermions represent the only matter fields and no elementary Higgs bosons exist, the necessity of fine-tuning and hence the hierarchy problem of the SM are avoided.

Technicolor models predict the existence of doublets of additional massless Dirac fermions, so-called technifermions. Between those a chiral symmetry exists that, if spontaneously broken, results in the technifermions to acquire a dynamical mass, and several massless Goldstone bosons being created. Three of these give masses to the W and Z bosons. In pure Technicolor theories however, a-priori no mechanism exists to also give masses to the ordinary fermions. To avoid the necessity of additional elementary scalars, the Technicolor model therefore was embedded into an "Extended Technicolor" (ETC) [120] gauge theory to allow for couplings of technifermions to quarks and leptons via additional gauge bosons arising in the enlarged gauge group. The ETC gauge group is then broken down to the former Technicolor gauge group at large scales of the order $\mathcal{O}(10^3$ TeV).

However, the ETC model is subject to severe constraints from LEP precision measurements since ETC interactions are predicted to allow for large FCNC interactions at tree-level. Further it lacks a mechanism to generate the large top-quark mass measured by experiments at the Tevatron and LHC accelerators. To account for these issues, the so-called topcolour-assisted Technicolour model (TC2) [121, 122] was proposed, which connects the top quark with the electroweak symmetry breaking and dynamically accounts for larger parts of the top-quark mass. As the main consequence the model predicts three top-pions, Π_t^0, $\Pi_t^\pm$ and one top-Higgs h_t. These are subject to large Yukawa

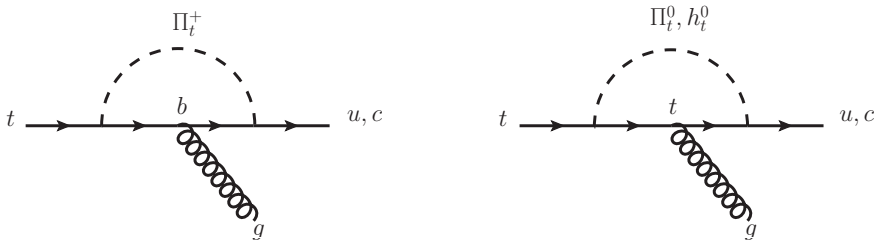

Figure 3.4.: Examples of Feynman diagrams contributing to the $t \to ug$ and $t \to cg$ decay amplitudes in the Top-Colour assisted Technicolour Model (TC2).

couplings to the third generation which induce new sources of top-quark FCNC interactions through virtual contributions (see Figure 3.4), since the non-universal topcolour interactions do not exhibit a GIM mechanism. Calculations within the TC2 framework have shown to produce large enhancements in the branching fractions of the strong FCNC top-quark decay modes up to $\mathcal{B}(t \to cg) \sim 10^{-5}$ [109, 123], which reach the level of detectability of the LHC experiments.

3.2. FCNC Searches in Top-Quark Physics

While FCNC top-quark interactions via the $q\gamma t$ and qZt vertices are best studied directly in decays, i.e. by searching for final states with the corresponding signatures, the qgt coupling is best studied indirectly through FCNC vertices at production since the final state signatures in the $t \to qg$ decay mode are expected to be dominated by the large QCD multijet background. Although the single top quarks produced via the qgt coupling are assumed to purely decay like in the SM, several kinematic properties allow for a distinction of its decay signature from SM backgrounds:

- The single top quarks produced via the considered FCNC processes are expected to have a much softer p_T spectrum than in SM production, since the $2 \to 1$ process is the dominant contribution where the top quark is produced almost without transverse momentum for reasons of momentum conservation.
- the strong FCNC top-quark production is highly charge asymmetric which is reflected in the identified charge of the reconstructed single lepton which provides additional separation power from the manifold SM background processes.
- Further, the W boson from the decay of the top-quark produced via strong FCNCs has a higher p_T spectrum which leads to smaller relative angles of its decay products in the laboratory frame.

A more detailed discussion of the expected differences in the kinematic signatures of the signal and the different background processes will be given in Section 8 after introducing the event reconstruction and selection in Sections 6 and 7. Table 3.2 shows a summary of the present experimental limits at 95% C.L. on the branching fractions of the FCNC top-quark decay channels established by experiments of the LEP, HERA, Tevatron and LHC accelerators. The values given for the branching fractions for the strong FCNC processes $t \to qg$ for the Tevatron are results of the limits derived from the search for FCNC direct top-quark production ($2 \to 1$) by the CDF collaboration [124] or production via a t-channel process ($2 \to 2$) by the D0 collaboration [125]. The values for $t \to qg$ shown for the LHC are the results of a former 7 TeV analysis by the ATLAS collaboration using parts of 2011 data [126].

In addition to direct searches at high-energy colliders, anomalous FCNC couplings would also affect low-energy processes involving the top quark at loop level [139]. These therefore provide complementary indirect bounds on the tqZ and $tq\gamma$ FCNC top-quark couplings, e.g. from measurements in flavour physics such as rare B- and K-meson

Table 3.2.: Present experimental limits at 95% C.L. on the branching fractions of the FCNC top-quark decay channels established by experiments of the LEP, HERA, Tevatron and LHC accelerators.

Coupling	LEP		HERA	
$\mathcal{B}(t \to q\gamma)$	2.4%	[127–131]	0.64% ($tu\gamma$)	[132]
$\mathcal{B}(t \to qZ)$	7.8%	[127–131]	49% (tuZ)	[133]
$\mathcal{B}(t \to qg)$	17%	[18]	13%	[133–135]
Coupling	Tevatron		LHC	
$\mathcal{B}(t \to q\gamma)$	3.2%	[136]	—	
$\mathcal{B}(t \to qZ)$	3.2%	[137]	0.07%	[138]
$\mathcal{B}(t \to qg)$	2.0×10^{-4} (tug), $(2 \to 2)$	[125]	—	
	3.9×10^{-3} (tcg), $(2 \to 2)$	[125]	—	
	3.9×10^{-4} (tug), $(2 \to 1)$	[124]	5.7×10^{-5} (tug), $(2 \to 1)$	[126]
	5.7×10^{-3} (tcg), $(2 \to 1)$	[124]	2.7×10^{-4} (tcg), $(2 \to 1)$	[126]

($b \to s$ mediated (semi-)leptonic or radiative) decays and studies of their potential deviations from the SM predictions. Analysis of data from e.g. the BaBar [140], Belle [141], CDF [142] and LHCb [143] experiments have proven to provide stringent indirect limits on the respective decay branching fractions, yielding competitive, or for particular coupling configurations even more stringent bounds than those of present direct searches [139, 144–146], see Table 3.3 for a summary.

Table 3.3.: Present indirect bounds on the FCNC top-quark decay branching fractions established by measurements of rare B- and K-meson decays.

Coupling	indirect upper limit	
$\mathcal{B}(t \to uZ)$	3.9×10^{-4}	[139]
$\mathcal{B}(t \to cZ)$	4.85×10^{-3}	[144]
$\mathcal{B}(t \to u\gamma)$	1.44×10^{-4}	[145]
$\mathcal{B}(t \to c\gamma)$	2.1×10^{-3}	[145]

3.3. FCNC Interactions in the Effective Theory Framework

Anomalous couplings, such as flavour-changing neutral currents involving the top quark, can be described in a model-independent manner using an effective operator formalism [147]. Instead of relying on specific assumptions and predictions of a particular theory or extension to the SM, whose direct effects manifest itself at energies above a few TeV – the SM is assumed to be the low energy limit or effective theory of an unspecified underlying theory valid at very high energies. The effects of many new physics models might not be directly accessible by the LHC experiments because e.g. new particles predicted by these are expected to be produced at energies not accessible at the

LHC. However, indirect effects, such as modifications of the SM particle properties or their couplings, could be perceived at a much lower energy scale Λ. The low energy limit can be described by extending the SM Lagrangian $\mathcal{L}^{(\mathrm{SM})}$ (dimension four in energy[5]), by a series of effective operators of dimension E^5 ($\mathcal{L}^{(5)}$) and E^6 ($\mathcal{L}^{(6)}$). The latter are required to be built with the SM fields and to be invariant under the gauge group of the SM. The full "effective Lagrangian" is then defined as follows:

$$\mathcal{L}^{(\mathrm{eff})} = \mathcal{L}^{(\mathrm{SM})} + \frac{1}{\Lambda}\mathcal{L}^{(5)} + \frac{1}{\Lambda^2}\mathcal{L}^{(6)} + \mathcal{O}\left(\frac{1}{\Lambda^3}\right) . \tag{3.2}$$

The effective operators $\mathcal{L}^{(5)}$ and $\mathcal{L}^{(6)}$ are suppressed by powers of the new physics scale Λ, which has a dimensionality of $[\Lambda] = E^{+1}$ and is related to the mass cut-off scale above which the effective theory breaks down. Hence the coefficients in Λ characterise the energy scale at which the new physics manifests itself in the theory. Further, they ensure that the dimensionality of $\mathcal{L}^{(\mathrm{eff})}$ remains four. A broad manifold of effective operators exists which fulfil the criteria described above. Therefore more criteria have to be employed to select only those of a particular interest for the type of physics processes investigated. Following [148], the number of effective operators can be further reduced by applying the following criteria:

- The dimension five effective operators $\mathcal{L}^{(5)}$ are neglected since they break baryon and lepton number conservation and hence are considered unphysical,
- only those operators are considered that have no sizeable impact on low energy physics, since their effects have been extensively constrained by the existing data of LEP and Tevatron experiments,
- the effective operators have to contribute to flavour-changing interactions in the strong sector, hence no operators with electroweak gauge bosons are considered,
- lastly, only those operators describing FCNC couplings to a single top quark are of interest within this analysis, hence such processes, in which an up (u) or charm quark (c) interacts with a gluon to produce a single top quark.

This leads to a set of operators describing strong FCNC vertices of the form qgt which can be written as [149]:

$$\mathcal{O}^{ij}_{qG\Phi} = \bar{q}^{\,i}_L \, \lambda^a \, \sigma^{\mu\nu} \, q^j_R \, \tilde{\Phi} \, G^{a\mu\nu} , \tag{3.3}$$

where q^j_R stands for a right-handed quark singlet, $\bar{q}^{\,i}_L$ for a left-handed quark doublet, $G^{a\mu\nu}$ is the gluon field strength tensor and $\tilde{\Phi}$ is the charge conjugate of the Higgs doublet. The indices of the spinors (i, j) are flavour indices which define the quark generation and λ^a are the Gell-Mann matrices (cf. Section 2.2). Since a single top quark is required to take part in the interaction, one of the indices can always be set equal to 3. Consequently

[5] Assuming natural units $\hbar$=c=1 (as implied throughout this thesis), in a dimensional analysis all quantities of the Lagrangian (such as fields, their derivatives, mass parameters, etc.) can be measured in units of energy to some power (dimensionality). By requiring the space-time integral of the Lagrangian density $\mathcal{L}$, the action $\mathcal{S} = \int \mathcal{L}\, \mathrm{d}^4x$, to be dimensionless in natural units to ensure its Lorentz-invariance, the Lagrangian of a 4D field theory is required to have dimensionality $[\mathcal{L}] = E^{+4}$.

the other index has to be either 1 or 2 since only flavour-changing interactions are of interest. Hence the remaining fermion field in the interaction is either a u or a c quark.

In addition to the direct single top-quark production $qg \to t$ these operators give rise to interactions of the form $gg \to tq$ and $gq \to tg$, as well as to processes of single top-quark production involving gluonic quark-quark (or quark-antiquark) scattering. In the analysis hence all such processes have to be considered, in which an up quark, charm quark or gluon originating from the colliding protons are interacting via strong couplings in a t-, s-, or u-channel process to produce a single top quark, including processes with the associated production of additional gluons or light quarks ($2 \to 2$ processes). Replacing $\tilde{\Phi}$ in Eq. 3.3 by its vacuum expectation value ($v/\sqrt{2} \approx 246$ GeV) leads to a dimension five-like operator which allows for writing the full strong FCNC Lagrangian as follows [149]:

$$\mathcal{L}_S = -g_s \sum_{q=u,c} \frac{\kappa_{qgt}}{\Lambda} \, \bar{q} \, \lambda^a \, \sigma^{\mu\nu} \, (f_q + h_q \gamma_5) \, t \, G^a_{\mu\nu} + h.c. \ , \tag{3.4}$$

where $\kappa_{gqt} \, (q = u, c)$ are dimensionless, real and positive parameters that relate the strength of the new couplings to the strong coupling constant $g_s = \sqrt{4\pi\alpha_s}$. The new physics scale described above is represented by Λ and the parameters f_q and h_q are real parameters which define the chirality of the produced top quark and satisfy the relation $|f_q|^2 + |h_q|^2 = 1$ for reasons of normalisation.

The FCNC processes may give rise to additional decay modes of the top quark and thus affect its total decay width. Consequently the strong FCNC processes have to be considered for calculating the branching fractions of the strong FCNC couplings. The calculation is done straightforward by dividing the partial width of the top-quark decay via FCNC processes, $\Gamma_{t\to qg}$, by the (modified) total top-quark decay width:

$$\mathcal{B}(t \to qg) = \frac{\Gamma_{t\to qg}}{\Gamma_{t\to bW} + \Gamma_{t\to qg}} \quad q = u, c \ . \tag{3.5}$$

Theory calculations and numerical results of the branching fractions and partial decay widths of the $t \to ug$ and $t \to cg$ decay at leading order (LO) and next-to-leading order (NLO) can be found in [150]. The partial decay width including the full NLO corrections is given as:

$$\Gamma^{\mathrm{NLO}}_{t\to qg} = \Gamma^{\mathrm{LO}}_{t\to qg} \left\{ 1 + \frac{\alpha_s}{72\pi} \left[174 \ln\left(\frac{\mu^2}{m_t^2}\right) - 12 N_f \ln\left(\frac{\mu^2}{m_t^2}\right) - 36 N_f - 38\pi^2 + 749 \right] \right\} \ ,$$

where α_s is the strong coupling constant, μ the renormalisation scale, N_f represents the number of involved quark flavours, and m_t is the mass of the top quark. $\Gamma^{\mathrm{LO}}_{t\to qg}$ is the respective partial decay width calculated at LO which is given as follows:

$$\Gamma^{\mathrm{LO}}_{t\to qg} = \frac{8\alpha_s m_t^3}{3} \left(\frac{\kappa_{qgt}}{\Lambda}\right)^2 \ .$$

Using $N_f = 5$, a top-quark mass definition of $m_t = 172.5$ GeV, and setting the renormalisation scale to be equivalent to m_t, one obtains the following values for the top-quark FCNC partial decay width at NLO:

$$\Gamma^{\mathrm{NLO}}_{t\to qg} = 1.613 \times \left(\frac{\kappa_{qgt}}{\Lambda\,[\mathrm{TeV}]}\right)^2 \ \mathrm{GeV} \ .$$

Using Equation 3.5 in combination with LO and NLO values for the SM top-quark decay width as calculated in [151], one can plot the branching fraction of the strong FCNC top-quark decay as well as the effect on the branching fraction of its SM decay ($t \to Wb$) as a function of the anomalous coupling constant κ_{qgt}. Both are shown in Figure 3.5 (a) and (b) for LO and NLO calculations respectively. The plots illustrate that for small coupling constants of e.g. $\kappa_{qgt}/\Lambda < 0.1$ TeV^{-1}, the influence of the anomalous top-quark decay on the total decay width is negligible. This allows for considering only SM decay modes and hence for simplifying Equation 3.5 to:

$$\mathcal{B}(t \to qg) = \frac{\Gamma_{t\to qg}}{\Gamma_{t\to bW}} \quad q = u, c. \tag{3.6}$$

This assumption is well supported by the present upper limits on the coupling constants from different experiments as summarised in Section 3.2. As a direct consequence for searches of strong FCNC single top-quark production, this allows the top quark to be reconstructed in the SM decay mode only. Using the parameters and theory calculations as described above one can calculate the branching fraction for the $t \to qg$ decay mode

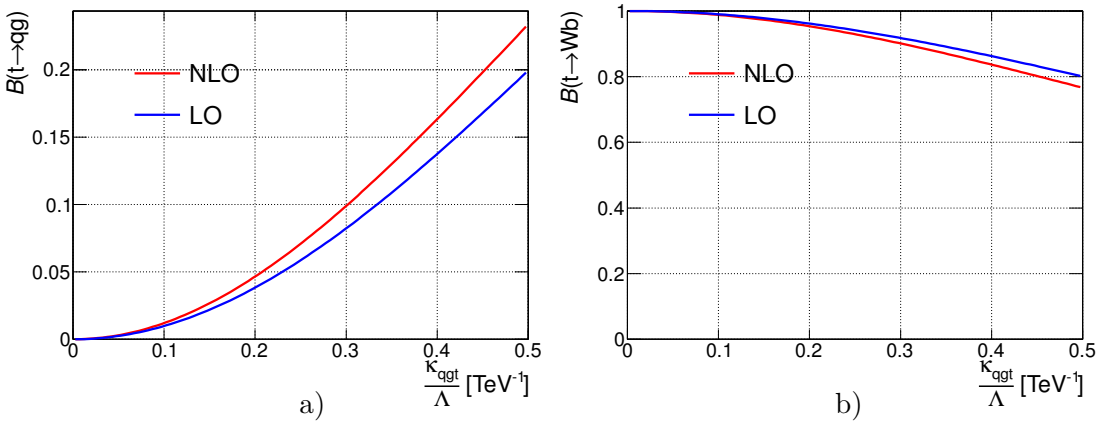

Figure 3.5.: Branching fraction of the FCNC top-quark decay $\mathcal{B}(t \to qg)$ (a) and of the SM top-quark decay $\mathcal{B}(t \to bW)$ (b) as a function of the FCNC coupling, calculated at leading and next-to-leading order.

as a function of the strong FCNC coupling constant κ_{qgt}:

$$\mathcal{B}(t \to qg) = 1.2205 \times \left(\frac{\kappa_{qgt}}{\Lambda\,[\mathrm{TeV}]} \right)^2 \quad . \tag{3.7}$$

To calculate the cross-sections at next to leading order, in addition to the LO direct top-quark production (cf. Figure 2.8), one loop virtual gluon corrections and real gluon bremsstrahlung contributions have to be included which is described in detail in [152]. Further, processes with two gluons or two quarks in the initial states have to be considered. Figure 3.6 gives an overview of exemplary NLO Feynman diagrams contributing to the two strong FCNC single top-quark processes. More comprehensive lists can be found e.g. in [148, 150]. In [16] LO and NLO cross-section calculations are carried out numerically at $\sqrt{s} = 7$ TeV using the CTEQ6L1 [153] LO and CTEQ6.6 [154] NLO parton distribution function (PDF) respectively and setting the normalisation and factorisation scales equal to a top-quark mass of $m_t = 173.1$ GeV. The cross-section is expressed as a

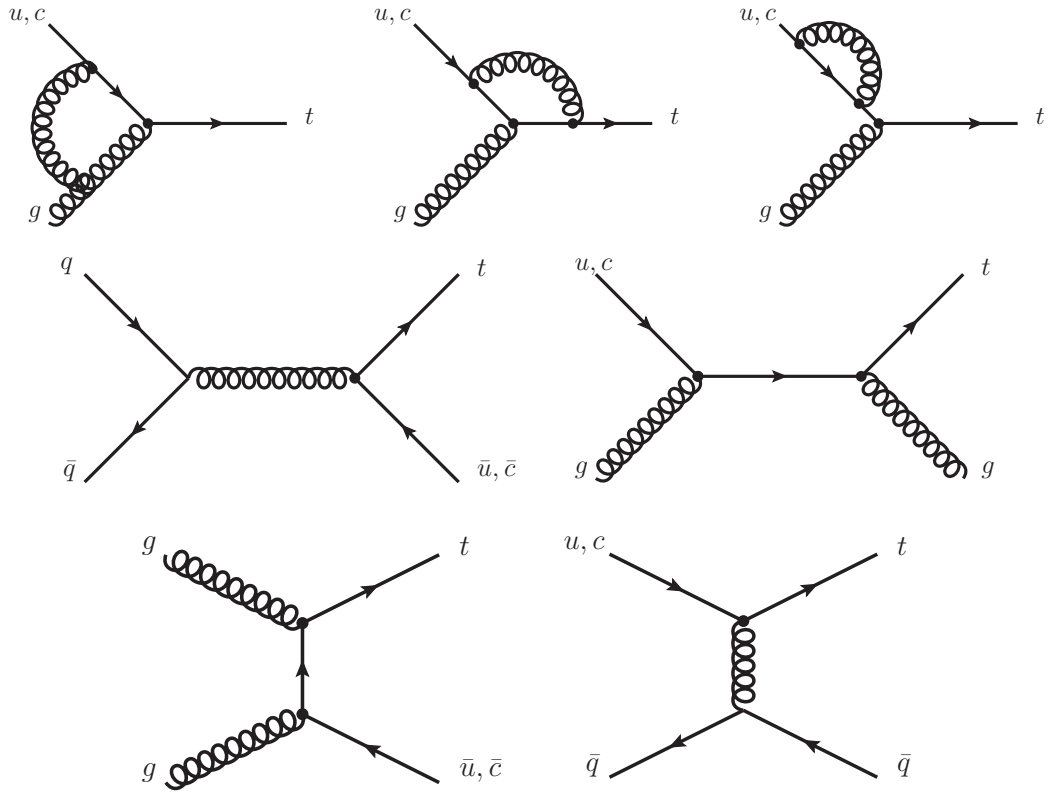

Figure 3.6.: Exemplary Feynman diagrams of anomalous single top-quark production via strong FCNCs at at next-to-leading order (NLO). The charge conjugated processes are always implied.

function of the coupling constants κ_{qgt}

$$\sigma_{qg\to t} = \sum_{q=u,c} \left(\frac{\kappa_{qgt}}{\Lambda}\right)^2 \left(b_{qL}|f_q^L|^2 + b_{qR}|f_q^R|^2\right) \ , \tag{3.8}$$

where b_{qL}, b_{qR} are real constants and f_q^L, f_q^R are chiral parameters projecting out the left- and right-handed polarisations, respectively. In order to calculate values of b_{qL} and b_{qR} for 8 TeV, the numerical results given in [16] are rescaled with the cross-section ratio $k_q = \sigma_{qg\to t}(8\text{ TeV})/\sigma_{qg\to t}(7\text{ TeV})$ as determined using the MEtop generator [149], cf. Section 5.2.1. Applying the resulting k-factors of $k_u = 1.22$ and $k_c = 1.32$, assuming purely left-handed couplings only ($f_q^L = 1$ and $f_q^R = 0$), and considering all leptonic decay channels, Equation 3.8 can be written as:

$$\sigma_{qg\to t}^{\text{NLO}} = \left(99.9^{+5.8}_{-5.2}\right) \times 10^3 \left(\frac{\kappa_{ugt}}{\Lambda\,[\text{TeV}]}\right)^2 \text{pb} + (19.5 \pm 1.0) \times 10^3 \left(\frac{\kappa_{cgt}}{\Lambda\,[\text{TeV}]}\right)^2 \text{pb}\,, \tag{3.9}$$

$$\sigma_{qg\to t}^{\text{LO}} = \left(74.8^{+5.8}_{-5.2}\right) \times 10^3 \left(\frac{\kappa_{ugt}}{\Lambda\,[\text{TeV}]}\right)^2 \text{pb} + (12.9 \pm 1.0) \times 10^3 \left(\frac{\kappa_{cgt}}{\Lambda\,[\text{TeV}]}\right)^2 \text{pb}\,. \tag{3.10}$$

Herein the error bands represent the uncertainties arising from the scale uncertainties, i.e. from varying the renormalisation and factorisation scales by factors of ½ m_t and $2\,m_t$. The resulting cross-sections as a function of the coupling constants are shown in Figure 3.7. In summary, given a cross-section measurement of the FCNC single top-quark production via the *ugt* and/or the *cgt* vertex, the effective theory calculations described above render it possible to derive the corresponding coupling constants and branching fractions by subsequently applying equations 3.10 and 3.7.

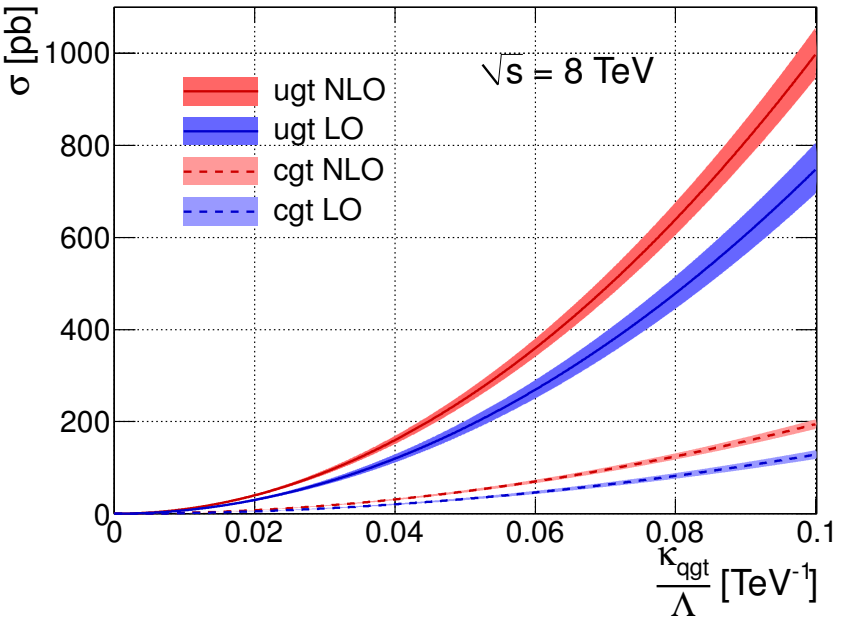

Figure 3.7.: The cross-section for single top-quark production as a function of the coupling constant for the $ug \to t$ (solid lines) and $cg \to t$ processes (dotted lines). The NLO calculation is shown in red, the LO cross-sections in blue. The uncertainty bands reflect the scale uncertainties as derived from varying the renormalisation and factorisation scales from ½ m_t to 2 m_t.

4. The ATLAS Detector at the The Large Hadron Collider

In view of the seminal results from past precision and discovery experiments at the former Tevatron, LEP and HERA accelerators, it was decided to built a new collider in order to extend the physics reach of future experiments towards even higher centre-of-mass energies. To study low-rate phenomena like the FCNC processes investigated in this work, and to enable for the production of heavy particles, such as top quarks, potential SUSY particles, Higgs or other heavy gauge bosons, a future accelerator needed to provide the highest possible event rates over a large kinematic range. To meet these requirements, and since circular electron-positron colliders of reasonable size are limited by the effects of synchrotron radiation, it was chosen to build a new hadron accelerator and collider, known as the Large Hadron Collider. The LHC is a proton-proton accelerator and storage ring serving four main, and several smaller experiments with the aim to provide answers to many of the open physics questions within the SM and beyond (cf. Section 3). In addition to protons, the LHC was designed to accelerate and collide heavy nuclei in order to study the quark-gluon plasma which could provide insights e.g. on the matter condensation process in the early universe. Section 4.1 provides an overview of the LHC accelerator chain and performance and introduces related quantities used throughout this thesis.

Four large experiments have been constructed at the LHC. Two of the experiments, ATLAS (A Toroidal LHC ApparatuS [155]) and CMS (Compact Muon Solenoid [156]) are general purpose experiments. Their design is driven by the requirements and performance needed in order to search for signatures of new highly energetic particles of potentially low production rates, and for the expected event topologies of the SM Higgs boson in particular. However, ATLAS should also be able to perform precision measurements of known Standard Model parameters. The ALICE (A Large Ion Collider Experiment [157]) and LHCb (Large Hadron Collider beauty [143]) experiments employ specialised detectors, designed to study the quark-gluon plasma in heavy ion collisions and to explore CP violation in B physics. The presented analysis, however, focuses on p-p collisions and uses collision data recorded by the ATLAS experiment in 2012. Section 4.2 therefore will provide an overview of the overall ATLAS detector design, its main components, and the ATLAS data-taking and trigger mechanisms.

4.1. The Large Hadron Collider

The Large Hadron Collider [158, 159] is a p-p collider of 26.7 km circumference, built 45-170 m below the ground at the European Particle Physics Laboratory CERN at the

French-Swiss boarder near Geneva, Switzerland. Located inside the tunnel of the former LEP accelerator [50], the LHC accelerates two protons beams in opposite directions through separate beam pipes along a nearly circular path of eight linear sections interleaved by eight arcs. The proton beams are generated and pre-accelerated in a chain consisting of accelerators formerly built and used in past experiments at CERN, see Figure 4.1. The protons are generated by ionising hydrogen gas in a duoplasmatron and subsequently extracted and transferred to the Radio Frequency Quadrupole (RFQ). The RFQ is a linear accelerator in which the protons are accelerated to 750 keV, focussed, and separated into bunches of approximately 10^{11} protons each. The bunches are transferred into the LINAC2 linear accelerator to be pre-accelerated to an energy of 50 MeV before being injected into the (circular) Proton Synchrotron Booster (PSB) that raises their energy by another factor of 28. Next, the protons are transferred to the Proton Synchrotron (PS) in which the initial bunches are split into 72 smaller bunches with a spacing of 25 ns, and the beam energy is raised to 25 GeV. The last facility in the pre-accelerator chain is the Super Proton Synchrotron (SPS), where the proton bunches

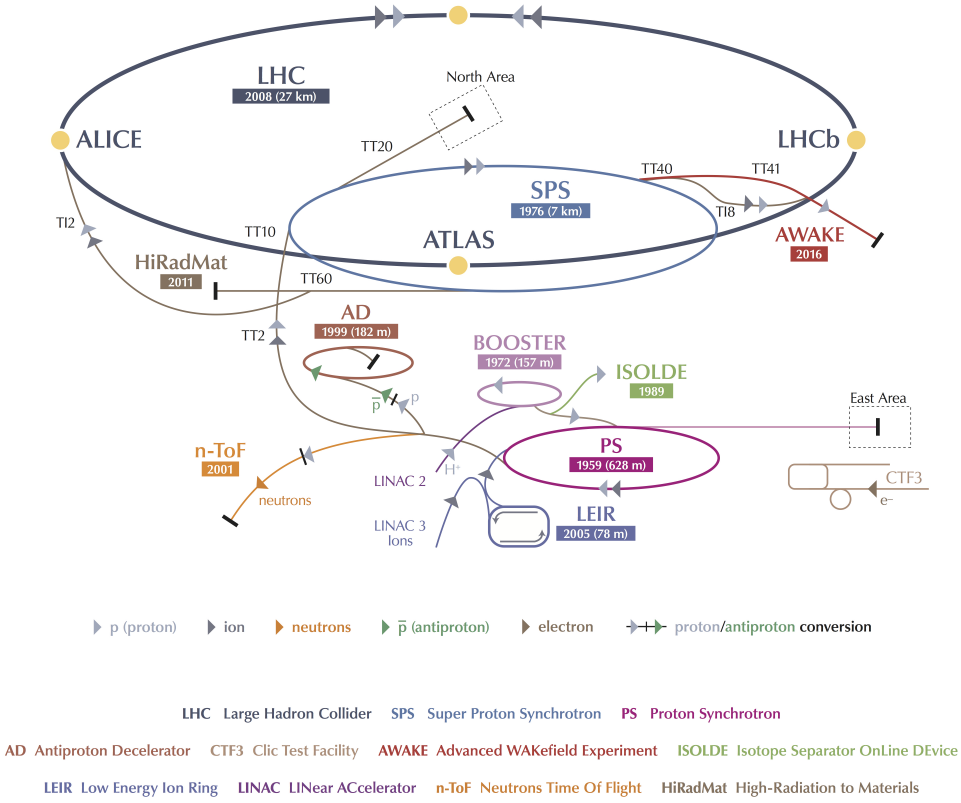

Figure 4.1.: Illustration of the CERN accelerator complex. Shown are the Large Hadron Collider and the various pre-accelerators (LINAC 2, PS Booster, PS and SPS) used to accelerate proton bunches to 450 GeV before injected into the LHC and accelerated further. [160]

are accelerated to 450 GeV before being injected into the two concentric beam pipes of the actual LHC ring via two transfer lines. The injection of up to 2808 bunches per beam is possible according to the design specifications. Radio-frequency (RF) cavities in the straight sections of the LHC accelerate the proton beams within approximately 20 minutes up to energies of 7 TeV each. The energy however has been limited to 3.5 TeV in 2010/11 and to 4 TeV per beam in 2012 for safety reasons. Runs at the full design energy are envisaged for the year 2015/16 and beyond, after having finished the necessary consolidation works in the LHC magnet systems (see Appendix F.1). To keep the proton beams on their quasi-circular path, a total of 1232 superconducting dipole magnets are installed in the arc sections of the LHC ring. The magnets are made of niobium-titanium (NbTi) and are cooled beyond critical temperature to 1.9 K using super-fluid helium in order to produce nominal magnetic field strengths of 8.33 T. Another 392 quadrupole and additional sextupole and octupole magnets are installed along the main ring to focus the proton beams and tune other beam parameters before the proton bunches are brought to collision inside sections with common beam pipes in four interaction points (IPs). At these points on the ring large caverns host the main experiments and their detectors.

The total inelastic event rate R in p-p collisions in the IPs is given by the product of the total (inelastic) hadronic interaction cross-section of the protons σ_{had} and the instantaneous luminosity $\mathcal{L}$. Assuming identical bunch sizes and Gaussian transverse bunch profiles, $\mathcal{L}$ is defined by the number of bunches n_b per beam, their revolution frequency f, by the number of protons per bunch N_{p}, and the geometrical beam parameters in the interaction point as follows:

$$\mathcal{L} = \frac{N_{\text{p}}^2 n_b f}{4\pi\sigma_x^\star\sigma_y^\star} F \,. \tag{4.1}$$

Herein $\sigma_x^\star$ and $\sigma_y^\star$ stand for the horizontal and vertical (RMS) widths of the (Gaussian) beam profile in the transverse plane, and F is a geometric reduction factor to account for the non-zero crossing angle of the bunches at the IP. Alternatively, the instantaneous luminosity can be expressed using the value of the beta-function at the IP ($\beta^\star$) and the beam emittance (ϵ) or its energy-independent equivalent, the normalised emittance $\epsilon_{\text{N}} = \epsilon/\gamma$, where γ is the relativistic gamma factor. Assuming a circular transverse beam profile and equal $\beta^\star$ values for both beams, $\mathcal{L}$ can be calculated as:

$$\mathcal{L} = \frac{N_{\text{p}}^2 n_b f \gamma}{4\pi\beta^\star\epsilon_{\text{N}}} F \,. \tag{4.2}$$

At the IPs of the CMS and ATLAS experiments the beam sizes are squeezed down to nominal diameters of approximately 16 μm and are crossed at angles of $\approx 285\,\mu$rad. Table 4.1 summarises the nominal LHC design parameters as well as the values achieved in the most recent run period in 2012. The parameters foreseen for the next operation period (Phase-0), starting in 2015/16, are also shown for comparison. Using Equation 4.2 and assuming the nominal LHC beam parameters given in Table 4.1, an instantaneous (design) luminosity of $\mathcal{L} = 10^{34}\,\text{cm}^{-2}\text{s}^{-1}$ can be achieved. The integral of the instanta-

Table 4.1.: List of nominal design parameters of the LHC and beam parameters during the 2012 run period and projected values for Phase-0 runs. [161]

Parameter	design value	2012 run	Phase-0
Number of bunches	2808	1374	2520-2760
Bunch length [cm]	7.55	≤ 9	7.55
Bunch spacing [ns]	25	50	25 (50)
Average bunch intensity [p/bunch]	1.15×10^{11}	$\sim 1.6 \times 10^{11}$	1.15×10^{11}
Normal. emittance at IP [mm $\cdot$ mrad]	3.75	2.5	1.9-3.75
$\beta^{\star}$ at IP [cm]	55	60	45-55
Peak luminosity [$\mathrm{cm}^{-2}\mathrm{s}^{-1}$]	1×10^{34}	7.7×10^{33}	$0.9\text{-}1.7 \times 10^{34}$
$\sqrt{s}$ [TeV]	14	8	13-14

neous luminosity over time, the integrated luminosity $\mathcal{L}_{\mathrm{int}} = \int \mathcal{L}\,\mathrm{d}t$, represents a common measure of the performance of the accelerator over time. It determines the total number of events produced for a process of a given cross-section (e.g. total inelastic proton interactions) and hence determines the total amount of physics data that can be recorded at a given detector efficiency. It is usually expressed as an inverse cross-section, i.e. in fb^{-1} or pb^{-1}. At typical operating conditions and availability of the machine, one year of data-taking at nominal design luminosity at ATLAS roughly corresponds to an integrated luminosity of approximately $\mathcal{L}_{\mathrm{int}} = 20\text{-}30\,\mathrm{fb}^{-1}$.

4.2. The ATLAS Detector

The ATLAS detector [155, 162] is a cylindrical, 44 m long and 25 m high multi-purpose particle detector. Its overall structure weights approximately 7000 t and is composed of several cylindrical subdetectors arranged in an onion-like layered manner. Their purpose is to detect and reconstruct the properties of as many particles as possible generated in a p-p collision event in order to draw conclusions on the primary interaction processes involved in their production. To reconstruct the final state products of an event in almost its entirety, the different subdetectors have to register particles within a large geometrical acceptance. Each covers almost the full solid angle[1] around the interaction point and obeys a radial and forward-backward symmetric layout. From inside to outside the ATLAS detector is composed of a tracking system close to the beam pipe, electromagnetic and hadronic calorimeters at intermediate radii, and a muon spectrometer system, see Figure 4.2. The functional principle and layout of each these subdetectors will be discussed in the following sections in more detail.

[1] In ATLAS a right-handed coordinate system with its origin at the nominal IP is used. It is defined either in Cartesian or polar coordinates by the x-axis pointing towards the centre of the LHC ring, the y-axis upwards, and the z-axis pointing parallel to the anti-clockwise beam direction (as viewed from above ground); or by the radius $r = \sqrt{x^2 + y^2}$, the pseudorapidity $\eta = -\ln[\tan(\theta/2)]$, where θ is the polar angle with respect to the the anti-clockwise beam direction, and the azimuthal angle ϕ around the beam axis as measured from the x-axis.

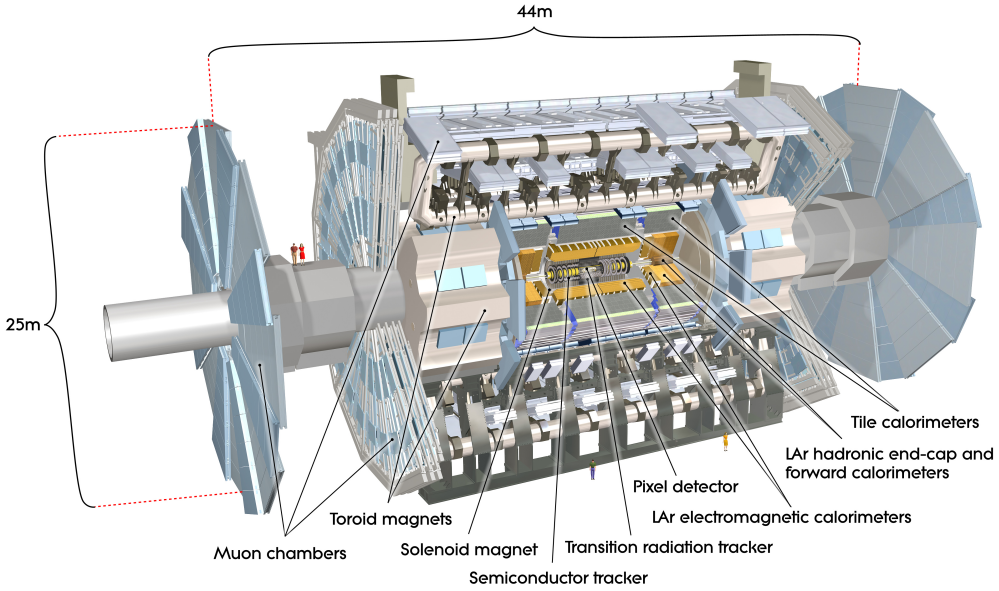

Figure 4.2.: Cutaway illustration of the ATLAS detector and its main subdetectors. [163]

4.2.1. Inner Detector

The detector part of ATLAS closest to the IP is formed by the so-called Inner Detector (ID). It is used to precisely measure the trajectories of charged particles, and to determine their momenta and charge by bending their tracks in a magnetic field. In addition, it allows to identify primary and secondary vertices and hence the origin of the interaction and the decay positions and flight lengths of short-lived particles such as hadrons containing b and c quarks or τ leptons.

The active volume of the ID extends over a length of $l \approx 5.3\,\mathrm{m}$ and a diameter of $d \approx 2.1\,\mathrm{m}$ (overall envelope $l \approx 7\,\mathrm{m}$, $d \approx 2.3\,\mathrm{m}$) [155]. It consists of three subdetectors arranged in three concentric cylindrical layers, which employ different detection and tracking technologies and cover a pseudorapidity range of $|\eta| < 2.5$ in total, see Figure 4.3. The innermost part closest to the beam pipe is formed by the Pixel detector that uses several layers of silicon pixel sensors as detecting elements. It is surrounded by the SemiConductor Tracker (SCT) which hosts layers of silicon microstrip sensors. The outermost part consists of the Transition Radiation Tracker (TRT) which uses various layers of gaseous straw tube elements. The overall goal of the tracking performance of the ID in terms of transverse momentum[2] resolution is $\sigma_{p_\mathrm{T}}/p_\mathrm{T} = 0.05\% \cdot p_\mathrm{T}[\mathrm{GeV}] \oplus 1\%$ [164]. The expected resolution in the reconstruction of transverse (d_0) and longitudinal impact parameters ($z_0 \sin\theta$) at the perigee[3] for 1 GeV pions, and neglecting effects of misalign-

[2] The transverse momentum and energy are defined as $p_\mathrm{T} = p \sin\theta$ and $E_\mathrm{T} = E \sin\theta$, respectively.

[3] The perigee is defined as the point on a reconstructed (and extrapolated) particles' trajectory with the closest approach to the nominal beam centre (global z-axis).

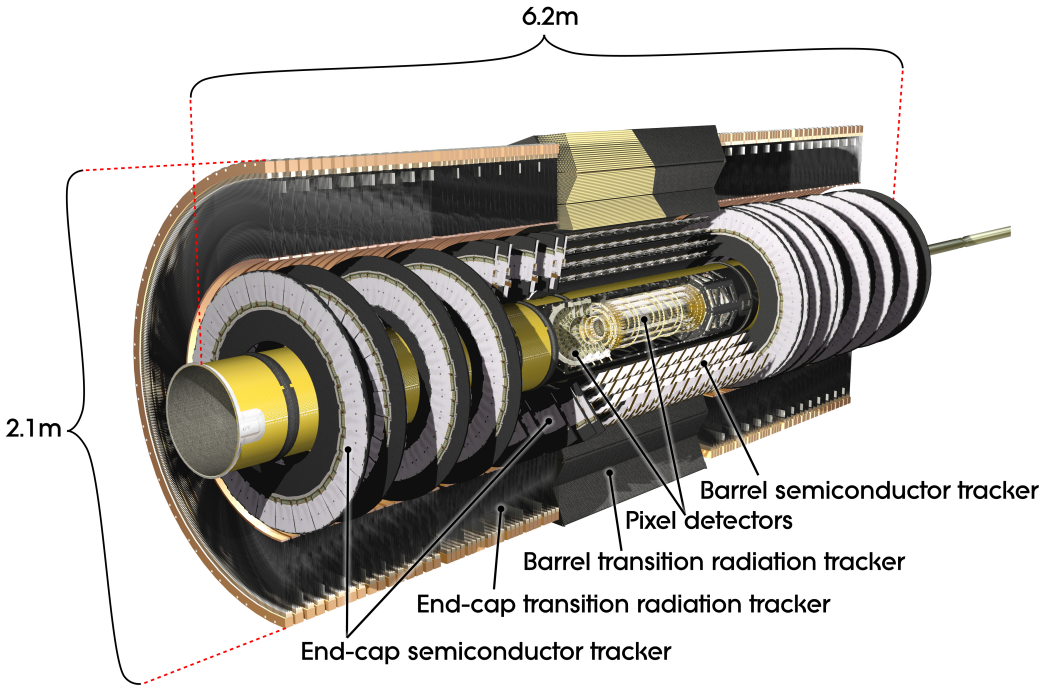

Figure 4.3.: Cutaway illustration of the ATLAS ID and its three subdetectors in the barrel and endcap regions. [165]

ment, calibration and pile-up, is $\sigma(d_0) \sim 10\,\mu\text{m}$ and $\sigma(z_0 \sin\theta) \sim 90\,\mu\text{m}$, where z_0 is the position of the primary vertex[4] in beam direction and θ is the polar angle of the track [164].

In order to measure the momenta of the charged particles and to identify their charges, the ID is embedded in a 2 T axial magnetic field that is generated by a superconducting NbTi solenoid surrounding the ID. The field is generated within a volume of an axial length of 5.8 m and a bore of 2.46 m and hence pervades the active volume of all three subdetectors in the ID. The (steel) absorber of the hadronic calorimeter is used as a flux return yoke. Since the solenoid precedes the electromagnetic calorimeter, its thickness has been minimised to have as little impact on the calorimeter performance as possible. A more comprehensive description of the ATLAS magnet system is given in [166].

Pixel Detector

The Silicon Pixel detector [167] consists of three cylindrical barrel layers, each 80 cm in length, placed at radii of 50.5 mm, 88.5 mm and 122.5 mm. The layers host a total of 1456 silicon pixel detector modules which are mounted onto pairs of staves that are arranged in an overlapping layout and host 2×13 modules each. The endcaps to each

[4] A vertex is defined as the position where several particle trajectories intersect and merge.

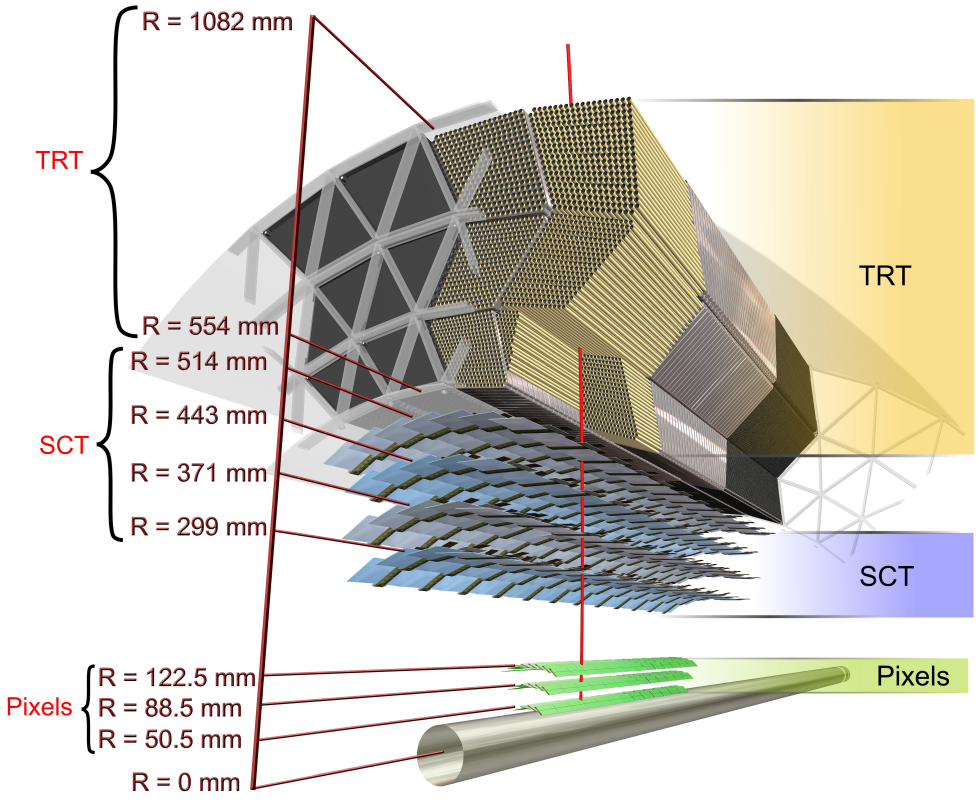

Figure 4.4.: Cutaway illustration of the different layers of all three subdetectors in the ID barrel region. [165]

side of the barrel are equipped with three disks at z-positions of $\pm 495\,\text{mm}$, $\pm 580\,\text{mm}$, and $\pm 650\,\text{mm}$, with a total of 48 pixel detector modules mounted onto each disk.

All pixel modules consist of a $19 \times 63\,\text{mm}^2$ large and $250\,\mu\text{m}$ thick n-in-n[5] silicon sensor as a detecting element. The segmented readout side hosts 47232 (328×144) pixel implants with a typical size of $50 \times 400\,\mu\text{m}^2$. The pixels are read out by 16 front-end ICs which are bump-bonded onto the sensor and connected to a flex circuit (hybrid) on their top via wire bonds at each front-end chips periphery. The hybrid hosts passive components and a module controller chip (MCC) which builds the interface to the off-detector data-taking, detector control and monitoring systems.

The Pixel detector covers a total active silicon area of $\approx 1.7\,\text{m}^2$ and features a total of ≈ 80.4 million readout channels. Each channel needs to provide a high time resolution

[5] The sensors use n^+-doped pixel implants (readout side) in an oxygenated n-type (n^--doped) Si bulk. The p^+-doped backplane requires an additional processing step since it hosts multiple guard ring implants to avoid shortcuts of the bias voltage at the sensor edges. Also see Appendix F.3.1 for more details.

($< 25\,\text{ns}$) in order to attribute hits to the correct bunch crossing and prevent saturation effects from the high particle multiplicities generated in the proton collisions. A high granularity of the Pixel layers is of particular importance at the innermost radii to achieve the required high-resolution track reconstruction and vertexing capabilities (cf. Section 6.1.3). The ATLAS Pixel detector therefore covers a pseudo-rapidity range of $|\eta| < 2.5$ and features an intrinsic position resolution of $10\,\mu\text{m}$ in r-ϕ and $115\,\mu\text{m}$ in z in the layers of the barrel part, and $10\,\mu\text{m}$ in r-ϕ and $115\,\mu\text{m}$ in r in the endcap disks.

The Pixel and Semiconductor Tracker (see next section) share a common cooling system to prevent overheating of electronics and to limit the leakage current of the sensors, in particular after irradiation for several years during the LHC operation. At nominal operating conditions the system has to remove approximately 85 kW from the ID and is based on evaporative C_3F_8 cooling. The coolant is distributed to, and integrated into, all Pixel and SCT barrel and disk support structures, reducing the temperature of the pixel and strip sensors to a target value of approximately $-7°\text{C}$. The TRT (see Section 4.2.1) is operated at room temperature and cooled using a mono-phase C_6F_{14} cooling system. A similar system is used to remove heat from the larger part of services and electronics outside the ID volume. More details on the ID cooling system can be found in [155].

Semiconductor Tracker

The Semiconductor Tracker (SCT) [168] layout consists of four cylindrical barrel layers, $149,3\,\text{cm}$ in length, at radii of 300 mm, 373 mm, 447 mm and 520 mm. The layers host a total of 2112 double-sided silicon strip detector modules which are mounted onto pairs of staves hosting 12 modules each, arranged in an overlapping layout akin to that of the Pixel detector as shown in Figure 4.4. The barrel part is complemented by two endcaps which are equipped with nine disks at z-positions between $\pm 835\,\text{mm}$ and $\pm 2388\,\text{mm}$, each hosting different numbers of double-sided silicon strip detector modules arranged in a maximum of three rings equipped with 40 (inner), 40 (middle) or 52 (outer) strip detector modules, respectively, cf. Figure 4.3.

In the barrel region, each detector module consists of four silicon microstrip detectors. Two daisy-chained $64 \times 63.6\,\text{mm}^2$ and $250\,\mu\text{m}$ thick p-in-n type sensors are mounted onto each side of a module, one pair aligned with the beam direction and the other rotated by a stereo-angle of 40 mrad with respect to the first, see Figure 4.5. This allows for an effective (stereo) measurement of both coordinates resulting in an intrinsic position resolution of $17\,\mu\text{m}$ in r-ϕ and $580\,\mu\text{m}$ in z in the layers of the barrel part.

The 768 strips on each sensor on one side of a barrel module have a pitch of $80\,\mu\text{m}$ and are electrically connected forming a single mechanical unit of 12.6 cm long strips (with 2 mm gap) per module side. All four sensors are glued onto a common $380\,\mu\text{m}$ thick thermal pyrolytic graphite (TPG) baseboard and heat spreader with beryllia facings. The (AC-coupled) strips are read out by 12 application-specific integrated circuits (ASICs) that connect to each strip via Al wire bonds. Six of these front-end ASICs are placed on each of two polyimide hybrids comprising a carbon-fibre substrate and bridging the sensors on each side of the module.

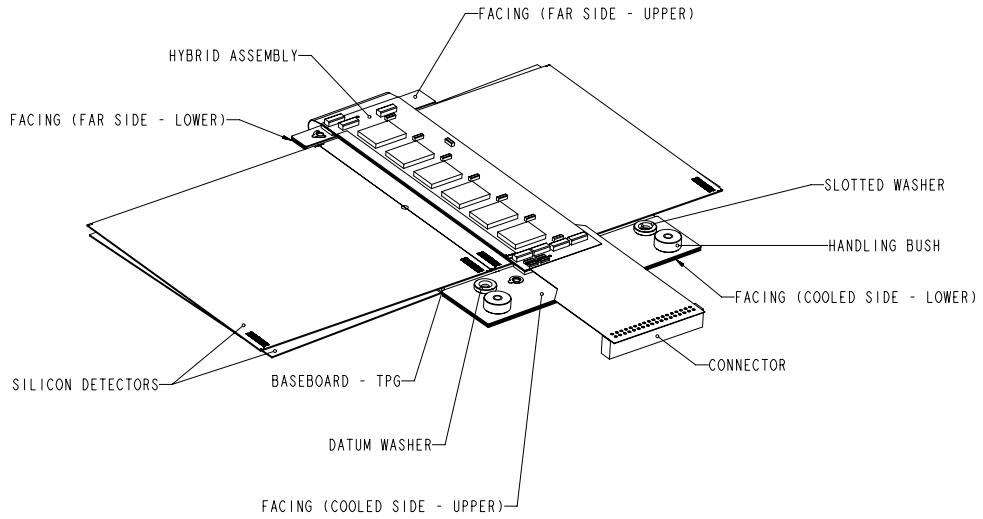

Figure 4.5.: Schematic view of an ATLAS SCT silicon strip detector barrel module. [155]

In the disks of the endcaps three different module types exist. Similar to the barrel layout, each module hosts two sets of daisy-chained sensors glued back-to-back onto a central TPG base plate for cooling and mechanical support. The trapezoidal p-in-n endcap sensors host 768 radial strips (constant orientation in ϕ) with a mean pitch of $\approx 80\,\mu$m. Again, two sensors are arranged at a stereo-angle of ± 20 mrad with respect to each other, which results in an intrinsic effective stereo space-point resolution of $17\,\mu$m in r-ϕ and $580\,\mu$m in r in the SCT disks. The strips on each module side are read out via 2×6 front-end ICs mounted onto two polyimide flex-hybrid on carbon base-plates that are attached via glass fan-ins on either side of one end of the TPG base plate.

The SCT in total covers an active area of silicon of $63\,\mathrm{m}^2$ and features a total of ≈ 6.3 million readout channels. Each of the 12 ASICs on a SCT module comprises 128 readout channels. Each readout channel implements two parts, an analog frontend consisting of a charge-sensitive pre-amplifier, signal shaper and programmable discriminator (nominal threshold 1 fC), and a digital part which implements a binary pipeline to store the hit information, and a de-randomiser and compression logic for sending out the data upon receipt of a L1 trigger signal (see Section 4.2.4). The data of one module are read out via two serial links connecting to all readout ASICs from both ends in a daisy-chained layout. The data are sent off-module at a rate of 40 Mbps via low-mass electrical links and are converted into optical signals on patch-panels outside of the active SCT volume. In the opposite direction similar links exist to provide the clock, trigger and control signals for each SCT module. The optical signals are then send further to/from off-detector electronics (readout drivers located in service caverns ~ 80 m away) via radiation-hard optical fibres. A similar data transmission scheme exists for the Pixel detector, although

higher data link counts and speeds (up to 2×80 Mbps) are required for connecting parts of the modules in order to account for the higher hit rates in the lower Pixel layers close to the IP.

Transition Radiation Tracker

The Transition Radiation Tracker (TRT) resides at the outermost radii of the ATLAS Inner Detector between $r = 563$ mm and $r = 1066$ mm [155]. The TRT consist of a total of approximately 300,000 Al-coated polyimide drift tubes (gaseous straw tubes) filled with a gas mixture of 70% Xe, 27% CO_2 and 3% O_2, and a gold-coated tungsten wire in their centre serving as the anode. The tubes are 4 mm in diameter, and in the barrel region are arranged in 73 layers of 144 cm long tubes in parallel with the beam axis, see Figure 4.4. In the barrel their anode wires are divided at half length (≈ 0) and readout from both sides to reduce the hit occupancy. In addition, two endcaps each are equipped with nine wheels of 37 cm long straw tubes that are arranged radially (constant orientation in ϕ) in 160 layers between $z = 827$ mm and $z = 2744$ mm.

All tubes are arranged in arrays which are interleaved with a transition radiation material which consists of carbon and polypropylene fibres in the barrel region, and polypropylene radiator foils in the wheels of the endcaps. Particles traversing the radiator material emit X-ray photons that are absorbed by the gas mixture. Depending on the particles' gamma factor, the amount of emitted X-ray photons differs. This allows for a discrimination of lighter particles (electrons) from others (pions) already in the ID region by combining the signal information with respect to two different thresholds, a low one (~ 300 eV) used for the actual tracking by registering charged particles ionising the gas in the tube, and a high threshold (~ 6 keV) used to register the absorption of transition radiation. On average, electrons with $E > 2$ GeV pass at least 36 straws and are expected to cause approximately seven to ten high-threshold hits from transition radiation. Apart from its particle identification capabilities the TRT provides additional track information at outer radii in the r-ϕ plane at an intrinsic accuracy of 130 μm per straw and within an pseudorapidity range of $|\eta| < 2.0$.

4.2.2. Calorimeters

The ATLAS calorimetry system [155, 169] covers a pseudorapidity range of $|\eta| < 4.9$ and comprises of two subdetectors using different technologies: an electromagnetic sampling calorimeter for the precise measurement of electrons and photons, and different types of hadronic sampling calorimeters at outer radii and z-positions, see Figure 4.6.

Electromagnetic Calorimeters

The Electromagnetic (EM) calorimeter [155, 171] is a sampling calorimeter which consists of lead absorbers interleaved with electrodes and liquid argon (LAr) in between the gaps as active material. They are arranged in an accordion-shaped geometry to provide full symmetry without inactive regions in ϕ. The EM calorimeter barrel part covers a pseudorapidity range of $|\eta| < 1.475$ and is divided into two half-cylinders of 3.2 m length,

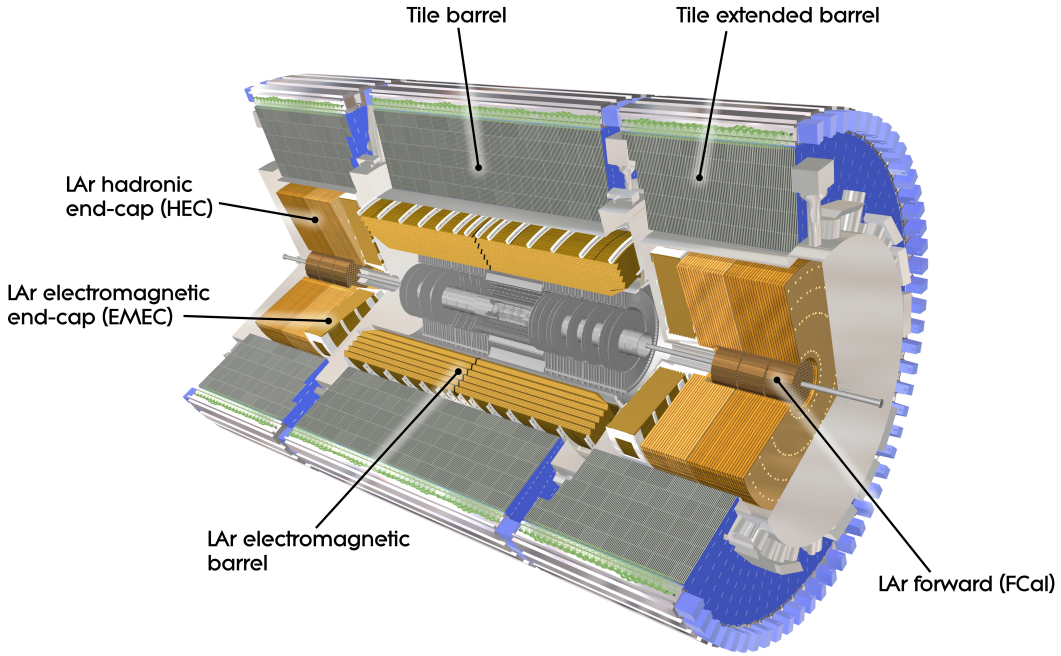

Figure 4.6.: Cutaway illustration of the different ATLAS electromagnetic and hadronic calorimeter subsystems. [170]

separated by a 4 mm gap at $z = 0$, and each hosting 1024 absorber layers interleaved with readout electrodes. The barrel part is complemented by two concentric wheels in the endcaps covering pseudorapidity regions of $1.375 < |\eta| < 2.5$ (outer wheel, 768 absorbers/electrodes) and $2.5 < |\eta| < 3.2$ (inner wheel, 256 absorbers/electrodes). The total thickness of the EM calorimeter in terms of radiation lengths amounts to $> 22\,X_0$ in the barrel part and $> 24\,X_0$ in the endcaps.

The region of the barrel and outer wheels ($|\eta| < 2.5$) to large parts is segmented into three sections in r – see Figure 4.7 for an illustration of a typical barrel module layout. The first layer is segmented into strips ($\Delta\eta \times \Delta\phi = 0.025/8 \times 0.1$) and serves as a preshower detector for improved photon separation. The second layer provides the highest granularity ($\Delta\eta \times \Delta\phi = 0.025 \times 0.025$) since it is in that layer with a depth of $\approx 16\,X_0$, where the largest fraction of the shower energy is deposited. The third layer collects the shower tails and provides a coarser granularity ($\Delta\eta \times \Delta\phi = 0.05 \times 0.025$). The inner wheels ($|\eta| > 2.5$) and the regions with $|\eta| < 1.5$ of the outer wheels only comprise a twofold segmentation in depth and have a coarser transverse granularity.To account for the early onset of the shower evolution and hence energy loss of electrons and photons due to the material of the ID and solenoid magnet, the region within $|\eta| < 1.8$ is equipped with additional presampler detectors inside the barrel cryostat. The presamplers consist of separate thin liquid-argon layers, 11 mm/5 mm in depth in

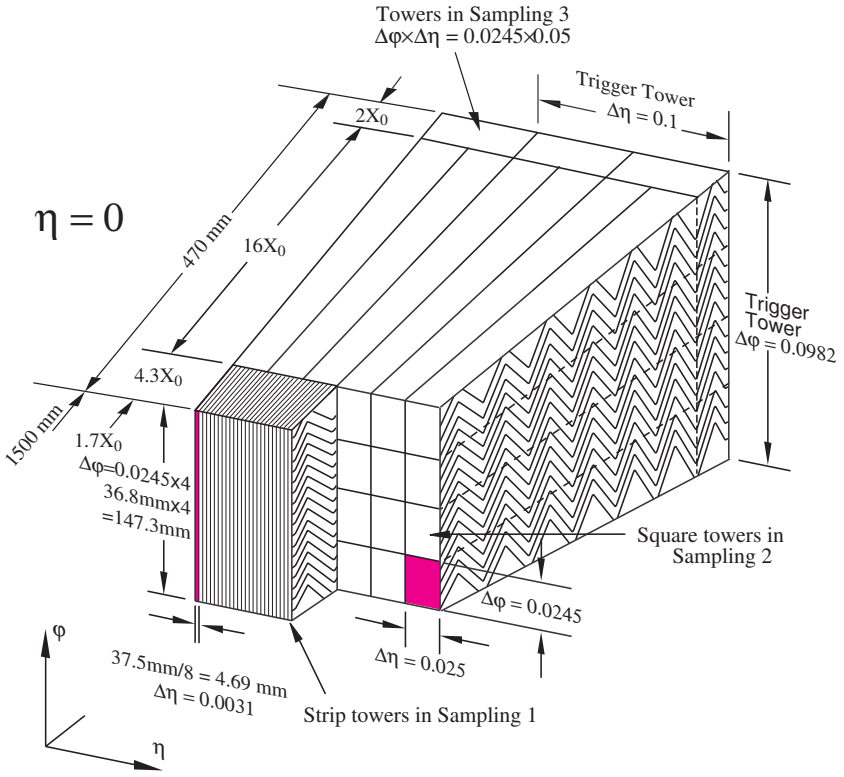

Figure 4.7.: Illustration of an ATLAS electromagnetic LAr calorimeter module in the barrel part. Each module consists of three absorber and detector layers and three segments in depth. The front segment is read out at the inner radius side, the middle and back segments at the outer radius side of the electrode. [171]

the barrel/endcap regions, which provide additional early sampling information of the electromagnetic showers. In total the EM calorimeter is designed to reach an energy resolution of $\sigma_E/E = 10\%/\sqrt{E[\mathrm{GeV}]} \oplus 0.7\%$ [164].

Hadronic Calorimeters

The ATLAS hadronic calorimeter [155, 172] provides high spatial granularity and sampling resolution for hadronic showers within a pseudorapidity range of $|\eta| < 3.2$ and features an additional high-density LAr forward calorimeter ($3.2 < |\eta| < 4.9$) to reconstruct jets at very small polar angles. The central part consists of two subsystems, the Tile Calorimeter and the Hadronic Endcap Calorimeter. The first radially follows the EM calorimeter and covers a pseudorapidity range of $|\eta| < 1.7$, at radii between 2.28 m and 4.25 m. It is build from 64 modules in ϕ, segmented into three layers in depth

with steel (absorber) plates ($d \approx$ 4-5 mm) alternating with scintillating plastic plates ($d \approx 3$ mm) as the active material. The latter are read out in groups from the inner and outer radius sides using wavelength shifting fibres connecting to photomultiplier tubes, thereby building cells of $\Delta\eta \times \Delta\phi = 0.1 \times 0.1$ (first two layers) and of $\Delta\eta \times \Delta\phi = 0.2 \times 0.1$ (last layer), respectively.

The Endcap Calorimeter covers a pseudorapidity range of $1.5 < |\eta| < 3.2$ and hence overlaps with the Tile Calorimeter and LAr forward calorimeters to provide full hermeticity. It precedes the EM calorimeter endcaps, and similar to these, consists of two wheels on either side. Each wheel is build from 32 modules divided into two segments in depth that consist of copper (absorber) plates ($d \approx 25$ mm or $d \approx 50$ mm) alternating with LAr gaps ($d \approx 8.5$ mm) as active material that is interleaved by three electrodes. The modules are read out in cells of $\Delta\eta \times \Delta\phi = 0.1 \times 0.1$ ($|\eta| < 2.5$ region) or $\Delta\eta \times \Delta\phi = 0.2 \times 0.2$ ($|\eta| > 2.5$). The total thickness of the Tile and Hadronic Endcap Calorimeters in terms of interaction lengths amounts to approximate $9.7\,\lambda$ and the nominal energy resolution is specified as $\sigma_E/E = 50\%/\sqrt{E[\text{GeV}]} \oplus 3\%$ [164].

The LAr forward calorimeter is placed approximately 1.2 m outwards in z with respect to the front-face of the EM calorimeter in order to reduce the amount of neutrons backscattered into the ID region (neutron albedo). It therefore is limited in depth ($\approx 10\,\lambda$) and implemented in a high-density design consisting of three three 45 cm deep modules per endcap comprising a metal (absorber) matrix with regularly spaced longitudinal channels filled with concentric metal rods and tubes in parallel to the beam axis. The latter serve as an electrode structure and LAr in the gaps between the rods and the tubes serves as the sensitive medium. The first module (copper), is optimised for electromagnetic shower measurements, whereas the other two (tungsten) are optimised for high absorption lengths to measure the energy of hadronic interactions. The forward calorimeter has a nominal energy resolution of $\sigma_E/E = 100\%/\sqrt{E[\text{ GeV}]} \oplus 10\%$ [164].

4.2.3. Muon System

The outermost subdetector of ATLAS comprises of the Muons Spectrometer (MS) [155, 173] that measures the trajectories and momenta of charged particles exiting the calorimeters (mostly muons) within a pseudorapidity range of $|\eta| < 2.7$ by bending their tracks in a magnetic field. The MS consists of four different types of trigger and high-precision tracking chambers that are arranged in three concentric cylindrical layers at radii of approximately 5 m, 7.5 m, and 10 m in the barrel part, and four wheels at z-positions of $\pm$7.4 m, $\pm$10.8 m, $\pm$14 m, and $\pm$21.5 m in the endcaps, see Figure 4.8.

Monitored Drift Tube (MDT) chambers provide precision momentum measurements and are installed over almost the full pseudorapidity range. The chambers consist of three to eight layers of Al drift tubes with a diameter of 30 mm. They are filled with a gas mixture of 93% Ar and 7% CO_2 and host a 50 μm W/Re wire in their centre serving as the anode. They provide an average resolution of 80 μm per tube (or $\approx 35\,\mu$m per chamber) in the track bending direction (η). Cathode-Strip Chambers (CSC) are used in the very forward region ($2 < |\eta| < 2.7$) of the innermost wheels to account for the higher muon track density in that region. They provide higher granularity and

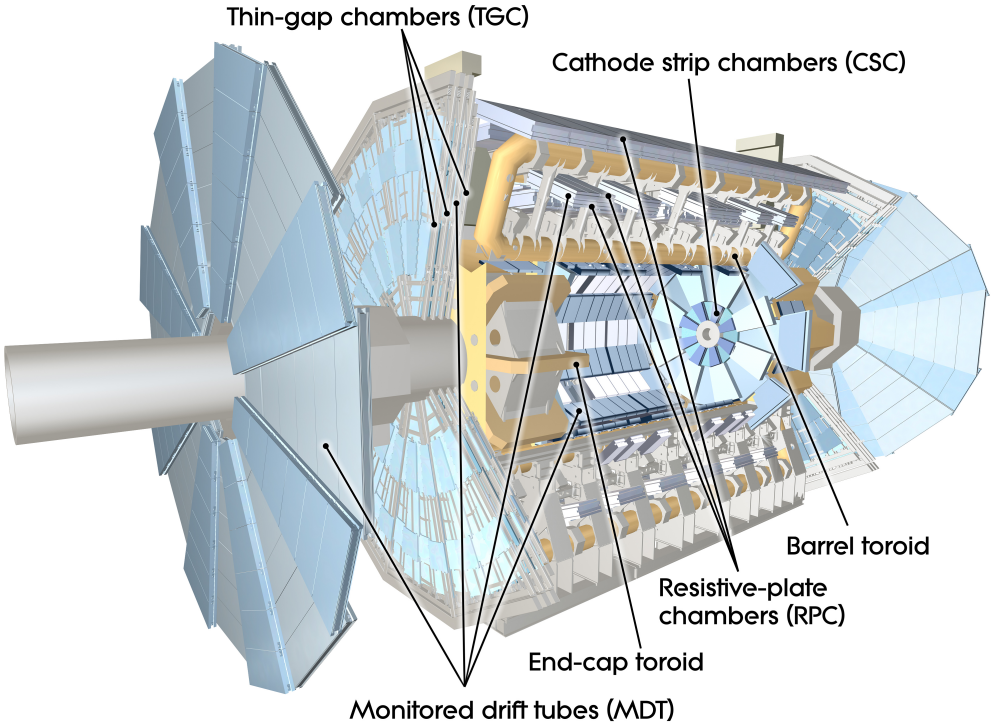

Figure 4.8.: Cut-away illustration of the ATLAS muon spectrometer subsystems. [174]

time resolution by measuring the muon tracks in four consecutive planes of multi-wire proportional chambers with cathodes segmented into strips on both sides.

The MS includes a dedicated trigger system (see also next section) that covers a pseudorapidity region of $|\eta| < 2.4$ and feature the high time resolution (bunch crossing identification) and a fast response, which the MDTs and CSCs cannot provide due to their intrinsically large drift times. It provides fast information on the muon track multiplicity and approximate energy information for triggering, and in addition complements the MDT information by a second coordinate measurement in the non-bending (ϕ- or r-) direction.

Within the pseudorapidity range of $|\eta| < 1.05$, Resistive Plate Chambers (RPCs) are used. The RPCs consist of two sets of parallel resistive electrode plates placed at at a distance of 2 mm and the gap filled with a gas mixture of $C_2H_2F_4$, C_4H_{10} and SF_6 (94.7%, 5% and 0.3%, respectively). The signals are read out via (AC coupled) metallic strips at the plates outer face (i.e. no wires are used). The latter are segmented in η and ϕ and hence allow for a measurement in both projective planes. The RPCs are arranged in three concentric cylindrical layers in the barrel, two of which enclose the MDTs of the middle layer at radii of approximately 5 m and 7.5 m, and the third located close to the outer MDT layer at $r \approx 10$ m. They are complemented by four layers in the endcaps, one in front and two behind the second MDT wheel plus an additional layer located in front of the innermost wheel.

In the range of $1.05 < || < 2.4$ so-called Thin Gap Chambers (TGCs) are used. These are multi-wire proportional chambers comprising a thin (2.8 mm) gap between two cathode (copper) planes, with two layers of wires (anodes) placed with a pitch of 1.8 mm in between. The gap is filled with a gas mixture of CO_2 and n-pentane. Like in the RPCs, the cathode planes are segmented into readout strips oriented orthogonally to the wires to also provide a measurement in the azimuthal coordinate. The TGCs are arranged in circular disks mounted in two concentric rings of seven and two layers of TGCs, covering pseudorapidity ranges of $1.05 < |\eta| < 1.92$ and $1.92 < |\eta| < 2.4$, respectively.

The overall goal for the (stand-alone) tracking performance of the MS in terms of transverse momentum resolution is specified as $\sigma_{p_T}/p_T = 10\%$ for 1 TeV muon tracks [164]. Similar to the ID, the MS is embedded in a strong magnetic field in order to bend the muon tracks for measuring their momenta and identifying their charge. The magnetic field of the muon system is provided by eight superelliptical-shaped coils with an axial extension of 25.3 m each. They are arranged symmetrically in an octagon with inner and outer diameters of 9.4 m and 20.1 m, respectively. The toroidal magnet system is complemented by two smaller toroid magnets at each end-cap of the muon spectrometer. Both magnet systems provide a nominal toroidal magnetic field of approximately 0.5 T in the central, and 1 T in the end-cap region of the MS, with a lower bending power in the overlap (transition) region of both. The resulting field (in its full extend) is highly non-uniform due to distortions from large magnetisable components in its surrounding volume, such as the Tile Calorimeter, the massive steel frame support of the MS, outer platforms, etc. It therefore needs to be modelled and monitored accurately ($\mathcal{O}(1\,\mathrm{mT})$) with the help of ~ 1800 B-field sensors to achieve the resolution in the muon momentum reconstruction given above.

4.2.4. Trigger and Data Acquisition System

The readout, processing and storage of all events created at the LHC at a bunch-crossing rate of 40 MHz is technically not feasible for reasons of limited bandwidth and storage capacities. On the other hand, the analysis of low rate phenomena with extremely low cross-section requires large data statistics and hence substantial amounts of collision events to be recorded. To select only those events which are of interest for physics analyses and to reduce the total number of events to be stored to the presently permitted rate of approximately 200-400 Hz, ATLAS employs a sophisticated trigger system [155, 175] which is organised in three levels. The first level (L1) trigger is based on custom purpose hardware, to large parts residing inside the detector. The second level (L2) trigger and third level Event Filter (EF) are both implemented in software that runs on dedicated commercial computing hardware outside of the detector volume and is collectively referred to as the High Level Trigger (HLT). The different trigger stages work inclusively, hence each trigger decision is refined in the consecutive level by applying additional, more stringent selection criteria.

The L1 trigger performs an initial event selection based on information of reduced granularity from the calorimeters and from the RPCs and TGCs in the Muon Spectrom-

eter. It searches for signatures of high-p_{T} leptons and photons, highly energetic jets and hadronic τ-decays, as well as for events with large total or missing transverse energy ($E_{\mathrm{T}}^{\mathrm{miss}}$, cf. Section 6.2.4). When an event meets one of the L1 selection criteria, data are read out from pipeline buffers on the front-end electronics in the different subdetectors by issuing a L1 accept signal (L1A). Upon its receipt within a maximum latency of $2.5\,\mu$s, the data corresponding to the bunch crossing of interest (encoded in the L1A) is send to custom ReadOut Buffers (ROBs) that store the data for subsequent access and processing by the HLT and data acquisition (DAQ) system. The typical L1 output rate during the first years of operation ranged from 20-75 kHz, which corresponds to a reduction factor of ~ 500 with respect to the nominal bunch-crossing rate. The maximum L1 rate is specified with 100 kHz. To reduce the total amount of data that needs to be read from the ROBs for processing at the L2 trigger stage, the L1 trigger defines Regions of Interest (RoIs) around the identified trigger objects.

The L2 trigger stage is seeded with the L1 RoI information and uses the full granularity and precision of calorimeter, MS and also ID measurements within the RoIs only, thereby reducing the data volume to be read and processed by the L2 trigger to a level of 2% of the full detector data. Within an average latency of ≈ 10 ms the L2 trigger reduces the event rate by another factor of ~ 20 to values below 3.5 kHz. If an event meets the L2 selection criteria, the full detector data of the event is read out and passed to the EF stage.

The EF accesses the full detector information at full granularity to select events using more complete and detailed calibration information and algorithms close to the final "offline" algorithms that are used to identify and reconstruct objects in the final processing and analysis of the stored data. Within an average latency of ~ 1 s the EF stage thereby reduces the number of events by another factor of 10-20, down to nominal rates of ~ 200 Hz at which the full event information is read out and stored for its subsequent offline analysis.

If the expected output rate for a particular trigger configuration and trigger level exceeds the rate permitted by the subsequent trigger stage or that of the final event readout and storage, so-called pre-scalings can be applied which reduce the trigger output rate as required by randomly discarding events for a given trigger chain, stage or particular trigger signature. In dependence of the initial trigger object found, the events passing the EF are associated and written to distinct data streams or channels which are later selected for offline analysis as appropriate. Hence, due to the inclusive trigger and streaming model, the same events may appear in different data streams reflecting a given trigger menu, i.e. when having passed triggers for electrons, muons, photons, τ-leptons, missing (transverse) energy, or jets.

5. Data and Simulated Samples

In this analysis it is searched for single top-quark production via strong FCNC interactions using data from p-p collisions at a centre-of-mass-energy of $\sqrt{s} = 8$ TeV taken by the ATLAS detector during 2012. Signal samples of the top-quark FCNC signal events as well as samples for SM background processes are generated using simulations from different Monte Carlo (MC) generators followed by a detector and trigger simulation. Finally, the same offline reconstruction methods as used with observed data are applied to the simulated samples.

The following section summarises the data samples used for the analysis, followed by a section which details the functional principles of the different steps in the MC simulation chain. A third and fourth section summarise the MC generators used to simulate the signal and the different background processes, including details on the predicted cross-sections and their uncertainties. In the last two sections the detector simulation and the pile-up reweighting are discussed.

5.1. Data Samples

During 2012 the LHC was operating at a centre-of-mass energy of 8 TeV, the highest energy ever reached at a hadron collider. In terms of instantaneous luminosity, the LHC broke its own record from 2011 by delivering up to $\mathcal{L} = 7.7 \times 10^{33}\,\mathrm{cm}^{-2}\mathrm{s}^{-1}$ with a total number of 1374 proton bunches colliding [161].
During the 2012 data taking period the LHC has delivered a total integrated luminosity of $\mathcal{L}_{\mathrm{int}} = 23.3 \pm 0.8\,\mathrm{fb}^{-1}$ with proton-proton collisions. The total recorded luminosity by ATLAS amounts to $\mathcal{L}_{\mathrm{int}} = 21.7\,\mathrm{fb}^{-1}$, corresponding to a data-taking efficiency of 93%. The total delivered and recorded integrated luminosity vs. day in 2012 is shown in Figure 5.1.

Within this analysis data-sets from proton-proton collisions recorded with the ATLAS detector between April 4th and October 24th 2012[1] are used. Events are selected using single electron and muon triggers without any pre-scaling applied. The events have to pass a filter, the Good Run List (GRL), which ensures that only those events are taken into account which were recorded during stable beam operation of the LHC (stable beams flag on) and with all detector components and trigger systems fully operational (all data quality flags set). The resulting data-set corresponds to a total recorded luminosity of $14.1 \pm 0.4\,\mathrm{fb}^{-1}$ out of $14.6\,\mathrm{fb}^{-1}$ delivered by the LHC. The fraction of the full 2012 dataset

[1] These correspond to the data-taking periods A1 (run number 200804) through H3 (run number 213155) – periods the data-sets are grouped into and which reflect the changes in the LHC beam parameters during the 2012 data-taking.

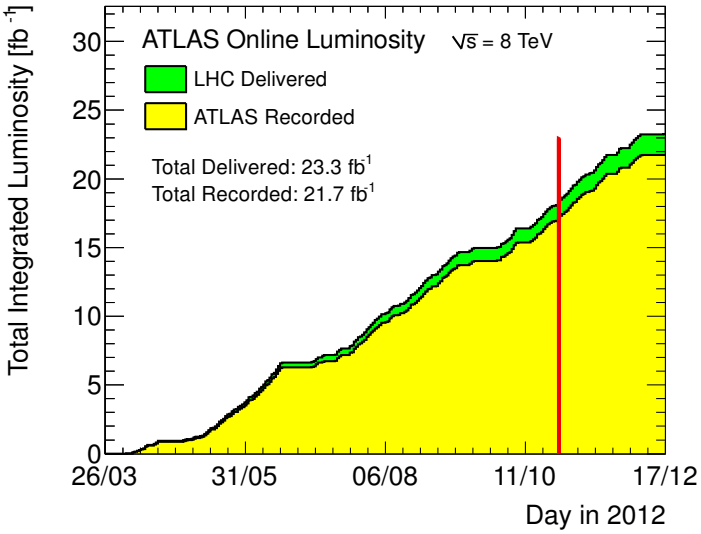

Figure 5.1.: Cumulative luminosity versus day delivered by the LHC (green), and recorded by the ATLAS experiment (yellow) for proton-proton collisions at 8 TeV centre-of-mass energy during stable beam conditions in 2012 [176]. Shown is the luminosity as determined from counting rates measured by the different luminosity detectors, which were calibrated using van-der-Meer scans [177, 178] performed in November 2012. The red line denotes the fraction of the dataset used in this analysis.

used in this analysis is indicated by a red line in Figure 5.1. The relative uncertainty on the integrated luminosity is 2.8% and was derived from a preliminary calibration of the luminosity scale using van-der-Meer scans performed in November 2012, following the same methodology as detailed in Ref. [179].

5.2. Monte Carlo Simulation

Monte Carlo (MC) techniques are employed to make predictions for collision events of physics processes contributing to the signal and all possible SM background processes. They play a key role in the data analysis of high energy physics experiments as they encode our current best knowledge of the kinematic properties and rates of particle interactions occurring in the SM, as well as the expected characteristics of the signal processes under investigation. As they are used to estimate the background yields after the event selection and to calculate the acceptance for the signal process, in particular for the search of low rate phenomena and precision measurements MC simulation with the highest possible accuracy need to be employed.

Events from hadron collisions at high energy particle accelerators usually contain a large number of particles originating from a complex manifold of interactions and pro-

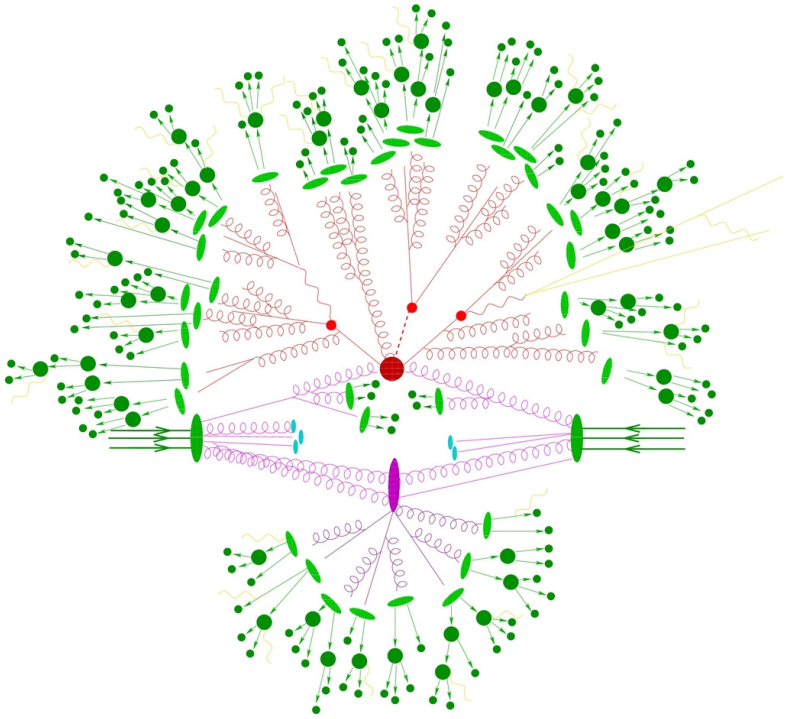

Figure 5.2.: Illustration of a p-p collision including the hard-process and underlying event interactions, parton-showering and the parton-to-hadron transition [181]. The red circles denote the hard interaction, the green ellipses interactions modelled in the parton shower. Additional spectator interactions are shown in purple and the decay of long-lived particles in dark green.

cesses as illustrated in Figure 5.2. To simulate events in the ATLAS detector, a sophisticated framework [180] exists which establishes a simulation chain consisting of several stages. First the proton-proton collision itself is simulated. Partons[2] from within the proton contribute to the actual hard interaction of interest. The hard interaction part is simulated using matrix element (ME) generators and is depicted in red in Figure 5.2. Unstable particles may be produced which decay after a short life-time and lead to a chain of intermediate particles and subsequent decay processes that have to be simulated taking into account conservation laws, spin and other correlations transferred from the incoming particles. The produced particles may split into, or radiate other particles, leading to a parton shower (PS) which is simulated at a subsequent stage by so-called

[2]Parton: The principle of asymptotic freedom allows for treating the constituents of hadrons as free particles in high-energetic collisions. The parton model provides a high-energy approximation and description of the compositeness of hadrons (such as protons), which are described within a reference frame where they have infinite momentum (high energy limit) and as being composed of a resolution scale-dependant superposition of point-like constituents, so-called "partons". For low resolution scales Q^2 the parton composition converges to the known 3 valence partons (quarks) for baryons and two ($q\bar{q}$-pair) for mesons.

PS generators. The further the shower evolves the lower the energy scales at which the subsequent processes occur. As the confinement becomes more and more effective, quark-antiquark pairs and quark triplets within the shower become strongly connected and transform into mesons and baryons. These hadronisation processes cannot be calculated but only be modelled due to their non-perturbative nature. In Figure 5.2 these are depicted by green ellipses. Multiple interactions may occur besides the hard interaction, originating e.g. from the proton remnants, which are referred to as the underlying event. In Figure 5.2 these spectator interactions are illustrated in purple. In the event simulation they are accounted for by tunes of the MC generators to observed data. Thereafter the decay of long-lived particles such as τ leptons and B hadrons are simulated, shown in dark green in Figure 5.2. In a last step called detector simulation, the interaction of all final-state particles with the detector material, the signal generation in the active detector material as well as the subsequent processing of these signals by the detector electronics are simulated. Hence, the format of the simulation output is identical to the output of the detector during real data-taking of collision events. In the following all steps considered in the full event simulation will be discussed in more detail.

The crucial quantity for a scattering experiment is the cross-section which provides a measure of probability to find a particular final state of particles from the interactions of two or more particles in a defined initial state. The interaction of two hadrons (e.g. two protons p) with the momenta p_1 and p_2 within the parton model [182] is defined as the combination of a hard interaction with a high invariant momentum transfer Q^2 and an underlying event. Using the factorisation theorem the perturbative and non-perturbative processes can be factorised (see e.g. [183, 184]), such that the total cross-section of the hadronic interaction can be written as

$$\sigma_{\text{had}} = \sum_{a,b} \iint F_a(x_1, \mu_f^2)\, F_b(x_2, \mu_f^2)\; \hat{\sigma}_{ab\to X}\left(x_1 p_1, x_2 p_2, \alpha_s(\mu_r^2), \frac{Q^2}{\mu_f^2}, \frac{Q^2}{\mu_r^2}\right) dx_1\, dx_2\,,$$

where x_1 and x_2 denote the momentum fractions of the partons (a, b) that contribute to the actual hard interaction with the cross-section $\hat{\sigma}$. The momentum distribution of the partons constituting the proton is described by the parton distribution functions (PDF) F_a and F_b. The PDFs provide a probability measure of a parton of a certain type and longitudinal momentum fraction x to be found in the proton at the resolution scale Q^2. The parton densities cannot entirely be obtained by perturbative QCD calculations. Therefore the variation of parton densities of the proton are measured experimentally with probes of different resolution scales, such as in collisions from hadron and e-p colliders, see e.g. [185]. Figure 5.3 gives an example of the proton PDF based on fits to combined datasets of the experiments at the HERA e-p and the Tevatron p-$\bar{\text{p}}$ accelerators [59]. The factorisation scale μ_f defines the separation between the contributions described by the PDFs and the partonic (hard) interaction. Choosing a large factorisation scale leads to more collinear partons being absorbed in the PDFs while small values for μ_f results in these partons being described in the hard interaction part. The renormalisation scale (cf. Section 2.2) and factorisation scale are usually set equal to the scale of the partonic interaction itself, $\mu_f^2 = \mu_r^2 = Q^2$, to avoid large logarithmic

terms leading to perturbation theory to break down.

Since the running coupling for the hard interaction is usually small, its cross-section can be expanded in a finite series of α_s

$$\hat{\sigma}_{ab\to X} = \alpha_s^k \sum_{m=0} \alpha_s^m \, \hat{\sigma}_m \,, \tag{5.1}$$

The contributions $\hat{\sigma}_m$ are calculated by integrating the respective matrix element (ME) over the phase space volume of interest. The differential cross-section for the hard interaction of the partons in an arbitrary $2 \to n$ scattering process is given by:

$$d\hat{\sigma} = \frac{(4\pi)^4 |\mathcal{M}|^2}{\sqrt[4]{(p_1 p_2)^2 - m_1^2 m_2^2}} \,, \tag{5.2}$$

where p_1 and p_2 are the four-vectors and m_1 and m_2 the masses of the particles in the initial state. The matrix element, $\mathcal{M}$, is Lorentz-invariant and encodes the full dynamics of the scattering processes including spins and couplings, i.e. how the free particles from the initial state are mapped to free particles in the final state. A full description of the calculation of the matrix elements from Feynman diagrams of different orders can be found in [23].

Matrix element or parton-level generators are used to generate events for a defined composition of particles in the initial and final state. They provide the identification of sub-processes contributing to the interaction and calculate the corresponding amplitudes or reduced matrix elements $\mathcal{M}_{fi}$ for each. Since the latter usually are only calculated up

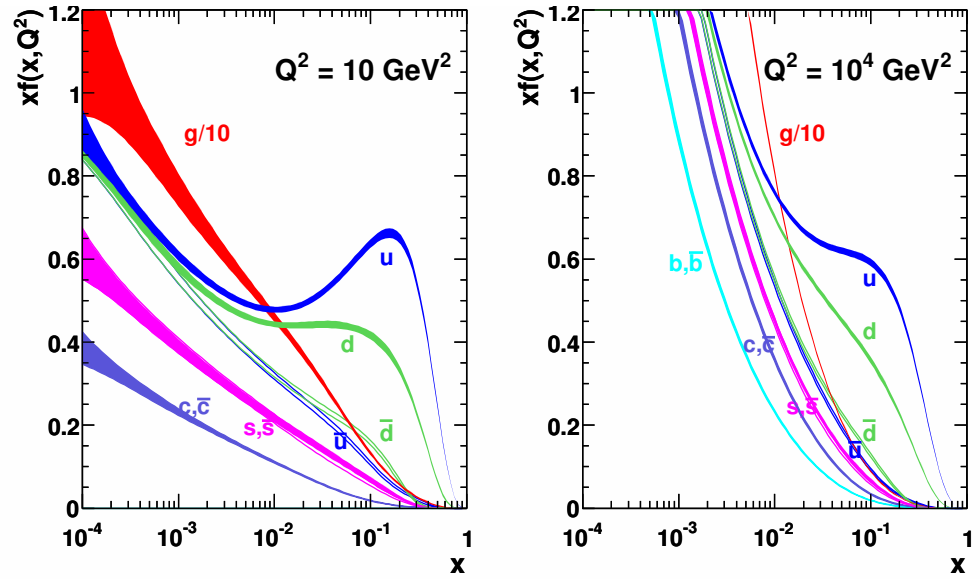

Figure 5.3.: MSTW 2008 NLO PDFs (at 68% C.L.) of the proton at resolution scales of $Q^2 = 10$ GeV^2 (left) and $Q^2 = 10^4$ GeV^2 (right) [59].

to a certain order in α_s by perturbative approximation, only a limited order of Feynman diagrams and thus number of particles in the final state can be described. The information from all contributing sub-processes is then used to calculate the cross-sections at the given order and to generate events at parton level, which means only elementary particles like leptons, single quarks and gluons are generated in the final states.

To obtain a more comprehensive description of the full interaction, additional collinear and soft emissions in the initial and final state, so-called initial and final state radiation (ISR/FSR), as well as hadronisation processes have to be accounted for. The first can be described by another factorisation term in Equation 5.2. Therefore ME generators usually are directly interfaced to so-called parton-shower (PS) generators. The parton shower model describes an iterative procedure to simulate higher order QCD emissions and hadronisation processes in a simplified manner. Additional collinear and soft emissions e.g. of gluons, like $q \to gq$ and $g \to gg$, or from gluon splitting $g \to qq$ are approximated by evolving the parent parton from the ME generator in a series of branchings of the form a $\to$ bc, where each daughter particle (b, c) may emit additional partons. A priori the order of these branchings is undefined which is why an evolution scale has to be introduced. It can be interpreted as a time scale providing an ordering mechanism in the shower evolution. In many cases variables like the invariant mass or virtuality Q^2, the transverse momentum (p_{T} ordering) or the angular distance between the outgoing partons (angular ordering) are used. In the parton shower model a process of the form $2 \to n$ is usually factorised into a set of plain $2 \to 2$ or $1 \to 2$ processes to approximate multiple soft and collinear emissions. To avoid the confinement effects in the non-perturbative region, a cut-off at energy scales of $\mathcal{O}(1\ \mathrm{GeV})$ is applied below which no soft emissions are simulated. To simulate the full set of processes the shower is factorised into, the PS formalism does not rely on explicit ME calculations. Instead it is based on branching fractions calculated at LO which are evolved to different momentum scales using the Dokshitzer-Gribov-Lipatov-Altarelli-Parisi (DGLAP) equations [186–188]. Divergences and their cancellations are accounted for using Sudakov form factors [189] which expand the DGLAP equations and assure that the probability for the branching of a parton never exceeds unity. A more comprehensive description of the parton shower formalism can be found in e.g. [65].

PS generators usually also implement the simulation of hadronisation processes, also referred to as fragmentation. Hadronisation occurs as a direct consequence of the confinement which prohibits the observation of free colour-charged particles at scales larger Λ^{-1} (cf. Section 2.2). In the fragmentation process partons from the shower merge to bundles of hadrons, creating so-called "jets". In practice the hadronisation can only be described by phenomenological models due to its non-perturbative nature. Common to all these models is that they obey parton-hadron-duality, which ensures that the conservation of quantum numbers at both, parton and hadron level is fulfilled. The most commonly used hadronisation models are the so called string fragmentation and cluster fragmentation models which are described in detail elsewhere [190–194].

In general the modelling of kinematic properties for a given process may differ between different combinations of ME and PS generators. In most cases this is a result of different orders of matrix elements (LO, NLO) used in ME generators or distinct showering

and fragmentation models used within the PS generators they are interfaced to. These variations therefore have to be accounted for as an additional source of systematic uncertainty. Usually higher order matrix element (e.g. NLO) generators are preferred over LO generators as they provide a more precise description of soft emissions and hence of the overall kinematics of the simulated process, which in turn increases the confidence in the predictions.

In the interaction of two protons multiple other, partially soft interactions may occur in addition to the hard process of interest. These spectator interactions are the result of additional hard interactions originating from the remaining partons of the colliding protons as well as of contributions from beam-beam remnants and initial and final state radiation. The sum of all additional processes except the hard scattering process itself is usually referred to as the "underlying event". As the spectrum of contributions to the underlying event includes non-perturbative processes, it is in general difficult to simulate. Therefore the MC generators are tuned by fitting models of the underlying event to observed data. The two MC tunes currently most used within ATLAS and also used in this analysis are the Perugia2011C tune [195] and the ATLAS underlying event tune 2B (AUET2B) [196].

5.2.1. Simulation of the Signal Processes

Former searches for single top-quark production via FCNCs in strong interactions by experiments at the Tevatron [124, 125] and the LHC accelerator [126] used leading order (LO) matrix element event generators, e.g. PROTOS [197] or TopReX [198], to simulate the signal processes. In this analysis, MEtop [149], a new generator for simulating strong FCNC processes at NLO approximation is used. For the first time this allows for the investigation of 2 →2 processes in combination with the formerly used (LO) direct FCNC single top (2 →1) process, leading to a more comprehensive description of the expected signal shape. MEtop allows for the generation of events of several topologies, including direct single top-quark production, top-quark + gluon and top- + light-quark production as shown in Figure 5.4.

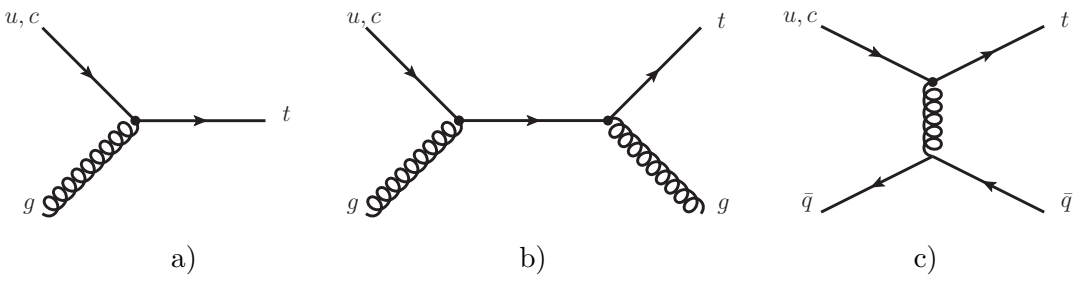

Figure 5.4.: Examples of Feynman diagrams of single top-quark production via strong FCNCs: direct single top-quark production (a), top-quark + gluon production (b) and top- + light-quark production (c).

The top-quark interactions through strong FCNCs of the form $ug \to t$ and $cg \to t$ are introduced through two different effective operators (cf. Equation 3.4):

$$\mathcal{O}_{uG} = i\frac{g_s}{\Lambda}\,\bar{u}\,\lambda^a\sigma^{\mu\nu}\,(f_u + h_u\gamma_5)\,t\,G^a_{\mu\nu} \quad \text{and} \tag{5.3}$$
$$\mathcal{O}_{cG} = i\frac{g_s}{\Lambda}\,\bar{c}\,\lambda^a\sigma^{\mu\nu}\,(f_c + h_c\gamma_5)\,t\,G^a_{\mu\nu}\,,$$

where f_q and h_q $(q = u, c)$ are real constants which define different chiralities of the produced top quark and which are normalised by requiring $f_q^2 + h_q^2 = 1$. The values for f_q and h_q have to be set as configuration parameters within METOP and were chosen such that only purely left-handed top quarks are produced. This represents the most conservative assumption since in the SM single top quarks are solely produced with left-handed polarisation. Allowing for any right-handed contributions would give rise to additional differences in the kinematic properties of the signal process in comparison to SM top-quark production. As these differences are to be used to distinguish signal from background events in the later analysis, a higher separation could be achieved since right-handed polarisations would reflect in particular in the angular distributions of the top-quark decay products. If right-handed contributions do not exist in nature, this would lead to an overestimation of the sensitivity of the analysis. Given Equation 5.3 the full strong FCNC Lagrangian as used within METOP can be written as:

$$\mathcal{L}_S = c_1\,\mathcal{O}_{uG} + c_2\,\mathcal{O}_{cG} = i\,\kappa_{ugt}\,\frac{g_s}{\Lambda}\,\bar{u}\,\lambda^a\sigma^{\mu\nu}\,(f_u + h_u\gamma_5)\,t\,G^a_{\mu\nu}$$
$$+\,i\,\kappa_{cgt}\,\frac{g_s}{\Lambda}\,\bar{c}\,\lambda^a\sigma^{\mu\nu}\,(f_c + h_c\,\gamma_5)\,t\,G^a_{\mu\nu}\,,$$

where c_1 and c_2 can directly be identified as parameters for the coupling constants κ_{ugt} and κ_{cgt} defining the coupling strengths of the ugt and cgt vertex, respectively. c_1 and c_2 are used as configuration parameters within the generator and have to be defined by the user. Both parameters are chosen equal to 0.01 to represent values close to the most stringent limits currently existing, $\kappa_{ugt}/\Lambda < 0.0069$ and $\kappa_{cgt}/\Lambda < 0.016$ [126]. The parameters for the masses of the top quark, W boson and Z boson are set to 172.5 GeV, 80.403 GeV and 91.1876 GeV, respectively. A full list of configuration parameters used for the event generation can be found in Appendix E.1.

Individual samples are generated for both, the $ug \to t$ and $cg \to t$ process, where the top quark is assumed to decay like in the SM as motivated earlier, and in which only the leptonic decay modes of the W boson are considered. Table 5.1 lists the cross-sections times the branching ratios ($\mathcal{B}$) of the $t \to Wb$ and the subsequent leptonic W decay, as calculated with METOP using the above values for c_1 and c_2. To ensure that the kinematic shapes of both samples are independent of the choice of the coupling constants, several samples are generated using different choices for κ_{ugt} and κ_{cgt}, both ranging from 0.002 to 0.05. From the comparison of their kinematic distributions after showering, no such dependence can be observed (see Appendix E). The CT10 [61] NLO PDF set is chosen to be used for the event generation with METOP. To simulate the parton shower and hadronisation processes METOP is interfaced to the PYTHIA 6.421 [199] generator.

Table 5.1.: Generated cross-sections times branching ratio for the $ug \to t$ and $ug \to t$ processes, determined using the METOP generator.

	t	$\bar{t}$	Total
$ug \to t$	3.41 pb	0.76 pb	4.17 pb
$cg \to t$	0.48 pb	0.45 pb	0.93 pb

For modelling the underlying event the AUET2B tune to the ATLAS data is used.

For the simulation of the inclusive direct single top-quark production at NLO, the parton level contributions to the direct top production, as well as the $gq \to gt$ process have to be considered. The latter is subject to soft and collinear divergences which can only be eliminated by including the NLO corrections. Although this can be circumvented easily for the analytical calculation of the total cross-section, it is not straightforward to handle at the level of event generation. To account for this problem, METOP uses an effective NLO approximation [200] by implementing a merging scheme between the $2 \to 1$ and $2 \to 2$ process. Each process separately populates two disjoint but contiguous regions in phase-space. Hence a matching variable must be defined which in METOP is given by the transverse momentum of the top quark, $p_{\mathrm{T}}^{\mathrm{match}}$. In the high p_{T} region events are generated using the $2 \to 2$ process. In the phase-space region with low p_{T} the hard $2 \to 1$ process is used in combination with a subsequent parton shower generated by PYTHIA.

Since PYTHIA will by default shower all direct top events produced, double counting has to be avoided. Therefore the phase-space region of the showered events of the $2 \to 1$ process have to be limited such that the first PS emission from the $2 \to 1$ process does not fall within the phase-space region populated by the hard $2 \to 2$ process generated using the ME. This can be assured using a p_{T}-ordered shower (cf. Section 5.2) as is provided by PYTHIA. In the output LHE [201] files used by the PS generator, METOP configures the starting scale for the branching in the $2 \to 1$ region to be equal to the value of $p_{\mathrm{T}}^{\mathrm{match}}$. The value for $p_{\mathrm{T}}^{\mathrm{match}}$ has to be chosen such that a smooth transition between both phase space regions is assured. Based on the studies and suggestions in [149] a value of $p_{\mathrm{T}}^{\mathrm{match}} = 10$ GeV was chosen as the matching scale since this was found to provide the best transition in the transverse momentum distribution of the produced top quark after applying the full showering with PYTHIA.

To assure the correct simulation of events and check for any errors in the implementation at least of the LO part of the event simulation within METOP, selected shape distributions of the event kinematics in samples before applying the detector simulation were compared to those of the MADGRAPH [202] and PROTOS generators which are summarised in Appendix E.3. Furthermore, the dependence on the renormalisation and factorisation scales was estimated by comparing simulation samples before the detector simulation using values of 1/2 and 2 times the nominal values, see Appendix E.4. Appendix E.4 also discusses additional comparisons, made to test the influence of a particular choice for $p_{\mathrm{T}}^{\mathrm{match}}$ within a range of 8 GeV $< p_{\mathrm{T}}^{\mathrm{match}} <$ 15 GeV and variations in the amount of initial (ISR) and final state radiation (FSR).

5.2.2. Standard Model Background Processes

Several SM processes have to be considered as background to the FCNC analysis, the simulation of which will be presented in the following in more detail. The data is searched for events in which a u or c quark interacts with a gluon to produce a single top quark. The top quark is assumed to decay like in the SM, i.e. $t \to Wb$, while for the subsequent decay of the W boson only the leptonic decay modes are considered. Consequently the full event signature in the 1-jet bin consists of a high-p_{T} b-quark jet, exactly one charged lepton and missing transverse energy ($E_{\mathrm{T}}^{\mathrm{miss}}$) from the neutrino. If searched in higher jet bins, the $2 \to 2$ processes and higher order QCD emissions from the subsequent parton shower of the $2 \to 1$ process may contribute to a similar event topology, but with extra light-jets in the final state. Hence, several SM processes are expected to have the same signature in the final state as the signal samples, the main of which are W+jets production, in particular W+jets with the associated production of heavy-flavour quarks (W+HF+jets). Additional contributions arise from SM top-quark production, Z+jets and diboson production as well as QCD multijet events. A full list of common configuration parameters used for the MC event generation of all background processes can be found in Appendix E.1.

In order to generate W, $Wb\bar{b}$, $Wc\bar{c}$, Wc as well as Z events with up to 5 additional partons in the final state, the ALPGEN v2.14 [203] LO matrix element generator is used. It is interfaced to PYTHIA v6.4 for the parton shower generation and combined with the Perugia2011C [195] tune for the underlying event simulation. For both, the ME and PS generator parts the CTEQ6L1 [153] LO PDF set is used. As in the case of signal event generation, overlaps in the phase space regions for events generated via the matrix elements and those generated using the PS mechanism occur. In case of the ALPGEN generator, overlaps between events generated for the n and $n+1$ parton samples are removed using the MLM matching scheme [203]. In addition, parts of the generated events are simulated twice across different sets of MC samples, i.e. in the inclusive W+n parton samples, in the following referred to as W+jets, and in the samples of associated heavy-flavour quark production ($Wb\bar{b}$, $Wc\bar{c}$, Wc), also denoted as W+HF+jets production. As an example, events with a W boson, a c and a u quark in the final state could arise in both, the W+2 parton and the Wc+1 parton samples. To remove those double-counted events, an overlap removal based on a ΔR matching scheme is applied which exploits the different strengths of the ME and PS generator parts, the first providing a better description for quark emissions with large opening angles, the second being better suited to simulate the collinear gluon splitting. The phase-space populated by W production in association with heavy-flavour quarks hence should not be limited by imposing phase-space cuts, since in the HF overlap removal those overlapping events should preferably be vetoed in the inclusive W+n parton samples. While feasible for the associated heavy quark pair production samples, in case of the Wc samples a cut on the transverse momentum of the final state c quark of $p_{\mathrm{T}}(c) > 10$ GeV needs to be applied. This is a consequence of the much larger production cross-sections involved. In addition, a cut on the angular distance between the c quark and the closest additional parton of $\Delta R(c, \mathrm{parton}) > 0.7$ is employed. In the Z+n parton samples the phase space is restricted to dileptons gen-

erated in the invariant mass range of 60 GeV $< m_{\ell^+\ell^-} <$ 2000 GeV. In all cases only the leptonic decay modes of the W and Z bosons are considered. The kinematic shapes and acceptances of the W+jets and Z+jets backgrounds are taken from the MC simulation. The normalisations of the samples are derived by rescaling the LO Monte Carlo results to the respective inclusive (N)NLO theory cross-section predictions. All W+jets, W+HF+jets and Z+jets samples, except the Wc+n parton samples, are normalised to the inclusive NNLO cross-section prediction given in [204, 205]. The normalisation for the Wc+n parton samples is obtained separately from the ratio between cross-sections calculated at NLO and LO precision using MCFM [206, 207]. The resulting k-factor value obtained using the CTEQ6L1 PDF set is 1.52. Details on these calculations are presented in [208], among further studies which prove the independence of the k-factor from the chosen value of the cut on $p_{\mathrm{T}}(c)$ used in the event generation. The overall flavour composition of the W+HF+jets samples is also taken from simulation.

Estimates of the cross-section uncertainties of the W+n parton and Z+n parton samples are derived using the Berends-Giele scaling [209, 210] uncertainty on the cross-section ratio $\sigma(W(Z)+\mathrm{n}+1)/\sigma(W(Z)+\mathrm{n})$ between the $W(Z)$+n+1 and the $W(Z)$+n parton samples. The relative uncertainty on the ratio is given as ±24% and is added n times in quadrature to the uncertainty of ±4% considered for the $W(Z)$+0 parton case, i.e. once for each additional parton in the final state. This results in a total relative cross-section uncertainty of ±24.3% and ±34.2% for the $W(Z)$+1 and $W(Z)$+2 parton samples respectively. From calculations in [208] the relative cross-section uncertainty of the Wc+n parton samples was estimated to be 24%, evaluated by calculating k-factors for different PDF sets and factorisation scales. However, the additional relative uncertainties from the heavy-flavour (HF) contributions are chosen to be 50% for all, the $Wb\bar{b}$, $Wc\bar{c}$ and Wc+jets samples in order to be consistent with ATLAS top-quark analysis group wide conventions. In Appendix D.2 it is shown that this rather conservative choice, despite a potential over-estimation of the resulting total cross-section uncertainty, has no impact on the final result since the normalisation uncertainties for the W+HF+jets are constrained a posteriori by observed data in the statistical analysis, see Section 10.3. The uncertainty from the HF contributions is applied as an additional uncorrelated uncertainty and thus is added in quadrature to the value of the cross-section uncertainty from the respective inclusive $W(Z)$+n parton sample. The total relative uncertainties obtained for the $W(Z)$+HF+1 and $W(Z)$+HF+2 parton samples hence are ±55.6% and ±60.6% respectively.

The matrix element generator POWHEG [211] is used in combination with with the CT10 NLO PDF set in order to generate simulated events of SM single top-quark production in the Wt- and s-channel, as well as events of SM $t\bar{t}$ production with at least one top quark decaying leptonically. To generate electroweak SM single top-quark events in the t-channel, the ACERMC v.3.7 [212] ME generator is used. Both, POWHEG and ACERMC use NLO matrix element calculations and are interfaced to PYTHIA v.6.4 using the the Perugia2011C tune for modelling the parton shower and underlying event. The $t\bar{t}$ sample cross-section is normalised to the NNLO theory prediction of $\sigma_{t\bar{t}} = 253^{+13}_{-15}$ pb for a top-quark mass of 172.5 GeV. The calculation includes resummation of next-to-next-to-leading logarithmic (NNLL) soft gluon terms with top++2.0 [52–

57]. The uncertainty includes the PDF and α_S uncertainties added in quadrature to the scale uncertainty. The PDF uncertainty was calculated using different PDF sets following the PDF4LHC prescription [58], including the MSTW2008 68% CL NNLO [59, 60], CT10 NNLO [61, 62] and NNPDF2.3 5f FFN [63] PDF sets. Consequently, a value of 6% is used for the uncertainty on the normalisation of the $t\bar{t}$ sample. The t-channel single top-quark production with the exchange of a virtual W boson has a predicted cross-section of $87.8^{+3.4}_{-1.9}$ pb [64] and the associated production of an on-shell W boson and a top quark (Wt-channel) has a predicted production cross-section of 22.4 ± 1.5 pb [65], both calculated at approximate NNLO using soft-gluon resummation at NNLL accuracy. In [66] a predicted production cross-section of 5.6 ± 0.2 pb was calculated at NNLO accuracy for the s-channel SM single top-quark production. The uncertainties reflect the scale and PDF uncertainties added in quadrature, the latter calculated using the MSTW2008 90% CL NNLO [59, 60] PDF set.

Diboson events (WW, WZ and ZZ) are simulated using the HERWIG [213] generator for the (LO) ME calculation, parton showering and hadronisation. As parton distribution function the CTEQ6L1 [153] LO PDF set is used. The underlying event is modelled using Jimmy [214] and lepton decays are modelled using Tauola [215]. Since the event signature searched for contains exactly one lepton, filtered samples are used which contain only events with a single lepton with $p_{\mathrm{T}} > 10$ GeV and $|\eta| < 2.8$ in the final state. k-factors are applied to scale the LO simulation results to the inclusive NLO theory cross-section which has been calculated using MCFM[206, 216]. The uncertainty on the cross-section prediction given for these processes amounts to 5%.

Tables 5.2 and 5.3 show a summary of all MC samples and ME/PS generators used for the simulation of the SM background processes, including their total event statistics and production cross-sections used throughout the analysis. The cross-section values include the k-factors and SM branching ratios of the simulated set of processes, as well as potential filter efficiencies of the respective sample. The latter are applied to account for the fraction of events that has been omitted in the event generation as compared to the fully inclusive simulation, such as in event samples where filters have been applied to constrain the general final state topology (e.g. WW, WZ, ZZ) or cuts were imposed on the kinematic properties of the final state objects (e.g. Wc+n, Z+n) to restrict the phase space.

Within the analysis, several MC event samples are merged, reflecting certain classes of processes with similar kinematic signatures. This is preferable since several sub-samples, e.g. of the W+jets or SM single top-quark production, show nearly indistinguishable kinematic shapes after the neural network classification, see Section 8.3 for details. In addition an individual treatment of all sub-samples would increase the number of free parameters for normalisation uncertainties drastically and lead to an impracticable increase in computation time for the final systematic analysis. Therefore all W+HF+jets, W+jets and Z+jets samples are merged into three single background samples. In accordance to the n$^{\mathrm{th}}$ jet-bin investigated, the respective W/Z+(HF)+n parton and +(n-1) parton samples dominate the event yields in the combined samples by far. For the normalisation uncertainty in the n-jet bin therefore the relative cross-section uncertainty of W/Z(+HF)+n parton sample is chosen. This results in a normalisation uncertainty

Table 5.2.: MC samples for SM single top-quark and $t\bar{t}$ production used within the analysis. The cross-section (σ) includes the filter efficiencies of the respective sample as well as the k-factors applied and SM branching ratios of the simulated set of processes. N_{MC} denotes the total event statistics of the sample.

	σ [pb]	generator	N_{MC}	k-factor
Wt all decays	22	Powheg+Pythia	1,000,000	1.09
t-channel (lepton+jets)	28	ACERMC+Pythia	9,000,000	1.10
s-channel (lepton+jets)	1.8	Powheg+Pythia	1,200,000	1.10
$t\bar{t}$ (no fully hadronic)	137	Powheg+Pythia	15,000,000	1.20

of $\pm 24.3\%$ in the 1-jet bin and $\pm 34.2\%$ in the 2-jet bin for both, the combined W+jets and the combined Z+jets samples. The uncertainty on the normalisation of the combined W+HF+jets sample hence amounts to $\pm 55.6\%$ and $\pm 60.6\%$, respectively. The diboson and Z+jets samples are treated as one background and the larger cross-section uncertainty of the Z+jets background is taken as the normalisation uncertainty for the combined sample. While the $t\bar{t}$ sample is treated as is, the samples of SM single top-quark production in the Wt-, s- and t-channel are merged into a single sample after the neural network analysis. An uncertainty on the normalisation of 5% is used for the combined contributions from all three SM single top-quark production processes. This reflects the weighted average of the cross-section uncertainties, accounting for the share the respective sample has on the combined cross-section of all three processes. Table 5.4 summarises the estimated relative uncertainties on the cross-sections of all background processes considered in case of requiring exactly one or exactly two jets in the final state.

5.3. QCD Multijet Events

The QCD multijet background arises mostly from misidentified physics objects, such as jets identified as isolated leptons. Muons and electrons are primarily subject to misidentification in semi-leptonic b-quark decays, e.g. from heavy-flavour hadrons, or from long lived weakly decaying states such as $\pi^{\pm}$ or K mesons, from which leptons are passing the isolation requirement[3]. If the leptons are emitted outside of their parent jet or the jets are not well reconstructed, the leptons may fulfil the isolation criteria and hence be wrongly accepted, mimicking the leptonic decay product of the W boson from the single top-quark decay. These fake rates are usually small ($\mathcal{O}(10^{-3})$) and the multijet background can be efficiently rejected, e.g. by requiring the event to contain a substantial amount of missing transverse energy (cf. Section 7). However, a significant amount of the background remains present due to the large production cross-section of QCD

[3] A detailed description of the identification and isolation criteria of all physics objects will be given in Section 6.

Table 5.3.: MC samples for W+jets, Z+jets and diboson production used within the analysis. The cross-section (σ) includes the filter efficiencies of the respective sample as well as the k-factors applied and SM branching ratios of simulated set of processes. N_{MC} denotes the total event statistics of the sample.

	σ [pb]	generator	N_{MC}	k-factor
$Z \to \ell\ell$ + 0 partons	848	ALPGEN+Pythia	6,620,000	1.18
$Z \to \ell\ell$ + 1 parton	203	ALPGEN+Pythia	1,330,000	1.18
$Z \to \ell\ell$ + 2 partons	70	ALPGEN+Pythia	405,000	1.18
$Z \to \ell\ell$ + 3 partons	18	ALPGEN+Pythia	102,000	1.18
$Z \to \ell\ell$ + 4 partons	5	ALPGEN+Pythia	30,000	1.18
$Z \to \ell\ell$ + 5 partons	1	ALPGEN+Pythia	10,000	1.18
$W \to \ell\nu$ + 0 partons	9219	ALPGEN+Pythia	3,450,000	1.13
$W \to \ell\nu$ + 1 parton	2030	ALPGEN+Pythia	2,500,000	1.13
$W \to \ell\nu$ + 2 partons	614	ALPGEN+Pythia	3,769,000	1.13
$W \to \ell\nu$ + 3 partons	166	ALPGEN+Pythia	1,010,000	1.13
$W \to \ell\nu$ + 4 partons	42	ALPGEN+Pythia	250,000	1.13
$W \to \ell\nu$ + 5 partons	13	ALPGEN+Pythia	70,000	1.13
$W \to \ell\nu + b\bar{b}$ + 0 partons	59	ALPGEN+Pythia	475,000	1.13
$W \to \ell\nu + b\bar{b}$ + 1 parton	52	ALPGEN+Pythia	356,000	1.13
$W \to \ell\nu + b\bar{b}$ + 2 partons	27	ALPGEN+Pythia	175,000	1.13
$W \to \ell\nu + b\bar{b}$ + 3 partons	14	ALPGEN+Pythia	50,000	1.13
$W \to \ell\nu + c\bar{c}$ + 0 partons	158	ALPGEN+Pythia	1,275,000	1.13
$W \to \ell\nu + c\bar{c}$ + 1 parton	163	ALPGEN+Pythia	1,048,000	1.13
$W \to \ell\nu + c\bar{c}$ + 2 partons	92	ALPGEN+Pythia	525,000	1.13
$W \to \ell\nu + c\bar{c}$ + 3 partons	41	ALPGEN+Pythia	170,000	1.13
$W \to \ell\nu + c$ + 0 partons	1154	ALPGEN+Pythia	6,500,000	1.52
$W \to \ell\nu + c$ + 1 parton	417	ALPGEN+Pythia	2,070,000	1.52
$W \to \ell\nu + c$ + 2 partons	109	ALPGEN+Pythia	520,000	1.52
$W \to \ell\nu + c$ + 3 partons	25	ALPGEN+Pythia	110,000	1.52
$W \to \ell\nu + c$ + 4 partons	7	ALPGEN+Pythia	20,000	1.52
WW	21	Herwig	2,500,000	1.68
WZ	6.9	Herwig	1,000,000	1.90
ZZ	1.5	Herwig	245,000	1.55

Table 5.4.: Summary of the relative uncertainty on the cross-sections of all background processes for the 1-jet and 2-jet bins.

	relative uncertainty	
Process	1-jet bin	2-jet bin
SM single top	5 %	5 %
$t\bar{t}$	6 %	6 %
W+light jets	24 %	34 %
W+HF+jets	55 %	60 %
Z+jets/diboson	24 %	34 %
Multijets	50 %	50 %

multijet events which amounts to approximately 0.01 to 0.1% of the total proton-proton cross-section which is at the order of $\sigma_{\mathrm{pp}}^{\mathrm{tot}} \approx 100\,\mathrm{mb}$ [217] at current centre-of-mass energies at the LHC. Additional fake-mechanisms for electrons arise from the conversion of directly produced photons or electromagnetic-like, pion-rich light flavour jets, in which a leading π^0 shower overlaps with a charged particle that is subsequently reconstructed as an electron.

Consequently, the QCD multijet background consequently is partially dependent on detector-related quantities such as efficiencies and parameters of the lepton identification and isolation. The misidentification (fake) rate and hence the multijet background itself is therefore difficult to model precisely using MC simulations alone which is why partially data-driven methods such as the "matrix method" or "jet electron model" are employed to obtain the shape and eventually the normalisation of this background. A detailed description of both models will be given in Section 7.3.1 after introducing the event reconstruction and selection in the Chapters 6 and 7.

5.4. Detector and Trigger Simulation

In the last step of the simulation chain the detector response to the generated events has to be simulated. The goal is to obtain an output format from simulated events which is identical to the output of the detector during real data-taking of collision events which allows to apply the same reconstruction algorithms for both types of events. The detector simulation is performed making use of GEANT4 [218], a toolkit for simulating the passage of particles through matter. GEANT4 is used to simulate the interaction of all final-state particles with the passive and active detector material and any signals (hits) obtained thereby, while accounting for resolution effects and inefficiencies in the different sub-components of the detector. In addition, the decays of long-lived particles produced by the MC generators are simulated. In a second step, called digitisation, the hits obtained by the interactions with the active detector material are transformed into analogue or digital signals to simulate the response of the detector electronics. In total, the full ATLAS detector simulation follows a inside-out scheme consisting of the following stages [180]:

- To obtain a distribution of the interaction points as close as possible to the one in the actual data taking, the events passed to the detector simulation have to be preprocessed. Using a database with records of the beam conditions during real p-p collisions the events are boosted, rotated, and their vertex positions are smeared accordingly.
- Starting from the interaction point, the passage of all final state particles through the different sub-detectors of ATLAS are simulated, including potential interactions with the detector material, showering and decay processes as well as charge depositions in the active material, the latter producing a collection of "hits" as an output for the subsequent digitisation step. The computationally most intensive part is the simulation of particle showers in the calorimeters. The total simulation time per event takes several minutes.
- In the digitisation step the obtained hits are transformed into electrical signals. Based on the detailed properties, like thresholds and noise of each readout channel, the response of the readout electronics is simulated, including dead-times and digitisation effects. A raw data object (RDO) file is created which is equivalent to the output of the readout drivers of the real detector from collision data but in addition contains the so-called truth information, i.e. the ("true") generator information of the events. Operating at high instantaneous luminosities leads to multiple proton-proton collisions occurring within one bunch-crossing, usually referred to as "pile-up" events. They are simulated by overlaying the hits from the primary interaction with those from multiple predefined events, also accounting for those from previous bunch crossings. For the MC samples used throughout this analysis, PYTHIA8 [219] minimum bias events[4] with the AM2 tune are used for the pile-up simulation. The additional pile-up collisions are then treated in the same way as the primary ones.

The detector geometry used by GEANT4 is obtained using a geometry database and model ("GeoModel" interface [220]), which are updated regularly to account for changes in the geometry or (mis-)alignment, and for studies comparing collision data and MC simulated events. They provide data on volume dimensions, positions and rotations of detector components, active and dead material as well as on the material compositions and densities. To allow accurate modelling of charged particles passing through the (position-dependent) magnetic field, a map of the ATLAS magnetic field is linked to the geometry database. A separate conditions database contains the information on the detector conditions during single data-taking runs, such as noisy or dead channels, temperatures, calibration states, as well as other information on the sub-detectors hardware and software status and configurations relevant to the event simulation. For all MC samples used in the analysis the ATLAS geometry model `ATLAS-GEO-20-00-01` is used. The settings for the geometry and database used for the different steps in the simulation of all MC samples are:

[4] Minimum bias events are measured using loose triggers to select inelastic interactions from p-p collisions with as little bias as possible. Minimum bias events may comprise diffractive and non-diffractive processes and are usually dominated by soft interactions with low momentum transfer and particle multiplicity.

- AtlasProduction 17.2.X.Y for the event generation (TAGProd 17.2.0.2.1-17.2.0.4.1)
- AtlasProduction 17.2.0.2, 17.2.2.6 and 17.2.6.2 for the GEANT4 simulation
- AtlasProduction 17.2.1.4 for digitisation and reconstruction

and the settings for the conditions database used

- GEANT4 simulation: `OFLCOND-MC12-SIM-00`
- digitisation and reconstruction: `OFLCOND-MC12-SDR-06`.

After digitisation, the RDO information from the simulation and collision data events are grouped into collections of different particle or object types using a set of "on-line" reconstruction algorithms. The outputs of these are the so-called event summary data (ESD), analysis object data (AOD) or derived physics data (DPD) files which then usually are processed further to only include the relevant information for a certain class of physics processes.

5.5. Pile-up Reweighting and z-Vertex Correction

Since the MC simulation samples were produced simultaneously with, or shortly after the actual data-taking in 2012, the variable pile-up rate used as an input for the digitisation step in the simulation chain was based on an extrapolation of the accelerator performance and beam conditions throughout the year. The pile-up events are assumed to follow a Poisson distribution given the average number of proton-proton interactions $\langle\mu\rangle$. In the simulations of all MC samples the value for $\langle\mu\rangle$ was varied between 5 and 40 to account for the changes in the luminosity conditions of the LHC in different periods of the data-taking. The actual average number of interactions in collision data is derived using the integrated luminosity measured in a defined period of time (luminosity block). Given the total inelastic cross-section for p-p collisions (σ_{pp}), $\langle\mu\rangle$ is defined as

$$\langle\mu\rangle = \frac{\mathcal{L}_{\text{int}}\,\sigma_{\text{pp}}}{N_{\text{b}}\,f} \quad . \tag{5.4}$$

where N_{b} is the number of colliding bunches, f is the revolution frequency of the protons in the LHC and $\mathcal{L}_{\text{int}}$ is the integrated luminosity in the luminosity block. Figure 5.5 shows distributions of the average average number of interactions in p-p collision data from 2012 (rescaled by 0.9) as well as the values used in the first (8 TeV) ATLAS MC simulation campaign in 2012/2013 (MC12a). Since the estimated and measured values for $\langle\mu\rangle$ differ, all MC events are re-weighted using the standalone `PileupReweighting` tool to get a more accurate description of the collision data. First, a random number is drawn to group each event of a MC sample into one of the different 2012 data-taking periods, accounting for the different recorded integrated luminosity of each. Since the periods reflect different LHC beam parameters, a $\langle\mu\rangle$ value is calculated for each and the $\langle\mu\rangle$ value of the MC event is compared to the value from the data-taking period it

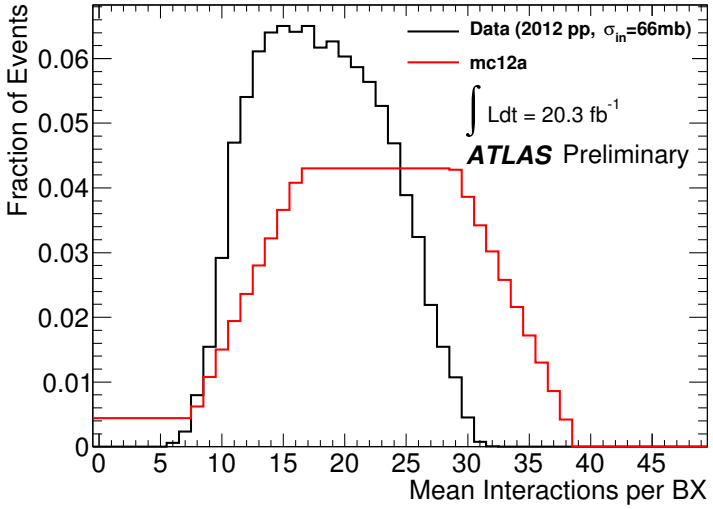

Figure 5.5.: Average number of interactions per bunch crossing ($\langle\mu\rangle$) used in the MC12a production campaign (red) based on pre-data-taking estimates and as obtained in observed events of the full 2012 p-p collisions dataset (black) [221].

was grouped into. Using the difference between both, a weight is calculated and applied to the simulated event.

In this analysis, MC simulated samples from the MC12a simulation campaign are used in which the average beam spot size σ_z along the beam line (z-vertex distribution) has been modelled too wide, with a value of 66 mm as opposed to $\approx$ 47 mm observed in data. Therefore the reconstructed vertex multiplicity (N_{PV}) tends to be lower in data with a larger number of vertices merged. However, this effect cannot be easily reweighted but is expected to have negligible effects except for the N_{PV} distribution itself.

6. Definition and Reconstruction of Physics Objects

The general purpose of the ATLAS detector is to identify and disentangle the vast amount of particles created in the p-p collisions at the LHC, to allow for a reconstruction of the kinematics and properties of the physics processes by which they have been produced. The particle reconstruction is mainly based upon tracks of charged particles in the inner detector and muon spectrometer, and upon energy clusters deposited in the EM and hadronic calorimeters. Depending on the combination of signatures left in the different sub-detectors, different classes of particles can be distinguished and their properties, such as their charge, momentum or energy, can be measured, see Figure 6.1. Higher level information, e.g. on the time of flight and vertex positions, allow for the identification of τ leptons or jets originating from b quarks. Various reconstruction algorithms are used to process the detector information during data-taking (online algorithms) or to post-process the stored data (offline algorithms) in order to identify and reconstruct "physics objects", candidates which match the expected signatures and properties of "real" particles and compound objects produced in the collision events as closely as possible. These objects are used to identify and select certain classes of events and their associated decay signatures from the large amount of events produced in (background) processes not of interest, for their comparison to MC simulations, and for the subsequent statistical analysis.

The final state signature of top-quark events which involve a subsequent leptonic W decay consists of electrons or muons, missing transverse energy from neutrinos, and hadronic jets originating from quarks and gluons. For their identification and reconstruction data from all ATLAS sub-detectors is required. The identification and reconstruction of the associated physics objects follows definitions and recommendations developed by the ATLAS top-quark working group that have been adapted and optimised for the purpose of this analysis. Details on the object definitions, their reconstruction performance and calibration, to a large extend are only documented internally to date [223] and therefore will be summarised in the following.

6.1. Fundamental Objects

6.1.1. Tracks

The trajectories of charged particles in the Inner Detector are bend onto helical paths due to the magnetic field from the central solenoid. When interacting with the active detector material the charged particles produce (raw) hits in the different layers of the

Pixel, SCT and the TRT sub-detectors. Since particles passing through the silicon tracker part usually produce hits in several neighbouring detector elements (pixels or strips) of a single layer, the raw hits are first combined into silicon clusters. From these, three-dimensional (3D) space-points are derived within the inner detector acceptance ($|\eta| < 2.5$) using the position and alignment information from the ATLAS geometry database. While clusters of raw hits in the Pixel detector can be directly converted into space-points, single strips of the SCT only provide precise position information in the r-ϕ plane. Therefore cluster pairs from both sides of a double-sided SCT module are combined to form single space-points in order to obtain sufficient precision in the position information along the z-axis ($\approx$ strip direction).

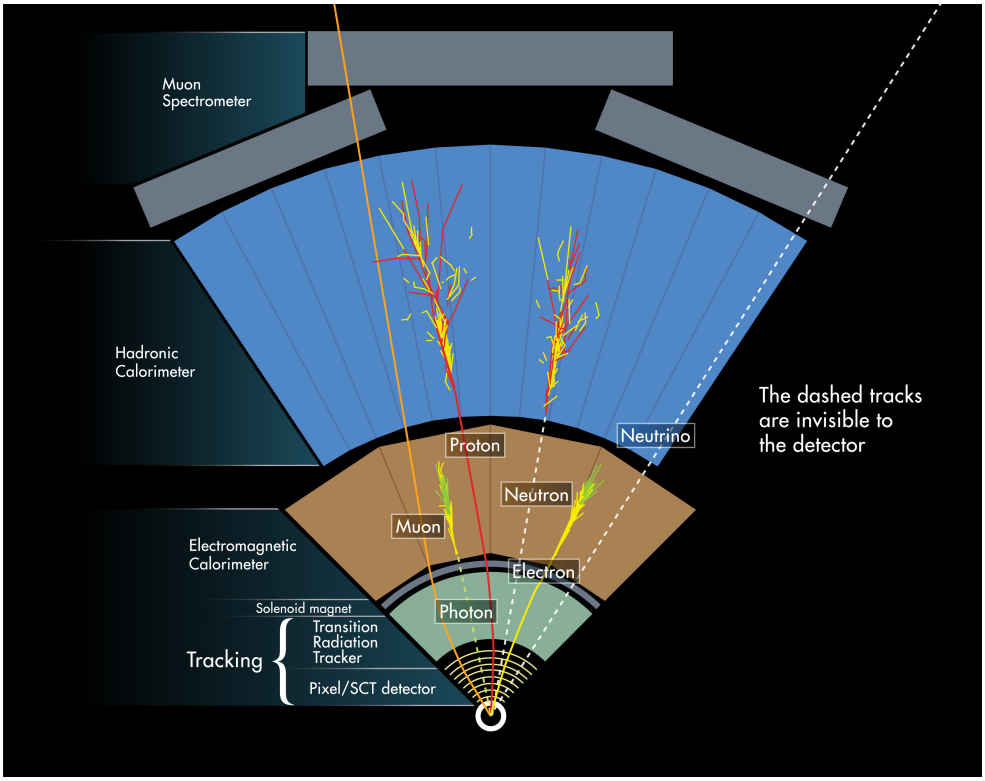

Figure 6.1.: Profile view of the ATLAS detector in the $r - \phi$ plane with different types of particles passing the sub-detector systems. Electrons (positrons) are detected from leaving bend tracks in the ID and depositing energy in the EM calorimeter, photons from clusters in the EM calorimeter only. Hadrons are identified from energy depositions mainly in the hadronic calorimeter, potentially associated to tracks in the ID (charged hadrons). Muons are identified from tracks in the muon spectrometer and ID. Lastly, neutrinos pass the detector without measurable interaction and are inferred from missing transverse energy calculated from the sum of all transverse momenta and energy deposits of all particles associated to a certain interaction. [222]

To reconstruct particle trajectories, first an inside-out sequence of the iterative track reconstruction chain [224] is applied. In the first iteration, track seeds are built from all possible combinations of three 3D space points of the Pixel detector. For each seed, matching track candidates are searched using Kalman filters [225] based on an estimation of the track parameters from the seed. A track is parametrised using five variables, the closest distance to the global z-axis (perigee) in the longitudinal and transverse plane, the (signed) impact parameters d_0 and z_0, the azimuthal and polar angle of the track at the perigee, ϕ_0 and θ, and the ratio of the particles charge and momentum, q/p, which defines the trajectories curvature at the perigee. In the iterative track finding procedure the estimated trajectory is followed and searched for further hits associated to the track candidate, by which in turn the track projection is updated progressively. The procedure is repeated in subsequent iterations, also including track seeds from the SCT. At the end in total 10% of the seeds yield a proper track candidate to be stored. In the next step ambiguities between the track candidates are resolved by scoring them [226] based on a more precise fit including material corrections. Apart from the quality of fit, in general tracks with more space points are preferred over small track segments, space points from the Pixel detector preferred over those from the SCT, and so on. Missing hits, from reconstructed trajectories passing instrumented and operational silicon layers without being registered, decrease the overall track score and are referred to as "holes". In an iterative procedure, low score tracks are removed and the remaining ones refitted in the subsequent iteration. Hits which were shared between tracks thereby are reassigned again and again to the tracks with the highest scores, thus bundling them increasingly. The obtained tracks are searched for matching extensions into the TRT, where TRT space-points are only added to the track in case they improve the overall fit quality, otherwise they are counted as outliers. In a last step the inside-out reconstruction is followed by an outside-in sequence to account for tracks from secondary vertices, e.g. from K_s decays or photon conversions, and for ambiguous track seeds in the silicon tracker part. The algorithm starts from seeds built in the TRT which are extrapolated into the silicon detector and tried to be matched to further silicon space points.

6.1.2. Clusters

Particles passing the ATLAS calorimeters deposit their energy in many calorimeter cells which is why cluster algorithms are employed to identify, group and sum cells with energy deposits originating from individual particles (or their showers) into calorimeter clusters. These energy sums are then calibrated with respect to a certain hypothesised particle of origin [227, 228] to account for cells missed to be added to the cluster, and for energy losses in dead material of the detector. Energy deposits from particle showers in cells of the EM and hadronic calorimeter are used to build clusters using two different algorithms [229]. In both cases, first, and before the actual clustering, calorimeter towers are built from the sum of energy deposits in all cells in longitudinal slices across a grid in the η-ϕ plane. If cells span several towers, their energies are distributed according to their fractional area in each tower.

The "sliding window clustering algorithm" builds fixed size clusters by summing neigh-

bouring cells within a rectangular window of fixed size in elements of the tower grid. The window is moved over each tower grid element and the total transverse energy in the window is measured. A pre-cluster is formed if the transverse energy reaches a local maximum and is above a certain threshold, $E_{\mathrm{T}}^{\mathrm{thresh}}$. In the final cluster building, the detailed cell information of all layers is used again to build clusters of different fixed sizes in the η-ϕ plane, depending on the location in the calorimeter and the assumed particle type. The cluster building is started from seeds given by the barycentre positions of the pre-clusters. The sliding window clustering algorithm is used mostly in the EM calorimeter, since it is fast and provides precise cluster energy calibration by using fixed cluster sizes. It is therefore best suited for reconstructing objects with uniform energy deposition patterns, such as electromagnetic showers. From the clusters build in the EM calorimeter, later electrons and photons are identified (egamma). The algorithm also is combined with information from the hadronic calorimeters for jet finding and τ-lepton identification (combined).

In the hadronic calorimeter the "topological cluster algorithm" is used. Starting from a set of seed cells which are selected by requiring the signal-to-noise ratio (SNR) of that cell to be above a (high) threshold, clusters are built by iteratively merging the seed cell with energy deposits (E_{cell}) in the neighbour cells. Neighbouring cells are only included if their SNR lies above a certain (however lower) threshold. If they have a SNR above an intermediate threshold, they may become seeds themselves making their direct neighbours to be collected as well. Further, this allows for two clusters to be merged depending on the SNR values of their intermediate cells. Choosing low threshold requirements for the peripheral cells of a cluster mostly avoids to cut off shower tails, while the rather high threshold requirement for the seeds suppresses noise, mostly arising from electronic noise and pile-up. The algorithm is best suited for isolated clusters. However, the typical situation in most ATLAS events involves overlapping showers with topological clusters covering large areas of the detector. Therefore in a last step the clusters are split between local maxima in the energy deposits which allows to disentangle individual particles' deposits. The topological cluster algorithm in total is very efficient at suppressing noise in clusters with varying and large cell count and therefore is best suited for the reconstruction of hadronic jets of a higher variability in their energy deposition patterns, and for the reconstruction of the missing transverse energy.

6.1.3. Vertices

A precise reconstruction of the primary interaction vertex of the p-p collision is crucial for identifying and suppressing non-collision backgrounds and superimposed interactions from pile-up events. Further, the reconstruction of secondary vertices allows for the identification of long-lived particles such as τ leptons or B hadrons that decay after a certain time-of-flight and hence displaced from the primary vertex.

In ATLAS, vertices are reconstructed using the information of particle tracks in the ID. Vertex reconstruction algorithms are employed to determine vertex candidates in two steps [230, 231]. First a procedure is applied to find vertex seeds in the form of

clusters of tracks satisfying certain quality requirements and with compatible position along the z-axis (beamline), measured at the point on the track closest to the beam spot centre. The tracks considered have to be built from at least six hits in the Pixel and SCT detectors (at least four of these in the SCT) and need to have a reconstructed track transverse momentum of $p_{\mathrm{T}} > 150$ MeV. To suppress tracks originating from secondary interactions, the transverse and longitudinal impact parameters of the tracks and their uncertainties ($\sigma(d_0)$, $\sigma(z_0)$) have to fulfil $|d_0| < 4\,\mathrm{mm}$, $\sigma(d_0) < 5\,\mathrm{mm}$, and $\sigma(z_0) < 10\,\mathrm{mm}$. In the second step, a vertex position is fitted from each seed by applying an adaptive χ^2-based algorithm [232] that weights the tracks of a seed cluster and its surrounding tracks according to their compatibility with a certain vertex. The position of the beam-spot and its size are used as a constraint during the vertex fitting step. If a track mismatches the fitted vertex by more than $\approx 7\sigma$, it is used as a new seed and the procedure is repeated until no additional seeds are found, or until no tracks not associated to any vertex remain. The vertex finding is followed by a fitting procedure in which the precise vertex positions and their uncertainties are determined.

6.2. Reconstruction of Physics Objects

6.2.1. Electron Reconstruction

Online Trigger Pre-selection

Electrons are selected online using different triggers to account for the changing pile-up conditions during the 2012 data taking period. In this analysis the electron channel events are triggered by the unprescaled single electron trigger with lowest E_{T}-threshold. At the L1 trigger stage an energy deposit in the EM calorimeter of $E_{\mathrm{T}} > 30$ GeV or $E_{\mathrm{T}} > 18$ GeV is required. At the HLT stage the full granularity of the calorimeter and all tracking information is available. At this stage fast seeding and tracking algorithms are used to match calorimeter clusters to tracks in the ID. Further, the trigger electron object is required to have a transverse energy of $E_{\mathrm{T}} > 60$ GeV (EF_e60_medium), or $E_{\mathrm{T}} > 24$ GeV in combination with a loose track isolation criterion (EF_e24vhi_medium1). The latter requires the scalar sum of the transverse momenta of all tracks falling within an η-ϕ cone of $\Delta R < 0.2$[1] around the trigger electron object divided by its E_{T} to be < 0.1.

Offline Reconstruction and Identification

Hereafter electrons are independently reconstructed offline in the central region of the detector ($|\eta| < 2.47$) by associating cell clusters in the EM calorimeter to reconstructed tracks in the ID using more sophisticated algorithms. In the first reconstruction step, cluster seeds in the middle layer of the EM calorimeter with an energy deposit > 2.5 GeV are preselected, which were determined by the sliding window algorithm (cf. Section 6.1) using a window size of 3×3 cells in the $\eta \times \phi$ plane. In a second step the angular position of a clusters barycentre and the corresponding extrapolated position in η and ϕ of the tracks in the middle layer are compared. Electron candidates are built, if at least one ID track with a transverse momentum of $p_{\mathrm{T}} > 0.5$ GeV is matched to the seed cluster

[1] The angular distance between two objects is defined as $\Delta R = \sqrt{\Delta\eta^2 + \Delta\phi^2}$.

within a certain threshold in the angular distance ΔR. If multiple tracks match the cluster position, only the track of smallest ΔR is taken into account. Candidates within the transition region of $1.37 < |\eta| < 1.52$ between the barrel and endcaps of the EM calorimeter are excluded. This is to account for the limited calorimeter instrumentation and large amount of inactive material from services in front of the first calorimeter layers which lead to an insufficient reconstruction efficiency.

After the matching procedure, the energy sum of the cluster is recomputed using an increased, position dependent window size (barrel: 3×7, endcap: 5×5 cells), where additional track information is also included to account for Bremsstrahlung effects, energy deposits outside the cluster (lateral and longitudinal leakage), and potential interactions of the electron candidate with the inactive detector material in front of the calorimeter. The recomputed cluster energy (E_{clus}) is later used as the energy of the electron four-momentum. If the matched track is constructed from more than four hits in the Pixel and SCT detectors, the remaining coordinates of the four-vector are derived from the η and ϕ coordinates of the track at the vertex position. Otherwise, the electron direction is derived from the cluster position. The transverse energy is defined by $E_{\text{T}} = E_{\text{clus}} \cdot \cosh(\eta)$, where the direction in η is taken from the associated track. Final electron candidates are selected if they have a transverse momentum larger than 25 GeV to avoid a larger part of the efficiency turn-on of the trigger at lower p_{T} values.

To identify electrons from the obtained candidates, a set of quality cuts is applied on calorimeter, tracker and combined variables to distinguish isolated electrons from hadronic jets mimicking electron signatures (fakes) or non-prompt (background) electrons, i.e. from photon conversions or neutral pion decays. Three different (inclusive) sets of cuts with increasingly stringent criteria (and hence background rejection) exist, which are referred to as loose, medium and tight. The loose selection criteria include requirements on the shower shape in the EM calorimeter (middle layer) and on the amount of longitudinal leakage into the hadronic calorimeter. The medium selection additionally requires energy depositions in the innermost (strip) layer of the EM calorimeter, more stringent quality criteria on the associated ID track, i.e. a larger number of Pixel and SCT hits and impact parameter constraints, and a better match between the calorimeter cluster and the associated track extrapolation. Lastly, the tight criteria employ additional cuts, e.g. on the ratio of the reconstructed cluster energy to the track momentum ($E_{\text{clus}}/p_{\text{track}}$), or on the number of hits in the TRT. A certain fraction of the TRT hits are required to be high-threshold hits to allow for a better separation from e.g. muons or charged hadrons such as pions (cf. Section 4.2.1). Further, increased track quality and track-matching cuts are employed. In particular the requirement of at least one b-layer hit and a veto against conversion vertices associated to the track allow for a better discrimination of background electrons from photon conversions. A full descriptions of all cuts in the different sets can be found in [233].

Isolation Requirements

Electrons from the W-boson decay in the leptonic single top-quark decay channel usually are isolated from jet activity in the EM and hadronic calorimeters, in contrast to e.g. electron fakes from hadronic jets or high-p_{T} electrons from heavy-flavour decays

as originating from the W+jets and QCD multijet background. Therefore the above backgrounds can be reduced by imposing additional isolation criteria.

On the one hand, an isolation in the EM calorimeter is required, which limits the amount of low energy deposits in calorimeter towers within an η-ϕ cone around the electron direction of $\Delta R < 0.2$, < 0.3 or < 0.4. The cut values are corrected for energy leakage outside of the cone and for energy depositions from underlying pile-up events. The cut on the maximum energy deposit in the cone, after subtracting the reconstructed energy of the electron itself, is parametrised in 9×9 bins in $|\eta_{\text{clus}}| \times E_{\text{T}}$. The values are tuned such that an uniform isolation efficiency is achieved in η and E_{T} with respect to a certain set of quality cuts (i.e. loose, medium, tight), ranging from 75 to 100% respectively. On the other hand, track isolation requirements are imposed on the electron candidates which limits the scalar sum of the transverse momenta of all tracks falling within an η-ϕ cone around the electron as defined above. Similarly, the cuts are parametrised in 9×9 bins in $|\eta_{\text{clus}}| \times E_{\text{T}}$. The working points for both isolations used within this analysis follow the ATLAS top-quark group recommendations for the early 2012 dataset and are a combination of an EM calorimeter isolation within a cone of $\Delta R = 0.2$ at a working point of 90% efficiency (EtCone20@90), and track isolation within a cone of $\Delta R = 0.3$ at 90% efficiency (PtCone30@90). Finally, all electron candidates are required to match a trigger electron object as reconstructed by the single electron trigger chain described at the beginning of this section.

Efficiency and Data/MC Scale Factors

To account for the limited efficiencies in the triggering (ϵ_{trig}), offline identification and reconstruction (ϵ_{id} & ϵ_{reco}) and in the isolation of electrons (ϵ_{iso}), scale factors are derived to match MC simulations with data. The total efficiency (ϵ) of the electron selection therefore is factorised as $\epsilon = \epsilon_{\text{reco}} \cdot \epsilon_{\text{id}} \cdot \epsilon_{\text{iso}} \cdot \epsilon_{\text{trig}}$, where ϵ_{reco} includes the efficiencies of the cluster-track matching, the track quality, and the energy leakage cuts with respect to the initial EM cluster formation (assumed to be 100%). The ϵ_{id}-term represents the efficiency of the identification criteria with respect to ϵ_{reco}. The efficiencies for the isolation requirement are then computed with respect to ϵ_{id} and those of the trigger are derived with respect to the combination of $\epsilon_{\text{id}} \cdot \epsilon_{\text{iso}}$. To derive the scale factors, efficiency maps for all four sources of inefficiencies are derived and compared for events from collision data and MC simulation using the tag-and-probe method [234]. Differences in the efficiencies are then corrected for by applying scale factors of the form $\text{SF} = \epsilon_{\text{data}}/\epsilon_{\text{MC}}$, weighting individual events depending on the electron kinematics. The efficiencies and scale factors for the offline reconstruction and identification are derived using the tag-and-probe method on $Z \to ee$ and $J/\psi \to ee$ events using the first $770\,\text{pb}^{-1}$ of the 2012 8 TeV data [235]. The resulting efficiencies for isolated electrons from $Z \to ee$ events are estimated to be $\epsilon_{\text{reco}} \approx 98\%$ and $\epsilon_{\text{id}} \approx 80\%$, see Figure 6.2. Similarly, the efficiency for the isolation requirement and the trigger efficiency were determined using the tag-and-probe method on $Z \to ee$ samples. The isolation efficiencies and scale factors are derived in nine bins of η and 12 bins in E_{T}. The trigger efficiencies and scale factors are derived for four different run periods (A-B3, B4-D3, C1-C5, D4+) and in nine bins of η and 15 bins in E_{T}.

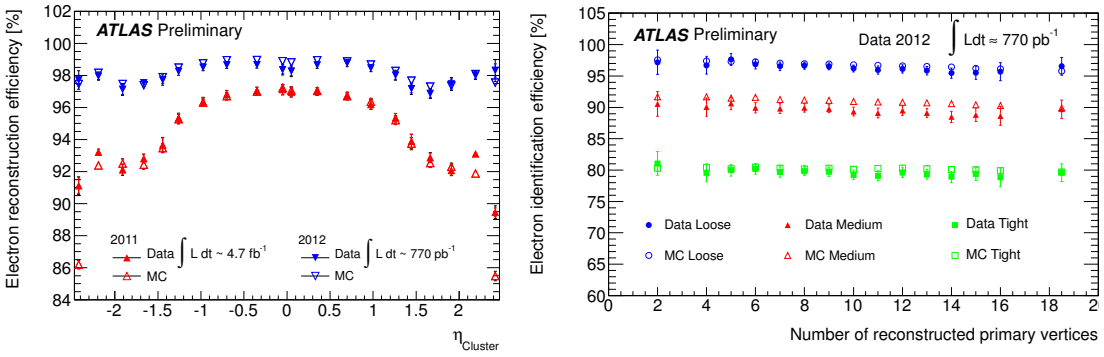

a) b)

Figure 6.2.: Electron reconstruction efficiency parametrised in different bins in η and electron identification efficiency vs. number of primary vertices (b), as estimated in the full 2011 (7 TeV) dataset, in 770 pb^{-1} of 2012 (8 TeV) data, and in MC simulated events. [235]

Energy Calibration and Resolution

The EM cluster energy used for the electron energies is corrected in data by data-to-simulation scale factors obtained in studies of $Z \to ee$ events after the full electron reconstruction and calibration procedure. The scale factors are parametrised in 34 bins of the electron η using two different methods, the line-shape fit and the template method. The first method employs an unbinned log-likelihood fit to the dielectron invariant mass of reconstructed $Z \to ee$ candidates for different η configurations of the reconstructed electrons in simulation and data events. Likewise, the template method builds template histograms of the mass of reconstructed Z boson from simulation and compares these to data for various electron pseudorapidity configurations. For each set a χ^2 test is performed between the data distribution and simulated templates, which results in a parabolic function in dependence of the assumed electron energy scale. The minima of the latter determine the electron energy scale. Figure 6.3 shows examples of reconstructed $Z \to ee$ invariant mass distributions for central and forward electrons in 2011 data after applying energy scale corrections determined with the line-shape fit method. The corrections applied typically are at the order of 0.5-1%.

The electron energy resolution in the calorimeter is parametrised as

$$\frac{\sigma(E)}{E} = \frac{a}{\sqrt{E}} \oplus \frac{b}{E} \oplus c \ ,$$

where a, b and c denote η-dependent parameters reflecting a sampling term, a noise term and a constant term, respectively. While the sampling term is well described in simulation ($\approx$ 10%) and the noise term is taken from calibration runs, the constant term is usually 1% larger in data with respect to simulated events. The parameter is measured in analogy to the energy scale determination by comparing the reconstructed dielectron invariant mass in $Z \to ee$ events in simulated and data events. Two different

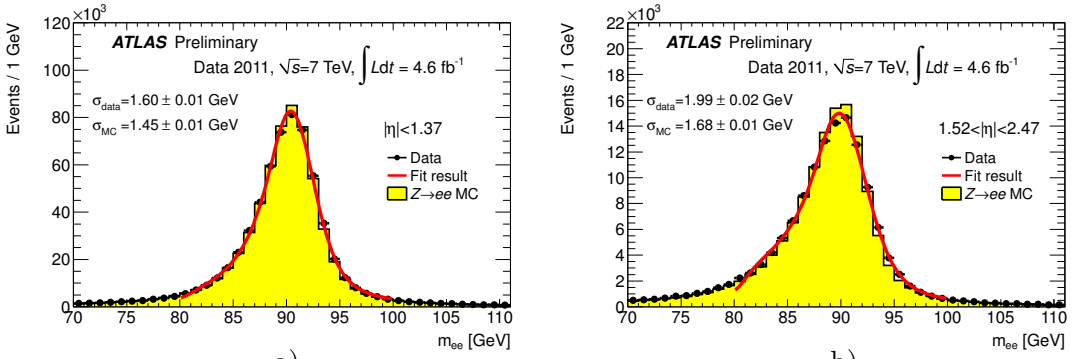

Figure 6.3.: Reconstructed $Z \to ee$ invariant mass distribution for electrons in the central (a) and forward region (b), after applying the electron energy scale corrections determined in 4.6 fb^{-1} of 2011 data. [236]

methods are employed, the template method, as described above, using templates with varied c-parameters, and the subtraction method which is based on fits to the invariant Z mass distributions using a (fixed) Breit-Wigner function convoluted with a Crystal-Ball function, the σ of the latter defining the energy resolution, see Figure 6.2. The c-parameters are then extracted by comparing the resolutions in data and simulated events for different electron η configurations.

An electron energy smearing is applied to the MC simulated events to match the energy resolution in data. The electron cluster energy is smeared on an event by event basis using random numbers drawn from Gaussian distributions reflecting the difference to the energy resolution in data, as a function of the energy deposit and direction in η of the electron candidate.

6.2.2. Muon Reconstruction

Online Trigger Preselection

In this analysis muon channel events are preselected using unprescaled single muon triggers [237]. The L1 trigger requires a muon chamber track with $p_{\mathrm{T}} > 15$ GeV (L1_MU15) which has later to be matched with a muon reconstructed at the HLT stage. At the L2 trigger stage, fast fitting and reconstruction algorithms using look-up-tables are employed to derive refined MS track parameters within the RoI defined by the L1 trigger stage. The MS tracks are then matched and combined with ID tracks, followed by a first coarse isolation requirement from adding calorimetric information. At the EF level, two different single muon triggers are used. The first requires a muon reconstructed with a threshold of $p_{\mathrm{T}} > 24$ GeV and applies an additional (loose) track isolation criterion (EF_mu24i_tight), which requires the scalar sum of the transverse momenta of all tracks falling within an η-ϕ cone of $\Delta R < 0.2$ around the trigger muon object (excluding the muon track itself) divided by its p_{T} to be < 0.12. The second one requires no isolation but muons with a higher p_{T} of at least 36 GeV (EF_mu36_tight).

Offline Reconstruction and Identification

Muon candidates are reconstructed in the central region of the detector ($|\eta| < 2.5$) by matching tracks reconstructed in the muon spectrometer to tracks in the Inner Detector, while accounting for effects from interactions with the ATLAS detector material. Several independent muon identification strategies exist, which combine the information from both sub-detectors in different ways [238, 239].

The "combined" (CB) reconstruction algorithm combines the full information from both sub-detectors and provides the highest purity muon candidates. Tracks are reconstruction independently in the ID and MS and a combined track is formed by matching and combining an extrapolated MS track with a track reconstructed in the ID in a global refit to all muon hits in the ID and the MS. First, MS track seeds are computed from straight line fits on RPC and TGC hits, which are subsequently fitted to derive muon tracks using the same mechanism as described in 6.1.1. The MS tracks are then extrapolated to the ID where they are matched with associated ID tracks. If several ID track candidates exist within a defined η-ϕ window, the best combination is determined from a χ^2 fit. The "combined" muon track is then reconstructed in a global refit to all muon hits along the associated ID and the MS tracks. The associated Inner Detector tracks have to pass a certain set of quality cuts to reduce the number of fake muons from secondary decays. The tracks are required to be reconstructed from at least one Pixel and at least four SCT space-points while no more than three Pixel or SCT holes[2] occur. Further, ID tracks within an pseudorapidity range of $0.1 < |\eta| < 1.9$ need to have a matching extension into the TRT built from at least five TRT hits (n_{TRT}) with no more than $0.9 \cdot n_{\mathrm{TRT}}$ outliers, and the longitudinal impact parameter has to fulfil $d_0 < 2\,\mathrm{mm}$.

In contrast, the "segment tagging" (ST) algorithms use ID tracks of the same criteria as described above as seeds, which are extrapolated to the Muon Spectrometer and subsequently associated with straight track segments reconstructed in the MS. In case a full track refit is possible, the muon is reconstructed similar to CB algorithms described above. The ST algorithms have higher efficiency than the CB algorithms and are better suited for muons which did not cross enough precision chambers (e.g. low-p_{T} muons) to independently derive their momenta in the MS. Lastly, the "standalone" (SA) reconstruction algorithms derive the muon track using hit information from the MS only. The track from the MS is extrapolated back into the ID and the track parameters at the interaction point are determined using a vertex constraint.

Within this analysis the so-called "Muid" collection is used, which contains muon candidates found by the three algorithms described above. Similar to the electrons case, the muon candidates are divided into three inclusive quality levels: tight, medium and loose, which refer to different levels of tightness and hence rejection of background (fake) muons. The tight selection criteria only include ("combined") muons reconstructed from a combined track refit. The medium criteria in addition include muons reconstructed with the ST algorithms where the ID track is associated to at least two track segments in the MS, or where the reconstructed muon direction lies within $|\eta| < 0.2$. By the latter, inefficiencies in the region around $|\eta| \approx 0$, which arise from only partially equipped muon chambers due to space occupied by services for the ID and calorimeters, can be recovered.

[2]Here, inoperable (dead) modules of a Pixel or SCT layer which are crossed by the muon are always counted as a hit and hence are excluded from the hole count.

Lastly, the loose selection includes muons found by all algorithms within the full detector acceptance, including the standalone algorithms. The final muon candidates used within this analysis are required to be "combined" muons (hence classified as "tight") and to have a transverse momentum above 25 GeV to avoid the turn-on in trigger efficiency at lower transverse momenta.

Isolation Requirements

As for electrons, muons are subject to be faked, e.g. in heavy-flavour decays, which is why candidates are required to fulfil additional (offline) isolation requirements which are tighter than those imposed at the trigger stage. In 2012, top-quark analyses in ATLAS use a new so-called "mini-isolation" [240] requirement as the default criterion for track and calorimeter isolation in order to account for the conditions of increased pile-up and to improve the performance in boosted top-quark decay topologies where the angular distance of the decay products is proportional to the inverse of the top quark p_{T}. The mini-isolation therefore defines a cone radius which is varied with the muon p_{T} as $\Delta R < 10\ \mathrm{GeV}/p_{\mathrm{T}}(\mu)$. Muon candidates are accepted, if the scalar sum of the transverse momenta of all tracks with $p_{\mathrm{T}} > 1$ GeV ($\sum p_{\mathrm{T}}^{\mathrm{track}}$), fulfilling additional track quality requirements ($d_0 < 10\,\mathrm{mm}$,$z_0 \cdot \sin(\theta_{\mathrm{track}}) < 10\,\mathrm{mm}$, > 4 ID hits), and falling within the respective cone around a muon candidate, is less than 5% of the reconstructed muon p_{T} (p_{T}^{ℓ}), hence $\sum p_{\mathrm{T}}^{\mathrm{track}}/p_{\mathrm{T}}^{\ell} < 0.05$.

Efficiency and Data/MC Scale Factors

As for electrons, identification, isolation and trigger efficiencies are derived [239] using the tag-and-probe method in $Z \to \mu\mu$, $J/\psi \to \mu\mu$ and $\Upsilon \to \mu\mu$ decays to derive scale factors in order to account for the difference in the efficiencies between observed data and MC simulation. The efficiencies and scale factors were derived using a dataset of

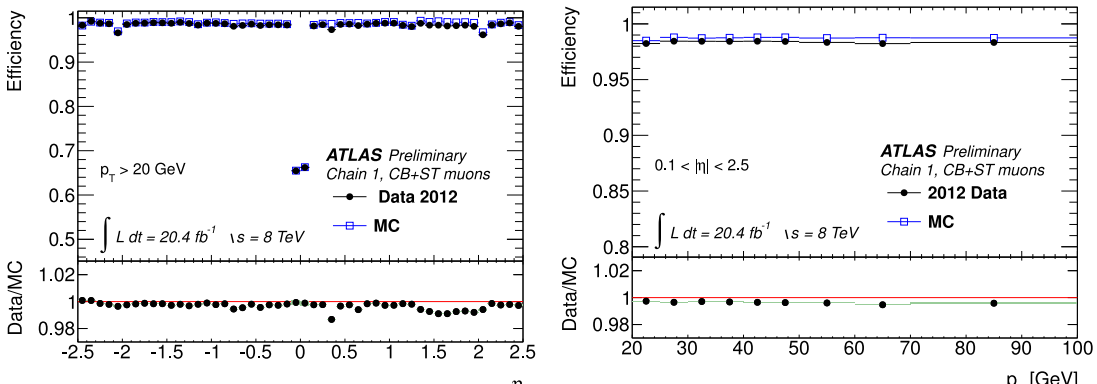

Figure 6.4.: Muon reconstruction efficiency for muons with $p_{\mathrm{T}} > 20$ GeV parametrised in different bins in η (a), and for muons with $0.1 < |\eta| < 2.5$ parametrised in different bins in p_{T} (b). The ratio pad shows the relative difference between the efficiencies in data and simulation. [239]

8 TeV p-p collisions recorded in 2012 and corresponding to an integrated luminosity of $20.4\,\text{fb}^{-1}$. The reconstruction efficiencies for "combined" muons are a superposition of the reconstruction efficiencies in the MS and ID, and the matching and refit efficiencies of the tracks from both measurements. The reconstruction efficiencies mostly range between 96% and 98%, depending on the muon η, see Figure 6.4. Charge dependent scale factors are obtained in bins of fine granularity in η-ϕ. The efficiency for the mini-isolation and trigger requirement is evaluated similarly using muons from Z boson decays. The isolation efficiency on average reaches $\approx 98\%$ for both, observed and simulated events and a scale factor of 1.00 ± 0.02 is assigned to the isolation cut. The trigger efficiencies and scale factors are derived in bins of η and ϕ for different run periods as described in [237], but were updated using 2012 data.

Momentum calibration and resolution

The muon momentum scale is corrected for all reconstructed muons and a resolution smearing is applied on events from MC simulation to match the momentum uncertainty with measurements performed in collision data [239]. The muon momentum scale and resolution are derived in studies of $Z \to \mu\mu$, $J/\psi \to \mu\mu$ and $\Upsilon \to \mu\mu$ decays after the complete muon reconstruction and calibration procedure. The parameters are derived using template fitting techniques similar to those used to derive the electron energy scale and resolution. Simulated templates of different Z mass distributions with varied correction parameters of the ID and MS measurements are generated and compared to those in data using a binned likelihood fit in order to find the one best matching. The scale factors are derived in 16 bins in η and are computed as the average of the ID and

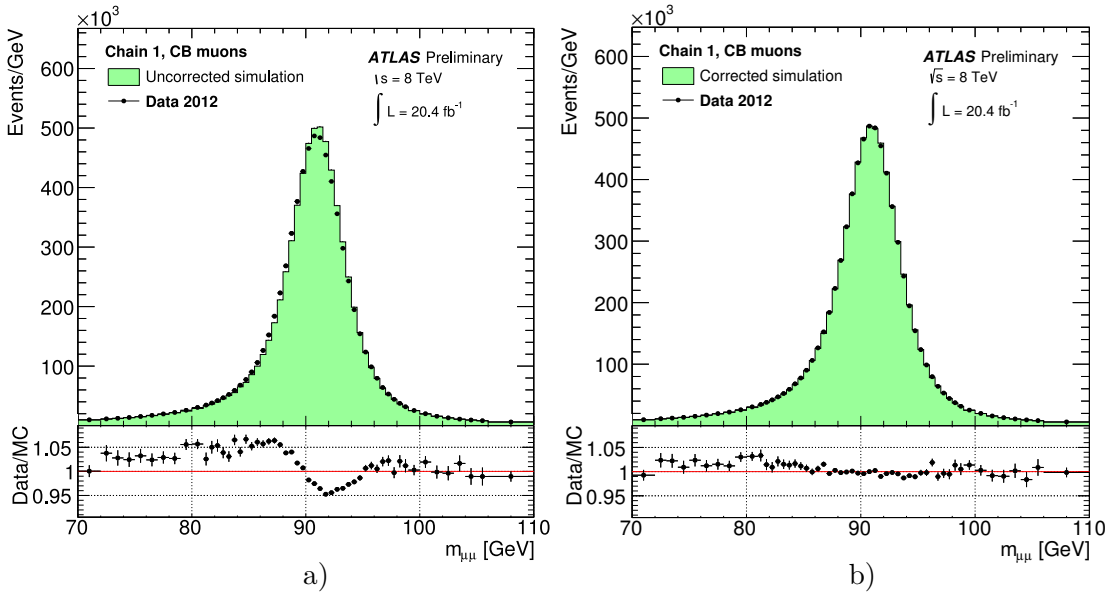

Figure 6.5.: Dimuon invariant mass for (isolated) CB muons with $p_{\text{T}} > 25$ GeV in 2012 data and for simulated $Z \to \mu\mu$ events, either without (a) or with muon momentum smearing and scale corrections applied (b). [239]

MS momentum corrections, weighted by the respective muon momentum resolutions.

The muon momentum resolution is parametrised as

$$\frac{\sigma(p_{\mathrm{T}})}{p_{\mathrm{T}}} = a \oplus b \cdot p_{\mathrm{T}} \ ,$$

where a is a correction term for contributions due to multiple scattering, and b accounts for the effect of the intrinsic (spatial) detector resolution and residual misalignments. Simultaneously to the momentum scale, the resolution in both sub-detectors is derived and compared to that of Z mass distributions in data. A muon momentum smearing is applied to the MC simulated events to match the higher resolution found in data. The momentum is smeared on an event by event basis using random numbers drawn from Gaussian distributions that reflect the difference to the resolution of each sub-detector in data, i.e. for the MS and ID measurements individually. Figure 6.5 shows a comparison of the Z mass spectrum obtained in simulated and observed $Z \to \mu\mu$ events before and after applying the muon momentum scale factors and momentum resolution smearing by which the data/MC agreement is improved significantly.

6.2.3. Jet Reconstruction

Offline Reconstruction and Identification

In this analysis jets are reconstructed within a pseudorapdity range of $|\eta| < 2.5$ using the anti-k_{T} algorithm [241, 242]. The algorithm computes a distance measure $d_{i,j}$ between two arbitrary objects (e.g. an energy cluster or a particle track) and a similar distance $d_{i,B}$ between each object and the beam direction B:

$$d_{i,j} = \min\left(p_{\mathrm{T},i}^{-2}, p_{\mathrm{T},j}^{-2}\right) \frac{\Delta R_{i,j}^2}{R^2} \ , \quad d_{i,B} = p_{\mathrm{T},i}^{-2} \ ,$$

$$\text{with} \quad \Delta R_{i,j}^2 = (y_i - y_j)^2 + (\phi_i - \phi_j)^2 \ ,$$

where $p_{\mathrm{T},i/j}$ is the transverse momentum, $y_{i/j}$ is the rapidity and $\phi_{i,j}$ the azimuthal angle of the respective object. The free resolution (or width) parameter R controls the size of the jets and their relative distance, i.e. the distance at which they are resolved from each other. In this analysis the AntiKt4LCJets algorithm is used which implies a width parameter of $R = 0.4$. It uses topological clusters (cf. Section 6.1.2) as input objects for the anti-k_{T} algorithm, which were calibrated using the local cluster weighting (LCW) method [243].

The LCW method partially corrects for the different response to hadronic and electromagnetic showers due to the non-compensating nature of the calorimeters. Further, it corrects for differences in their reconstruction efficiencies and for energy deposits outside the calorimeters. The LCW method calibrates topological clusters individually and "locally", i.e. without considering the final jet it may later be associated with. The calibration is based on a classification into hadronic and EM-like cluster shapes which is achieved using different sets of cell and topological cluster variables, such as the clusters

barycentre, isolation and longitudinal depth. The method then applies different weights to energy deposits from either shower type (obtained from MC simulations), and thereby improves the jet energy resolution.

The iterative anti-k_{T} algorithm reconstructs jets from the calibrated topological clusters by determining the smallest of the distances $d_{i,j}$ or $d_{i,B}$. If the smallest is a distance between two topological clusters ($d_{i,j}$), they are subsequently merged into one combined cluster object. If the smallest value is given by a $d_{i,B}$ entry, the respective cluster object i is removed from the list of inputs and is declared as a final jet candidate if it has a $p_{\mathrm{T}} > 7$ GeV, otherwise it is discarded. The distances of the new or remaining cluster objects are recalculated and the procedure is repeated until no topological clusters are left. The key feature of the algorithm is that clusters with low energy deposits from soft particles predominantly merge with neighbouring calorimeter clusters of high energy deposits (i.e. from hard particles) before they may cluster among themselves. Clusters from soft particles or calorimeter noise thereby do not significantly modify the final jet boundaries which instead are predominantly defined by clusters of high energy deposits.

Additional quality and pile-up rejection cuts are imposed on the obtained jet candidates in observed and simulated events to suppress jets from secondary interactions and so-called "bad jets" originating from leptons faking hadronic jets, beam-gas and beam-halo interactions, cosmic-ray showers, or noise bursts in the calorimeter [244]. Jet candidates with $p_{\mathrm{T}} > 20$ GeV are removed if:

- they overlap with an identified electron candidate within a cone of $\Delta R < 0.2$, since they likely correspond to the same physics object. In case several jets overlap with the same electron candidate, only the closest is removed;
- they fail to pass a set of "looser" quality cuts, e.g. on the energy fractions in the calorimeters and several jet variables described in detail in [245], which efficiently reduces fake jets from calorimeter noise and non-collision backgrounds;
- their absolute value of the jet vertex fraction |JVF| is below 50%, where the jet vertex fraction (JVF) [246] provides a measure of probability that a jet is originating from the respective primary vertex associated to the hard interaction of interest. It is defined as the summed p_{T} of tracks associated to the jet and originating from the primary vertex, divided by the p_{T} sum of all tracks associated to the jet. Tracks are counted as associated to a jet if they lie within a cone of $\Delta R < 0.4$ around the jet candidate. A cut in the minimal JVF value therefore significantly reduces the effect of secondary interactions within the same bunch crossing (in-time pile-up).

Efficiencies and Data/MC Scale Factors

The efficiency of the jet reconstruction from (LCW calibrated) topological clusters is derived by comparisons with jets reconstructed from tracks of charged particles in the Inner Detector using the tag-and-probe method [247]. The efficiency, defined as the fraction of (probe) jets reconstructed from ID tracks matched to a (tag) jet reconstructed from calorimeter clusters, was found to be approximately at unity for both, MC and data events, with minor deviations only affecting jets with a transverse momentum of $p_{\mathrm{T}} < 30$ GeV. Since the final event selection of this analysis requires jets with a

$p_{\mathrm{T}} > 30$ GeV (see Chapter 7), no correction for the reconstruction efficiency needs to be applied to MC events.

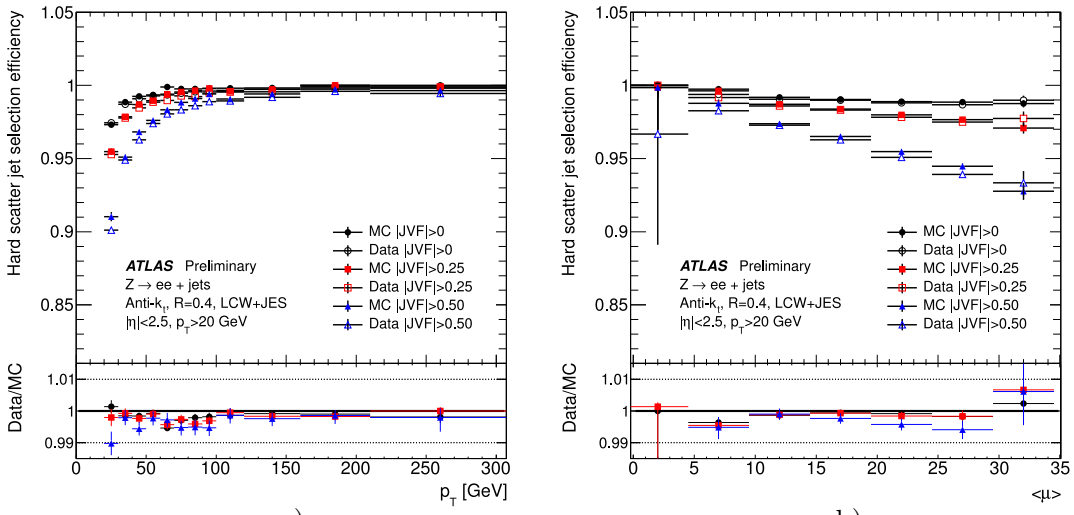

Figure 6.6.: Efficiencies of the JVF cut for jets with $p_{\mathrm{T}} > 20$ GeV and $|\eta| < 2.4$ from hard interactions in simulated and observed $Z(ee)$+jets events as a function of the jet p_{T} (a), and as a function of the average number of interactions per bunch crossing (b), for different JVF cut values. [246]

The cut in the jet vertex fraction affects (in)efficiencies in MC simulated and observed events differently. Hence, scale factors are applied to match both, which have been derived using the tag-and-probe method in data-MC comparison of $Z \to \mu\mu$+jets and $Z \to ee$+jets events in separate signal (jets from hard interactions) and background-enriched regions (jets from pile-up). Figure 6.6 exemplarily shows the derived JVF cut efficiencies for jets from hard interactions as a function of the jet p_{T} and of the average number of interactions per bunch crossing ($\langle\mu\rangle$). The method was validated using MC truth information[3], and JVF efficiencies/inefficiencies in the signal and background region were parametrised using exponential functions in the jet p_{T}. More details on the corresponding analysis and the JVF principle in general can be found in [246].

Energy calibration and resolution

Despite the LCW calibration, the final jet energy scale (JES) has to be calibrated to the hadronic scale, which represents the second part of the so-called LC+JES calibration scheme, albeit corrections are smaller than for the former default EM+JES calibration scheme used in analyses of ATLAS data recorded in 2010 and 2011. The energy scale of each jet is calibrated using scale factors derived in three subsequent steps:

Pile-up correction: The average contribution from secondary p-p interactions within the same and previous bunch crossings is subtracted from the measured jet transverse

[3]MC truth refers to objects reconstructed from MC "truth" particles (e.g. jets) on generator level, i.e. before parton showering and detector simulation are applied.

energy (E_{T}) using offset correction constants derived from measurements in minimum bias collision data. Their values are parametrised in bins of N_{PV} (number of reconstructed primary vertices), τ_{bunch} (spacing between consecutive bunches) and the jet pseudorapidity η, to account for the variable in-time and out-of-time pile-up conditions and the calorimeter geometry.

Jet vertex correction: The jet four-momenta of an event are corrected such that their origins point back to the primary vertex associated to the hard interaction of interest, instead of the centre of the ATLAS coordinate system. The correction does not alter the jet energy itself but increases the angular resolution and (to a lesser extend) the response in the jets p_{T}.

Jet energy and direction correction: Finally, each jet is corrected in its energy and direction using correction constants derived by matching reconstructed with MC truth jets in samples of inclusive QCD jet events generated using PYTHIA, and comparing their kinematic properties. The correction factors are parametrised in bins of the (uncorrected) E_{T} and η. Figure 6.7 shows the average jet energy for LC calibrated jets in 7 TeV data and MC simulation as a function of the jet pseudorapidity, and the fractional jet energy resolution as a function of the average jet p_{T}. A detailed description of the calibration procedure can be found in Chapter 8 of [243].

Contrary to the muon p_{T} and electron E_{T}, the jet energy resolution approximately agrees in events from collision data and MC simulations, see Figure 6.7. Therefore no nominal resolution smearing is applied in MC simulated events, but residual data/MC disagreements in particular regions of the jets p_{T} and η are accounted for by means of an additional smearing as a systematic uncertainty, see Section 9 for details.

Identification of b-quark jets

The identification of b-quark jets (b-jets) is of particular importance to this analysis since it allows for identifying events containing top quarks with high purity and discriminating against a large fraction of the background processes. Several properties allow for a distinction of b- from light-quark jets:

- The life time of b-flavoured hadrons of $\mathcal{O}(1\,\mathrm{ps})$ on the one hand is small enough so they still decay within the detector volume, on the other hand sufficiently large to lead to a significant flight path length L of $\mathcal{O}(1\,\mathrm{mm})$. This results in secondary vertices displaced from the primary vertex (beam-beam collision point) which can be reconstructed and constitute the main ingredient for b-tagging algorithms.
- B hadrons have large masses (> 5 GeV) and large branching ratios for decays into leptons. Therefore they fragment into much lighter decay products carrying large transverse momenta.
- For the same reason, b-jets tend to have higher invariant masses and tend to have higher particle multiplicities with larger opening angles making the b-jets wider.

Several b-tagging algorithms take advantage of the above properties to weight jets in events according to their probability to be originating from a b quark. For the selection of the signal sample (cf. Section 7), the *MV1c* b-tagging algorithm is used. It is derived

from the *MV1* algorithm (used in the control sample), but is optimised to provide a better rejection of *c*-quark jets. The *MV1* and *MV1c* algorithms are based on neural networks (cf. Section 8) that combine the output weights of several stand-alone *b*-tagging algorithms, namely the *IP3D*, *SV1* and *JetFitterCombNN* algorithms, described in detail in [250]. The three algorithms make use of the (signed) impact parameter significances and their correlations of all the tracks associated to a jet, of properties of the inclu-

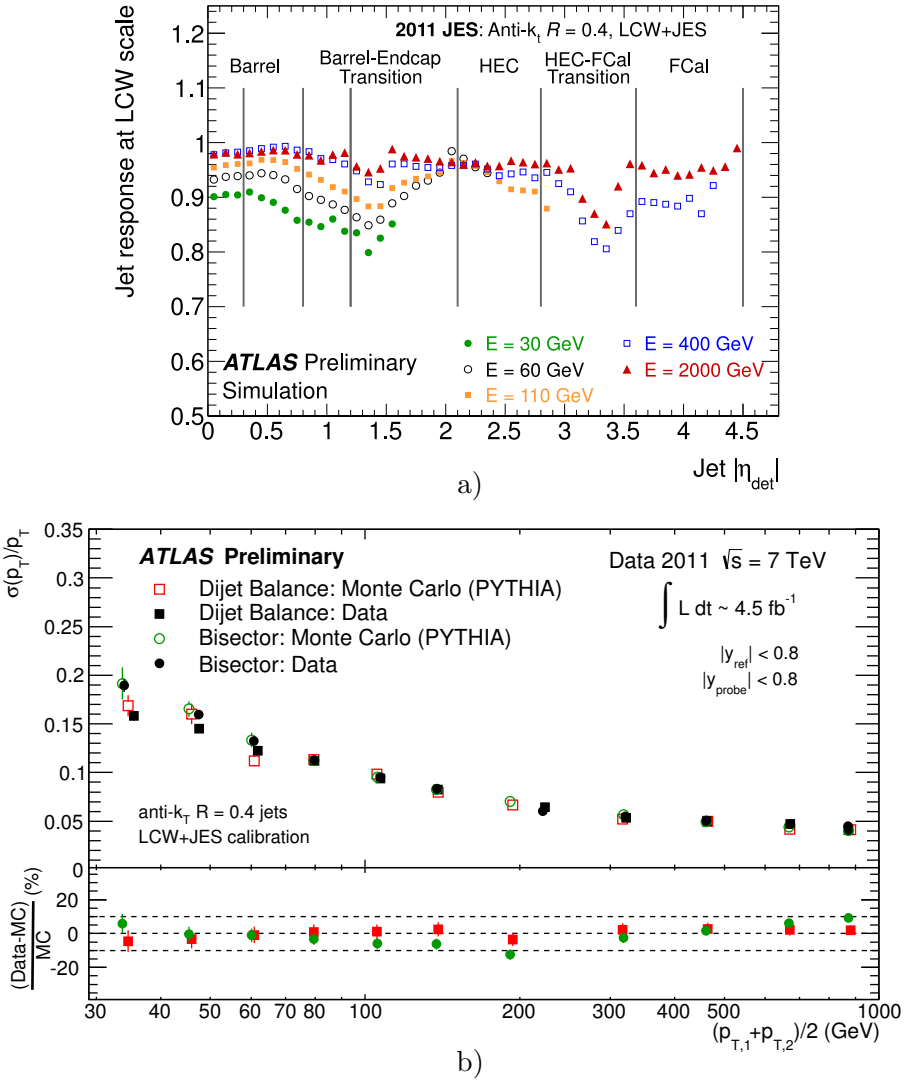

Figure 6.7.: Average energy of jets (at the LCW scale) with respect to the truth jet energy in MC simulation (PYTHIA) as a function of the jet pseudorapidity before the jet vertex correction is applied (a), and fractional jet energy resolution as a function of the average jet p_{T} (b), measured with the dijet balance (squares) and bisector (circles) in-situ techniques. [248, 249]

sive B-hadron decay vertex and its associated tracks from within the jet, as well as of properties of the reconstructed b- and c-hadron decay chain and flight path topology inside the jet. The flavour tagging algorithms compute an output weight for each jet which is low for c- and light-quark jets and tends to be large for b-quark jets. Different neural networks are trained for the *MV1* and *MV1c* algorithms using simulated events, optimised to achieve a high light-jet or a better c-jet rejection in the region of lower b-tagging efficiency (higher output weight), respectively.

To match the tagging efficiencies in MC simulations and collision data, scale factors are applied to simulated events which are parametrised in bins of the jet p_{T} and η. For each algorithm several operating points of different b-tagging efficiency and purity are defined, each corresponding to a certain cut value in the output weight. The operation points are calibrated by estimating the efficiencies to correctly tag a jet as originating from a b quark, referred to as b-tagging efficiency, and the rate of misidentifying a c- or light-quark jet as a b-jet, referred to as c-tag and mistag rate.

The b-tagging efficiencies and scale factors are derived from a combination of measurements in collision and MC simulated events using different methods, called $p_{\mathrm{T}}^{\mathrm{rel}}$ and system8 method [251], or tag counting, kinematic selection and kinematic fitting method [252]. The first two are based on dijet samples with muons in the final state. The $p_{\mathrm{T}}^{\mathrm{rel}}$ method derives tagging efficiencies from a subset of b-jets which contain a reconstructed muon, using the muon momentum transverse to the combined muon+jet axis ($p_{\mathrm{T}}^{\mathrm{rel}}$). The $p_{\mathrm{T}}^{\mathrm{rel}}$ spectrum from b-jets is harder than that of c- or light-quark jets, which allows to derive templates from MC simulations to be fitted to data to obtain the number of b-, c- and light-flavour jets before and after applying a particular tagging algorithm. The system8 method defines three sets of selection criteria of little correlation, one of which is the b-tagging algorithm under study. The criteria are used to construct a fully constrained equation system built with the number of events passing given combinations of these criteria. The equation system is then solved for eight unknowns, namely the efficiencies for b-/non-b-jets passing each set of selection criteria and the number of b-/non-b-jets present before applying any selection.

The latter three methods use the kinematic properties of $t\bar{t}$ events in the semi-leptonic and dileptonic decay channels, which feature naturally large b-jet contents to measure the b-tagging efficiency in data. They became competitive with the above methods with the larger integrated luminosity collected in 2011 and 2012 becoming available. The methods rely on the assumed fractions of b-, c- and light-flavour jets, and on the expected c-tag and mistag rates derived from MC simulations in which the flavour of a jet is labelled by matching it with generator level (truth) particles. The tag counting method extracts the b-tagging efficiency by fitting the distribution of the expected number of events with n b-tagged jets to that in observed $t\bar{t}$ candidate events. Lastly, the kinematic selection method derives the b-tagging rate by measuring the total fraction of b-tagged jets in data events and comparing it with the expected fractions of b-, c- and light-flavour jets from simulation. The kinematic fit method derives the b-tagging efficiency from a highly enriched sample of b-jets obtained in a kinematic fit to the $t\bar{t}$ event topology by which jets in the final state are directly associated to jets originating from top-quark decays.

The final b-tagging efficiencies used in this analysis were derived using a combination

of the calibrations with the $p_{\mathrm{T}}^{\mathrm{rel}}$ and system8 methods with the $t\bar{t}$ kinematic selection method, while the other independent methods are employed as cross-checks to ensure the reliability of the calibration. Figure 6.8 shows exemplary b-tagging efficiency scale factors as obtained from the kinematic selection and system8 methods for the *MV1* b-tagging algorithm at 70% efficiency.

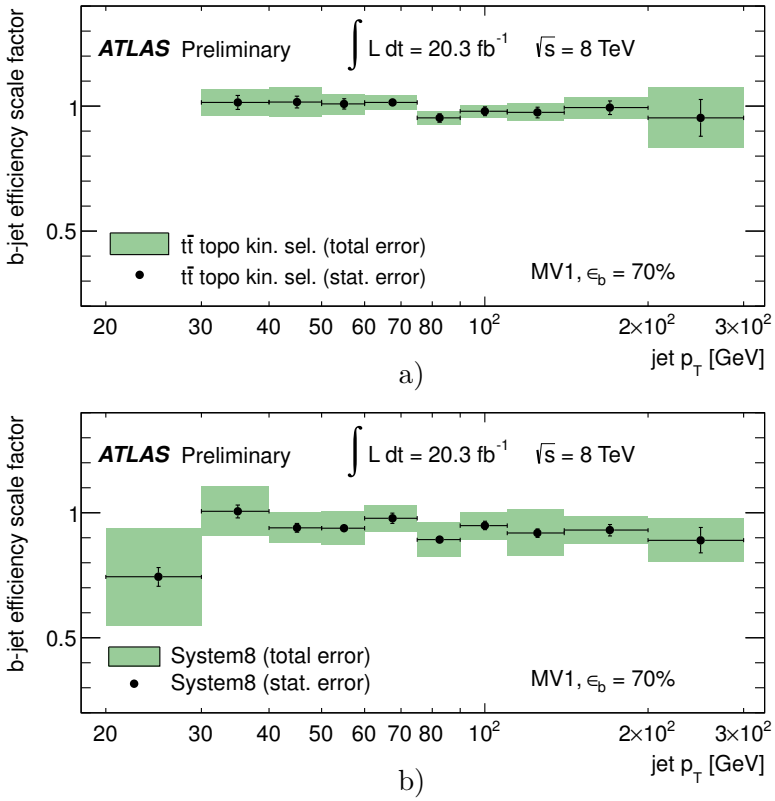

Figure 6.8.: b-tagging efficiency data-to-simulation scale factors as obtained from the kinematic selection (a) and system8 method (b) for the *MV1* b-tagging algorithm at 70% efficiency on 8 TeV data. [253]

The c-tagging efficiencies and scale factors have been derived using samples of $D^{\star+}$ mesons by comparing the yield of reconstructed $D^{\star+}$ mesons selected in samples with or without b-tagging requirements applied [254]. An inclusive tagging efficiency is first obtained for jets associated to $D^{\star+}$ meson decays by performing a combined fit in both samples which is decomposed into efficiencies for tagging b- and c-jets using the jet flavour composition as obtained from fits in data, and the b-tagging efficiency as derived from the combined $p_{\mathrm{T}}^{\mathrm{rel}}$ and system8 methods in simulated events.

Lastly, the mistag rates and scale factors are obtained in an analysis using the "negative tag method" in inclusive jet samples [255]. The method separates light- from heavy-flavour jets by practically inverting the tagging algorithms, i.e. negating their internal impact parameter and the decay length selections. The rate of data events con-

taining jets tagged with negative algorithm outputs is corrected for effects of e.g. the finite jet direction resolution, or secondary vertices from long-lived particles or material interactions, and is then used as an approximation of the mistag rate due to detector resolution effects.

The expected number of events after applying the full event selection (see Section 7) and the b-tagging requirement using the *MV1* and *MV1c* algorithms in dependence of their tagging weights is shown in Figure 6.9. It can be seen that the *MV1c* tagger outperforms the *MV1* b-tagging algorithm in terms of rejection against the Wc and Wcc and multijet backgrounds, while the decrease in the signal acceptance stays relatively small. Standard calibration points for the *MV1* tagger exist for b-tagging efficiencies of

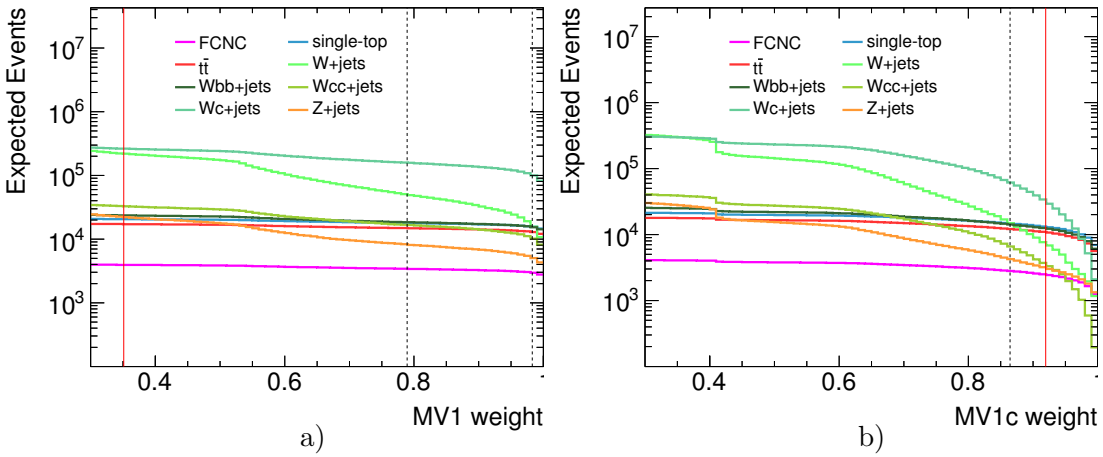

Figure 6.9.: Expected number of events after applying the *MV1* (a) and *MV1c* (b) b-tagging algorithms on different MC simulated background samples after the full event selection in dependence of the respective tagging weights. The chosen weight cuts used in the selection of the control sample (*MV1*) and signal sample (*MV1c*) are marked with red lines respectively.

80%, 70% and 60%, and for 57% and 50% efficiency for the *MV1c* tagger, measured in $t\bar{t}$ events respectively and denoted as vertical lines in Figure 6.9. To better suppress the dominant W+HF+jets background, an algorithm at a calibration point of low b-tagging efficiency but high light- and particularly c-jet rejection is favourable to achieve a higher purity of signal events after the event selection [208]. Therefore the *MV1c* tagging algorithm is chosen and applied with a weight cut at > 0.9195 to identify b-jets in the signal sample. In $t\bar{t}$ events this working point corresponds to a b-tagging efficiency of 50% and a c-tag and mistag rate of 3.9% and 0.07%, respectively. For the control sample used within this analysis (see next Section 7) a much looser b-tagging requirement is used in order to obtain a sample enriched in background events while maintaining the possibility to identify all final state objects and to construct the same kinematic variables as in the signal sample. Here, jets are identified to be originating from b quarks employing the *MV1* b-tagging algorithm with a weight cut of > 0.3511, which corresponds to a b-tagging efficiency of 80% measured in $t\bar{t}$ events.

6.2.4. Missing Transverse Energy

The $E_{\mathrm{T}}^{\mathrm{miss}}$ is a measure of the transverse energy or momentum and direction of particles escaping the detector without any measurable interaction, such as the neutrino from the leptonic $W \to e\nu$ decay in the FCNC signal process. It therefore is used to discriminate signal events from several background processes, in particular QCD multijet production, using the magnitude of the $\vec{E}_{\mathrm{T}}^{\mathrm{miss}}$ vector or its direction with respect to other final state decay objects. The $\vec{E}_{\mathrm{T}}^{\mathrm{miss}}$ vector is calculated from the negative sum of the transverse energy vectors (or momentum vectors if neglecting particle masses) of all particles in the detector, accounting for energy losses due to the limited coverage, efficiency and resolution of all ATLAS sub-detectors. In contrast to the unknown longitudinal component, the $\vec{E}_{\mathrm{T}}^{\mathrm{miss}}$ ideally should approximately sum to zero if all particles were detected. However, it will not fully cancel if any high-p_{T} object has escaped undetected.

In this analysis an "object-based" $\vec{E}_{\mathrm{T}}^{\mathrm{miss}}$ [256] is derived starting from the calculation of a vector sum of all calorimeter cells associated to a topological cluster which are subsequently associated to, and calibrated for, individual reconstructed high-p_{T} physics objects, such as electrons, jets and muons. The recalibrated energy deposits from the different classes of objects are grouped into terms denoted as *RefEle*, *RefJet* and *RefMuon* respectively. To avoid double-counting, cells belonging to several objects in the event are associated to the first reconstructed object a match was searched and found for, done in the same order the object types are denoted above:

The *RefEle* term is built from topological clusters matched to (tight) electron candidates, but with $p_{\mathrm{T}} > 10$ GeV and whose cells are recalibrated to the EM scale using the nominal energy calibration described in Section 6.2.1, except the lateral (out-of-cluster) leakage correction.

The *RefJet* term is constructed from topological clusters associated to jets whose calibrated p_{T} (LC-JES scheme) is larger than 20 GeV. Topological clusters associated to "soft" jets with low transverse momenta down to 10 GeV are collected in an additional *RefSoftJet* term with their energies calibrated using a different, local hadron (LocHad) based scheme which locally weights topological clusters, optimised from single pions.

The *RefMuon* term is calculated from the p_{T} of all muons from the MuidMuonCollection, hence is including "combined" isolated muons from within the region of $|\eta| < 2.5$, but also (non-isolated) muons within the extended acceptance range of the muon spectrometer not covered by the ID ($2.5 < |\eta| < 2.7$), reconstructed using the stand-alone algorithm. The energy deposits of muons in the calorimeter is either included in the jet term if the muon overlaps with a reconstructed jet within $\Delta R = 0.3$ or otherwise counted to the cell-out-term (see below).

The *RefCellOut* term collects any remaining clusters not associated to a reconstructed physics objects and sums them with their energies calibrated to the EM scale.

The final calibrated $\vec{E}_{\mathrm{T}}^{\mathrm{miss}}$ is referred to as *MET_RefFinal_AntiKt4LCTopoJets_tightpp*, in accordance to the physics objects the calibration is based on. Similar $E_{\mathrm{T}}^{\mathrm{miss}}$ descriptions are available which are based on the same terms but are constructed using less

stringent object selection and reconstruction criteria, i.e. loose or medium identification criteria for electrons reflect in the name of the $E_{\mathrm{T}}^{\mathrm{miss}}$-collection which are called accordingly *MET_RefFinal_AntiKt4LCTopoJets_loosepp* or *_mediumpp*. The fully calibrated $\vec{E}_{\mathrm{T}}^{\mathrm{miss}}$ in either case is then calculated from the sum of all terms described above:

$$\vec{E}_{\mathrm{T,RefFinal}}^{\mathrm{miss}} = \vec{E}_{\mathrm{T}}^{\mathrm{RefEle}} + \vec{E}_{\mathrm{T}}^{\mathrm{RefMuon}} + \vec{E}_{\mathrm{T}}^{\mathrm{RefJet}} + \vec{E}_{\mathrm{T}}^{\mathrm{RefSoftJet}} + \vec{E}_{\mathrm{T}}^{\mathrm{RefCellOut}} \quad .$$

The $\vec{E}_{\mathrm{T}}^{\mathrm{miss}}$ vector usually is parametrised in its components in the x-y (transversal) plane to derive its magnitude as

$$E_{\mathrm{T}}^{\mathrm{miss}} = \left|\vec{E}_{\mathrm{T}}^{\mathrm{miss}}\right| = \sqrt{(E_{\mathrm{x}}^{\mathrm{miss}})^2 + (E_{\mathrm{y}}^{\mathrm{miss}})^2} \quad \text{, where} \quad \vec{E}_{\mathrm{T}}^{\mathrm{miss}} = \begin{pmatrix} E_{\mathrm{x}}^{\mathrm{miss}} \\ E_{\mathrm{y}}^{\mathrm{miss}} \end{pmatrix} \quad .$$

Figure 6.10 shows the $E_{\mathrm{T}}^{\mathrm{miss}}$ measured in observed and simulated $Z \to \mu\mu$ events as well as the $E_{\mathrm{x}}^{\mathrm{miss}}$ and $E_{\mathrm{y}}^{\mathrm{miss}}$ resolution as a function of the total transverse energy in the event ($\sum E_{\mathrm{T}}$), derived in observed and simulated $Z \to \mu\mu$ and $Z \to ee$ events. The $Z \to \ell\ell$ channel is suited in particular since it is has a very clear event signature, large cross-section, and is expected to contain only very low contributions of genuine $E_{\mathrm{T}}^{\mathrm{miss}}$ (i.e. from background processes). Therefore a large fraction of the reconstructed $E_{\mathrm{T}}^{\mathrm{miss}}$ is a direct result of the limits in the reconstruction and detector performance. Performance studies in events containing genuine $E_{\mathrm{T}}^{\mathrm{miss}}$ (e.g. $W \to \ell\nu$), on the other hand, are used for a validation of the $E_{\mathrm{T}}^{\mathrm{miss}}$ scale and response. More details on the $E_{\mathrm{T}}^{\mathrm{miss}}$ reconstruction and its performance in 2012 data can be found in [256].

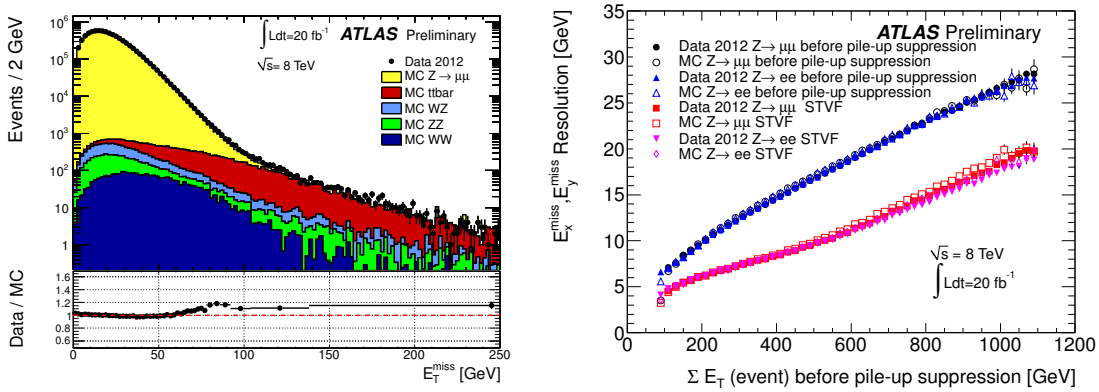

a) b)

Figure 6.10.: Distribution of $E_{\mathrm{T}}^{\mathrm{miss}}$ as measured in $Z \to \mu\mu$ events (before pile-up suppression) in observed data and simulation (a) and the expected and observed $E_{\mathrm{x}}^{\mathrm{miss}}$ and $E_{\mathrm{y}}^{\mathrm{miss}}$ resolution derived in $Z \to \mu\mu$ and $Z \to ee$ events as a function of the total transverse energy of the event ($\sum E_{\mathrm{T}}$) [256].

7. Event Selection

Events are selected based on the objects identified and reconstructed as described in the previous Section 6. While the object definitions are generally optimised for analyses searching for top quarks in the final state, the final selection criteria of candidate events from data and MC samples are usually refined and adopted to the the specific measurement and physics process under investigation, i.e. to simultaneously obtain high signal purity in a sample of sufficiently large statistics. However, before any final event selection criteria are applied, events are preselected based on general event quality and cleaning cuts applied on all data and MC samples as detailed in the following section.

7.1. Preselection

7.1.1. Data Quality and Event Cleaning Cuts

Only those events are selected which pass the Good Run List[1] (GRL), rejecting events from periods of unstable beam operations or with inoperable or malfunctioning detector components or trigger systems. Further, events are required to have at least one primary vertex reconstructed from at least five tracks. In addition, several event cleaning criteria are applied to avoid rare cases in which data corruption occurred at the event level, i.e. incomplete or duplicate events have been recorded, or certain detector malfunctions or noise bursts occurred which were not accounted for in the GRL:

LAr noise bursts : Events with noise bursts and data integrity errors in the LAr calorimeter are removed using an error flag provided in the input datasets.

TileCal corruption: Since 2011 the Tile Calorimeter has suffered from frequent module errors (trips). Events with trips or neighbouring unpowered modules in the TileCal are therefore removed.

Incomplete events: Due to restarts of the central ATLAS timing, trigger and control system (TTC) events in the lumi-block after any such restart may be produced with some part of the detector information missing. Those events therefore are rejected using an error flag provided in the input datasets.

Duplicate events: In very rare occasions malfunctions of the DAQ system may result in events being written out twice. In addition, the inclusive trigger and streaming model implicates that the same event may be triggered simultaneously in different

[1] For this analysis the revision *PHYS-StandardGRL-All-Good* in combination with the detector status and defects databases *DetStatus-v54-pro13-04* and *DQDefects-00-00-33* is used.

chains and hence is written out in more than one output stream. Therefore any such duplicate events are removed to avoid double-counting and to obtain statistically independent samples of both lepton channels.

7.1.2. Checks for Redundantly Reconstructed Objects

In addition, several overlap criteria are applied by which objects identified and reconstructed redundantly by different algorithms, but likely having their origin in the same physics object in the detector, are removed or whole events are rejected as follows:

Jet-electron overlap removal : Apart from the removal of the closest jet within $\Delta R < 0.2$ of an electron (see Section 6.2.3), remaining electron candidates overlapping with jets within a cone of $\Delta R < 0.4$ are rejected subsequently;

Muon-jet overlap removal: Muons are rejected if their momentum vector falls within a cone of $\Delta R < 0.4$ around any jet with $p_{\mathrm{T}} > 25$ GeV and $|JVF| > 0.5$, since these usually stem from semi-leptonic heavy-flavour decays inside the jet;

Electron-muon overlap removal: Events are rejected if a reconstructed electron and muon share the same ID track.

7.2. Event Selection Cuts

After the offline object reconstruction, extra cuts are applied to the physics objects. The event selection is adapted to the final state signature of the FCNC signal processes illustrated in Figure 7.1. Hence events are selected containing a lepton and a neutrino, measured as missing transverse energy, one b quark, and potentially additional light-flavour jets originating from $2 \to 2$ or higher order processes, such as top-quark+gluon or top+light quark production (cf. Section 5.2.1).

Therefore events are selected, which contain exactly one isolated electron or muon, missing transverse energy and one or two jets, one of which is required to be identified as a b-quark jet. The final event selection is applied to two different types of datasets or samples, recorded either via the single electron (Egamma stream) or muon trigger chains (Muon stream) during data-taking, or in the detector simulation for MC simulated events, respectively. Equally, events are selected in two different categories (channels) defined by the lepton flavour if they contain:

- exactly one central ($|\eta| < 2.47$) electron (electron channel) or exactly one central ($|\eta| < 2.5$) muon with $p_{\mathrm{T}} > 25$ GeV (muon channel);
- a substantial amount of missing transverse energy of $E_{\mathrm{T}}^{\mathrm{miss}} > 30$ GeV,
- exactly one or exactly two central jets with $p_{\mathrm{T}} > 30$ GeV within a pseudorapidity range of $|\eta| < 2.5$,

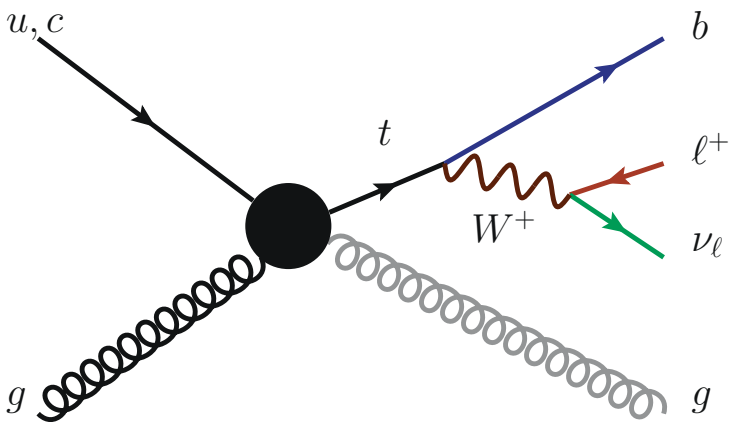

Figure 7.1.: Final state signature of the signal FCNC processes containing a single lepton and neutrino, one b-quark jet, and potentially additional light-flavour jets originating from $2 \to 2$ and higher order processes.

- exactly one jet which has been identified as a b-quark jet using the MV1c algorithm at 50% b-tagging efficiency,
- and pass a cut in the reconstructed transverse W mass of $m_{\mathrm{T}}(W) > 50$ GeV, to be defined in the following.

Apart from a cut on $E_{\mathrm{T}}^{\mathrm{miss}}$, the transverse W-boson mass is an effective way to distinguish signal from fake electrons from QCD multijet events since the $m_{\mathrm{T}}(W)$ distribution of the multijet background tends to be softer with respect to single-top events containing a real W boson in the decay chain. The transverse W-boson mass is reconstructed from the transverse momentum vectors of the lepton and neutrino, the latter of which is derived from the $\vec{E}_{\mathrm{T}}^{\mathrm{miss}}$ vector as described in Section 8.2.1:

$$m_{\mathrm{T}}(W) = \sqrt{2 p_{\mathrm{T}}(\ell) p_{\mathrm{T}}(\nu) - \vec{p}_{\mathrm{T}}(\ell)\vec{p}_{\mathrm{T}}(\nu)} = \sqrt{2\, p_{\mathrm{T}}(\ell)\, E_{\mathrm{T}}^{\mathrm{miss}} \left(1 - \cos\Delta\phi\left(\ell, \vec{E}_{\mathrm{T}}^{\mathrm{miss}}\right)\right)} \ ,$$

where $p_{\mathrm{T}}(\ell)$, $p_{\mathrm{T}}(\nu)$ denote the transverse momentum of the lepton or neutrino and $\Delta\phi\left(\ell, E_{\mathrm{T}}^{\mathrm{miss}}\right) = \phi(\ell) - \phi(\nu)$ stands for their reconstructed azimuthal angular distance.

Using the event selection described above, an event sample is selected which will form the basis of the later statistical analysis, hereafter called signal sample or signal region. A second, disjoint selection sample is defined in a different kinematic region using almost identical selection criteria, the only difference lying in a looser b-tagging requirement. This event sample, hereafter called control sample or control region, is obtained using the MV1 algorithm calibrated at a higher b-tagging efficiency of 85% while events with jets passing the tighter nominal (MV1c) b-tagging requirement of the signal sample are rejected. The control sample thereby obtained is dominated by W+jets production and

allows for the same definitions of objects and kinematic variables to be used as in the signal region in order to check their correct modelling in MC simulation. The signal and control samples are further divided according to their jet multiplicity reconstructed in the final state, in the following referred to as (exclusive) 1-jet and 2-jet bin. Assuming a cross-section of 1 pb for FCNC single top-quark production, about 450 signal events in 14.1 fb^{-1} of collision data are expected in the 1-jet bin signal region and about 350 signal events in the 1-jet bin control region, while the overall statistics of the control region is approximately four times larger.

7.3. Background Estimation

The background shapes and rates of all except the QCD multijet background are estimated from MC simulations scaled to their respective theory cross-section prediction and to the integrated luminosity of the data sample as detailed in Section 5. Since the multijet background is difficult to model precisely using MC simulations (cf. Section 5.3), different methods are employed to estimate its shape and normalisation in the electron and muon channel separately, as will be detailed in the following sections.

7.3.1. Estimation of the QCD Multijet Background

In total, three different methods are investigated to obtain shapes and, if possible, also the normalisations of the multijet background: the matrix method, the jet-electron model and the so-called anti-muon model. In general these partially data-driven techniques require a selection which to a large extend is similar to the nominal selection criteria. Only certain cuts and object criteria are modified or inverted, such that the obtained sample is enriched in QCD multijet (fake) events, while staying mostly independent of the original signal selection. To obtain a multijet sample in the electron channel the "jet-electron model" is chosen while the "matrix method" is applied in the muon channel. To obtain the normalisation for the multijet background sample in the electron channel a fit in the $E_{\text{T}}^{\text{miss}}$ distribution is performed, whereas in the muon channel the rate estimation is obtained from the matrix method itself.

Matrix method: The data-driven matrix method estimates the number and the kinematic shape of fake events in the muon or electron channel of the signal region using two samples selected via loose and tight (nominal) lepton isolation criteria, where the latter is a subset of the loose definition. The loose selection hence is defined to contain leptons of mostly similar kinematics, but resulting in much higher yields. Except from the isolation requirement, both selections are set mostly identical. Using the measured efficiencies of real and fake leptons of the loose selection to also pass the tight isolation requirements, ϵ_{real} and ϵ_{fake}, one can express the number of fake leptons ($N_{\text{tight}}^{\text{fake}}$) passing the tight (nominal) isolation requirements as follows:

$$N_{\text{tight}}^{\text{fake}} = \frac{\epsilon_{\text{fake}}}{\epsilon_{\text{real}} - \epsilon_{\text{fake}}} \left(N_{\text{loose}} \cdot \epsilon_{\text{real}} - N_{\text{tight}}\right) \ ,$$

where

$$N_{\text{tight}} = N_{\text{tight}}^{\text{fake}} + N_{\text{tight}}^{\text{real}} \quad \text{and} \quad N_{\text{loose}} = N_{\text{loose}}^{\text{fake}} + N_{\text{loose}}^{\text{real}}$$

are the respective numbers of leptons passing the loose and tight selection, and the efficiencies ϵ_{real} and ϵ_{fake} are defined as:

$$\epsilon_{\text{real}} = \frac{N_{\text{tight}}^{\text{real}}}{N_{\text{loose}}^{\text{real}}} \quad \text{and} \quad \epsilon_{\text{fake}} = \frac{N_{\text{tight}}^{\text{fake}}}{N_{\text{loose}}^{\text{fake}}} \ .$$

The loose selection criteria (to obtain N_{loose}) used in the electron channel are identical to the nominal (tight) identification and reconstruction criteria, except:

- only "medium" lepton identification criteria are required (cf. Sec. 6.2.1),
- a conversion match veto is applied,
- no isolation is required (muon-jet overlap removal nevertheless is applied),
- accordingly, for the calculation of the $E_{\text{T}}^{\text{miss}}$ (cf. Section 6.2.4) the collection used is `MET_RefFinal_AntiKt4LCTopoJets_mediumpp`.

In the muon channel the loose definition is identical to the nominal (tight) object reconstruction criteria, except no isolation requirement, i.e. no mini-isolation is applied.

The efficiencies of real and fake loose leptons to also pass the tight selection criteria are measured in collision data using event samples of dedicated control regions, enriched with real leptons or fake leptons, respectively. In the electron channel both efficiencies were measured in the same 8 TeV ($14.1\,\text{fb}^{-1}$) dataset that is used in this analysis. Also the event selection mostly follows the nominal selection described in Section 7.2, except for including higher multiplicities of jets (with $p_{\text{T}} > 25$ GeV), a different b-tagging requirement (MV1 at 70% b-tagging efficiency), and requiring exactly one loose electron as defined above. The fake enriched region is selected with a low amount of missing transverse energy of $E_{\text{T}}^{\text{miss}} < 20$ GeV or by fulfilling $E_{\text{T}}^{\text{miss}} + m_{\text{T}}(W) < 60$ GeV, while the efficiency for real leptons is measured in events with $E_{\text{T}}^{\text{miss}} > 120$ GeV. Events with real electrons in the fake enriched region are subtracted using estimates from MC simulation. To avoid any remaining dependencies on the event topology, the efficiencies were parametrised in variables they most vary in, namely the p_{T} and η of the electron, the azimuthal distance $\Delta\phi$ between the electron and the $\vec{E}_{\text{T}}^{\text{miss}}$ vector, the angular distance ΔR between the electron and the closer jet, $E_{\text{T}}^{\text{miss}}$ itself, and $\sum E_{\text{T}}$.

In the muon channel the efficiencies for fake/real loose muons to pass the tight selection criteria are measured in collision data using the same dataset and event selection as is used to estimate the efficiencies in the electron channel. Similarly, exactly one loose muon is required, using the loose and tight muon definitions as described initially. The fake efficiencies were determined in a control region of high muon d_0 impact parameter significance ($|d_0^{\text{sig}}| > 0.5$). The real muon enriched region is defined by requiring $m_T(W) > 100$ GeV. The contributions from real

muons in the fake enriched region are again subtracted using predictions from MC simulated events. To account for remaining dependencies on the muon isolation, the detector acceptance or on the hadronic activity from hard jets, both efficiencies are parametrised in the p_T and $|\eta|$ of the muon, the distance ΔR between the muon and the closest jet, and in the number of b-tagged jets. To obtain the final multijet sample in the electron or muon channel, the measured efficiencies are applied to data in the form of weights for events passing the loose or tight selection criteria, respectively.

Jet-electron model: The jet-electron model derives a shape for the multijet background in the electron channel by selecting events with similar kinematics to the signal selection, but with jets intentionally misreconstructed as an electron and used in place of it. The method thereby intends to mimic the dominant fake mechanisms in nominally reconstructed events. The model is used on events selected from a PYTHIA dijet sample using jet triggers, where each jet resembling an electron has to fulfil almost the same selection criteria as a signal lepton, i.e. requiring an $E_{\mathrm{T}} > 25$ GeV calibrated at the EM scale within an pseudorapidity range of $\eta < 2.47$ which requires a different algorithm for the $E_{\mathrm{T}}^{\mathrm{miss}}$ calculation. In order to reduce contributions from converted photons the jet has to be associated to at least four ID tracks. Further it has to deposit a fraction of $f_{\mathrm{EM}} = 80-95\%$ of its energy in the EM calorimeter. To reduce the contributions from real electrons, e.g. from W+jets processes, a veto cut is placed on events in which a lepton was identified according to high-efficiency (loose) criteria. Lastly, the event is accepted if exactly one jet fulfils the above criteria. Albeit a-priori counter-intuitive, the same method and selection as described above resembles a model that also provides a reasonable description of the background from fake leptons in the muon channel. In either case the selected jet-electron events are only used to obtain a background shape model for the multijet events, hence no special trigger requirement is applied. For the same reason the normalisation of the template has to be derived by fitting the model to observed data together with all remaining SM backgrounds in either lepton channel, which will be discussed in more detail later in this section.

Antimuon model: The data-driven antimuon method provides an estimate of the fake background shape in the muon channel by inverting or changing several criteria of the nominal event selection:

- the mini-isolation requirement is loosened, requiring $\sum_{\mathrm{tracks}} p_{\mathrm{T}}^{\mathrm{track}} \,/\, p_{\mathrm{T}}^{\ell} < 0.1$ (cf. Sect. 6.2.2),
- no z_0 constraint is applied as an additional track quality requirement in the mini-isolation,
- the ratio of the energy deposits in the calorimeter within a cone around the muon of $\Delta R = 0.2$ to its p_{T} is *larger* than 30%,
- fake muons are to be selected preferably inside jets by requiring a special flag provided by the calorimeter (`EnergyLossType`=1 or "NotIsolated"), and

- fake jets from real muons losing large amounts of energy are rejected by requiring an energy loss of at most 6 GeV.

Similar to the jet-electron model, a fake enriched sample with low contribution from signal muons is obtained. Same as for the jet-electron method, the normalisation of the template has to be derived by fitting the model to observed data.

All above models are studied to make a particular choice for each lepton channel based on the quality of the shapes and rates of the templates obtained by each method. In the electron channel a comparison is made between the matrix method and the jet-electron model. In the muon channel templates are obtained using the matrix method, antimuon and jet-electron model. In the following, the results are presented exemplarily for the 1-jet bin signal and control regions. The respective results for the 2-jet bin can be found in Appendix A. To determine the normalisation of the multijet background template using the jet-electron or anti-muon model, a binned maximum likelihood fit of the template, together with all MC simulated backgrounds, is performed to the observed data in the full $E_{\mathrm{T}}^{\mathrm{miss}}$ distribution after applying all nominal selection criteria, but leaving out the cut on $E_{\mathrm{T}}^{\mathrm{miss}}$ itself. The $E_{\mathrm{T}}^{\mathrm{miss}}$ distribution is of particular utility since the QCD multijet background is expected to have a much softer $E_{\mathrm{T}}^{\mathrm{miss}}$ distribution than the signal and most SM background processes.

In case of the jet-electron model in the electron channel, the fits are performed separately in two channels for electrons in the endcaps ($|\eta| \geq 1.5$) and in the central ($|\eta| < 1.5$) part of the electromagnetic calorimeter, for the signal and control region respectively. This is required, since it was found that the model does not properly describe the fraction of QCD events in the central and forward regions simultaneously. The multijet template is fitted together with templates for all other background processes derived from MC simulation, which are normalised to their respective theory cross-section predictions, namely top-quark, W+jets, W+HF+jets, Z+jets and diboson production. The rate uncertainties of the latter are accounted for by means of additional constrained nuisance parameters, whereas the multijet template is left as a free parameter in the fitting process.

In order to improve the stability of the fits, it has to be accounted for the similar shapes of particular backgrounds in the $E_{\mathrm{T}}^{\mathrm{miss}}$ distribution. Consequently the contributions from W+jets and W+HF+jets, the contributions from $t\bar{t}$ and single top-quark production, and the contributions from Z+jets and diboson production were each joined into one template, while keeping the relative fractions according to the theory predictions. Due the still similar shape of the joined Z+jets/diboson template with respect to the W+(HF)+jets backgrounds, the rate of the first is fixed since it represents the smallest background in the analysis. In case of the matrix method, the shape and the normalisation of the multijet background are both obtained from the model itself. Nevertheless a fit in the $E_{\mathrm{T}}^{\mathrm{miss}}$ distribution is performed in this case as well, but with the normalisation of the multijet template being fixed and varying the remaining background processes within their constraints only. The Gaussian constraints of the combined background templates reflect the larger of the cross-section uncertainties of each sub-process in the joined template, namely 55% for the combined W+jets and 6% for the top-quark

template.

Figure 7.2 shows the corresponding $E_{\mathrm{T}}^{\mathrm{miss}}$ distributions in the 1-jet bin signal and control region after applying the binned maximum likelihood fit in the electron channel for multijet estimates derived using the matrix method or jet-electron model. Here, the different backgrounds and the multijet template are shown rescaled to their respective fit results. The fit results of the jet-electron model are shown for both, the forward/central regions as well as for their combination. Figure 7.3 shows the corresponding fit results in the $E_{\mathrm{T}}^{\mathrm{miss}}$ distribution in the 1-jet bin muon channel, obtained using multijet estimates derived with the matrix method, antimuon and jet-electron model. The corresponding distributions for the 2-jet bin can be found in Appendix A.

The estimated values of the rates and relative fractions of the multijet background in the $E_{\mathrm{T}}^{\mathrm{miss}}$ region of the final event selection ($E_{\mathrm{T}}^{\mathrm{miss}} > 30$ GeV) and in the 1-jet bin are given in Table 7.1, for both lepton channels and the signal and control samples, respectively. Here, also the individual fit results for the jet-electron model in the electron central and forward region are shown. Similar tables showing the rates and relative fractions obtained with all models in the 2-jet bin are given in Appendix A. Table 7.2 shows

Table 7.1.: Estimates of the multijet background rates and fractions in the 1-jet bin signal and control region using the matrix method, jet-electron and antimuon model. The quoted numbers denote the (rounded) expected number of events in each region. The uncertainties reflect the statistical uncertainty from the limited template size, which in case of the jet-electron or antimuon model is combined with the uncertainty of the fit to the $E_{\mathrm{T}}^{\mathrm{miss}}$ distribution in data.

1-jet bin		signal region		control region	
Method	Channel	Events	Fraction	Events	Fraction
Jet-electron model	el. (cent.)	2830 ± 190	9%	14600 ± 500	9%
Jet-electron model	el. (fwd.)	2550 ± 180	20%	12100 ± 500	16%
Jet-electron model	el. (comb.)	5380 ± 250	12%	26700 ± 700	11%
Matrix method	electron	2970 ± 40	13%	14190 ± 70	6%
relative difference wrt. jet-electron model			+4%		−47%
Matrix method	muon	12700 ± 100	18%	21660 ± 190	6%
Antimuon model	muon	17800 ± 500	26%	72100 ± 1500	21%
relative difference wrt. matrix method			+46%		+240%
Jet-electron model	muon	9000 ± 300	13%	18600 ± 600	5%
relative difference wrt. matrix method			−28%		−12%

the simultaneously obtained scale factors for the combined contributions of W+jets and W+HF+jets, and for the joined $t\bar{t}$ and single top-quark production template. From the plots in Figure 7.3 it can be seen that in the muon channel the antimuon model overestimates the multijet background in the control region, which is confirmed by the small scale factors obtained for the combined W+jets/W+HF+jets and $t\bar{t}$/single top-quark background templates. This is likely to be caused by the antimuon multijet template having a shape much closer to the W+jets background than in case for all other models.

Table 7.2.: Scale factors for the combined contributions from W+jets/W+HF+jets and from $t\bar{t}$/single top-quark production in the 1-jet bin signal and control region as obtained from the simultaneous binned maximum likelihood fit in the $E_{\mathrm{T}}^{\mathrm{miss}}$ distribution.

1-jet bin		signal region		control region	
Method	Channel	W+jets	top	W+jets	top
Jet-electron model	el. (cent.)	1.05 ± 0.02	1.02 ± 0.03	1.01 ± 0.00	0.87 ± 0.04
Jet-electron model	el. (fwd.)	1.00 ± 0.03	1.14 ± 0.03	1.01 ± 0.01	1.01 ± 0.05
Jet-electron model	el. (comb.)	1.05 ± 0.02	1.04 ± 0.03	1.01 ± 0.00	0.93 ± 0.04
Matrix method	electron	0.90 ± 0.01	1.22 ± 0.03	1.06 ± 0.00	0.73 ± 0.04
Matrix method	muon	1.14 ± 0.02	1.10 ± 0.03	1.11 ± 0.00	0.89 ± 0.04
Antimuon model	muon	1.02 ± 0.02	1.01 ± 0.02	0.93 ± 0.01	0.65 ± 0.04
Jet-electron model	muon	1.23 ± 0.02	1.05 ± 0.03	1.12 ± 0.00	0.63 ± 0.04

Similarly, the jet-electron model tends to mismodel the multijet shape in both, the signal and control region towards lower $E_{\mathrm{T}}^{\mathrm{miss}}$, leading to unphysical scale factors for the other backgrounds. In the muon channel therefore the matrix method was chosen to be used as the nominal multijet model since it provides the best shape modelling and in turn results in the most reasonable scale factors for the remaining background processes. In the electron channel, however, the jet-electron model was chosen as the default method. As can be seen in Figure 7.2 the matrix method provides comparatively poor shape modelling in the electron channel and tends to overestimate the multijet contribution in the low $E_{\mathrm{T}}^{\mathrm{miss}}$ region, which also reflects in the respective scale factors derived for the W+jets and SM top-quark production processes.

Table 7.1 also shows the relative rate difference of all alternative models with respect to the default method in each channel. Apart from the highly overestimated rates from the antimuon model in the muon channel control region, all yields obtained with the alternative methods differ by at most -47/+46% in the 1-jet bin, and at most -56/+2% in the 2-jet bin (see Appendix A). Therefore a generic systematic rate uncertainty of 50% is assigned to the multijet background in each channel. The choice for this value is compatible with earlier estimates used in related single-top analyses in ATLAS [126, 257] and studies in 7 TeV data [258, 259], and is further supported by cross-checks in which the binned likelihood fit was performed in the less sensitive variable $m_{\mathrm{T}}(W)$, leaving out the $m_{\mathrm{T}}(W)$ cut instead of the $E_{\mathrm{T}}^{\mathrm{miss}}$ cut in the final event selection.

The scale factors for the combined contributions of W+jets/W+HF+jets and of $t\bar{t}$/single top-quark production as obtained in the fit to the E_T^{miss} distribution are not used in the later analysis and are only applied to scale the respective backgrounds in control plots in order to check the modelling of kinematic distributions, i.e. of the variables later used as input to the neural network (see Section 8). For the actual neural network training as well as for the final statistical analysis the normalisation of all backgrounds, except for that of the multijet background, is taken solely from MC simulations scaled to their respective theory cross-section predictions as described in Section 5.2.2. All rate

and cross-section uncertainties are then fully accounted for in the final limit evaluation.

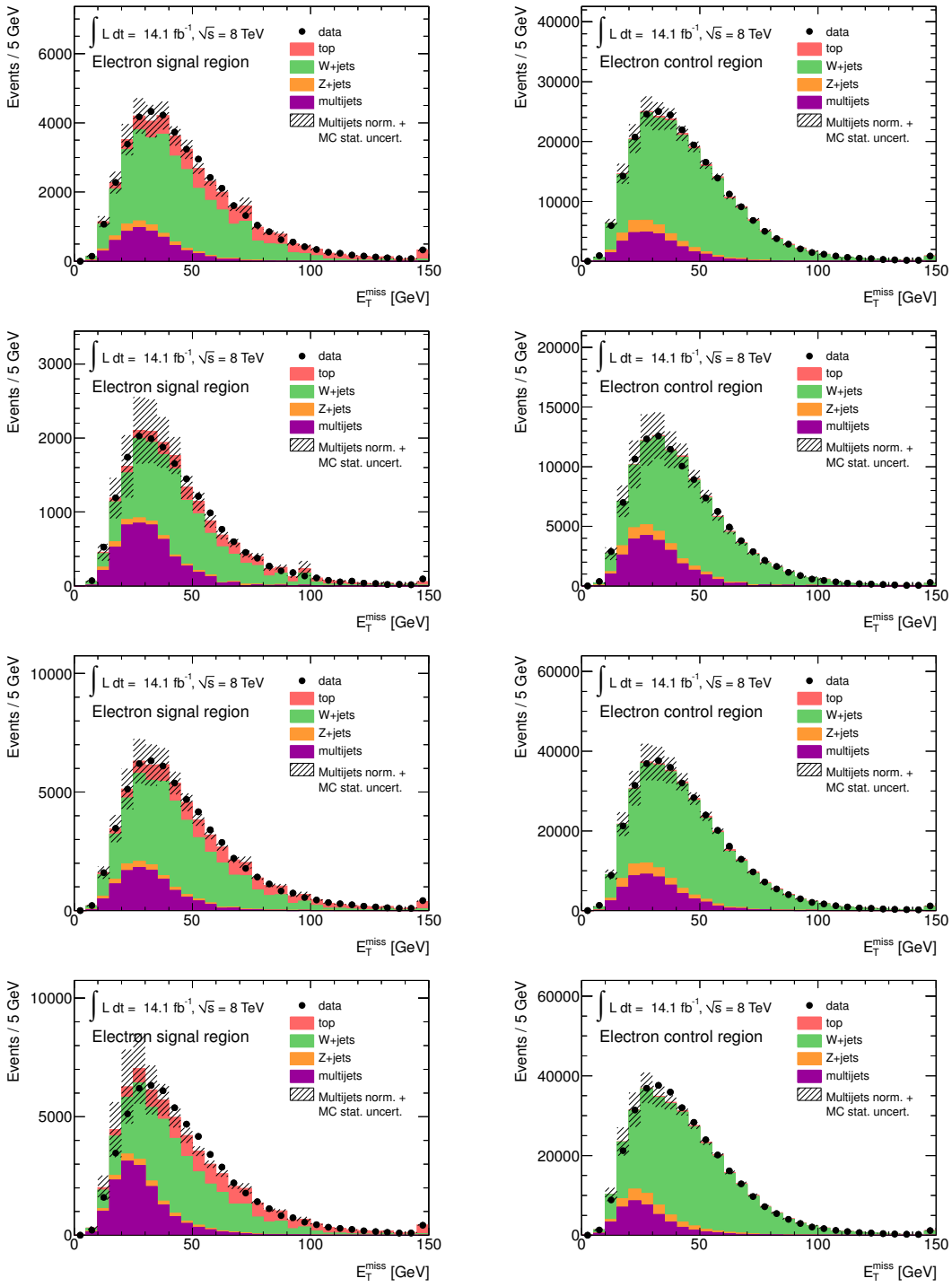

Figure 7.2.: Fitted $E_{\mathrm{T}}^{\mathrm{miss}}$ distributions for the 1-jet bin electron channel in the signal (left) and control region (right), using the jet-electron model in the central/forward regions (first/second row), and their combination (third row), as well as using the matrix method (bottom row). The error bands denote the combined MC statistical and assigned multijet rate uncertainty of 50 %.

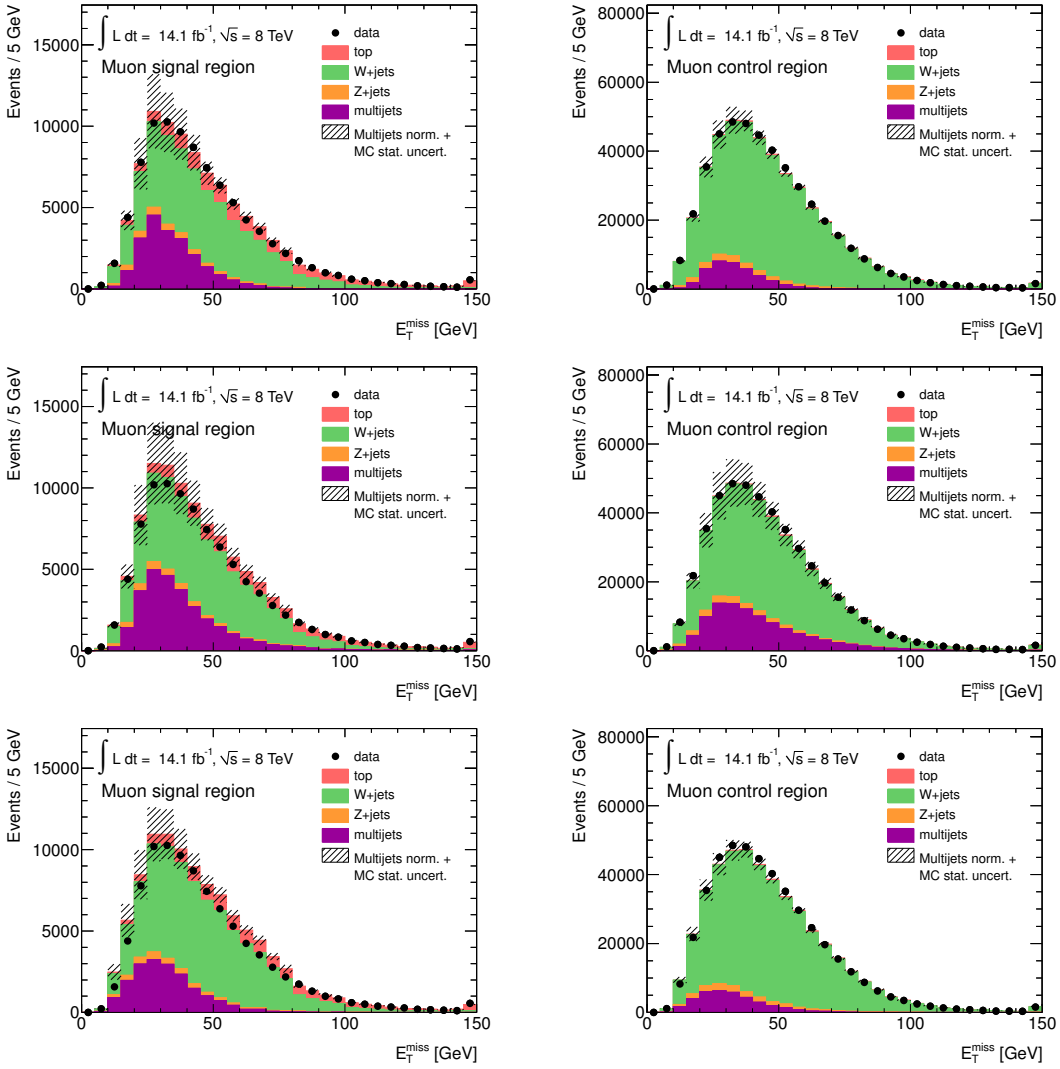

Figure 7.3.: Fitted $E_{\mathrm{T}}^{\mathrm{miss}}$ distributions for the 1-jet bin muon channel in the signal (left) and control sample (right), using the matrix method (top row), anti-muon model (middle row), and using the jet-electron model (bottom row). The error bands denote the combined MC statistical and assigned normalisation uncertainty of the multijet template of 50 %.

7.4. Event Yields and Basic Control Distributions

Table 7.3 summarises the event yields in the 1-jet bin signal and control region after applying the full object and event selection, for observed events and for each of the simulated background processes considered. Table 7.4 provides a summary of the respective event yields in the signal and control regions of the 2-jet bin. Also shown in both tables are the number of selected signal events for an assumed signal cross-section of 5 pb for the combined $ug \to t$ and $cg \to t$ FCNC processes. All yields in the respective signal

Table 7.3.: Number of observed events in collision data and expected number of background events for the signal and control region in the 1-jet bin, split up into the contributions from the different SM background processes. The number of selected signal events is shown for an assumed signal cross-section of 5 pb for the combined $ug \to t$ and $cg \to t$ processes. The (rounded) event yields reflect the acceptance from MC samples normalised to their respective theory cross-section and the data-driven multijet estimates. The uncertainties reflect the statistical uncertainties arising from the limited sizes of the simulation samples, combined with the cross-section or the multijet normalisation uncertainty respectively.

control region	electron channel			muon channel
process	central	forward	total	total
FCNC 5 pb	571 ± 11	174 ± 6	745 ± 12	988 ± 14
SM single top	2990 ± 150	814 ± 43	3800 ± 190	4920 ± 250
$t\bar{t}$	2480 ± 150	660 ± 42	3140 ± 190	3830 ± 230
W+jets	55000 ± 14000	30000 ± 7000	85000 ± 21000	124000 ± 30000
W+HF+jets	90000 ± 50000	30000 ± 16000	110000 ± 60000	160000 ± 90000
Z+Jets	5900 ± 1400	2900 ± 700	8800 ± 2100	10000 ± 2500
multijets	15000 ± 7000	12000 ± 6000	27000 ± 13000	22000 ± 11000
total expected	170000 ± 50000	76000 ± 19000	240000 ± 70000	320000 ± 90000
data	168996	76487	245483	351104
signal region	electron channel			muon channel
process	central	forward	total	total
FCNC 5 pb	761 ± 11	212 ± 6	973 ± 13	1296 ± 15
SM single top	4160 ± 210	1082 ± 56	5240 ± 260	6810 ± 340
$t\bar{t}$	3270 ± 200	863 ± 53	4140 ± 250	5220 ± 320
W+jets	2400 ± 700	1100 ± 400	3500 ± 1000	5000 ± 1300
W+HF+jets	16000 ± 9000	6500 ± 3500	23000 ± 12000	31000 ± 17000
Z+jets	710 ± 180	278 ± 71	990 ± 240	2000 ± 500
multijets	2800 ± 1400	2500 ± 1300	5400 ± 2700	13000 ± 6000
total expected	30000 ± 9000	12000 ± 4000	42000 ± 13000	63000 ± 18000
data	31271	12680	43951	68574

Table 7.4.: Number of observed events in collision data and expected number of background events for the signal and control region in the 2-jet bin, split up into the contributions from the different SM background processes. The number of selected signal events is shown for an assumed signal cross-section of 5 pb for the combined $ug \to t$ and $cg \to t$ processes. The (rounded) event yields reflect the acceptance from MC samples normalised to their respective theory cross-section and the data-driven multijet estimates. The uncertainties reflect the statistical uncertainties arising from the limited sizes of the simulation samples, combined with the cross-section or the multijet normalisation uncertainty respectively.

signal region	electron channel			muon channel
process	central	forward	total	total
FCNC 5 pb	237 ± 6	64 ± 3	301 ± 7	400 ± 8
SM single top	6000 ± 300	1177 ± 61	7200 ± 400	9100 ± 500
$t\bar{t}$	13100 ± 800	2930 ± 180	16000 ± 1000	20000 ± 1200
W+jets	1100 ± 400	300 ± 110	1400 ± 500	2000 ± 700
W+HF+jets	9000 ± 5000	3900 ± 2300	12500 ± 7500	17000 ± 10000
Z+jets	910 ± 310	360 ± 120	1300 ± 400	1500 ± 500
multijets	3000 ± 1500	1300 ± 700	4300 ± 2200	4400 ± 2200
total expected	33000 ± 6000	10018 ± 2463	43000 ± 8000	54000 ± 11000
data	32902	10920	43822	59838
control region	electron channel			muon channel
process	central	forward	total	total
FCNC 5 pb	179 ± 6	56 ± 3	234 ± 7	291 ± 8
SM single top	3600 ± 180	754 ± 40	4350 ± 220	5540 ± 280
$t\bar{t}$	6800 ± 400	1700 ± 100	8500 ± 500	10900 ± 700
W+jets	20000 ± 7000	11000 ± 4000	31000 ± 11000	45000 ± 15000
W+HF+jets	32000 ± 19000	12000 ± 7000	45000 ± 27000	60000 ± 40000
Z+Jets	3800 ± 1300	1700 ± 600	5500 ± 1900	5600 ± 1900
multijets	9000 ± 5000	6000 ± 3000	15000 ± 8000	9000 ± 4000
total expected	76000 ± 21000	33884 ± 8948	110000 ± 30000	140000 ± 40000
data	73258	33320	106578	143310

and control regions are calculated using the acceptance from MC samples normalised to their theoretical cross-sections, including the respective (N)NLO k-factors. Additional scale factors, e.g. as obtained in the likelihood fits for the multijet estimation, are not applied. In the electron channel the acceptance of the multijet background reflects the yields obtained from the binned maximum likelihood fit to the full $E_{\mathrm{T}}^{\mathrm{miss}}$ distribution in observed data, using a multijet template derived with the jet-electron model. The respective yields in the muon channels are obtained from the matrix method. The uncertainties in Tables 7.3 and 7.4 reflect the combination of the statistical uncertainty

due to the limited size of the simulated background samples with the cross-section or multijet rate uncertainty. The observed event yields in collision data agree well with the sum of all background predictions within the given uncertainties.

The main background contributions in the 1-jet bin arise from W+jets production, in particular in association with the production of heavy-flavour quarks, followed by contributions from multijet and SM top-quark production. While in the 2-jet bin control region the situation is similar to the 1-jet bin, in the signal region $t\bar{t}$ production represents the dominant background, followed by W+HF+jets and SM single top-quark production.

In order to check for any disagreement in the shape or rate of the simulation with respect to the observation in data, distributions of several basic kinematic variables in the control region were used to verify the correct modelling of the data. Figures 7.4 and 7.5 show distributions for the combination of the electron and muon channel of the transverse momentum and pseudorapidity of the lepton and jets as well as of the $m_{\mathrm{T}}(W)$ and $E_{\mathrm{T}}^{\mathrm{miss}}$ distributions, in the 1-jet and 2-jet bin respectively. The distributions are normalised using the scale factors obtained in the binned maximum likelihood fit to the $E_{\mathrm{T}}^{\mathrm{miss}}$ distribution used to determine the fraction of multijet events. Within the combined statistical (limited sample sizes) and multijet rate uncertainty very good agreement between the observed and simulated distributions is found.

Since any hypothetical contribution of FCNC events in the signal region is expected to contribute only marginally ($\approx 1 - 2\%$)) to the total number of expected events (cf. Tables 7.3 and 7.4), similar distributions for the signal region are used in order to have a coarse cross-check on potential shape mismodelling that could not be explained by a potential signal contribution. Figures 7.6 and 7.7 therefore show the same distributions of basic kinematic variables in the signal region for the combination of electron and muon channel, including a hypothetical FCNC signal contribution from the combined ugt and cgt processes that corresponds to a cross-section times branching ratio of 50 fb. Overall good agreement is found between the observed and simulated distributions.

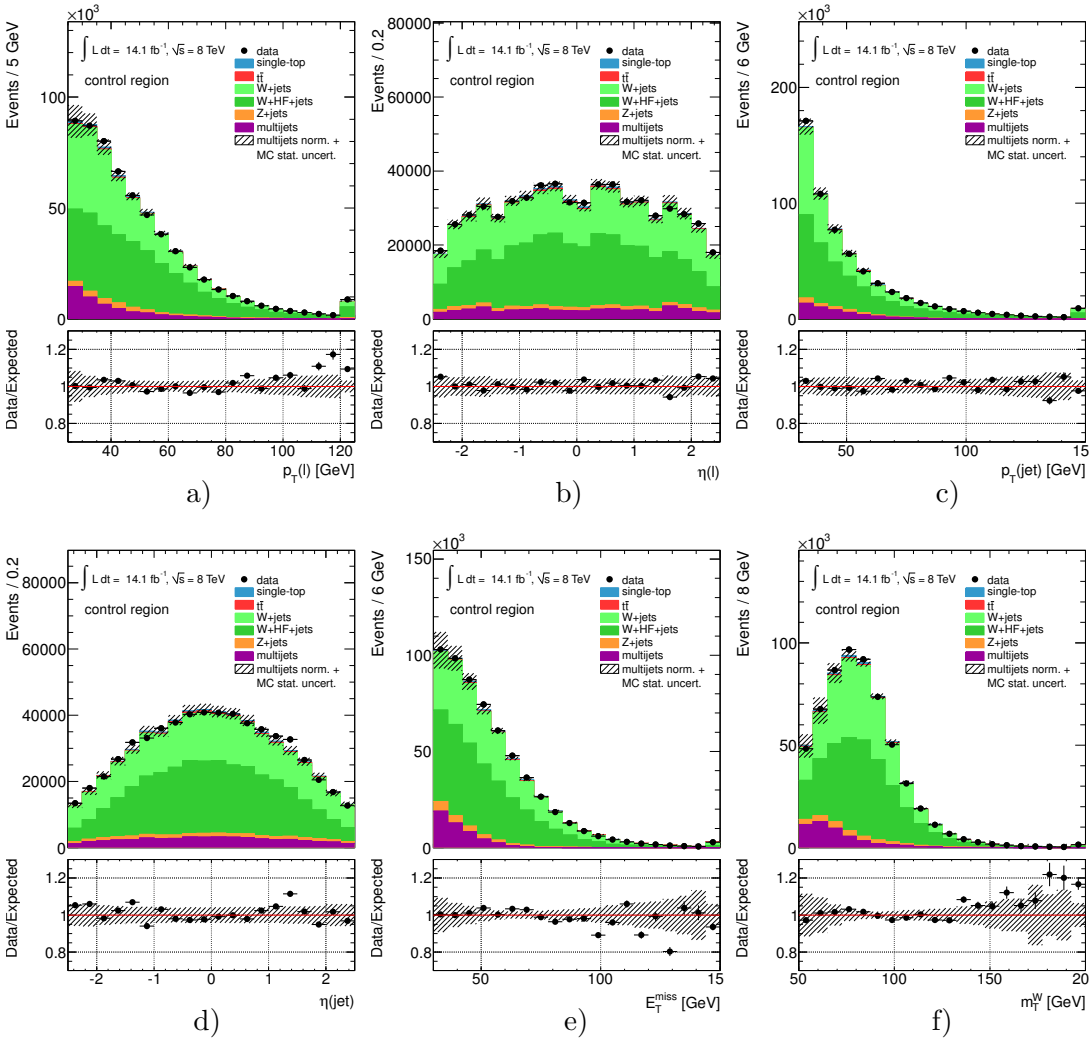

Figure 7.4.: Basic kinematic distributions for the combination of muon and electron channels in the 1-jet bin control region. The distributions are normalised using the scale factors obtained in the binned maximum likelihood fit to the $E_{\mathrm{T}}^{\mathrm{miss}}$ distribution used to determine the fraction of multijet events. Shown are the distributions of: a) the transverse momentum and b) pseudorapidity of the lepton, c) the transverse momentum and d) pseudorapidity of the jet, e) the missing transverse energy and f) the transverse W-boson mass. The last histogram bins include overflow events and the hatched error bands in the main and ratio plot reflect the combination of the statistical uncertainties (limited sample sizes) and the multijet normalisation uncertainty.

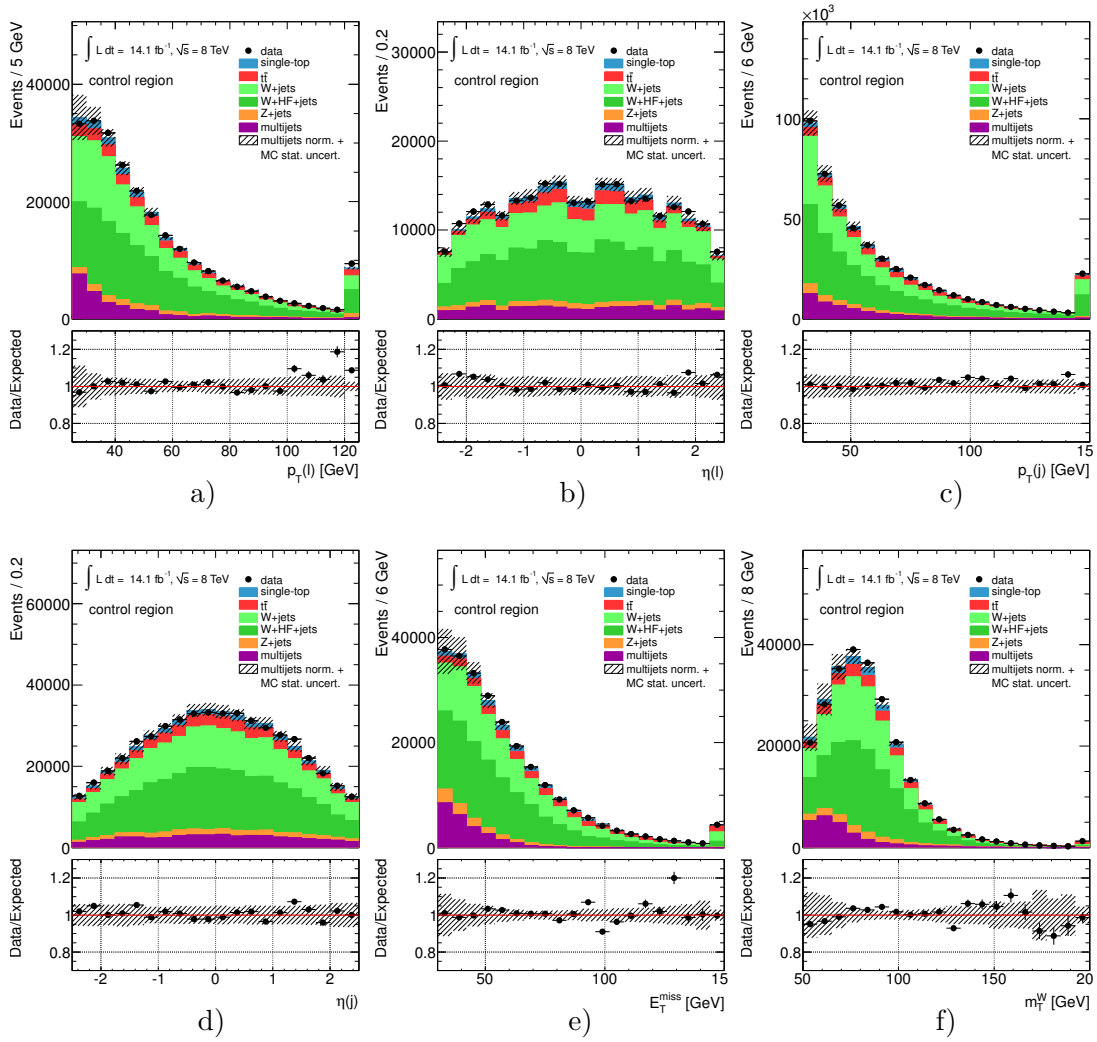

Figure 7.5.: Basic kinematic distributions for the combination of muon and electron channels in the 2-jet bin control region. The distributions are normalised using the scale factors obtained in the binned maximum likelihood fit to the $E_{\mathrm{T}}^{\mathrm{miss}}$ distribution used to determine the fraction of multijet events. Shown are the distributions of: a) the transverse momentum and b) pseudorapidity of the lepton, c) the transverse momenta and d) pseudorapidities of the jets, e) the missing transverse energy and f) the transverse W-boson mass. The last histogram bins include overflow events and the hatched error bands in the main and ratio plot reflect the combination of the statistical uncertainties (limited sample sizes) and the multijet normalisation uncertainty.

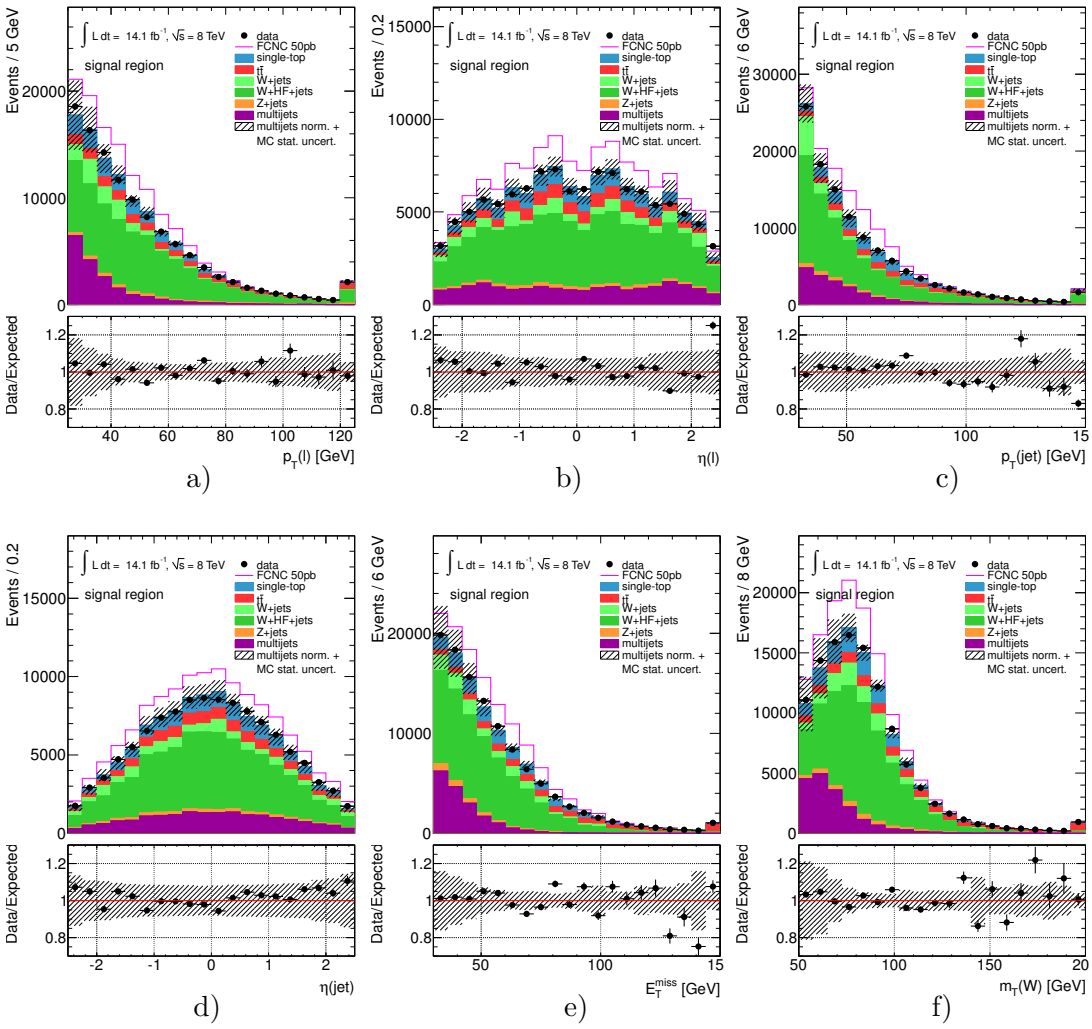

Figure 7.6.: Basic kinematic distributions for the combination of muon and electron channels in the 1-jet bin signal region. The distributions are normalised using the scale factors obtained in the binned maximum likelihood fit to the $E_{\mathrm{T}}^{\mathrm{miss}}$ distribution used to determine the fraction of multijet events. Shown are the distributions of: a) the transverse momentum and b) pseudorapidity of the lepton, c) the transverse momentum and d) pseudorapidity of the jet, e) the missing transverse energy and f) the transverse W-boson mass. A hypothetical FCNC signal contribution from the combined *ugt* and *cgt* processes corresponding to a cross-section of 50 pb is shown stacked on top of all SM background contributions. The lower pads show the relative difference between the observed distribution and that of the SM only expectation. The last histogram bins include overflow events and the hatched error bands in the main and ratio plot reflect the combination of the statistical uncertainties (limited sample sizes) and the multijet normalisation uncertainty.

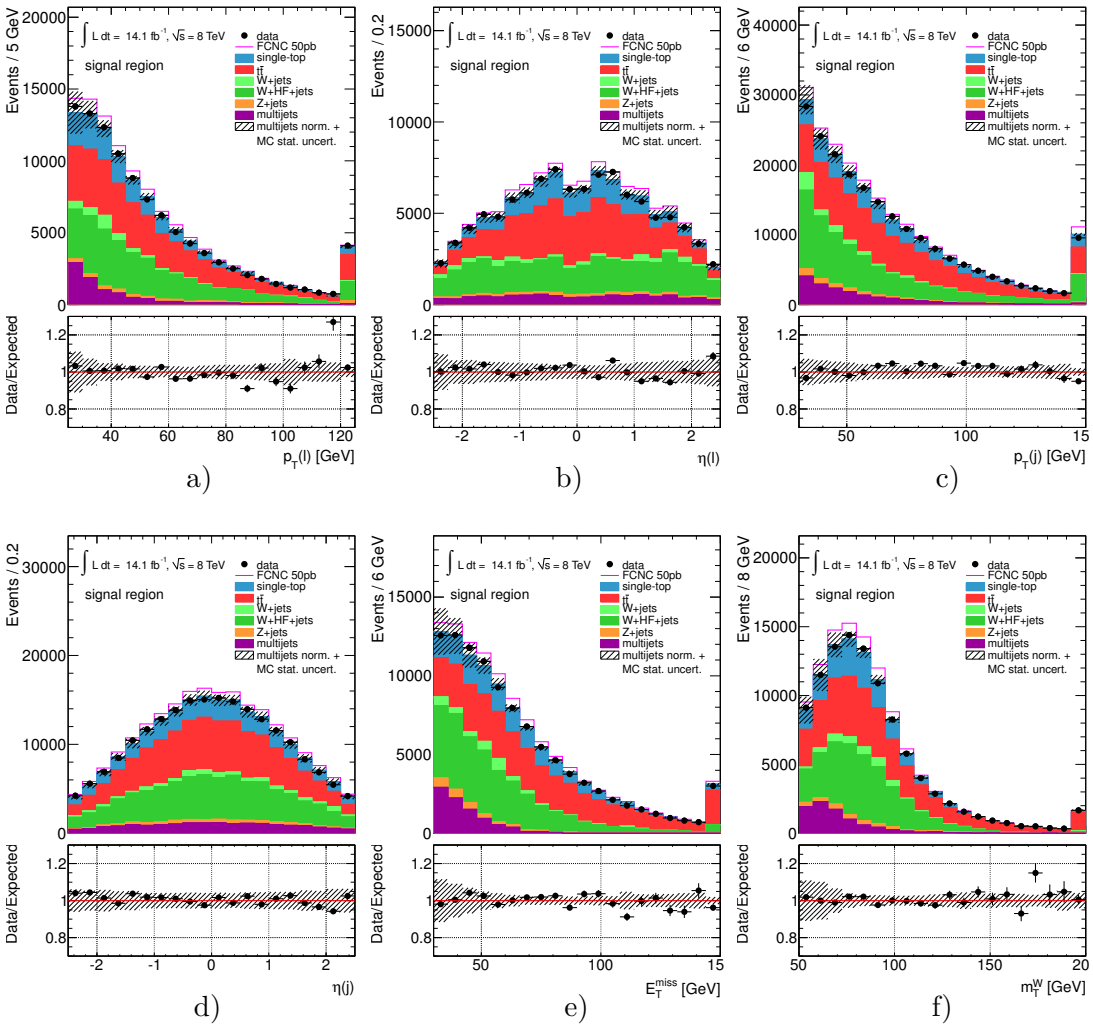

Figure 7.7.: Basic kinematic distributions for the combination of muon and electron channels in the 2-jet bin signal region. The distributions are normalised using the scale factors obtained in the binned maximum likelihood fit to the $E_{\mathrm{T}}^{\mathrm{miss}}$ distribution used to determine the fraction of multijet events. Shown are the distributions of: a) the transverse momentum and b) pseudorapidity of the lepton, c) the transverse momentum and d) pseudorapidity of the jet, e) the missing transverse energy and f) the transverse W-boson mass. A hypothetical FCNC signal contribution from the combined ugt and cgt processes corresponding to a cross-section of 50 pb is shown stacked on top of all SM background contributions. The lower pads show the relative difference between the observed distribution and that of the SM only expectation. The last histogram bins include overflow events and the hatched error bands in the main and ratio plot reflect the combination of the statistical uncertainties (limited sample sizes) and the multijet normalisation uncertainty.

8. Neural Network Analysis

Since no prominent variable exists which provides sufficient discriminating power on its own in order to distinguish signal from background events, a simple cut-based analysis does not provide enough sensitivity to search for single top-quark production in FCNC processes mediated via the strong force. The low signal-to-background ratio of at most 1:50 for a 5 fb FCNC signal in the 1-jet bin and not least the shape and rate uncertainties would severely limit any signal cross-section measurement. Therefore, a multivariate analysis (MVA) is indispensable to exploit the full separation power that is distributed over many correlated variables. In this analysis a neural network classifier is employed which is optimised for this task and combines the information of many kinematic and topological variables of the final state objects and their correlations to form a single continuous classifier output of high shape-wise differentiation between signal and background events. The basic principles of neural network techniques and their implementation in this analysis are discussed in the next section, followed by a description of the neural network training process and the variables used as inputs to the network in Section 8.2.

8.1. Basics and Implementation

Artificial neural networks (ANNs) provide (approximate) solutions to complex optimisation and generalisation problems which cannot easily be expressed algorithmically. ANNs generalise and associate data in an iterative procedure, inspired by the adaptive learning capabilities of biological neural networks. In analogy to the latter, they are built from sets of interconnected (technical) "neurons" or nodes which compute scalar output values in each discrete time step (iteration) from a vector of inputs using a non-linear mapping. The inputs are variably weighted, depending on the weight $\omega_{i,j}$ (or "strength") of the directed connection between two neurons i and j. The non-linear mapping between the input vector of a neuron j, usually a linear composition of scalar outputs of other neurons i $(o_1, ..., o_n)$, is given by a set of transformations consisting of a so-called propagation, an activation or transfer function, and an output function. The propagation function (f_{prop}) defines the actual input to the neuron by transforming the outputs o_i of all neurons i that are connected to the neuron j of interest, accounting for the weights of each connection, respectively. The propagation function is usually chosen to be the weighted sum of all connected outputs o_i:

$$p_j = f_{\text{prop}}(o_i, \omega_{i,j}) = \sum_i \omega_{i,j}\, o_i \quad . \tag{8.1}$$

The activation function defines the actual mapping to the activation (output) value of the neuron j, potentially taking into account the neurons former activation state $a_j(t-1)$, that is given by the output of the activation function in the previous iteration $(t-1)$. Further, it depends on a threshold or bias value (b_j) which is given by the position at which the activation function reaches its maximum gradient (in analogy to the potential needed to make biological neurons fire):

$$a_j(t) = f_{\text{act}}\left(p_j, b_j, a_j(t-1)\right) \quad . \tag{8.2}$$

The activation function is usually defined globally for all neurons and often is chosen to be a binary threshold (Heavyside) or sigmoid function, e.g. hyperbolic tangent or Fermi function. Finally, the output function defines the output of a neuron from its current activation state and is usually set to identity, i.e. the activation is directly taken as the neurons output:

$$o_j = f_{\text{out}}(a_j) = a_j \quad . \tag{8.3}$$

Several network topologies exist, which are defined by the arrangement of neurons and the connections between them. In this analysis the NeuroBayes® package [260, 261] is used, which implements a three-layer feed-forward topology that arranges neurons in three distinct levels, an input layer, a hidden layer and an output layer. In a feed-forward network each neuron is allowed to have directed connections to neurons of the subsequent layer only, thereby forming a directed non-cyclic graph. Hence, neurons from the input layer connect to neurons in the hidden (processing) layer, also referred to as hidden nodes, and the latter connect to neurons in the output layer, in the following referred to as output nodes. Several other topologies exist which are not detailed here. A comprehensive discussion of the neural network techniques described in this section, including further common network topologies, can be found in e.g. [262] or [263]. Since the ANN is destined to classify events as signal- or background-like based on kinematic variables of the final state objects, the input layer consists of one node for each input variable plus one bias node. These are connected to an arbitrary number of hidden nodes in the second layer which themselves conjointly connect to a single output node in the last layer. The extra bias node has the purpose of simplifying the activation function for computational reasons, such that it replaces the threshold value in the activation function that defines the nodes response. This can be achieved by a constantly active node with output 1, which allows to represent the negative threshold values of all j nodes in the subsequent layer in the form of connection weights $(\omega_{\text{bias},j})$ from the bias node to each. The threshold value is already subtracted from the network input at the stage of calculating the propagation function, which facilitates the learning algorithms applied later to train the connection weights and node thresholds at the same time. The NeuroBayes package uses a sigmoidal activation function which maps a continuous infinite/unconstrained input $p \in [-\infty, +\infty]$ from the propagation function to a continuous output in the interval $[-1, +1]$ as shown in Figure 8.1:

$$f_{\text{act}} = S(p) = \frac{2}{1 + e^{\,-p}} - 1 \quad . \tag{8.4}$$

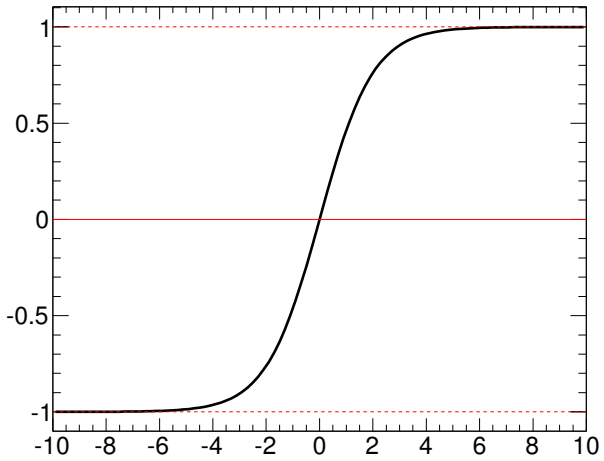

Figure 8.1.: Sigmoidal activation function as given in Equation 8.4. The function is particularly sensitive to inputs from the propagation function (p) within the range around zero. For large input values immediate saturation is reached.

Using the propagation and output functions defined in Equations 8.1 and 8.2, the full ANN output consequently provides a continuous classification variable in the same output interval and is given as follows:

$$O_{\mathrm{ANN}} = f_{\mathrm{act}} \left(\sum_j \omega_{j,k} \cdot \sum_i \left(\omega_{i,j}\, x_i + \omega_{\mathrm{bias},j} \right) \right) \quad , \tag{8.5}$$

where the x_i represent the values of the variables used as inputs to the nodes i in the first layer, and $\omega_{i,j}$, $\omega_{j,k}$ are the connection weights on the input nodes to the hidden nodes (j), or of the hidden nodes to the output node k.

The learning capability is the main characteristic of ANNs which enables them to familiarise solutions to problem in a training procedure (i.e. the classification of signal/background-like simulated events) and to generalise them in order to provide solutions to unknown problems of the same class (i.e. to apply the classification to observed data). The training in general is an iterative procedure by which the neural network is altered via changes in its components, i.e. by adding or deleting connections or nodes, varying the nodes propagation or activation function, or more commonly by only changing connecting weights and threshold values (hence bias node connection weights). The NeuroBayes package implements the latter case, leaving the overall network topology and the global transfer functions of the nodes fixed. In a so-called supervised learning procedure the training inputs are entered in form of simulated signal and background events, provided together with appropriate output values (targets), namely the desired binary classification into signal ($+1$) or background events (-1). In the actual train-

ing, in each iteration the difference between the target and the actual output value is compared using an error function (Err(W)), that is defined on the set of all connection weights between the nodes (W). In the case of NeuroBayes, the entropy loss function, also referred to as cross-entropy function, is used as an error function and is defined as

$$\mathrm{Err}(W) = \sum_n \log\left(\frac{1}{2}\cdot(1 + T_n \cdot O_n(W) + \epsilon)\right) \quad , \tag{8.6}$$

where T_n is the desired (binary) output value or target (-1 or $+1$) of the network in a subset of training events n, O_n is the actual neural network output value for a set of connection weights (W), and ϵ is a regularisation constant. The loss function hence is a measure of how well the network is trained to produce the desired output and therefore represents the quantity to be minimised. The error function (Err(W)) is minimised numerically and provides information on how to change the connection weights by calculating its gradient: $\Delta W = -\eta \bigtriangledown \mathrm{Err}(W)$. To obtain information on how to change each single connection weight in the next iteration, the gradient of the error function is rewritten in form of the usual partial derivatives to the single weights

$$\Delta\omega_{i,j} = -\eta \frac{\partial \mathrm{Err}(W)}{\partial \omega_{i,j}} \quad . \tag{8.7}$$

The parameter η represents a global step width by which the weights are changed in proportion to the gradient of the current training iteration. They are adapted for each weight individually in the training process. In order to improve the generalisation performance and to avoid overtraining, Bayesian regularisation techniques are employed by which the absolute weights are continuously reduced during the training process, in addition to the variations calculated from the gradient of the error function (weight decay). Thereby statistical fluctuations are reduced and only recurring training patterns become subject to the learning. The Bayesian regularisation approach allows for an automated optimisation of the weight decay parameters during the training and thereby simultaneously prevents overfitting and oversmoothing [264]. Since weights of connections might become zero and thus even whole nodes could become insignificant, they are removed by a pruning mechanism. The training then is continued with the reduced network which minimises possible noise sources and leads to an optimised network topology and overall better generalisation performance. The whole training process is repeated until either the maximum of training iterations is reached, or the training is stopped by mechanisms to prevent the loss of generalisation capabilities from memorising the training patterns "by heart" (see Section 8.2.4). More details on the above training procedure and the regularisation techniques employed in NeuroBayes can be found in [260, 261].

8.2. Neural Network Training and Preprocessing

The training is performed using simulated events of the signal and all background processes, except the multijet background. The latter is excluded, since it is not based on

simulated samples but on approximate models derived from data. Hence, this conservative choice is made to avoid the data-driven patterns to be learned by the network rather than learning the "real" signature of multijet events – for the price of slightly decreased discrimination power against the multijet background. However the effect of the latter is already minimised by the application of stringent selection criteria, by which the total contribution from the multijet background in the signal samples is reduced significantly. Nonetheless, tests were performed to quantify the impact on the overall separation power of the network and on the results of the final statistical analysis, which however is found to be negligible, see Appendix C.5.

Different networks are trained for events in the 1-jet and 2-jet bin signal samples to account for differences in the event kinematics and particle multiplicities in the final state. The training is performed with events in the combined electron and muon channel and using a ratio of signal to background events at unity (50:50). The different background processes are weighted according to their relative contributions in the signal sample. They are scaled to the number of expected events according to their respective theory cross-section predictions and their sum is normalised to the total number of events in the combined FCNC signal samples.

8.2.1. Construction and Preselection of Input Variables

Before training the neural network, input variables have to be selected, based on which the ANN learns to distinguish signal from background events. As briefly discussed in Section 3.2, the $qg \to t \to b\ell\nu$ process is characterised by three main differences from the various SM background processes. Firstly, single top quarks produced in the ugt and cgt FCNC processes are expected to be produced almost without transverse momentum, since the main contribution of the total production originates from the $2 \to 1$ process. The p_{T} spectra of top quarks produced in SM processes (e.g. $t\bar{t}$ production) or of top quarks misidentified from non-top-quark events (e.g. W+jets processes) are harder, and often broader, due to the larger particle multiplicities in their decay processes and final states. For the same reason, the angular distributions of the top-quark decay products differ. The W boson and the b-quark jet tend to be directed almost back-to-back in the transverse plane, whereas their azimuthal angular distance is smaller in most background processes. Since the top quark is the heaviest elementary particle, the W boson and the b-quark jet from its decay carry higher energies and typically have harder momentum spectra than those in Z+jets or W+jets background events. For the same reason the lepton and neutrino from the subsequent W boson decay tend to be subject to higher boosts in top-quark events, resulting in small angular distance between them, and hence large azimuthal angular distances around π with respect to the b-jet. Lastly, strong FCNC top-quark production is highly charge asymmetric. Approximately three times more single top quarks than top antiquarks are expected to be produced in the combination of the considered FCNC processes. The charge asymmetry arises mostly from the (dominant) ugt process and is caused by the ratio of the parton density functions of u to $\bar{u}$ quarks in the proton at typical momentum transfers of x=[0.02..0.5] at the LHC energies (cf. Figure 5.3 in Section 5.2). The c- to $\bar{c}$-quark PDF ratio, In contrast,

is close to unity, hence the *cgt* process contributes only marginally to this effect. For the remaining background processes the charge asymmetry is near unity with the exception of SM single top-quark production processes. However, this ratio is at most two in t-channel single top-quark production [259], given by the ratio of the parton density distribution of u and d quarks in the proton.

Consequently several categories of variables have to be considered as potential inputs to the neural networks. These include basic kinematic variables of the final state objects in the event, such as the transverse momenta, energies or reconstructed masses of all final state particles, their direction in η and ϕ, or the $E_{\mathrm{T}}^{\mathrm{miss}}$. Various compound variables built from combinations of properties of final state objects are explored, such as the transverse W boson mass ($m_{\mathrm{T}}(W)$), derived from the $\vec{E}_{\mathrm{T}}^{\mathrm{miss}}$ and lepton $\vec{p}_{\mathrm{T}}$ vectors (cf. Section 7.2), or the sum of the transverse momenta of all final state objects (H_{T}). Further, the kinematic properties of reconstructed intermediate objects in the decay chain are considered as potential inputs to the ANNs, i.e. kinematic variables of the W boson or the top quark itself. To reconstruct the four-vectors of the W boson and top quark, the neutrino four-momentum has to be estimated first. Since its longitudinal momentum ($p_z(\nu)$) cannot be measured directly, additional information on the lepton originating from the assumed leptonic W decay is needed to derive the full momentum four-vector from the $\vec{E}_{\mathrm{T}}^{\mathrm{miss}}$ vector. Assuming energy and momentum conservation and that no other undetectable particles than one SM neutrino are produced in the event, the $E_{\mathrm{T}}^{\mathrm{miss}}$ can be directly identified with the neutrino transverse momentum ($p_T(\nu) = E_{\mathrm{T}}^{\mathrm{miss}}$). Given the lepton four-momentum, the neutrino's longitudinal momentum can be derived by imposing a constraint on the invariant mass of the W boson:

$$(p_W)^2 = (p_\ell + p_\nu)^2 = m_W^2 = (80.425\ \mathrm{GeV})^2,$$

where p_W, p_ℓ and p_ν are the four vectors of the W boson, lepton and neutrino, respectively. The quadratic equation has twofold real or imaginary solutions:

$$p_z(\nu) = \frac{\mu \cdot p_z(\ell)}{p_{\mathrm{T}}(\ell)^2} \pm \sqrt{\frac{\mu^2\, p_z(\ell)^2}{p_{\mathrm{T}}(\ell)^4} - \frac{E_\ell^2 \cdot p_{\mathrm{T}}(\nu)^2 - \mu^2}{p_{\mathrm{T}}(\ell)^2}}\ ,$$
$$\text{with} \quad \mu = \frac{m_W^2}{2} + p_{\mathrm{T}}(\ell) \cdot p_{\mathrm{T}}(\nu) \cdot \cos\Delta\phi(\ell,\nu)\ .$$

Herein $\Delta\phi(\ell,\nu)$ denotes the azimuthal angular distance between the lepton and the neutrino (or $\vec{E}_{\mathrm{T}}^{\mathrm{miss}}$) vector and E_ℓ is the energy of the lepton. In case of real solutions for $p_{z,\nu}$, the one of smaller value is chosen, since the W boson and hence its decay products tend to be produced with small pseudorapidity. In approximately one third of the events the equation has imaginary solutions, mostly arising from the limited precision in the $E_{\mathrm{T}}^{\mathrm{miss}}$ measurement. In this case, the $E_{\mathrm{T}}^{\mathrm{miss}}$ is progressively scaled down until the imaginary part vanishes and a real solution is obtained.

Subsequently, the W boson four-vector can be reconstructed from the sum of the neutrino and lepton four-vectors. Likewise, the top-quark four-vector is given by the sum of the four-vectors of the W boson and the jet which has been identified to be

originating from a b quark.

Distances between final or intermediate state objects contribute additional inputs to the neural network, i.e. the relative angles $\Delta\eta$ and $\Delta\phi$ or their combination ($\Delta R = \sqrt{\Delta\eta^2 + \Delta\phi^2}$) as observed in the laboratory frame, or their reconstructed equivalents in the rest frames of the W boson and top quark. Lastly, integer variables like the charge of the lepton are considered as possible discriminators between signal and background events, since the charge of the top quark is reflected in the charge of the W boson and subsequently in that of the final state lepton.

All potential input variables to the neural network are preselected based on the quality of the modelling of the data distribution by MC simulated events in the control (and signal) region as described in Section 7.4. Each variable is further checked for data/MC agreement in the electron and muon channel separately and is omitted if large deviations are found.

8.2.2. Preprocessing of Input Variables

Variables are chosen to be included as inputs to the neural network based on their separation power, while accounting for potential correlations among them. For this task the NeuroBayes package provides a complex and robust preprocessing mechanism to decorrelate the variables and rank them in their discrimination power.

In an automated procedure each input variable is first transformed into flat distributions between -1 and $+1$ using a non-linear transformation. This is favourable in order to fully exploit the sensitive region of the activation function around zero and to avoid the saturation region at very small/large inputs passed from the propagation function. Further, it reduces the influence of extreme outliers in the input variables which otherwise could saturate individual nodes.

In the next step, the normalised distributions are transformed into Gaussians with a mean value of $\mu = 0$ and a standard derivation of $\sigma = 1$ using the inverse integrated χ^2 function. This is to allow the network to reach fast learning speed right from the beginning of the training process, since it avoids node saturation caused by the plateaus of the activation function and ensures that the input values at the output node similarly are distributed as Gaussians ($\mu = 0$, $\sigma = 1$).

As next, the input variables are decorrelated. First the covariance matrix of all N input variables is computed which afterwards is transformed into a unit matrix using the Jacobi eigenvalue algorithm and dividing each rotated input vector by the square root of its determined eigenvalue. At this point the variables are ranked in their discrimination power using an iterative procedure. First the total (linear) correlation of the set of input variables to the target value is computed. This is done by performing $N - 1$ Jacobi rotations such that a single decorrelated variable represents the total correlation to the target and the correlations of the remaining variables are zero. Now a single variable is left out and the total correlation of the remaining input set to the target is recomputed. This is repeated for each individual variable one at a time, yielding a list of the variables and the total correlation loss caused by their exclusion. The least significant variable found, hence the one which causes the least loss of correlation, is removed

entirely. The procedure then is repeated with the remaining input set. Again, the $N-1$ variables are decorrelated and the total correlation of the set and the loss of correlation by omitting individual variables from the set are recomputed again. The next least significant variable is removed as well, and the procedure repeated with the remaining $N-2$ input variables, and so on, until only the most significant one is remaining. The final ranking of the variables by their significance is based on the loss of total correlation caused by their entire removal after decorrelation of the respective reduced set of input variables, multiplied by the square root of the training sample size. The total correlation to the target is given in %. The significance of this correlation is denoted in terms of σ and will be used as the measure of choice throughout this thesis. The preprocessing procedure can also deal with non-continuous input variables by setting individual preprocessing flags for each variable, as is done for the lepton charge in this analysis.

8.2.3. Final Selection of Input Variables

A threshold can be set in the training to only include those variables which are contributing to the total target correlation with a defined minimal significance after having performed the full ranking procedure described above. The network topology thereby can be optimised automatically by removing irrelevant input nodes and thus potential noise sources. To identify the final list of input variables to be used, a preliminary ANN is trained with all potential input variables having passed the preselection, such that the variables with the highest significances can be identified. Finally, only those variables are included which contribute with a significance of at least $3\,\sigma$. Thereby the best possible discrimination between signal and background events is achieved while keeping the set of input variables reasonably small. It was checked for that including more variables does not improve the separation power significantly. Likewise, excluding more variables (with significances up to $5\,\sigma$) showed only marginal losses in the networks performance, see Appendix C.4. This leads to 13 variables remaining for the network of the 1-jet bin and 10 variables chosen as inputs to the ANN of the 2-jet bin. All final variables are listed in Table 8.1 ordered by their importance.

It can easily be seen that variables correlated to the top-quark p_{T}, i.e. the transverse momenta of its decay products or the invariant mass of the top quark as derived from the reconstructed W boson and b-jet four-vectors, form the most significant variables in both networks. Another variable of high significance represents the lepton charge. This is due to the high ratio in the rate of top-quark to top-antiquark production in the FCNC signal processes. As expected, several angular differences between the W boson and top-quark decay products form the third class of significant variables for the reasons explained in Section 8.2.1. The distributions of all variables used as input to the neural networks in the 1-jet bin and 2-jet bin are shown in Appendix B, for the combined electron and muon channel in the signal and in the control region, respectively.

The topology of the network in the hidden layer was adapted to the number of input nodes. In the hidden layer 20 nodes are used, since this results in the best separation power of the final networks in both jet bins, see Appendix C.1 for a detailed discussion.

Table 8.1.: Variables used as input to the neural networks of the 1-jet and 2-jet bin ordered by their significance, as estimated from the total correlation loss to the target caused by its removal.

1-jet bin		2-jet bin	
Variable	Significance (σ)	Variable	Significance (σ)
$p_{\mathrm{T}}(b)$	44.9	$m(t)$	30.4
$\Delta\phi(\ell, W)$	22.9	$q(\ell)$	21.1
$\eta(\ell)$	18.9	$m_{\mathrm{T}}(W)$	19.6
$p_{\mathrm{T}}(W)$	16.4	$p_{\mathrm{T}}(\mathrm{l\text{–}jet})$	13.7
$\eta(t)$	16.2	$\Delta R(\mathrm{l\text{–}jet}, t)$	12.4
$q(\ell)$	15.1	$\eta(b)$	9.0
$\Delta\phi(\ell, b)$	11.2	$\eta(\ell)$	5.1
$\Delta\phi(W, \nu)_{\mathrm{t\text{–}rest}}$	8.0	$\Delta\phi(b, W)$	4.8
$\Delta\phi(W, t)$	7.2	$\Delta R(\ell, \nu)$	4.6
$E_{\mathrm{T}}^{\mathrm{miss}}$	4.8	$\Delta\phi(\ell, b)_{\mathrm{t\text{–}rest}}$	4.3
$\eta(\nu)$	4.6		
$\Delta\phi(b, t)$	4.4		
$\Delta R(\ell, t)$	4.1		

8.2.4. Avoiding Overtraining

Multivariate analysis methods, such as ANNs, usually are subject to learning the information from kinematic variables of single training events "by heart". This worsens the generalisation performance and could bias the ANN output when applying the network on collision data. NeuroBayes therefore implements cross-checks for overtraining in spite of the weight-decay techniques applied during the training process itself. A so-called early-stop procedure is implemented which ends the training of the network as soon as its generalisation performance decreases or a minimum in the entropy error is reached. The cross-entropy error function therefore is measured on an independent validation or test sample which consists of 20% of the total number of events available for the training. The remaining 80% are used as the actual training sample. The entropy loss function on the test sample is calculated after each training iteration. The training process is stopped if it increases or stops improving, eventually discarding the last iteration in which an overtraining occurred. Thereby the point of minimal cross-entropy error on the training sample, at the point of maximum generalisation performance, is used for the final network. Figure 8.2 shows the values of the error function for training and test samples in dependence of the training iteration. One can see the initial decrease in the entropy error in both, training and validation samples, which quickly reaches a plateau after which the training is stopped. Following this procedure the training of the neural networks is finished after 8 and 12 iterations for the network of the 1-jet and 2-jet bin, respectively.

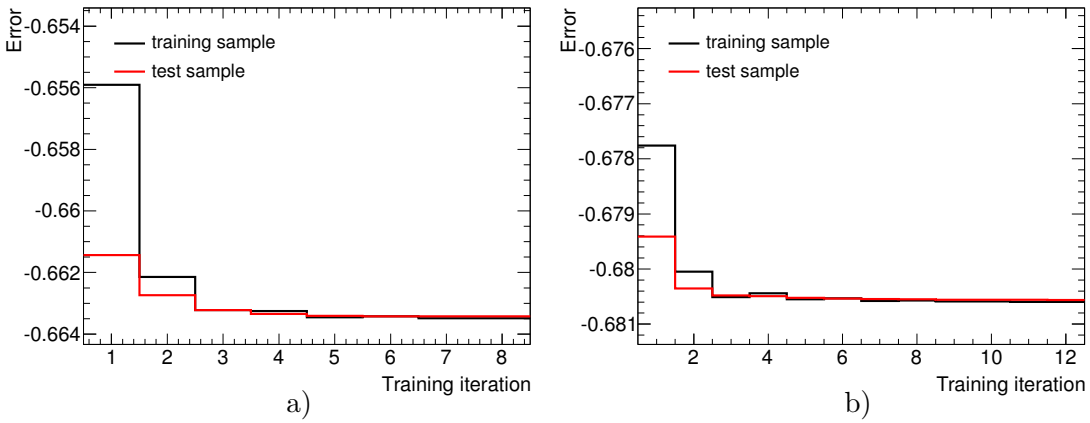

Figure 8.2.: Value of the entropy error function for the training (black) and test sample (red) in dependence of the training iteration of the neural networks for the 1-jet bin (a) and 2-jet bin (b).

8.2.5. Training Results

Figure 8.3 shows the training result of the ANNs for the 1-jet and 2-jet bin. Shown are the ANN output distribution normalised to unit area for the simulated background and signal events used in the training. In accordance to the respective target outputs, signal events accumulate towards discriminator values of +1 while background events are concentrated towards low discriminator values (target output −1). It can be seen that the ANN of the 1-jet bin provides a better signal/background separation than the network trained for the 2-jet bin. On the one hand, this is caused by the lower number of training events available in the 2-jet bin signal sample (14.000 compared to 22.000

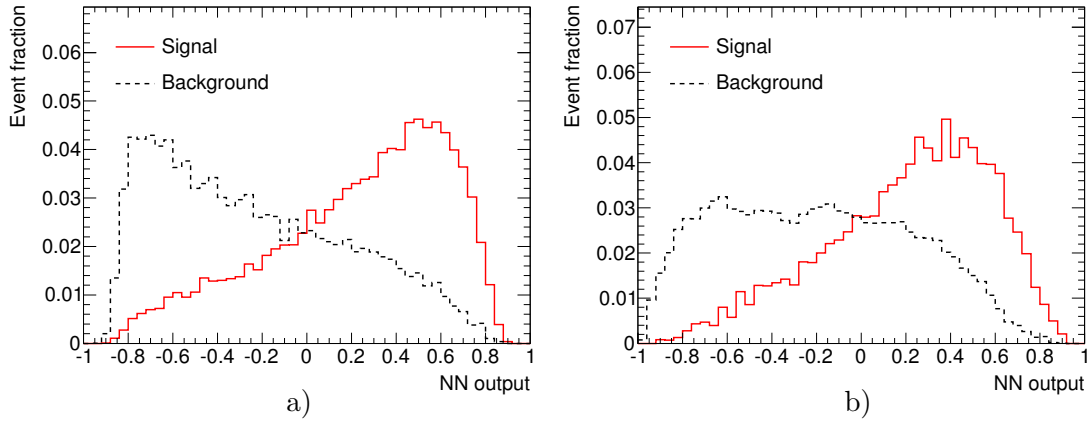

Figure 8.3.: ANN output distributions normalised to unit area for simulated background (hatched lines) and signal events (solid lines) of the networks for the 1-jet bin (a) and 2-jet bin (b).

for the 1-jet bin). This was confirmed by studying the discrimination power of the network when training both networks with only half of the available events. Whereas the performance of the network for the 1-jet bin was nearly unaffected, the ANN for the 2-jet bin showed a much higher dependence on the training sample size. On the other hand, the most determining factor is the FCNC signal event signature in the 2-jet bin, which is much closer to that of different background processes. Figure 8.4 shows the output distributions from the ANNs of both jet bins normalised to unit area, split up into the different background and the combined signal processes. In the 2-jet bin, in particular the separation against the SM single top-quark production processes is worse, since their final state signature is much closer to that of the FCNC signal processes.

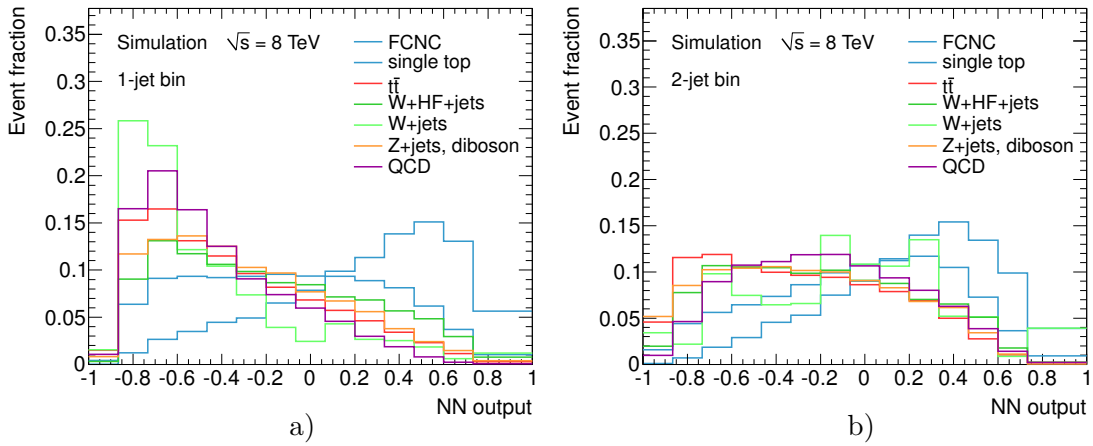

Figure 8.4.: Output distributions of the ANNs of the 1-jet bin (a) and 2-jet bin (b) for the SM background and the signal processes normalised to unit area.

The overall quality of the training is cross-checked in distributions of the signal purity in dependence of the ANN output in which a proper training of both networks is verified. Details on the procedure and the resulting distributions are summarised in Appendix C.2. Appendix C.3 in addition provides details of the correlations between the input variables as determined during the preprocessing step of the training, as well as on the final topology for both fully trained networks.

8.3. Application on Data

As for the fit in the $E_{\mathrm{T}}^{\mathrm{miss}}$ distribution the shape of the ANN output distributions of several background processes are very similar and therefore difficult to distinguish in the final statistical analysis and cross-section (limit) evaluation. When left floating individually in their rate within constraints derived from their respective theory cross-section prediction, templates of similar shape lead to ambiguities and unjustified (anti-)correlations of their (posterior) systematic rate uncertainties in the statistical analysis described in Section 10.3. Therefore the output templates of certain background processes are com-

bined into single templates with their relative fractions corresponding to their respective theory cross-section prediction (see Section 5.2.2). Figure 8.5 shows the classifier outputs from the ANNs in the 1-jet and 2-jet bin normalised to unit area for events of the different MC simulated background (sub)samples in the signal region, namely the Z+jets, W+jets, $Wb\bar{b}$, $Wc\bar{c}$, Wc processes, the Wt-, s- and t-channel single top-quark production processes, as well the $t\bar{t}$ and diboson production samples. Due to the similar shape of the $Wb\bar{b}$, $Wc\bar{c}$, Wc+n partons samples, see Figure 8.5 (a,b), their ANN outputs are merged into a single W+HF+jets template. Similarly the Z+jets and diboson production processes are grouped into a single ANN output template, since they represent the least dominant backgrounds with reasonably similar shapes. The different SM single top-quark production processes, as well as the $t\bar{t}$ production are also grouped into single templates. Including the output for multijet events, this leads to a total of six different background templates to be used in the later statistical analysis: W+jets, W+HF+jets, $t\bar{t}$, Z+jets plus diboson, multijets, and SM single top-quark production. The FCNC signal processes are modelled by one individual template. Although both processes in principle are subject to minor differences in their kinematical properties, this simplification is justified by the fact that the templates of the $ug \to t$ and $ug \to t$ signal processes exhibit almost identical shapes in the ANN output distributions, see Figure 8.5 (a,b). Nonetheless, a more detailed discussion on the prospects and implications of an individual treatment of both signal contributions in the ANN training and later statistical analysis are given in Section 11.2.

The neural network outputs for the different groups of background processes are validated with observed events by applying the networks (trained with events of the signal region) on the event sample of the control region. The event composition in the latter is dominated by the W+jets, W+HF+jets and $t\bar{t}$ backgrounds and therefore provides a good cross-check to demonstrate that the ANN output correctly models their shape outside of the signal region.

Lastly, the trained neural networks are applied on observed events in the signal sample. Figure 8.6 shows the neural network output distributions for the combined electron and muon channel in the 1-jet and 2-jet bin, and in the control and signal region, respectively. Shown are the ANN outputs for observed events and for the different simulated SM background contributions grouped as explained before. Herein again all processes are normalised with the scale factors obtained in the binned maximum likelihood fit to the $E_{\mathrm{T}}^{\mathrm{miss}}$ distribution in data. The hatched bands indicate the combined statistical uncertainty from the limited MC samples size and the uncertainty on the multijet normalisation of 50%. In the plots for the signal region the combined FCNC signal contribution of the $ug \to t$ and $cg \to t$ processes is shown stacked on top of all backgrounds with an assumed cross-section of 20 pb. Similar distributions of the ANN outputs for simulated and observed events, split up into electron and muon channel, can be found in Appendix C.6. Overall good agreement between data and prediction is found in both jet-bins of the control samples, respectively. Similarly good agreement between observed data and simulation is demonstrated in the signal region. No visible signal excess can be observed, which however is expected for small signal contributions at the order of the formerly excluded cross-sections (times $t \to bW$ branching frac-

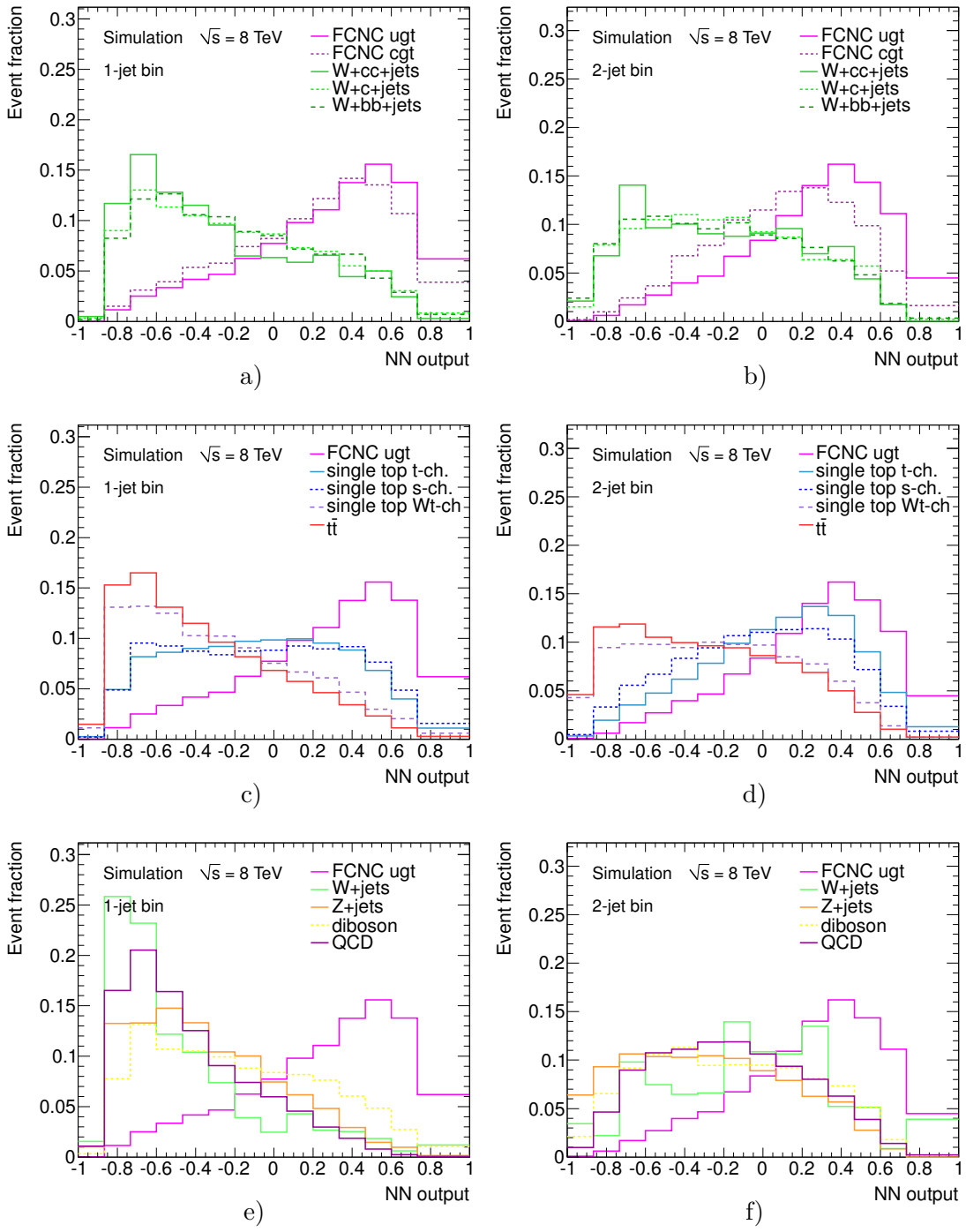

Figure 8.5.: Neural network output distributions normalised to unit area split up into individual background samples and the different signal processes, for the ANNs of the 1-jet bin (left) and 2-jet bin (right). Shown are the ANN output for the different W+HF+jets and the two signal samples (a,b), the outputs for the different SM top-quark processes (c,d), and of the Z+jets, diboson and multijet samples (e,f).

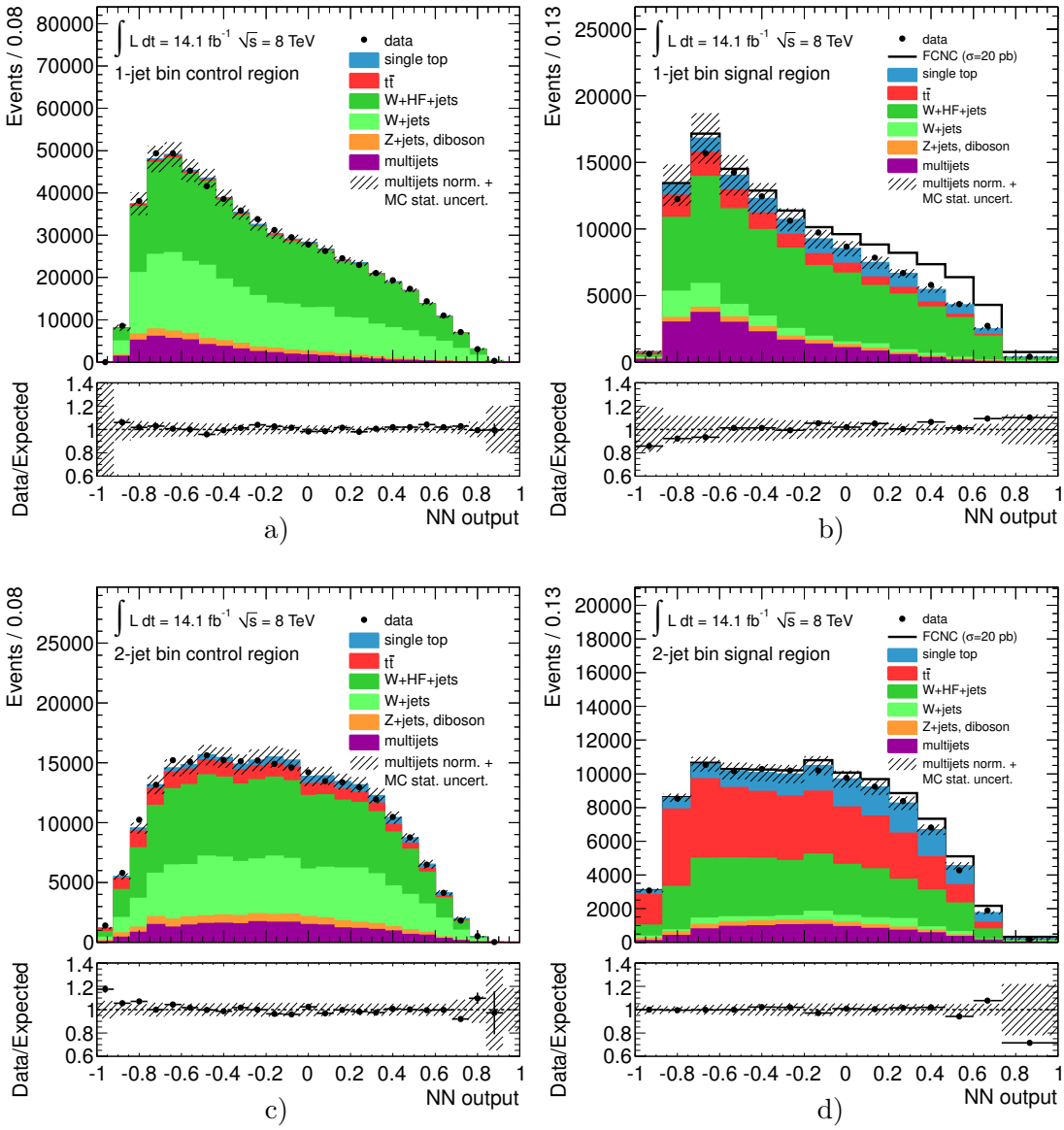

Figure 8.6.: Neural network output distributions for simulated and observed events of the 1-jet bin (top row) and 2-jet bin (bottom row) in the control (a,c) and in the signal region (b,d), for the combined electron and muon channels respectively. Figures b) and d) show the signal template stacked on top of all SM backgrounds and scaled to a cross-section of 20 pb. All processes are normalised with the scale factors obtained in the binned maximum likelihood fit to the $E_{\mathrm{T}}^{\mathrm{miss}}$ distribution in data, used to determine the fraction of multijet events. The lower pads show the relative difference between the observed distribution and that of the SM only expectation. The hatched bands in the main and ratio plots indicate the combined statistical uncertainty from the simulated samples size and the uncertainty on the multijet normalisation.

tion) of $\sigma_{qg\to t} \times \mathcal{B}(t \to bW) < 3.9$ pb [126] or below. To determine a potential FCNC signal contribution or set a respective upper cross-section limit on the FCNC single top-quark production, a comprehensive statistical analysis is employed, accounting for various sources of systematic uncertainties in the measurement and simulation that will be discussed in the next chapter.

9. Systematic Uncertainties

To extract plausible information on the cross-section or derive a cross-section limit of a potential FCNC signal contribution, several sources of systematic uncertainties have to be accounted for in the analysis. Systematic uncertainties are introduced to estimate the effects from intrinsic limitations of e.g. the detector and LHC performance, measurement procedures or the limited precision of theory calculations. Since the knowledge on the direction and size of systematic errors arising therefrom is limited, they cannot be corrected for entirely and hence have to be accounted for in the form of uncertainties. Systematic uncertainties may affect both, the normalisation or acceptance of the individual background and signal processes (rate uncertainties), and the shape of the distributions of kinematic variables, and hence that of the ANN output distributions for the different background and signal templates (shape uncertainties). Later, the templates will form the input to the statistical analysis performed to extract the size of a potential signal contribution. Separate background and signal templates of varied event kinematics and yields are obtained for $+1\,\sigma$ and $-1\,\sigma$ shifts of each systematic uncertainty considered. Their variety, characteristics and the manner of their formal treatment follow common prescriptions and procedures which were developed and continuously refined within ATLAS and the ATLAS top-quark physics group over the past years of LHC physics operation.

9.1. Object Identification and Reconstruction

Lepton trigger, identification and reconstruction efficiencies:
The electron trigger, identification and reconstruction, as well as isolation efficiencies are corrected for in simulated events using scale factors derived from measurements using the Tag-and-Probe method on e.g. $Z \to ee$ samples in data (cf. Section 6.2.1). Systematic uncertainties [235] are assigned to these scale factors, which were evaluated by variations of the tag electron selection requirements and in general are found to be below 0.5%. An additional uncertainty arises from the varying pile-up conditions and is accounted for by evaluating the dependence of the scale factors on the reconstructed number of primary vertices. Half of the resulting variation is used as an uncertainty, which is found to amount to less than 0.5%. Differences in the isolation efficiency between electrons from Z-boson decays (used to evaluate the scale factors) and electrons in SM top-quark events are accounted for by adding an additional uncertainty of 2% in quadrature.

Uncertainties on the scale factors for the identification and reconstruction efficiency of muons (cf. Section 6.2.2) are derived similarly from comparisons of different types of probe muons used for the scale factor extraction. These are combined with the uncertainty on the residual background contamination of the employed $Z \to \mu\mu$ sample

and amount to approximately 0.2%. Additional sources of uncertainties arise for the reconstruction efficiencies of muons with very low ($p_{\mathrm{T}} < 10$ GeV) and very high momenta ($p_{\mathrm{T}} > 100$ GeV) [239]. A conservative value of 2% is applied as an uncertainty on the mini-isolation efficiency scale factor. The uncertainties above are applied to the simulation samples by individually varying the respective lepton scale factors by $+1\,\sigma$ and $-1\,\sigma$ in their uncertainty during the object reconstruction.

Lepton charge identification:
For electrons the uncertainty from differences in the charge misidentification probabilities in data and MC simulation are found to be negligible [234]. For muons the situation differs due to the toroidal magnetic field of the Muon Spectrometer. The muon reconstruction and trigger efficiencies differ for positively and negatively charged muons produced in the forward/backward direction at large $|\eta|$ values, since muon trajectories may be bent outside of the MS geometrical acceptance in either direction. The effects are accounted for in the form of charge dependent efficiency scale factors and in the muon (ID) momentum resolution uncertainty.

Jet reconstruction efficiency:
The jet reconstruction was estimated to be fully efficient for jets with $p_{\mathrm{T}} > 30$ GeV (cf. Section 6.2.3). Since jets are selected with a minimum transverse momentum of $p_{\mathrm{T}} > 30$ GeV, no efficiency scale factors are applied and hence no related systematic uncertainty is to be considered.

Jet vertex fraction scale:
The performance of the JVF requirement is measured in data and MC simulation using the tag-and-probe method on $Z \to \mu\mu$+jets and $Z \to ee$+jets events [223]. Two different sources of systematic uncertainty are associated to the JVF scale factors. The first results from the quality of fit in the signal and control regions used to extract the efficiency and inefficiency scale factors, and the second from the selection criteria used to define the (tag) jets from the hard interaction. The latter criteria are varied and the resulting scale factors are refitted. The absolute value of the difference between the variations and the nominal fit are taken as the selection uncertainty on the hard scatter jet efficiency and inefficiency scale factors which typically amount to $\sim 1\%$ and $\sim 4\%$, respectively. These uncertainties are then added in quadrature to the respective fit uncertainties ($<1\%/\sim 10\%$) to obtain the total systematic uncertainty for a given JVF scale factor.

b-tagging efficiency scale factors:
The uncertainties on the b-tagging efficiency arise from statistical and systematic uncertainties associated to the different calibrations analyses (i.e. $p_{\mathrm{T}}^{\mathrm{rel}}$/system8 method and $t\bar{t}$ kinematic selection) by which the scale factors have been extracted initially (cf. Section 6.2.3). The total uncertainties typically range from 5% to 19%, depending on the jet p_{T} and calibration analysis, and are dominated by uncertainties arising from the limited knowledge of the jet energy scale and resolution, and (for the $p_{\mathrm{T}}^{\mathrm{rel}}$/system8 method) by uncertainties from the modelling of the production and decay of heavy flavour jets and differences in the b-tagging efficiencies between hadronic and semi-leptonic b-jets (i.e. containing a reconstructed muon) [251, 252]. Similarly, the uncertainties of the

analyses used to obtain the c-tagging efficiencies and mistag rates in data and simulation are accounted for as uncertainties of the c-tag and mistag rate scale factors. The total uncertainties on the c-tagging rate scale factors range from 12% to 25%, depending on the jet p_{T}, and are dominated by uncertainties related to the fit that is used to extract the yields of $D^{\star+}$ mesons and jet flavour fractions, and by the uncertainty on the b-tagging efficiency that is used as an input to the respective analyses [254]. The main uncertainties in the mistag rate measurement arise from the limited jet energy and impact parameter resolution, and from differences in the (jet) trigger efficiency in observed and simulated events, and typically amount to values within 18% and 49%, see [255] for details.

9.2. Object Energy/Momentum Scale and Resolution

Electron energy scale and resolution:
Systematic uncertainties associated to the electron energy scale are derived simultaneously with the determination of the electron energy scale factors using the line-shape fit and the template method (cf. Section 6.2.1). The uncertainty lies within ±1-2% for $|\eta| < 2.47$ and arises from comparisons of both methods and uncertainties associated to each individual method, as well as from presampler energy scale uncertainties (i.e. the difference between presampler and calorimeter energy scale). Additional contributions arise from pile-up and from the detector material and hardware modelling. The selection of simulated events is repeated with the electron energy varied by $\pm 1\sigma$ in the total energy scale uncertainty.

Uncertainties on the correction for the electron energy resolution in simulated events arise from statistical and systematic uncertainties of the different methods employed for their determination and the differences in the results obtained by these in the data/MC comparisons. They are accounted for in the cluster energy smearing through additional up/down variations using random numbers drawn from modified Gaussian distributions which reflect the associated uncertainties.

Muon momentum scale and resolution:
Uncertainties on the muon momentum scale are included by repeating the event selection of MC simulated events with the muon momentum varied within the uncertainty derived simultaneously with the muon momentum scale correction factors (see Section 6.2.2). The scale uncertainty lies within ±1-2% for $|\eta| < 2.5$ and is dominated by the uncertainty of the template fit used to extract the corrections, the intrinsic resolution uncertainty of the measurements in the ID and MS (spatial resolution & misalignment), and the uncertainty from multiple scattering in the detector material.

Similar to the electron energy measurement, an uncertainty is assigned to the muon momentum resolution, which originates from the same sources as described above and is dominated by the uncertainty of the template fit derived using varied Z mass windows. The uncertainty is applied by means of additional up/down variations in the smearing of the muon momentum measurement from the ID and MS individually, using random numbers drawn from Gaussian distributions reflecting the respective uncertainty.

Jet energy scale and resolution:
The uncertainty on the jet energy scale is derived in an in-situ analysis of EM+JES calibrated jets in 2010 data [243]. The estimates were refined by studies in 2011 data, i.e. on flavour and topology uncertainties [265], η inter-calibration studies in dijet events [266], and pile-up uncertainties [267]. The results were subsequently validated in studies of 2012 data and are found to be applicable as such also for LCW+JES calibrated jets. The total uncertainty on the jet energy scale hence originates from several sources, such as uncertainties arising from the (light-quark/gluon) flavour composition of the samples, mismeasurements from overlapping close-by jets, pile-up, and additional uncertainties applied for b-quark jets [268] that account for differences in the uncertainties associated to the jets originating from light-quarks and gluons that were used in the studies. The total uncertainty is parametrised in the jet p_{T} and η and ranges from 2.5% to 8% and 3.5% to 14% for jets in the central and forward region, respectively (see Figure 9.1). The energy of each jet is scaled up or down by $1\,\sigma$ in the total scale uncertainty.

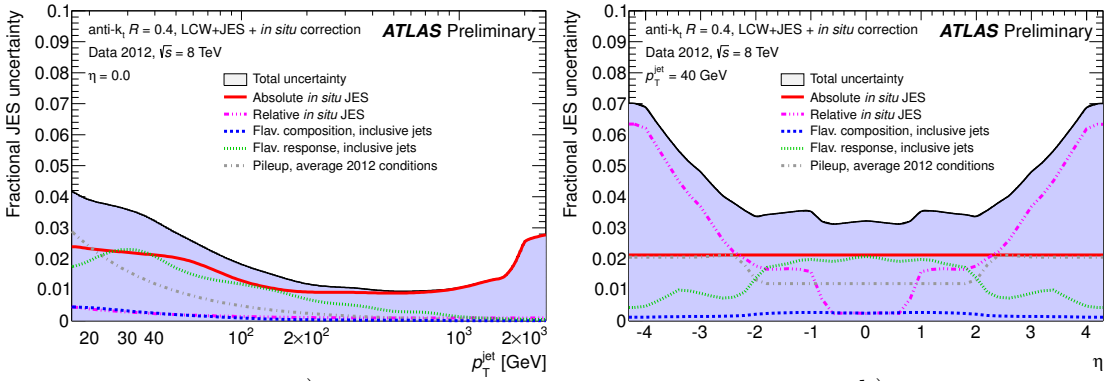

Figure 9.1.: Fractional jet energy scale uncertainty and its components as a function of the jet p_{T} at $|\eta| = 0$ (a), and as a function of the jet η for jets with $p_{\mathrm{T}} = 40$ GeV (b). [269]

The jet energy resolution was measured in dijet events using the bisector technique as described in [247], but was updated using 8 TeV data and MC simulations. The bisector method defines an imbalance vector in the transverse jet p_{T}, defined as the vector sum of the transverse momenta of the two leading jets. Ideally this vector is zero and hence allows to study sources of mismeasurements that lead to imbalances and to fluctuations in these due to the limited energy resolution. The imbalance is parametrised in projections along an orthogonal coordinate system defined in the transverse plane using the direction that bisects the azimuthal angle formed by both jets. The obtained imbalance distributions are then fitted with Gaussian functions and the variances are compared between observed and MC simulated events. The resolution in data in general agrees with that in simulation, but residual data/MC disagreements in particular jet p_{T} and η regions, and additional uncertainties on the measurements in data, are accounted for as a systematic uncertainty by means of a jet p_{T} smearing in simulated events. The

variations are parametrised as a function of the original jet transverse momentum and momentum direction in η.

Missing Transverse Energy:
The uncertainties from the scale and resolution corrections of lepton and jet momenta and energies are propagated to the $E_{\mathrm{T}}^{\mathrm{miss}}$ calculation, respectively. Additional (inherent) uncertainties arise in the contributions of calorimeter cells not associated to any reconstructed objects (*RefCellOut* term) and low p_{T} jets with 7 GeV $< p_{\mathrm{T}} <$ 20 GeV (*RefSoftJet* term), see Section 6.2.4. Both terms, commonly referred to as "soft terms", are varied simultaneously for uncertainties in their energy scale and resolution, uncertainties arising from effects of pile-up, topoclusters energy scale and threshold uncertainties, and uncertainties associated to the MC modelling, i.e. in the PS modelling or from the limited knowledge on the dead material in the detector. The scale and resolution uncertainties were determined in $Z \to \ell\ell$ events in 8 TeV data and simulation [256]. Two different methods are applied which compare observables in $Z \to \ell\ell$ events without jets, dominated by lepton and soft term contributions, or evaluate the balance between the contributions from soft terms and those of the reconstructed (hard) objects, see [270] for a detailed description. Both uncertainties on the (combined) soft terms are considered as uncorrelated and hence individual sets of systematic samples of up/down variations in the $E_{\mathrm{T}}^{\mathrm{miss}}$ soft term scale or resolution are generated.

9.3. Uncertainties in MC Simulation

ME generator:
Systematic effects from MC modelling of the $t\bar{t}$ process are estimated by comparing several different generators. The full difference between an MC@NLO and POWHEG sample, as well as the difference between an MC@NLO and ALPGEN sample, each interfaced to HERWIG for parton showering, are estimated. The largest of the two is symmetrised[1] and taken as a (two-sided) systematic uncertainty for the $t\bar{t}$ background sample.

PS generator:
The effect of using different parton shower and fragmentation models for the $t\bar{t}$ process is accounted for by comparing two samples generated with the POWHEG ME generator interfaced to either the HERWIG or PYTHIA generators for parton showering. The full difference between both samples is symmetrised and included as a two-sided systematic uncertainty.

Initial and final state radiation:
The amount of initial (ISR) and final state radiation (FSR) is varied for the $t\bar{t}$ and SM single top-quark production samples by modifying parameters in samples produced with the ACERMC ME generator interfaced to PYTHIA for parton showering. The parameters were varied in PYTHIA within a range similar to that used in the Perugia

[1] The full relative difference between both samples is taken as the positive error, and the respective value of same size but opposite sign is taken as the negative error on the nominal background sample.

Soft/Hard tune variations [195]. Since the nominal samples are partly generated using a different ME generator, the full difference between the samples of up and down ISR/FSR variations is used as a systematic uncertainty for the respective nominal sample. The following parameters are varied in PYTHIA, also see the PYTHIA manual [199] for their detailed description:

- ISR: `PARP(67)` and `PARP(64)`
  Parameter `PARP(67)` is multiplied with the scale of the hard scattering and hence defines the maximum scale (Q^2_{max}) or parton virtuality allowed in the shower. The parameter `PARP(64)` is used as a scale to control the strong coupling constant, $\alpha_s(p^2_{\text{T}})$, as a function of the squared evolution scale in a space-like (p_{T}-ordered) shower.
- FSR: `PARP(72)` and `PARJ(82)`
  The parameter `PARP(72)` controls the Λ value (cf. Section 2.2) used in running coupling (α_s) in time-like parton showers. The parameter `PARJ(82)` controls the invariant cut-off scale in p_{T} below which no further parton splitting is allowed.

The default values of the parameters in the nominal samples are:
`PARP(67)=1.0, PARP(64)=2.0, PARP(72)=0.260` [GeV], `PARJ(82)=1.00` [GeV].
In the systematics samples the parameters are varied as follows:

- *more PS*: `PARP(67)=1.75, PARP(64)=1.02, PARP(72)=0.425, PARJ(82)=0.50`
- *less PS*: `PARP(67)=0.75, PARP(64)=4.08, PARP(72)=0.150, PARJ(82)=1.66`

PDF sets:
The systematic uncertainties related to the parton distribution functions are taken into account for all samples using simulated events. Since the generation of separate MC samples for different PDF sets and each nominal background sample is computationally too expensive, the events are reweighted a-posteriori in accordance to each of the PDF uncertainty eigenvectors using a parametrisation that allows for an emulation of the behaviour of real variations of the samples at the time of their production. Depending on the PDF set used in the MC simulation of a particular background, templates of rate and shape variations are created by calculating an envelope of inter- and intra-PDF uncertainties originating from different variations within single PDF uncertainty eigenvector sets, as well as from the spread between those variations among the CT10, MSTW2008NLO [59] and NNPDF2.3 [271] PDF sets. The envelope is calculated following the procedure of the PDF4LHC recommendations [58]. The uncertainty is applied to all MC simulated processes, including the signal processes. For samples which were generated using LO ME generators in combination with LO PDF sets, the relative uncertainty calculated from the envelope of NLO PDF sets is applied on the original central (LO) value of the event weight.

Cross-section & multijet rate uncertainty:
The uncertainties on the normalisation of the various background processes are estimated either by using the uncertainties on the theoretical cross-section predictions as detailed in Section 5.2.2 and Table 5.4, or in case of the multijet background, by using the

assigned rate uncertainty of 50% from comparisons of different models for the multijet background estimation, see Section 7.3.1.

MC sample statistics:
The limited statistics of the MC samples, in particular of the W+jets samples, causes large scale factors (up to $\mathcal{O}(40)$) by which the respective samples are multiplied in order to match the integrated luminosity of the data sample. These weights, in addition to others arising from e.g. the k-factors or different data/MC scale factors applied to match the efficiencies of object reconstruction and identification in data, are accounted for and propagated through the analysis to the ANN outputs of each sample and in each bin of the output distributions. The uncertainties due to the limited size of the MC samples are then included in the final cross-section (limit) evaluation as additional sources of uncertainty independent for each bin and background sample, also see the next chapter for more details.

W+jets kinematic modelling:
Since the W+jets production processes represent the dominant backgrounds of the analysis, uncertainties of their kinematic modelling have to be considered. The production of many additional W+jets MC samples is computationally very expensive due to the large cross-sections, low selection efficiencies, and hence large sample sizes needed in order to obtain sufficient statistics after the event selection. However, modelling uncertainties in the MC event generation of the W, Wcc, Wc and Wbb+n parton samples can be parametrised in the final event kinematics in order to allow for an a-posteriori variation on the nominal samples using event weights, thereby emulating the behaviour of real variation at the time MC production. Studies were performed at MC truth level using samples generated with the ALPGEN generator and varying different parameters of the event generation with respect to the nominal values. Based on a comparison of the resulting event kinematics, it was found that the p_{T} of the leading jet (of highest p_{T}) in general provides a good estimator of the overall event kinematics and is used to parametrise systematic variations of the parameters `iqopt3` and `ptjmin10` within ALPGEN. Parametrisation functions are derived in the form of first order polynomials for each parameter variation using an event selection at MC truth level that is close to the primary selection criteria applied in top analyses, i.e requiring jets with $p_{\mathrm{T}} > 25$ GeV and $|\eta| < 2.5$, a single lepton with $p_{\mathrm{T}} > 20$ GeV and $|\eta| < 2.5$ and $E_{\mathrm{T}}^{\mathrm{miss}} > 20$ GeV. The obtained functions are used to compute additional event weights for each variation which are added in quadrature and applied to the nominally selected MC events. The difference to the nominal samples is then symmetrised, normalised to the nominal event yield, and used as the final systematic shape uncertainty.

Multijet kinematic modelling:
Because not only large differences in the predicted rate of the multijet background can be observed, but also the kinematic shape obtained with the various models differs, uncertainties on the kinematic modelling of the multijet background have to be accounted for. In order to construct a respective systematic shape uncertainty, the differences in the kinematic shape between templates obtained via different multijet background models are considered, namely the difference of the nominal templates to those obtained

with the matrix method in the muon channel and to those of the jet-electron model in the muon channel. For each lepton channel individually, the full differences from the alternative predictions to those obtained with the nominal methods are calculated and symmetrised. Since the multijet rate uncertainty is already accounted for in the form of a systematic uncertainty on the template normalisation, the templates of the variations are normalised to the expected yield predicted by the default method in each channel and hence are used as pure shape uncertainties.

Luminosity:
The relative uncertainty on the measured integrated luminosity is 2.8% and was derived from a preliminary calibration of the luminosity scale using Van-der-Meer scans performed in November 2012, following the same methodology as detailed in [179]. The uncertainty is applied as an additional (fully correlated) rate uncertainty to all MC simulated backgrounds.

Tables 9.1 and 9.1 summarise the resulting relative uncertainties in the expected events yields (rate uncertainties) for the different background and the signal processes in the 1-jet and 2-jet bin, and for the combination of electron and muon channels, respectively.

Figures 9.2 and 9.3 show exemplary ANN output shape distributions for different nominal signal and background templates and those of $\pm 1\sigma$ shifts in those uncertainties with the largest impact on the results of the final statistical analysis (see next chapter), i.e. the uncertainties on the jet energy scale, b-tagging efficiency and the PDF uncertainty. Shown are the ANN output distributions normalised to unit area for the combined electron and muon channel in the 1-jet and 2-jet bin, respectively. Similar distributions for all other systematic uncertainties also were checked for any unexpected behaviour in order to cross-check for the correct implementation of each in the analysis.

The uncertainty on the jet energy scale has an impact on the kinematic shape of the FCNC and SM top-quark processes, including on that of the $t\bar{t}$ template not shown here. This is related to the uncertainties associated to the flavour composition (i.e. including at least one b-quark jet) and the generally high jet multiplicity of these samples. Large effects also can be seen in the respective rate uncertainties in Tables 9.1 and 9.2, since the JES influences the number of jets passing the event selection criteria in the two jet bins. The effect on the rate of the FCNC signal processes in the 1-jet bin, however, is rather small since most FCNC events possess a single jet in the final state which results in almost similar amounts of events migrating from the 0-jet to the 1-jet bin as are doing from the 1-jet to the 2-jet bin, and vice versa. On the other hand, large and oppositely signed rate variations are found for the W+jets and SM top-quark production processes (also see Appendix D.1 for a more detailed discussion on this effect of bin migration). Different to the JES (and JER), effects from the uncertainties on e.g. the lepton energy/momentum scale and resolution show almost negligible effect on the shapes of all MC processes. Also the effects on the ANN output shape from the uncertainty on the b-tagging efficiency and the PDF uncertainty shown in Figures 9.2 and 9.3 are comparatively small. Their large impact on the statistical analysis instead is caused by their relatively large influence on the rates of the different background and signal processes (cf. Table 9.1/9.2).

Table 9.1.: Relative systematic uncertainties on the number of expected events from each signal and background source for a plus/minus variation of a systematic uncertainty for the combined electron and muon channels in the 1-jet bin.

Systematic uncertainty	Signal	W+jets	W+HF+jets
Jet energy scale	$\pm 0.3\%$	$\mp 14.2\%$	$\mp 2.7\%$
Jet vertex fraction scale	$^{+0.3}_{-0.2}\%$	$^{+3.0}_{-1.2}\%$	$^{\pm+0.4}_{-0.3}\%$
Jet energy resolution	$\pm 2.4\%$	$\pm 27.1\%$	$\pm 2.8\%$
b-tagging eff. SF	$\pm 4.6\%$	$\pm 0.9\%$	$\pm 1.0\%$
c-tagging eff. SF	$\pm 0.1\%$	$\pm 3.0\%$	$\pm 20.2\%$
mistag rate SF	$\pm 0.0\%$	$\pm 25.6\%$	$\pm 0.5\%$
Muon momentum scale	$\pm 0.1\%$	$\pm 0.1\%$	$\pm 0.2\%$
Muon momentum smearing (ID)	$\pm 0.0\%$	$\pm 0.0\%$	$^{-0.1}_{0.0}\%$
Muon momentum smearing (MS)	$\pm 0.0\%$	$\pm 0.0\%$	$\pm 0.1\%$
Muon Reco/ID eff. SF	$\pm 0.2\%$	$\pm 0.2\%$	$\pm 0.2\%$
Muon Trigger eff. SF	$\pm 1.1\%$	$\pm 1.1\%$	$\pm 1.1\%$
Electron energy scale	$\pm 0.7\%$	$\pm 0.4\%$	$\pm 0.8\%$
Electron energy smearing	$\pm 0.0\%$	$\pm 0.0\%$	$\pm 0.1\%$
Electron Reco/ID eff. SF	$\pm 1.1\%$	$\pm 1.0\%$	$\pm 1.1\%$
Electron Trigger eff. SF	$\pm 0.2\%$	$\pm 0.2\%$	$\pm 0.2\%$
$E_{\mathrm{T}}^{\mathrm{miss}}$ Cellout/Softjet term resolution	$^{0.3}_{-0.1}\%$	$\pm 0.4\%$	$\pm 0.1\%$
$E_{\mathrm{T}}^{\mathrm{miss}}$ Cellout/Softjet term scale	$\pm 0.2\%$	$\pm 0.7\%$	$\pm 0.8\%$
PDF	$\pm 2.9\%$	$\pm 4.1\%$	$\pm 7.8\%$
Systematic uncertainty	$t\bar{t}$	**single-top**	Z+jets
Jet energy scale	$\mp 12.7\%$	$^{-4.1}_{+3.7}\%$	$\pm 3.8\%$
Jet vertex fraction scale	$^{+0.7}_{-0.5}\%$	$^{+0.4}_{-0.3}\%$	$^{+0.8}_{-0.4}\%$
Jet energy resolution	$\pm 1.2\%$	$\pm 1.6\%$	$\pm 7.0\%$
b-tagging eff. SF	$\pm 4.9\%$	$\pm 4.7\%$	$\pm 3.7\%$
c-tagging eff. SF	$\pm 0.3\%$	$\pm 0.1\%$	$\pm 4.7\%$
mistag rate SF	$\pm 0.0\%$	$\pm 0.1\%$	$\pm 2.8\%$
Muon momentum scale	$\pm 0.1\%$	$\pm 0.1\%$	$\pm 0.2\%$
Muon momentum smearing (ID)	$\pm 0.0\%$	$\pm 0.0\%$	$\pm 0.2\%$
Muon momentum smearing (MS)	$\pm 0.0\%$	$\pm 0.0\%$	$\pm 0.1\%$
Muon Reco/ID eff. SF	$\pm 0.2\%$	$\pm 0.2\%$	$\pm 0.2\%$
Muon Trigger eff. SF	$\pm 1.0\%$	$\pm 1.0\%$	$\pm 1.2\%$
Electron energy scale	$\pm 0.5\%$	$\pm 0.6\%$	$^{0.9}_{-0.7}\%$
Electron energy smearing	$^{-0.1}_{0.0}\%$	$\pm 0.0\%$	$\pm 0.2\%$
Electron Reco/ID eff. SF	$\pm 1.1\%$	$\pm 1.1\%$	$\pm 0.8\%$
Electron Trigger eff. SF	$\pm 0.2\%$	$\pm 0.2\%$	$\pm 0.2\%$
$E_{\mathrm{T}}^{\mathrm{miss}}$ Cellout/Softjet term resolution	$\pm 0.1\%$	$\pm 0.0\%$	$^{2.3}_{-0.9}\%$
$E_{\mathrm{T}}^{\mathrm{miss}}$ Cellout/Softjet term scale	$\pm 0.1\%$	$\pm 0.1\%$	$^{3.5}_{-2.4}\%$
PDF	$\pm 4.2\%$	$\pm 1.6\%$	$\pm 4.4\%$
PS generator	$\pm 11.7\%$	—	—
MC generator	$\pm 9.6\%$	—	—
ISR/FSR	$\pm 3.2\%$	$\pm 5.0\%$	—

Table 9.2.: Relative systematic uncertainties on the number of expected events from each signal and background source for a plus/minus variation of a systematic uncertainty for the combined electron and muon channels in the 2-jet bin.

Systematic uncertainty	Signal	W+jets	W+HF+jets
Jet energy scale	$^{+4.2}_{-3.0}$%	±10.1%	$^{+5.6}_{-5.1}$%
Jet vertex fraction scale	$^{+0.7}_{-0.6}$%	$^{+3.5}_{-1.7}$%	$^{+0.8}_{-0.5}$%
Jet energy resolution	±5.5%	±24.1%	±3.2%
b-tagging eff. SF	±4.8%	±1.2%	±2.0%
c-tagging eff. SF	±0.2%	±2.4%	±14.3%
mistag rate SF	±0.0%	±21.9%	±0.7%
Muon momentum scale	±0.2%	±0.1%	±0.3%
Muon momentum smearing (ID)	±0.0%	±0.0%	±0.0%
Muon momentum smearing (MS)	$^{-0.1}_{0.0}$%	±0.0%	±0.1%
Muon Reco/ID eff. SF	±0.2%	±0.2%	±0.2%
Muon Trigger eff. SF	±1.1%	±0.8%	±0.8%
Electron energy scale	±0.8%	±0.8%	±0.8%
Electron energy smearing	$^{-0.1}_{0.0}$%	$^{-0.2}_{-0.1}$%	±0.0%
Electron Reco/ID eff. SF	±1.1%	±1.0%	±1.0%
Electron Trigger eff. SF	±0.2%	±0.2%	±0.2%
$E_{\mathrm{T}}^{\mathrm{miss}}$ Cellout/Softjet term resolution	±0.5%	$^{-1.0}_{-0.2}$%	±0.5%
$E_{\mathrm{T}}^{\mathrm{miss}}$ Cellout/Softjet term scale	$^{+0.5}_{0.0}$%	$^{-0.3}_{0.0}$%	±0.2%
PDF	±2.8%	±4.9%	±5.2%
Systematic uncertainty	**$t\bar{t}$**	**single-top**	**Z+jets**
Jet energy scale	$^{-7.1}_{+6.8}$%	$^{-0.3}_{+0.1}$%	$^{+5.7}_{-2.4}$%
Jet vertex fraction scale	$^{+0.8}_{-0.7}$%	$^{+0.7}_{-0.5}$%	$^{+1.2}_{-0.7}$%
Jet energy resolution	±1.1%	±1.8%	±6.8%
b-tagging eff. SF	±3.3%	±4.1%	±3.3%
c-tagging eff. SF	±0.1%	±0.1%	±4.2%
mistag rate SF	±0.0%	±0.0%	±1.9%
Muon momentum scale	±0.1%	±0.1%	±0.2%
Muon momentum smearing (ID)	±0.0%	±0.0%	±0.0%
Muon momentum smearing (MS)	±0.0%	±0.0%	±0.0%
Muon Reco/ID eff. SF	±0.2%	±0.2%	±0.2%
Muon Trigger eff. SF	±1.0%	±1.0%	±1.0%
Electron energy scale	±0.4%	±0.7%	$^{+2.0}_{-1.0}$%
Electron energy smearing	±0.0%	±0.0%	±0.3%
Electron Reco/ID eff. SF	±1.1%	±1.1%	±1.1%
Electron Trigger eff. SF	±0.2%	±0.2%	±0.3%
$E_{\mathrm{T}}^{\mathrm{miss}}$ Cellout/Softjet term resolution	$^{-0.1}_{0.0}$%	±0.1%	±1.1%
$E_{\mathrm{T}}^{\mathrm{miss}}$ Cellout/Softjet term scale	±0.1%	±0.2%	$^{+4.1}_{-1.5}$%
PDF	±4.7%	±1.7%	±4.2%
PS generator	±6.7%	—	—
MC generator	±10.6%	—	—
ISR/FSR	±2.6%	±3.7%	—

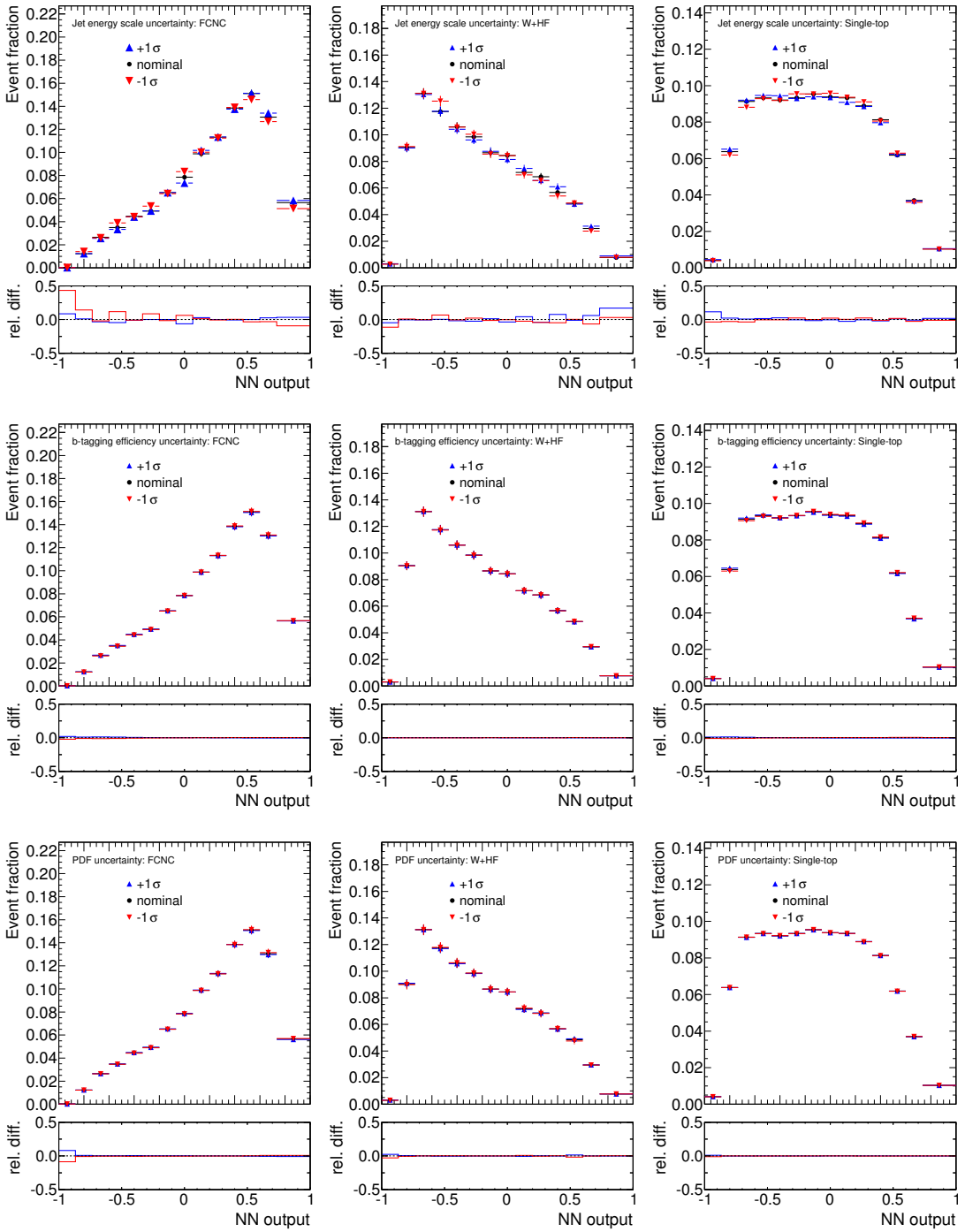

Figure 9.2.: ANN output distributions in the 1-jet bin normalised to unit area for $\pm 1\sigma$ shifts in the uncertainty of the jet energy scale (top row), the b-tagging efficiency (middle row) and the PDF uncertainty (bottom row), for signal (a), W+HF+jets (b) and SM single top-quark events (c), respectively.

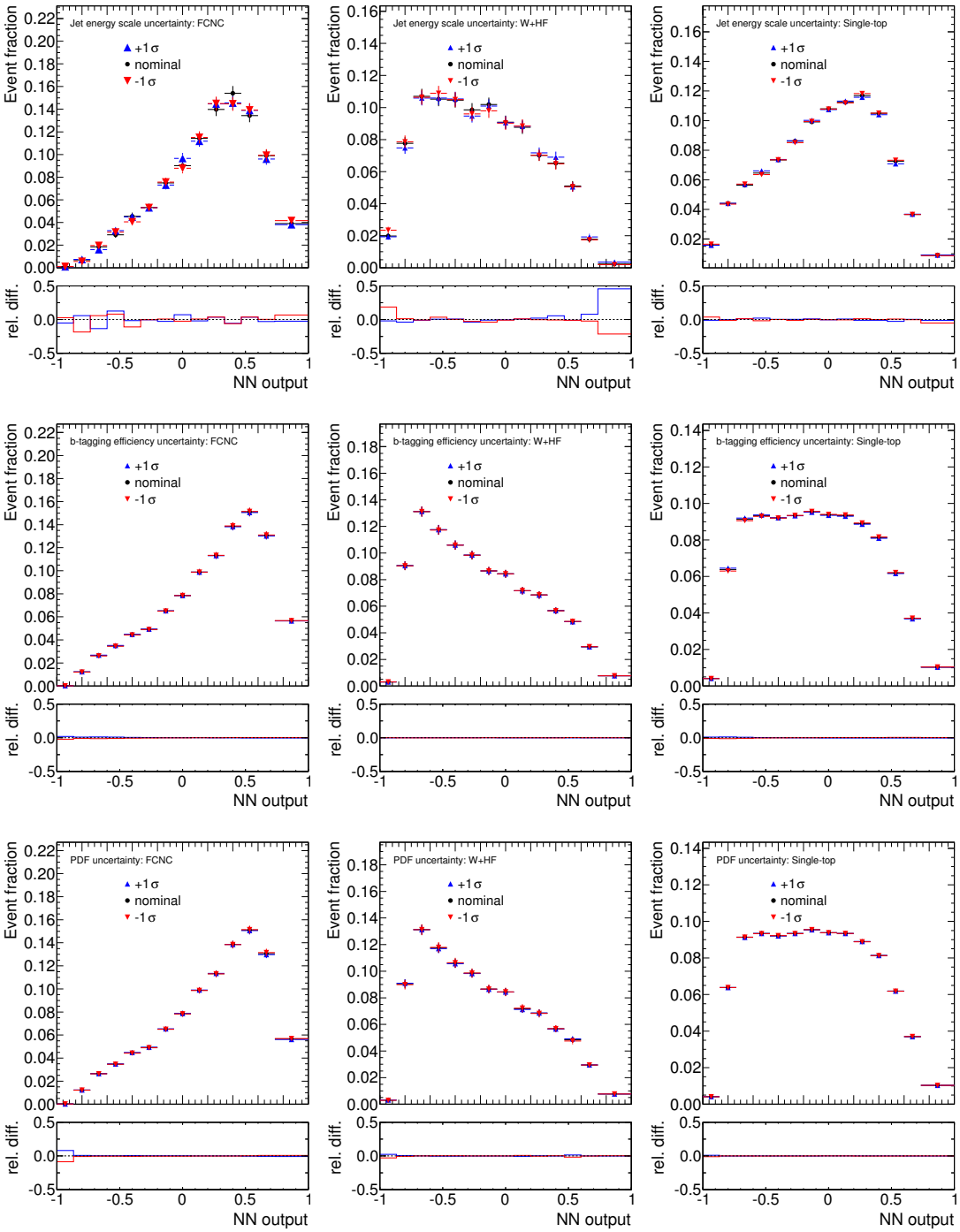

Figure 9.3.: ANN output distributions in the 2-jet bin normalised to unit area for $\pm 1\sigma$ shifts in the uncertainty of the jet energy scale (top row), the b-tagging efficiency (middle row) and the PDF uncertainty (bottom row), for signal (a), W+HF+jets (b) and SM single top-quark events (c), respectively.

10. Statistical Analysis

In order to measure or set an upper limit on the cross-section of the anomalous single top-quark production via flavour-changing neutral currents, a Bayesian statistical analysis [272] is performed by applying a binned likelihood method on the full neural network output distribution. Using theory calculations, the limits on the cross-section can be converted into limits on the branching ratios and coupling constants of the FCNC processes under investigation.

10.1. Cross-section and Limit Evaluation

For a single bin j of a distribution the likelihood L to observe a certain event count D_j is defined by the Poisson distribution:

$$L(D_j|\lambda_j) = \frac{e^{-\lambda_j}\lambda^{D_j}}{D_j!}\,, \tag{10.1}$$

where λ_j is the expected or mean count (yield) in bin j. Hence, λ_j is the sum of the predicted contributions from all N background sources and a particular signal contribution for a given signal acceptance α_j, signal cross-section σ, and integrated luminosity $\mathcal{L}$:

$$\lambda_j = \alpha_j\,\mathcal{L}\,\sigma + \sum_{i=1}^{N} b_{ij} \equiv a_j\,\sigma + b_j\,. \tag{10.2}$$

Here b_j represents the sum of all background yields b_{ij} and $a_j = \alpha_j\mathcal{L}$ denotes an effective luminosity, determined by the signal acceptance α_j in the j^{th} bin. Since the probabilities for observed counts in multiple bins of a distribution are disjoint, the likelihood for a distribution of observed events in M bins is given by the product of all single-bin likelihoods:

$$L(\mathbf{D}|) = L(\mathbf{D}|\sigma,\mathbf{a},\mathbf{b}) = \prod_{j=1}^{M} \frac{e^{-\lambda_j}\lambda_j^{D_j}}{D_j!}\,, \tag{10.3}$$

where $\mathbf{D}$ and represent vectors of the observed and total expected number of events in M bins, and $\mathbf{a}$ and $\mathbf{b}$ are the corresponding vectors of the effective luminosity and the total background yield.

According to Bayes' theorem [273], the posterior probability density for a hypothesis

$\mathrm{H}(\sigma, \mathbf{a}, \mathbf{b})$, given the observed distribution $\mathbf{D}$ can be expressed as

$$P(\mathrm{H}(\sigma, \mathbf{a}, \mathbf{b})|\mathbf{D}) = \frac{P(\mathbf{D}|\mathrm{H}(\sigma, \mathbf{a}, \mathbf{b})) \cdot P(\mathrm{H}(\sigma, \mathbf{a}, \mathbf{b}))}{P(\mathbf{D})}\,, \tag{10.4}$$

where

- $P(\mathbf{D}|\mathrm{H}(\sigma, \mathbf{a}, \mathbf{b}))$ is the conditional probability to observe the distribution of events $\mathbf{D}$ if the hypothesis $\mathrm{H}(\sigma, \mathbf{a}, \mathbf{b})$ is true. Given that the data are known, it is equivalent to the likelihood of the hypothesis parameters denoted in Equation 10.3;
- $P(\mathrm{H}(\sigma, \mathbf{a}, \mathbf{b}))$ is the prior probability function which reflects the degree of belief that the hypothesis $\mathrm{H}(\sigma, \mathbf{a}, \mathbf{b})$ is true;
- $P(\mathbf{D})$ is the unconditional or marginal probability of $\mathbf{D}$ which is independent from the particular hypotheses considered. It acts as a normalising constant to provide a proper probability measure by ensuring that the sum over all possible hypotheses is at unity.

The prior probability $P(\mathrm{H}(\sigma, \mathbf{a}, \mathbf{b}))$, often also denoted as $\pi(\sigma, \mathbf{a}, \mathbf{b})$, encodes the knowledge available a-priori on the parameters σ, $\mathbf{a}$ and $\mathbf{b}$. Assuming that any prior knowledge of $\mathbf{a}$ and $\mathbf{b}$ is independent of the signal cross-section, the prior probability can be factorised as

$$\pi(\sigma, \mathbf{a}, \mathbf{b}) = \pi(\sigma)\,\pi(\mathbf{a}, \mathbf{b})\,. \tag{10.5}$$

In general this assumption is valid, since neither the signal acceptance nor the background yield are expected to depend on the signal cross-section. To support this, it was proven that the signal shape, and hence acceptance α_j in a particular bin, is independent of the coupling constant and thus the cross-section chosen for generating the signal event sample, see Appendix E. Further, it was shown that for the range of coupling constants coming into consideration in this analysis, the effect on the SM single-top decay branching ratio is negligible. A common convention for the choice of the prior density for the signal cross-section $\pi(\sigma)$ is to assume a positive probability function flat in σ:

$$\pi(\sigma) = \begin{cases} 1/\sigma_{\mathrm{max}} & \forall \;\; 0 < \sigma < \sigma_{\mathrm{max}} \\ 0 & \text{otherwise}\,. \end{cases} \tag{10.6}$$

The range of the signal prior $\pi(\sigma)$ has to be constrained with an upper bound σ_{max}, since it represents an improper probability function. The lower bound is set to 0, since a negative cross-section is considered unphysical. The value for σ_{max} has to be chosen such that it is large enough to make the posterior probability fall to zero to fulfil the requirement on the normalisation

$$\int_0^{\sigma_{\mathrm{max}}} P(\mathrm{H}(\sigma, \mathbf{a}, \mathbf{b})|\mathbf{D})\, d\sigma = 1 \;\; . \tag{10.7}$$

To obtain the signal posterior probability density function (pdf) which reflects the probability of the signal hypothesis to be true, as a function of the signal cross-section σ, Equation 10.4 is integrated with respect to the parameters $\mathbf{a}$ and $\mathbf{b}$:

$$p(\sigma|\mathbf{D}) = \iint P(\mathrm{H}(\sigma, \mathbf{a}, \mathbf{b})|\mathbf{D})\, d\mathbf{a}\, d\mathbf{b} \tag{10.8}$$

$$= \frac{1}{\mathcal{N}\sigma_{\max}} \iint L(\mathbf{D}|\sigma, \mathbf{a}, \mathbf{b})\pi(\mathbf{a}, \mathbf{b})\, d\mathbf{a}\, d\mathbf{b}\,, \tag{10.9}$$

where the $P(\mathbf{D}) = \mathcal{N}$ is the overall normalisation parameter to ensure that Equation 10.7 remains true. The vectors $\mathbf{a}$ and $\mathbf{b}$ are altered for all systematic uncertainties considered. The priors for these are chosen to be Gaussian distributions with the width of the respective estimated uncertainty. Details on the implementation of systematic uncertainties are discussed in the following Section 10.2.

Since the signal posterior pdf gives the probability for a true signal hypothesis as a function of the signal cross-section, any measure of the location of the posterior density, e.g. the mean, median or mode, can be used as a measure of the signal cross-section. If no evidence for observing the signal is found, the Bayesian upper limit on the cross-section at a certain confidence level (C.L.), $\sigma_{\mathrm{C.L.}}$, can be calculated by integrating the posterior pdf as follows:

$$\int_0^{\sigma_{\mathrm{C.L.}}} p(\sigma|\mathbf{D})\, d\sigma = \mathrm{C.L.}\ . \tag{10.10}$$

10.2. Systematic Uncertainties

Both, normalisation and shape systematic uncertainties are accounted for in the statistical analysis using a direct sampling approach. For each bin of the distribution a Gaussian prior with the width of the corresponding uncertainty for a given signal or background process is used. The choice of a Gaussian prior is motivated by the fact that all uncertainties are given as the 1σ variance of a Gaussian distributed over the mean or expected count. Further this choice ensures that that the posterior distribution itself is a Gaussian distribution since the Gaussian family is self-conjugate with respect to a Gaussian likelihood function, hence is a conjugate prior of it. For each systematic uncertainty included, a large number of random samples of systematic shifts is drawn from the prior distributions and a separate likelihood distribution is computed for each sample. Finally, the posterior density distribution is obtained by averaging over all individual likelihoods, i.e. by calculating the sum over all likelihoods and dividing by the number of samples drawn.

For each sample a systematic yield shift caused by a particular systematic uncertainty s is calculated in each bin. First, a random number $(g(0,1)_s)$ is drawn from a normal distribution with mean of zero and width of one. This random number represents a particular systematic shift of the systematic uncertainty s in terms of its standard deviation and is applied to all bins of the distribution simultaneously. The yield shifts, $\Delta\lambda_{ij,s}$, for

all bins j and all background or signal sources i are then calculated as follows:

$$\Delta\lambda_{ij,s} = g(0,1)_s \times \begin{cases} \left(\lambda_{ij,s}^{+\sigma} - \lambda_{ij}^{0}\right) & \forall\ g(0,1)_s > 0 \\ \left(\lambda_{ij}^{0} - \lambda_{ij,s}^{-\sigma}\right) & \forall\ g(0,1)_s < 0 \end{cases} , \tag{10.11}$$

where $\Delta\lambda_{ij,s}$ is the yield shift of the background or signal source i in bin j, caused by a given source of systematic uncertainty s. The nominal yield in bin j is denoted by λ_{ij}^{0}, while $\lambda_{ij,s}^{+\sigma}$ and $\lambda_{ij,s}^{-\sigma}$ represent the shifted yields of the source i for a $\pm 1\,\sigma$ variation of the systematic uncertainty. The shifted yields are derived from two additional MC samples of $\pm 1\,\sigma$ variations from each systematic uncertainty, all passed through the same neural network analysis beforehand. In cases in which only one-sided systematic uncertainties are given, the templates of the neural network output distribution for the $\pm 1\,\sigma$ shifts are symmetrised, see Section 9 for details about which systematic uncertainties this applies to. In cases of asymmetric systematic uncertainties, where a systematic shift leads to differently shifted positive and negative bin counts, a quadratic approach [274] is used to get a smooth transition at zero shift (λ_{ij}^{0}). The yield shift in these cases are given by

$$\Delta\lambda_{ij,s} = \left[g(0,1)_s \times \frac{\lambda_{ij,s}^{+\sigma} - \lambda_{ij,s}^{-\sigma}}{2} + g(0,1)_s^2 \times \frac{\lambda_{ij,s}^{+\sigma} + \lambda_{ij,s}^{-\sigma} - 2\lambda_{ij}^{0}}{2} \right] . \tag{10.12}$$

To include multiple sources of systematic uncertainties simultaneously, the procedures described above are repeated for each of them. Hence, for each sample a set of random numbers and yield shifts is generated. The total yield of a background or signal source i in the bin j used to calculate the new likelihood, is obtained by summing over all shifts obtained for all sources of systematic uncertainties considered:

$$\lambda_{ij} = \lambda_{ij}^{0} + \sum_{s} \Delta\lambda_{ij,s} \,. \tag{10.13}$$

For large shifts in one or more systematic uncertainties the total yield λ_{ij} might become negative and the bin content is set to zero. If for a particular sample more than 30% of the bins have been set to zero for this reason, the sample is discarded and a new set of random numbers is drawn. Sampling distributions showing the number of samples drawn vs. the systematic shift are obtained for each systematic uncertainty in the statistical analysis and are checked for any modification of the expected Gaussian shape, such as possible truncation effects due to large negative systematic fluctuations. No such deviations is found in any of the distributions, hence assuring the correct accounting for all uncertainties in their full extend.

The final signal posterior density function is obtained by integrating over the priors of all systematic uncertainties. This is performed by drawing a large number of random samples from the Gaussian priors and computing a likelihood for each. Lastly the integration is approximated by summing over all systematic sample likelihoods. The integral (magnitude) of each individual likelihood is a measure of how well a particular set of shifts of systematic uncertainties is compatible with the data. Hence only those likeli-

hoods with a large integral will contribute considerably to the final posterior density. It has to be assured that a sufficiently large number of samples is obtained to cover the full phase space of possible combinations of systematics shifts. As the number of samples grows large, the relative uncertainty arising from the finite size of sampling statistics is then calculated from the k individual likelihood integrals I_k using the standard error and the samples estimate of the mean posterior pdf as follows:

$$\sigma^{\mathrm{rel}}_{k_{\mathrm{samples}}} = \frac{\mathrm{Var}\left(p(\sigma)\right)}{\langle p(\sigma)\rangle} = \frac{\sqrt{\sum\limits_k I_k^2}}{\sum\limits_k I_k}\,. \tag{10.14}$$

In all calculations it was therefore assured that $\sigma^{\mathrm{rel}}_{k_{\mathrm{samples}}} < 0.05$ to obtain reasonably accurate measurements.

The uncertainties arising from the limited size of the MC samples have to be treated differently. Since the MC statistical uncertainty is considered independent from bin to bin and among all backgrounds, no common Gaussian prior can be used. Instead, separate priors are required to be sampled from, one for each individual background or signal source and bin. This would result in a very large phase space for the integration and hence require drawing a vast amount of samples of systematic shifts to obtain sufficiently large sampling statistics. Since this in impractical for reasons of computation time, a Gamma distribution is used instead of a Gaussian prior to model the MC statistical uncertainty. Using a Gamma prior allows for using an algebraic expression to analytically compute the integral over the systematic uncertainty instead of summing over individual sample likelihoods and is implemented by modifying Equation 10.1 to

$$L(D_j|\lambda_j) = \int L(D_j|\lambda_j, \sigma^{\mathrm{MC}}_{d_j})\; d\sigma^{\mathrm{MC}}_{d_j} \tag{10.15}$$

$$= \frac{y_j^{D_j}}{(y_j+1)^{D_j+k_j+1}} \cdot \frac{1}{\beta(D_j+1, k_j)} \tag{10.16}$$

where $\sigma^{\mathrm{MC}}_{d_j}$ denotes the statistical uncertainty for the yield d_j in bin j, β is the beta function, and $k_j = (d_j/\sigma^{\mathrm{MC}}_{d_j})^2$ and $y_j = d_j/k_j$. In the calculation of the statistical uncertainty $\sigma^{\mathrm{MC}}_{d_j}$ of each bin all scalings of the original MC samples (e.g. k-factors, luminosity) are propagated and individual event weights applied during the analysis (e.g. from efficiency / scale corrections) are fully accounted for.

10.3. Expected and Observed Limits

By integrating the posterior probability function an upper limit on the anomalous FCNC single top-quark production cross-section is calculated individually for the signal samples in the 1-jet and 2-jet bin. To determine whether the statistical analysis performs as

expected and the claimed sensitivity is justified, studies using pseudo-data samples with characteristics as close as possible to the observed data sample are employed. To determine the a-priori sensitivity, a pseudo-dataset corresponding to the nominal distribution of expected events from MC simulations (Asimov dataset [275, 276]) is used in place of the observed data. Thereby an expected limit is determined including all sources of systematic uncertainties and using the same method as for the observed data sample. The resulting posterior probability functions obtained for events in the 1-jet and 2-jet bins are shown in Figure 10.1 (c) and (d), together with the 95% C.L. expected upper limit calculated by integrating the posterior probability function. Including all systematic uncertainties, the expected upper limit in the 1-jet bin is 2.4 pb, and 5.7 pb for the signal sample in the 2-jet bin. As expected, a much lower sensitivity is reached in the 2-jet bin (cf. Section 8.2.5). To study the influence of individual systematic uncertainties on the expected sensitivity in each jet bin, expected upper limits on the signal cross-section are calculated including only single sources of uncertainties at a time, in addition to the MC statistical uncertainties. The resulting expected limits are summarised in Table 10.1. To get an estimate on how purely statistical and normalisation uncertainties affect the final result, the posterior probability function and the expected 95% C.L. upper limits including only the statistical uncertainties and those on the theoretical cross-section and multijet normalisation are shown in Figure 10.1 (a) and (b) for each jet bin. From these pdf distributions and Table 10.1 it can be seen that in particular the uncertainty on normalisation of the W+HF+jets and single-top backgrounds dominate the uncertainty since they represent the largest background or the one closest to the kinematic shape of the signal processes.

In accordance to the studies in Section 9, Table 10.1 shows that most of the (shape affecting) systematic uncertainties have negligible impact on the expected upper limit, while some particular systematic uncertainties, such as the b-tagging efficiency, c-tag and mistag rate uncertainties, as well as uncertainties on the jet energy resolution and those of the PDF sets, dominate the width of the signal posterior pdf. However, the most important source of uncertainty is the MC statistical uncertainty itself, which is a result of the limited MC sample size available in early 2013, in particular of the W+HF+jets and W+jets background samples.

The results obtained from collision data reflected in the signal posterior pdf are shown in Figure 10.2 (a) and (b) for the 1-jet bin and 2-jet bin, and including only the statistical uncertainties and those on the theoretical cross-sections and multijet rate. The corresponding pdf distributions obtained when including all systematic uncertainties are shown in Figure 10.2 (c,d). No significant rate of FCNC single top-quark production can be observed in any of the distributions. The cross-section at the maximum value (mode) of the signal pdf in the 1-jet bin is zero and hence in full agreement with the SM expectation (null hypothesis, H0). In the 2-jet bin, however, the signal posterior pdf peaks at non-zero, albeit small cross-section values. To estimate the significance of the observed difference with respect to the expectation, the Bayes ratio [277] (B_{10}) of the signal hypothesis for a cross-section at the most probable value of the signal posterior pdf (H1) to the SM background-only hypothesis (H0) is calculated as described in [277]. The resulting significance ($Z = \sqrt{2 \log B_{10}}$) of the peak is derived as $0.43\,\sigma$

and the signal hypothesis therefore is clearly excluded. Consequently upper limits are set on the signal cross-section by integrating the signal posterior pdfs in both jet bins. For the 1-jet bin the observed 95% C.L. upper limit on the anomalous FCNC single top-quark production cross-section, including all systematic uncertainties, is found at 2.5 pb. Including only the statistical uncertainties and those on the theoretical cross-sections and multijet normalisation it is calculated as 2.4 pb. In the 2-jet bin the observed 95% C.L. upper limits are measured as 6.8 pb when including all systematic uncertainties, and 7.1 pb when only the uncertainties on the normalisation of the SM background processes and the uncertainty from the limited MC samples statistics are included. This a-priori

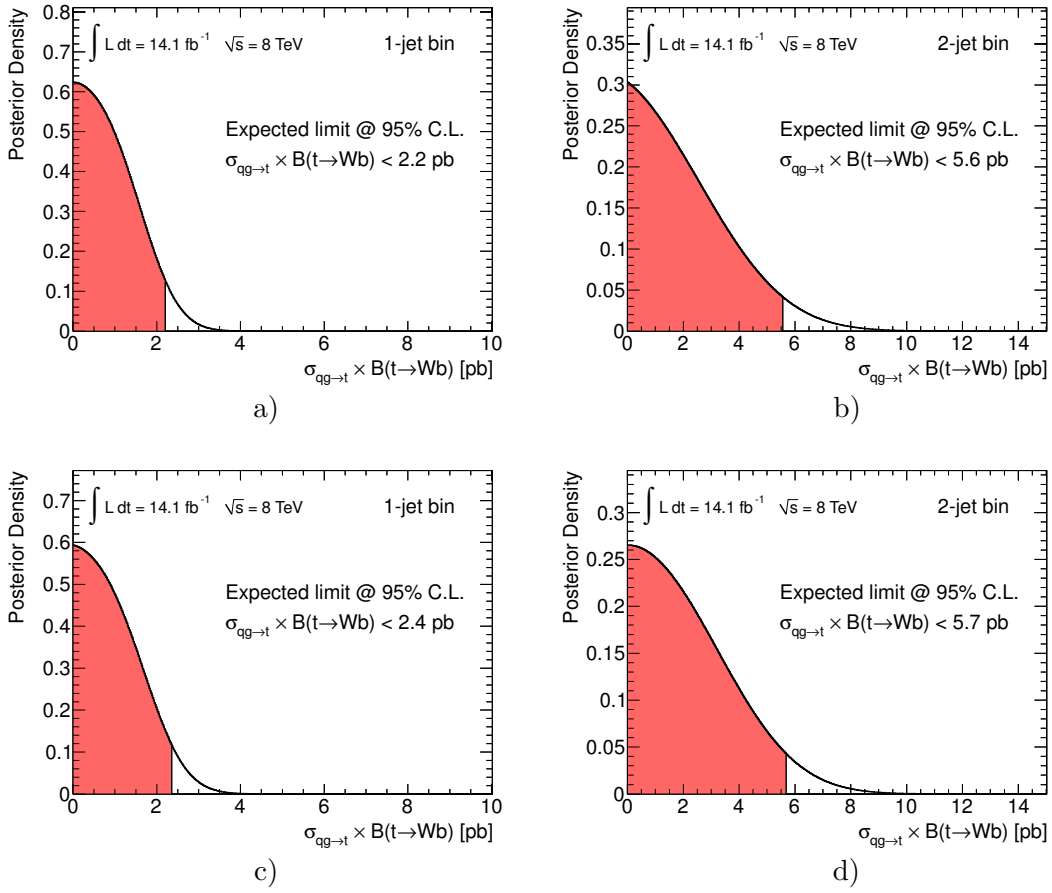

Figure 10.1.: Distributions of the signal posterior probability function of the Asimov dataset used to calculate the expected upper limit, including only the statistical uncertainties and those on the theoretical cross-section and multijet normalisation (top row), and including all systematic uncertainties (bottom row), for the signal sample in the 1-jet bin (a,c) and 2-jet bin (b,d) respectively. The red area covers 95% of the integral up to which the signal pdf is integrated in order to derive the upper limit on the cross-section.

Table 10.1.: The effect of each single systematic uncertainty in addition to the MC statistical uncertainties alone (top row) on the expected 95% C.L. upper limits on the anomalous FCNC single top-quark production $qg \to t \to b\ell\nu$ in the 1-jet bin and 2-jet bin.

Source	expected 95% C.L. upper limit	
	1-jet bin	2-jet bin
MC statistical uncertainties	1.39 pb	4.02 pb
Luminosity	1.79 pb	5.20 pb
$E_{\mathrm{T}}^{\mathrm{miss}}$ Cellout&SoftJet scale and resolution	1.51 pb	4.07 pb
Electron ID, Reco & trigger efficiency	1.63 pb	4.84 pb
Electron energy scale and resolution	1.46 pb	4.13 pb
Muon ID, Reco & trigger efficiency	1.61 pb	4.78 pb
Muon momentum scale and resolution	1.44 pb	4.02 pb
b-tagging eff., c-tag & mistag rate	1.99 pb	5.27 pb
Jet energy scale	1.67 pb	4.03 pb
Jet energy resolution	1.40 pb	4.18 pb
Jet vertex fraction scale	1.41 pb	4.46 pb
W+jets shape	1.39 pb	4.03 pb
Multijet shape	1.41 pb	5.17 pb
PDF	1.94 pb	4.96 pb
ISR/FSR	1.51 pb	5.26 pb
MC generator	1.58 pb	4.60 pb
PS generator	1.63 pb	5.16 pb
W+HF+jets cross-section	1.95 pb	5.21 pb
W+jets cross-section	1.48 pb	5.05 pb
Z+jets cross-section	1.49 pb	4.56 pb
$t\bar{t}$ cross-section	1.45 pb	4.63 pb
Single-top cross-section	1.57 pb	5.41 pb
Multijet rate	1.48 pb	5.14 pb
All systematic uncertainties	2.37 pb	5.67 pb

counter-intuitive difference can be explained by individual systematic uncertainties shifting the most probable value of the posterior probability density up- or downwards due to asymmetries in the yields obtained for shifted systematic uncertainties affecting the background and signal contributions differently. The most probable cross-section value in the 2-jet bin, including only the statistical uncertainties and those on the theoretical cross-sections and multijet normalisation is $2.2^{+2.1}_{-2.1}$ pb and gets shifted downwards to $1.4^{+2.4}_{-1.4}$ pb when including all systematic uncertainties. Hence, while making a non-zero posterior mean value less probable as intuitively expected, the addition of the shape uncertainties also increases the upper error bound of the most probable value. A summary of the expected and observed 95% C.L. upper limits is given in Table 10.2.

To visualise how each systematic uncertainty is constrained by the data, histograms

of the systematic shifts, sampled from their respective prior distributions and with each entry weighted by its likelihood integral, are shown in Appendix D. This systematics posterior pdf is obtained by integrating the likelihood as done in Equation 10.8 to obtain the signal posterior pdf, but replacing the signal by the shift for a particular systematic uncertainty, see Appendix D for more details. Figure 10.3 shows a summary of the mean and width of the systematics posterior pdfs for all sources of systematic uncertainty. In case the observed data do not constrain a particular systematic, the resulting posterior pdf is expected to have a mean of zero and width of one, in accordance to the systematic uncertainties Gaussian prior. Overall little spread in the most probable values of sys-

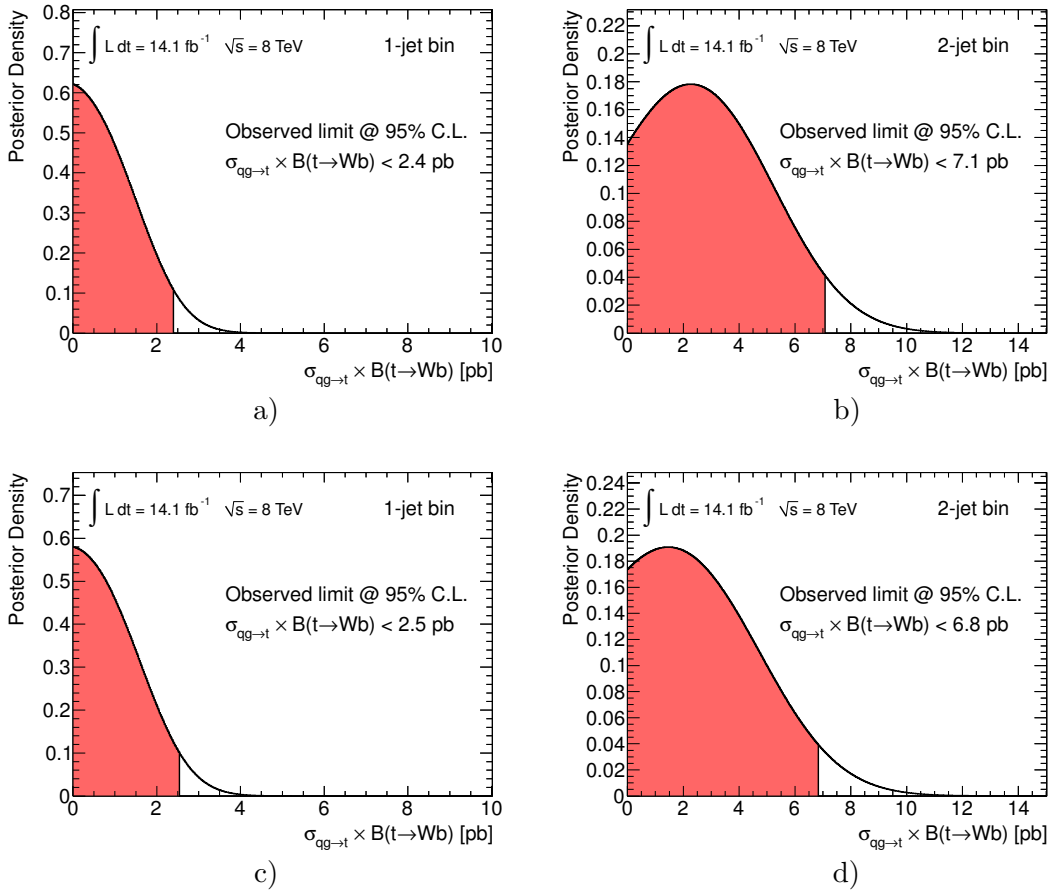

Figure 10.2.: Distributions of the signal posterior probability density function of the observed events, including only the statistical uncertainties and those on the theoretical cross-sections and multijet normalisation (top row), and including all systematic uncertainties (bottom row), for the signal sample in the 1-jet bin (a,c) and 2-jet bin (b,d). The red area covers 95% of the integral up to which the signal pdf is integrated in order to derive the upper limit on the cross-section.

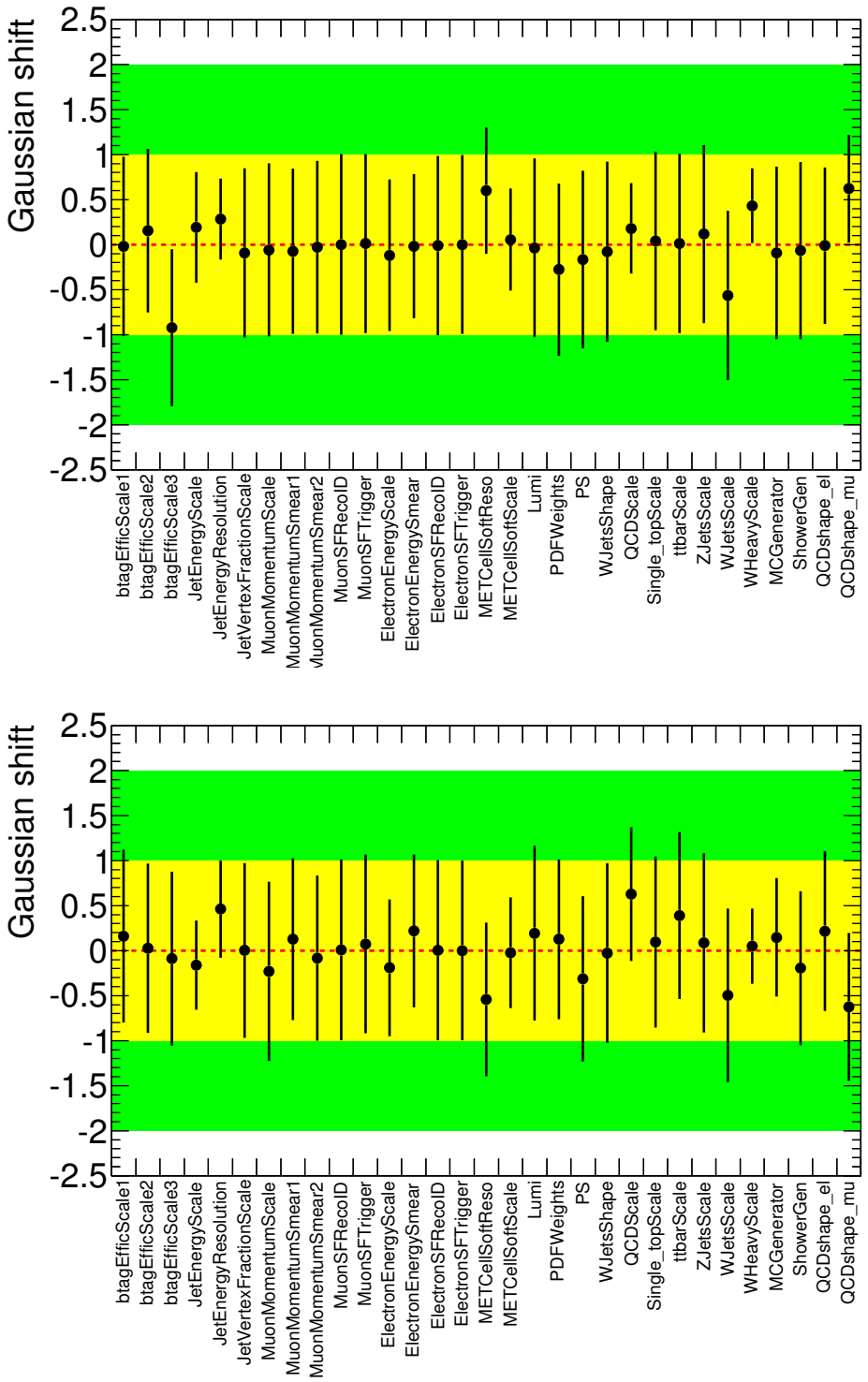

Figure 10.3.: Summary of the systematics posterior pdf mean and standard deviation in units of (Gaussian) σ for all sources of systematic uncertainty considered in the statistical analysis in the 1-jet bin (top) and 2-jet bin (bottom).

Table 10.2.: Expected and observed 95% C.L. upper limits on the anomalous FCNC single top-quark production cross-section obtained in the 1-jet and 2-jet bin, including either all or only the statistical uncertainties and those on the theoretical cross-section predictions and multijet background rate.

	expected		observed	
jet bin	1-jet bin	2-jet bin	1-jet bin	2-jet bin
normalisation & MC stat. unc.	2.2 pb	5.6 pb	2.4 pb	7.1 pb
all systematic uncertainties	2.4 pb	5.7 pb	2.5 pb	6.8 pb

tematics shifts can be observed which are all found within $\pm 1\sigma$ in the standard deviation of their respective Gaussian priors. In particular the uncertainties on the normalisation of the W+HF+jets and multijet backgrounds get largely constrained by data due to the a-priori conservative choice for the uncertainty of the W+HF+jets cross-section (55%) and the multijets rate (50%). In order to check if this potential overestimation has an impact on the results, the statistical analysis is repeated using smaller a-priory uncertainty values for the normalisation of the W+HF+jets background processes as shown exemplarily for the 1-jet bin in Appendix D.2. No visible deterioration of the results can be found for uncertainty values on the W+HF+jets background normalisation as low as approximately 50% of the original value, which is in accordance with the width of the respective systematics posterior probability distribution.

The systematics posterior density distributions can be used to correct the normalisations of the background processes by deriving scale factors using the systematics pdf mean values for the respective cross-section and multijets rate uncertainties. A summary is given in Table 10.3 for the 1-jet bin and 2-jet bin. respectively. The same table shows the widths of the systematics posterior density distributions from which is concluded that the uncertainties on the cross-sections for the W+HF+jets and W+jets backgrounds as well as those on the multijets normalisation are smaller than the a-priori uncertainties given by the theory predictions and the assigned multijets rate uncertainty. This is a

Table 10.3.: Mean values of the systematics posterior density distributions in units of (Gaussian) σ for the cross-section and multijets rate uncertainties and resultant scale factors (SF) for the respective backgrounds.

	1-jet bin systematics pdf			2-jet bin systematics pdf		
Process	mean [σ]	width [σ]	SF	mean [σ]	width [σ]	SF
SM single top	+0.04	$\pm$0.99	1.00	+0.10	$\pm$0.95	1.01
$t\bar{t}$	+0.01	$\pm$0.99	1.00	+0.39	$\pm$0.93	1.02
W+jets	$-$0.56	$\pm$0.94	0.86	$-$0.50	$\pm$0.96	0.83
W+HF+jets	+0.43	$\pm$0.41	1.24	+0.05	$\pm$0.42	1.02
Z+jets	+0.12	$\pm$0.99	1.03	+0.09	$\pm$0.99	1.03
Multijets	+0.18	$\pm$0.50	1.09	+0.62	$\pm$0.74	1.31

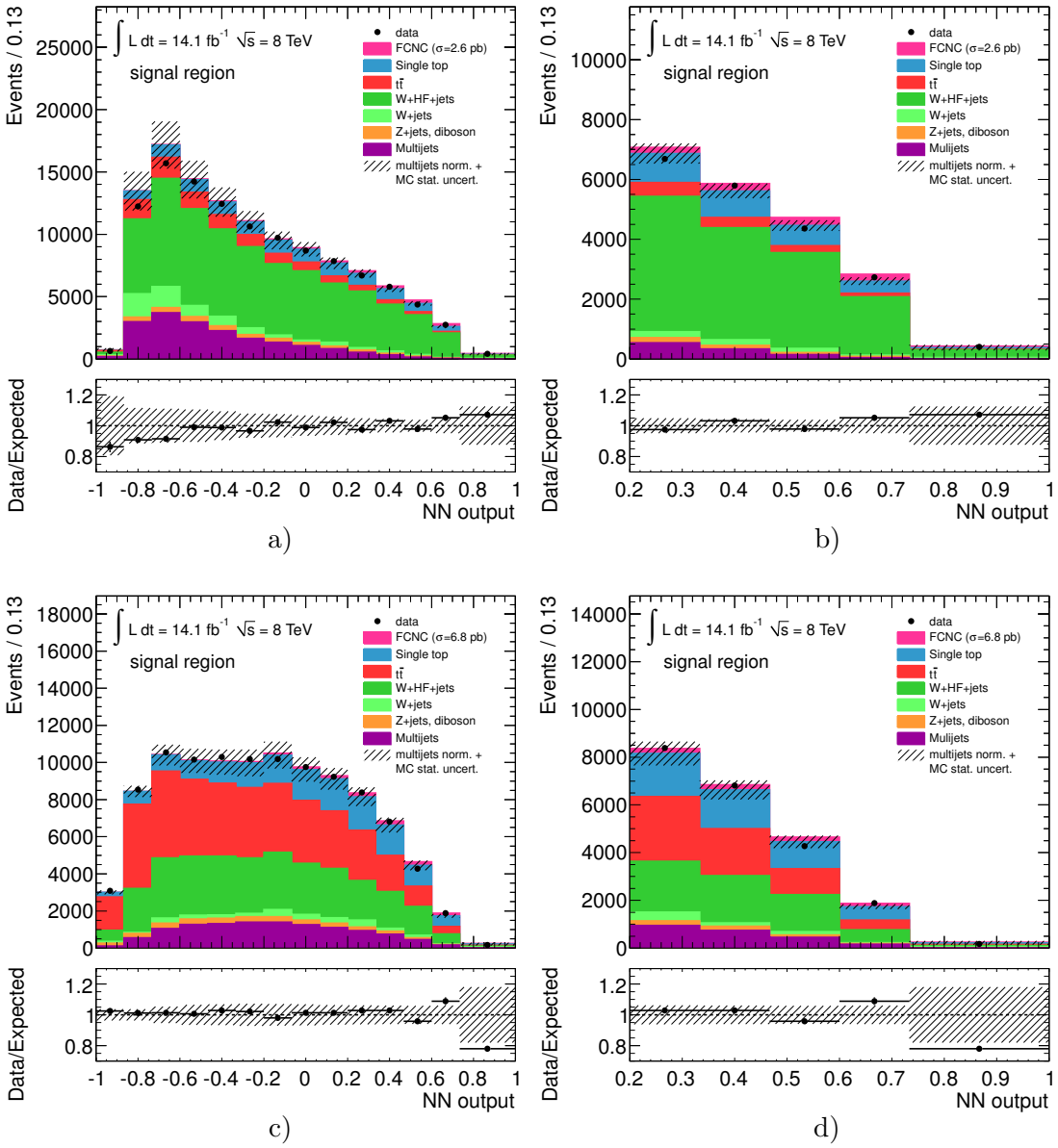

Figure 10.4.: Neural network output distribution in the signal region (a,c), and in the signal region with neural network output values above 0.2 (b,d), for the 1-jet bin (top row) and 2-jet bin (bottom row), respectively. The signal contribution is shown scaled to the observed upper limit at 95% C.L. stacked on top of the backgrounds. All background processes are shown normalised to the systematics posterior pdf mean values of their respective cross-section or rate uncertainties as obtained in the limit calculation. The lower pads show the relative difference between the observed distribution and that of the SM only expectation. The hatched bands indicates the combined statistical uncertainty from the simulated samples size and the uncertainty on the multijet rate.

result of the constraints on the background fluctuations by the observed data given the shape differences between the different background contributions in the full neural network output distribution. It turns out that best compatibility with the observation in the 1-jet bin is obtained by scaling the cross-sections of the W+jets and W+HF+jets backgrounds by 0.86 and 1.24, respectively, while increasing the multijet rate by 9% and leaving the remaining SM backgrounds mostly unchanged. Similarly in the 2-jet bin the most probable value for the normalisation of the W+jets and W+HF+jets backgrounds is found to be at 0.83 and 1.03, while increasing the overall rate of the multijet background by 31%.

To depict the observed upper limit in the neural network output distribution, the signal processes are shown stacked on top of the SM background processes and scaled to the observed upper cross-section limit of 2.6 pb or 6.8 pb in the 1- or 2-jet bin, see Figures 10.4 (a) and (c). To test the agreement between prediction and observed data using the posterior scales, all background processes in this figure are normalised to the mean values of the systematics posterior pdf of their respective cross-section or rate uncertainty as summarised in Table 10.3. Figure 10.4 (b) and (d) show a version of the distributions with a zoom into the region of high neural network output values where the signal contributions are expected to accumulate. In all sub-figures the ratio pad shows the relative difference between data and the expected contributions from SM background processes only; in this ratio the signal contribution shown in the main pad hence is not included. From the latter it can be confirmed that the observation from collision data can be described by the SM background processes alone, which is compatible with the results seen in the signal posterior pdfs.

10.4. Ensemble Tests

To further justify the claimed sensitivity and in order to validate that the observed limits lie within a reasonable range around their corresponding expected values, the purely Bayesian statistical analysis approach is extended by a frequentist procedure. Instead of using a single pseudo-dataset fixed to the nominal expected event yield in each bin, multiple pseudo-experiments are run using ensembles of pseudo-datasets. The pseudo-datasets are generated by randomly sampling events from the distributions of simulated events in the ANN outputs. The full statistical analysis procedure is run for each, which yields separate limits for each pseudo-experiment.

The same direct sampling approach as described in Section 10.2 is used to include the full phase space of systematic uncertainties in the pseudo-dataset generation. To generate a single set, a random sample corresponding to a particular set of systematic yield shifts is chosen, and in each bin a new number of events is sampled from a Poisson distribution with its mean set to the sum of background yields in that bin. A total of 1000 pseudo-experiments are performed and the expected 95% C.L. upper limit is calculated for each. The resulting distributions of expected limits for the 1-jet and 2-jet bins are shown in Figure 10.5. The medians of the distributions are compatible with the expected upper limits formerly derived using the single pseudo-dataset fixed to the

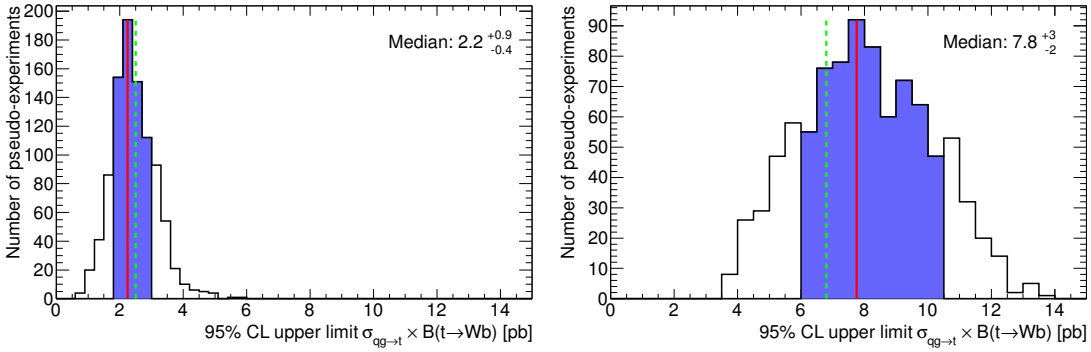

a) b)

Figure 10.5.: Distribution of the 95% C.L. upper limits on the FCNC signal cross-section in 1000 pseudo-experiments using simulated events in the 1-jet bin (a) and 2-jet bin (b). The red line denotes the median of the distribution and the blue area represents the $\pm 1\sigma$ band (standard deviation). The value of the observed limit is shown as a hatched green line for comparison.

nominal distribution of expected events. The standard deviation is calculated as the difference between 16th and 84th percentile of the distribution. It provides a measure of uncertainty of the median expected limit and therefore represents a range wherein an observed limit is likely to be found, if the statistical analysis performs well and the data is fully described by the SM prediction within the statistical and systematic uncertainties. The observed limits lie well within the $\pm 1\sigma$ bands of these distributions.

In order to validate that the claimed sensitivity to measure or exclude a hypothetical FCNC signal contribution in the analysis is reasonable, additional pseudo-experiments are performed in the (more sensitive) 1-jet bin, with non-zero signal contributions included in the generation of the pseudo-datasets. The added signal contributions correspond to cross-sections of 2.5 pb, 5 pb and 10 pb, respectively. The distributions of the maxima (most probable value) of the signal posterior distributions from all pseudo-experiment of a particular ensemble and signal cross-section are shown in Figure 10.6. Figure 10.7 shows the mean values of these distributions in dependence of the cross-section of the additional signal contribution in the pseudo-datasets for the 1-jet bin. The mean values match the injected signal cross-sections very well and only a minimal bias is visible when applying a linear fit, which confirms that the claimed sensitivity of the analysis is well justified.

10.5. Limits on Coupling Constants and Branching Ratios

Using the NLO predictions for the FCNC single top-quark production cross-section (cf. Equation 3.10 in Section 3.3) the more stringent upper limit on the production cross-section derived in the 1-jet bin is converted into limits on the coupling constants κ_{ugt}/Λ and κ_{cgt}/Λ. Assuming a purely SM-like top-quark decay with $\mathcal{B}(t \to Wb) = 1$

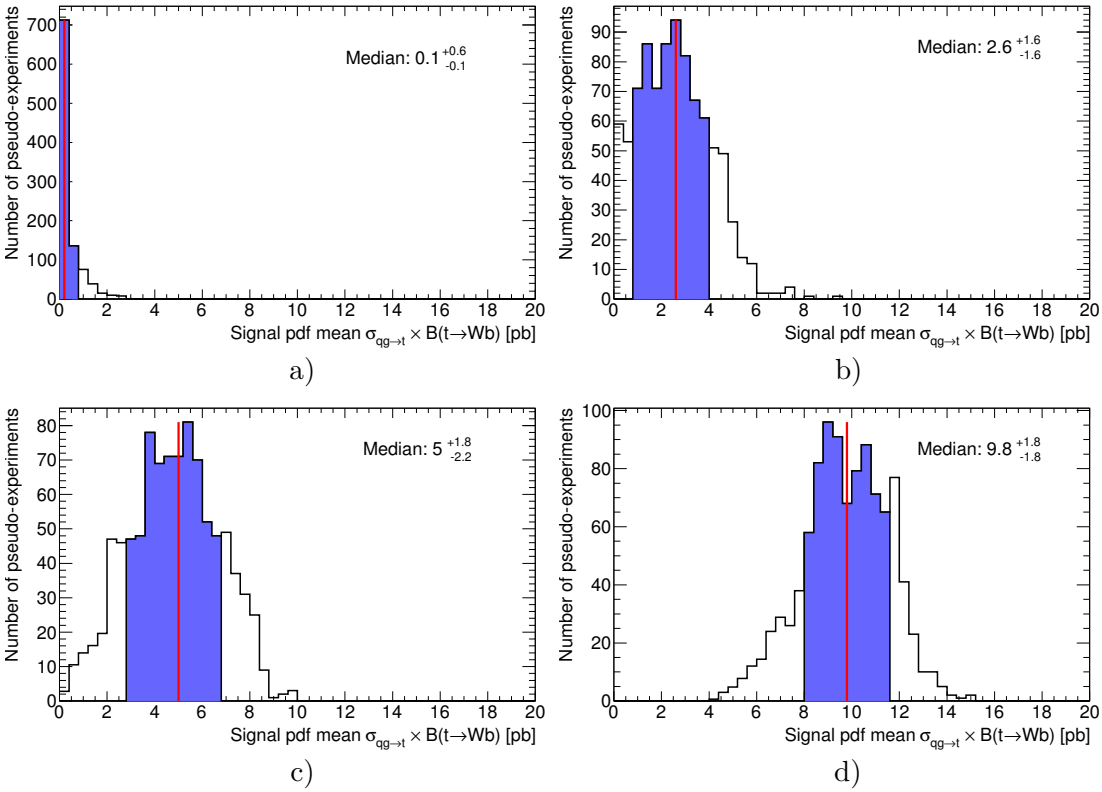

Figure 10.6.: Distribution of the maxima of the signal posterior pdfs obtained in 1000 pseudo-experiment in the 1-jet bin using pseudo-datasets derived from SM background processes only (a), and including different signal contributions corresponding to 2.5 pb (b), 5 pb (c) and 10 pb (d). The red lines denote the median of each distribution and the blue areas represent the $\pm 1\sigma$ band.

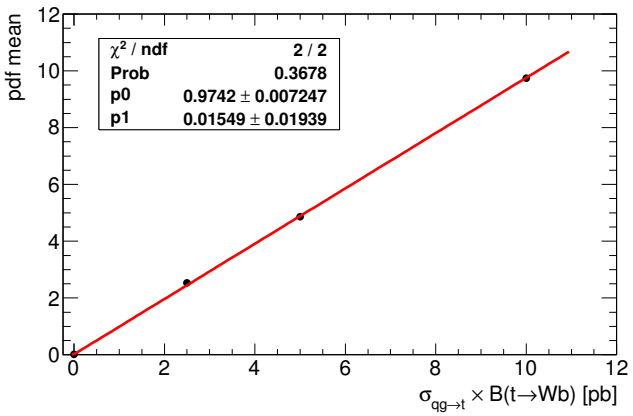

Figure 10.7.: Mean values of the most probable values in the signal pdfs vs. cross-section of the included signal contribution from both FCNC processes.

one obtains

$\kappa_{ugt}/\Lambda < (5.0 \pm 0.2) \cdot 10^{-3}$ TeV $^{-1}$, assuming $\kappa_{cgt}/\Lambda = 0$, and

$\kappa_{cgt}/\Lambda < (1.1 \pm 0.1) \cdot 10^{-2}$ TeV $^{-1}$, assuming $\kappa_{ugt}/\Lambda = 0$.

The errors reflect the uncertainties of the relation between cross-section and coupling constants as given in Equation 3.10, arising from the uncertainties on the theory cross-section derived from variations in the renormalisation and factorisation scales within $\frac{1}{2}\, m_t \leq \mu \leq 2\, m_t$. Figure 10.8 (a) shows the distribution of the upper limit for combinations of κ_{ugt}/Λ and κ_{cgt}/Λ as considered in [16]. Shown are the observed limits and their uncertainty from the theory cross-section prediction as described above, as well as the expected limits and their uncertainty derived using ensemble tests as described in the previous section. The limits on the coupling constants allow to derive limits on the branching fractions, converted using Equation 3.7 as detailed in Section 3.3. The upper limits on the branching fractions thereby obtained are

$\mathcal{B}(t \to ug) < (3.1 \pm 0.2) \cdot 10^{-5}$, assuming $\mathcal{B}(t \to cg) = 0$, and

$\mathcal{B}(t \to cg) < (1.6 \pm 0.1) \cdot 10^{-4}$, assuming $\mathcal{B}(t \to ug) = 0$.

Again, the errors reflect the (propagated) scale uncertainties on the relation between cross-section and coupling constants in Equation 3.10. Possible combinations of the branching fraction for both FCNC sub-processes are shown in Figure 10.8 (b).

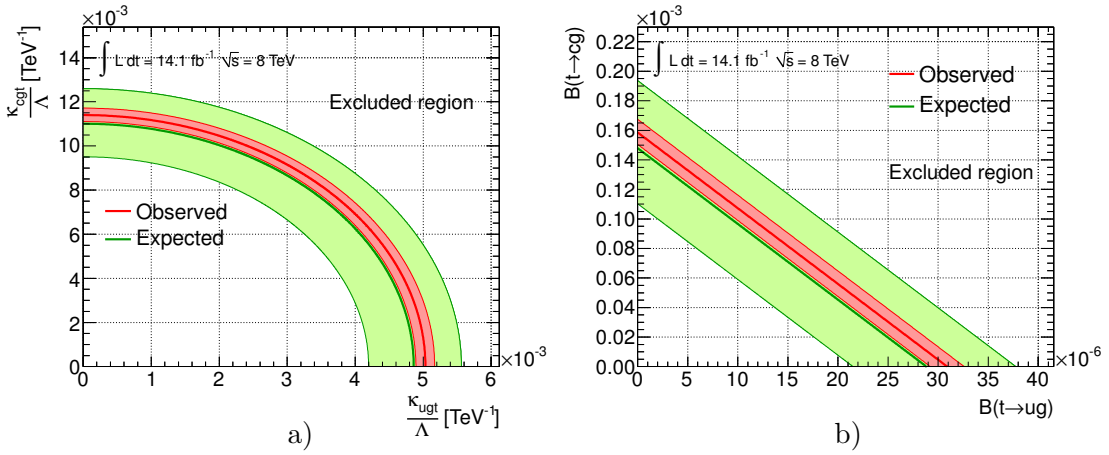

Figure 10.8.: Upper limit on the coupling constants κ_{ugt} (a) and κ_{cgt} and on the branching fractions $\mathcal{B}(t \to ug)$ and $\mathcal{B}(t \to cg)$ (b). The green bands represent the uncertainties on the expected upper limit on the FCNC single top-quark production cross-section derived using ensemble tests as described in Section 10.4. The shaded red areas represent the uncertainties arising from the scale uncertainties on the theory cross-section/coupling relation as given in Equation 3.10.

11. Discussion of the Results

In the previous chapter new upper limits on the $\sigma_{qg\to t} \times \mathcal{B}(t \to bW)$ FCNC single-top production cross-section and the respective coupling constants and branching fractions for the $ug \to t$ and $cg \to t$ FCNC processes have been derived. In order to evaluate the improvement with respect to previous results and their impact on the BSM theories discussed in Chapter 3, the findings are compared to different theory predictions and to the results of a previous 7 TeV ATLAS analysis [126] that up to now has set the world's most stringent limits on FCNC single top-quark production processes in strong interactions. Apart from the increased data statistics at a higher centre-of-mass energy, the main differences with respect to the former ATLAS analysis lie in the use of a new NLO signal generator (formerly LO generators were used) and the extension to the 2-jet bin to account for the additional contributions from $2 \to 2$ signal processes. Further, several changes in the object definition and their reconstruction, in the event selection and QCD multijet estimates, and in the choice of input variables to the neural network are made, in order to optimise the analysis for the different conditions in 8 TeV data (e.g. pile-up, trigger setup) and changes in the prerequisites and measurement setup (e.g. detector/reconstruction performance, available MC statistics). As a result the new observed upper limits on the FCNC single top-quark production cross-section were improved by nearly a factor of two with respect to the 7 TeV analysis. The following section will provide a detailed comparison with the previous results, discuss the main differences and improvements and their impact on the overall analysis sensitivity. In Section 11.2 possible aspects for improvements in future searches for strong FCNC single top-quark production using the ATLAS detector are discussed, and estimates of the impact of larger data statistics at higher centre-of-mass energies are presented in Section 11.3. Lastly, in Section 11.4 the results are evaluated in the context of the theory predictions by the different BSM models discussed in Chapter 3.

11.1. Comparison with ATLAS 7 TeV Results

In order to compare the performance of the analysis with the results from the former 7 TeV ATLAS analysis [126] in which a LO FCNC signal sample was used, three additional networks are trained for the 1-jet bin using the default NLO and a LO signal sample for comparison. The LO sample is produced with the MEtop ME generator using the CTEQ6L1 (LO) PDF sets and only includes the direct single top-quark production via strong FCNCs in order to reflect the Protos sample formerly used in [126]. Very good agreement is found in the kinematic modelling between the LO samples generated with the Protos, MadGraph and MEtop ME generators, see Appendix E.3. For training and running both networks on observed data the same input variables are

employed as were used in [126]. In a third training, the nominal input variables of this analysis are used, but the network is trained and run using the LO FCNC samples. As a further comparison, the nominal 8 TeV results of this analysis are shown, hence using an ANN trained with and run on the NLO sample.

The influence of each single systematic uncertainty on the expected upper limits in addition to the MC normalisation and statistical uncertainty are summarised in Table 11.1 for the three different cases described above, and in comparison with the former 7 TeV results. The number of expected background and observed events for the 1-jet bin signal region in the electron and muon channel of the present analysis in comparison with the event yields of the former 7 TeV ATLAS analysis are shown in Table 11.2. Here also the number of selected signal events for an assumed signal cross-section of 5 pb for the combined $ug \to t$ and $cg \to t$ processes are shown. The (rounded) event yields reflect the acceptance from MC samples normalised to their respective theory cross-section and multijet rate estimates. The uncertainties reflect the statistical uncertainties arising from the limited sizes of the MC samples, combined with the respective cross-section or the multijet rate uncertainty.

While the overall signal-to-background ratio of the event selection stays almost identical with respect to the 7 TeV analysis, the expected limits get improved by approximately 45% when using a neural network trained and run with the LO signal samples and using the input variables used in the former analysis. This improvement is mainly caused by the larger dataset available in the 8 TeV analysis, but is reduced to approximately 35% when switching to a similar network trained and run with the NLO FCNC signal samples. This is an expected consequence of the slight deterioration in the separation power of the network in the NLO case due to the fact that the kinematic shape of the signal processes is much closer to that of the SM background processes. The pure LO case hence leads to better separation from the SM top-quark production processes in particular, see Figure 11.1.

The same effect is observed between the results from the networks trained using the present set of input variables. The expected limits obtained are less stringent with these inputs in both cases, i.e. using simulations of the signal processes simulated at LO and NLO, since the networks provide overall better separation between signal and background events when trained and run with the former set of input variables. Nonetheless more stringent observed limits are obtained with the present inputs to the neural network, see Table 11.1. This is a result of omitting input variables used in the former analysis which were found to be subject to mismodelling in the present (8 TeV) control sample. In particular the distributions of the reconstructed b-jet and top-quark mass were excluded from the initial list of input variables to the network of the 1-jet bin since they are known to be subject to imperfections in the modelling due to their high dependence on the precise kinematic modelling of multiple inputs, i.e. of the final state lepton, $E_{\mathrm{T}}^{\mathrm{miss}}$ and/or the modelling of the jet kinematics and b-tagging performance. This tendency already could be observed in the control distributions of the former 7 TeV analysis, however to a more moderate extent which did not yet justify an exclusion of the variable as input to the ANN. The larger discrepancy between expected and observed events results from the poorer modelling of the kinematics in these variables at 8 TeV, potentially overlaid

Table 11.1.: The effect of each single systematic uncertainty considered on the expected 95% C.L. upper limits on the anomalous FCNC single top-quark production $qg \to t \to b\ell\nu$ in the 1-jet bin in comparison to the former 7 TeV ATLAS analysis [126].

dataset / E_{CM}	7 TeV analysis [126]	8 TeV analysis			
input variables	old	old	old	new	new
signal sample	LO	LO	NLO	LO	NLO
Cross-section, multijets rate & MC stat.	2.26 pb	1.28 pb	1.61 pb	1.91 pb	2.21 pb
Luminosity	2.31 pb	1.29 pb	1.61 pb	1.93 pb	2.22 pb
LAr-hole	2.30 pb	na	na	na	na
$E_{\mathrm{T}}^{\mathrm{miss}}$ Cellout&SoftJet scale and resol.	—	1.27 pb	1.62 pb	1.91 pb	2.18 pb
Electron ID, reco & trigger efficiency	2.27 pb	1.30 pb	1.64 pb	1.98 pb	2.27 pb
Electron energy scale and resolution	2.28 pb	1.28 pb	1.60 pb	1.92 pb	2.26 pb
Muon ID, reco & trigger efficiency	2.28 pb	1.29 pb	1.63 pb	1.95 pb	2.22 pb
Muon momentum scale and resolution	2.16 pb	1.28 pb	1.57 pb	1.89 pb	2.16 pb
b-tagging efficiency, c-tag & mistag rate	2.93 pb	1.31 pb	1.63 pb	1.93 pb	2.21 pb
Jet energy scale	1.69 pb	1.27 pb	1.57 pb	1.90 pb	2.17 pb
Jet reco efficiency	2.29 pb	na	na	na	na
Jet energy resolution	2.28 pb	1.26 pb	1.57 pb	1.85 pb	2.14 pb
Jet vertex fraction scale	—	1.27 pb	1.59 pb	1.89 pb	2.20 pb
ISR/FSR	2.44 pb	1.27 pb	1.59 pb	1.89 pb	2.17 pb
PDF	2.29 pb	1.30 pb	1.63 pb	1.94 pb	2.23 pb
W+jets shape	2.31 pb	1.29 pb	1.61 pb	1.91 pb	2.21 pb
Multijet shape	—	1.30 pb	1.66 pb	1.90 pb	2.13 pb
MC generator	2.28 pb	1.29 pb	1.61 pb	1.94 pb	2.22 pb
PS generator	2.28 pb	1.27 pb	1.61 pb	1.95 pb	2.21 pb
All systematics - expected limit	2.36 pb	1.31 pb	1.57 pb	1.86 pb	2.37 pb
All systematics - observed limit	3.91 pb	2.67 pb	2.61 pb	2.33 pb	2.53 pb

Table 11.2.: Comparison of the number of observed and expected events in the 1-jet bin signal region in the present and former 7 TeV ATLAS analysis [126]. The number of selected signal events is shown for an assumed signal cross-section of 5 pb for the combined $ug \to t$ and $cg \to t$ processes. The (rounded) event yields reflect the acceptance from MC samples normalised to their respective theory cross-section and the data-driven multijet estimates. The uncertainties denote the statistical uncertainties arising from the limited sizes of the simulation samples, combined with the cross-section or the multijet rate uncertainty.

	7 TeV		8 TeV	
	electron ch.	muon chan.	electron ch.	muon chan.
FCNC 5 pb	265 ± 5	300 ± 5	973 ± 135	1296 ± 155
SM Single-top	700 ± 70	760 ± 80	5240 ± 260	6810 ± 340
$t\bar{t}$	310 ± 30	340 ± 40	4140 ± 250	5220 ± 320
W+jets	2100 ± 500	2500 ± 600	3500 ± 1000	5000 ± 1300
W+HF+jets	7000 ± 4000	8000 ± 5000	23000 ± 12000	31000 ± 17000
Z+jets	190 ± 50	510 ± 120	990 ± 240	2000 ± 500
Multijets	800 ± 400	800 ± 400	5400 ± 2700	13000 ± 6000
Sum MC (SM only)	10900 ± 3200	13000 ± 3800	42000 ± 13000	63000 ± 18000
data	11704	14519	43951	68574

with effects from the low MC sample statistics available for the dominant W(+HF)+jets background, which also reflects in their respective kinematic distributions in the signal sample. As a consequence, the most probable values of the signal pdf for observed events gets shifted towards larger values when applying the same statistical analysis to the output distributions of the ANNs that were trained with the former set of input variables. These output distributions hence yield less stringent observed limits with larger differences to the respective expected upper limits. In order to improve the credibility of the results in the present analysis, it was chosen to omit these variables in the training. Variables highly correlated to the former then get a higher rank in their significance which results in only marginal loss in the total separation power of the network. The overall sensitivity of the analysis hence is deteriorated only slightly by the different choice of variables, for the sake of improved reliability of the results.

11.2. Prospects for Future Improvements

The results of this analysis have been made public in [278]. Updates of these results are planned for the near future, with the possibility to improve the analysis and sensitivity in several aspects which will be discussed in the following. Since the sensitivity of the analysis to a large extend is dominated by the limited MC sample and data statistics, the straightforward measure for increasing the analysis performance will be the inclusion

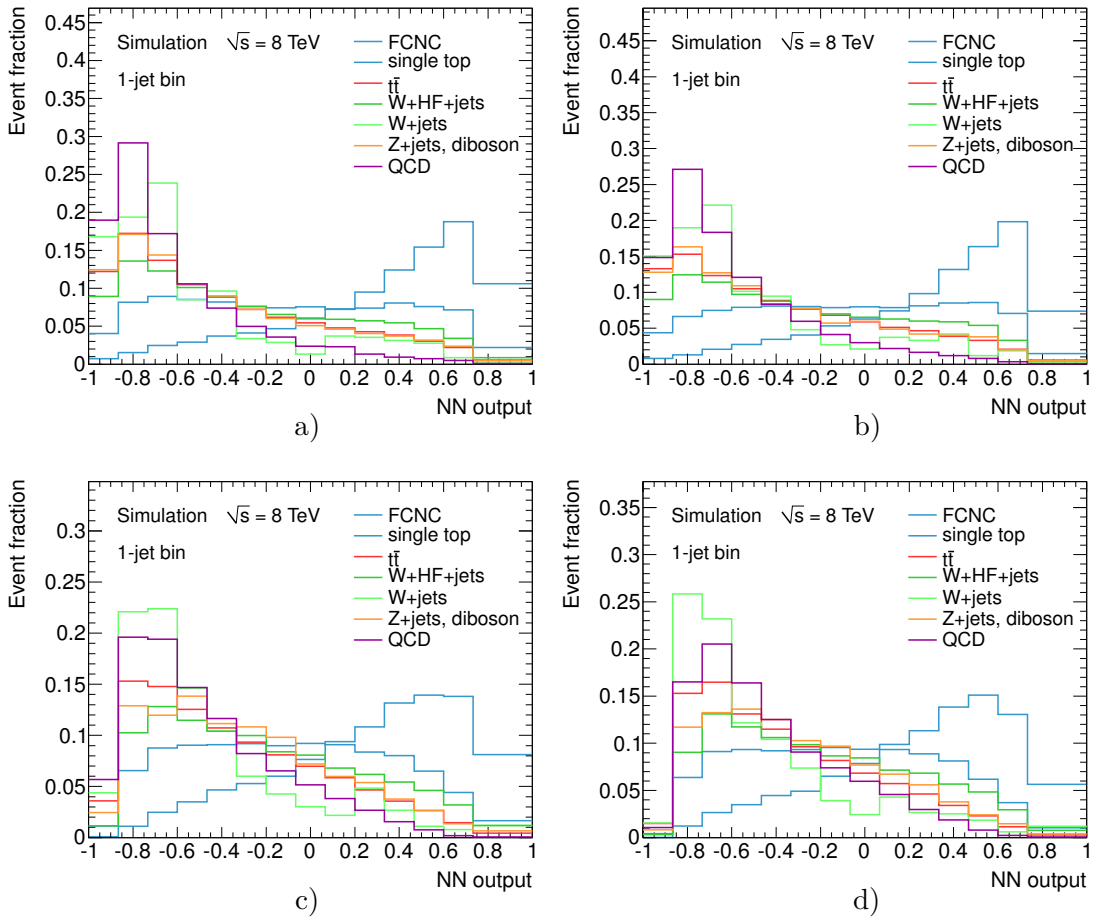

Figure 11.1.: Neural network output distributions normalised to unit area for the different background and the signal processes, for networks trained with the variables which were used in the former ATLAS analysis (top row) or using the nominal set of input variables used within this analysis (bottom row). Shown are the results from networks trained using the LO FCNC signal samples (a,c) and the NLO signal samples (b,d) for training and running the network on.

of the full 8 TeV dataset recorded with the ATLAS detector in 2012, amounting to an integrated luminosity of 21.7 fb^{-1}. However, the key point will be the availability of larger MC samples with significantly improved statistics, in particular of the W+jets samples (by at least a factor of ten). The large statistical fluctuations of the W+jets production background lead to MC/data disagreements in the distributions of several kinematic variables which are indistinguishable from mismodellings originating from the MC event generation itself. Those variables consequently were chosen to be excluded from the initial list of inputs to the neural networks. Additional samples for the W+jets

and W+HF+jets processes are in official production, the generation of which however has not been completed and validated at the time of writing. With these samples becoming available, new neural networks of potentially higher separation power could be trained, including those variables which might have been subject to mismodelling as a result of purely statistical effects. In addition, large shape and rate uncertainties are associated to the W(+HF)+jets samples due to the fact that these are limited to simulations at leading-order accuracy. Although alternative generators like Sherpa [181] already exist which circumvent this drawback by using NLO ME calculations in combination with sophisticated matching schemes (variants of the MC@NLO algorithm [279]), most analyses currently use the recommended default generators since their limitations are thought to be better understood, they are long-tested, and continuously validated, and provide good comparability to former results. However, these arguments will become more and more questionable in sight of the clear benefits of alternatives for the production of inclusive W+jets samples becoming more mature.

Possible improvements with respect to the simulation of the signal processes lie in the production of additional systematics samples for parton shower variations. Such variations have not yet been included in this analysis due to the limited computing resources available in early 2013. However, the production of new samples with MEtop using the more recent Perugia2011C tune and of corresponding systematics samples for parton shower variations is already in process. Also the production of additional MC samples that reflect potential shape uncertainties arising from the choice of the factorisation and renormalisation scales, and for the particular choice for the $p_{\mathrm{T}}^{\mathrm{match}}$ variable within MEtop, is presently under discussion.

The computational performance of the statistical analysis could be improved by changing to a different analysis tool-kit and/or strategy used to extract the signal cross-section or their upper limit. The direct sampling approach becomes increasingly computational expensive with more sources of systematics being included. The "brute-force" sampling from the prior-distributions leads to a large number of samples being discarded or contributing only with very low likelihoods to the final posterior probability. The performance could be improved drastically by implementing Markov chain Monte Carlo (MCMC) or other importance sampling techniques that allow to approximate the signal pdf more efficiently.

Concerning the analysis strategy itself, an individual treatment of the two signal processes ($ug \to t/cg \to t$) in the neural network training, in principle, could improve the separation power and hence sensitivity of the analysis, given that sufficiently large signal samples are available to prevent the training performance from being deteriorated by the reduced statistics. This may be achieved by making use of different, optimized sets of inputs to the ANNs which reflect particular properties in the distributions of kinematic and topological variables that are characteristic to an individual signal subprocess. However, this requires a more complex and computationally more expensive statistical analysis in which the cross-section of the two individual signal processes is measured, or set a limit upon, by constructing a posterior probability density in a two-dimensional plane, each axis reflecting the production cross-sections of one of the two independent signal processes. Despite the doubled effort from training and optimizing individual

ANNs and potentially increased computational expenses in the signal sample generation and statistical analysis, the reliability of the analysis results in general could be improved further by intrinsically ensuring its immunity to any unperceived dependence on the ratio of events from $ug \to t$ and $ug \to t$ processes in the combined FCNC signal sample that is used in the training of the ANNs in the present analysis.

Another measure to improve the sensitivity of the analysis is the combined statistical analysis of events from both (or more) jet bins. However, this requires detailed studies of possible correlations between the systematic uncertainties in both jet categories, accounting for differences in the effects on the individual sets of input variables to both neural networks. Assuming total correlation between identical sources of systematic uncertainties across both jet bins, in the present analysis the expected limit obtained from running the statistical analysis on the combination of both jet categories improves slightly from 2.4 pb to 2.3 pb. The observed limit however is deteriorated by almost 30%. Also when assuming the rate (and shape) uncertainties of the multijet background in both jet bins to be totally uncorrelated, since their rates are derived separately using data-driven techniques, no improvement for the combined result is found. Consequently, a more promising approach in future analyses would be to avoid the commonly used distinction between different jet-bins from the beginning and to include the jet-multiplicity as another (integer) variable as an input to a common neural network, with the side-effect of even increased overall statistics from including events of jet-multiplicities > 2. In addition, the classifier output of the b-tagging algorithm used to identify jets to be originating from a b-quark of the top decay could directly be used as an input to the ANN. This however would require a (quasi-)continuous calibration of the respective efficiencies and mistag rates which have only very recently become available.

11.3. Extrapolation Towards Future LHC Runs

After the two-years shutdown of the LHC accelerator in 2013/14 (Long Shutdown 1 or LS1) for consolidation works on the LHC magnet system and repairs and first upgrades of the detectors (cf. Appendix F.1), the LHC is projected to be restarted in early 2015. The accelerator is foreseen to be run at increased beam energy of at first 6.5 TeV per beam, which is later to be raised to achieve the full design energy, enabling the LHC to provide p-p collisions at a centre-of-mass energy of 14 TeV. The LHC is projected to deliver a total of approximately $300\,\mathrm{fb}^{-1}$ of data from p-p collision in several run-periods within the following eight years of operation. A major upgrade towards the so-called high-luminosity LHC (HL-LHC) has been proposed [280] for the years around 2024. Its aim is to extend the discovery potential by means of major upgrades of the accelerator complex and of the experiments by means of which an increase in the deliverable instantaneous luminosity by a factor of ten beyond its current design value is to be achieved. A total of $3000\,\mathrm{fb}^{-1}$ of additional collision data are expected to be delivered within another operation period of approximately ten years in total.

To gain a coarse estimate on the impact on future searches for FCNC single top-quark production in strong interactions using the ATLAS detector, studies are conducted that

extrapolate the results presented in this work towards future 14 TeV runs in a simplistic approach, for assumed integrated luminosities of $300\,\text{fb}^{-1}$ and $3000\,\text{fb}^{-1}$, respectively. Scale factors for all MC simulated samples are derived from the ratio between their 8 TeV and 14 TeV theory cross-section predictions. The number of expected events in the 1-jet bin is recalculated for each (sub-)process by applying the scale factors and by rescaling to an integrated recorded luminosities of $300\,\text{fb}^{-1}$ and $3000\,\text{fb}^{-1}$, respectively. Hence, for simplicity the same kinematic shapes as for 8 TeV centre-of-mass energy are assumed for all SM background and the signal processes. The full statistical analysis is then performed in the same way as in the presented 8 TeV analysis, and assuming the same systematic, but different statistical uncertainties of the MC simulated samples. In contrast to the present analysis it was presumed that samples with a size corresponding at least to the statistics in collision data are available for all (sub-)processes.

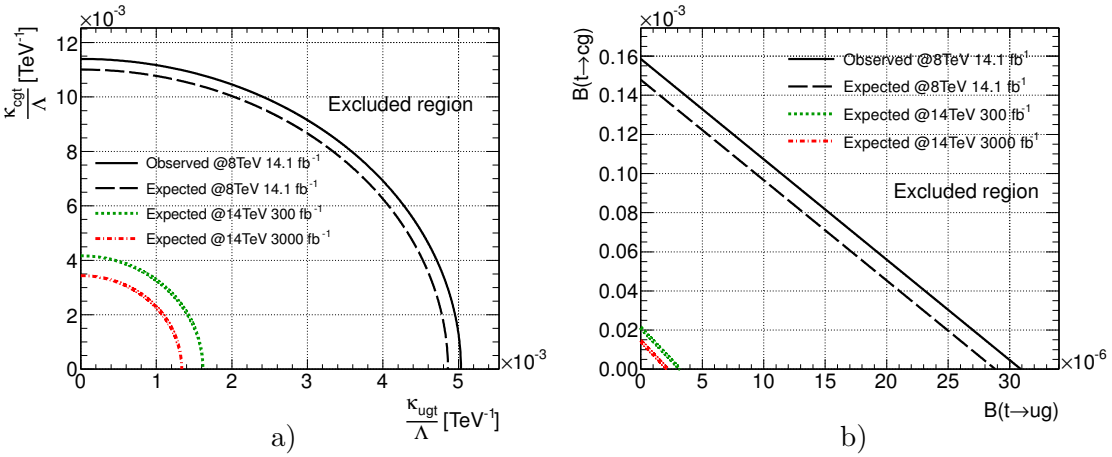

Figure 11.2.: Estimates of the expected upper limits on the coupling constants κ_{ugt} and κ_{cgt} (a) and on the branching fractions $\mathcal{B}(t \to ug)$ and $\mathcal{B}(t \to cg)$ (b) for different projections of future 14 TeV runs with assumed integrated luminosities of $300\,\text{fb}^{-1}$ and $3000\,\text{fb}^{-1}$. The estimates are based on the 8 TeV event selection in the 1-jet bin in which all background and signal samples are rescaled to their respective 14 TeV theory cross-section prediction and to the assumed integrated luminosities.

First coarse estimates on the reachable sensitivity are derived in terms of projected expected limits on the coupling constants and branching fractions for integrated luminosities of $300\,\text{fb}^{-1}$ and $3000\,\text{fb}^{-1}$ of 14 TeV data. The projections are shown in Figure 11.2 in comparison to the present results. It can be clearly seen that with larger datasets becoming available the expected performance of the analysis is likely to be improved significantly and tends to be increasingly limited by systematic uncertainties. However, the quantitative results have to be interpreted with caution. In particular the projection towards an integrated luminosity of $3000\,\text{fb}^{-1}$ is subject to large uncertainties. It has to be emphasised that this rather simplistic projection is based on several tentative assumptions, the most important of which are summarised as follows:

1. The expected event yields for all SM background and the FCNC signal processes are based on a simple rescaling of the 8 TeV samples. However the kinematic shapes of most background and the signal processes are subject to changes with increased collision energies.

2. The study is based on the current ATLAS detector layout and performance in both projections, which represents a large simplification since the detector is foreseen to undergo several upgrades in the current (LS1) and future large shutdowns. Major changes in the detector layout are planned, in particular for an upgrade towards operation at the HL-LHC (Phase II), aiming for improved granularity, radiation hardness and trigger capabilities, see Appendix F.1 for a detailed summary.

3. The same trigger and reconstruction efficiencies as those present in the 8 TeV run are assumed. This represents an optimistic assumption since they are likely to decrease with higher energies, instantaneous luminosities and more challenging pile-up conditions becoming present.

4. The sources and sizes of systematic uncertainties are kept unchanged although, on the one hand, their magnitude is likely to decrease with better knowledge of the detector performance and more precise theory calculations becoming available. On the other hand, several systematic uncertainties likely have to be increased in size, or new sources of systematic uncertainties will have to be included in order to account for the more challenging future LHC beam conditions, changes in the reconstruction procedures, etc.

A detailed study hence would require a more sophisticated approach which includes e.g. the generation of new MC samples for increased beam energies and of much larger statistics, the detector simulation based on a prospected future ATLAS detector layout, an adapted trigger and pile-up simulation, and new selection cuts and revised descriptions of all systematic uncertainties included. A more precise and reliable estimation of the future sensitivity therefore represents a very time and resource consuming task but nonetheless is planned to be conducted in the future. In spite of its limitations this extrapolation nevertheless provides a first qualitative impression of the improvements feasible with larger datasets and higher centre-of-mass energies becoming available in the future.

11.4. Comparison with Theory Predictions

The presented analysis improves the previous most stringent experimental limits on the branching fractions of the FCNC top quark decay via the tqg vertex by almost a factor of two. Thereby the new limits on $\mathcal{B}(t \to ug)$ enter further into regions of values predicted by BSM theories – for the first time this is also true for the $t \to cg$ process. Figure 11.3 (a) shows a summary of the most recent observed upper limits set on the respective FCNC branching fractions by experiments at the Tevatron and LHC accelerators (cf. Section 3.2). Also shown are the values for $\mathcal{B}(t \to ug)$ and

$\mathcal{B}(t \to cg)$ as predicted by the SM and the group of new physics models discussed in Section 3.1, i.e. the quark-singlet model (QS), the two-Higgs doublet model with (2HDMII) or without flavour-conservation (2HDMIII), the minimal supersymmetric model (MSSM), SUSY models with R-parity violation ($\not{R}$ SUSY) and the Topcolour-assisted Technicolour model (TC2).

In particular the regime of supersymmetric models is probed further since these allow for the highest FCNC branching fractions among the discussed models. Since top-quark production mediated via gluonic FCNC interactions has not been observed at the maximum rates predicted by i.e. the MSSM and $\not{R}$ SUSY models, continuously more stringent upper bounds may need to be set on the parameters of R-parity, and potentially specific soft breaking terms in the superpotential of the respective SUSY Lagrangians (cf. Section 3.1.3) in the future, or their exclusion can be confirmed independently if already constrained otherwise more recently. With the larger datasets and higher centre-of-mass energies becoming available with the future 14 TeV runs, the sensitivity may be driven even an order of magnitude higher with respect to that of the present analysis. This may also allow to probe the regime of rates predicted by certain two-Higgs doublet models in the future, see Figure 11.3 (b).

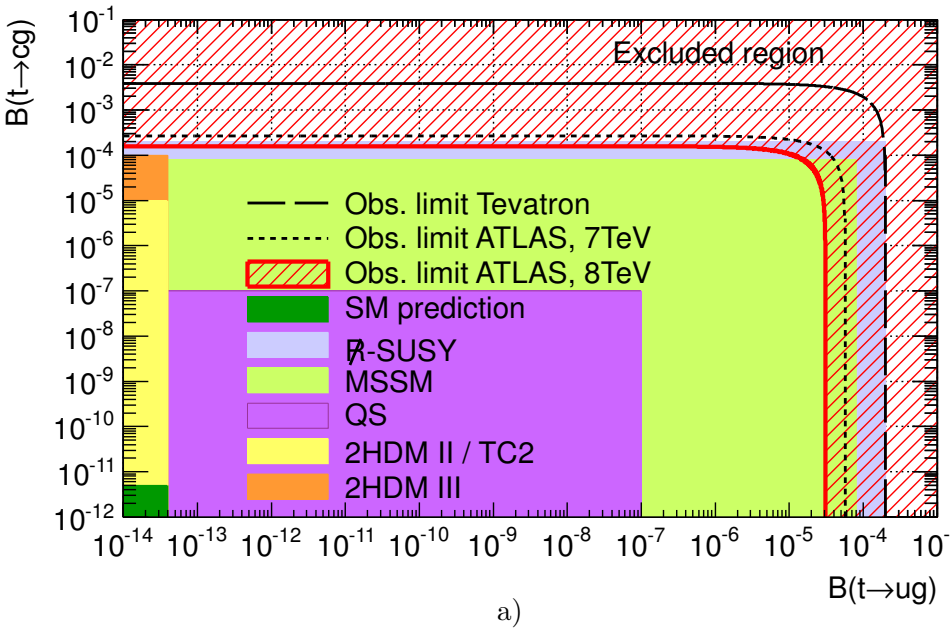

a)

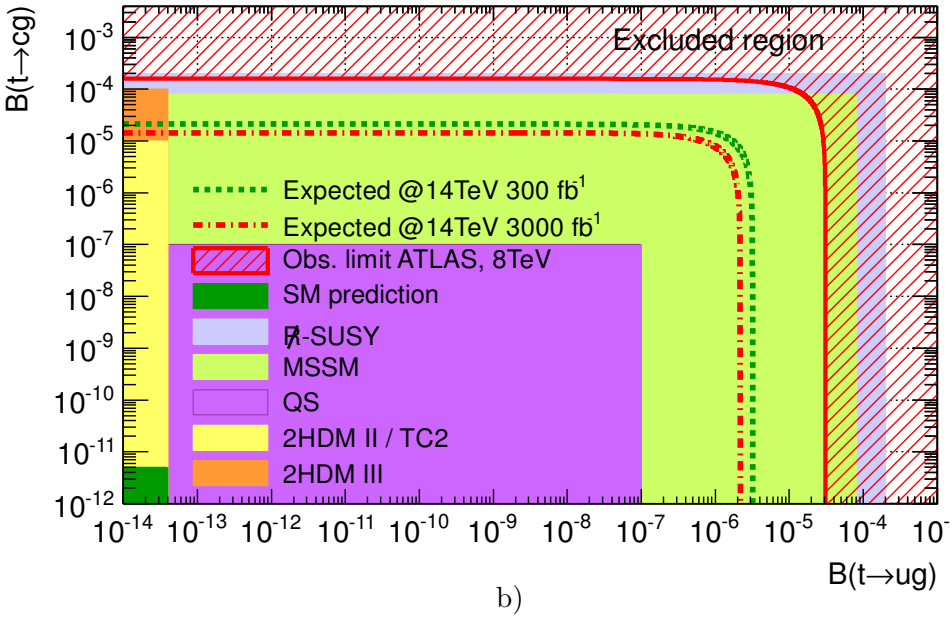

b)

Figure 11.3.: Observed upper limits from different experiments and predictions of the SM and different BSM theories on the FCNC branching fractions $\mathcal{B}(t \to ug)$ and $\mathcal{B}(t \to cg)$ (a), as well as estimates of the expected upper limits on the FCNC branching fractions for different projections of future 14 TeV runs, with assumed integrated luminosities of $300\,\mathrm{fb}^{-1}$ and $3000\,\mathrm{fb}^{-1}$ and in comparison with the predictions of the SM and different BSM theories (b). The new exclusion region derived in this analysis is marked as the (red) hashed area.

11.5. Conclusions

A search for anomalous single top-quark production via flavour-changing neutral currents (FCNCs) in strong interactions was performed. A data sample collected with the ATLAS detector in 2012 at a centre-of-mass energy of $\sqrt{s} = 8$ TeV, and corresponding to an integrated luminosity of $\mathcal{L}_{\text{int}} = 14.1\,\text{fb}^{-1}$ was used. It was searched for events in which a light quark (u or c) interacts with a gluon to produce a single top quark, including potential production modes with additional light-flavour jets in the final state. Therefore events with an isolated electron or muon, missing transverse momentum, a single b-quark, and either none or exactly one additional light-flavour jet were selected and searched for FCNC production of left-handed single top quarks. To discriminate between signal and background processes, multivariate techniques employing three-layer feed-forward neural networks were applied to the two disjoint selection samples of different jet multiplicity. The final statistical analysis was performed using Bayesian techniques, applying a binned maximum likelihood method to the full neural network output distributions. Systematic uncertainties were included via a direct sampling approach.

The obtained signal posterior probability density function was not found to support any significant signal contribution. Consequently, Bayesian upper limits on the FCNC production cross-section were derived by integrating the posterior probability density for events with exactly one or exactly two jets in the final state. The observed 95% C.L. limit on the cross-section times branching fraction was derived as $\sigma_{qg\to t} \times \mathcal{B}(t \to bW) < 2.5$ pb in the 1-jet bin and < 6.8 pb in the 2-jet bin. The expected sensitivity was estimated by applying an identical statistical analysis to a pseudo-dataset corresponding to the distribution of the expected events. The resulting expected upper limit at 95% C.L. was found to be $\sigma_{qg\to t} \times \mathcal{B}(t \to bW) < 2.4$ pb in the 1-jet bin and < 5.7 pb in the 2-jet bin. From the more stringent observed limit of the 1-jet bin, new upper limit on the coupling constants and branching fractions were derived using NLO theory calculations. The obtained limits on the coupling constants are $\kappa_{ugt}/\Lambda < 5.0 \cdot 10^{-3}$ TeV^{-1} (assuming $\kappa_{cgt}/\Lambda = 0$) and $\kappa_{cgt}/\Lambda < 1.1 \cdot 10^{-2}$ TeV^{-1} (assuming $\kappa_{ugt}/\Lambda = 0$), and those on the branching fractions $\mathcal{B}(t \to ug) < 3.1 \cdot 10^{-5}$ (assuming $\mathcal{B}(t \to cg) = 0$) and $\mathcal{B}(t \to cg) < 1.6 \cdot 10^{-4}$ (assuming $\mathcal{B}(t \to ug) = 0$). These limits improve previous results [126] by nearly a factor of two and represent the world's most stringent limits on FCNC single top-quark production processes in strong interactions to date.

* * *

A. Estimation of the QCD Multijet Background in the 2-Jet Bin

This appendix presents the results of the binned maximum likelihood fits in the $E_{\mathrm{T}}^{\mathrm{miss}}$ distributions in the signal and control regions of the 2-jet bin. The fits were performed the same way as described in Section 7.3.1 with the only difference being the Gaussian constraints on the normalisation of the combined W+jets background templates which is set to 60% to reflect the larger cross-section uncertainty of this background sample at higher jet multiplicities (cf. Section 5.2.2). Figure A.1 shows the $E_{\mathrm{T}}^{\mathrm{miss}}$ distributions in the 2-jet bin signal and control region after applying the binned maximum likelihood fit in the electron channel for multijet estimates derived using the matrix method or jet-electron model. Again, the different backgrounds (and the jet-electron multijet template) are shown rescaled to their respective fit results. The results of the jet-electron model are shown for both, the forward/central regions as well as for their combination. Figure A.2 shows the corresponding fit results in the 2-jet bin muon channel, obtained using multijet estimates derived with the matrix method, antimuon model, and jet-electron model.

The estimated values of the rates and relative fractions of the multijet background in the $E_{\mathrm{T}}^{\mathrm{miss}}$ region of the final event selection ($E_{\mathrm{T}}^{\mathrm{miss}} > 30$ GeV) in the 2-jet bin are given in Table A.1, for both lepton channels and for the signal and control sample, respectively. Again, also the individual fit results for the jet-electron model in the electron central and forward region are shown. Table A.2 shows the simultaneously obtained scale factors in the 2-jet bin for the combined contributions of W+jets and W+HF+jets, and the joined $t\bar{t}$ and single top-quark production template, respectively.

Similar to the case of the 1-jet bin, in the electron channel the best fit results are obtained using the jet-electron model. Again, the matrix method tends to overestimate the multijet contribution towards lower $E_{\mathrm{T}}^{\mathrm{miss}}$ values in both, the signal and control region. In the muon channel the situation also is akin to that of the 1-jet bin. The antimuon model in general tends to overestimate the multijets rate, caused by larger fake contributions in the tail towards larger $E_{\mathrm{T}}^{\mathrm{miss}}$ values. The obtained shape is more similar to that of the combined W+jets background in particular, which consequently is scaled downwards in the fitting process. Lastly, in the muon channel the matrix method is favoured over the jet-electron model, since it provides a better shape model in the low $E_{\mathrm{T}}^{\mathrm{miss}}$ region.

Table A.1.: Estimates of the multijet background rates and fractions in the 2-jet bin signal and control region using the matrix method, jet-electron and antimuon model. The quoted numbers denote the (rounded) expected number of events in each region. The uncertainties reflect the statistical uncertainty from the limited template size, which in case of the jet-electron or antimuon model is combined with the uncertainty of the fit to the $E_{\mathrm{T}}^{\mathrm{miss}}$ distribution in data.

2-jet bin		signal region		control region	
Method	Channel	Events	Fraction	Events	Fraction
Jet-electron model	electron (cent.)	3040 ± 240	9%	9200 ± 400	13%
Jet-electron model	electron (fwd.)	1290 ± 140	12%	6100 ± 400	18%
Jet-electron model	electron (comb.)	4320 ± 280	10%	15300 ± 600	14%
Matrix method	electron	3060 ± 30	7%	6730 ± 50	6%
relative difference wrt. jet-electron model			−29%		−56%
Matrix method	muon	4420 ± 60	7%	8850 ± 150	6%
Antimuon model	muon	9900 ± 600	17%	32000 ± 1200	22%
relative difference wrt. matrix method			+125%		+260%
Jet-electron model	muon	3500 ± 250	5.8%	9000 ± 500	6%
relative difference wrt. matrix method			−21%		+2%

Table A.2.: Scale factors for the combined contributions from W+jets/W+HF+jets and from $t\bar{t}$/single top-quark production in the 2-jet bin signal and control region as obtained from the simultaneous binned maximum likelihood fit in the $E_{\mathrm{T}}^{\mathrm{miss}}$ distribution.

2-jet bin		signal region		control region	
Method	Channel	W+jets	top	W+jets	top
Jet-electron model	el. (cent.)	0.85 ± 0.06	1.09 ± 0.02	0.94 ± 0.01	1.04 ± 0.04
Jet-electron model	el. (fwd.)	1.24 ± 0.05	0.94 ± 0.04	1.08 ± 0.01	0.91 ± 0.05
Jet-electron model	el. (comb.)	0.98 ± 0.05	1.05 ± 0.02	0.99 ± 0.01	1.02 ± 0.04
Matrix method	electron	1.03 ± 0.03	1.04 ± 0.02	1.08 ± 0.01	0.78 ± 0.03
Matrix method	muon	1.12 ± 0.04	1.05 ± 0.02	1.05 ± 0.01	1.01 ± 0.04
Antimuon model	muon	1.08 ± 0.05	0.96 ± 0.02	0.87 ± 0.01	0.90 ± 0.03
Jet-electron model	muon	1.31 ± 0.04	1.03 ± 0.02	1.06 ± 0.01	0.95 ± 0.03

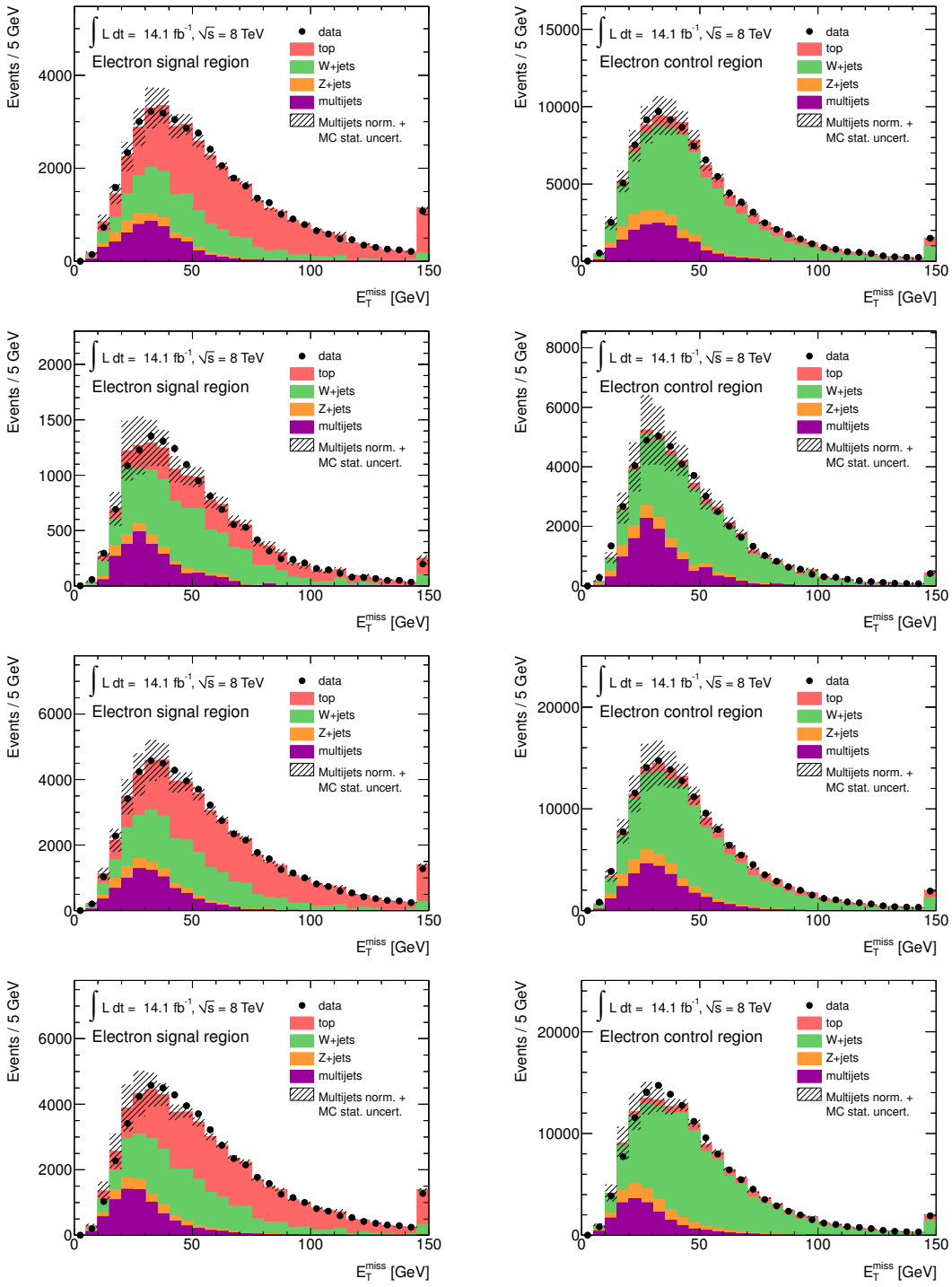

Figure A.1.: Fitted $E_{\mathrm{T}}^{\mathrm{miss}}$ distributions for the 2-jet bin electron channel in the signal (left) and control region (right), using the jet-electron model in the central/forward regions (first/second row), and their combination (third row), as well as using the matrix method (bottom row). The error bands denote the combined MC statistical and assigned multijet rate uncertainty of 50 %.

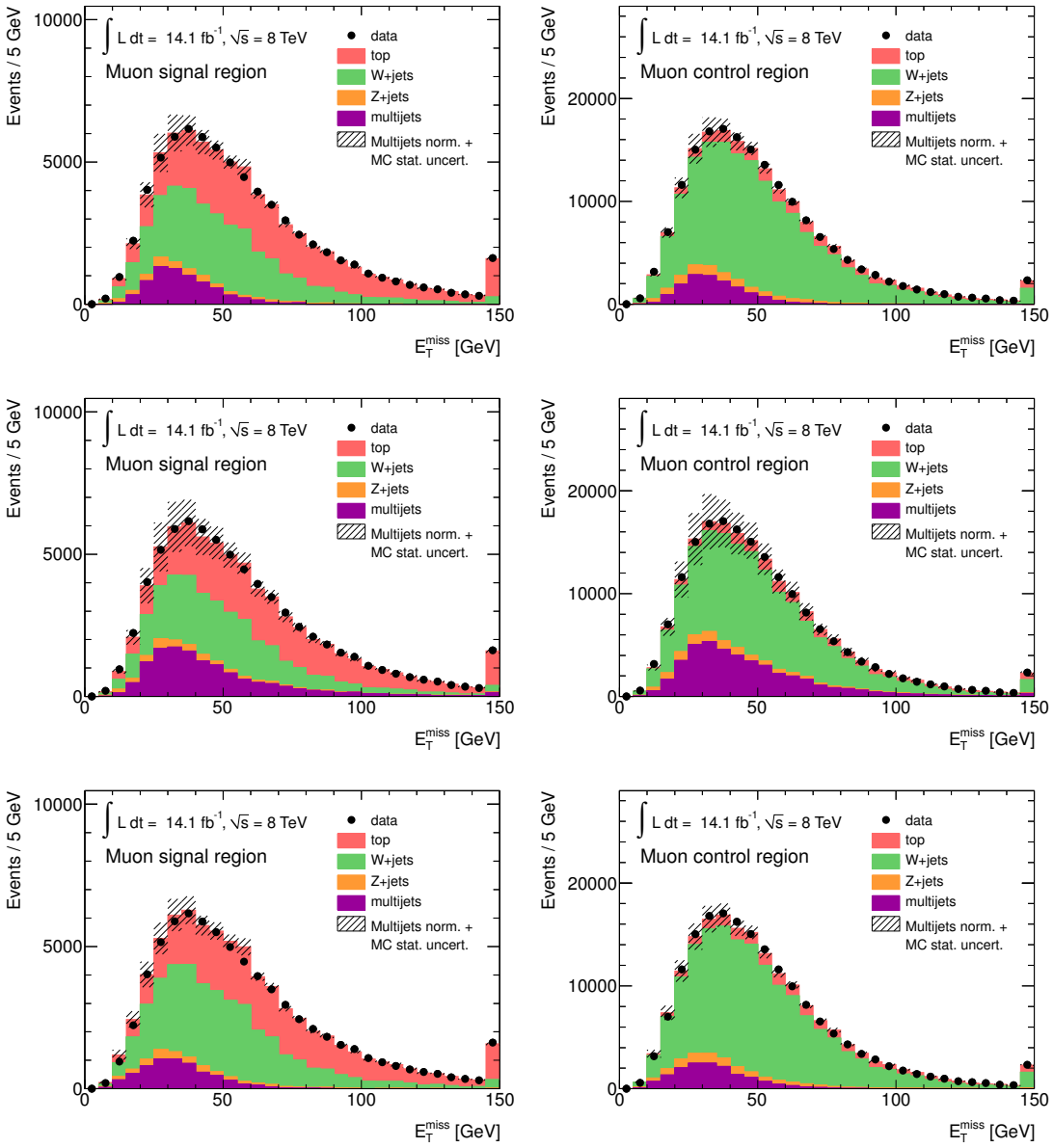

Figure A.2.: Fitted $E_{\mathrm{T}}^{\mathrm{miss}}$ distributions for the 2-jet muon channel in the signal (left) and control sample (right), using the matrix method (top row), anti-muon model (middle row), and using the jet-electron model (bottom row). The error bands denote the combined MC statistical and assigned normalisation uncertainty of the multijet template of 50 %.

B. Validation of Input Variables to the Neural Network

In this Appendix all variables are shown, which were used in the training of the neural networks of the 1-jet bin and 2-jet bin in the control and signal sample, respectively. The distributions are used to check the modelling of each single variable in a high statistics sample, as well as in that used for the final selection and statistical analysis. Therefore the expected distributions obtained from simulated events are normalised to the result of the binned maximum likelihood fit in the $E_{\mathrm{T}}^{\mathrm{miss}}$ distributions used to determine the fraction of multijet events (cf. Section 7.3.1). Figures B.1 through B.4 show the control and signal sample distributions of the variables used in the neural network for the 1-jet bin for the combination of the electron and muon channel, respectively. The corresponding distributions of the input variables to the network of the 2-jet bin are shown in Figures B.5 - B.8. Also shown are the respective shape distributions normalised to unit area from simulated evens of the FCNC signal and the three most important background processes in the signal region. Similar distributions of the input variables to both networks split in the electron and muon channel were also checked for any signs of mismodelling, but are not shown here for the sake of brevity.

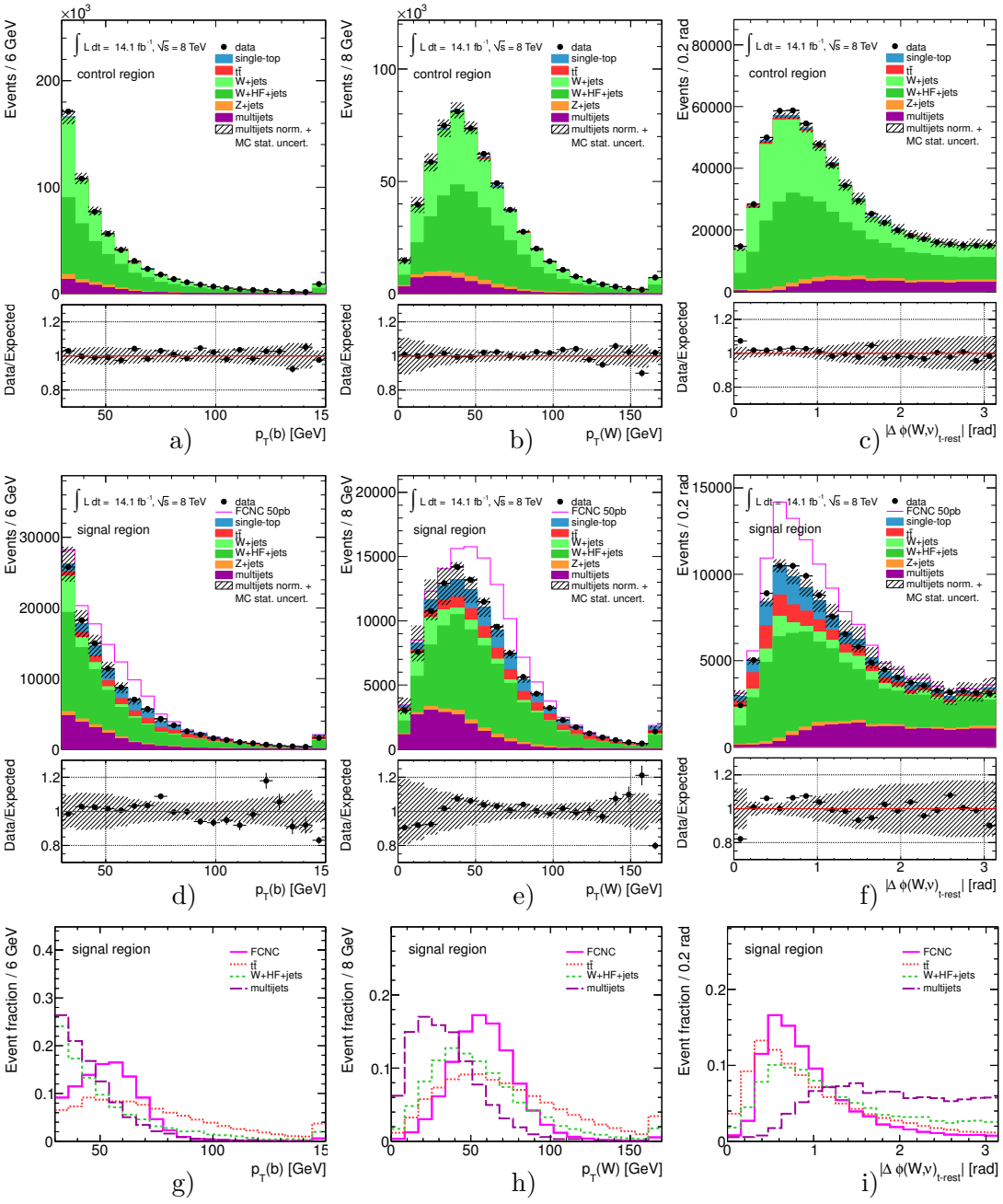

Figure B.1.: Kinematic distributions of the input variables to the neural network for the combined lepton channels in the 1-jet bin control (top row) and signal region (middle row) with all processes normalised to the result of the binned maximum likelihood fit used to determine the fraction of multijet events, or in the signal region with all processes normalised to unit area (bottom row). The hatched bands represent the combination of statistical uncertainties and the uncertainty of the multijet background normalisation. The panels shows the transverse momentum of the b-jet (a,d,g) and of the W boson (b,e,h), and the azimuthal angular distance between the W boson and the neutrino in the top-quark rest frame (c,f,i).

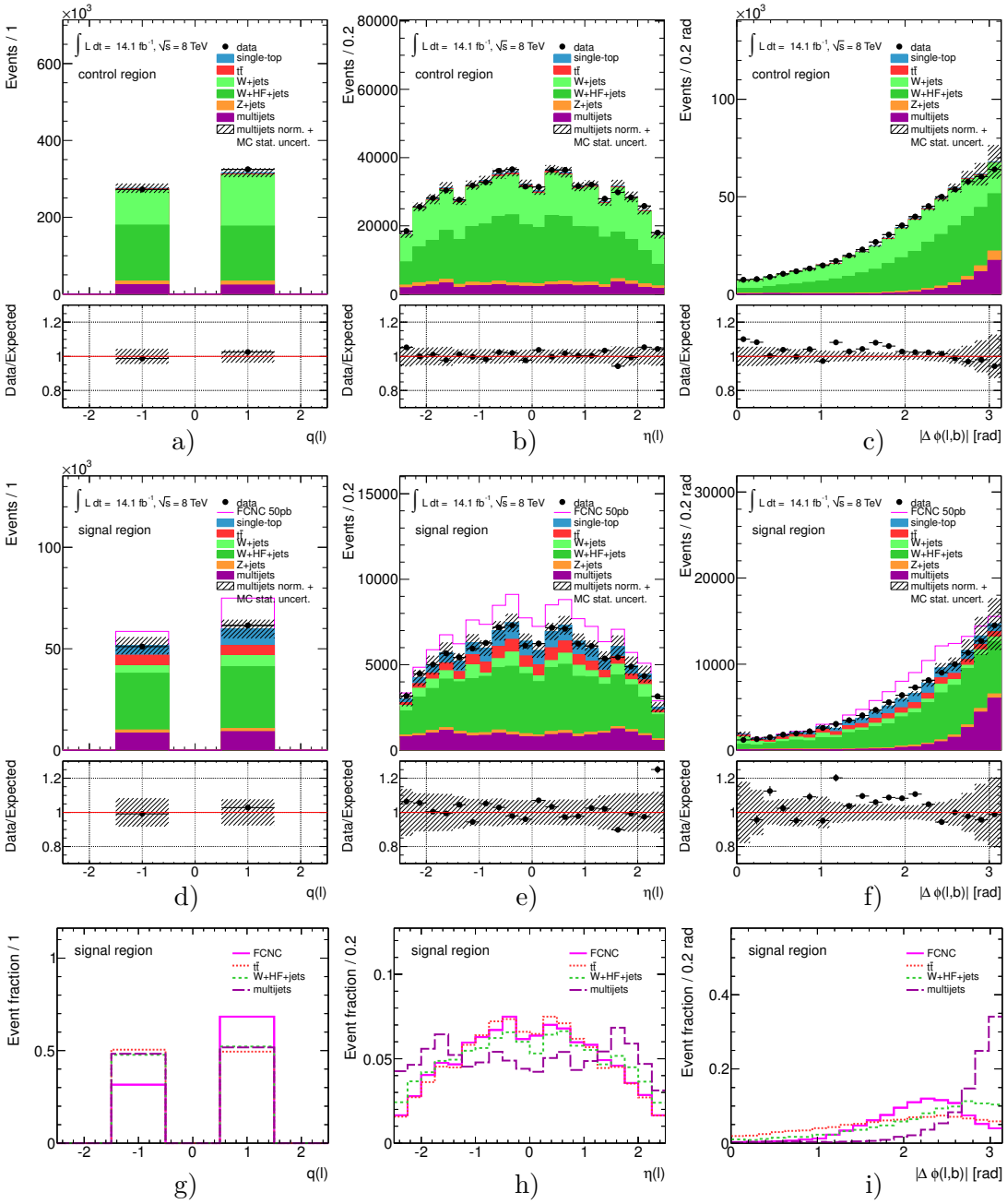

Figure B.2.: Kinematic distributions of the input variables to the neural network for the combined lepton channels in the 1-jet bin control (top row) and signal region (middle row) with all processes normalised to the result of the binned maximum likelihood fit used to determine the fraction of multijet events, or in the signal region with all processes normalised to unit area (bottom row). The hatched bands represent the combination of statistical uncertainties and the uncertainty of the multijet background normalisation. The panels show the charge (a,d,g) and the pseudorapidity of the lepton (b,e,h), and the azimuthal angular distance between the lepton and the b-jet (c,f,i).

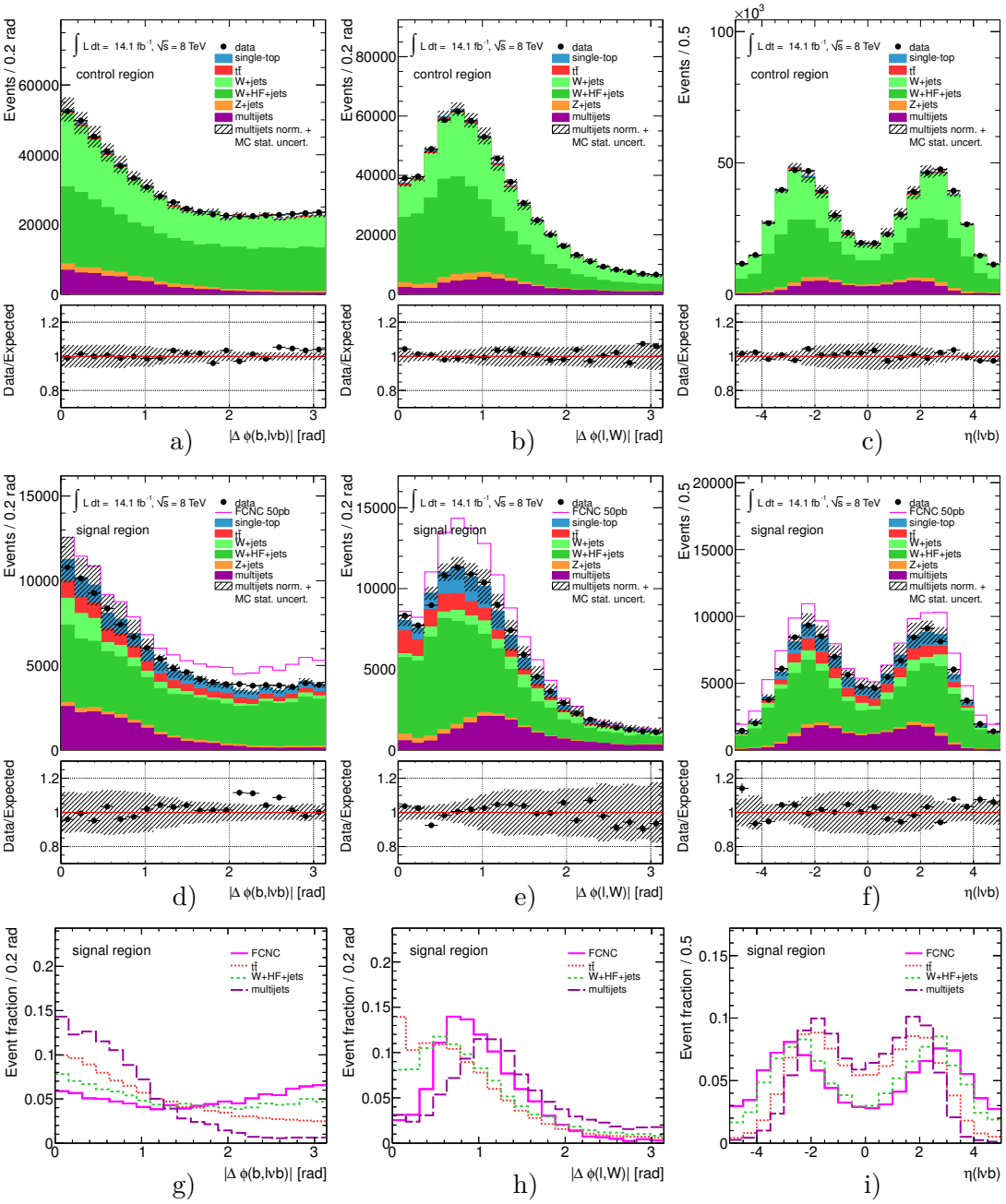

Figure B.3.: Kinematic distributions of the input variables to the neural network for the combined lepton channels in the 1-jet bin control (top row) and signal region (middle row) with all processes normalised to the result of the binned maximum likelihood fit used to determine the fraction of multijet events, or in the signal region with all processes normalised to unit area (bottom row). The hatched bands represent the combination of statistical uncertainties and the uncertainty of the multijet background normalisation. The panels show the azimuthal angular distance between the b-jet and the top quark (a,d,g), between the lepton and the W boson (b,e,h), and the pseudorapidity of the top quark (c,f,i).

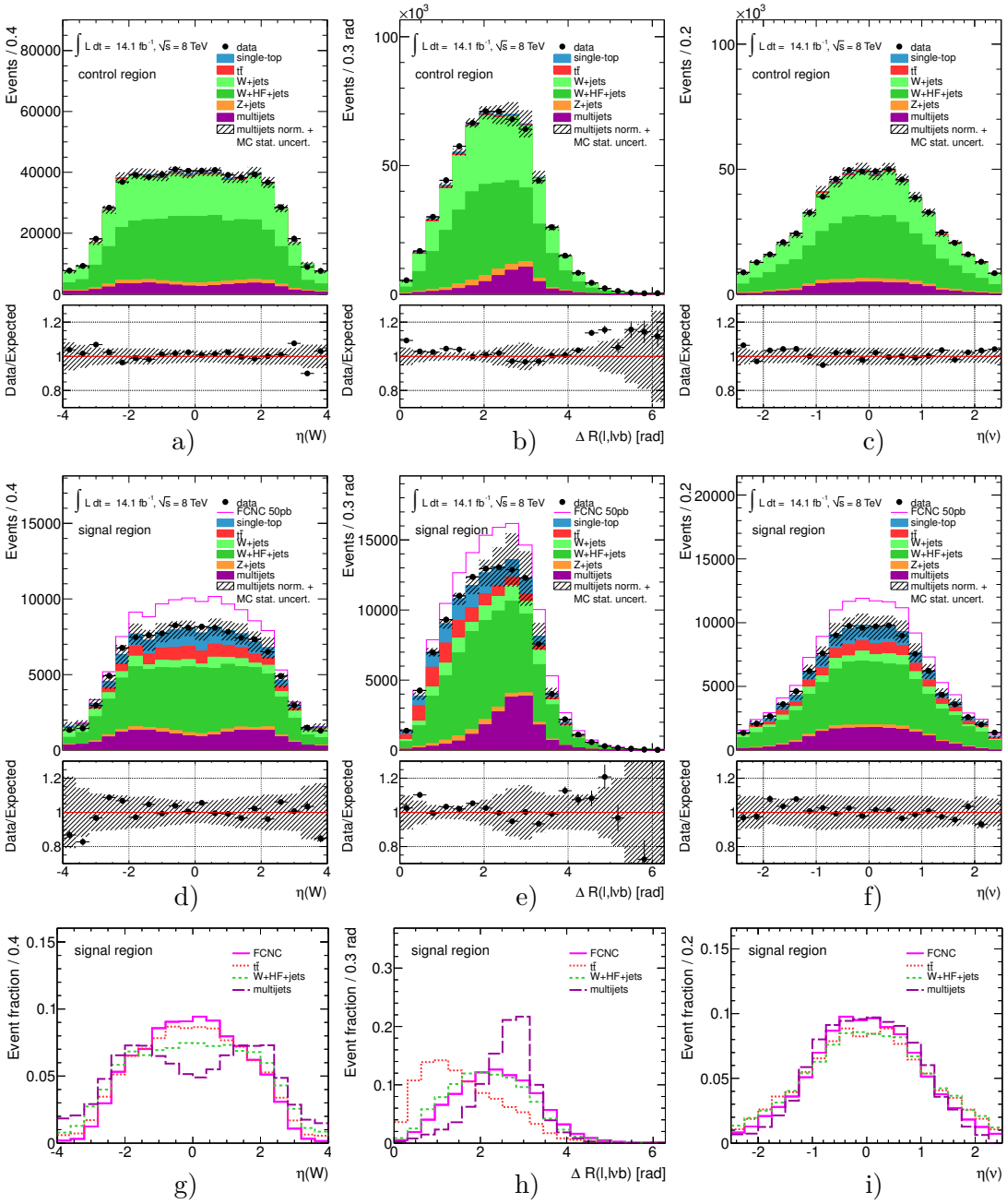

Figure B.4.: Kinematic distributions of the input variables to the neural network for the combined lepton channels in the 1-jet bin control (top row) and signal region (middle row) with all processes normalised to the result of the binned maximum likelihood fit used to determine the fraction of multijet events, or in the signal region with all processes normalised to unit area (bottom row). The hatched bands represent the combination of statistical uncertainties and the uncertainty of the multijet background normalisation. The panels show the angular distance between the lepton and the top quark (a,d,g), the azimuthal angular distance between the W boson and the top quark (b,e,h), and the neutrino pseudorapidity (c,f,i).

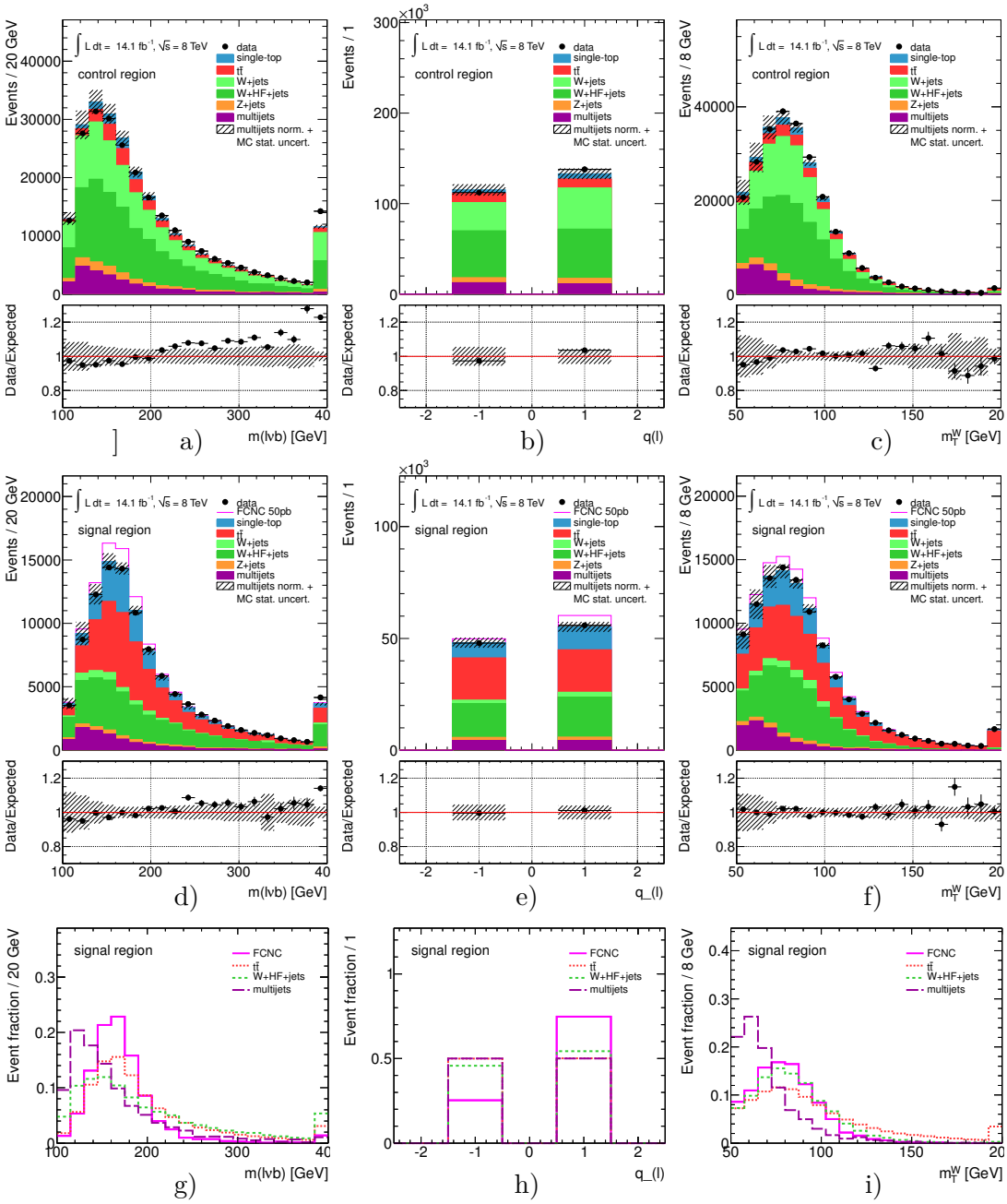

Figure B.5.: Kinematic distributions of the input variables to the neural network for the combined lepton channels in the 2-jet bin control (top row) and signal region (middle row) with all processes normalised to the result of the binned maximum likelihood fit used to determine the fraction of multijet events, or in the signal region with all processes normalised to unit area (bottom row). The hatched bands represent the combination of statistical uncertainties and the uncertainty of the multijet background normalisation. The panels shows the invariant mass of the reconstructed top quark (a,d,g), the charge the lepton (b,e,h), and the transverse mass of the W boson (c,f,i).

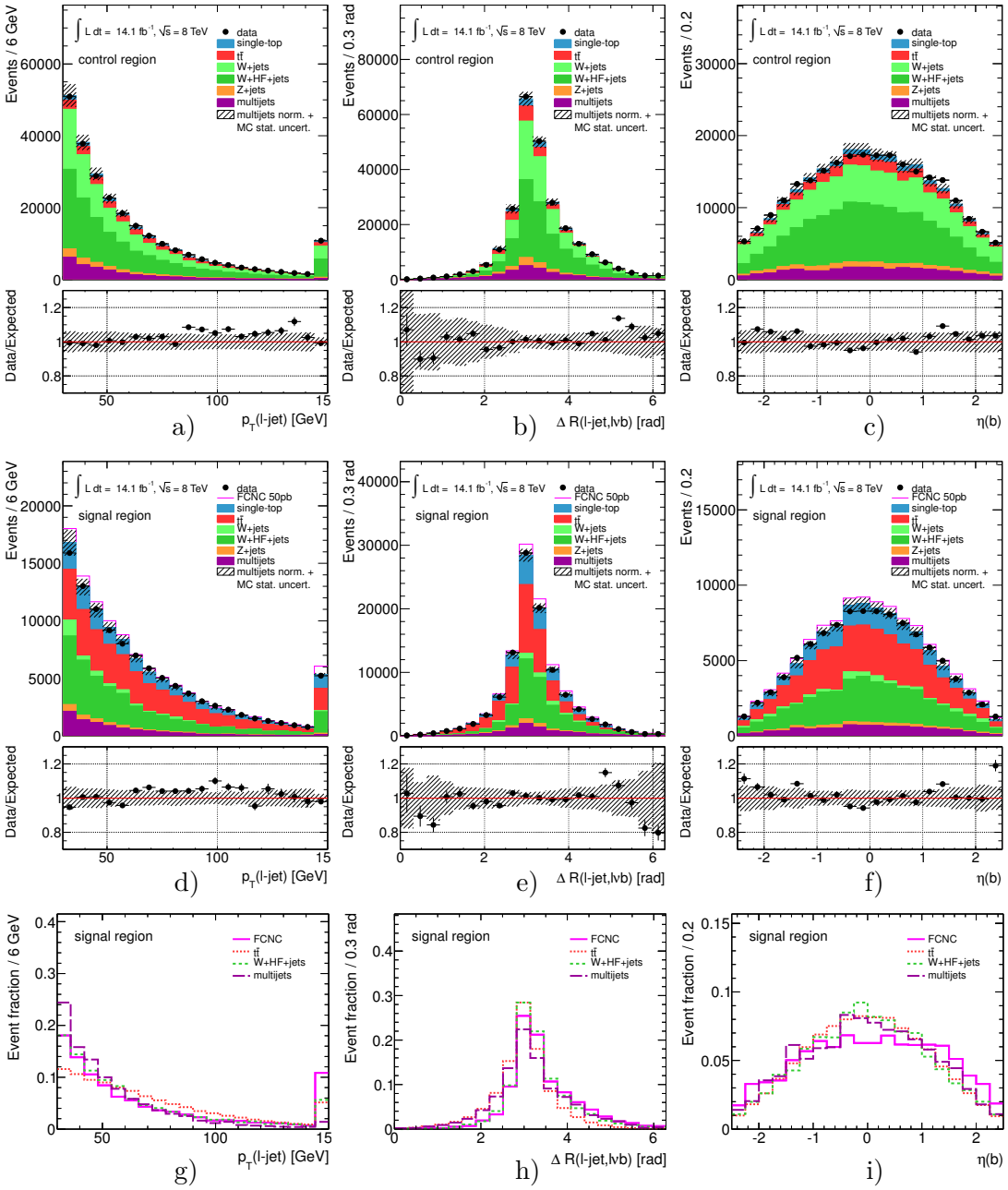

Figure B.6.: Kinematic distributions of the input variables to the neural network for the combined lepton channels in the 2-jet bin control (top row) and signal region (middle row) with all processes normalised to the result of the binned maximum likelihood fit used to determine the fraction of multijet events, or in the signal region with all processes normalised to unit area (bottom row). The hatched bands represent the combination of statistical uncertainties and the uncertainty of the multijet background normalisation. The panels show the transverse momentum of the light-jet (a,d,g), the angular distance between the light-jet and the top quark (b,e,h), and the pseudorapidity of the b-jet (c,f,i).

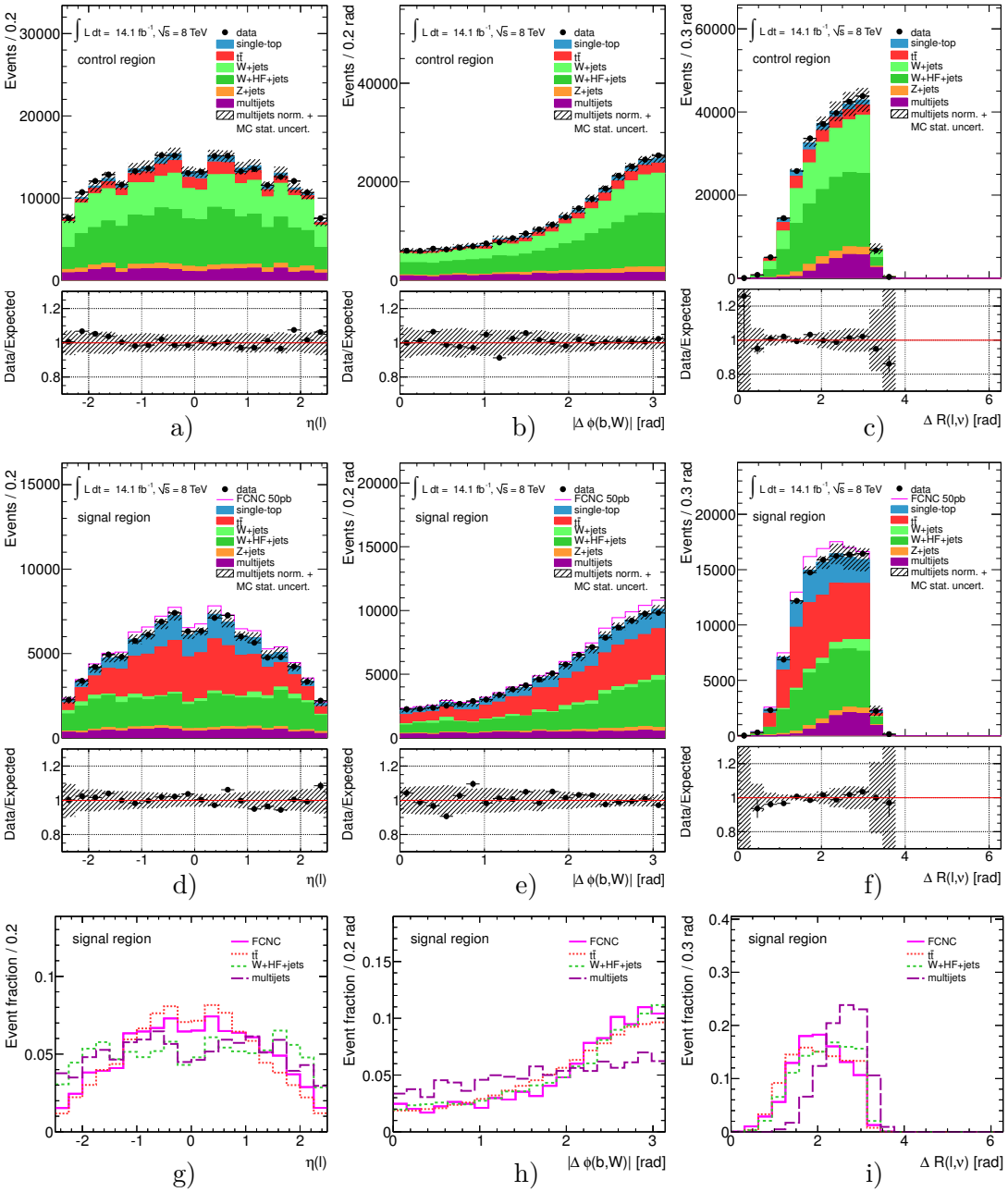

Figure B.7.: Kinematic distributions of the input variables to the neural network for the combined lepton channels in the 2-jet bin control (top row) and signal region (middle row) with all processes normalised to the result of the binned maximum likelihood fit used to determine the fraction of multijet events, or in the signal region with all processes normalised to unit area (bottom row). The hatched bands represent the combination of statistical uncertainties and the uncertainty of the multijet background normalisation. The panels show the pseudorapidity of the lepton (a,d,g), the azimuthal angular distance between the b-jet and the W boson (b,e,h), and the angular distance between the lepton and the reconstructed neutrino (c,f,i).

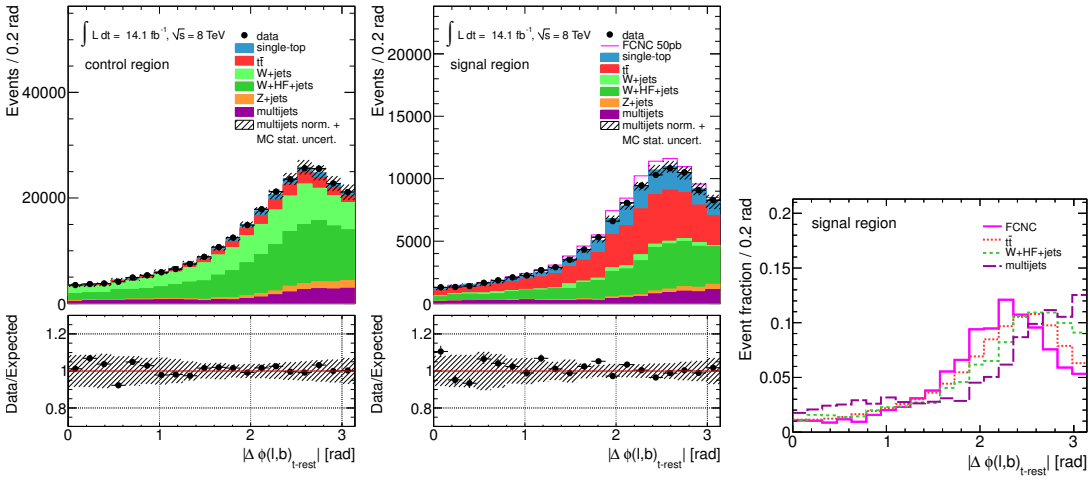

Figure B.8.: Kinematic distributions of the input variables to the neural network for the combined lepton channels in the 2-jet bin control (top row) and signal region (middle row) with all processes normalised to the result of the binned maximum likelihood fit used to determine the fraction of multijet events, or in the signal region with all processes normalised to unit area (bottom row). The hatched bands represent the combination of statistical uncertainties and the uncertainty of the multijet background normalisation. The panels show the azimuthal angular distance between the lepton and the b-jet in the top quark rest frame.

C. Neural Network Analysis

C.1. Choice for Number of Hidden Nodes

The number of hidden nodes in the network is to be chosen freely. Too few nodes in the hidden layer may limit learning capabilities, choosing too many may lead to faster overtraining and an overall decrease in learning speed. To find the optimal number for each network, several training runs have been performed using different numbers of nodes in the hidden layer within a range from 5 to 100. Figure C.1 shows the resulting ANN output distributions normalised to unit area for a selection of these. As expected, only

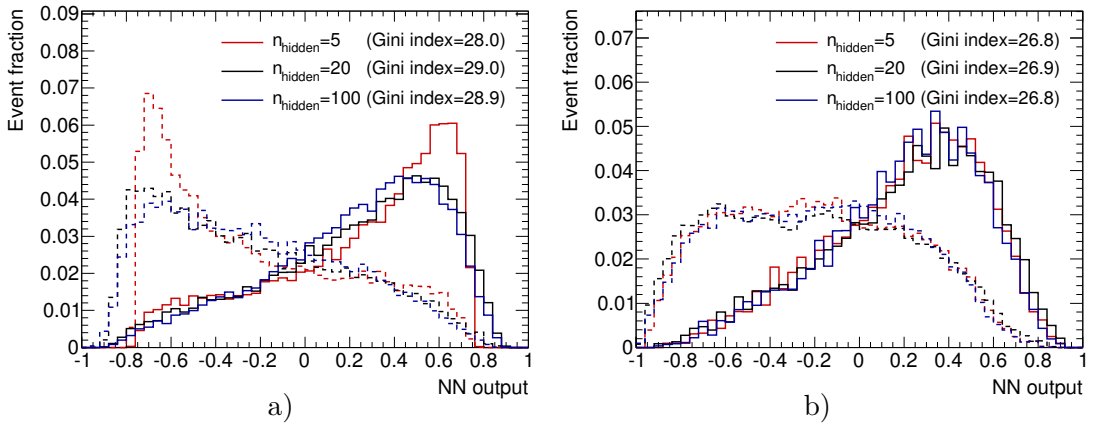

Figure C.1.: Neural network output distribution normalised to unit area for simulated signal (solid lines) and background events (hatched lines) used in the neural network training for the network of the 1-jet bin (a) and 2-jet bin (b), and using different numbers of nodes in the hidden layer (n_{hidden}).

marginal impact on the overall signal and background shape of the ANN outputs can be observed in the upper range of the hidden node count. This is a result of the effective pruning capabilities during the training procedure (cf. Section 8.1). Only with very high node counts the discrimination performance decreases visibly, which is caused by the slower learning speed. However, with too few nodes in the hidden layer the learning performance decreases significantly since the network is too limited in its number of free parameters to successfully match minima on the rather complex error function manifold. Figure C.1 also shows the respective Gini index reached for each network topology, which provides a measure of the overall separation power of the network, see Section C.4 for details. Based on this study a value of 20 hidden nodes is chosen for both ANNs.

C.2. Quality of Training

The quality of the training is verified in distributions of the signal purity in dependence of the ANN output, see Figure C.2. The signal purity is defined as the ratio of the number of signal events to the total number of (signal plus background) events in each bin of the ANN output distribution. If the network is properly trained and its error function is minimised, the distribution should follow a linear function through the origin, or in this case, through (-1,0) for ANN outputs $\in [-1, +1]$ (blue line in Fig. C.2) [260].

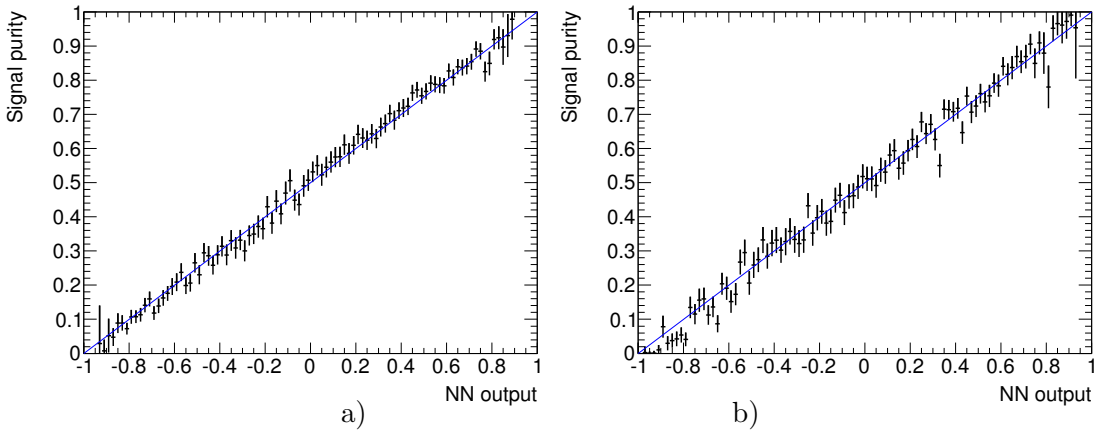

Figure C.2.: Signal purity as a function of the ANN classifier output in each bin for the ANNs of the 1-jet bin (a) and 2-jet bin (b). The linear behaviour verifies proper training of the network.

The ideal distribution of the purity (P) then is given as

$$P = \frac{O_{\mathrm{ANN}} + 1}{2} \quad .$$

which can be interpreted as a probability that an event classified with a certain ANN output is a true signal event. In the purity distributions of both networks nearly all points follow the diagonal within their statistical uncertainties which demonstrates their proper training.

C.3. Correlation of Input Variables and Final Network Topology

The correlations between the input variables, as determined during the preprocessing step of the neural network training, are shown in Figure C.3 for the 1-jet and 2-jet bin, respectively. The mapping of the variables to the numeric labels used in the plots is given in Table C.1. The final topology for both fully trained networks is show in Figure C.4. The mapping of the variables to the node numbers of the input layer is the same as in the correlation plots (see Table C.1). The final weights of the connection between the nodes are represented by the widths of the lines.

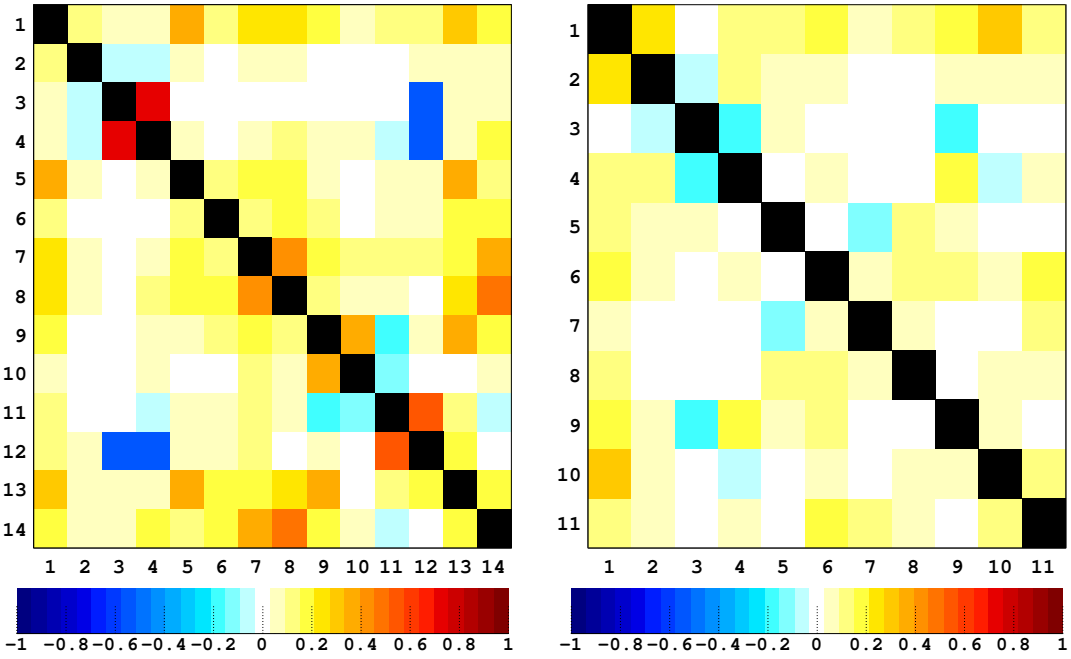

a) b)

Figure C.3.: Correlation matrix of the variables used as input to the network for the 1-jet bin (a) and 2-jet bin (b). The first entry represents the bias node of the respective network. The mapping of the variables to the numeric labels used in the plots is given in Table C.1.

Table C.1.: Numbering of the variables used in the training for the neural network.

1 jet bin				2 jet bin	
No	Variable	No	Variable	No	Variable
1	bias node	12	$\eta(t)$	1	bias node
2	$q(\ell)$	13	$p_{\mathrm{T}}(W)$	2	$q(\ell)$
3	$\eta(\ell)$	14	$\Delta\phi(W,\nu)_{\mathrm{t-rest}}$	3	$\eta(\ell)$
4	$\eta(\nu)$			4	$p_{\mathrm{T}}(b)$
5	$p_{\mathrm{T}}(b)$			5	$p_{\mathrm{T}}(\mathrm{l\text{–}jet})$
6	$E_{\mathrm{T}}^{\mathrm{miss}}$			6	$m_{\mathrm{T}}(W)$
7	$\Delta\phi(\ell,b)$			7	$\Delta\phi(b,W)$
8	$\Delta\phi(\ell,W)$			8	$\Delta R(lep,\nu)$
9	$\Delta\phi(b,t)$			9	$\Delta R(\mathrm{l\text{–}jet},t)$
10	$\Delta\phi(W,t)$			10	$m(t)$
11	$\Delta R(\ell,t)$			11	$\Delta\phi(\ell,b)_{t-rest}$

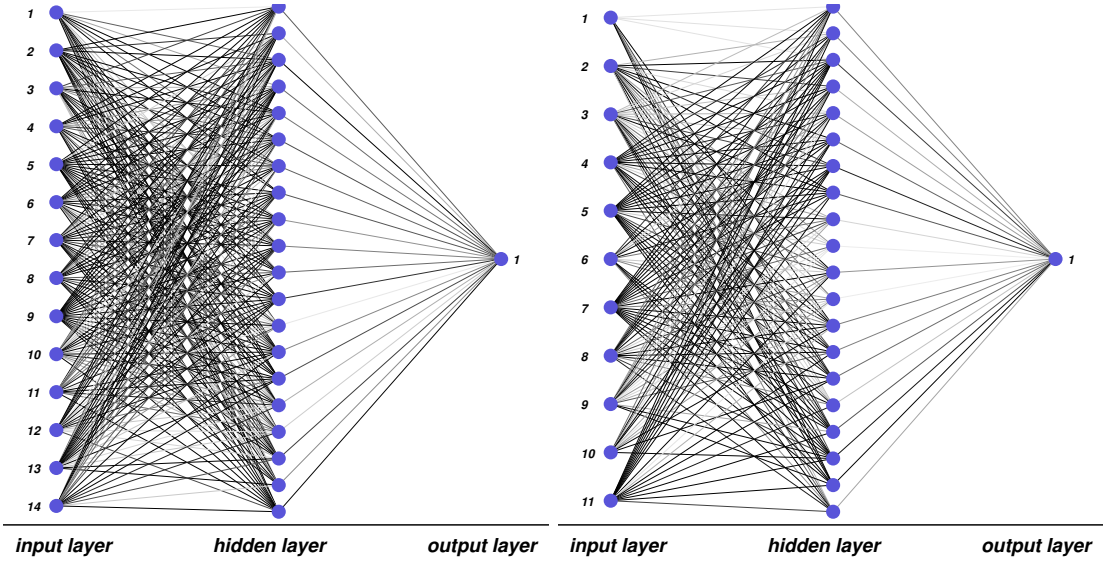

Figure C.4.: Final topology of the trained networks for the 1-jet bin (a) and 2-jet bin (b). The widths of the lines correspond to the connection weights between the nodes. The mapping of the variables to the node numbers in the input layer is given in Table C.1.

C.4. Criteria for Including Input Variables

The decision to include variables as inputs to the network is based on two criteria. First, all variables are checked for correct modelling in the control and signal regions, in both lepton channels individually and for their combination. If large disagreements between simulated and observed distributions are found or variables are known to be subject to poor modelling in general (i.e. jet masses), they are removed from the preliminary list of variables to be included in the initial training in which the variables are ranked in their significance (cf. Section 8.2.3).

After preprocessing and ranking, the variables of highest significance from the list are chosen such that with a reasonably large set of variables, i.e. < 15, almost the maximal discrimination power between the signal and background events still is achieved. A measure of the overall separation power of the network is given by the so-called Gini index, which provides a measure of statistical dispersion and is determined as follows. First, the so-called Lorentz-curve is derived from the ANN outputs of signal and background events. The Lorentz-curve describes the dependence of the signal efficiency (ratio of selected signal events over all signal events) on the total efficiency (ratio of selected events over all events), see Figure C.5 (blue curves). The Gini index then is determined from the area between the Lorentz-curve and the line at unity (diagonal through origin), divided by the area below that line. If the Lorentz-curve lies on the diagonal itself (Gini index = 0), no separation is achieved at all, since signal and background events

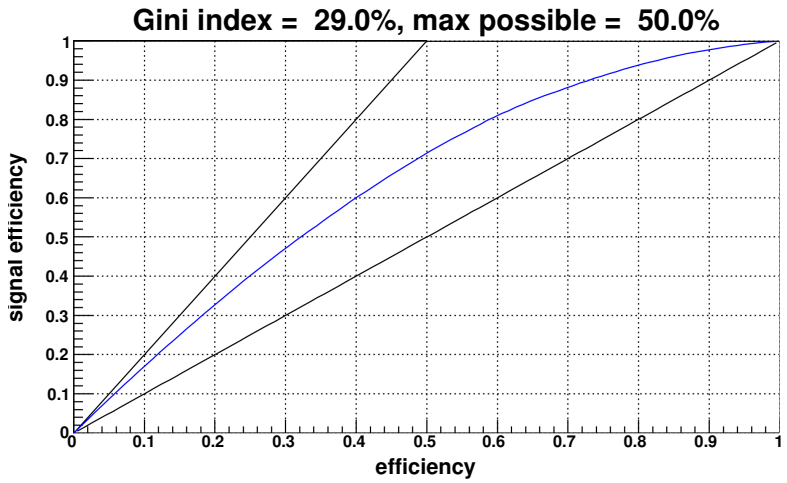

a)

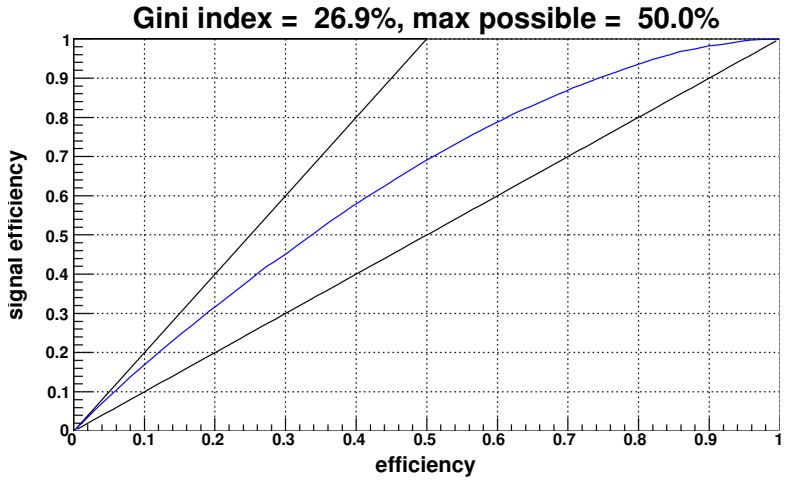

b)

Figure C.5.: Lorentz-curve (blue) for the networks used in the 1-jet (a) and 2-jet bin (b).

are classified equally by the network and hence are uniformly distributed in its outputs. The maximum possible value of the Gini index is limited to 0.5 (or 50%) since the ratio of signal to background events in the training was chosen to be at unity (50:50). It is found, that removing variables with a significance below $3\,\sigma$ has no measurable effect on the Gini index and hence on the overall separation power of the network. As a further cross-check, a network is trained for the 1-jet bin, where only those (7) variables are included which contribute with a significance $\geq 10\,\sigma$. The Gini index of the ANN thereby decreased from 29.0% to 28.2%. Figure C.6 shows the classifier outputs for signal (solid lines) and background events (hatched lines) from the newly trained net-

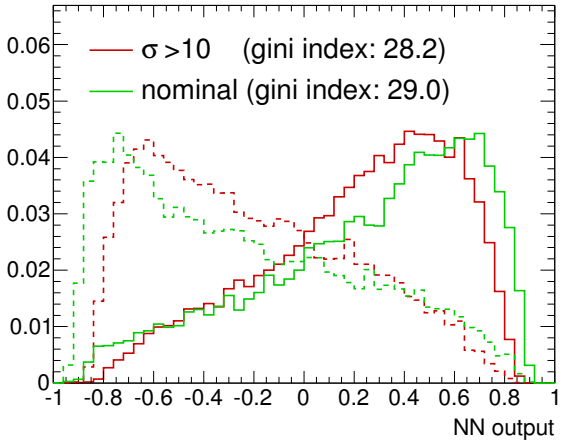

Figure C.6.: ANN output distribution for simulated signal (solid lines) and background events (hatched lines) used in the neural network training for the 1-jet bin using the seven most significant variables only (red), and using all input variables in the training (green).

work for the 1-jet bin in comparison to the nominal ANN used in the analysis. When using the new network for the event classification, the resulting expected 95% CL upper limit on the anomalous FCNC single top-quark production cross-section deteriorates by approximately 15%. This justifies that variables with lower significances should be included since they contribute to the overall sensitivity of the analysis. Based on the studies above it was decided to keep those variables which contribute with a significance above $3\,\sigma$ in their correlation to the target, leading to the 13 variables remaining for the network of the 1-jet bin and 10 variables used as inputs to the network of the 2-jet bin as listed in Table 8.1 in Section 8.2.3.

C.5. Excluding the Multijet Background in the ANN Training

In order to test the effects of excluding multijet background events in the training, different networks are trained with simulated events from the combined electron and muon channel, with and without using events from the multijet templates as an additional input to the training. Figure C.7 shows the resulting discriminator outputs normalised to unit area, for the different background contributions and the signal processes in the 1-jet and 2-jet bin, respectively. No large difference can be observed in the discrimination of signal events from the different backgrounds. While in the networks which were trained including the multijet templates the discrimination against QCD multijet events is increased slightly as expected, the separation from the other backgrounds stays almost same, with small improvements towards lower classifier outputs and slight deteriorations towards very large ANN output values. The Gini indices of the corresponding Lorentz curves for both networks hence only change marginally from 29.0 to

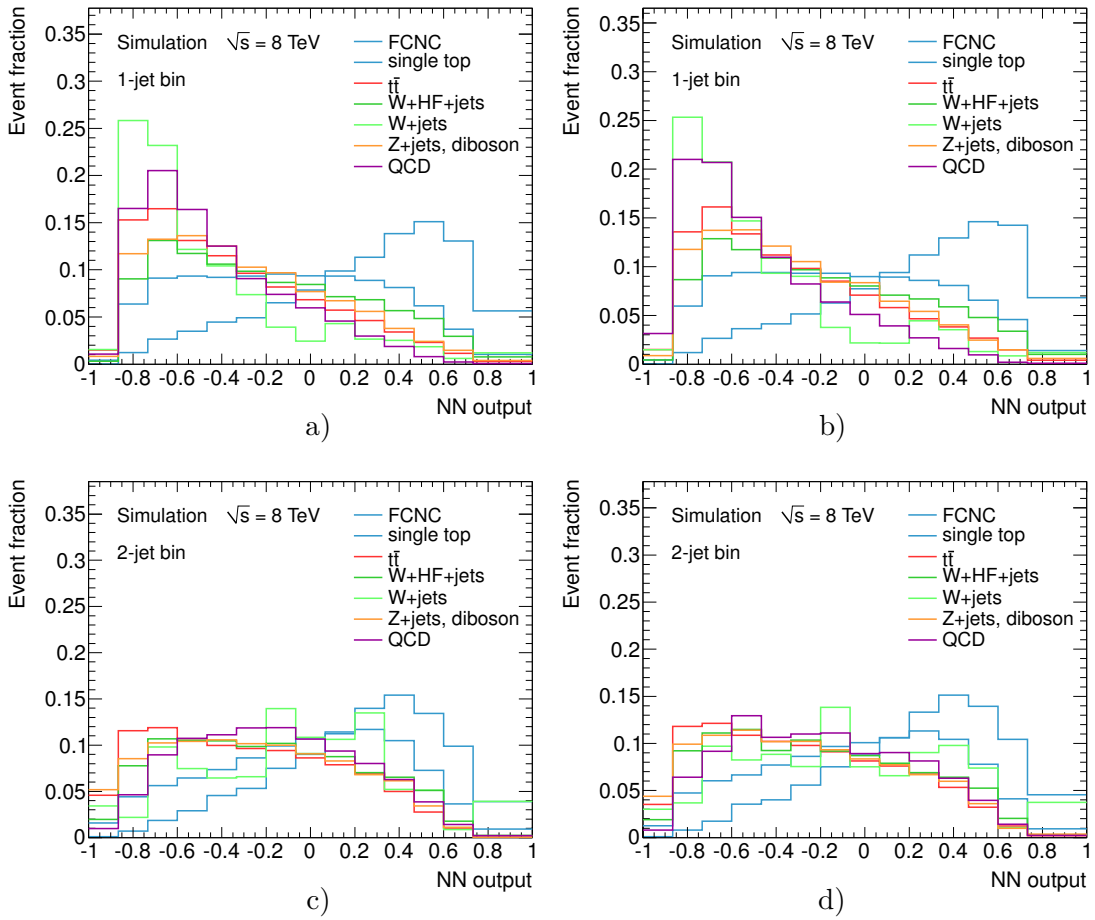

Figure C.7.: Neural network output distributions normalised to unit area for the different background and the signal processes using neural networks trained for the 1-jet bin (a,b) and 2-jet bin (c,d), either excluding multijet events in the training (left) or including the multijet templates (right), respectively.

29.1 for the ANN of the 1-jet bin, and from 26.9 to 27.1 for the network of the 2-jet bin. In summary, only negligible impact on the overall separation power is found when training the network without the multijets template. To quantify the impact on the final statistical analysis, limits have been derived as described in Section 10 but using the ANN outputs generated with the alternative networks, i.e. trained with the multijet templates included. Table C.2 shows the resulting expected 95% CL upper limits on the anomalous FCNC single top-quark production cross-section for the 1-jet and 2-jet bin (including all uncertainties) in comparison with the nominal results derived in Section 10. The expected limits obtained with the new networks decrease by 8% in the 1-jet bin and increase by approximately 8% in the 2-jet bin. Albeit the differences are small and lie well within the expected range of variation estimated using pseudo-experiments,

Table C.2.: Expected 95% CL upper limits on the anomalous FCNC single top-quark production cross-section in the 1-jet and 2-jet bins, derived using ANN outputs from networks trained without (nominal) or with multijet events.

ANN trained	expected 95% CL limit 1-jet bin	2-jet bin
without multijet events	2.37 pb	5.67 pb
with multijet events	2.17 pb	6.03 pb

the a-priori counter-intuitive increase in the case of the 2-jet bin can be explained by the small deterioration in the separation against non-multijet backgrounds towards higher classifier outputs when using the respective network. Although the separation against the multijet background itself is slightly improved, the total expected event count in the (most sensitive) last bins of the ANN output distributions are dominated by the W+jets and SM top-quark events.

C.6. ANN Output Distributions for Electron/Muon Channel

Figure C.8 shows the ANN output distributions separated into electron and muon channel events for the 1-jet bin and 2-jet bin control region, respectively. Shown are the ANN outputs for observed events and the different SM background contributions grouped as explained before. Herein all processes are normalised with the scale factors obtained in the binned maximum likelihood fit to the $E_{\mathrm{T}}^{\mathrm{miss}}$ distribution in data, used to determine the fraction of multijet events (cf. Section 7.3.1). The hatched bands indicate the combined statistical uncertainty from the limited MC samples size and the uncertainty on the multijet normalisation of 50%.

Figure C.9 shows the respective ANN output distributions for the electron and muon channels in the signal region. Therein the combined FCNC signal contribution of the $ug \to t$ and $cg \to t$ processes is shown stacked on top of all backgrounds with an assumed cross-section of 20 pb.

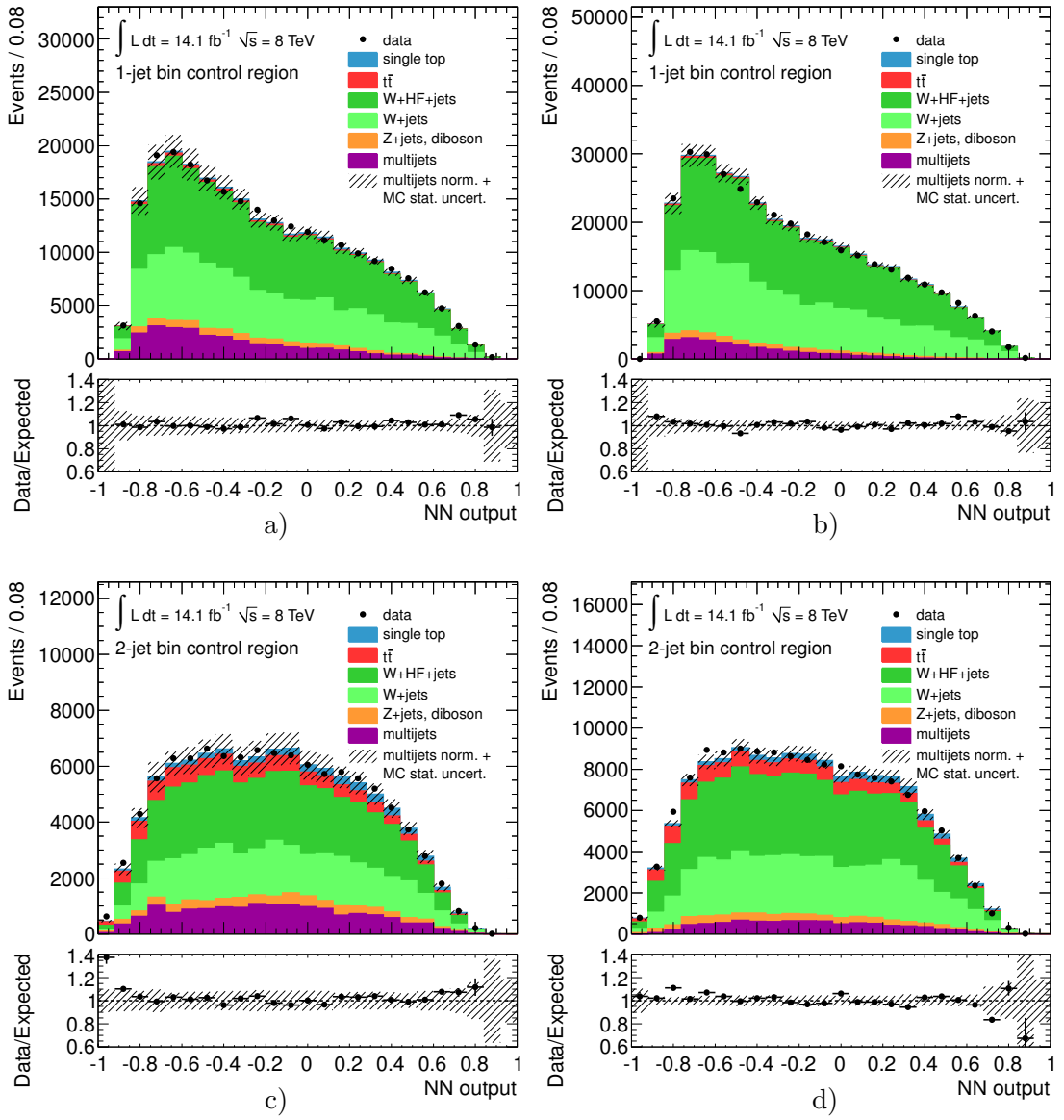

Figure C.8.: Neural network output distributions for simulated and observed events of the 1-jet bin (top row) and 2-jet bin (bottom row) in the control region, split up for events in the electron channel (a,c) and muon channel (b,d). All processes are normalised with the scale factors obtained in the binned maximum likelihood fit to the $E_{\mathrm{T}}^{\mathrm{miss}}$ distribution in data, used to determine the fraction of multijet events. The hatched bands in the main and ratio plots indicate the combined statistical uncertainty from the simulated samples size and the uncertainty on the multijet normalisation.

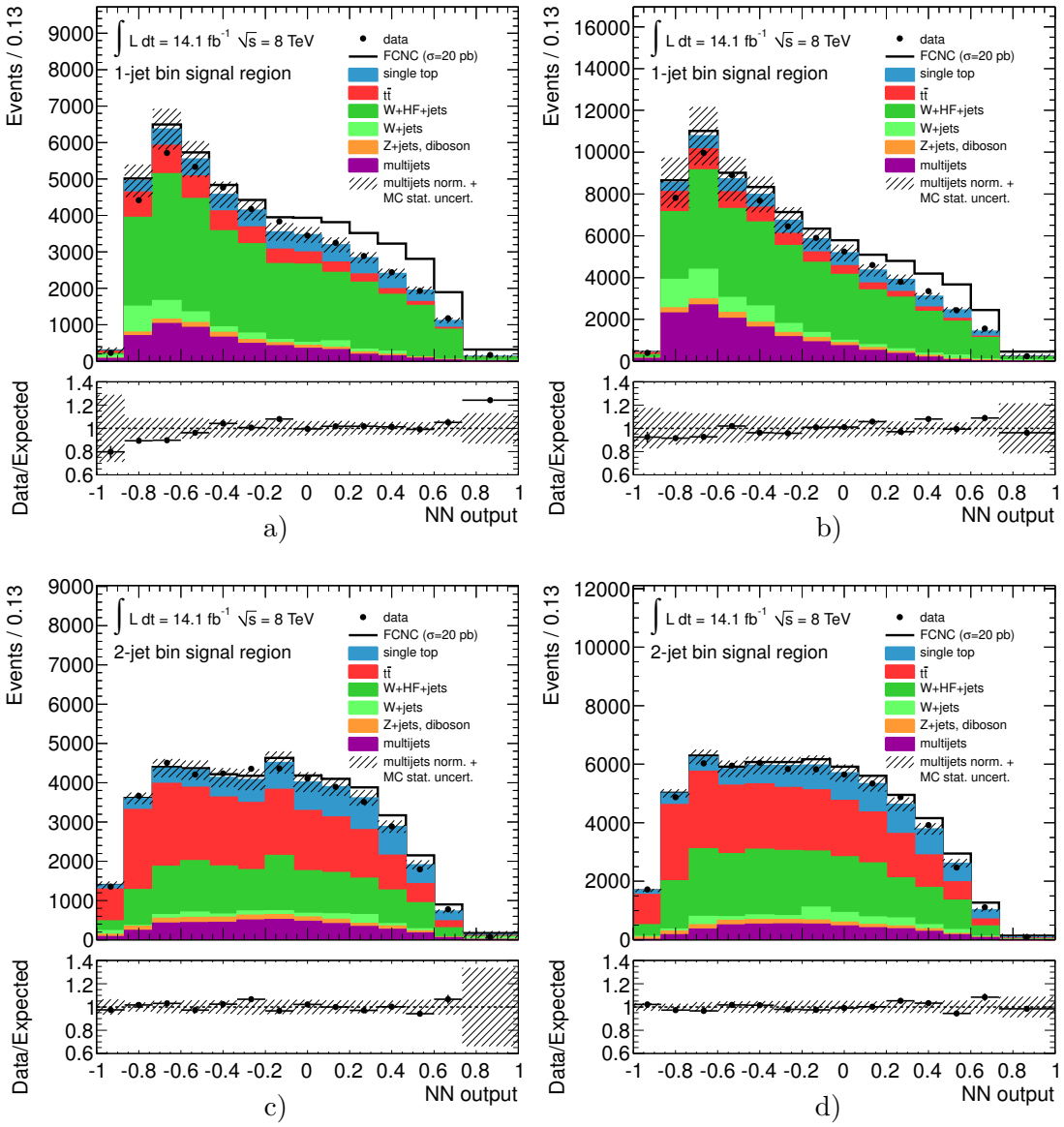

Figure C.9.: Neural network output distributions for simulated and observed events of the 1-jet bin (top row) and 2-jet bin (bottom row) in the signal region, and split up for events in the electron channel (a,c) and muon channel (b,d). The figures show the signal template stacked on top of all SM backgrounds and scaled to a cross-section of 20 pb. All processes are normalised with the scale factors obtained in the binned maximum likelihood fit to the $E_{\mathrm{T}}^{\mathrm{miss}}$ distribution in data, used to determine the fraction of multijet events. The lower pads show the relative difference between the observed distribution and that of the SM only expectation. The hatched bands in the main and ratio plots indicate the combined statistical uncertainty from the simulated samples size and the uncertainty on the multijet normalisation.

D. Limit Evaluation

D.1. Systematics Posteriors

Figures D.2-D.4 show histograms of the posterior probability density for each systematic uncertainty in the 1-jet bin. Corresponding distributions for the 2-jet bin are shown in Figures D.5-D.7. The distributions provide information on the systematics likelihood as a function of their systematic shift by integrating over the signal cross-section instead of the sampled shifts of the systematic uncertainty of interest. The systematics posterior probability density for a particular systematic uncertainty hence is obtained similarly to the signal posterior density as described in Equation 10.8, but replacing the signal cross-section by the shift of the systematic uncertainty of interest:

$$p(g_s|\mathbf{D}) = \frac{1}{\mathcal{N}\sigma_{\max}} \iiint L(\mathbf{D}|\sigma, \mathbf{a}, \mathbf{b})\pi(\mathbf{a}, \mathbf{b})\, d\mathbf{a}_{!\mathbf{s}}\, d\mathbf{b}_{!\mathbf{s}}\, d\sigma\,, \tag{D.1}$$

where g_s denotes the shift for the systematic uncertainty s. Herein the integrals over the priors for the effective luminosity $\mathbf{a}$ and the total background yield $\mathbf{b}$ hence exclude the integration over the systematic shift s itself, which is denoted as "$!s$" in the differentials $d\mathbf{a}_{!\mathbf{s}}, d\mathbf{b}_{!\mathbf{s}}$.

In case the observed data do not constrain a particular systematic uncertainty, the resulting posterior pdf is expected to have a mean of zero and width of one, in accordance to the systematic uncertainties Gaussian prior. The posterior mean values (or modes) thereby provide an estimate of the direction and value of the most probable systematics shifts in view of the observed data, or of how much each source of systematic uncertainty is constrained by the data in its priorly assessed size (width). Very large shifts in the mean value (e.g. $> 2\,\sigma$) instead could point to individual systematics being underestimated.

The double peak structure of the systematics pdf distribution of the jet energy scale uncertainty is studied in more detail in order to investigate its origin and estimate a potential impact on the overall performance of the statistical analysis. The origin of this effect lies in the the number of jets passing the jet selection criteria in the different jet bins for variations in the jet energy scale. In particular the number of W+jets events that pass the event selection in the 1-jet bin increases with a higher jet energy scale, since more events from samples of low parton multiplicities (i.e. the W+0 or W+1 parton samples) migrate into the 1-jet bin. Similarly, fewer events from samples of higher parton multiplicities migrate out of the 1-jet bin into higher ones due to the much lower associated cross-sections. While the jet energy scale has a smaller impact on the signal processes since FCNC events to great extend feature a single jet in the

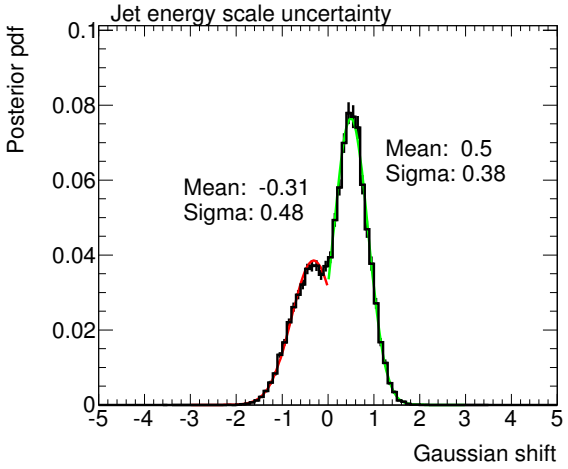

Figure D.1.: Systematics posterior pdf in the 1-jet bin jet for the energy scale uncertainty.

Table D.1.: Observed limits in the 1-jet bin for the jet energy scale being fixed to the two most probable values in its systematics pdf distribution.

systematics shift	observed 95% C.L. upper limit
nominal	2.53 pb
$-0.31\,\sigma$	2.42 pb
$+0.50\,\sigma$	2.36 pb

final state, the opposite is observed for the SM top-quark production processes. Most events of the latter type possess three or more jets in the final state. Hence more of these are reconstructed in the 1-jet bin category with *lower* jet energy scales since more jets potentially could fall below the jet p_{T} cut of 30 GeV. Since the shapes of both backgrounds in the ANN output of the 1-jet bin are fairly similar (cf. Section 8.2.5), the effect of W+jets events with low parton multiplicities migrating into the 1-jet with increasing jet energy scale is comparable to that of SM single top-quark events of higher jet multiplicities migrating into the same jet bin when decreasing it. This penalty results in the most probably value of the jet energy scale to be found at two points, for an up- and for a downward fluctuation of the systematic uncertainty. Albeit this result reflects the real situation and an impact on the performance of the statistical analysis is expected to be avoided "by design" since it is integrated over the full distribution of systematic shifts and associated likelihoods, its influence on the observed limit nevertheless is studied in more detail. Therefore two Gaussian distributions are fitted to the systematics posterior distribution in different ranges of systematic shifts, i.e. in the intervals [-5,0] and [0,5], and their mean values are extracted, see Figure D.1. The calculation of the observed upper limits on the FCNC signal cross-section is then repeated with the shift in the jet energy scale being fixed to either of the two modes (most probable values) of the systematics posterior distribution. The results are summarised in Table D.1. As expected, neither

of the two choices causes any larger deterioration in the observed limit. The resulting slight improvement in its value is expected since one of the largest systematics is being "artificially" constrained.

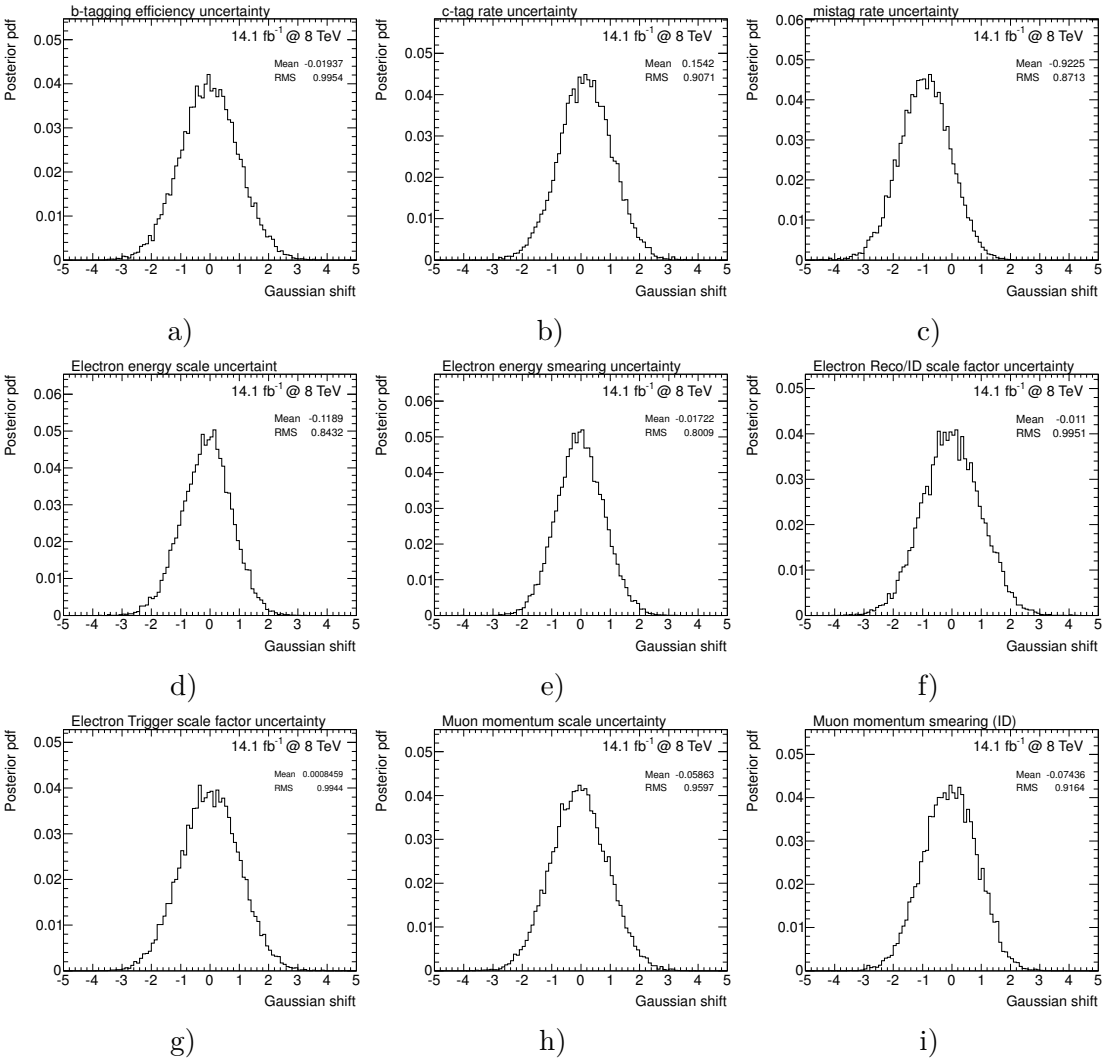

Figure D.2.: Distributions of the posterior probability density in the 1-jet bin for the b-jet efficiency scale factor uncertainty (a), c-jet efficiency scale factor uncertainty (b) and mistag rate efficiency scale factor uncertainty (c), for the electron energy scale uncertainty (d), electron energy resolution uncertainty (e) and electron reconstruction and ID scale factor uncertainty (f), as well as for the electron trigger scale factor uncertainty (g), muon momentum scale uncertainty (h) and muon momentum resolution (ID) uncertainty (i).

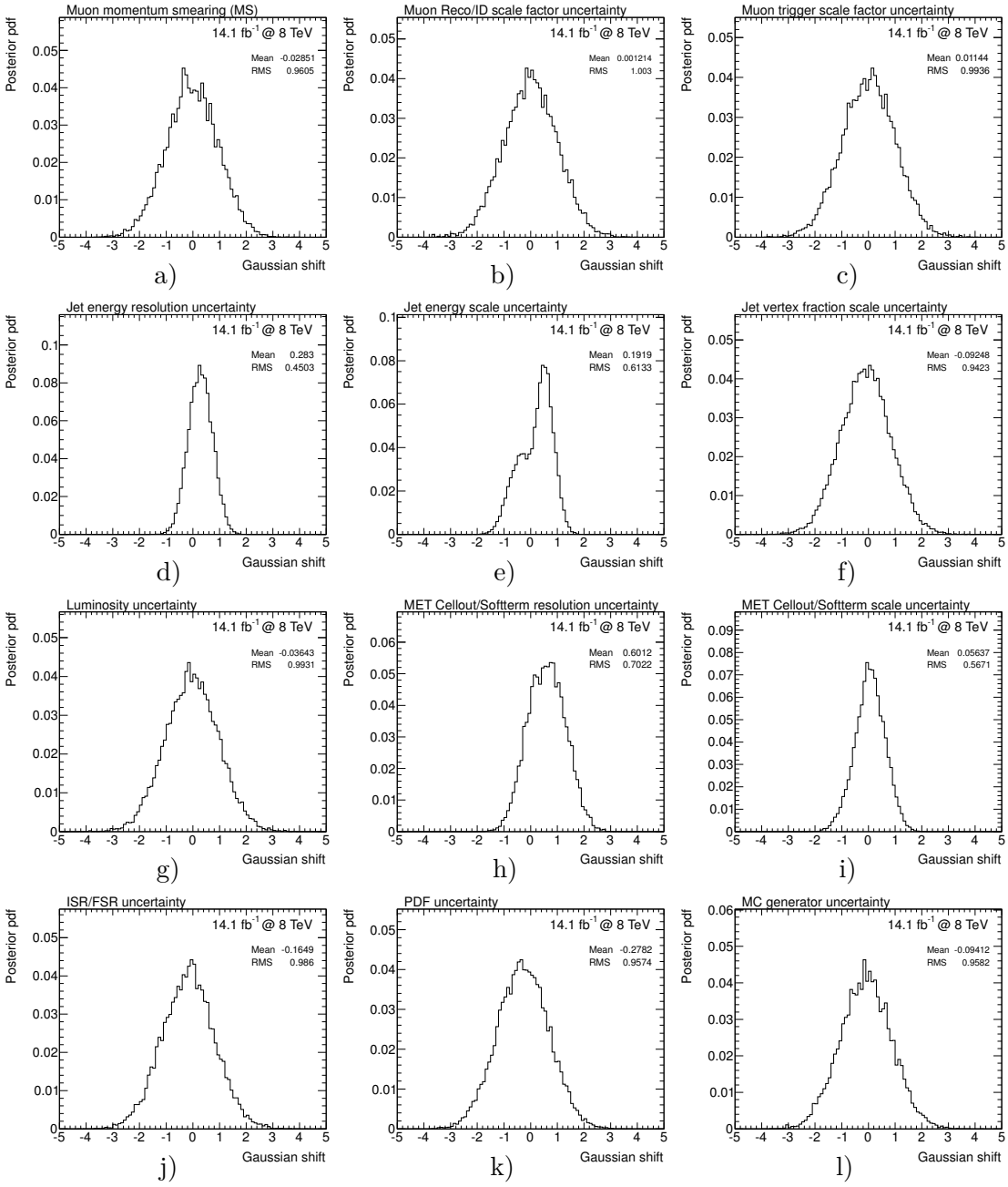

Figure D.3.: Distributions of the posterior probability density in the 1-jet bin for the muon momentum resolution (MS) uncertainty (a), muon reconstruction and ID scale factor uncertainty (b) and muon trigger scale factor uncertainty (c), for the jet energy resolution (d), energy scale (e), and jet vertex fraction scale uncertainty (f), for the luminosity uncertainty (g), MET Cellout&Softterm resolution (h) and scale uncertainty (i), as well as for the ISR/FSR uncertainty (j), PDF uncertainty (k) and $t\bar{t}$ MC generator uncertainty (l).

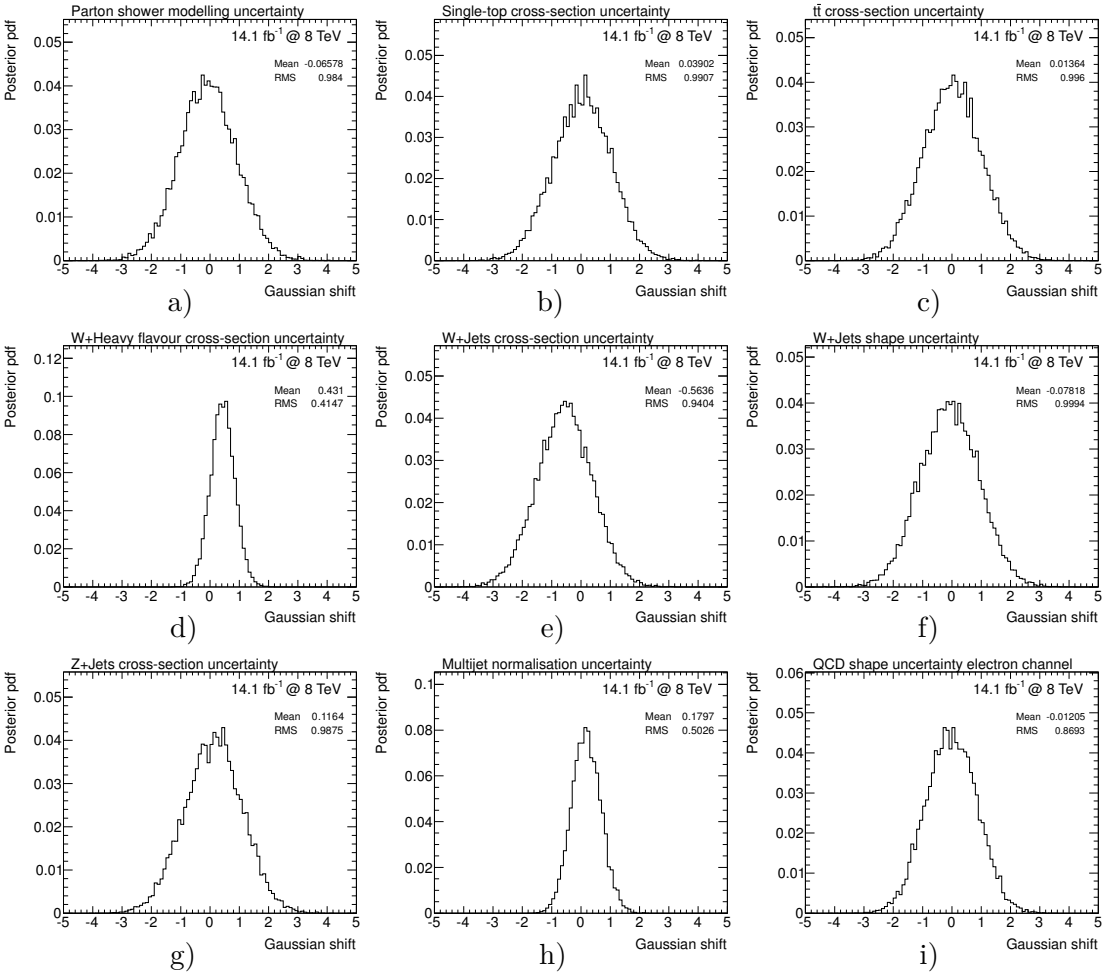

Figure D.4.: Distributions of the posterior probability density in the 1-jet bin for the parton shower modelling uncertainty (a), the single-top (b), $t\bar{t}$ (c), and W+HF+jets cross-section uncertainty (a), for the W+jets cross-section (b) and shape uncertainty (c), as well as for the Z+jets cross-section (d) and multijets normalisation uncertainty (e).

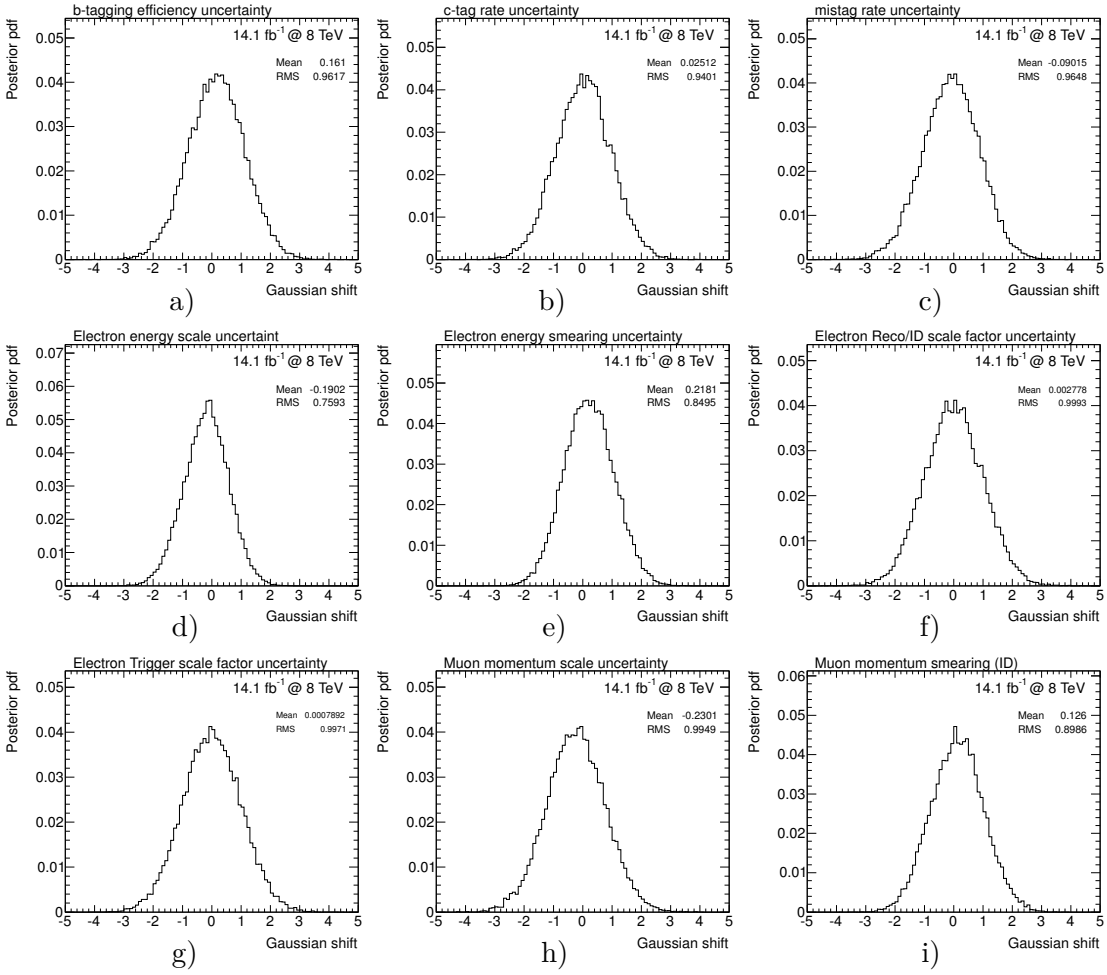

Figure D.5.: Distributions of the posterior probability density in the 2-jet bin for the b-jet efficiency (a), c-jet efficiency (b) and mistag rate efficiency scale factor uncertainty (c), for the electron energy scale (d) and resolution (e) and electron reconstruction and ID scale factor uncertainty (f), as well as for the electron trigger scale factor uncertainty (g), muon momentum scale uncertainty (h) and muon momentum resolution (ID) uncertainty (i).

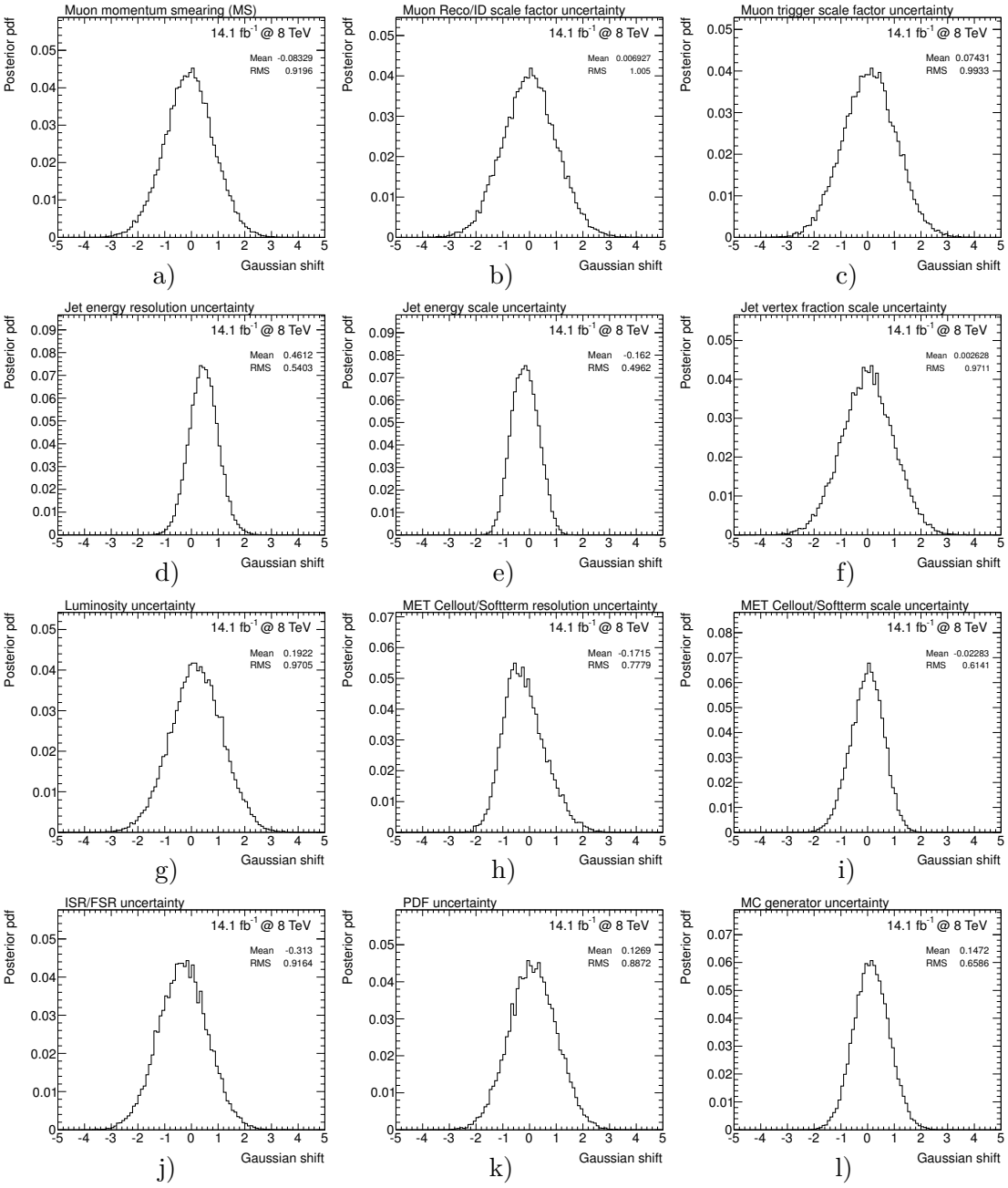

Figure D.6.: Distributions of the posterior probability density in the 2-jet bin for the muon momentum resolution (MS) uncertainty (a), muon reconstruction and ID scale factor uncertainty (b) and muon trigger scale factor uncertainty (c), for the jet energy resolution (d), energy scale (e), and jet vertex fraction scale uncertainty (f), for the luminosity uncertainty (g), MET Cellout&Softterm resolution (h) and scale uncertainty (i), as well as for the ISR/FSR uncertainty (j), PDF uncertainty (k) and $t\bar{t}$ MC generator uncertainty (l).

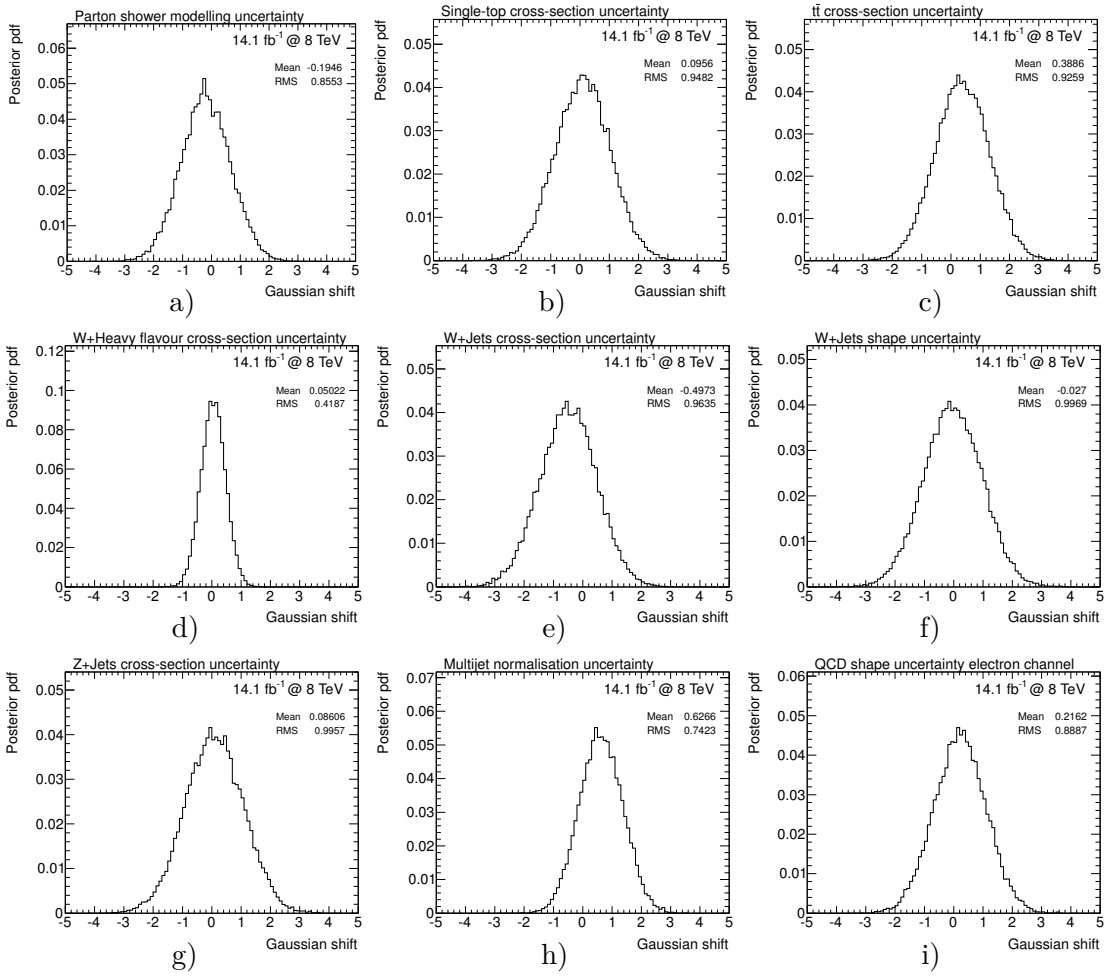

Figure D.7.: Distributions of the posterior probability density in the 2-jet bin for the parton shower modelling uncertainty (a), single-top (b), $t\bar{t}$ (c), and W+HF+jets cross-section uncertainty (a), for the W+jets cross-section (b) and shape uncertainty (c), as well as for the Z+jets cross-section uncertainty (d) and multijets normalisation uncertainty (e).

D.2. Effect of W+HF+jets Normalisation Uncertainty

The W+HF+jets normalisation uncertainty is likely to be overestimated as can be seen in the width of its corresponding systematics posterior distribution (see previous section). To evaluate the effect of choosing the rather conservative value of originally 55%, several limit calculations using different, smaller uncertainty values have been run. The observed limits in the 1-jet bin were calculated including all systematics using their nominal values, changing only the value for the W+HF+jets normalisation uncertainty to values ranging from 45% down to 15%. The resulting limits and the respective posterior mean and width of the W+HF+jets normalisation uncertainty for each of the chosen prior uncertainty values are shown in Table D.2. It turns out that for values down to 30%

Table D.2.: Observed limits for the 1-jet bin and the corresponding posterior mean and width of the W+HF+jets normalisation uncertainty for different choices of uncertainty values.

uncertainty	observed 95% C.L. upper limit	pdf mean [σ]	pdf width [σ]
55% (nominal)	2.53 pb	0.54	$\pm$0.42
45%	2.56 pb	0.57	$\pm$0.45
40%	2.52 pb	0.64	$\pm$0.54
35%	2.54 pb	0.66	$\pm$0.59
30%	2.48 pb	0.69	$\pm$0.65
25%	2.59 pb	0.72	$\pm$0.72
20%	2.70 pb	0.69	$\pm$0.78
15%	2.69 pb	0.62	$\pm$0.86

the observed limits stays within 2% of the original value, the remaining differences of which can easily be explained by statistical fluctuations in the sampling process of the limit evaluation and the limited resolution of 0.1 pb in the integration of the final posterior density. Hence, the nominal W+HF+jets normalisation provides a rather good description of the data without the need for large systematic shifts and the choice for a particular value of its systematic uncertainty does not impact the results and performance of the limit calculation within a large range. The posterior widths and mean values are increasing respectively for lower uncertainties. However, for values starting from 25% or lower the mean value of the systematic posterior probability density does not get shifted accordingly to higher values any more, which then is compensated by other systematics showing higher shifts instead. Hence, when assuming values lower than 30% the uncertainty tends to be underestimated.

E. Signal Generator

E.1. Common Parameters Used for the MC Event Generation

Table E.1 shows a list of configuration parameters and values such as particle masses, widths, and the Weinberg mixing angle common to all generators used for the MC event generation of all processes considered in the analysis. All values given follow the ATLAS-wide conventions for the MC production in 2012/13 which are based on the PDG2010 [281] values. The value for the top-quark mass reflects a common value agreed upon within the ATLAS top-quark analysis group in 2011, for the values for bottom- and charm-quark masses each generator's (and process') default value (including zero mass for certain processes) is used. Table E.2 shows all nominal parameters, constants

Table E.1.: Summary of configuration parameters and values of constants common to all generators used in the MC event simulation.

Option	Description	Value
Mtop	t-quark mass	172.5
MZ	Z-boson mass	91.1876
MW	W-boson mass	80.399
wW	W-boson width	2.085
wZ	Z-boson width	2.4952
SW^2	$\sin^2\theta_W$ (θ_W = Weinberg angle)	0.23113

and configuration options used for the signal event generation with the MEtop matrix element generator as set in the respective "param.dat" configuration file.

E.2. Dependence on Coupling Constant

To check for any dependence of the (NLO) signal kinematics on the choice of the coupling constants, two additional samples were produced for both the $ug \to t$ and $cg \to t$ process using the same random seeds as in the nominal sample but different couplings constants of $\kappa_{qgt} = 0.002$ and $\kappa_{qgt} = 0.05$, respectively. Figure E.1 shows the normalised kinematic distributions of the top quark and jets after showering with Pythia in comparison to the nominal sample with $\kappa_{qgt} = 0.01$. No deviation is found for any of the two samples, thus only the cross-section is affected by the choice of the coupling constant.

Table E.2.: Summary of parameters used in METOP for the signal event generation.

Option	Description	Value
Mu	u-quark mass [GeV]	0.32
Md	d-quark mass [GeV]	0.32
Mc	c-quark mass [GeV]	1.55
Ms	s-quark mass [GeV]	0.50
Mb	b-quark mass [GeV]	4.95
Mtop	t-quark mass [GeV]	172.5
MZ	Z-boson mass [GeV]	91.1876
MW	W-boson mass [GeV]	80.399
MH	Higgs-boson mass [GeV]	115
Me	electron mass [GeV]	0.000511
Mm	muon mass [GeV]	0.1057
Mt	tau mass [GeV]	1.777
wW	W-boson width [GeV]	2.085
wtop	t-quark width [GeV]	1.320
wH	Higgs-boson width [GeV]	0.005753
wZ	Z-boson width [GeV]	2.4952
s12	Values for CKM matrix element $\|V_{us}\|$	0.221
s23	Values for CKM matrix element $\|V_{cb}\|$	0.040
s13	Values for CKM matrix element $\|V_{ub}\|$	0.0035
SW	$\sin\theta_W$ (θ_W is the Weinberg angle)	0.480791
EE	Electromagnetic coupling constant $g_{em} = \sqrt{4\pi\alpha_{em}}$	0.3133
cox	Coupling constants κ_{ugt} (x=1) / κ_{cgt} (x=2)	0.01
fx	Chirality parameter from co1 and co2	+0.7071
hx	Chirality parameter from co1 and co2	−0.7071
Q	Factorisation scale μ_f [GeV]	172.5
miuR	Renormalisation scale μ_r [GeV]	172.5
L	"New physics" energy scale Λ	1000 (GeV)
ECM	Centre-of-mass energy $\sqrt{s}$ [GeV]	8000 (GeV)
PTmatch	p_{T} for matching ME/PS part $p_{\mathrm{T}}^{\mathrm{match}}$ [GeV]	10 (GeV)
PTmin	Cut in PT for LO 2⇒2 processes [GeV]	10 (GeV)
pdf	PDF name according to LHAPDF	CT10.LHgrid
pp	Type of collider: 1 for pp and -1 for p$\bar{\mathrm{p}}$	1
DecMod	W boson decay modes (e, μ, τ, u, c)	11100 (leptonic)
SpCorr	Spin Correlations (0-off, 1-on)	1
ttbar	t,$\bar{t}$ or both (0- t only, 1- $\bar{t}$ only, 2- t and $\bar{t}$)	2

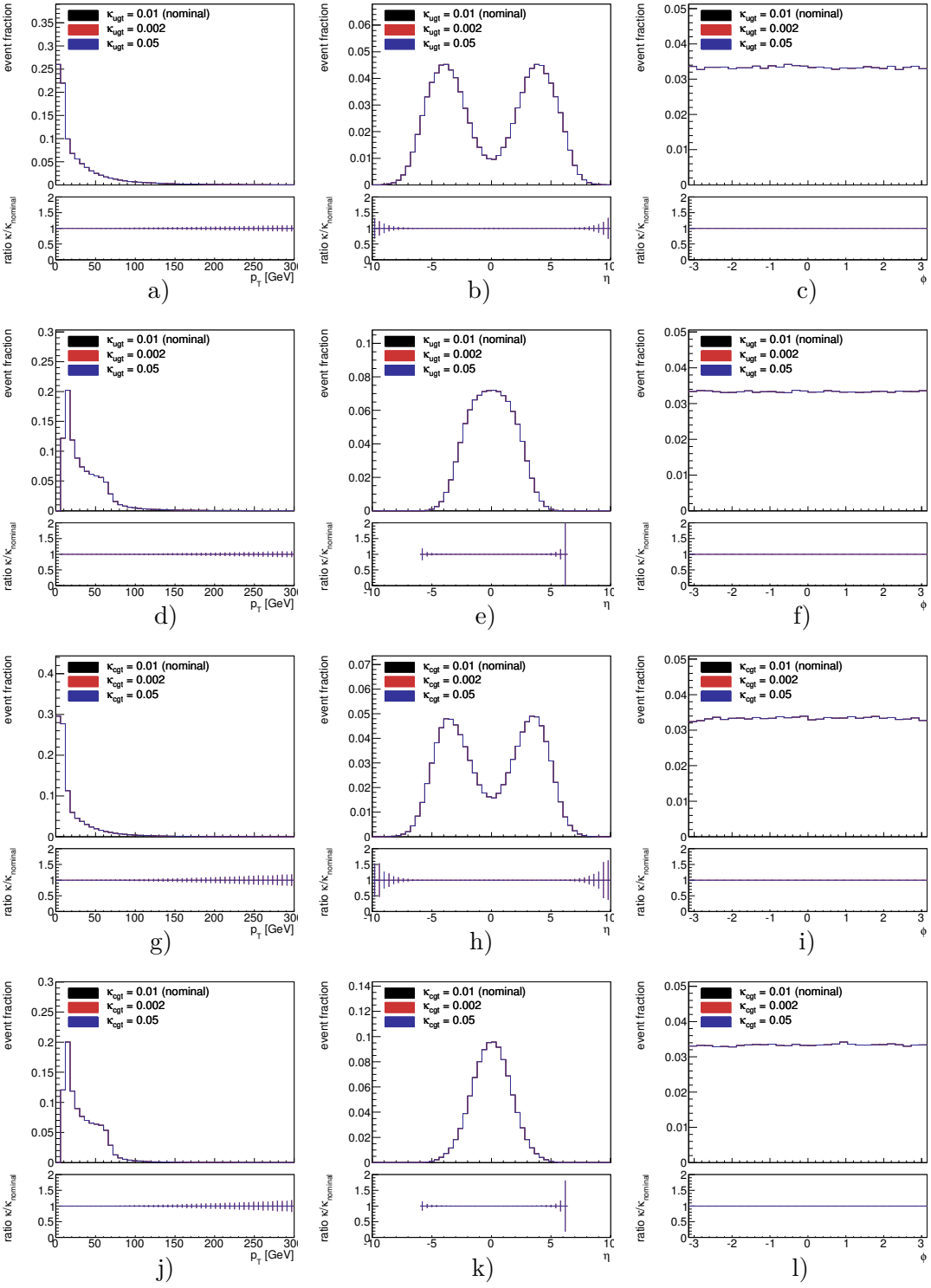

Figure E.1.: Basic kinematic distributions of the top quark, (a-c) and (g-i), and of jets, (d-f) and (j-l), for the $ug \to t$ and $cg \to t$ processes in NLO, respectively, produced with the METOP ME generator interfaced to PYTHIA using different values for the coupling constant κ_{ugt} and κ_{cgt}, respectively.

E.3. Comparisons with Alternative LO MC Generators

Comprehensive studies of the event kinematics of the METOP output are conducted to validate the new NLO signal generator against well established existing generators. As a cross-check for the event simulation in METOP, the event kinematics before applying the detector simulation of the LO $qg \to t$ process are compared to the output of the (LO) PROTOS and MADGRAPH [202] generators. For all generators the CTEQ6L1 [153] LO PDF set and a top-quark mass of $m_t = 172.5$ GeV are used.

The event kinematics are compared in a variety of variables, ranging from basic properties like the total momentum p and energy E, transverse and longitudinal momenta (p_{T}, p_{z}), η and ϕ of the final state objects (t, b, ℓ, ν) and the intermediate W boson, and using (MC truth) information on (tagged/untagged) jets, like their number and p_{T}, and η, ϕ in different p_{T} regions. Further, angular variables like $\cos\theta^*$, the angle between the momentum of the charged lepton in the W boson rest frame, and the momentum of the W boson as seen in the top-quark rest frame, are used to ensure the correct handling of spin correlations and the W boson helicity. The kinematic distributions after showering with PYTHIA are shown exemplary for the top quark and jets in Figure E.2 for the ugt and cgt processes, respectively. All distributions show good agreement within the statistical fluctuations. Further, the $qg \to tg$ ($2 \to 2$) sub-process was generated at LO and compared to events simulated using the MADGRAPH generator. Figure E.3 shows the respective kinematic distributions of the top quark and jets after showering for both processes. Neither here significant deviations can be observed despite statistical fluctuations.

With the agreement between the LO processes, which were also presented at generator level within the ATLAS MC group, and additional studies comparing the LO and NLO event generation with METOP, the generator was formally validated within ATLAS allowing for the official production of the two signal event samples for the ugt and cgt processes using the ATLAS simulation framework in early 2013.

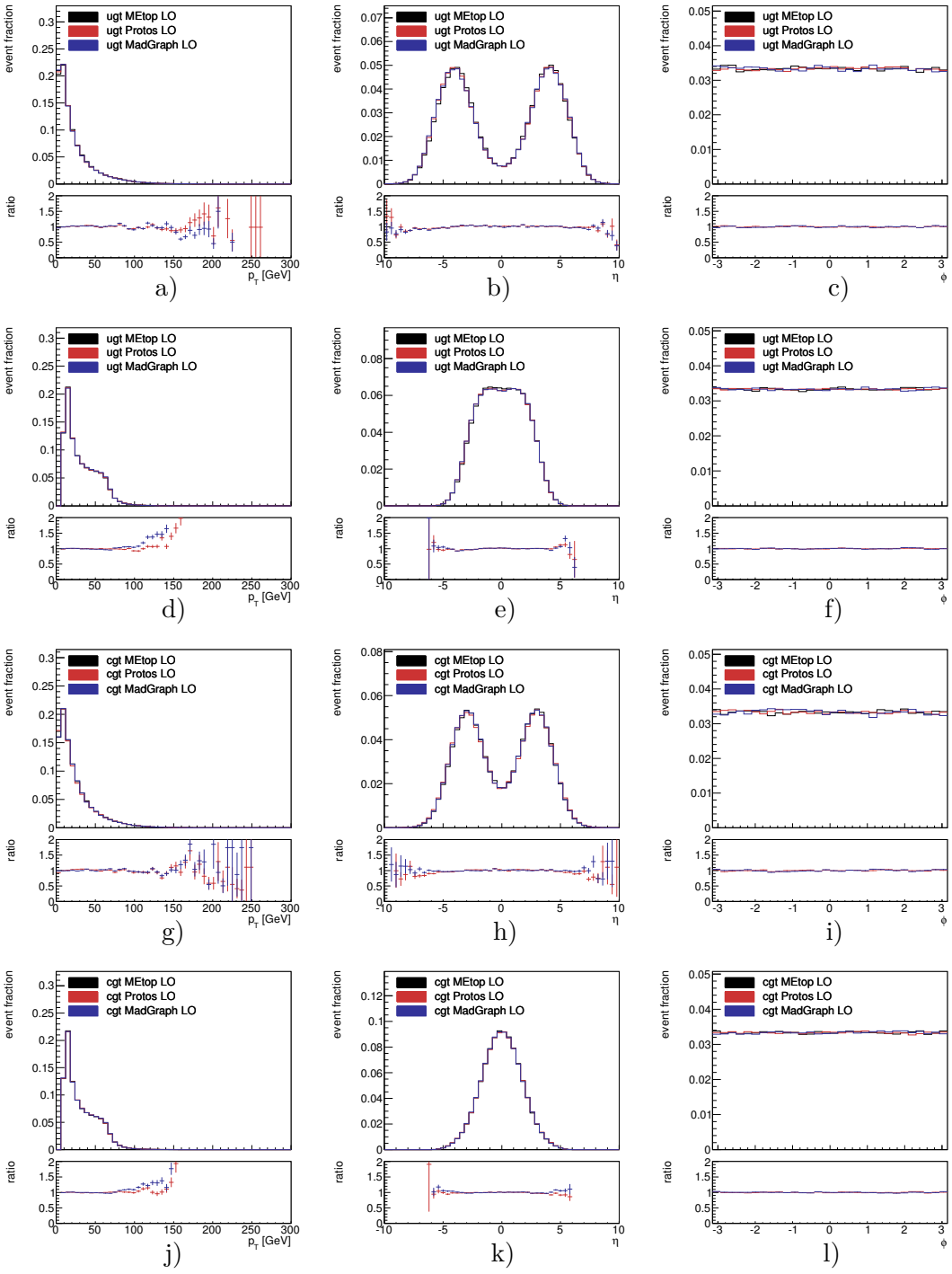

Figure E.2.: Basic kinematic distributions of the of the LO $ug \to t$ and $cg \to t$ process for the top quark, (a-c) and (g-i), and for jets, (d-f) and (j-l), generated using the MEtop, PROTOS and MadGraph generators, respectively.

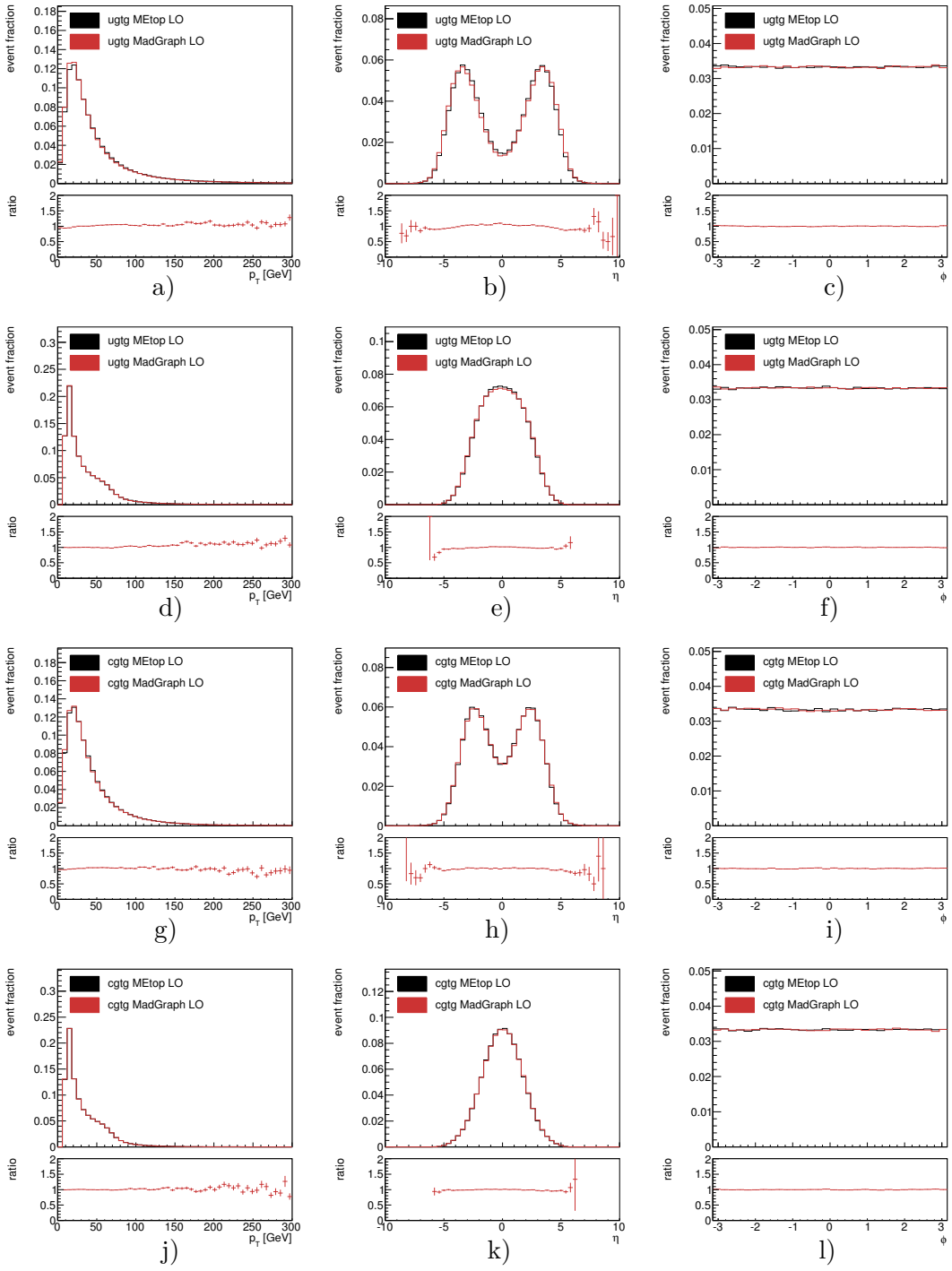

Figure E.3.: Basic kinematic distributions of the of the LO $ug \to tg$ and $cg \to tg$ processes for the top quark, (a-c) and (g-i), and for jets, (d-f) and (j-l), generated using the MEtop and MadGraph generators.

E.4. Comparisons of Event Kinematics for Different ME and PS Parameters

To estimate the dependence on the renormalisation and factorisation scales, comparisons of the event kinematics are made for the inclusive direct top-quark production process at NLO approximation, which is also used within this analysis to simulate the signal processes using the METOP event generator. Different NLO simulation samples are generated and compared before the detector simulation, simultaneously varying the renormalisation and factorisation scales by factors of 1/2 and 2. The nominal value is set to $\mu = \mu_r = \mu_f = 172.5$ GeV, corresponding to the top-quark mass and following the common convention of all generators used within this analysis. Figure E.4 shows the resulting kinematic distributions of the top quark and jets after showering for the *ugt* and *cgt* processes, respectively. As expected, deviations at the order of 10% can be seen in the relevant range of the top-quark pseudorapidity ($\eta < 2.5$) and transverse momentum ($p_{\mathrm{T}} > 20$ GeV) distributions.

In addition, comparisons are made to test the influence of a particular choice for $p_{\mathrm{T}}^{\mathrm{match}}$ within a range of 8 GeV $< p_{\mathrm{T}}^{\mathrm{match}} <$ 15 GeV. Figure E.5 again shows the respective kinematic distributions of the top quark and jets after showering for the *ugt* and *cgt* processes. The shape differences at most amount to approximately 10% for the relevant range of the p_{T} and η distributions of the top quark, however they are less prominent than for variations of the renormalisation and factorisation scales.

Further, comparisons for variations in the amount of initial (ISR) and final state radiation (FSR) are made by varying parameters in the subsequent showering with the PYTHIA PS generator interfaced to METOP, see Section 9 for details. Figure E.6 shows the resulting kinematic distributions of the top quark and jets after showering for the *ugt* and *cgt* processes. The shape differences amount to approximately 5% for the relevant range of the p_{T} and η distributions.

To account for all of the above uncertainties in a correct manner, several additional MC simulation samples have to be produced for variations of μ, $p_{\mathrm{T}}^{\mathrm{match}}$ and ISR/FSR respectively, allowing to include each variation as an additional uncertainty in the limit evaluation, see Section 10.2. This results in a total of 12 additional systematics samples that need to be produced using the official ATLAS simulation framework. Since the event simulation requires extensive computational power, requesting such large numbers of additional samples was not feasible in early 2013, since simulation resources are limited and were used to capacity with simulation requests from the ATLAS SM and Higgs groups. In addition, no official prescription for the ISR/FSR variations in PYTHIA was available at that time. However, since these became available in July 2013, the generation of at least the ISR/FSR systematics samples are in progress to be available for an update of the present analysis in 2014.

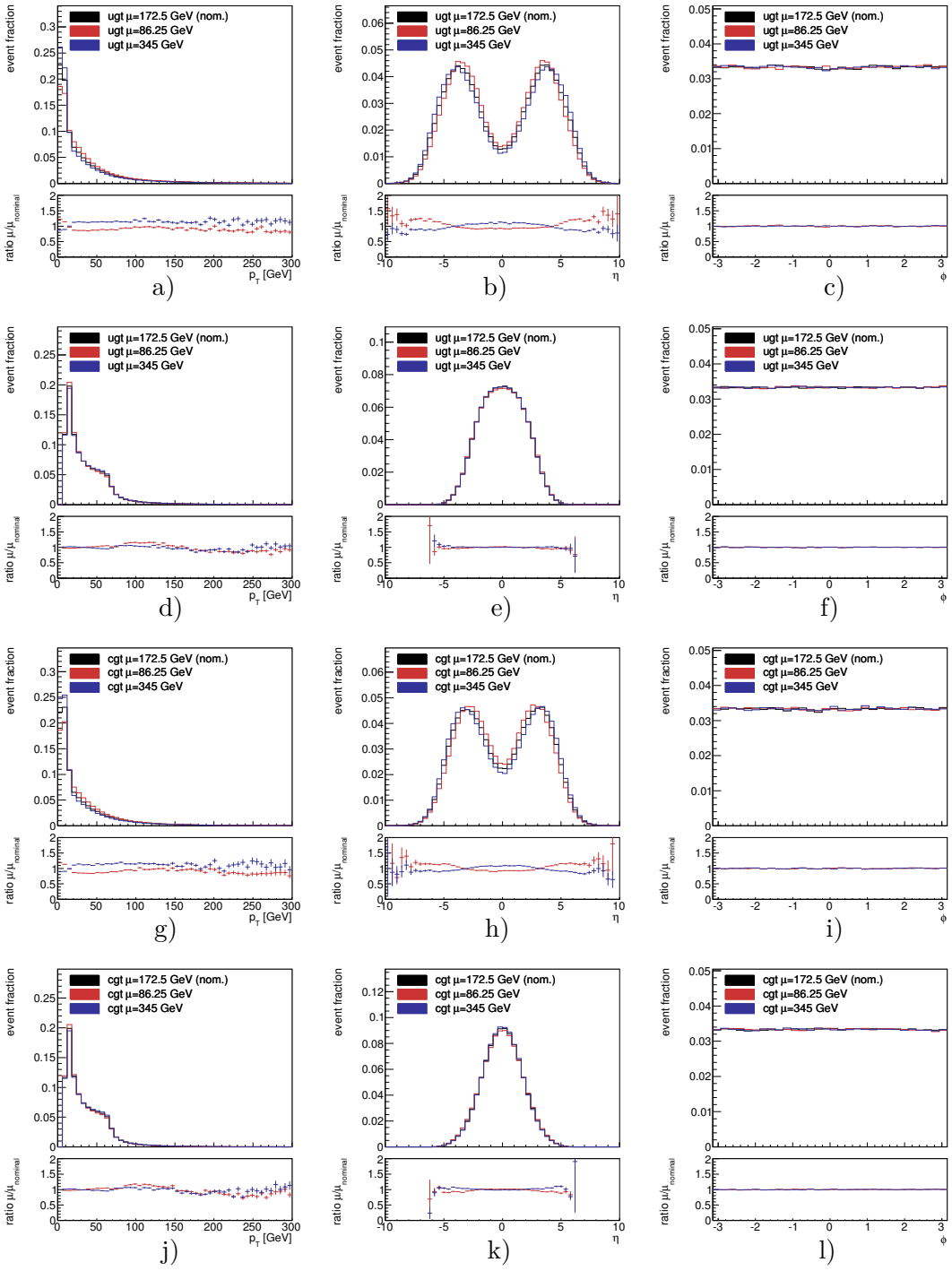

Figure E.4.: Basic kinematic distributions of the top quark, (a-c) and (g-i), and of jets, (d-f) and (j-l), for the $ug \to t$ and $cg \to t$ process in NLO, respectively, produced via METOP using different values for the factorisation and renormalisation scales $\mu = \mu_r = \mu_f$.

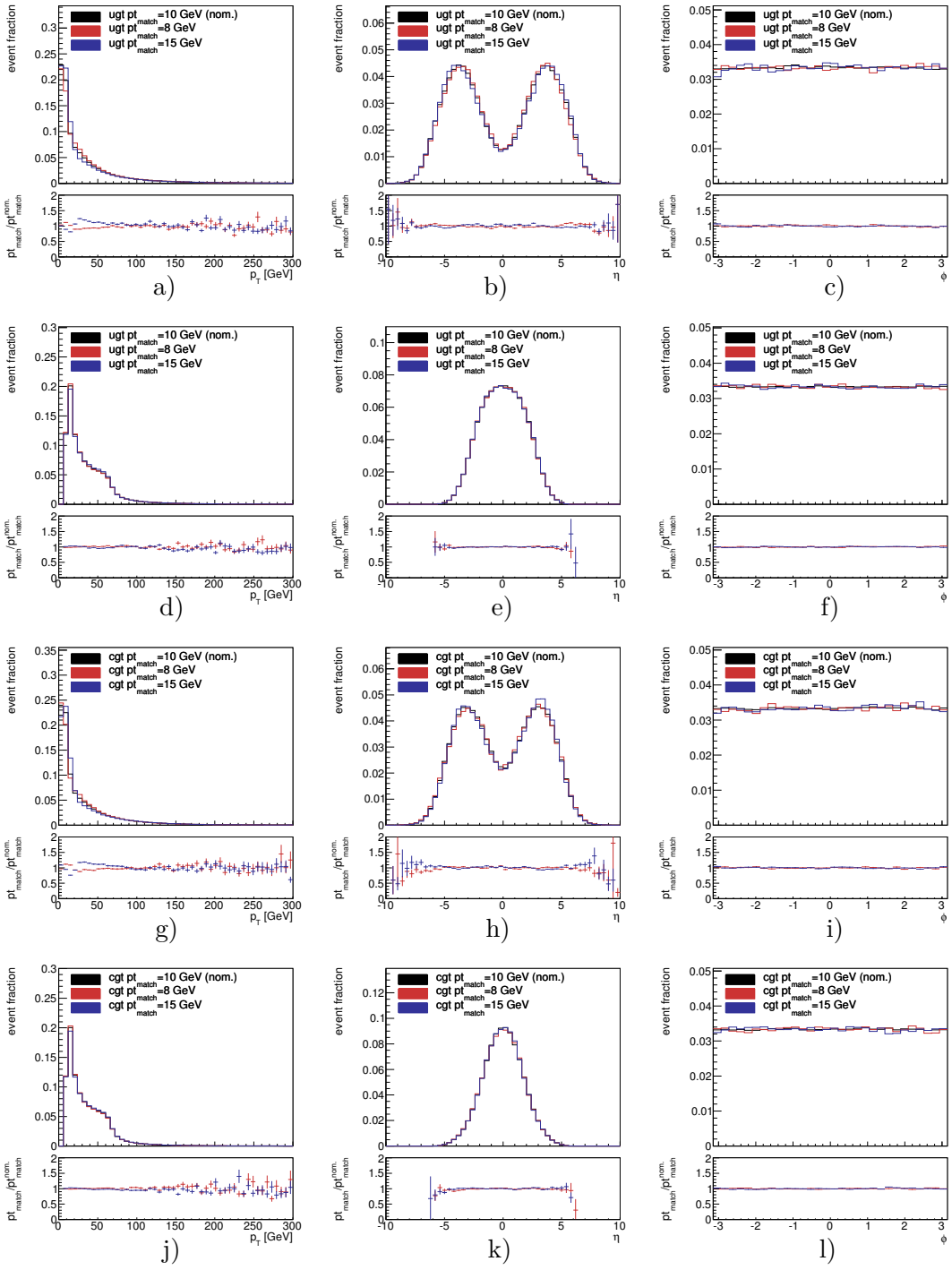

Figure E.5.: Basic kinematic distributions of the top quark, (a-c) and (g-i), and of jets, (d-f) and (j-l), for the $ug \to t$ and $cg \to t$ processes in NLO, respectively, produced via METOP using different choices for $p_{\mathrm{T}}^{\mathrm{match}}$.

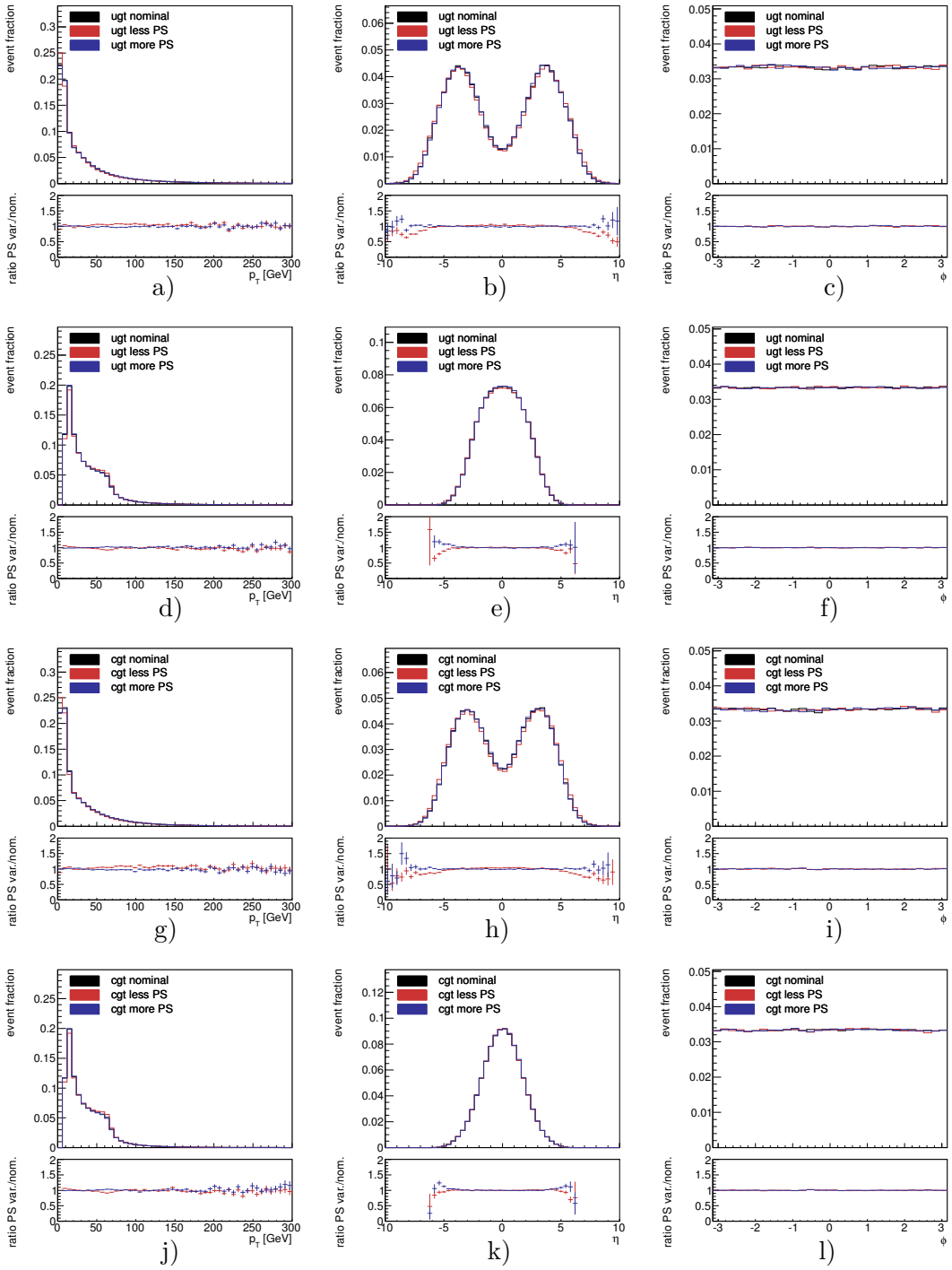

Figure E.6.: Basic kinematic distributions of the top quark, (a-c) and (g-i), and of jets, (d-f) and (j-l), for the $ug \to t$ and $cg \to t$ processes in NLO, respectively, produced via MEtop, varying the amount on initial and final state radiation in the subsequent showering with PYTHIA.

F. HL-LHC Upgrade of the ATLAS Silicon Microstrip Detector

Another part of this PhD work consists of contributions to several R&D projects towards an upgrade of the present silicon microstrip detector (SCT) that will constitute one of two sub-detectors of a future all-silicon tracker operated at the so-called High-Luminosity LHC (HL-LHC). The HL-LHC project aims for an extended 10-years operation of the LHC and its main experiments at an instantaneous luminosity that is roughly five times larger than the present design value. As a consequence of the much higher technical demands imposed by the higher particle multiplicities at the HL-LHC, major upgrades and replacements of the present ATLAS detector will be required, which will affect almost all sub-detectors and off-detector systems. The following sections will provide a chronological overview of the different phases of the LHC and ATLAS upgrades towards a potential HL-LHC, followed by an introduction to the technical demands imposed on a future detector, and on the ATLAS Inner Detector in particular. A large part of the contributions lie in the installation of infrastructure, measurement setups for future prototyping and mass-production of silicon microstrip detector elements and their integration into modules and macro-assemblies. The knowledge and expertise gained herein form the basis for several on-going research and development projects towards the design, technical implementation and assembly of the future ATLAS microstrip detector endcaps. Larger parts of this project build upon the experience gained in the prototyping of the silicon microstrip detector barrel modules and the optimisation of the tools and techniques employed for their construction and testing during this PhD work, see Section F.3. Other studies represent e.g. calculations for estimating the electrical performance and efficiency of several topologies of alternative powering concepts for detector elements of the future microstrip detector. These have been continuously updated in the course of maturing layout decisions and technical specifications of the detector components and front-end electronics and are summarised in Section F.2.2.

F.1. The LHC High-Luminosity Upgrade

The luminosity of the proton-proton collisions delivered to the experiments at the LHC has been increasing continuously since the restart of the LHC in 2009. To fully exploit its physics potential, a larger technical shutdown is currently ongoing after which the LHC is expected to stepwise reach its design energy of 7 TeV per proton beam and its nominal instantaneous luminosity of $10^{34}\,\mathrm{cm}^{-2}\mathrm{s}^{-1}$. During this first long shutdown (LS1), extensive consolidation work of the machine, in particular of the magnet system [282] is envisaged in order to enable the accelerator to safely operate at larger beam energies.

Already during the first years of operation at the LHC, the performance, particularly of the ATLAS Inner Detector, will continuously degrade due to accumulated radiation damage and ageing of the detector components. Especially at the innermost layers of the Pixel detector the high radiation near the interaction point results in a gradual degradation of sensors and readout electronics. At the time of design the technology did not permit to operate the innermost layer of the Pixel detector barrel part (B-Layer) at the nominal luminosity for the full envisaged operation time of the LHC. It was estimated that, after reaching a lifetime corresponding to a recorded integrated luminosity of $\sim 300\,\mathrm{fb}^{-1}$, irradiation effects will have lead to an intolerable reduction in tracking efficiency. Therefore the replacement of the Pixel B-Layer has already been envisaged at the time of design. However, instead of a replacement, more recently it has been proposed to insert an additional Pixel layer between the existing sub-detector and a new beam-pipe of smaller radius. This concept was approved and the so-called Insertable B-Layer (IBL [283]) is installed during the LS1. Several new technologies were under development to enable the IBL for the perennial operation at LHC design luminosities and to withstand an even increased radiation dose and pixel occupancy caused by its closer proximity to the interaction point. Apart from a more stringent material budget, the pixel sizes of its sensor modules will get significantly reduced. A shrinkage from currently $400 \times 50\,\mu\mathrm{m}^2$ down to $250 \times 50\,\mu\mathrm{m}^2$ represents a key ingredient of the new design in order to ensure the maintenance or even improvement of the tracking performance throughout the remaining years of the LHC physics program. Further changes involve the ATLAS HLT trigger system, which will be restructured into a single stage, merging the L2 and EF stages, which allows for an optimisation of the tracking algorithms and HLT CPU resource consumption [284]. The LS1 is to be followed by a three years long period of operation (Phase-0) after the restart of the LHC, currently projected for early 2015. During this run period the instantaneous luminosity is projected to be increased towards the design value of $10^{34}\,\mathrm{cm}^{-2}\mathrm{s}^{-1}$ and thereby enable the ATLAS and CMS experiments to collect integrated luminosities of up to $100\mathrm{fb}^{-1}$, each.

A second long shutdown (LS2) is currently scheduled to follow in 2018 which will presumably last one year. Its intention, on the one hand, is to enable the machine to increase the instantaneous luminosity beyond its nominal value up to approximately $2\text{-}3 \cdot 10^{34}\,\mathrm{cm}^{-2}\mathrm{s}^{-1}$, which corresponds to 55-80 interactions per bunch crossing at 25 ns bunch spacing. This is to be achieved by the integration a new linear accelerator (Linac4) in the pre-accelerator chain, upgrades to the PS Booster in order to increase its energy and to allow for a reduction in the beam emittance, and upgrades to the LHC collimator systems – for a detailed review see e.g. [285]. On the other hand, enhancements of the detectors are indispensable in order to be able to cope with the increase in radiation and particle densities (pile-up). The upgrades of the ATLAS detector [286] involve major improvements of the Level-1 trigger system in order to maintain an acceptable (lepton) trigger performance at increased interaction rates. These include the installation of a new tracking and trigger device in the forward muon spectrometer (Small Wheels) and new trigger electronics in the EM and forward LAr calorimeters in order to raise the granularity of the L1 trigger information from the calorimeter up to a level comparable to that presently only available at the full (EF level) readout. Further changes in the

trigger architecture involve the implementation of a hardware-based track trigger at the HLT stage. This so-called Fast TracKer (FTK) will allow for early access to more precise and in particular global track reconstruction information at an early stage in the HLT chain and thereby circumvent the CPU constraints of the former L2 tracking. Lastly, it was proposed to install two new forward detectors (ATLAS Forward Proton, AFP) at 206 m and 214 m on either side of the ATLAS detector in order to maintain and extend the forward physics capabilities at increased luminosities. After performing the upgrades during the LS2 a running period (Phase-I) of another three years at nominal energy and firstly at nominal luminosity is planned. Later the instantaneous luminosity is envisaged to be increased by up to a factor of three beyond the present design value, with the goal of delivering approximately 300-400 fb^{-1} in p-p collisions at 14 TeV to the experiments by 2022.

The upgrades during LS2 are the basis for a major machine upgrade towards the HL-LHC which has been proposed to be performed in the years around 2024 [280]. The plans for this third long shutdown (LS3) aim for an extension of the physics program by approximately 10 years (Phase-II), targeting a total delivered integrated luminosity of 3000 fb^{-1} in p-p collisions at 14 TeV. This is to be achieved by increasing the instantaneous luminosity by yet another factor of two to three, hence reaching up to $\mathcal{L}_{\mathrm{int}} = 7 \cdot 10^{34}\,\mathrm{cm}^{-2}\mathrm{s}^{-1}$ which corresponds to 140-200 interactions per bunch crossing at 25 ns bunch spacing [287]. The upgrade is based on the mentioned changes in the different (pre-)accelerator systems during the LS2 that aim for increased beam brightness by means of an two-fold increase of the number of protons per bunch while maintaining the beam emittance constant. The increased beam currents imply the need for an upgrade of the cryogenics system, the magnets in the interaction regions and matching sections, and to install a more powerful collimation system [288]. Further measures in the interaction regions during LS3 aim for a reduction of $\beta^{\star}$ by means of the installation of new quadrupoles in combination with "crab cavities" that compensate for the reduction in the geometric factor (F), cf. Equation 4.2. These introduce a transverse electric field in order to torque the beam and rotate the bunches such that they collide head on and with maximal overlap in the collision point. The high instantaneous luminosities reached at the HL-LHC also will make it necessary to limit the peak luminosity in order to restrict the energy deposition in the interaction region magnets and to limit the peak pile-up in the detectors. One key concept of the HL-LHC baseline therefore will be the implementation of luminosity levelling for the ATLAS and CMS experiments as already implemented at the LHCb experiment. The latter refers to procedures that limit the maximum instantaneous luminosity by intentionally detuning beam parameters (e.g. of the crab cavities) such that it is fixed to a predefined levelled maximum value over longer time by continuously retuning these parameters to compensate for protons lost in the collisions (proton burning) or an increase in the beam emittance. Other measures include the increase in the overall machine availability and hence efficiency by reducing the turn-around time between subsequent fills of the storage ring and a further consolidation of the quench protection system.

The higher statistics recorded are expected to permit measurements of higher precision within the Standard Model, i.e. enabling access to rare decay modes, Higgs couplings

to second generation fermions and Higgs self-couplings. Further it will allow to extend the mass reach for signatures of physics scenarios beyond the Standard Model that yet are not accessible at the LHC. For a detailed review of the envisaged physics capabilities and performance goals of the ATLAS detector at the HL-LHC see e.g. [289, 290]. The Phase-2 machine upgrades result in increased technical requirements for the experiments and inevitably lead to the exigency for upgrades of their detectors. Using the example of the ATLAS detector, the following section provides an overview of the demands and upgrade plans for a continuous operation at the HL-LHC. The impact on the performance of the ATLAS Inner Detector, the resulting requirements and their consequences for a future design of the ATLAS tracker will be discussed in Section F.2.1.

F.2. HL-LHC Upgrades of the ATLAS Detector

The higher particle fluxes and increased requirements on radiation hardness at the HL-LHC cause stringent technical requirements which can only be met by upgrades in different ATLAS sub-detectors. In addition, most of the current detector components and readout electronics will have reached a life-time of 15–20 years and demand for replacements. For those reasons the front- and back-end electronics of the LAr calorimeters are to be replaced. Further, upgrades in the trigger system impose higher demands on the processing speed and granularity of the EM calorimeter electronics than the present systems are capable to provide, despite the Phase-I upgrades discussed earlier. Since the average energy deposit and particle flux in the calorimeters would exceed the current design specifications by up to a factor of ten, further upgrades were proposed for the forward LAr detector systems. Similar reasons require a replacement of the on- and off-detector electronics of the hadronic (Tile) calorimeter which will be modularised and decreased in size. In addition, optional upgrades of the (cold) electronics of the hadronic endcap calorimeters are proposed. Substantially increased demands on the muon tracking and trigger system require the replacement of the MDT readout electronics. This will also allow to use the high-precision MDT information to assist the proposed track triggering. Further upgrades affect the RPC (barrel) and TGC (endcap) trigger chambers and their electronics that will have to be replaced in order to cope with higher demands on the spatial resolution in η.

Not least due to the fact that the performance of the current ID will be continuously degrading, a new ATLAS tracker must be designed and constructed for the operation at the future HL-LHC. Therefore the most extensive changes in layout and technology are needed in the ATLAS Inner Detector, which according to current planning will be replaced entirely by a new all-silicon tracker during the LS3. In addition to improved radiation hardness, the new tracker design must ensure a sufficiently low detector occupancy to guarantee good tracking performance in an environment of largely increased particle densities. A more detailed descriptions of the demands and consequences for its layout will be given in Section F.2.1.

The expected trigger rates and increased data volume at HL-LHC will exceed the capabilities of the present detector DAQ and trigger electronics in spite of the upgrades

performed during LS1 and LS2. In order to maintain the current trigger efficiencies for lepton p_{T} thresholds around 20-25 GeV and to increase the flexibility to adapt to new physics scenarios in view of potential future discoveries, an entirely new trigger architecture is developed. The new baseline trigger system consists of a hardware trigger part which is split into two subsequent trigger stages, Level-0 and Level-1, featuring a combined trigger rate of 200 kHz within a total latency of 20 μs. The new Level-0 trigger (L0) functionally replaces the current hardware (L1) trigger but features an increased accept rate of at least 500 kHz within a latency of 6 μs. The new Level-1 trigger subsequently reduces the rate to 200 kHz within the remaining 14 μs. Similar to the present design, the L0 trigger is used to predefine regions of interest based upon information from the EM and hadronic calorimeters and from the (upgraded) muon trigger systems. The information is brought together and processed in a central L0 trigger system which provides basic topological trigger capabilities at the earliest stage in the trigger chain in order to decide for the release of a L0 accept signal. The L0 trigger is then broadcast to the front-ends of the different detector subsystems that participate in the L1 decision in order to flag their data to be stored and be available to the subsequent trigger stage. When the L1 trigger stage is initiated upon a L0 accept, the readout of the full calorimeter information (L1Calo), track information of the ID within RoIs found at L0 (L1Track), and data from the MS (L1Muon) is triggered, including the additional information from the MDTs. The refined information of the three subsystems is again merged in a central (L1) trigger processor, based upon which the decision is made to issue a L1 accept signal using refined criteria applied to the event topologies. The L1 accept signals are distributed to all ATLAS detector subsystems and trigger the readout of their data for the HLT processing and final data acquisition. Similarly to the Phase-I L2 trigger design, software algorithms at a single HLT stage are used to select final events for readout at an anticipated rate of 5-10 kHz using objects reconstructed at almost the full final (offline) precision. Consequently the hardware and software of the HLT trigger farms require to be upgraded in order to cope with the increased L1 accept rate and significantly larger event sizes due to the increase in pile-up, while using more sophisticated algorithms that process larger amounts of information in order to reach a reduction in the event rate by a factor of 20-40. For the same reasons the DAQ systems of all sub-detectors will have to provide the capability to read out data at bandwidths at least four times higher than those available in Phase-I.

F.2.1. Inner Detector Upgrade for HL-LHC

The design of the new ATLAS ID is mainly driven by the aim to maintain or even improve its performance in the presence of the demands and constraints dictated by the HL-LHC environment. Similar to the current ATLAS tracker it should provide high precision transverse momentum and direction measurements of isolated particles in combination with information from the muon spectrometer, and good vertex resolution in order to distinguish between vertices of pile-up events and those originating from hard interactions. In particular the measurement of tracks and the identification of secondary vertices in highly boosted jets will put new challenges and requirements on the tracking

performance of the future tracker. Further requirements lie in the ability to identify tau lepton decays and their associated impact parameters as well as in the reconstruction of tracks originating from converted photons.

The large increase in particle multiplicity from overlapping inelastic proton-proton collisions will produce higher radiation damage in the detectors and their electronics. Commonly two different quantities are employed to express the expected radiation damage after a certain time of operation at a given instantaneous luminosity. The total ionising dose (TID), measured in Gray ($1\,\mathrm{Gy} = 1\,\mathrm{J/kg}$) expresses the energy loss of high-energetic particles due to direct ionisation processes in the material. It therefore mainly accounts for the radiation damage arising from photons, electrons and positrons in MOS[1] and bipolar devices that are used in the front-end electronics, e.g. from charges trapped in the gate oxides that impact the transistor threshold voltages. A second quantity is used to account for non-ionising energy losses (NIEL) that occur via displacements in the atomic lattice of a material. It is expressed in terms of a 1 MeV neutron equivalent (n_{eq}) fluence that describes the time integrated flux of arbitrary particles in terms of the equivalent integrated flux of neutrons of a defined incident energy (1 MeV) that is needed to produce approximately the same displacement damage in a given material (usually silicon). It hence is mostly used to quantify the expected bulk damage in semiconductor devices such as of the silicon sensors used in the Pixel and Si microstrip detectors. Their irradiation results in increased sensor leakage currents and hence noise present in the analog front-ends, larger overall power dissipation, and a larger bias voltage required to fully deplete the sensors. A detailed description of the processes and effects of radiation damage in semiconductor devices can be found e.g. in [291].

Figure F.1 illustrates the expected accumulated 1 MeV n_{eq} fluence for the ID region after an one year operation at nominal luminosity at the LHC, and after the full envisaged operation period at nominal luminosity at the HL-LHC. First comparisons of 2011 data and LHC simulations show good agreement between predicted and measured fluences and doses at a level of 30% or lower in the barrel regions [294]. Scaling the expected values shown in Figure F.1 by a factor of approximately 5×10^2 gives a rough estimate on the expected accumulated fluence after the full operation period of the LHC with an integrated luminosity of $300\,\mathrm{fb}^{-1}$. It then is evident that the values after the full operation period at the HL-LHC will have reached levels even up to a magnitude higher. A similar increase is expected for the total ionising dose in the ID region. The design specifications of the current ATLAS Pixel detector and SCT technologies do not fulfil the increased requirements on radiation hardness. Its sensors and electronics need to withstand a much harsher radiation environment with expected 1 MeV n_{eq} fluences up to $1.4 \times 10^{16}\,\mathrm{cm}^{-2}$ and a total ionising dose of 7.7 MGy for the innermost Pixel and up to $5 \times 10^{14}\,\mathrm{cm}^{-2}$ and 0.2 MGy for the innermost strip layers in the barrel region [293].

[1] Metal–oxide–semiconductor (MOS) structures consist of an insulation (e.g. SiO_2) layer with a metal or poly-silicon layer on its top, and both placed on a semiconductor substrate (e.g. Si). Thereby a planar capacitor is formed with can be used to control the charge distribution in the semiconductor by applying a voltage across the MOS structure. It is commonly used to control the conducting channel of field-effect transistors (MOSFETs) by placing the MOS capacitance (forming the gate) between two highly (oppositely) doped implants in the substrate (forming the drain and source).

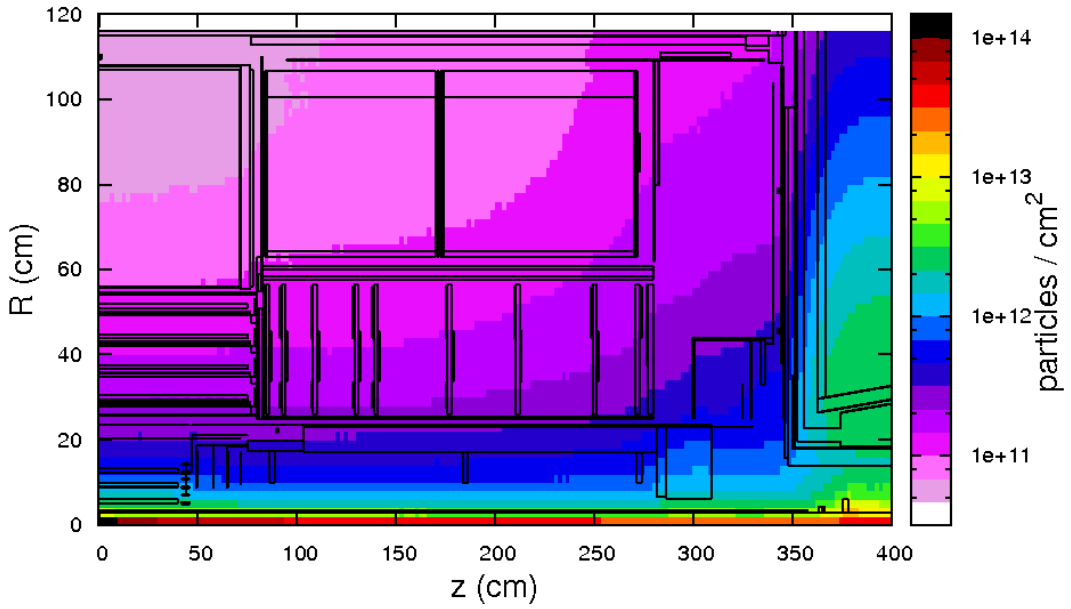

a)

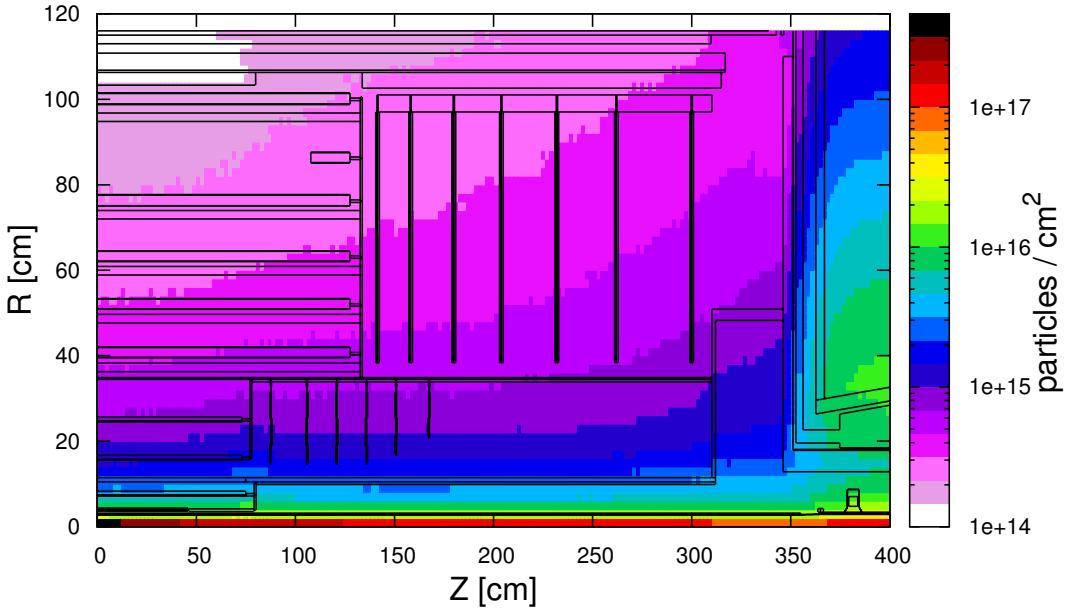

b)

Figure F.1.: 1 MeV n_{eq} fluences for the LHC ID region after an operation at nominal centre-of-mass energy and $\mathcal{L} = 1.3 \cdot 10^{34}\,\mathrm{cm}^{-2}\mathrm{s}^{-1}$ cumulating to an integrated luminosity of $1\,\mathrm{fb}^{-1}$ (a) [292], and for the HL-LHC ID region after reaching the full envisaged integrated luminosity of $3000\,\mathrm{fb}^{-1}$ at nominal energy in Phase-II (b) [293].

The current Pixel and SCT detectors however were only designed to withstand fluences up to 10^{15} 1 MeV $n_{\mathrm{eq}}\,\mathrm{cm}^{-2}$ and 2×10^{14} 1 MeV $n_{\mathrm{eq}}\,\mathrm{cm}^{-2}$, respectively.

With the higher instantaneous luminosity at the HL-LHC the number of pile-up events will raise from 23 interactions per bunch-crossing, as predicted for an operation at the LHC design luminosity, up to approximately 200 overlapping events per bunch-crossing at the HL-LHC [280]. Consequently the track multiplicities per rapidity unit are expected to raise to values > 1000, or even higher within the core of high-p_{T} jets. In the present tracker this would lead to an intolerable increase in occupancy and thus disallow to maintain the required tracking performance.

For the reasons above it is planned to replace the existing ATLAS ID by an overall new and improved tracker during the LS3 shutdown. Its design is mainly driven by the demand for increased radiation hardness and a higher granularity in order to enable it to distinguish tracks within an environment of extremely increased particle density. The current TRT will suffer from intolerable occupancy and won't be able to provide sufficient granularity which is why it is foreseen to be removed entirely. The future ATLAS tracker thus will be an entirely silicon-based system. The present baseline layout of the future tracker is shown in Figure F.2. Although details of the design are still subject to changes and optimisations, it provides an adequate overview of the current baseline layout. According to that, the innermost region is covered by pixel detectors, complemented with silicon microstrip detectors at intermediate and outer radii. Several alternative layout options have been proposed, details of which however are beyond the scope of this overview. More details of the baseline and alternative layouts currently investigated can be found in [280, 295–297].

In the baseline layout the barrel part of the new pixel detector consists of four layers extending from $R \sim 3.9\,\mathrm{cm}$ to a larger outer radius of $R \sim 25\,\mathrm{cm}$. The barrel part is complemented by six pixel detector disks in the forward region to provide more pixel hits in the very forward direction where particle densities are highest. To increase the modularity the innermost pixel layers in the barrel part will not be integrated with the beam pipe in order to be replaceable without its entire removal and breaking the beam pipe vacuum. For the same reason the outer barrel layers and discs are planned to be removable without the need for any intervention at the silicon microstrip detector. The Si microstrip detector is composed of three barrel layers of short strips ($\approx 2.4\,\mathrm{cm}$), followed by two layers of long strips ($\approx 4.8\,\mathrm{cm}$ in length) at larger outer active radii than presently are covered by the TRT, which allows to improve the overall momentum resolution. In the forward region the microstrip detector is composed of two endcaps consisting of seven strip disks each. The layout of this new all-silicon tracker allows to register particles within a large geometrical acceptance that covers a pseudo-rapidity range of $|\eta| = 2.5$, while ensuring at least 14 hits along a particle track in order to keep the number of misidentified or ambiguous tracks associated to a single particle constant with increased pile-up. In order to maintain the present tracking performance the granularity of the tracker is increased by a factor larger than four using sensors devices with smaller pixels (down to $25 \times 150\,\mu\mathrm{m}^2$) and shorter strips sizes at the inner layers. The overall number of channels in the Pixel and silicon strip detectors thereby increases to presumably 638 M and 74 M, respectively. At the same time the overall

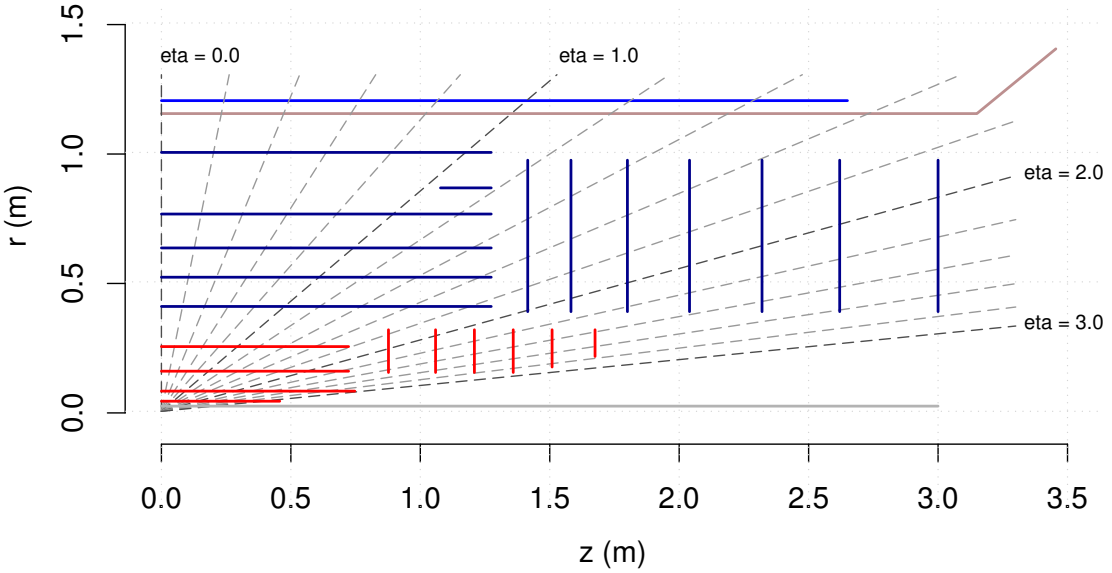

Figure F.2.: Proposed baseline layout of the ATLAS ID for the Phase-II [280] run. Shown is a projection of one quadrant of the ID in the r-z plane with the active cylinder and disk layers of the Pixel (red) and the silicon microstrip detectors (blue).

material budget of the tracker is reduced by nearly a factor of two which has the benefit of reduced tracking inefficiencies due to hadronic interactions, Bremsstrahlung effects and multiple scattering.

In conjunction with the increased channel count new front-end and back-end electronics will be required. The current readout electronics have been designed to cope with occupancies corresponding to 50 pile-up events at most, twice the design value of the LHC. With higher pile-up rates the electronics will suffer from bandwidth saturation in the on-detector electronics and optical links towards the off-detector readout drivers (RODs). This would lead to inefficiencies and data-losses in the Pixel detector and SCT for luminosities above $\mathcal{L} = 3 \cdot 10^{34}\,\mathrm{cm}^{-2}\mathrm{s}^{-1}$, i.e. rendering it impossible to resolve multiple near-by tracks passing single detector modules such as in the core of high-p_T jets.

F.2.2. Upgrade of the Silicon Microstrip Detector

Already during the construction phase of the current LHC efforts have been started and organised in several working groups in order to find and implement new technologies for sensors, readout electronics, mechanical supports and services for a future ATLAS silicon microstrip detector at the HL-LHC. The present baseline layout hence has been a result of over 10 years of development, nonetheless a rather short lead-time in sight of several years required to run mass-production, system tests and to prepare the integration of the final detector elements with a total silicon area of almost $200\,\mathrm{m}^2$.

The baseline design of the sub-detector follows the basic layout principle of the present SCT detector, i.e. consisting of a barrel part and endcaps to either side of the detector and covering a total of ±2.5 units in pseudorapidity. The barrel parts consists of five full length cylinders that extend up to ±1.3 m in z-direction along the beampipe. The innermost layer is placed at a radius of $r = 40.5$ cm with respect to the beam pipe centre, the outermost at $r = 100$ cm. A sixth long strip layer ("stub") has been added in the outer barrel part of the layout in order to avoid inefficiencies from lower hit-coverage in the barrel-endcap transition region, see Figure F.2. The two end-caps consist of seven disks extending from ±1.4 m to ±3 m in z-direction and from approx. ±0.4 m to ±1.0 m in r, leaving sufficient distance to the barrel part to allow for routing the services. The detailed positions of the different strip detector layers in the baseline layout are summarised in Table F.1.

Table F.1.: Positions of the different Si microstrip detector layers or disks and number of staves or petals per layer/disk in the present baseline layout for the Phase-II Upgrade of the ATLAS ID. [298]

Layer/Disk	barrel		endcaps	
	Position in r [mm]	Staves	Position in z [mm]	Petals
1	407	2×28	±1415	2×32
2	525	2×36	±1582	2×32
3	643	2×44	±1800	2×32
4	762	2×56	±2040	2×32
5	862	2×64 (stubs)	±2320	2×32
6	1000	2×72	±2620	2×32
7	—	—	±3000	2×32

The different layers and disks are composed of different substructures hosting multiple microstrip detector elements (modules). In the barrel part these are formed by 472 rectangular staves arranged in a turbine-like layout in lengthwise pairs of two units matched at $z = 0$. They are tilted by 10° along their long sides and are arranged in an overlapping manner along ϕ, see Figure F.3 (a). This way the detector stays hermetic for tracks with a p_{T} down to 1 GeV. The tilt angle is chosen such that the charge distribution between neighbouring strips due to the Lorentz drift of charge carriers in the bulk substrate of the Si microstrip sensors is minimised. The disks in the endcap region are formed by 224 trapezoidal petals. Two different layout options exist for the arrangement of 32 petals in each disk. The first, so-called turbofan option follows the layout of the barrel part with petals tilted by 13° along their long sides and arranged in a turbine-like and overlapping manner. The second, so-called castellated option refers to the placement of 16 petals side-by-side on each side of a disk. Both options are illustrated in Figure F.3 (b). Studies are currently ongoing to determine the optimal choice considering aspects of integrability and modularity, tracking performance and overall material budget.

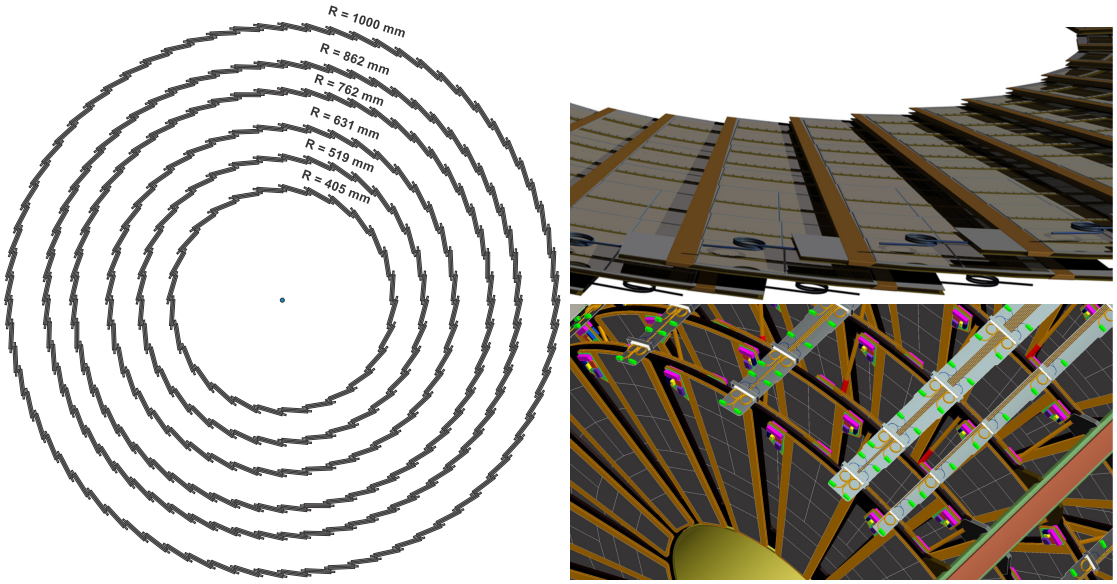

a) b)

Figure F.3.: View of the Si microstrip detector barrel part in the r-ϕ plane (a) and the endcaps (b) according to the current baseline layout for the HL-LHC. The endcap disks are composed of 32 petals in a turbine-like layout (top), or in a two-sided castellated layout (bottom). [280]

Stave Concept

The stave concept [299, 300] describes the placement of 13 single-sided silicon strip detector modules onto each facing of a common 1, 3 m long structure which provides electrical and optical services, cooling and mechanical support. The stave support itself consists of a lightweight rectangular sandwich structure made of carbon fibre laminates covering a spacing material made of carbon foam and carbon fibre honeycomb structures. The design is optimised for minimal material usage while providing high thermal conductivity and stiffness against gravitational sag. The present design of a stave consists of 26 modules (13 per side) and is shown conceptually in Figure F.4. A U-shaped cooling loop is embedded into the sandwich core and is surrounded by carbon foam, minimising the distance and hence temperature differences from coolant to the heat sources, i.e. sensors and front-end electronics on the modules. The integration of the cooling pipes leads to a further economisation of material and allows for higher coolant temperatures by reducing the cooling paths. A polyimide "bus" cable is glued onto each facing of the mechanical support structure. It provides the module services such as clock, command and data lines as well as power and sensor bias for each module. The data and power lines are concentrated in an extension at one end of the stave where an so-called End-Of-Stave or End-Of-Substructure (EoS) card resides that hosts components of the detector control system (DCS) and provides optical interconnects, buffers and HV multiplexers for powering and communication with the trigger system and the off-detector electronics.

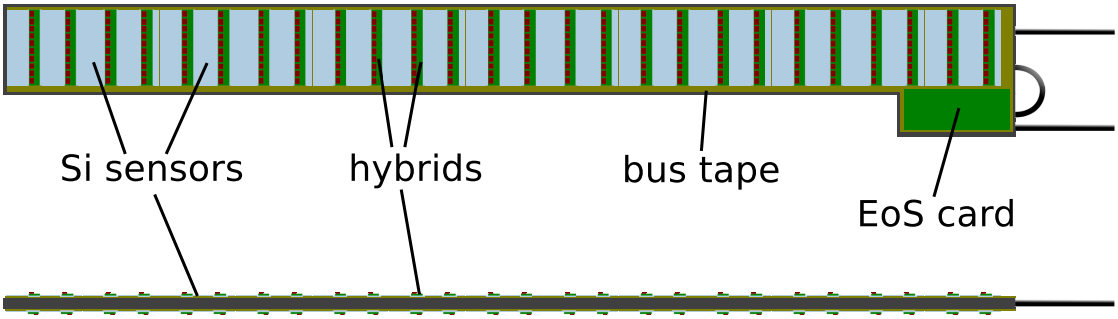

Figure F.4.: Conceptual layout of a stave structure populated with 13 Si strip detector modules on each facing as proposed for the ATLAS Si microstrip detector at the HL-LHC.

The fully assembled staves are mounted onto five support cylinders made of carbon fibre and reinforced plastic. The integration concept aims for allowing a lateral insertion and removal rather than a placement along the radial direction of the barrel cylinders which allows for easier and faster replacement of single staves during the last testing stages.

The Si microstrip detector modules are glued edge-to-edge on top of the bus cable on either side of the stave with a 200 μm spacing. Each module of a stave hosts a $97.54 \times 97.54\,\mathrm{mm}^2$ large Silicon microstrip sensor. Within the first three layers of the barrel part the sensors integrate four rows of 1280 strips, each 23.82 mm in length. At the outer two barrel layers sensors of similar size but longer strips of 47.755 mm organised in two rows are used. Figure F.5 shows a conceptual layout of a single-sided (short-strip) stave module as used in the inner three layers of the future Si microstrip tracker.

Two different options exist in order to provide an effective double-sided (stereo) measurement. In the first, strips at one half of the square-shaped sensor are rotated by

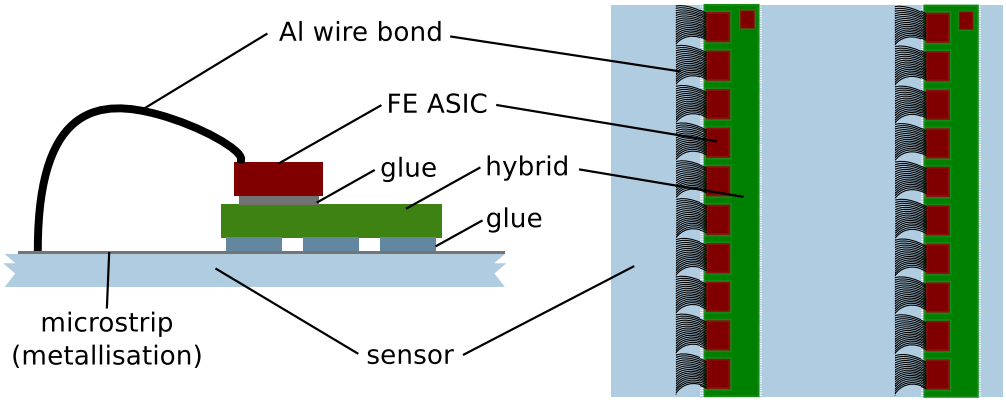

Figure F.5.: Conceptual layout of a single-sided module in the barrel part of the ATLAS Si microstrip detector at the HL-LHC - cross-section profile (left) and top view (right).

40 mrad and thereby provide a stereo-angle with the sensor glued on the opposite side of the stave. The second option is to use sensors with straight (axial) strips in the sensor layout, but rotating the sensors themselves on either or both sides of a stave, respectively. A more detailed description of the sensors and their properties is given in Section F.3.1. The optimal solution in terms of dead material or inactive strips and achievable precision of the positioning of the modules onto the polyimide sheet is currently under investigation.

Two substrate-less flex circuits (hybrids) are glued onto the sensitive side of the sensor, distributing data I/O and powering lines to a single column of ten ABC130 [301] readout ASICs glued on them. The ASICs provide 256 readout channels each, which are directly connected to the sensor strips via Al wire bonds. Hence each column of ASICs is used to read out two rows with 2×1280 microstrips on the sensor. As for the overall stave structure, the module design is optimised for minimised material, e.g. by using wire bonds for all off-circuit connections instead of connectors as implemented in the current SCT design.

Supermodule Concept

An alternative integration concept [302, 303] has been developed and is currently considered as a backup solution. The so-called Supermodule concept is akin to the substructure layout of the current SCT and describes the integration of double-sided silicon microstrip detector modules into a local support structure which itself is end-inserted into the overall support structure of the barrel. Two silicon sensors of the same type as used on

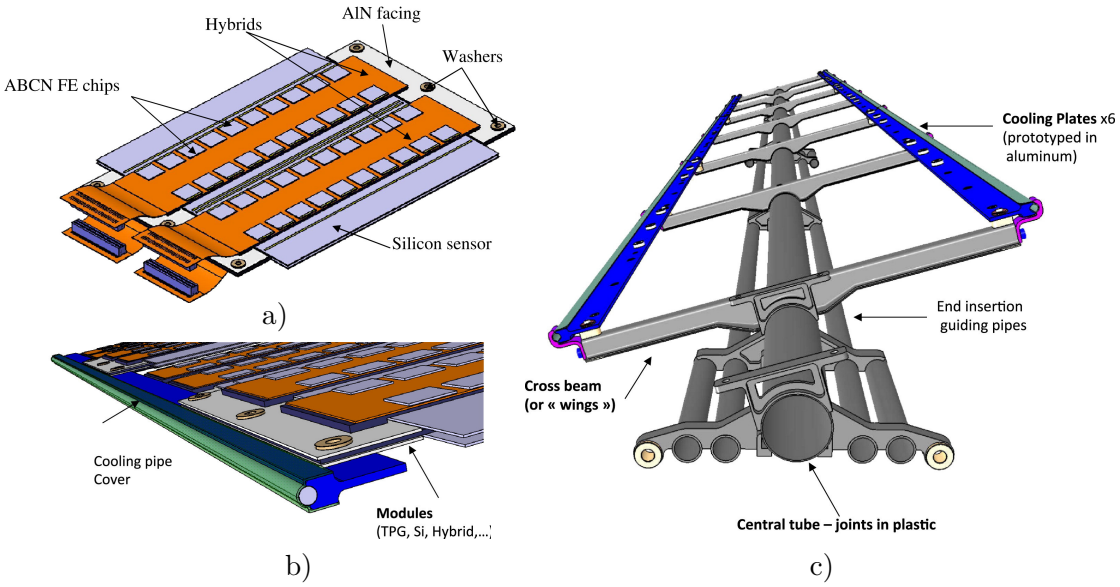

Figure F.6.: Schematic views of the different components of a double-sided microstrip detector module (a), and of the main components of a fully assembled Supermodule (b), including support and cooling structures (c) [302].

the single-sided (stave) modules are placed onto a central base-board made of thermal pyrolitical graphite (TPG) which provides mechanical stability and thermal contact, see Figure F.6 (a). Two flex hybrids on either side of a module host the readout ASICs and provide the necessary routing of power and signals. They themselves are glued onto a carbon-fibre bridge that is supported on Aluminium-Nitride (AlN) facings at both ends on the central base-board. Thereby any contact with the sensor readout (top) side is avoided. Thirteen double-sided modules are integrated into a single Supermodule, with the local support consisting of a central carbon fibre tube and attached cross-beam structures to support the modules as shown in Figure F.6 (b) and (c). Cooling plates are attached along the sides of the cross-beam structures to provide mechanical stiffness and thermal contact from the modules to cooling pipes residing at the lateral sides. The highly modular Supermodule approach provides mechanically independent subcomponents which is aimed to minimise mechanical stress and to ease the integration and potential rework of individual components at the latest stages in the assembly and testing process.

Endcaps

So-called petals are planned to form the basic substructure in the microstrip detector endcaps. In analogy to the generic layout of staves in the barrel region, a petal consists of an approximately 60 cm long trapezoidal, wedge-shaped support structure made of carbon fibre laminates covering a single U-shaped cooling pipe embedded in carbon foam and a carbon fibre honeycomb core. A total of nine silicon microstrip sensors are placed directly on the carbon fibre face-sheets on each petal side. The sensors are organised in six rings of which the three outermost ones are populated with two sensors placed side by side in ϕ direction, whereas the innermost three rings host single sensors, see Figure F.7. Akin to the stave modules, each sensor is equipped with a flex-circuit hybrid glued on top of its segmented side, holding the readout ASICs and providing the electrical lines for detector control, data transmission and powering. The microstrip sensors feature an axial strip layout pointing to the centre of the beam pipe on one side of the petal. The sensors on the back side are rotated by 40 mrad to provide an effective (double-sided) stereo space point measurement. A total of six different sensor geometries are needed in order to cover each facing without producing dead areas or unnecessary overlap at the petal edges. For the same reason up to 13 different hybrid layouts hosting different numbers of ABC130 ASICs are planned in order to match the different channel counts and geometries of the various sensors. In contrast to the stave layout, a polyimide bus tape is placed alongside the petal edges instead of covering the full surface underneath the sensors. A narrower bus tape is feasible since fewer modules and less than half the readout channels need to be powered and readout in comparison to a (short-strip) stave. Hence, placing a full-sized bus-tape on each facing would add unnecessary material and increase the thermal paths from the ASICs to the embedded cooling tubes. The bus tapes from one edge and from both facings of a petal connect to one of two EoS cards placed on either side of a square shaped extension at the top of the petal support structure. Each of the cards provides optical and electrical

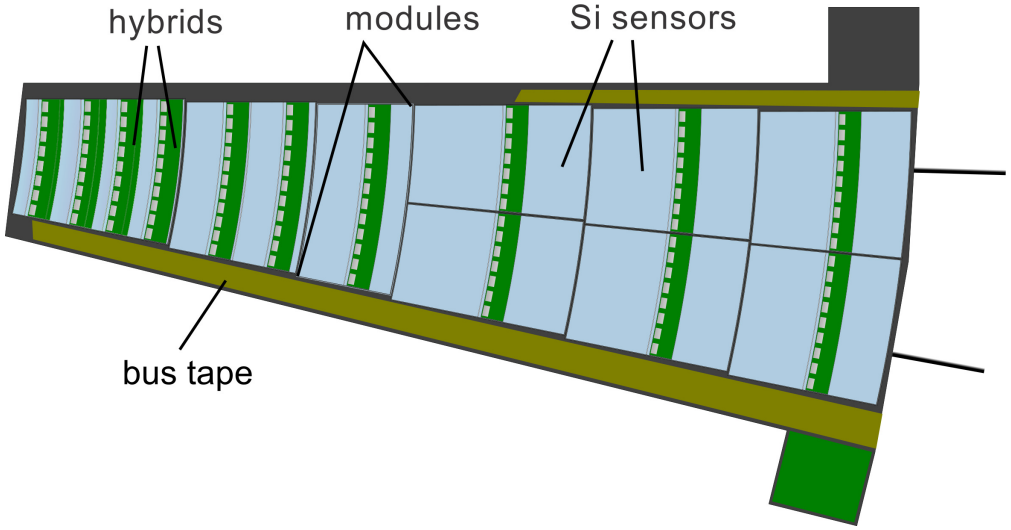

Figure F.7.: Conceptual layout of a petal structure in the endcaps populated with nine Si strip detectors on each facing as proposed for the ATLAS Si microstrip detector at the HL-LHC. Based on Figure 6.28b in [280]

interconnects for DCS, powering and data readout to the three upper right and three bottom sensors on the front side, and to the three upper left sensors of the backside of a petal, as seen from both facings respectively. The petals are mounted into an overall support structure forming seven disks from 32 petals each. They are held by an inner and outer support ring structure mostly made of carbon fibre which constitute an inner and outer cylindrical frame stabilised by three axial cross-structures (cf. Figure F.3). The outer cylinder in addition holds supports for service strains along the z-direction, each connecting to 14 petals of all subsequent disks of an endcap.

Front-end Electronics

To account for the increased channel count and the larger overall hit and trigger rates, the readout architecture of the silicon microstrip detector has to be renewed in order to provide higher bandwidths, additional trigger capabilities, but also increased radiation hardness of all associated hardware components. A detailed description of the future front-end electronics and trigger/readout architecture can be found e.g. in [280, 304]. An overview of their main characteristics and most important differences with respect to the present system is given in the following.

The smallest configurable electrical unit of the detector is built by the 130 nm CMOS readout ASICs (ABC130) residing on each hybrid. The ASICs implement a binary readout architecture which provides hit information of all strips in which charges above a defined threshold were deposited by ionising particles crossing the active sensor material. Each strip segment of a sensor is connected to one of 256 analog front-ends of a readout ASIC via Al wire bonds. The analog front-ends contain a charge sensitive preamplifier

and shaper that integrate the charge collected at the strip through a capacitive feedback loop and produce an output voltage equal to the charge present at its input. The preamplifier is followed by a discriminator with allows for setting a global threshold for amplitude discrimination of the amplifier output and individual threshold offsets per single front-end and hence trimming capabilities by configuring programmable digital-to-analog converters (DACs) in the ASICs. In the digital logic part of the ASIC the binary output of the discriminator is sampled at the raising edge of a central, globally distributed bunch crossing clock (BC) of 40 MHz, and then is stored in pipeline memory (`L0_Buffer`) upon receipt of a L0 trigger signal for further processing [304].

The implementation of the readout request from the newly introduced L0 hardware trigger system represents one key difference of the new ABC130 front-end ASIC with respect to its predecessor readout chip (ABCD [305]) used in the present SCT detector and manufactured in the radiation-hard 0.8 μm DMILL [306] technology. The L0 trigger signal is sent to all front-end ASICs at a maximum rate of 500 kHz. Alongside with the trigger signal an address for a region of interest (RoI) is generated which covers approximately 10% of the Inner Detector area. The ASICs first store all event data and meta information into the `L0_Buffer`, such as the corresponding bunch crossing ID (BCID) and a L0 counter value (L0ID). Upon the arrival of a L0 signal within a fixed but programmable latency ($\leq 6.4\,\mu$s) the event data are transferred from the end of the buffer pipeline into a random access memory (`R3L1_Buffer`), or otherwise are discarded. A schematic diagram of the different functional blocks of the ABC130 chip is given in Figure F.8. When an intermediate L1 RoI readout request (`R3`) is issued, the data from ASICs belonging to that RoI and associated to the L0ID of interest are read

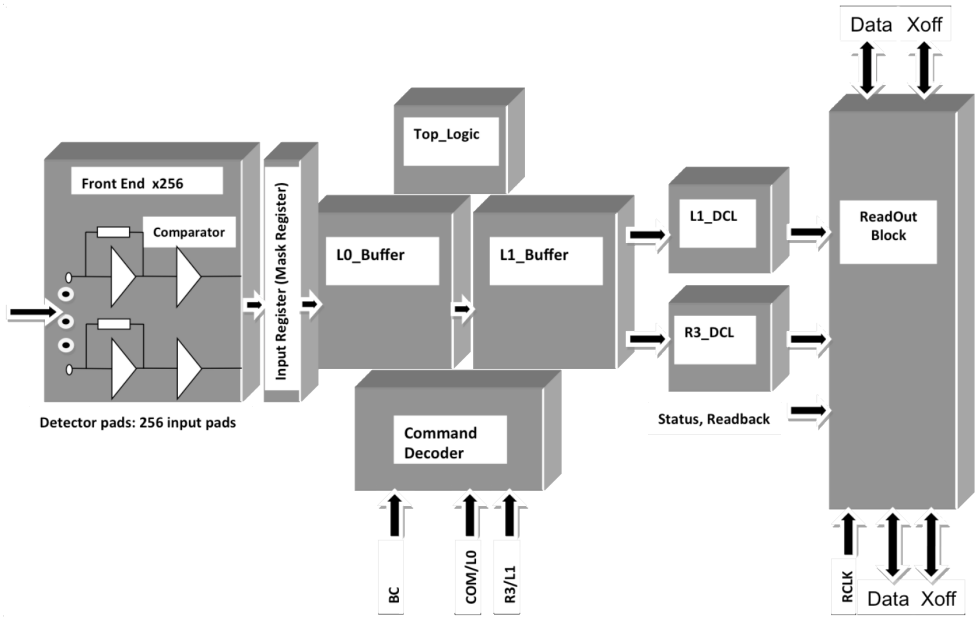

Figure F.8.: Block diagram of the ABC130 front-end ASIC. Based on Figure 3-1 in [301].

from the `R3L1_Buffer`. The data is subsequently processed by a special dedicated data compression logic (`R3_DCL`) to perform a fast zero suppression, cluster identification, and compression of the data in order to be transferred off the ASICs to the end of stave controller. From there they are sent further to the level-1 trigger electronics to assist in the decision whether to accept the full event for final readout by issuing a L1 accept signal (L1A) with an expected maximum rate of 200 kHz. Upon the arrival of the latter the data of the corresponding event is read from the `R3L1_Buffer` of all ASICs, processed by a different `L1_DCL` block and is sent off the modules to the readout system. The related off-detector electronics and services will be discussed in more detail in the next sections.

The hybrids are multi-layered substrate-less polyimide circuits optimised for a low material budget and equipped with passive components and circuits which interconnect the ASICs in a ring bus-like structure [299, 300]. They further provide lines for powering the chips, as well as for routing the control and trigger signals. In addition each hybrid contains a Hybrid Controller Chip (HCC) [304] with a unique address that builds the interface for data, trigger and control signals between the ASICs on each hybrid and the EoS card at the petal or stave periphery. Similar to the ABC130 ASIC the HCC is fabricated in a 130 nm process. It provides basic DCS information, such as on the hybrid temperatures and the sensor bias current. Further, it is used to de-serialise and multiplex the data from the readout ASICs in order to be sent over two line pairs on the bus tape to the EoS card using LVDS-like (Low Voltage Differential Signalling) techniques. On each hybrid, data from the ASICs are send off each chip through a

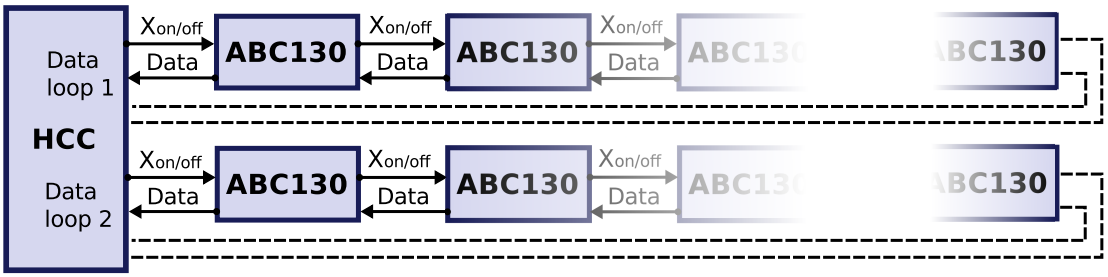

Figure F.9.: Schematic of the readout of a chain of ABC130 front-end ASIC.

readout block (cf. F.8) via two sets of bi-directional (differential) signal line pairs, either connecting to neighbouring chips arranged in a ring, or to the HCC itself in case of the first/last chip in a chain, see Figure F.9. The data readout is controlled via a Xon/Xoff flow-control mechanism and may occur in either direction of the serial chain of ABC130 ASICs. This way the readout can be configured to be split and occur from either side of the chain in case a malfunction in a single ASIC interrupts the readout path.

Upon receipt of a L1A or R3 readout request at a hybrid, the HCC redistributes the respective command to each ASIC via a bus of differential control line pairs terminated at each ABC130 ASIC on the hybrid. Upon its receipt the chips transfer the corresponding data to their readout block which compresses and formats the data in packets of 60 bits. The packets are transferred to a serialiser which sends them off at a configurable data

rate of 80 or 160 Mbs. According to the position in the chain different priorities are assigned to each chip, defining the order in which data packets from adjacent ASICs are passed through, or own data packets are sent off over the data line. The first chip in the chain has the highest priority (1) and immediately sends off its own data package upon arrival of a readout request. Subsequent ASICs in the chain obtain priorities of 2, 3, etc. which configures them to prioritise subsequent data packets for pass-through from the adjacent, the adjacent two, etc. ASICs before data pending from its own DCLs are send out [301]. The readout chips therefore exhibit several FIFO buffers to queue the packets from adjacent chips and their internal data until being forwarded to the readout block according to the configured priority. To prevent buffer overflows, the ASICs present an Xoff signal to the adjacent chip on a dedicated signal line pair to inhibit it from sending out a packet when the chip is not yet ready to forward data, i.e. when data from another queue is pending to be readout with higher priority or data is currently processed by the readout block and/or serialiser.

On the HCC side the incoming data packets from the ASICs need to be formatted into a single output stream in order to be sent off to the EoS and further off the detector. Arriving data packets therefore are further processed by an de-serialiser, multiplexer and encoder in the HCC. Each HCC sends data to the EoS receiver via a dedicated line pair using two redundant drivers connected in parallel to the data lines. Hence on a each stave facing 26 data line pairs need to be routed on the bus tape in order to read out all 13 modules of a single stave side. The layout for the petals will be mostly similar in spite of the different channel, ASIC and hybrid counts. The drivers operate at a data rate of 160 or 320 Mbps, hence allowing to readout two multiplexed 80 or 160 Mbps data streams of two chains of ASICs on a hybrid, interleaved with DCS data from the HCC itself [304]. Three other differential line pairs from the EoS connect to all HCCs on a single stave side in parallel. They are used to transmit command and control signals from the EoS side that are either interpreted as monitoring requests or configuration commands by the HCC of a matching HCC ID, or if unrecognised, are redistributed as required to the ASICs on the hybrid. They further provide the bunch crossing clock (40 MHz), as well as the L0, R3 and L1 trigger signals to the HCC and frond-end ASICs on each hybrid.

Services and Off-Detector Electronics

The aim for the HL-LHC upgrade of the ATLAS tracker is to provide a mostly common readout and control system for both the pixel and microstrip sub-detectors while maintaining compatibility with ATLAS wide standards and technologies. A block diagram of the key components of the data acquisition (DAQ) and detector control system (DCS) is shown in Figure F.10. The readout data, timing, trigger and most of the signalling for the DCS will be transmitted over the two individual optical fibres per stave or petal side. The EoS card hosts a respective number of GigaBit Transceivers (GBTs [307]) that build the interface from the HCC data lines to two optical drivers which send/receive the data to/from the off-detector DAQ and DCS system. However, a limited number of copper data lines connect to each EoS card in order to preserve an independent channel

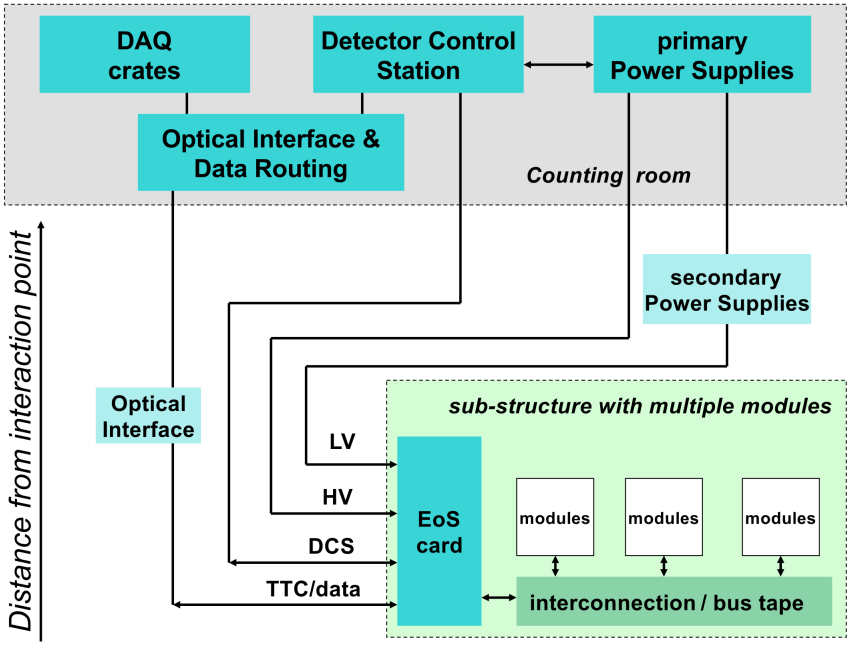

Figure F.10.: Block diagram of the proposed detector readout and control system of the ATLAS ID at the HL-LHC. [280].

for low-level DCS functionality such as interlocks and over-temperature protection.

The DCS provides all necessary control, monitoring and interlock functionality and is designed to be largely identical for both sub-detectors of the future ID. The interlock system itself is implemented purely in hardware, independent of the detector state and independent of the operational status of the DAQ system. A dedicated DCS chip resides on each EoS card to control the state of each module. Future implementations of the HCC are planned to provide information on temperature and humidity, voltage/current of the readout electronics and bias (leakage) current and voltage of the sensors. Since the DCS information from the HCC is send out in the same stream alongside with the module data, the interface for the optical fibres in the counting room splits the physics from DCS data and routes it to the respective subsystems (DAQ/DCS) [280].

The DAQ system processes the data from the pixel and microstrip detectors that are transmitted over 3196 optical links arriving at electronics in the counting room [304]. It is designed to allow for a readout of the microstrip detector at a rate of 200 kHz (500 kHz for L0) and a maximum rate of 500 kHz for the full readout of the pixel detector. It hence provides sufficient head-room for the data rates expected at the luminosities envisaged for the HL-LHC. Also the transmission rates on the fibres will be increased significantly in comparison to the 80 Mbit/s signalling speed used in the present ID. The link speed will be raised to 4.16 Gbits/s for the Si microstrip detector which corresponds to the data rate needed for the multiplexed transmission of all 26 160 Mbit/s data streams from the hybrids of a single stave side. Therefore new radiation hard optical fibres and

electronics based on modifications of well tested commercial components were developed in a common R&D project by the ATLAS and CMS collaborations [307]. Future versions of the optical interfaces currently are being optimised for lower power consumption and even increased link speeds of up to 9.6 Gbits/s. In summary, the services to and from each stave or petal consist of clock, trigger and control data signals sent over two optical fibres per petal/stave side; cooling tubes and dedicated copper lines for the low-level DCS signals; as well as additional low voltage (LV) and high voltage (HV) copper lines for providing power to the front-end electronics and the sensor bias voltage.

Although the new ATLAS ID will exhibit a significantly increased channel count, the total material per channel required for services will be reduced significantly due to the usage of high-bandwidth and multiplexing techniques, but also by sharing powering and sensor bias voltage lines among several modules, see Section F.2.2 for details. The services of each stave are routed along the outer cylinder of the endcaps in 16 or 32 axial runs (cf. Figure F.3) and connect to a series of patch panels outside of the active ID region and on platforms outside of the detector to provide interconnects for easy removal and maintenance of individual macro-components. Since larger parts of the present services cannot be removed or exchanged without major interventions at the muon spectrometer system, or would require prohibitively long work in a radiation environment, most of the existing services are planned to be reused for the future detector. While this is feasible for the LV, HV and DCS copper lines by using alternative powering schemes and HV multiplexing (see next Section), the current ID optical fibres do no permit the required high-speed transmission rates. They will need to be complemented by new, radiation hard graduated index multi-mode fibres. Lastly, the change towards a CO_2-based cooling system requires the installation of new insulated tubing of higher pressure rating [280].

Powering

Direct powering of each individual module via dedicated powering lines and individual power supplies as implemented in the present ATLAS tracker will lead to large inefficiencies and an intolerable increase in the number of service. Consequently an substantial increase in the demand on the cooling system and in the inactive material within the active volume of the future tracker would be imposed. Although the overall power consumption per channel will be reduced largely, for example by using new front-end ASICs produced in smaller manufacturing processes, the increase in the overall channel count largely over-compensates this effect. In the Si microstrip detector the estimated power consumption per channel (dominated by the front-end ASICs) will drop from currently $\sim 3.5\,\mathrm{mW/channel}$ down to $\sim 1.1\,\mathrm{mW/channel}$ [304], including the power consumption of the HCCs and the EoS card. However, the overall channel count will raise from presently 6.3 M to approximately 75 M. The estimated total power consumption of the strip detector will roughly threefold, with a total estimated power consumption of approximately 50 kW and 30 kW for the barrel and end-cap parts of the detector, respectively. Already due to the limited space for services in the Inner Detector an individual powering of the four times more modules will not be feasible. In addition, the new manufacturing processes used for the front-end ASICs implies lower operation voltages and an

increased overall current consumption of the front-end electronics. This will inevitably lead to higher resistive losses in the LV supply lines and bus tapes ($P_{\text{loss}} \propto I^2$), exceeding the power actually delivered to the tracker by up to a factor of five. In order to limit the power dissipation in the cables and retain an overall efficiency of the powering system which is comparable to that of the present SCT detector (∼60% [308]), alternative powering schemes will need to be implemented. Two different options currently are under investigation, a DC-DC conversion and a serial powering scheme [309] as illustrated in Figure F.11.

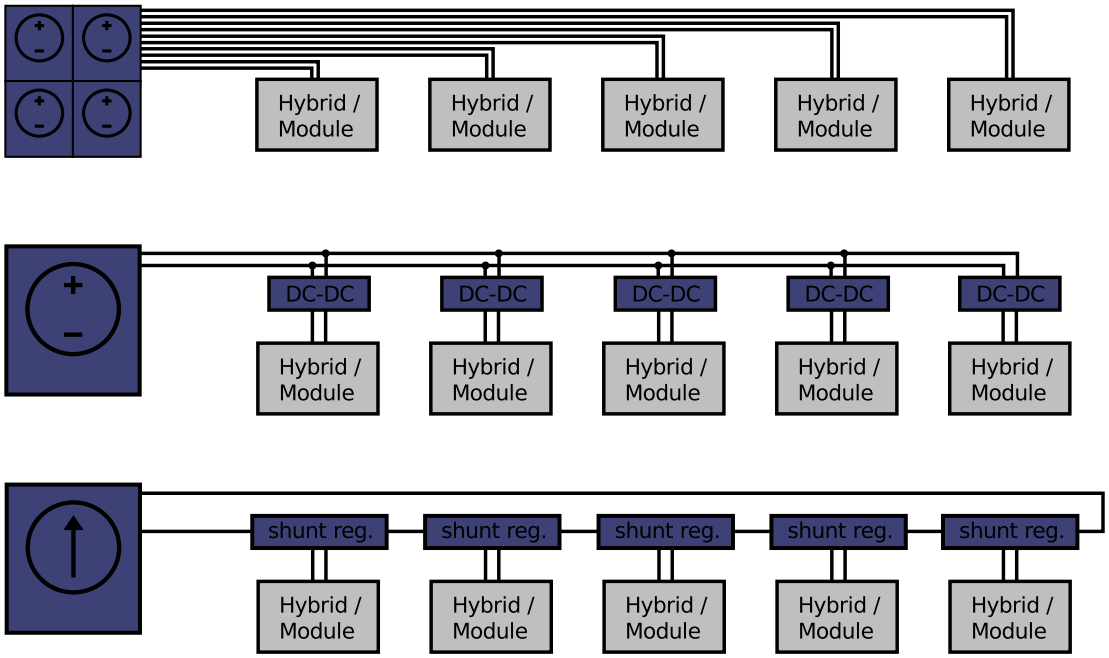

Figure F.11.: Schematic representation of different powering schemes: Independent powering of modules or hybrids using individual power supplies and supply lines (top), powering of several modules/hybrids in parallel at a higher voltage via a single constant voltage source with subsequent local DC-DC voltage conversion (centre), and powering of several modules/hybrids in a series via a single constant current source and local shunt regulators providing the final operation voltage.

In the case of DC-DC powering, current is transferred to the hybrids at higher voltage (≈ 10-12 V) over a single LV power line on the bus tape. The higher voltage then is converted locally down to the supply voltage required by the front-end ASICs using DC-DC converters residing on the bus tape next to each hybrid. Thus the current, the power losses and the mass/dimensions of the bus tapes and LV lines can be reduced significantly in comparison to an individual powering of each single hybrid or module. Custom radiation hard DC-DC converters currently are being developed [310] that will provide currents up to 4 A at a voltage step-down ratio of $r \approx$ 8-10.

In a serial powering scheme several individual hybrids are powered in series using a constant current source. Thereby the current and hence power losses on the services and bus tapes are reduced by "recycling" the current among the different loads. Shunt regulators provide a constant voltage drop across each load that corresponds to the supply voltage needed by the front-end ICs and the HCC. The regulators will be composed of two components, a dedicated serial power protection ASIC (SPP) [304] residing on the bus tape, which controls distributed shunt transistors integrated into each ABC130 ASIC on the hybrids via an analogue control signal generated in the external feedback loop. The SPP ASIC further provides fault protection capabilities in order to bypass individual modules. This is required to avoid an interruption of the chain and hence a blackout of a full stave side in case of malfunctions on individual modules. Since each hybrid is at a different potential with respect to the global ground, control and data lines have to be AC coupled. The voltage applied at the input of the serial chain and hence the voltage on the LV services is equal to the voltage required by each load multiplied by the number of loads powered in series (n). The minimal current that is required to be supplied on the line is defined by the hybrid with the highest power consumption in the chain.

Similar to both schemes are the advantages in terms of current reduction on the LV input lines and in the cable count when powering n hybrids or modules in parallel or in series. For example only a single LV line is planned to be used to power all modules on a single stave side – a reduction by a factor of 13 with respect to the present powering scheme. The total current that needs to be supplied to a stave in a serial powering scheme hence is reduced by the same factor. Likewise, in a DC-DC powering scheme the total current is reduced by a factor corresponding to the DC-DC voltage conversion ratio r. Under the assumption of fully efficient converters and regulators the power losses in the LV lines are reduced by a factor n or r^2/n, respectively. Since the current needed on the serial powering line is defined by the load with highest power consumption, in a petal layout with non-uniform module sizes it is defined by the module or hybrid hosting the largest number of front-end ICs. Hence for the end-caps a DC-DC powering scheme has been chosen as the baseline option since the efficiency in a serially powered petal is expected to be lower than for a serially powered chain of identical sensor modules, i.e. as given on a stave. For the barrel part the final choice for one of the schemes however will be based of future results of prototypes using the final ABC130 ASICs, SPPs and custom DC-DC converters. Apart from the overall powering efficiency and noise performance, the decision will rely on the detailed material budget and fault tolerance of each design.

As part of first efficiency estimates for powering petals in the future endcaps of the ATLAS microstrip detector, comparisons between different serial and DC-DC powering options were made. Calculations of the expected power consumption and powering efficiency were published e.g. in [304, 309]. The following estimates however are based upon more recent assumptions on the petal layout and the power consumption for the ABC130 front-end ASICs, the HCC and electronics on the EoS card as provided in [301, 304, 311] and summarised in Table F.2.

For the digital supply voltages a value of $V_{\mathrm{DDD}} = 1.2\,\mathrm{V}$ is assumed, equal to that for the analogue part of the ABC130 ASICs. Earlier variants based on lower digital

Table F.2.: Nominal DC supply currents and voltages of the different electrical components on a stave or petal. The values are based upon the assumption of nominal operating conditions and exclude additional loads from the regulators in the front-end ASICs. [301, 311]

	component / part	V_{in} [V]	I_{in} [mA]
ABCN130 front-end ASIC	analog (V_{DDA})	1.2	70
	digital (V_{DDD})	1.2	140
Hybrid control chip (HCC)		1.2	100
End-of-Substructure card	optical drivers	2.5	200
	EoS controller	1.2	1080
	DCS ASIC	1.2	50

voltages of $V_{\text{DDD}} = 0.9\,\text{V}$ were abandoned for reasons of higher single-event upset (SEU) sensitivity of the 130 nm CMOS process [304]. Due to the lack of final specifications or measurements of prototypes of the front-end ASICs and the HCC, the estimated power consumptions presented herein will likely to be subject to minor changes in the future. Similarly the final layout of the endcap sensors is currently under revision in order to optimise the strips length, pitch, angular distribution, and the overall sensor geometries for improved coverage and minimised material usage, occupancy, and potential hybrid design constraints imposed by the final ABC130 ASIC specifications.

The analogue and digital parts of the ABC130 ASIC can either be powered directly from an external voltage source (1.2 V) connected to dedicated power pins for both chip parts, or via two intermediate linear low drop-out (LDO) voltage regulators which derive the supply voltages for the analogue and digital circuitry from an external voltage source of up to 1.6 V (nominally 1.5 V). Consequently two different voltage conversion schemes are considered for estimating the overall efficiency of a DC-DC powered petal: the direct conversion of $\approx 10\,\text{V}$ applied on the bus tape down to the supply voltage of the ASICs in a single step, or a two-step conversion scheme with external DC-DC converters delivering 1.5 V to the ASICs and on-chip regulators deriving the final supply voltages on each ASIC. Both versions are illustrated in Figure F.12. The latter case has the advantage of providing higher immunity to potential differential mode noise created by the switching regulators used at the first conversion step. Table F.3 summarises the conversion efficiencies of the DC-DC converters taking into account the different conversion ratios needed in a single or two step conversion scheme. The values are based on the estimates and measurements of the latest custom DC-DC converter prototypes (AMIS5MP [312]) which shows efficiencies up to 82% for typical load conditions ($\approx 2\,\text{A}$) at an assumed output voltage of $V_{\text{out}} = 2.5\,\text{V}$ and a conversion ratio of four. However, an efficiency of 75% is assumed in the calculations to account for larger losses expected with the higher conversion ratios needed in order to provide the lower supply voltages of 1.2-1.5 V needed by the ABC130 ASICs. For the shunt regulator circuitry in the serial powering case usually an overall efficiency of 85% is assumed [304]. Similar to the DC-DC case, the voltage drop across the shunt regulators could be set to 1.2 V to power

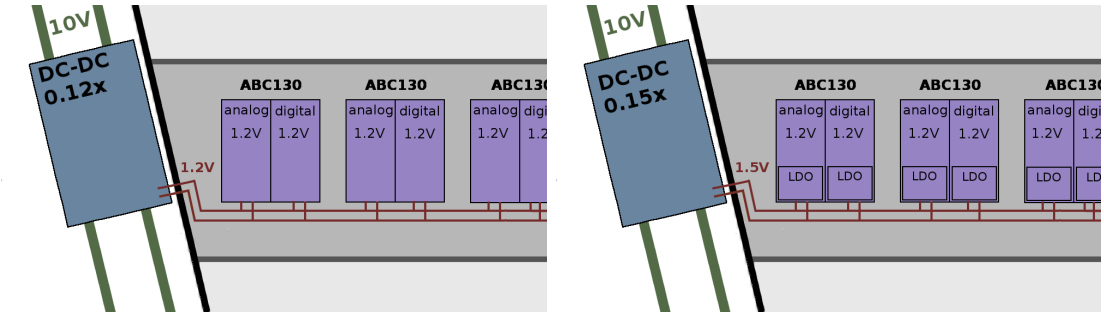

a) b)

Figure F.12.: Voltage conversion options for DC-DC powering scheme: Direct (single) step-down conversion of the supply voltage down to the ASIC operating voltage (1.2 V), and two-step conversion scheme (right) with external DC-DC converters delivering 1.5 V to the ASICs and on-chip linear regulators deriving the nominal operating voltage internally.

the analogue and digital parts of the front-end ASICs directly, or to 1.5 V when it is intended to use the internal linear voltage regulators for reasons of higher immunity to conductive noise. Based on the petal and stave layout given in [313] the total current and power consumption of a single-sided petal and stave are estimated and results detailed in Table F.4.

The total power dissipated on a single stave or petal side, provided the converter and shunt-regulator efficiencies given in Table F.3, are calculated for the DC-DC and serial powering options and for the one-step and two-step conversion schemes, respectively, see Table F.5. The calculations include rough estimates on the resistive losses on the bus tapes. Since final designs of these are currently ongoing, copper traces for the LV bus of 18 μm thickness were assumed for both, the bus tapes of petals and staves, whereas in the serial powering case a width of 5 mm (7 mm) throughout the full length of the tape of a stave (petal) is assumed. For the DC-DC powering case decreasing trace widths along the bus tape, approximately between 32 mm and 1 mm for staves, or between 11 mm (2 mm) and 0.5 mm (0.5 mm) for the bus tapes on the petal front (back) side are assumed, in accordance to recommendations of the IPC-2221/IPC-2223 standard (for a

Table F.3.: Estimated conversion efficiencies of the DC-DC converters, shunt and linear regulators, taking into account different conversion ratios in a single or two-step conversion scheme.

	V_{in} [V]	V_{out} [V]	conversion factor	estimated efficiency
DC-DC converter	10	1.5	0.15	75%
(AMIS5MP)		1.2	0.12	75%
linear regulator	1.5	1.2	0.80	80%
shunt regulator	1.5	1.2	0.80	85%

Table F.4.: Estimated current and power consumption of individual modules on a single stave and petal side and resulting total current/power consumption including peripheral electronics.

Stave (one side)	13 sensors												
Sensor (Module)	1	2	3	4	5	6	7	8	9	10	11	12	13
No. of strips / row	1280	1280	1280	1280	1280	1280	1280	1280	1280	1280	1280	1280	1280
Short strip rows	4	4	4	4	4	4	4	4	4	4	4	4	4
No. of hybrids	2	2	2	2	2	2	2	2	2	2	2	2	2
No. of ABCN13	20	20	20	20	20	20	20	20	20	20	20	20	20
I_{DDA} [mA]	1400	1400	1400	1400	1400	1400	1400	1400	1400	1400	1400	1400	1400
I_{DDD} [mA]	2800	2800	2800	2800	2800	2800	2800	2800	2800	2800	2800	2800	2800
Total power consumption for single-sided short strip stave (incl. EoS) [W]													68.9
Long strip rows	2	2	2	2	2	2	2	2	2	2	2	2	2
No. of hybrids	1	1	1	1	1	1	1	1	1	1	1	1	1
No. of ABCN13	10	10	10	10	10	10	10	10	10	10	10	10	10
I_{DDA} [mA]	700	700	700	700	700	700	700	700	700	700	700	700	700
I_{DDD} [mA]	1400	1400	1400	1400	1400	1400	1400	1400	1400	1400	1400	1400	1400
Total power consumption for single-sided long strip stave (incl. EoS) [W]													35.4

Petal (one side)	front side (6 sensors)						back side (3 sensors)		
Sensor	1		2	3	4-1	5-1	6-1	4-2	5-2	6-2
No of strip rows	8		4	2	2	2	2	2	2	2
No. of hybrids	4		2	1	1	1	1	1	1	1
No. of strips	2048	2304	2816	3072	1792	2048	2304	1792	2048	2304
Hybrid No.	1	2	5	7	8-1	9-1	10-1	8-2	9-2	10-2
No. of ABCN13	8	9	11	12	7	8	9	7	8	9
I_{DDA} [mA]	560	630	770	840	490	560	630	490	560	630
I_{DDD} [mA]	1120	1260	1540	1680	980	1120	1260	980	1120	1260
P_{total} [W]							24.9			6.4
Total power consumption for single-sided petal (incl. EoS) [W]										33.1

Table F.5.: Efficiency estimates for different powering schemes in the Si microstrip detector barrel (short strips) and endcaps. Also shown are the resulting current (I_{in}) and voltage (V_{in}) required to be applied at the end of stave/petal, and the resulting total power dissipation, including the power consumption of the EoS card and resistive losses in the bus tapes (P_{bus}).

	stave		petal		stave		petal	
	DC-DC	serial	DC-DC	serial	DC-DC	serial	DC-DC	serial
	1-step conversion scheme				2-step conversion scheme			
I_{in} [A]	9.4	2.6	4.4	3.1	11.7	2.6	5.5	3.1
V_{in} [V]	10	31.2	10	15.6	10	39	10	19.5
P_{bus} [W]	4.6	2.9	1.0	1.9	7.6	2.9	1.5	1.9
P_{tot} [W]	98.3	86.0	44.1	52.4	124.1	106.2	54.5	64.4
Efficiency	72%	82%	74%	63%	57%	66%	59%	51%

max. temperature increase of 10°C), respectively.

The estimated power consumption is roughly 10-20% higher than in previous estimates (e.g. [304, 309]), which is mostly driven by newer and more conservative assumptions on the ABC130 power requirements. In addition lower DC-DC conversion ratios and efficiencies are assumed in compliance with more recent recommended operating conditions and absolute maximum ratings of the custom DC-DC converters [312]. The total power dissipation nonetheless still lies well within the estimated budget of the cooling system and its safety margins, see next section. The power dissipation in the LV services towards the off-detector power supplies are not included in these calculations since their final layout and routing, and the feasibility of reusing existing cable plants of the present TRT/SCT detectors are still under revision. However, a rough estimate can be provided when assuming a total resistance of $R \approx 0.5\,\Omega$ for the LV lines powering each stave or petal, i.e. corresponding to a Cu cross-section of $d \approx 3.5\,\text{mm}$ as was assumed in past studies [309]. The additional power is dissipated partially inside and (to larger extend) outside of the active ID volume and amounts to $P_{\text{loss}} \approx 44\,\text{W}$ in the (1-step) DC-DC case, and to $P_{\text{loss}} \approx 4\,\text{W}$ in a serial powering scheme in the barrel region. In the endcaps these values are closer to each other, with $P_{\text{loss}} \approx 10\,\text{W}$ (DC-DC) and $P_{\text{loss}} \approx 5\,\text{W}$ (serial powering). The LV cabling hence has to be adapted to the respective powering option, optimised for acceptable voltage drops in particular along the cables reaching from the last patch panels beneath the outer endcap rings into the active ID volume ($\approx$ 2m). Consequently larger Cu cross-sections will be required for the DC-DC option. In the serial powering case, however, additional cable pairs are needed to individually power the EoS cards that are presently not intended to be included in the serial chain powering the modules.

In analogy to the LV power distribution, changes to the layout of the high-voltage (HV) supply for biasing the individual sensors in the modules on each petal or stave are indispensable. The limited space for additional services and for large amounts of traces on the bus tape prohibits each sensors to be biased via an individual HV line. Instead it is

planned to supply at least four sensors in parallel through a single HV bus on the bus tape which then connects to a single HV line towards the off-detector power supplies through the EoS card. To avoid several modules to be affected by malfunctions of individual sensors or connections (e.g. excessive leakage currents or shortcuts), radiation-hard HV switches are presently developed and planned to be placed on the EoS card to allow for disconnecting individual sensors via the DCS system. To even further reduce the HV cable count and hence inactive material in the tracker it is discussed to extend this scheme to bias all sensors on one side of a full stave or petal via a single HV line.

Cooling System

The total power consumption of a future ATLAS tracker at the HL-LHC is expected to raise from present values of $\approx 7\,\mathrm{kW}$ for the Pixel detector and $\approx 22\,\mathrm{kW}$ for the SCT to $\approx 12\,\mathrm{kW}$ and $\approx 75\,\mathrm{kW}$, respectively. These values do not include power losses in the cables and bus tapes, converters and peripheral electronics. Accounting for cooling losses or heat leakage through the IDs thermal enclosure, the total required cooling power in the tracking volume is expected to be approximately two times higher – currently estimated at 180 kW and hence roughly threefold with respect to the present value. In order to remove that large amount of power from the ID volume a novel cooling system based on a two-phase CO_2 cooling system and a coolant temperature of $-35°C$ is developed. The present implementation based on fluorocarbon cooling is kept as a backup. However, using liquid CO_2 brings the advantage of a larger heat transfer coefficient that allows for smaller cooling tube diameters and thus less inactive material in the tracker volume, easier handling, non-toxicity and lower mechanical forces due to thermal expansions. A similar CO_2 cooling system is implemented in the IBL and will provide crucial expertise for the future up-scaling of a similar system for the entire tracker.

The different components of pixel and microstrip modules and supports are already being optimised for such a design choice. The baseline layouts of staves and petals aim for low material and efficient thermal paths, i.e. by using small diameter Ti cooling pipes and sensors directly glued on the staves bus tape or carbon face sheet, making use of the full cross-sectional area of the module. The new cooling system transports the coolant at temperatures as low as $-40°C$ and therefore requires the installation of new insulated lines with higher pressure rating up to ≈ 100 bar. The cooling lines are multiplexed and connect to one inlet and one outlet tube per stave or petal, with the coolant boiling on the way through their core and leaving in a gaseous phase. Details on the proposed cooling system, including requirements, model calculations and initial layouts for a distribution scheme are given in [314]. The future cooling system presently is designed to provide a maximum total cooling power of 240 kW for the entire tracker and hence will provide sufficient safety margins to cope with fluctuations and ensure a safe operation of the ID.

F.3. Microstrip Detector Prototyping and Testing

As part of the research activities towards an upgrade of the ATLAS Si microstrip detector endcaps, various prototype stave modules have been fabricated and tested at DESY. The expertise gained therein forms the basis for first endcap module prototypes that are currently being developed, assembled and tested within an international community formed by a collaboration of presently six different institutions in Germany, Spain, Sweden, the Czech Republic and the Netherlands. The present goal is to develop and build a fully functional and full size petal prototype by 2014 and to optimise the associated simulation, fabrication and quality assurance techniques in preparation for a second prototyping phase and large scale production of detector components in the future. The prototyping of detector modules for both, the barrel and endcap region requires sophisticated infrastructure and tooling, readout systems and setups for sensor qualification and electrical testing, which were installed and continuously enhanced over the past years in the course of this PhD work.

Section F.3.2 provides an overview of the different components and assembly steps involved in the production of barrel module prototypes and introduces the necessary tooling where appropriate. However, before the actual module assembly, the microstrip sensors have to be tested for meeting the design specifications. Section F.3.1 therefore provides an overview of the functional principle and design on the future microstrip sensors using the example of present barrel sensor prototypes, as well as details on the different tests and associated measurement setups required for their electrical characterisation. The main steps of the electrical testing of hybrids and fully assembled modules as well as an overview on the associated DAQ test setup and software will be provided in Section F.3.3. A respective overview of the construction and testing of first prototypes of endcap detector modules is given in Section F.3.4, followed by a summary on the present status and plans for prototyping and testing of first macro-assemblies hosting multiple strip detector modules, see Section F.3.5.

F.3.1. Sensor Testing

Semiconductor detectors such as those based on silicon are used to measure the tracks of ionising particles by the generation of electron-hole pairs in the (depleted) bulk material at the time of the particles passage through the sensor, see Figure F.13. The silicon sensors therefore form a diode-like structure with a p-n-junction generated through doping one or both sides of the silicon bulk surface and/or the substrate itself with opposite type (p- and n-type) dopants. The generated electrons or holes can be collected at either (or both) sides of the sensor by applying a constant high (bias) voltage to the sensor. The latter on the one hand reverse biases the diode to create a depletion region in the bulk necessary to create quasi-free charge carriers and to prevent their recombination, and on the other hand generates the electric field causing the charge carriers to drift to either side of the sensor such that they can be collected and registered as a signal current at the sensor surface. Usually at least one side of the highly doped sensor surface is segmented to allow for a spatial resolution of the position at which the particle has passed

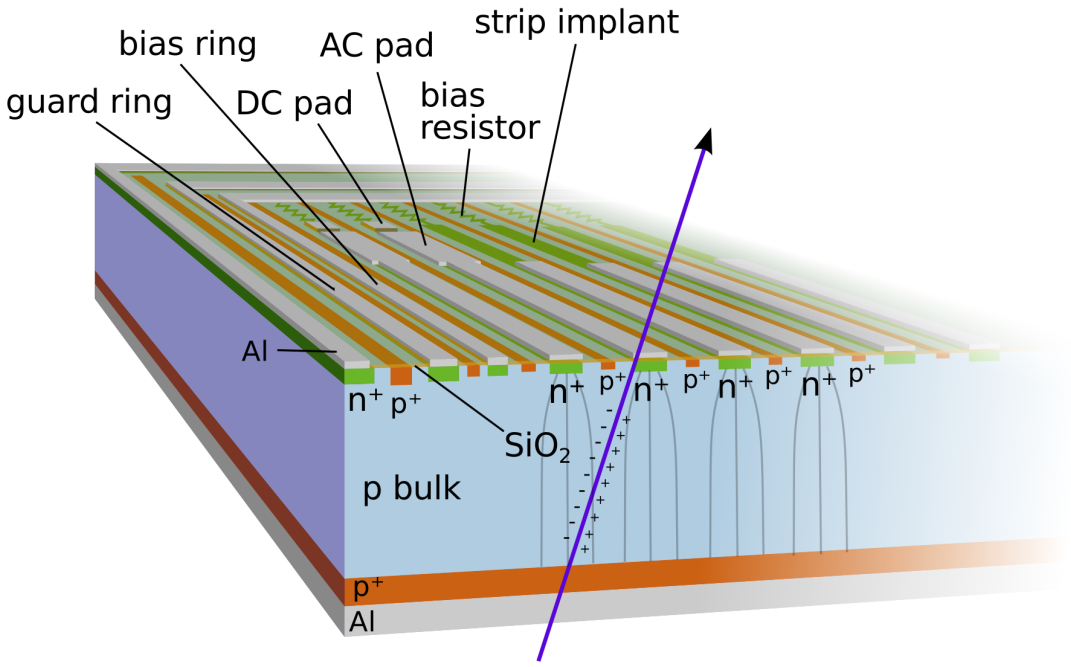

Figure F.13.: Illustration of the basic layout and principle of charge collection of a n-in-p type silicon microstrip sensor.

the sensor. In the case of silicon microstrip sensors this segmentation is performed in elongate strips of typically 50-100 μm width on the sensor top side while the sensor back side usually is left unsegmented, cf. Figure F.13.

In general three classes of sensor types are distinguished depending on the doping type and concentration of the bulk material and readout (strip) side. The most common are p-in-n type sensors which consist of a n-type sensor bulk with p-type strip implants, e.g. as used in the present ATLAS SCT. Their back side consists of a highly doped n-type layer usually fabricated by a simple diffusion process [315]. So-called n-in-n type sensors feature a weakly n-doped bulk and highly n^+-doped implants and are known to feature a higher radiation tolerance than p-in-n type sensors which is why this technology has been chosen for the present ATLAS Pixel detector. However, the latter requires a two-sided processing since the sensor back side requires an additional segmentation to incorporate isolation structures (guard rings) that isolate the readout from the back side at the sensor cutting edges. Lastly, n-in-p type sensors feature a p-type bulk and n-type implants and recently have become more prevalent with the availability of high-purity p-type silicon substrates.

Depending on the energy of a passing ionising particle, the sensor material and its thickness, typically $\mathcal{O}(10000)$ electron-hole pairs are created in the sensor bulk resulting in a relatively weak signal charge pulse of a few (tens of) nanoseconds that hence has to be amplified and converted into a signal voltage in order to be processed by the sub-

sequent readout electronics. Since the detector elements are high-impedance capacitive devices, the amplifiers are commonly built from operational amplifier integrators with a feedback capacitance and feedback resistor featuring a high-impedance input and low-impedance output, i.e. built from low-noise FETs in the first stage and low-impedance buffers driving an external (output) stage, see Figure F.14. These so-called charge sensi-

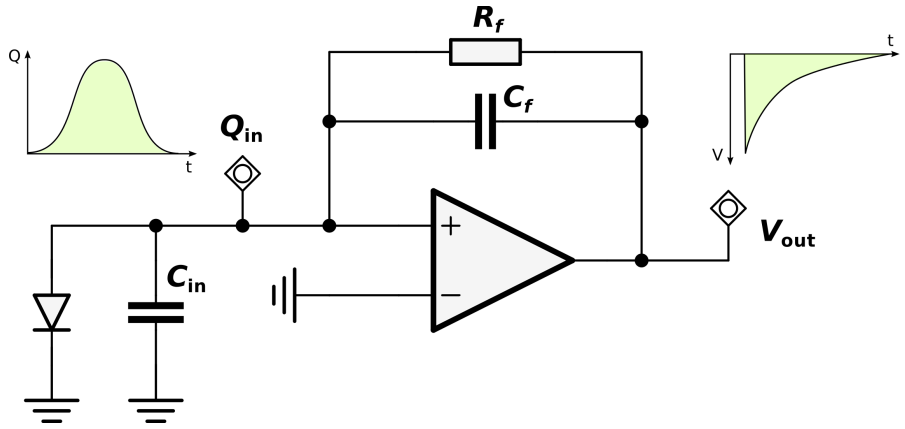

Figure F.14.: Illustration of the basic functional principle of a charge sensitive amplifier. A charge present at the input is integrated to the feedback capacitance which is constantly discharged by the feedback resistor resulting in an amplified voltage pulse (of opposite potential) at the output.

tive amplifiers integrate the charge pulses (Q_{in}) and convert them into voltage pulses (of opposite potential) at their output (V_{out}) by integrating the signal charge to the feedback capacitance (C_f) and the constant discharge of the latter by the feedback resistor (R_f) connected in parallel.

The detecting element of the future ATLAS microstrip detector modules consists of a n-in-p type silicon sensor. The choice for this technology is motivated by the higher radiation tolerance in comparison to the p-in-n type sensors presently used in the SCT. Their radiation hardness reaches levels comparable to that of n-in-n type sensors while being more cost efficient than the latter whose manufacturing requires a two-sided lithographic processing. Contrary to the commonly used p-in-n technology, no type-inversion[2] of the bulk material occurs due to the creation of effective acceptor states from exposure to large radiation doses. Consequently also after irradiation the depletion zone grows from the segmented (top) side which allows for an operation of partially depleted sensors, if required. Lastly, in p-in-n sensors electrons are collected to generate the signal at the strip implants as opposed to holes in p-in-n type sensors. This results in faster and more efficient charge collection due to the higher charge mobility and lower charge-trapping

[2] Type-inversion refers to the change in the effective doping concentration of the silicon bulk material from positive to negative values (space charge sign inversion). This effect occurs in p-in-n type sensors since radiation-induced defects predominantly manifest themselves in the form of additional deep acceptor like states (traps), while in p-type bulk materials the effective doping concentration is increased without causing any type-inversion.

efficiency of electrons in the substrate.

In case of single-sided stave modules a $97.54 \times 97.54\,\mathrm{mm}^2$ large silicon microstrip sensor fabricated on 6 inch (150 mm) p-type, float-zone silicon substrates (crystal orientation $\langle 100 \rangle$) are used, whereas in the endcaps sensors of similar technologies but six different geometries are presently under development. The barrel sensors used for the stave module production (ATLAS07 Series III a) were fabricated by Hamamatsu Photonics (HPK) [316], have a thickness of $\approx 320\,\mu$m and contain four rows of 1280 strips with a pitch of $74.5\,\mu$m, width of $16\,\mu$m and a length of 23.82 mm each. Two of the rows consists of axial strips, the other two of stereo strips inclined by 40 mrad. Figure F.15 (a) shows the respective mask layout of an ATLAS07 barrel type sensor. The single-sided n-type

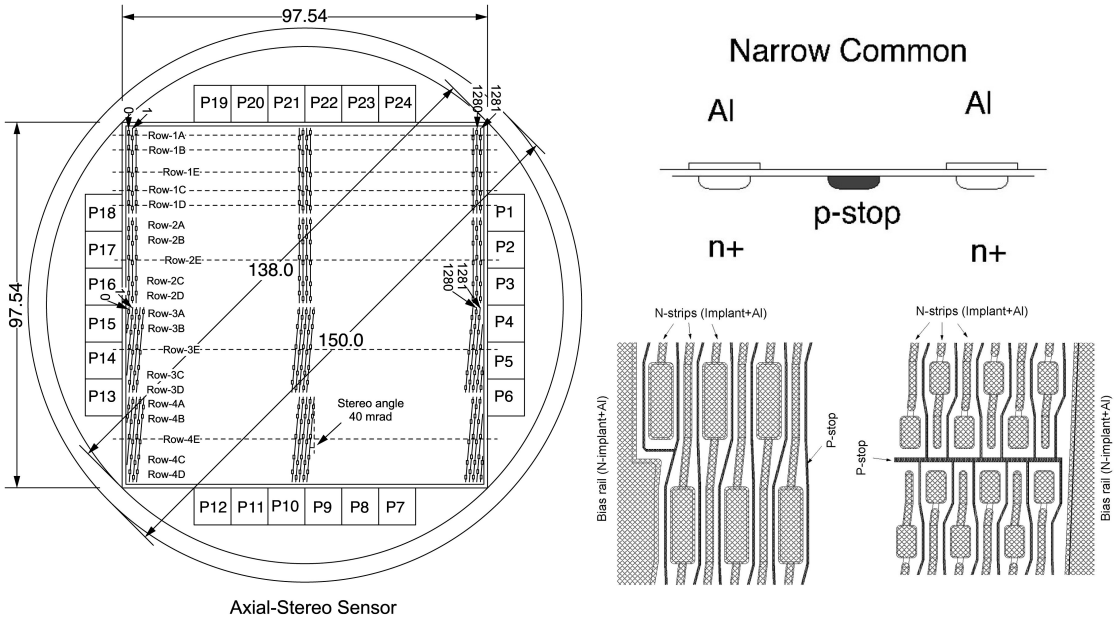

a) b)

Figure F.15.: Mask layout for the ATLAS07 barrel type sensor on a 150 mm wafer (a) and details on the p-stop structure layout (b). Apart from the central main sensor, several miniature sensors of $1 \times 1\,\mathrm{cm}^2$ are placed at the wafers periphery that are used for the qualification of different layout (p-stop and PTP) options and irradiation studies. [317]

strip implants are biased through a so-called bias ring that surrounds each strip row and connects to each strip implant through an individual poly-silicon resistor. The charge collected at each strip is read out via capacitively coupled metallisations on top of each strip, see Figure F.13. The metallisation layer of the sensor also provides several galvanically (DC) and capacitively (AC) coupled contact pads to each strip that are used for testing purposes and to wire bond each strip to a readout cell of the front-end ASICs. An additional outer single (floating) p-type guard ring structure protects the top layer strip implantations and bias ring from HV short-cuts at the sensor edges. An implication

Table F.6.: Comparison of design specifications and measured values of the different characteristics of ATLAS07 barrel Si microstrip sensors. [318]

Parameter	Specification	Measurement
Total leakage current $I_{\text{leak}}^{\text{bulk}}$	20 mA at 600 V	$210 - 450$ nA
Strip leakage current $I_{\text{leak}}^{\text{strip}}$	not specified	≤ 0.1 nA
Bulk capacitance C_{bulk}	not specified	1.13-1.21 nF
Full depletion voltage V_{depl}	≤ 500 V	$260 - 310$ V
Coupling capacitance (at 1 kHz) C_{coupl}	≥ 20 pF/cm	≥ 26 pF/cm
Silicon bias resistance R_{bias}	1.5 ± 0.5 M	~ 1.2 M
Inter-strip capacitance C_{int}	≤ 1.1 pF/cm	≤ 0.8 pF/cm
Inter-strip resistance per cm R_{int}	$\geq 10 \times R_{\text{bias}}$	≥ 200 G cm

of the n-in-p technology is the electron accumulation layer at the interface between the silicon and silicon oxide. To avoid potential shortcuts induced between neighbouring n-type implants additional p-type structures have to be introduced in between those. Two technologies are commonly employed, a "p-spray" isolation technique in which a distributed medium-dose p-implant covers the whole readout side, or additional highly p-doped "p-stop" structures surrounding each n-type implant as shown in Figure F.13. The latter technology is employed on the full-size ATLAS07 barrel sensors. Here all strip implants are surrounded by a common 6 μm wide p-implantation that isolates each strip from its neighbour and the bias ring, see Figure F.15 (b).

Before assembling the modules each sensor is tested for meeting its electrical design characteristics, in particular in terms of maximum bias voltage applicable and the resulting leakage current which impacts the overall noise performance of the detector. A summary of the full design specifications [318] of the current version of ATLAS Si microstrip barrel sensors (ATLAS07) and results of measurements performed in the course of manufacturing prototype barrel-type detector modules are given in Table F.6. The following subsections provide details on the measurement setup used for the electrical characterisation of a total of 10 barrel-type sensors as well as details on the procedure and exemplary results of each measurement performed.

Measurement Setup

In order to characterise the sensors, a semi-automatic probe station (CMicro PA200 [319]) is used to provide electrical contact between the sensor structures and the peripheral measurement instrumentation. The sensor is placed on a steel chuck that provides an electrical contact with its backplane. Bias (or guard) rings and the AC/DC contacting pads of single strip implants are contacted via needle probes. Attached to these are at least one lab power supply (Keithley 2410 [320]), e.g. to provide the sensor bias or additional test voltages, as well as Picoammeters (Keithley 6485 [321]), Capacitance (Agilent E4981A-001 [322]) or LCR-meters (Agilent 4263B [323]) required to measure the electrical properties of the whole sensor or single structures. All measurements are

performed at a temperature of 22°C and a humidity $\leq 5\%$, regulated by an integrated (dry) air chiller/heater system that keeps the chuck and the volume within a surrounding enclosure at a constant temperature during the measurement. Since the ATLAS07 sensor prototypes obey a floating single guard ring structure to prevent an avalanche breakdown at the sensor edges, no contact is required to bias the latter, i.e. as opposed to multiguard ring structures where the innermost ring in general is required to be biased to the same potential as the actual strip implants or bias ring to keep the leakage current of the inactive and active areas apart. Although in all measurements no such contact is made, in the following figures illustrating the different measurement setups also the connections to a potential "biased" guard ring are shown as dotted lines for the sake of generality.

Total Sensor and Single Strip Leakage Current

Before any other measurement is performed first all sensors are tested for meeting the design specifications for the maximum leakage current and the maximum bias voltage applicable before a break-down of the diode structure sets in. Therefore an increasing bias voltage (V_{bias}) is applied between the sensor back plane and a single probe contacting the bias ring, and the total leakage current is measured using a picoammeter placed in series, see Figure F.16 (a). At each voltage step the current is measured at least five times, starting after an initial delay of ten seconds and intermediate delays of three seconds between each measurement in order to prevent capacitive effects to influence the measurement. The mean value of the individual measurements at a certain voltage step then can be plotted against the bias voltage by which the so-called IV curve is obtained as shown in Figure F.17 (a). All tested sensors result to have absolute leakage

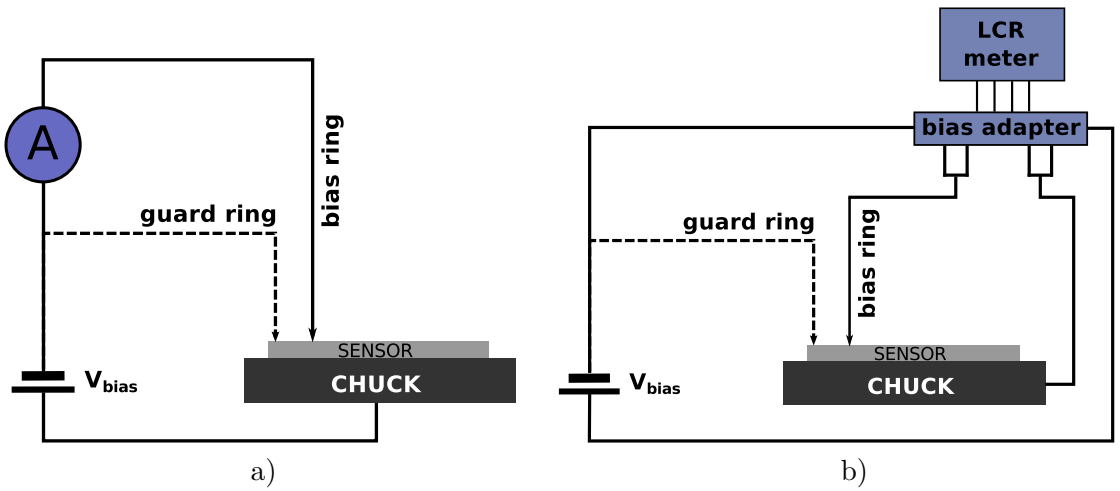

Figure F.16.: Measurement setup for determining the total sensor leakage current (a) and the total sensor bulk capacitance (b) as a function of the bias voltage.

currents far below the design specifications ($\leq 500\,\text{nA}$ at $V_{\text{bias}} = 600\,\text{V}$) and their IV

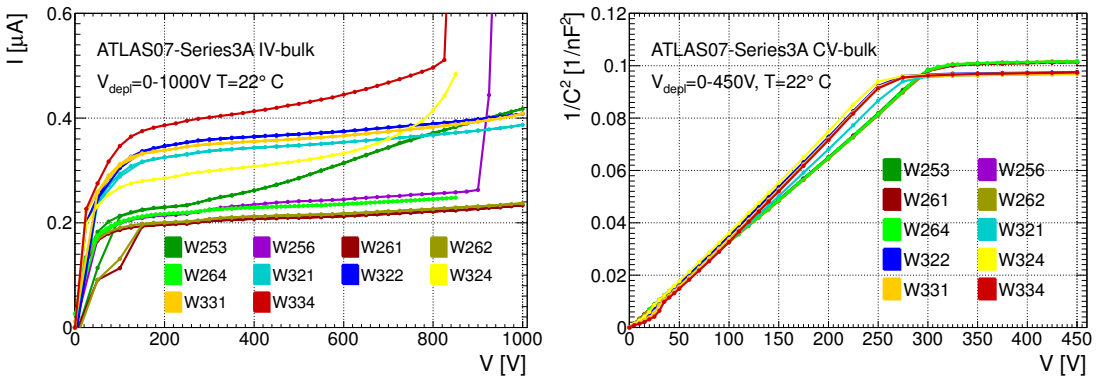

a) b)

Figure F.17.: Results of the total sensor leakage current vs. bias voltage (a) and of the (inverse square of the) total sensor bulk capacitance vs. bias voltage (b) for all tested ATLAS07 barrel sensor prototypes.

characteristics agree with earlier measurements performed by HPK and provided on data-sheets. All sensors can be biased with voltages as high as 800 V, with two sensors showing early onsets of micro-discharges or slow break-down (W234, W253). Two other show clear signs of a early break-down at $V_{\text{bias}} \sim 820\,\text{V}$ (W334) and $V_{\text{bias}} \sim 900\,\text{V}$ (W356).

Similar to the IV measurement of the full sensor, the leakage current of each single strip implant is measured with respect to the sensor back plane in order to test for inhomogeneities in the sensor bulk and its strip implants. In analogy to the former measurement, the sensor is biased by contacting a probe to the bias ring, but contacting an additional probe to the DC pad of a single strip implant and measuring the respective current to the common bias ring potential (ground). The measurement is repeated for each (n^{th}) strip of a sensor row respectively. An example of the results of a measurement of each tenth strip on an outer row of stereo-strips (Row4) of an ATLAS07 sensor is shown in Figure F.18 (a). It can be seen that all strips show uniform leakage with increasing bias voltage across the full sensor width. The remaining fluctuations most likely are caused by irreducible electrostatic interference usually associated with such high resistance or low current measurements.

Total Sensor and Single Strip Bulk Capacitance

The bulk capacitance between the sensor backplane and the bias ring (and hence strip implants) was measured in dependence of the bias voltage for all sensors. The resulting CV-curve allows to derive the minimum bias voltage needed to fully deplete the sensor across its full width. As soon as the depletion zone reaches the back plane of the sensor the decrease in capacitance with higher depletion voltage is reduced, since the depletion zone stops growing and the remaining CV-dependence is dominated by effects which can be expressed as an equivalent voltage dependence of the permittivity of the depleted

bulk material.

The bulk capacitance is measured using an LCR meter interfaced to an bias adapter which decouples the device from the high (bias) potential that otherwise would be applied to its terminals directly and thereby could damage the device. The LCR meter is connected to the back plane and bias ring of the sensor and the bias voltage is applied through the bias adaptor via the same terminals, see Figure F.16 (b). The measurement is performed at a frequency of 1 kHz, using the Cs/Rs configuration of the LCR-meter, and for increasing bias voltages of up to 450 V. Figure F.17 (b) shows the resulting CV-curves for all sensors. Plotted is the inverse bulk capacitance squared ($1/C^2$) vs. the applied bias voltage which allows to read off the full depletion voltage at the point where the linear extrapolations of both slopes cross, hence at the point where the slope suddenly decreases when the depletion zone stops growing. All tested sensors reach full depletion at bias voltages between $\approx$ 250-300 V, in compliance with the design specification that requires $V_{\text{depl}} \leq 500\,\text{V}$.

Similar to the measurement of the bulk capacitance, the capacitance of single strips with respect to the sensor backplane is measured. The test procedure hence is similar to the one before, but connecting the LCR meter to the back plane and a (DC) pad of a single strip instead of the full bias ring. The bias voltage is simultaneously applied to the bias ring and to the bias adaptor. The measurement is performed at a frequency of 1 MHz to account for the lower capacitance values, using the Cp/Rp configuration of the LCR-meter, and for bias voltages of up to 450 V. Figure F.18 (b) shows the resulting CV-curves for each tenth strip of a single row of a sensor. Plotted is the single strip capacitance vs. the bias voltage which shows an overall uniform distribution with capacitances lying within 0.7-0.8 pF/cm after reaching full depletion voltage.

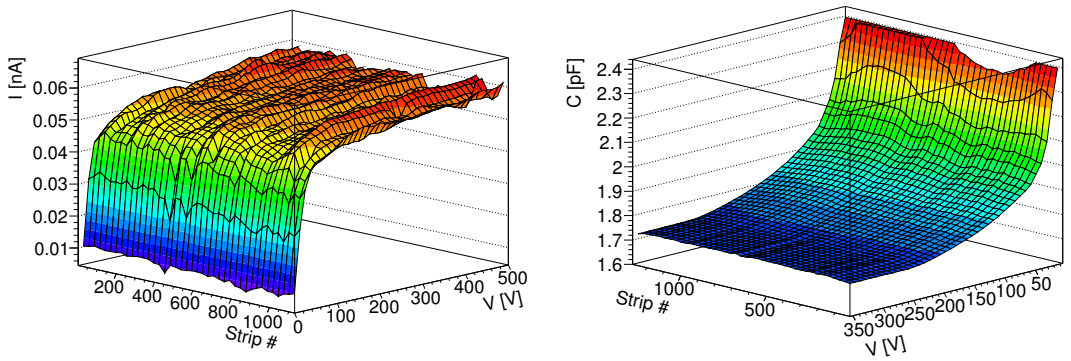

a) b)

Figure F.18.: Exemplary result of a single strip leakage current vs. bias voltage measurement (a) and of the single strip capacitance wrt. the backplane vs. bias voltage (b) for a single strip row of an ATLAS07 barrel sensor prototype.

Inter-Strip Capacitance

The inter-strip capacitance represents the dominant contribution to the total input capacitance at each readout cell of the front-end ASICs. The input capacitance (C_{in}) determines the noise gain ($\propto C_{\text{in}}^2$) of the frequency-independent thermal noise component at the first-stage FET in the charge sensitive amplifier and hence determines a large part of the total noise level of the readout signal. The inter-strip capacitance therefore in general is kept as low as possible.

In order to measure the inter-strip capacitance, two different methods have been defined. In the so-called 3-probe method the capacitance is measured between a central strip implant and the two closest adjacent strips, while all remaining strips are left floating, see Figure F.19 (left). In the second, so-called 5-probe method, two additional

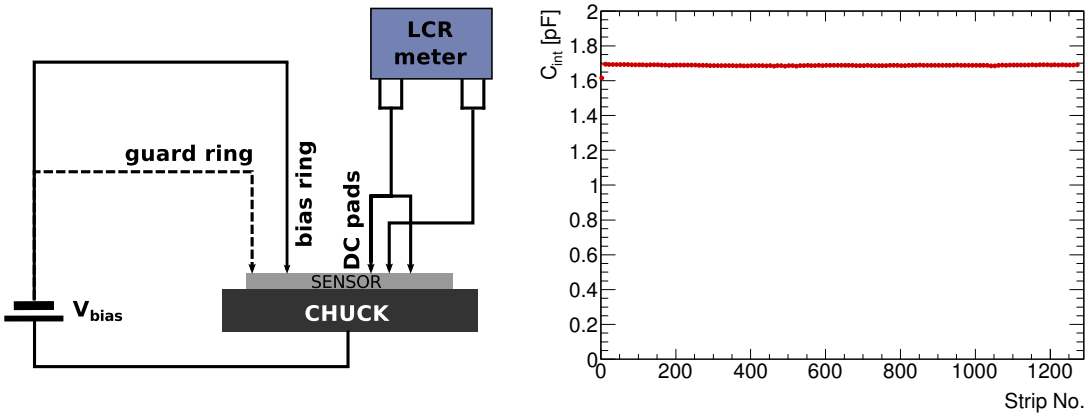

Figure F.19.: Measurement setup (left) and exemplary result of an inter-strip capacitance measurement on a single strip row of an ATLAS07 barrel sensor prototype (right).

probes connect the next-nearest two neighbour strips to ground in order to provide an effective shielding usually resulting in more precise results. However their dependency on the measurement method and test frequency usually lies within 10% [324]. The test frequency is set to 100 kHz or 1 MHz, and using the Cp/Rp LCR-meter configuration, respectively. Figure F.19 (right) shows an example of the results from a (3-probe) inter-strip capacitance measurement on a single strip row of an ATLAS07 barrel sensor at a bias voltage of 300 V. The values lie within 1.6-1.7 pF per strip, hence within 0.67-0.72 pF/cm, which is in agreement with the specifications that require less than 1.1 pF/cm at 100 kHz test frequency using the 3-probe method.

Coupling Capacitance

The coupling capacitance provides information on potential strip defects, such as openings or shorts in the metallisation layer between adjacent strips or shortcuts of the strip implants themselves. The coupling capacitance is measured between the strip metal

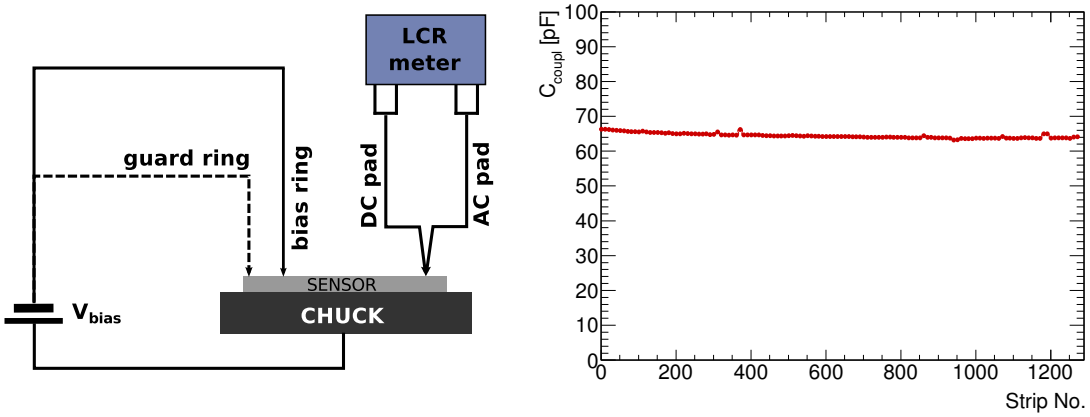

Figure F.20.: Measurement setup (left) and exemplary result of a coupling capacitance measurement of an ATLAS07 barrel sensor prototype (right).

layer and the strip implant by contacting the terminals of the LCR-meter via probes on the AC and DC pads of a single strip, see Figure F.20 (left). The bias voltage is applied between backplane and guard ring as usual and is set to 300 V to ensure full depletion. The measurement is performed at a test frequency of 1 kHz and using the Cs/Rs configuration of the LCR-meter. Figure F.20 (right) shows exemplary results of the coupling capacitance as a function of the strip number for a single row of an ATLAS07 barrel sensor prototype. The measured values are larger than 63 pF per strip ($\geq$ 26 pF/cm) and hence meet the specified limit of $C_{\text{coupl}} \geq 20\,\text{pF/cm}$.

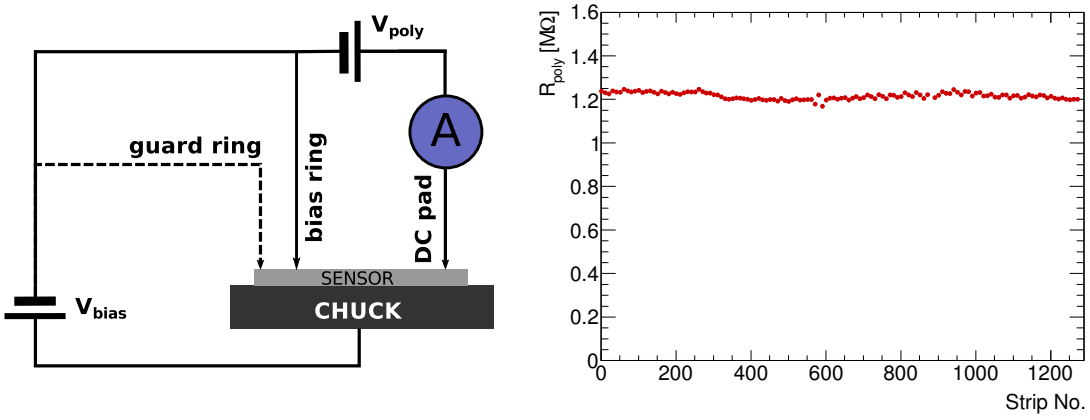

Figure F.21.: Measurement setup (left) and exemplary result of a bias resistance measurement for an single strip row of an ATLAS07 barrel sensor prototype (right).

Bias Resistance

Potential defects in the bias resistors can be identified by measurements of the IV-characteristics of the conducting path between the strip implant and the bias ring.

The bias resistance is measured directly by applying small voltages ($-5\,\mathrm{V} \leq V_{\mathrm{poly}} \leq +5\,\mathrm{V}$) in several steps (1V) to the DC pad of a single strip via an additional voltage source. The ground terminal of the voltage source is interconnected to the respective terminal of the source providing the voltage at the bias ring, see Figure F.21 (left). The resulting current between the strip implant and the guard ring is measured for each voltage step on the fully depleted sensor ($V_{\mathrm{bias}} = 300\,\mathrm{V}$). The resulting IV-dependence is then fit with a linear function to extract the bias resistance (R_{bias}). Figure F.21 (left) shows exemplary results of the bias resistance measurement for a single strip row of a barrel sensor prototype. All values lie within $1.16\,\mathrm{M} \leq R_{\mathrm{bias}} \leq 1.26\,\mathrm{M}$, which complies with the design specifications of $R_{\mathrm{bias}} = 1.5 \pm 0.5\,\mathrm{M}$ and agrees with earlier measurements performed by HPK after manufacturing that are provided on data-sheets.

Inter-Strip Resistance

The inter-strip resistance provides information on the homogeneity of the p-stop implantations isolating each strip from neighbouring strips and the bias ring. The measurement procedure is akin to that of the bias resistance measurement, but with the additional voltage of $-5\,\mathrm{V} \leq V_{\mathrm{int}} \leq +5\,\mathrm{V}$ applied in steps of 1 V between the DC pads of a single strip and one of its nearest neighbours, see Figure F.22 (left). The current at the outer strips (I_{meas}) is measured to avoid the current through the bias resistor (of much lower R) to the guard ring to spoil the measurement. The inter-strip resistance is then calculated from the slope of the measured IV-dependence $R_{\mathrm{int}} = \Delta V_{\mathrm{int}} / \Delta I_{\mathrm{meas}}$. Figure F.22 (right) shows exemplary results of an inter-strip resistance measurement on a

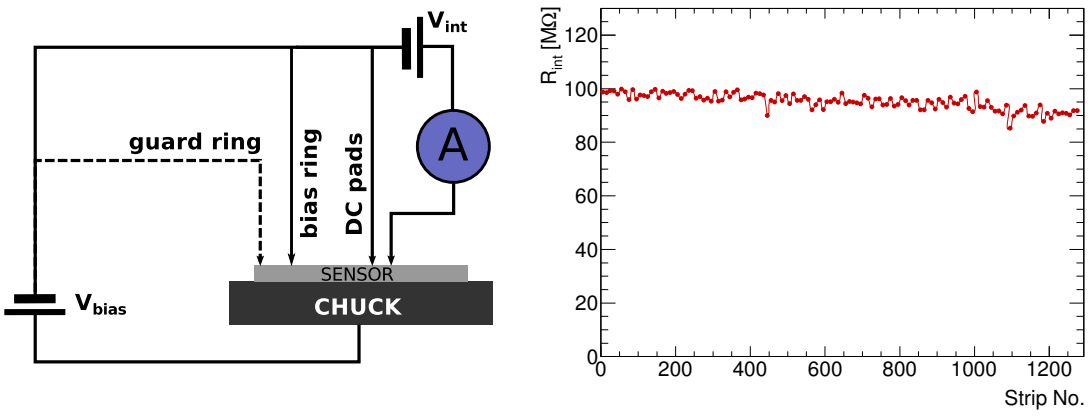

Figure F.22.: Measurement setup (left) and exemplary result of an inter-strip resistance measurement for a single strip row of an ATLAS07 barrel sensor prototype (right).

single row of an ATLAS07 barrel sensor prototype. The residual slope can be explained by the high sensitivity to small temperature (humidity) fluctuations given the small currents of $\mathcal{O}(10\,\mathrm{pA})$ being measured. Also surface charging effects at the insulating (SiO_2) layer could contribute to such a time dependence, in particular when biasing the sensor in low humidity environments as is provided here, see e.g. [325]. The obtained values lie within 200-240 $\mathrm{G}\cdot\mathrm{cm}$, which is in accordance with the specifications requiring $R_{\mathrm{int}} \geq 10 \times R_{\mathrm{bias}} \approx 15\mathrm{G}$.

F.3.2. Stave Module Assembly

Despite of their different geometries, the steps involved in the assembly and testing of prototype stave and petal microstrip detector modules are very similar. Apart from different tooling needed for both types, the construction and testing procedures of a module commonly consist of the following steps:

1. Glueing of readout ASICs onto hybrids,
2. Wire bonding of ASICs to hybrids,
3. Electrical testing of hybrids,
4. Quality tests of sensors,
5. Glueing of hybrids onto sensors,
6. Wire bonding of ASIC readout cells to single strips on the sensors, and
7. Final electrical (mechanical) testing of the module.

To date all module prototyping has been done using the ABC250 front-end ASICs, a 250 nm CMOS successor to the ABCD chip that is used in the present ATLAS SCT. In opposite to the final ABC130 readout ASIC [301] it is manufactured in a 250 nm process, features only 128 readout channels and does not yet provide the extended trigger (i.e. L0,L1/R3), readout and bandwidth capabilities implemented in the final version. However, at the time of writing a first submission of the new ABC130 prototypes has been finished and first batches of the new ASICs are already under testing. The final ABC130 readout ASIC [301] will feature 256 readout channels per ASIC and hence will be used to read out strips from two adjacent sensor rows from a single hybrid in the final design in order to save mass and reduce the overall power consumption.

Likewise the hybrids underwent several design changes and improvements over the past years in order to minimise their material usage in particular. While first versions of barrel-type hybrids are manufactured in a five-layered layout in a (polyimide) substrate-less flex-circuit technology [299] and host two columns of ten ABC250 front-end ASICs each, more recent versions feature a four-layered (shield-less) layout. The final versions are planned to have only three metal-layer layers and to host a single column of ten ABCN130 readout ASICs each, which will significantly reduce the overall hybrid size and associated material [313].

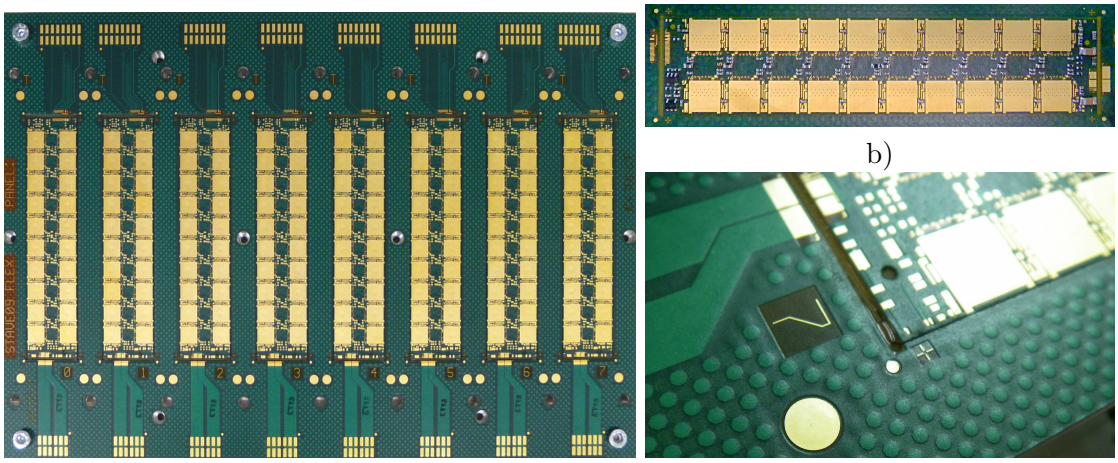

a) b) c)

Figure F.23.: View of an (unpopulated) panel with eight barrel-type hybrids (a). Each individual circuit (b) is laser cut on on its four sides except for four cut-out tabs at the long ends (c), retaining each hybrid in its position on the panel.

Glueing and Wire-bonding of Readout ASICs on Hybrids

The flex hybrids are produced on a selectively laminated FR4 panel hosting eight laser-cut units, see Figure F.23. The carrier serves as a temporary substrate during the manufacturing process, i.e. for easier mechanical handling and population with passive components. In the later module assembly process they also act as mechanical support for positioning in the glueing or subsequent wire bonding steps and provide break-outs and connectors for the hybrids power and data lines for the subsequent electrical testing. The present hybrid prototypes for barrel (stave) modules are manufactured in a five-layered layout featuring four active copper layers interleaved with 50 μm polyimide dielectrics (from top to bottom 2×signal, power and ground) plus an additional shield layer on their back-side, closest to the sensor. Each flex circuit holds 20 landing pads with thermal vias at the positions where the ASICs are to be attached. The hybrids provide the traces (100 μm track/gap) for powering, control and data lines to each ASIC, and host all needed passive components to safely operate the ASICs, i.e. filter capacitors for powering, terminations for data lines and reference voltages sources for the optional serial powering of several hybrids.

The glueing process for attaching ASICs onto a hybrid is illustrated in Figure F.24. First, 20 ASICs are placed and aligned in a precision tray composed of a plastic support with a laser-cut steel stencil attached to its top as shown in Figure F.24 (a). The ASICs are aligned in the cut-outs with a precision of approximately 50 μm in the x-y plane, mostly limited by the precision of the ASICs cut edges, but still much below the rather relaxed precision tolerances for their later placement on the hybrid ($\sim$ 200 μm) [313]. In the second step the ASICs are simultaneously picked up with a custom vacuum tool, as shown in Figure F.24 (b). The vacuum tool consists of a metal base plate and a plastic

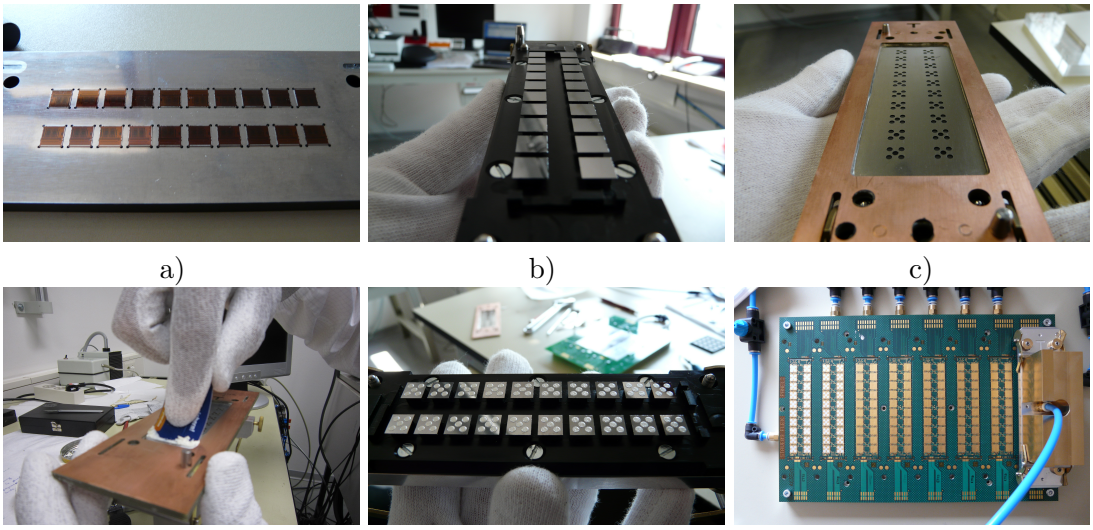

Figure F.24.: The different steps and tools involved in the glueing process for attaching 20 readout ASICs onto hybrids for barrel modules. The ASICs are positioned in a chip tray (a), picked up with a vacuum tool (b) on which subsequently a glue mask is attached (c). The glue is applied through the mask openings onto the ASICs back side (d), after which the mask is removed (e) and the ASICs are placed onto one of eight hybrids on a panel attached to a vacuum jig for curing (f).

stencil with 20 openings holding one ASIC, each. The tool has two steel positioning pins by which it can be precisely aligned onto respective precision holes in all jigs, hybrid panels or glue masks, including the chip tray described above. Next, a silver-loaded electrical grade epoxy (Hysol TRA-DUCT 2902 [326]) is applied to the back sides of each ASIC in a defined pattern and volume. This is achieved by attaching a 120 μm thick laser-cut steel stencil onto the pickup vacuum tool, aligned by its two positioning pins, see Figure F.24 (c). The stencil is enclosed between two frames for improving its rigidity and closely attaches to the ASICs back sides. It thereby serves as a glue mask to which the adhesive is applied via a scraper, ideally in one or two strokes over the full mask length to prevent excessive amounts of adhesive to be pushed through the mask openings while avoiding underfillings, see Figure F.24 (d). After the glue has been applied the stencil is removed and the resulting glue spots can be inspected, cf. Figure F.24 (e). In the last step the ASICs have to be positioned at a defined height onto the respective landing pads of a hybrid on the panel as shown in Figure F.24 (f). The hybrid panel therefore resides on an 8-way vacuum jig which allows to flatly vacuum-attach each hybrid to ensure all chip landing position to reside at a defined and constant height (i.e. preventing the hybrid to curl or bend up). Both, the hybrid panel and the subjacent vacuum jig exhibit precision positioning holes at each circuit position by which the vacuum pick tool is aligned in x-y direction. The final glue height is defined by four precision steel jacks

integrated into the pick tool which touch-down on respective reference landing pads on the panel periphery that reside at the same height as the actual ASIC landing positions. In a preceding calibration run the precision jacks hence need to be adjusted such that a uniform glue height of ideally $70 \pm 20\,\mu$m is achieved between the ASICs and hybrid landing locations.

The resulting glue heights and their uniformity were checked in calibration runs using glass dummy ASICs and reject hybrids as well as for all working hybrids produced using micrometer screw gauges or a confocal laser scanning microscope. Figure F.25 shows an exemplary result of a glue height measurement of the ASIC-to-hybrid gluing step using a mechanical prototype consisting of a reject hybrid and ASIC glass dummies as were used in initial gluing trials for the calibration of all associated tooling. For each chip position the total thickness of the final assembly is measured and the thicknesses of the hybrid at the ASIC landing positions and of the ASICs themselves are subtracted. The resulting glue heights range from $80\,\mu$m to $100\,\mu$m and hence are lying reasonably well within a tolerable range around the target thickness. In practise this result has not always been easy to achieve, since for instance, early hybrid prototypes were subject to inhomogeneities of their surface lamination or were bending as a result from being heated up in the solder-reflow process when populated with passives during the manufacturing process. This effect is also visible in the gluing results shown in Figure F.25, where the glue heights tend to lower values at the lowest/highest chip positions as a result of the early hybrid prototype bending up at its long ends. Other sources of misalignment were identified to originate from unequal heights of the vacuum pedestals of initial versions of the pickup tool or miscalibrated precision jacks. At least the former is likely to be avoided in future versions of the tool by means of replacing the contact face presently made of plastic with anodised aluminium that can be machined with higher precision and

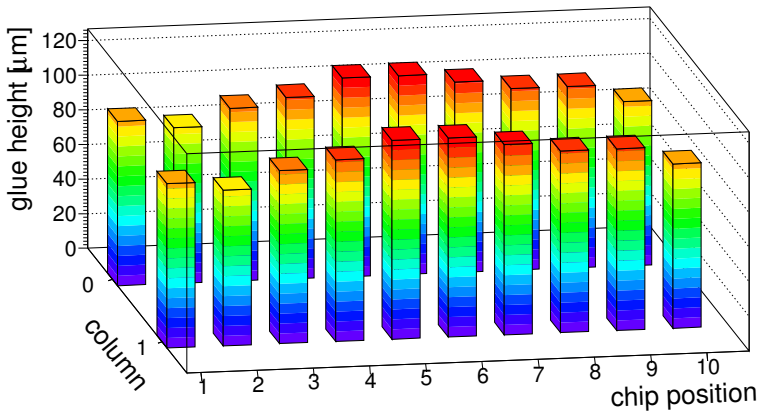

Figure F.25.: Exemplary result of a glue height measurement of the ASIC-to-hybrid gluing step. Shown are the resulting thicknesses of the adhesive for each of the 10 different ASIC position for both chip columns on the barrel hybrid.

furthermore improves the overall rigidity. Nonetheless the glue pattern was chosen such that an over-compression of the glue is tolerable up to a certain extend. No overfillings or excessive glue leaking onto surrounding pads could be observed for glue heights down to 45 μm. After its placement the pickup tool is weighted by a brass block to ensure that it is fully touching all four height marks and ideally needs to reside on the hybrid for the full curing time of the adhesive ($\sim$ 6-12 h). After the glue has set the pick tool is removed and the final assembly is ready for the first wire bonding step.

On average 80 25 μm thick Al wire bonds contact designated Al-bond pads on the ASICs to Au-plated bond pads on the hybrid side as illustrated in Figure F.27 (a). These provide the necessary connections to the powering and control lines, for setting address bits or for directly interconnecting adjacent ASICs via longer bond loops that serve as transmission lines for the tokenised data readout of multiple chips in a serial chain.

Before glueing the readily bonded hybrids onto a silicon sensor, each hybrid has to pass a set of intermediate electrical qualification tests. Each hybrid exhibits sets of larger bonds pads at its long ends that later serve as electrical connections to the stave bus tape. While still being attached to the panel, these pads are connected via additional wire bonds to breakout lines on the panel periphery that hosts connectors for easy access to the hybrids power and data lines in the subsequent electrical testing. Details on the different functional tests of powering, control and readout of the hybrids will be detailed in Section F.3.3.

Glueing and Wire-bonding of Hybrids/ASICs to Sensors

Final modules are assembled by subsequently glueing two hybrids onto the segmented (readout) side of a silicon sensor as depicted in Figure F.26. First a fully bonded and tested single hybrid is fixed in its position on the vacuum jig and loosened from the panel by cutting four tabs at its long ends as illustrated in Figure F.26 (a). These cut-out tabs have been left out in the laser cutting step during manufacturing to retain the hybrid in its position on the panel, see Figure F.23 (c) for a detailed view. The same vacuum pick-up tool is used to lift a single hybrid from the panel by the ASICs glued onto it previously. Similar to the procedure of glueing ASICs to hybrids a laser cut steel stencil is placed onto the pick-up tool that closely attaches to the hybrids back side, see Figure F.26 (b). The thickness of this second glue mask has been chosen somewhat larger (200 μm) than that of the ASIC glue mask since a larger target glue thickness and lower areal coverage have been found to improve the overall noise performance of the module by reducing parasitic capacitances induced by the closely attached hybrids [313]. The hybrids glued onto the segmented (strip) side of the sensor effectively behave as a parallel-plate capacitor with the adhesive and hybrids back-side solder-resist acting as a dielectric. The pattern of the openings and spare areas hence has been optimised to minimise the increase in inter-strip capacitance (roughly $\propto$ 0.3 pF per cm coverage). At the same time and similar to the ASIC glue stencil, it needs to provide high tolerance against over-compression of the adhesive and inhomogeneities in the hybrid's thickness or flatness, while avoiding excessive underfillings that could cause difficulties for wire-

bonding. Similarly contacts of the glue with the guard ring at the sensor edges are problematic since they could cause an early breakdown of the sensor or shortcuts of the bias voltage from deteriorating the guard ring isolation. Next a different electrical grade epoxy (Fuller Epolite FH-5313 [327]) is applied onto the mask using a scraper. Subsequently the mask is removed which leaves the glue pattern on the hybrids back side as shown in Figure F.26 (c). It is found that due to the low viscosity of this glue type a pre-curing for 30-40 minutes is recommendable to avoid excessive deliquescence of the adhesive and prevent it from flowing under the mask spare areas by capillary forces.

Finally the hybrid is placed onto the top side of a barrel sensor that is positioned inside a PCB frame and onto a vacuum assembly jig and weighted with a brass block for the adhesive curing time of another approximately $\sim$ 6-12 h, see Figure F.26 (d). The module assembly jig has a central pedestal around which first the PCB frame is attached via vacuum holes in the jigs periphery it resides on. The frame is used to distribute power to both hybrids, serves as a grounding point for the hybrids and sensor, and provides break-outs and connectors to data and powering lines used in the

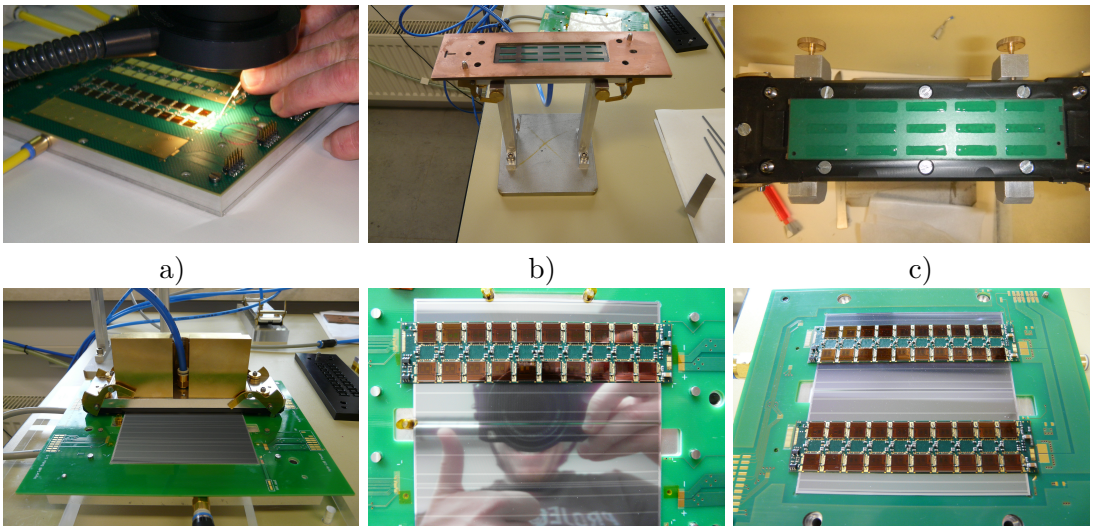

a) b) c)

d) e) f)

Figure F.26.: The different steps and tools involved in the glueing process for attaching two hybrids onto a barrel module sensor. The hybrids are cut out from the panel (a), and picked up using the vacuum tool on which subsequently a glue mask is attached (b). The glue is applied through the mask openings onto the hybrid back side after which the mask is removed (c). Finally the hybrid is placed onto the top side of a barrel sensor that is positioned onto a PCB frame on a vacuum assembly jig (d) for curing. After removing the pick tool the glueing result is checked (e) and the procedure repeated on the second hybrid position after which the fully assembled module (f) is ready to be detached from the jig together with its PCB frame for the subsequent wire-bonding steps and its electrical testing.

subsequent electrical testing steps. Secondly, a silicon barrel sensor is placed inside of the PCB frames cut-out area and onto the central pedestal of the assembly jig. Three precision pins on the jig serve as alignment points in x-y with respect to the sensors cut edges and several rows of vacuum holes in the pedestal hold the sensor flatly attached during the glueing process. The precision pins are usually covered with polyimide tape to prevent excessive mechanical stress to the sensor edges when attaching or releasing the sensor with the vacuum. Similar to all mentioned tools the assembly jig features two precision holes per hybrid location for alignment of the vacuum pick tool, and hence hybrid, relative to the sensor. Again the glue height is adjusted via the four precision jacks of the pick tool which touch-down onto the surface of four pedestals on the jig. In a preceding calibration run the precision jacks are adjusted to create a uniform glue height of ideally $120 \pm 30\,\mu$m between the hybrid back side and sensor surface resulting in a targeted area of $\sim 60\%$ being covered by the adhesive. After removing the pick tool the glueing result can be inspected, see Figure F.26 (e). The procedure then is repeated on the second hybrid position after which the module is fully assembled, Figure F.26 (f) and ready to be detached from the jig together with its PCB frame for the subsequent mechanical qualification and wire-bonding steps, and the final electrical testing. Similar to the ASIC-to-hybrid glue heights, the resulting glue thicknesses of the hybrid-to-sensor gluing step are checked using a confocal laser scanning microscope in an intermediate metrology step before wire bonding. In general all measurements performed on mechanical assemblies consisting of glass dummy sensors and reject hybrid / glass ASICs result in final glue thicknesses ranging from $80\,\mu$m to $160\,\mu$m and hence are reasonably close to the target value. The larger spread in the glue heights from this gluing step is a result of the inhomogeneities of the hybrid and in the results of the previous gluing step. These are intended to get balanced out by the hybrid-to-sensor glue such that the final distances between the ASIC top sides and sensor surface are as uniform as possible in order to facilitate the bonding.

For wire bonding, the module is placed onto a dedicated vacuum bonding jig, a simplified version of the assembly jig without any positioning pins or holes that only is used to flatly attach the module and PCB frame. In the second wire-bonding step the 10×128 readout cells of the ten ASIC of one hybrid column are connected to the 1280 strip metallisations of a single row on the sensor. The ASICs therefore provide Al bond pads in two rows that are connected via $\sim 1\,$cm long $25\,\mu$m thick Al wire bonds to the AC pads of the sensor strips, see Figure F.27 (b). The challenging part is the large bond angles occurring at the very first and last pads of each double-column of bond pads on the ASIC side, see Figure F.27 (c). Furthermore the close proximity of the rather long wires that are arranged in two height levels above each other requires narrow bond tools and high accuracy in the bonding process and later handling. With the new ABC130 ASIC the situation will be even more challenging, since 4 layers of 64 wire bonds per ASIC connect to the AC pads of two adjacent trip rows of the sensor. However, in first trials with test patterns on glass dummy sensors/ASICs the feasibility of this bond layout could already be proven with only minor modifications to the bond tools and parameters required.

During the course of the prototyping work several optimisations in the glueing process

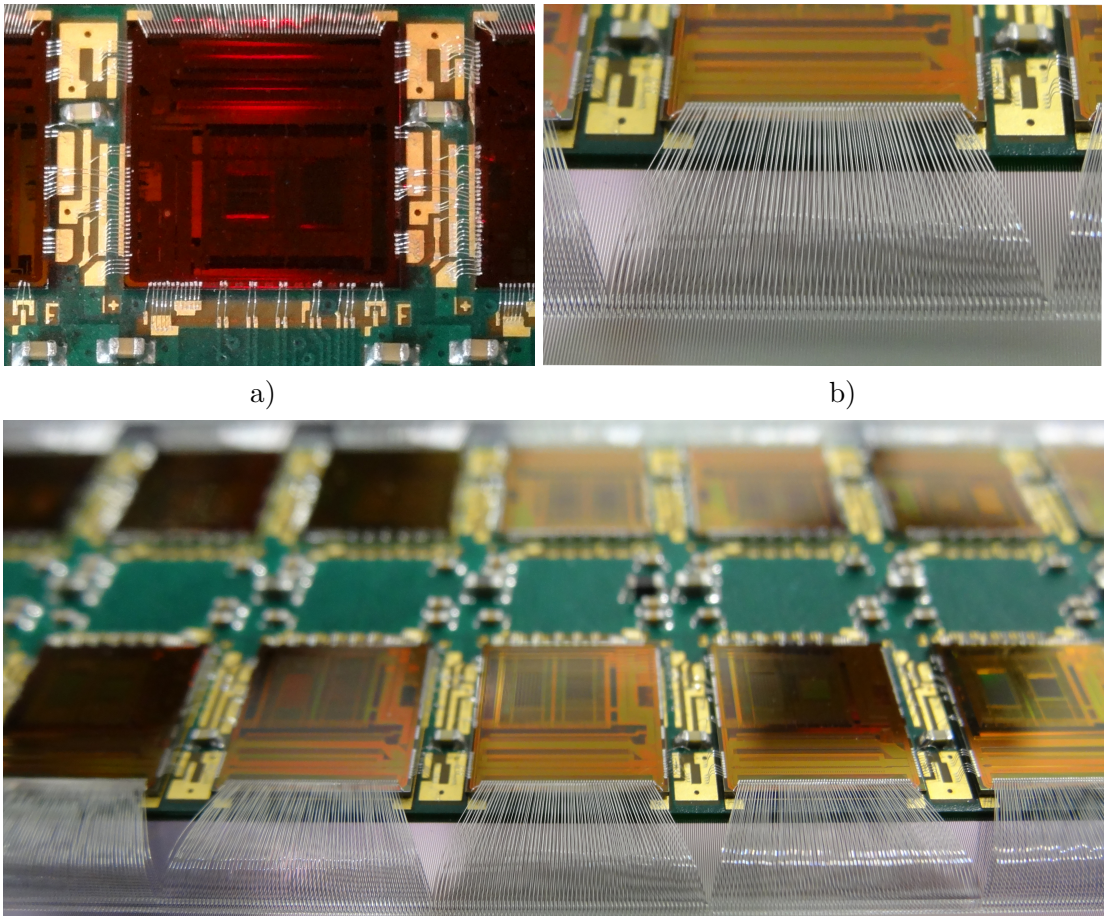

a) b)

c)

Figure F.27.: Top-side view of the wire bonds connecting each front-end ASIC to the hybrid (a), as well as of the double-layered bond layout for connecting the ASICs readout cells to individual strip metallisations of a single strip row of a barrel-type silicon sensor (b,c).

and the design of mechanical tools have been implemented with the input and support of in-house engineers and technicians. For instance, the second glueing step described above originally required the adhesive to be directly applied to the top side of the sensor using a paper stencil mask. However this required direct operation and contact of tools with the sensitive sensor surface. The method therefore was abandoned in favour of a glue application on the hybrid back-side, akin to the glueing step of ASICs onto hybrids. Other improvements reflect the precuring of the adhesive described above, the layout of the chip tray or the design of jigs and enclosures for transportation and storage.

In total about 25,000 hybrids and approximately 18,000 modules will need to be produced according to the present baseline layout. Hence the overall time required for their construction, bonding and electrical qualification is a crucial parameter in the planning

of the industrialised mass production within a presumably three year long assembly period, yet excluding the time budget required for their integration into larger structures (i.e. staves/petal) and macro-assemblies (i.e. disks/barrel layers).

The glueing steps presently take up a large part of the total time needed for the manufacturing and basic electrical qualification of a module. This is mainly due to the large curing times (8-16 hours) associated with the presently employed adhesives. Therefore studies of alternative electrical grade adhesives have been conducted in the course of a Master's thesis work at DESY [328] in order to identify and qualify candidates which obey faster curing times and at the same time fulfil the technical requirements and long-term stability for a 10-years operation within the harsh radiation environment of the ATLAS Inner Detector at the HL-LHC. At the time of writing a total of seven potential candidates were selected in a market survey, among those for instance UV-curing adhesives and adhesive tapes. The candidates were subsequently tested for meeting the technical specifications in terms of their rigidity after curing (crucial for bonding), long-term stability after thermal cycling, including adhesion and shear strength tests, their radiation hardness, thermal conductivity and chemical interaction with other materials such as the potential corrosion of aluminium. Initial calculations of their radiation lengths were performed as well. As expected the latter show large improvements, in particular with respect to the silver-loaded epoxy ($\sim 1/3X_0$) used in the first glueing step. More details on the studies and results described above can be found in the respective thesis [328]. In the near future additional studies are planned in order to investigate the impact of irradiations with higher energetic particles, potential chemical interactions with silicon, effects from outgassing of the adhesives during their curing and the ease of their mechanical handling in general, i.e. in terms of volumetric dosing and general manageability of their application and curing.

The bonding of a single hybrid takes roughly 5-20 minutes, depending on speed of the machinery and the amount of manual intervention required during the bonding process. Connecting all 20 ASICs of a single hybrid to two neighbouring strip rows of a barrel sensor will require an additional 10 to 40 minutes. In total, the required time for the wire bonding steps sums to approximately one hour per module. However, the largest part of the time-budget of the module production process will need to be accounted for the mechanical qualification and electrical testing, since this should also include thermal cycling and long-term operation (burn-in) tests of all final assemblies since (quasi-)defective components and bond connections or imperfections in the mechanical construction usually manifest themselves in abnormalities or malfunctions already at the very early stage of the nominal module life-time.

F.3.3. Electrical Testing

In the course of this PhD work a total of 10 barrel-type hybrids have been populated with ASICs, and an additional 15 hybrids were equipped with rejected ASICs or glass dummy chips for initial glueing and bonding trials. Using these, a total of three initial barrel module prototypes have been fully assembled and used to gain first expertise in the electrical testing. The first module is equipped with an non-functional sensor and

was used for initial ASIC-to-sensor bonding trials. The following three sections will provide an overview of the test setup and the different steps involved in the electrical testing procedure of single hybrids and fully assembled modules. In addition, at the end of this section results from a comparison in the electrical performance of single sided stave and double-sided Supermodule prototypes are presented, which were conducted during a research visit at CERN in 2011.

The HSIO Readout System

The central component of the readout system used for the data acquisition and detector control of the strip detector prototypes consists of the so-called High-Speed I/O (HSIO) system [329]. The HSIO is a stand-alone DAQ system that consists of a generic base board in the Advanced Telecommunications Computing Architecture (ATCA) standard form factor. The base board hosts a central processing unit presently formed by a Xilinx Virtex-4 Field Programmable Gate Array (FPGA) and provides several interface options, ranging from standard network connections (RJ45 GigE, SFP(+), XFP) over USB to headers and connectors for general purpose Input/Output (GPIO). The main communication with the peripheral DAQ (PC) computing hardware hence was chosen to be packet based, using a raw Ethernet protocol without any network/transport layer services on top.

The generic idea of the HSIO was to define a standardised design for processing data from different types of front-end electronics. Its generic functionality has been adapted by many ATLAS Upgrade projects and is planned to build the basis for the DAQ of as many of the ATLAS sub-detectors as possible in order to reduce the variety and complexity of the manifold custom hardware and software designs presently employed in ATLAS. The interface to the actual detector front-end electronics therefore is built by an additional custom interface board, in terms of the ATCA standard a so-called Rear Transition Module (RTM) attached to the HSIO main board via its Zone-3 connector. It provides the specific break-outs of signal lines, connectors, terminations and buffers required for a certain type of detector front-end electronics, in this case for individual ATLAS strip detector hybrids or modules, or connectors to interface with the EoS cars of whole staves and petals. Presently up to 32 160 Mbps data stream ($\equiv$ 16 modules) can be read simultaneously which likely is even to be increased with future hardware and firmware versions.

In the course of the development of the HSIO and its firmware also the corresponding DAQ control software on the PC side has been subject to continuous updates i.e. for implementing the packet based communication with the HSIO and its data and command structure required to initiate operations on the readout electronics interfaced to it. The so-called SCTDAQ software package forms the core of the readout software and provides the interface to the HSIO board to initiate commands to be send to the front-ends, write data to their registers for configuration, read-back status registers, command responses and the actual sensor hit data send back from the ASICs.

Hybrid and Module Testing

The electrical testing of hybrids and full modules is almost identical and includes general powering tests, initial calibration steps, and different gain and noise measurements. For testing of fully bonded hybrids a hybrid panel is placed on the 8-way vacuum jig to flatly attach a single circuit onto the panel in order to provide the necessary thermal contact with the jig during testing. This is necessary since the typical power consumption of a single flex hybrid reaches values of $> 10\,\mathrm{W}$, too much to be dissipated over air without additional cooling. As mentioned earlier, the panel provides connectors for the power and all required lines to the HSIO for sending command, clock and trigger (L1A) signals to the ASICs, as well as for receiving the data packages sent back over two individual LVDS line pairs (one per chip column).

Similarly a full module is attached onto a special module testing jig which provides the necessary connection of the bias voltage to the sensor, cooling loops for removing the dissipated heat using a liquid cooling systems, and the mechanical support and vacuum holes for securely fixing and providing good thermal contact of the module and its PCB frame. The jig therefore consists of a central isolated aluminium insert which serves as a pedestal similar to that of the module construction jig that is used to flatly attach the sensor and apply the sensor bias voltage to its back side. The remaining jig acts as a common grounding point for the low-voltage (ASIC power) and/or the (sensor bias) high-voltage return. Different powering options and grounding schemes can be tested by using different versions of PCB frames connecting the module. Currently two versions exist to power both hybrids either in series or via DC-DC powering. They therefore provide the respective connections between both hybrids, connectors to external HV/LV power supplies and the HSIO, and potentially host the necessary DC-DC converters. In either case they are equipped with two additional PCB boards that are populated with an early off-hybrid prototype version of the future HCC ASICs (cf. Section F.2.2), the so-called Buffer Control Chip (BCC). Similar to the HCC the latter is used to de-serialise and multiplex the data streams from the four columns of readout ASICs on a module in order to be sent over two line pairs at doubled bandwidth. Figure F.28 provides an overview of the common test setup employed for testing modules and hybrids at DESY. The device under test (DUT) is placed into an air-tight test box which is flushed with nitrogen to avoid condensation in case low temperature test are conducted. Also shown is the overall test setup, including the different HV/LV power supplies, the HSIO and a detailed view of the test box with a barrel module prototype placed on its vacuum testing jig that is cooled using a water-glycol mixture from a chiller situated outside of the lab space for thermal reasons. The whole setup is placed inside of a laminar flow tent to provide a clean and dust free test environment. The typical test procedure for the qualification of single hybrids and modules consists of seven steps which are detailed in the following.

Initial powering tests are performed to ensure the correct operation and initialisation of all ASICs, identify potential faults in traces, wire bonds and connectors and prevent damage of the front-end electronics or sensors during testing. In addition the thermal dissipation of all front-end ASICs is checked using thermal cameras or contact-less IR

Figure F.28.: Overview of the test setup used for the electrical qualification of hybrids and modules for the ATLAS strip detector upgrade. Shown are the laminar flow tent used to provide a clean and dust-free test environment (top left), the overall test setup (bottom left), including power supplies, the main test box hosting the DUT, and a 19″ unit hosting HSIO board. Also shown are detailed views of the HSIO system (top right) and the air-tight test box with a module mounted onto a testing jig (bottom right).

thermometers. Excessive power consumption or heat dissipation, for instance could identify potential shortcuts or malfunctioning ASICs, too low values provide hints for faults in the transmission of clock signals or configuration commands, malfunctions of internal voltage regulators, etc.

Burst tests of different kinds are performed in order to check the basic functionality of the communication with the front-end electronics. In either case a series (burst) of L1A triggers is send to the front-end ASICs. Upon their receipt the hit data, which is sampled at the bunch crossing clock from the discriminators and stored in a pipeline memory, is transferred to buffers for readout. This mechanism hence is similar to the

operational principle of the future ABC130 ASIC upon receipt of a L0 trigger signal. However the ABC250 predecessor does not feature the sophisticated data flow control using the three different trigger types (L0,L1/R3) as implemented in the final ABC130 ASIC. Also the principle of the serial readout of a chain of ASICs differs. Different to the Xon/Xoff flow-control mechanism of the ABC130 ASICs the ABC250 front-end chips implement a tokenised readout where the first chip of the chain is configured as a "Master", intermediate ASICs as "Slaves" and the last one as "End". When receiving a L1A signal, the "Master" chip sends a header to indicate the start of the readout followed by its own hit data. Afterwords it passes a token to the adjacent chip of the column. Upon receipt of this token by the consecutive chip (configured as slave), the latter subsequently sends its own hit data and passes the token to the next chip, and so on. When the token arrives at the last (end) chip, it sends is own data plus a trailer which indicates the end of the readout. The burst tests consequently are used to validate the correct operation of this readout mechanism. Either the raw data returned by a chain of ASICs is recorded for each L1A response and histogrammed and summed over in software (CaptureBurst), or the header/trailer information and/or the full hit data is decoded (RawBurst/ABCNBurst). This allows to identify corrupted header/trailer information, individual chip malfunctions or interruptions in the readout chain (i.e. by failures in wire bonds or the chips configuration).

Calibration scans of two types are performed before starting the actual gain and noise measurements. Initially, for each hybrid or module an IDelay or Stream delay scan is performed in order to accommodate for the phase shift between the clock signal sent from the HSIO to the hybrid/module and that of the hit data being returned on each stream. This phase shift differs in dependence of the total data cable lengths and the number and type of buffers/BCC chips placed on the data lines. To compensate for this effect a 6 bit Idelay register exists on the HSIO which defines the phase point at which the HSIO samples the data being sent back by the DUT within a range of approximately 5 ns. The Idelay scan sweeps through the full range of register settings and performs a kind of ABCNBurst for each. Usually one or more broader working ranges of Idelay settings exist for which the returned hit data from all ASICs is correctly sampled and decoded. Consequently the centre of the largest continuous range of working values is chosen and stored for the following tests.

The second calibration step is used to tune the timing of an integrated charge self-injection functionality of the ASICs analog front-ends that is used throughout all gain and noise tests performed later on. The analog front-end of each channel hosts an internal 50 fC calibration capacitor that is connected to the preamplifier input and allows to simulate a strip hit by charging the capacitor with a DAC-tunable voltage using an internal chopper circuit. This calibration (strobe) signal is triggered after a tunable delay with respect to the clock phase upon the receipt of a special control command. The delay for issuing the calibration pulse signal is set with 6 bit resolution in a register within a range of approximately 50 ns (two clock cycles at 40 MHz). The Strobe delay scan sweeps through the full range of delay settings while sending commands for injecting charges of approximately 4 fC into the capacitors, and issuing a trigger signal afterwords.

At the same time the threshold of the discriminators is set to a value corresponding to a charge of 2 fC, hence making sure that each injected charge should be registered as a hit. Each step in the scan is repeated 200 times and the number of hits returned by each channel is recorded. Within a certain range of the strobe delay (usually ~ 20 DAC units) the injected charge is registered correctly, hence the phase at which the charge is injected is in sync with the phase at which the discriminator output is sampled from. If the delay is too short, the discriminator output will be read too late and won't provide a hit anymore. If it is too long, the discriminator fires too late and the injected signal is not yet "seen" when sampling its output. The working Strobe delay range differs per ASIC (and to a lesser extend also per channel) due to production process variations. It hence is set for each ASIC individually to a value corresponding to a point at 25% or 40% of the functional range determined in the scan.

Threshold scans are performed in order to quantify the amplifier performance in terms of gain (slope), offset and linearity in its response to different charges injected at its input. An initial threshold scan is performed for three different charges (usually 0.5 fC, 1 fC and 1.5 fC) and therefore also is referred to as 3-point gain scan. The threshold for the amplitude discrimination is applied as a differential voltage offset to the comparator and can be tuned by a DAC with 8 bit resolution within a range from 0 fC to 9 fC. For each of the three different charges the threshold of the discriminator is systematically varied and the discriminator output for each channel is sampled various times. The resulting channels occupancy hence ranges from 0% (all samples below threshold) to 100% (all injected signals produce a hit) and follows the typical s-curve shape when plotted as a function over the full threshold range. Ideally this curve would have a shape of a step function but in reality is smeared out due to the noise present in the system. The threshold point at which 50% occupancy is reached (point of largest slope of the s-curve) is referred to as the Vt50 point and determines the mean amplifier response to the injected charge. It is determined by fitting a complementary error function, the width of which also provides a measure of the noise present at the amplifier output. Plotting the values of the Vt50 points as a function of the three injected charges yields a so-called response curve to which a linear fit is applied to extract approximate values of the discriminator offset (response at 0 fC) and the channels gain (slope [mV/fC]). Figure F.29 shows exemplary results of the offset and gain for all channels of a single column of ASICs of a single barrel-type hybrid. Also shown is the distribution over all 1280 channels of the Vt50 points for 1 fC injected charge. Typical values for the charge amplifiers gain lie around 110 mV/fC for the ABC250 ASICs (> 90 mV/fC according to specifications [330]). When dividing the estimated amplifier output noise (for 1 fC injected charge) by the estimated amplifier gain, the equivalent noise charge (ENC) at the amplifier input can be calculated. The ENC is commonly used to express the overall noise performance of charge amplifying systems and represents the required variation in charge present at the input of an "ideal" charge amplifier in order to produce the output noise measured (i.e. from the s-curve width). The typical noise values of single hybrids with ABC250 prototypes range from 380 to 410 ENC, see Figure F.30 for an example. This noise mainly originates from thermal noise of the first-stage FET and

the feedback resistor of the charge sensitive amplifier ($\propto \sqrt{\mathrm{T}}$) and from shot noise from the gate current I_g of the first-stage FET ($\propto \sqrt{I_g}$). For full modules with short strips connected to each readout channels the values are usually somewhat higher, ranging from 590 to 640 ENC due to additional contributions of shot noise from the leakage current of the sensor and the capacitive load added to the amplifier inputs that raises the noise gain $(1 + C_{\mathrm{in}}/C_f)$ for the thermal noise components, determined by the input (C_{in}) and feedback capacitance (C_f).

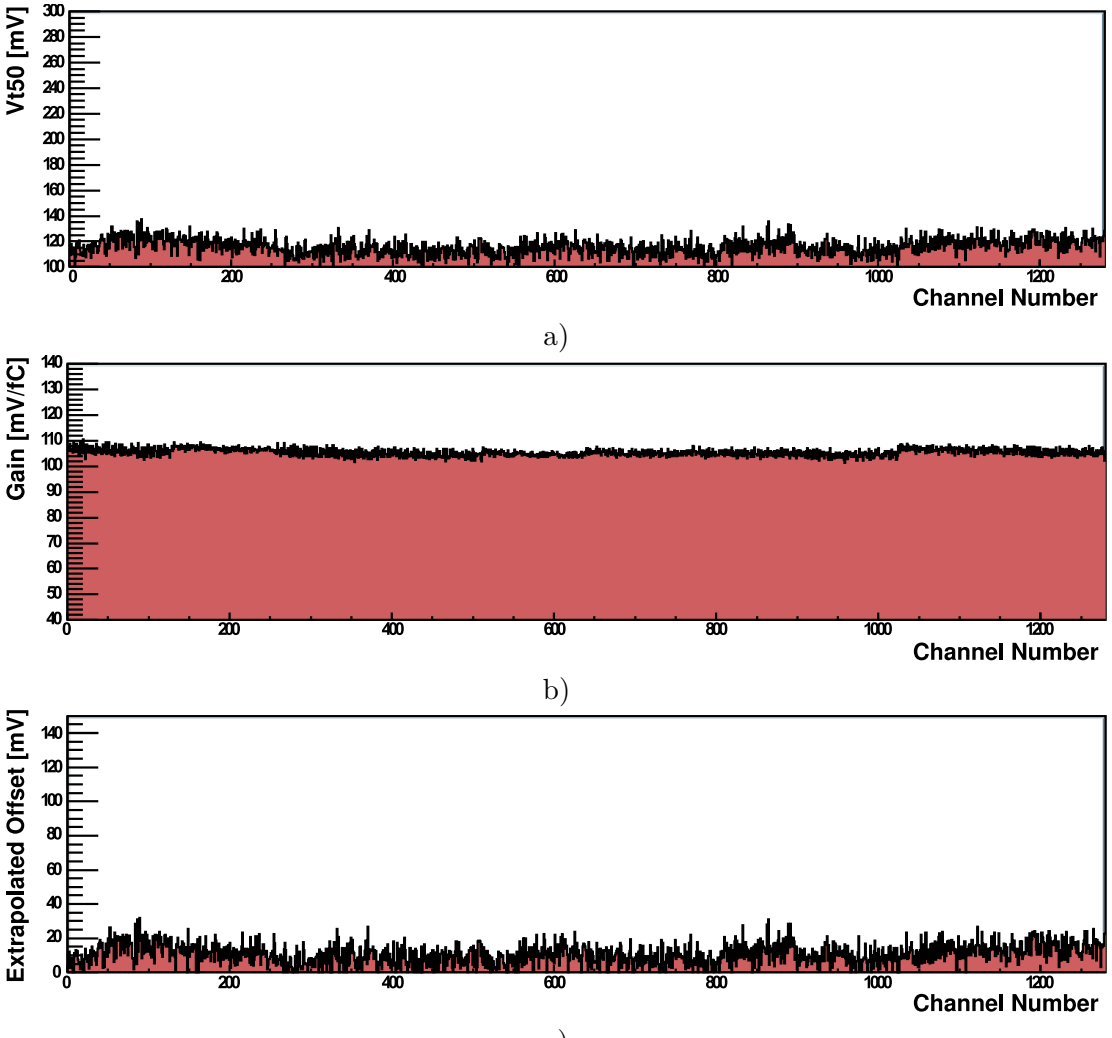

Figure F.29.: Exemplary result of a 3-point gain test of a single hybrid before the trimming step. Shown are the distributions over the 1280 channels of a single chip column for the calculated Vt50 point for 1 fC injected charge (a), the measured channels gain (b) and the extrapolated discriminator offset (c).

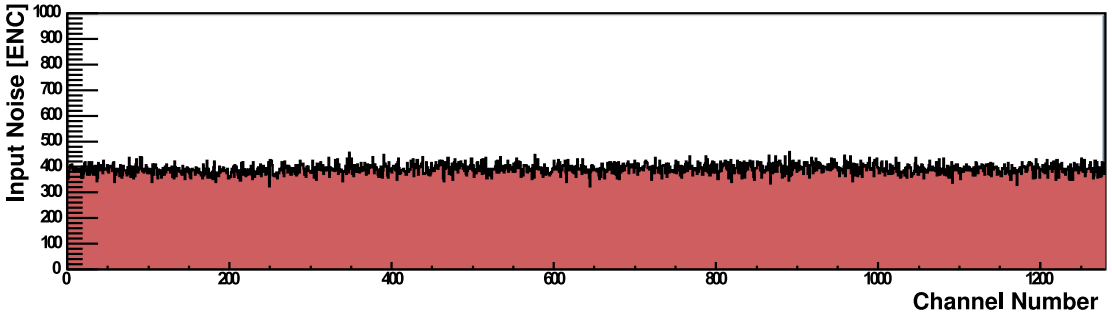

Figure F.30.: Exemplary result of the channels noise determined in a 3-point gain test of a single hybrid before the trimming step. Shown is the distribution over the 1280 channels of a single chip column for estimated input noise (in ENC) at the amplifier input.

Trimming: In order to assure a uniform response of each channel for a given charge at its input, channel-to-channel variations in the discriminator offset (cf. Figure F.29 (c)) have to be compensated for, which is also referred to as trimming. Each individual channel provides a trim DAC of 5-bit resolution by which an offset correction in the threshold can be applied within different ranges and hence with different resolutions or step sizes. Eight different trim ranges ranging from 0.48 mV to 2.88 mV can be set globally per ASIC using three bits in a configuration register. A TrimRange scan is performed to select the optimal trim range which allows to individually calibrate each channel to an equal target response per hybrid or module with highest possible precision. First, a threshold scan is performed for each range and the Vt50 points are compared to a target threshold in order to determine the maximum number of channels that can be aligned using trim DAC values of the given trim range. Thereafter the lowest possible trim range is chosen for each chip, such that the number of trimmable channels is maximised while minimising the residual spread due to the limited trim DAC resolution. The determined trim DAC values for all channels of a hybrid or module are instantaneously applied and written to a trim file for their later reuse. Those channels not trimmable within the chosen range are masked, i.e. excluded from the readout as a result of shorts or opens in the wire bonds, and are stored in a mask file respectively. Figure F.31 shows exemplary results of the trimming step for a single column of front-end ASICs on a single hybrid with the determined trim DAC steps for the chosen trim range and the resulting distribution of the Vt50 points for 1 fC injected charge. When compared to Figure F.29 (a) the large reduction in the spread of the channels response can be seen.

Response curve: An extended threshold scan using ten different charge values is performed which provides higher accuracy information on the channels response than the 3-point gain test performed before trimming. Instead of a linear fit, the distribution of Vt50 points vs. injected charge is fitted with a quadratic function to account for non-linearities in the amplifier response, in particular for higher charge values present at the input. This yields more precise values of the channels gain, discriminator offsets and

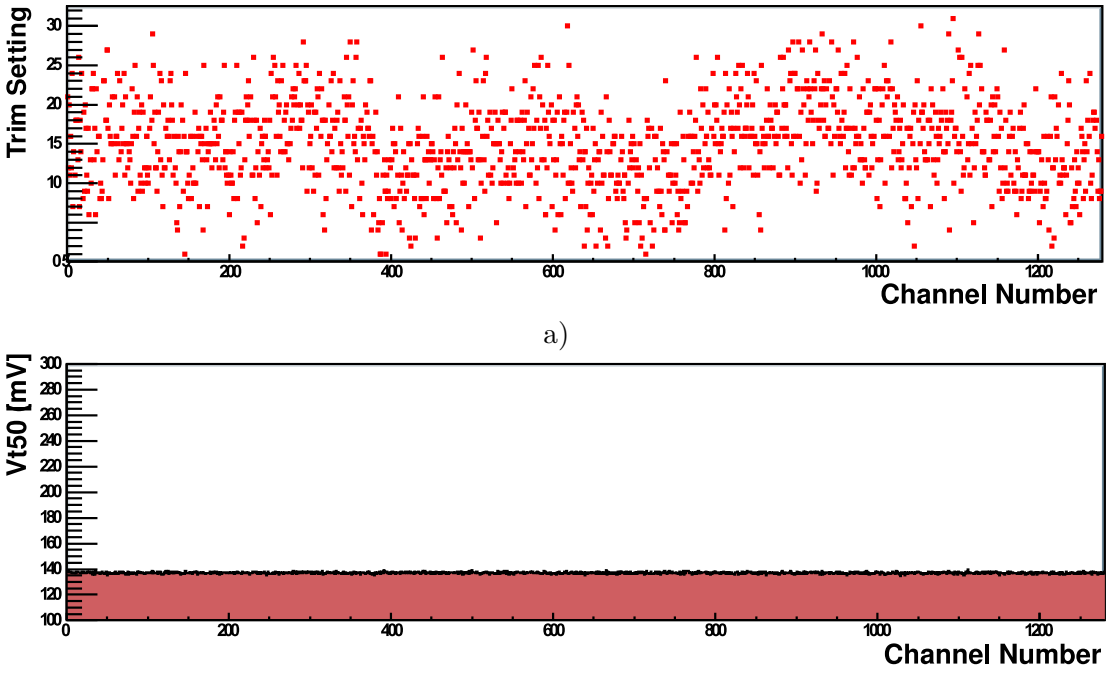

Figure F.31.: Exemplary result of the trimming step for a single hybrid. Shown are the distributions over the 1280 channels of a single chip columns for the determined trim DAC values of the chosen range and the resulting distributions of the Vt50 points for 1 fC injected charge after trimming with the respective trim DAC values (b).

input noise.

Noise occupancy: The detector occupancy from noise hits is required to stay below a certain level ($\mathcal{O}(10^{-5})$) to avoid a deterioration of the track reconstruction performance, i.e. from additional ambiguities introduced by noise hits. The noise occupancy is determined by measuring the number of hits returned from the front-ends for increasing threshold values without injecting any charge. In order to obtain sufficient statistics for occupancies down to $\mathcal{O}(10^{-7})$, up to 10^6 measurements are performed in the upper region of threshold values, while for low thresholds (where the occupancy approaches 1) only ~ 2000 samples are recorded. The minimal number of iterations per threshold point is chosen such that a minimum of 50 hits are recorded in $> 50\%$ of the active channels. Figure F.32 shows a logarithmic plot of the noise occupancy from all channels of a single hybrid on a barrel module prototype as a function of the discriminator threshold.

All single hybrids and the two fully assembled modules that host a working (b-grade) barrel short-strip sensor are tested using the full set of test procedures described above. Overall adequate gain ($> 105\,\mathrm{mV/fC}$) and noise performance ($< 650\,\mathrm{ENC}$) is measured with only few occasions of malfunctioning ASICs or noise excesses in particular sensor

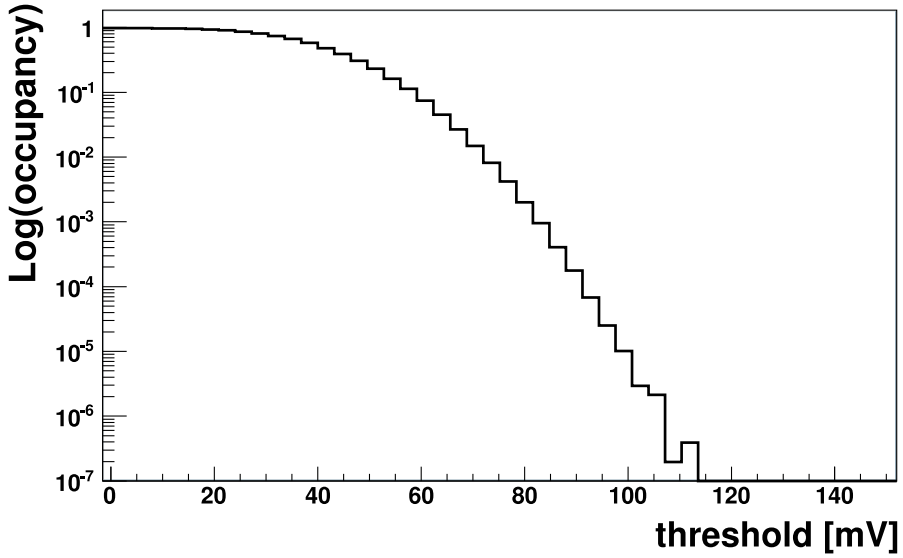

Figure F.32.: Exemplary result of the noise occupancy test for one of the two hybrids on a DC-DC powered barrel module. Shown is a logarithmic plot of the noise occupancy from all channels of the two ASIC columns vs. the discriminator threshold.

regions, e.g. due to the low-quality sensors that have been used for these first prototypes or faults in their bond connections. The signal-to-noise (S/N) ratio of a sensor provides an effective measure of the overall detector performance. It has been shown that to achieve a reasonable tracking performance and efficiency a S/N ratio of at least 10:1 and a signal-to-threshold value of at least 2.2:1 is required [313]. The charge collection efficiency of $1 \times 1\,\mathrm{cm}^2$ miniature ATLAS strip sensor prototypes has been measured before and after irradiation with protons, neutrons and pions with fluences up to 1×10^{16} 1 MeV $n_{eq}\,\mathrm{cm}^{-2}$ [280]. Figure F.33 shows the measurements after different steps in the irradiation, after annealing for 80 minutes at 60 °C respectively. The maximum expected fluence for the sensors was calculated as 8.1×10^{14} 1 MeV $n_{eq}\,\mathrm{cm}^{-2}$, whereas usually 2×10^{15} 1 MeV $n_{eq}\,\mathrm{cm}^{-2}$ are assumed to include safety factors accounting for the uncertainties in these calculations. At the end of the sensors lifetime roughly 8-11 ke^- are expected to be collected for minimum ionising particles of the different types. With an expected input noise of 640-680 ENC after irradiation, thresholds around 0.75 fC will suffice in terms of S/N performance ($\gtrsim 15:1$) while meeting with the requirements on signal efficiency and noise occupancy.

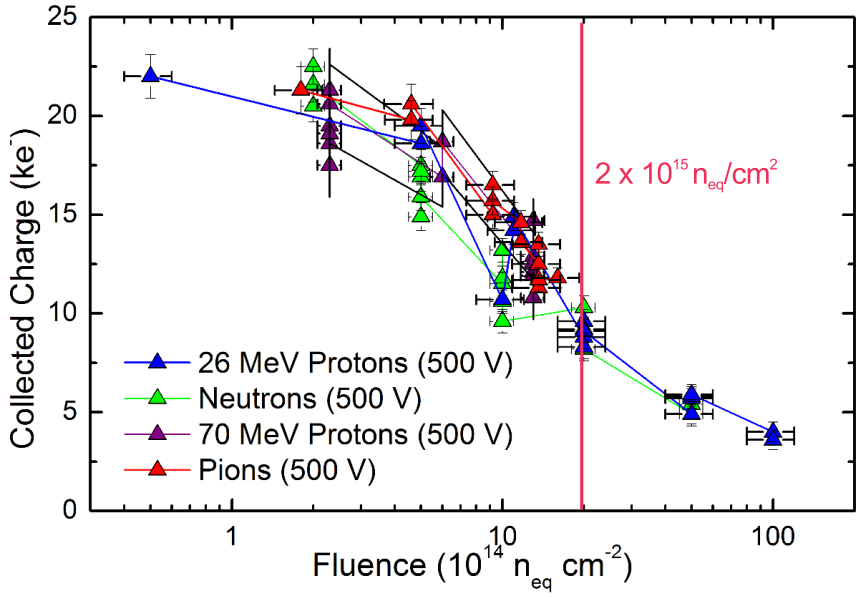

Figure F.33.: Measured charge collection efficiency for minimum ionising particles of different type and using a sensor bias voltage of 500 V as a function of the 1 MeV $n_{eq}\,\mathrm{cm}^{-2}$ fluence. [280]

Performance Comparisons of Single and Double-sided Modules

The electrical performance of a (single-sided) DC-DC powered stave module and a double-sided Supermodule prototype are compared. The DC-DC module was tested and operated on a module testing jig placed into an air and light-tight thermal enclosure flushed with nitrogen. The Supermodule prototype on the other hand is embedded into a small (air/light-tight) metal enclosure, see Figure F.34 (c). The modules were tested for different settings of coolant temperatures ranging from 8-20 °C to account for the differences in the cooling performance of both setups. The temperatures on the actual hybrids are measured by negative temperature coefficient (NTC) thermistors residing at the middle of each hybrid between both ASIC columns. Both modules are read out using the HSIO and the SEABAS system [331], the latter being an alternative readout system developed at KEK, Japan. The SEABAS readout system consists of a small $10 \times 30\,\mathrm{cm}$ base board that hosts two Xilinx Virtex-4 FPGAs providing TCP/IP and UDP connections to a controller PC and the capabilities for customisable data processing and connectivity to the front-end electronics.

For each temperature step the calibration steps, threshold and trim range scans were repeated to account for the temperature dependence of e.g. the optimal strobe delay setting as shown exemplary for the single-sided module in Figure F.35 (a). The bias voltage was set at $V_{\mathrm{bias}} = 200\,\mathrm{V}$ for both modules to ensure full depletion while avoiding excessive leakage currents from early/slow breakdowns of the sensor. Figure F.35 (b) shows the measured input noise as a function of the sensor leakage current. The noise

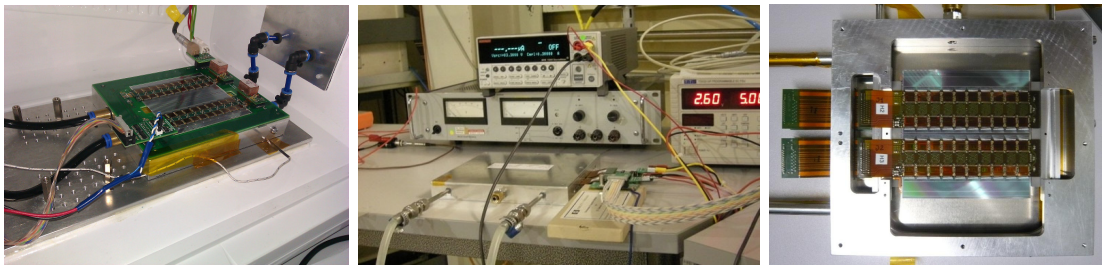

a) b) c)

Figure F.34.: Overview of the test setup used for the comparison of single and double-sided modules. Shown are the single-sided module placed on a module testing jig inside the thermal enclosure (a), the double-sided module enclosed in its metal housing with the cooling pipes data and powering lines attached (b), as well as a detailed view of the double-sided module placed in its enclosure (c).

values are calculated as the average of five different measurements from threshold scans performed around 1 fC. For values > 150 V no significant dependence on the sensor bias voltage is observable. Figure F.36 (a) shows the measured input noise as a function of the hybrid temperature. The noise values again are calculated by taking the average of five threshold scans performed around 1 fC. As expected, for similar hybrid temperatures the double-sided module on average shows a 5% lower input noise than the single-sided prototypes. This is mainly caused by the additional load capacitance ($\sim$ 10-20%) present at

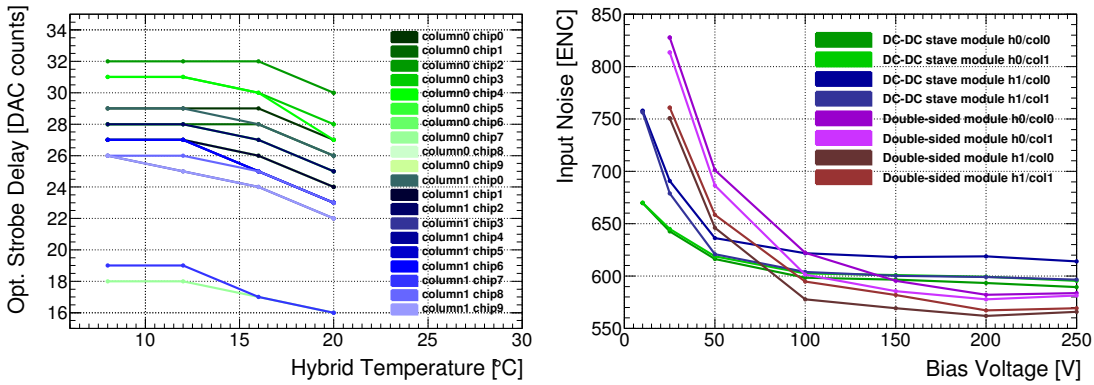

a) b)

Figure F.35.: The optimal strobe delay setting as derived in the respective calibration scan as a function of the hybrid temperature of the DC-DC powered stave module (a), and the measured input noise as derived from threshold scans around 1 fC as a function of the sensor bias voltage of both, the single and double-sided module (b).

the preamplifier inputs that is induced by glueing the hybrids directly on top of the segmented sensor surface in case of the single-sided modules. Additional contributions arise from the higher leakage current of the sensor used in the latter case, see Figure F.36 (b). A precise correction for the latter however is not feasible without knowledge on the single strip leakage current. Table F.7 shows a comparison of the gain and input noise values

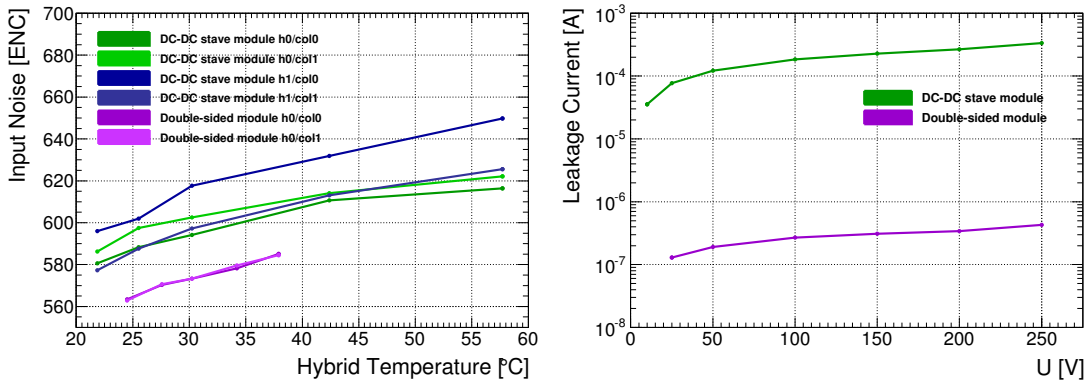

a) b)

Figure F.36.: Measured input noise as derived from threshold scans around 1 fC as a function of the hybrid temperature (a), and sensor IV curve of both modules (b).

of a single hybrid on a single and double-sided module as derived in threshold scans performed around 1 fC using the HSIO and SEABAS readout systems, respectively. All measurements are performed at a hybrid temperature of approximately 27 °C. As before it can be seen that the average input noise of the hybrid on the double-sided module is approximately 20 to 30 ENC counts ($\sim$ 4-5%) lower. Also visible is a difference in the average gain which is approximately 3% lower for the ASICs on the hybrid of the double-sided module. This is caused by a somewhat lower supply voltage present at the ASICs of the latter which is applied from an external power supply set to 2.6 V of which 2.35 V are measured at the hybrid pigtail connector (cf. Figure F.34 (b)). In case of the single-sided module 2.6 V are derived by the DC-DC converters residing directly beneath the hybrids on the module testing frame. This results in shorter powering lines and lower resistive losses with approximately 2.45 V being available at the ASICs. This in turn results in a higher value of the gain which shows an almost linear dependence on the supply voltage applied to the analog part of the circuitry.

When comparing the results between both readout systems, a higher average gain ($\sim$ 9%) and lower input noise ($\sim$ 1-4%) is measured with the SEABAS system. A definite cause for this effect could not be identified at the time the studies were performed. Potential sources of this effect could lie in the calculation of the gain (i.e. the determination of the Vt50 points) and differences in the fitting procedure used by both systems that is performed to extract the channels response curve and its slope. Also the use of different trigger rates in the threshold scans with both systems could impact the results.

Table F.7.: Comparison of the average gain, input and output noise values of a single hybrid on a single and double-sided module as derived in threshold scans performed around 1 fC using the HSIO and SEABAS readout systems.

		SEABAS			HSIO		
module (hybrid) / column		gain [mV/fC]	input noise [ENC]	output noise [mV]	gain [mV/fC]	input noise [ENC]	output noise [mV]
Single-sided	/ 0	116.3	571.9	10.66	109.2	589.9	10.32
module (h0)	/ 1	116.9	576.9	10.81	109.7	596.0	10.48
Double-sided	/ 0	113.6	546.1	9.93	105.9	570.3	9.68
module (h0)	/ 1	113.3	546.0	9.91	105.7	570.6	9.66

Table F.7 therefore also shows the respective values of the output noise as calculated from the product of gain and input noise as measured with both systems. The values of the output noise result to show a smaller difference (1-3%) in the values obtained with both readout systems.

In summary the double-sided module shows a somewhat lower input noise, as is expected from the different construction principle and from additional noise sources introduced by the usage of DC-DC converters on the single-sided module. However this difference is negligible in sight of the expected deterioration of the overall noise performance after irradiation at the end of the modules lifetime. Overall adequate gain ($> 105\,\mathrm{mV/fC}$) and noise performance ($< 650\,\mathrm{ENC}$) is given for both module types which hence meet the requirements to provide adequate tracking performance at an HL-LHC environment. The final choice for the module and integration layout hence will need to be based upon comparisons of further criteria, such as more precise estimates on the final material budget of both concepts, the ease of manufacturing, testing and replacement of modules and macro-assemblies, their cooling performance and the overall material and construction costs accounted to both integration concepts.

F.3.4. Petal Module Assembly and Testing

The methodologies of production and electrical characterisation of single-sided stave modules successively have been adopted in the construction of first prototypes of endcap modules. Similar to the prototyping of larger barrel-type assemblies (cf. Stavelets, see next section), the modules are to be mounted onto small scale versions of the final macro-assemblies, so-called Petalets hosting six end-cap silicon strip sensors each. This allows to mimic the electrical and mechanical properties of full size petals in order to identify the technical requirements and challenges in their assembly and optimise the methodologies of their integration. The results will also provide crucial input for steering the decision on the layout and scheme of powering and readout (and hence of the final bus tape design) of full-size petals, and will be used optimise the hybrid layouts and potentially also the endcap sensor geometries themselves. A Petalet consists of

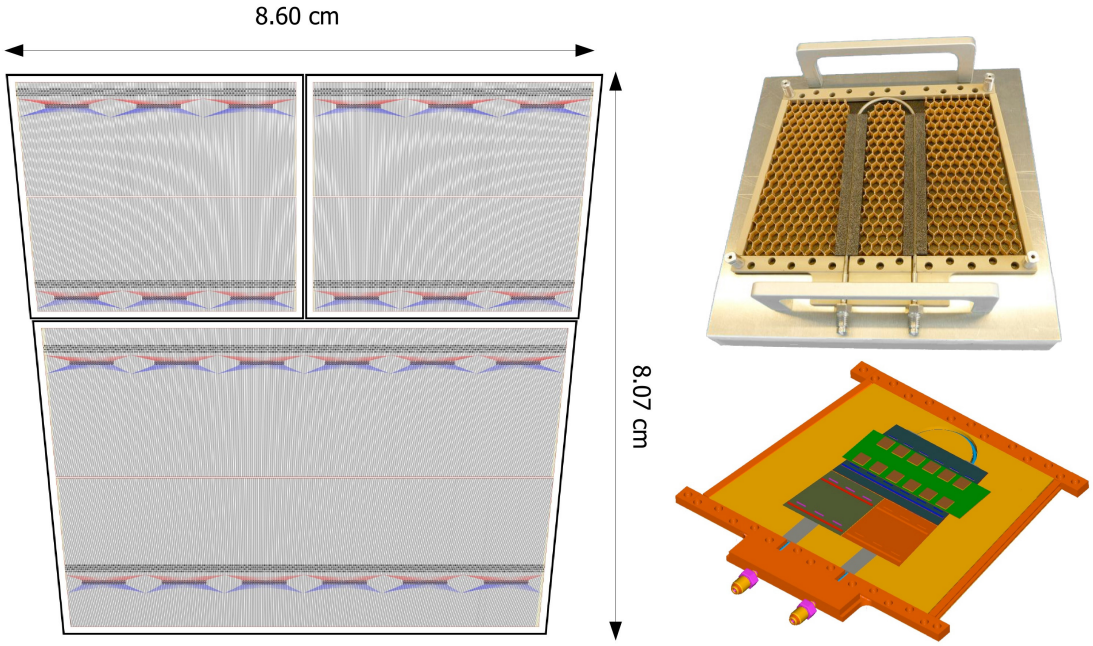

a) b)

Figure F.37.: Conceptual layout of a Petalet structure hosting three different types of sensors (a) which are placed onto each side of a carbon foam and carbon fibre honeycomb core with an embedded cooling pipe and carbon fibre facings (b).

three different types of sensors that are placed onto either side of a common trapezoidal support and cooling structure made of a carbon foam and carbon fibre honeycomb core and an embedded cooling pipe, covered with carbon fibre laminates on either facing as shown in Figure F.37. The layout hence follows the generic mechanical structure of a stave or full-size petal, with the sensor geometries chosen such that they resemble the area of a petal at the innermost radius hosting the sensor with the smallest strip pitch, and the central intersection region on the petal where the ring with single sensors adjoins the ring hosting two sensor columns (cf. Figure F.7). Presently two different options exist for the layout of the powering and readout in total 48 ABCN ASICs per Petalet. In the first, all three sensors on either facing are populated with individual hybrids forming three individual detector modules per side, see Figure F.38 (b). The traces for readout and powering are placed onto two similar bus tapes that connect to the two front left (back left) and back right (front left) modules and hence are folded around the Petalet top-side edge, respectively. In the second option the two top-side sensors share a common hybrid spanning over the full width of both sensors as illustrated in Figure F.38 (a). On the one hand, this allows to reduce the number of DC-DC converters (and BCC boards) required. On the other hand the traces for powering are routed on a dedicated bus tape and those for the data, command and clock signals on a bus tape at the opposite side,

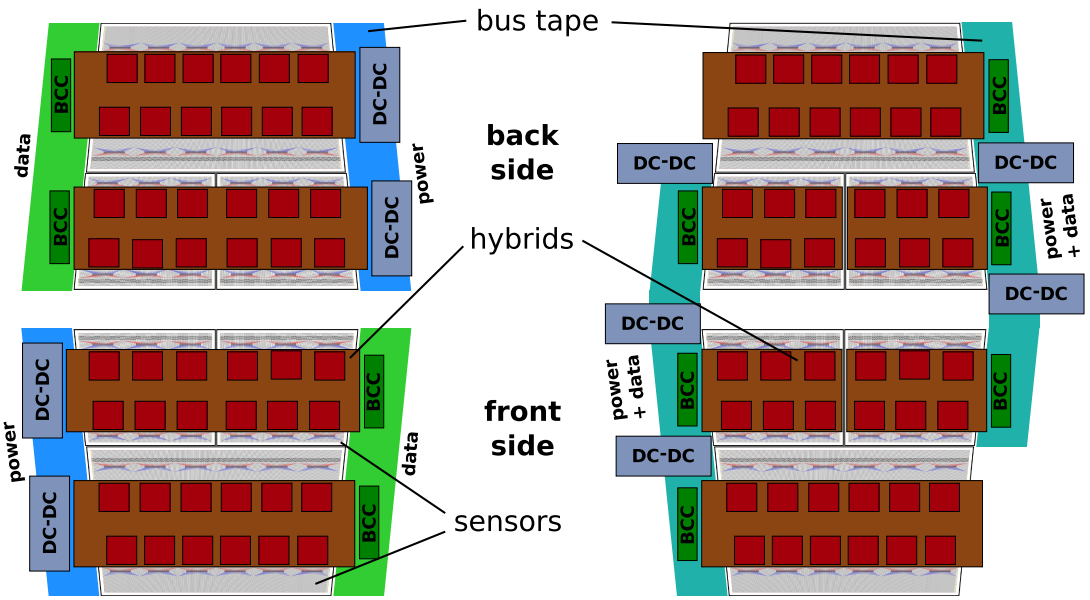

a) b)

Figure F.38.: Bus tape and hybrid layout options for the powering and readout of a Petalet. Shown is the front side (bottom) and flipped up back side (top) for both layouts. In the "Bear" layout (a) a common hybrid spans over the full width of both top-side sensors on each facing. Power and data lines are routed on dedicated bus tapes on either side of each Petalel facing. In the "Lamb & Flag" layout option (b) each sensor is populated with an individual hybrid. A common bus tape routes power and signals to the two front left and the back right module, as seen from either facing respectively. The bus tape therefore is folded around the Petalet top-side edge.

which in turn reduces the required tape widths and material.

At the time of writing first prototypes of Petalet support structures, sensors and hybrids in all variations have been developed and first prototype modules have been assembled and tested successfully at several institutions. The construction of fully populated Petalets therefore will likely follow in the very near future, i.e. with the final bus tapes and all the required tooling for the module placement becoming available. In the course of this PhD work initially six Petalet prototype sensors of all three geometries were tested to meet the design specifications. The sensors are produced on 6″ wafers by the Barcelona Microelectronics Institute of the National Microelectronics Centre (IMB-CNM) [332]. From these a total of three Petalet module prototypes have been assembled at DESY, which includes two mechanical assemblies for gluing and bonding trials and a fully functional prototype of the lower (large) sensor module that is to be mounted on the lower part of a Petalet facing. The modules were successfully assembled, wire

bonded and are presently undergoing electrical testing. The construction and electrical characterisation of the modules closely follows that of barrel-type modules. However the wire bonding layouts and a new set of tools had to be adapted from the stave versions to account for the different sensor and hybrid geometries. More details on the assembly procedures, tooling and testing of first Petalet hybrid and module prototypes at DESY can be found in [328].

F.3.5. Macro-Assemblies and Testing

The prototyping of macro-assemblies in the barrel region already is in an advanced state in which a number so-called "Stavelets" have been successfully assembled and tested since 2011. A Stavelet represents a short version of a full length stave and hosts up to four full-size barrel-type silicon microstrip detector modules on each facing, see Figure F.39 (a). Apart from minor layout differences it comprises the same mechanical structure as a full-sized stave. Presently two different versions of Stavelets have been developed which feature different bus tape layouts for serially or DC-DC powering the hybrids and modules. A first two prototypes of a serially powered Stavelets have been

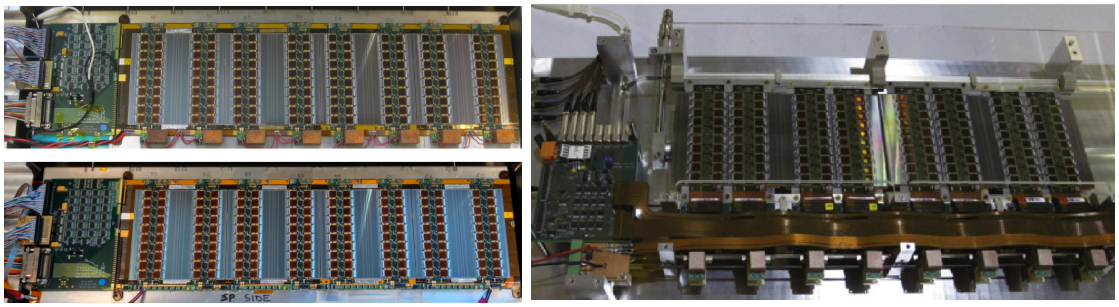

a) b)

Figure F.39.: Photographs of Stavelet prototypes hosting four barrel-type silicon strip detector modules (a) in both layout options for DC-DC (top) and serial powering (bottom), as well as of a short-version of a (DC-DC powered) Supermodule hosting four double-sided modules (b). [303, 333]

built and were successfully tested. The prototypes were built using commercial shunt regulators and four barrel type modules populated with 2×20 128-channel ABCN-25 readout ASICs. Similarly two DC-DC powered Stavelets were constructed and tested using commercial DC-DC step-down converters, with comparable powering efficiency and noise performance found [333, 334]. The serially powered Stavelets consistently showed a slightly lower average noise performances ($\sim$ 25-30 ENC), while the DC-DC powered versions exhibit a higher immunity to so-called double trigger noise (DTN) than the serial powering version. The DTN thereby reflects the potential noise interference from simultaneous charge integration and readout activity. It is tested by sending a series of two triggers within a variable latency with only the data returned for the second one being read back. Since no charge is injected the number of hits returned

ideally would be zero. In reality, however, a small occupancy is measured as a result of noise interference from the readout activity from the first trigger sent. This effect was identified to be originating from high-frequency common-mode noise on the LVDS data lines that in particular develops in the serial powering case where signal lines are AC coupled and all modules reside at different potentials with respect to the LV return (ground). Nonetheless good performance was demonstrated with all prototypes and both powering schemes. Similarly, for the second integration option small-scale versions of Supermodules have been fabricated using four modules populated with the ABC250 ASICs, see Figure F.39 (b). Overall good and uniform noise performance was found [302, 303] and a separate prototype Supermodule hosting eight double-sided modules already has been assembled, e.g. to perform further studies on grounding and shielding issues with more modules powered in parallel [280].

F.3.6. Summary and Outlook

As part of this PhD work various infrastructure and tooling, readout systems and setups for qualification and electrical testing were installed and continuously enhanced in order to prepare and conduct the prototyping of detector components for the barrel and endcaps of a future ATLAS silicon microstrip detector. At the time of writing a total of 15 hybrids and three barrel modules as well as first Petalet modules have been produced at DESY. The in-house assembly lately has been gaining a lot of momentum with new machinery for the wire bonding and qualification of the gluing processes becoming available.

The prototyping of barrel-type macro-assemblies will naturally evolve towards larger scale structures of single-sided modules populated with the future ABCN130 ASICs. Currently it is planned to fully assemble and test a full-size stave prototype until the end of 2014, the powering scheme of which, however, still has to be decided for. Additional work within the scope of this PhD topic concerns the installation of infrastructure and test setups for studies on large-scale structures and tests of irradiated modules at CERN, which however have not been detailed here. While in the barrel part at most two different hybrid layouts will be required, the Petals in the endcaps make it necessary to design and produce six or nine different hybrid types depending on the final layout decision, i.e. “Bear” or “Lamb & Flag”. With first versions of Petalets presently being assembled and tested and a first version of the final ABCN130 ASICs becoming available, the necessary design decisions and the goal of developing and constructing first fully functional full-size petals will be in reach within 2014/15. The methodologies developed and the expertise gained in the different fabrication and testing steps, as well in the installation, enhancement and usage of tooling and test setups contribute a large part of the necessary prerequisites for the large scale production of detector components planned for the years 2016 onwards.

Bibliography

[1] CDF Collaboration. Observation of top quark production in $\bar{p}p$ collisions. *Phys. Rev. Lett.*, 74:2626–2631, 1995. doi:10.1103/PhysRevLett.74.2626.

[2] D0 Collaboration. Observation of the top quark. *Phys. Rev. Lett.*, 74:2632–2637, 1995. doi:10.1103/PhysRevLett.74.2632.

[3] CERN, Geneva (Press Office). Update on the search for the Higgs boson by the ATLAS and CMS experiments at CERN, Dec 2011. URL `https://cds.cern.ch/record/1406786`.

[4] CMS Collaboration. Combined results of searches for the standard model Higgs boson in pp collisions at $\sqrt{s} = 7$ TeV. *Phys. Lett.*, B710(1):26–48, 2012. doi:10.1016/j.physletb.2012.02.064.

[5] ATLAS Collaboration. Combined search for the Standard Model Higgs boson using up to 4.9 fb^{-1} of pp collision data at $\sqrt{s} = 7$ TeV with the ATLAS detector at the LHC. *Phys. Lett.*, B710(1):49–66, 2012. doi:10.1016/j.physletb.2012.02.044.

[6] ATLAS Collaboration. Observation of an Excess of Events in the Search for the Standard Model Higgs boson with the ATLAS detector at the LHC. ATLAS-CONF-2012-093, CERN, Geneva, Jul 2012.

[7] CMS Collaboration. Observation of a new boson with a mass near 125 GeV. CMS-PAS-HIG-12-020, CERN, Geneva, Jul 2012.

[8] CMS Collaboration. Observation of a new boson at a mass of 125 GeV with the CMS experiment at the LHC. *Phys. Lett.*, B716(1):30–61, 2012. doi:10.1016/j.physletb.2012.08.021.

[9] ATLAS Collaboration. Observation of a new particle in the search for the Standard Model Higgs boson with the ATLAS detector at the LHC. *Phys. Lett.*, B716(1): 1–29, 2012. doi:10.1016/j.physletb.2012.08.020.

[10] A. J. Whitbeck (for the CMS Collaboration). Measurements of Higgs Boson Properties in CMS, In: Proceedings of the 48th Rencontres de Moriond on QCD and High Energy Interactions, La Thuile, Italy, 9 - 16 Mar 2013. CERN-CMS-CR-2013-145, CERN, Geneva, Jun 2013.

[11] T. Adye (for the ATLAS Collaboration). Measurements of Higgs boson properties in ATLAS, In: Proceedings of the 48th Rencontres de Moriond on QCD and

High Energy Interactions, La Thuile, Italy, 9 - 16 Mar 2013. ATL-PHYS-PROC-2013-122, CERN, Geneva, May 2013.

[12] S. Chatrchyan. Erratum: Study of the Mass and Spin-Parity of the Higgs Boson Candidate via Its Decays to Z Boson Pairs [Phys. Rev. Lett. 110, 081803 (2013)]. *Phys. Rev. Lett.*, 110:189901, May 2013. doi:10.1103/PhysRevLett.110.189901.

[13] ATLAS Collaboration. Evidence for the spin-0 nature of the Higgs boson using ATLAS data. *Phys. Lett.*, B726:120–144, 2013. doi:10.1016/j.physletb.2013.08.026.

[14] Particle Data Group. Review of particle physics and 2013 partial update for the 2014 edition. *Phys. Rev.*, D86:010001, Jul 2012. doi:10.1103/PhysRevD.86.010001.

[15] J. A. Aguilar-Saavedra. Top flavour-changing neutral interactions: Theoretical expectations and experimental detection. *Acta Phys. Polon.*, B35:2695–2710, 2004.

[16] J. Gao, C. S. Li, L. L. Yang, and H. Zhang. Search for anomalous top quark production at the early LHC. *Phys. Rev. Lett.*, 107:092002, 2011. doi:10.1103/PhysRevLett.107.092002.

[17] ATLAS Collaboration. Study of ATLAS sensitivity to FCNC top decays. *Eur. Phys. J.*, C52:999–1019, 2007. doi:10.1140/epjc/s10052-007-0434-0.

[18] M. Beneke, I. Efthymiopoulos, M. L. Mangano, et al. Top quark physics, In: Proceedings of the 1999 CERN Workshop on SM physics (and more) at the LHC. Cern-th-2000-100, fermilab-conf-00-398-t, CERN, Geneva, 2000. `arXiv:hep-ph/0003033`.

[19] S. L. Glashow. Partial Symmetries of Weak Interactions. *Nucl. Phys.*, 22:579–588, 1961. doi:10.1016/0029-5582(61)90469-2.

[20] A. Salam. Weak and Electromagnetic Interactions. *Conf. Proc.*, C680519:367–377, 1968. Originally printed in Svartholm: Elementary Particle Theory, Proceedings of the Nobel Symposium held 1968 at Lerum, Sweden, Stockholm.

[21] S. Weinberg. A Model of Leptons. *Phys. Rev. Lett.*, 19:1264–1266, 1967. doi:10.1103/PhysRevLett.19.1264.

[22] G. Zweig. An SU(3) model for strong interaction symmetry and its breaking. , CERN, Geneva, Feb 1964. CERN-TH-412.

[23] M. E. Peskin and D. V. Schroeder. *An Introduction To Quantum Field Theory*. Advanced book classics. Addison-Wesley Publishing Company, 1995. ISBN 9780201503975.

[24] E. Noether. Invariante Variationsprobleme. *Nachrichten von der Gesellschaft der Wissenschaften zu Göttingen, Mathematisch-Physikalische Klasse*, 1918:235–257, 1918. URL `http://eudml.org/doc/59024`.

[25] F. Englert and R. Brout. Broken symmetry and the mass of gauge vector mesons. *Phys. Rev. Lett.*, 13:321–323, Aug 1964. doi:10.1103/PhysRevLett.13.321.

[26] P. W. Higgs. Broken symmetries and the masses of gauge bosons. *Phys. Rev. Lett.*, 13:508–509, Oct 1964. doi:10.1103/PhysRevLett.13.508.

[27] G. S. Guralnik, C. R. Hagen, and T. W. B. Kibble. Global conservation laws and massless particles. *Phys. Rev. Lett.*, 13:585–587, Nov 1964. doi:10.1103/PhysRevLett.13.585.

[28] P. W. Higgs. Spontaneous symmetry breakdown without massless bosons. *Phys. Rev.*, 145:1156–1163, May 1966. doi:10.1103/PhysRev.145.1156.

[29] Y. Nambu. Quasi-Particles and Gauge Invariance in the Theory of Superconductivity. *Phys. Rev.*, 117:648–663, Feb 1960. doi:10.1103/PhysRev.117.648.

[30] J. Goldstone. Field theories with « Superconductor » solutions. *Il Nuovo Cimento*, 19(1):154–164, 1961. doi:10.1007/BF02812722.

[31] J. Goldstone, A. Salam, and S. Weinberg. Broken symmetries. *Phys. Rev.*, 127: 965–970, Aug 1962. doi:10.1103/PhysRev.127.965.

[32] H. Yukawa. On the Interaction of Elementary Particles. I. *Prog. Theor. Phys. Suppl.*, 1:1–10, 1955. doi:10.1143/PTPS.1.1.

[33] M. Kobayashi and T. Maskawa. CP-Violation in the Renormalizable Theory of Weak Interaction. *Prog. Theor. Phys.*, 49(2):652–657, 1973. doi:10.1143/PTP.49.652.

[34] G. 't Hooft. Renormalization of massless Yang-Mills fields. *Nucl. Phys.*, B33(1): 173–199, 1971. doi:10.1016/0550-3213(71)90395-6.

[35] G. 't Hooft and M. Veltman. Regularization and renormalization of gauge fields. *Nucl. Phys.*, B44(1):189–213, 1972. doi:10.1016/0550-3213(72)90279-9.

[36] F. Hasert, S. Kabe, W. Krenz, et al. Observation of neutrino-like interactions without muon or electron in the Gargamelle neutrino experiment. *Phys. Lett.*, B46(1):138–140, 1973. doi:10.1016/0370-2693(73)90499-1.

[37] UA1 Collaboration. Experimental observation of isolated large transverse energy electrons with associated missing energy at $\sqrt{s} = 540$ GeV. *Phys. Lett.*, B122(1): 103–116, 1983. doi:10.1016/0370-2693(83)91177-2.

[38] UA2 Collaboration. Observation of single isolated electrons of high transverse momentum in events with missing transverse energy at the CERN pp collider. *Phys. Lett.*, B122(5–6):476–485, 1983. doi:10.1016/0370-2693(83)91605-2.

[39] UA1 Collaboration. Experimental observation of lepton pairs of invariant mass around $95\,\mathrm{GeV/c^2}$ at the CERN SPS collider. *Phys. Lett.*, B126(5):398–410, 1983. doi:10.1016/0370-2693(83)90188-0.

[40] UA2 Collaboration. Evidence for $z^0 \to e^+e^-$ at the cern pp collider. *Physics Letters B*, 129(1-2):130–140, 1983. doi:10.1016/0370-2693(83)90744-X.

[41] M. Gell-Mann. A schematic model of baryons and mesons. *Phys. Lett.*, 8(3): 214–215, 1964. doi:10.1016/S0031-9163(64)92001-3.

[42] F. Tkachov. A contribution to the history of quarks: Boris Struminsky's 1965 JINR publication. `arXiv:0904.0343 [physics.hist-ph]`, April 2009.

[43] H. D. Politzer. Reliable perturbative results for strong interactions? *Phys. Rev. Lett.*, 30:1346–1349, Jun 1973. doi:10.1103/PhysRevLett.30.1346.

[44] D. J. Gross and F. Wilczek. Ultraviolet behavior of non-abelian gauge theories. *Phys. Rev. Lett.*, 30:1343–1346, Jun 1973. doi:10.1103/PhysRevLett.30.1343.

[45] G. 't Hooft and M. Veltman. Regularization and Renormalization of Gauge Fields. *Nucl. Phys.*, B44:189–213, 1972. doi:10.1016/0550-3213(72)90279-9.

[46] R. K. Ellis, W. J. Stirling, and B. R. Webber. *QCD and Collider Physics*, volume 8 of *Camb. Monogr. Part. Phys. Nucl. Phys. Cosmol.* Cambridge University Press, 1996. ISBN 9780521545891.

[47] G. Sterman, J. Smith, J. C. Collins, et al. Handbook of perturbative QCD. *Rev. Mod. Phys.*, 67:157–248, Jan 1995. doi:10.1103/RevModPhys.67.157.

[48] PLUTO Collaboration. Evidence for Gluon Bremsstrahlung in e^+e^- Annihilations at High Energies. *Phys. Lett.*, B86:418, 1979. doi:10.1016/0370-2693(79)90869-4.

[49] D. P. Barber, U. Becker, H. Benda, et al. Discovery of Three-Jet Events and a Test of Quantum Chromodynamics at PETRA. *Phys. Rev. Lett.*, 43:830–833, Sep 1979. doi:10.1103/PhysRevLett.43.830.

[50] CERN. LEP Design Report Vol.2: The LEP Main Ring. CERN-LEP-84-01, CERN, Geneva, 1984.

[51] TeVI Group. Design Report Tevatron 1 Project. FERMILAB-DESIGN-1984-01, FERMILAB, Batavia, IL, 1984.

[52] M. Cacciari, M. Czakon, M. Mangano, A. Mitov, and P. Nason. Top-pair production at hadron colliders with next-to-next-to-leading logarithmic soft-gluon resummation. *Phys. Lett.*, B710:612–622, 2012. doi:10.1016/j.physletb.2012.03.013.

[53] P. Baernreuther, M. Czakon, and A. Mitov. Percent Level Precision Physics at the Tevatron: First Genuine NNLO QCD Corrections to $q\bar{q} \to t\bar{t} + X$. *Phys. Rev. Lett.*, 109:132001, 2012. doi:10.1103/PhysRevLett.109.132001.

[54] M. Czakon and A. Mitov. NNLO corrections to top-pair production at hadron colliders: the all-fermionic scattering channels. *JHEP*, 1212:054, 2012. doi:10.1007/JHEP12(2012)054.

[55] M. Czakon and A. Mitov. NNLO corrections to top pair production at hadron colliders: the quark-gluon reaction. *JHEP*, 1301:080, 2013. doi:10.1007/JHEP01(2013)080.

[56] M. Czakon, P. Fiedler, and A. Mitov. The total top quark pair production cross-section at hadron colliders through $O(\alpha_S^4)$. *Phys. Rev. Lett.*, 110:252004, 2013. doi:10.1103/PhysRevLett.110.252004.

[57] M. Czakon and A. Mitov. Top++: A Program for the Calculation of the Top-Pair Cross-Section at Hadron Colliders. `arXiv:1112.5675 [hep-ph]`, 2011.

[58] M. Botje, J. Butterworth, A. Cooper-Sarkar, et al. The PDF4LHC Working Group Interim Recommendations. `arXiv:1101.0538 [hep-ph]`, 2011.

[59] A. Martin, W. Stirling, R. Thorne, and G. Watt. Parton distributions for the LHC. *Eur. Phys. J.*, C63:189–285, 2009. doi:10.1140/epjc/s10052-009-1072-5.

[60] A. Martin, W. Stirling, R. Thorne, and G. Watt. Uncertainties on α_S in global PDF analyses and implications for predicted hadronic cross sections. *Eur. Phys. J.*, C64:653–680, 2009. doi:10.1140/epjc/s10052-009-1164-2.

[61] H.-L. Lai, M. Guzzi, J. Huston, et al. New parton distributions for collider physics. *Phys. Rev.*, D82:074024, 2010. doi:10.1103/PhysRevD.82.074024.

[62] J. Gao, M. Guzzi, J. Huston, et al. The CT10 NNLO Global Analysis of QCD. `arXiv:1302.6246 [hep-ph]`, 2013.

[63] R. D. Ball, V. Bertone, S. Carrazza, et al. Parton distributions with LHC data. *Nucl. Phys.*, B867:244–289, 2013. doi:10.1016/j.nuclphysb.2012.10.003.

[64] N. Kidonakis. Next-to-next-to-leading-order collinear and soft gluon corrections for t-channel single top quark production. *Phys. Rev.*, D83:091503, 2011. doi:10.1103/PhysRevD.83.091503.

[65] N. Kidonakis. Two-loop soft anomalous dimensions for single top quark associated production with a W^- or H^-. *Phys. Rev.*, D82:054018, 2010. doi:10.1103/PhysRevD.82.054018.

[66] N. Kidonakis. NNLL resummation for s-channel single top quark production. *Phys. Rev.*, D81:054028, 2010. doi:10.1103/PhysRevD.81.054028.

[67] CDF Collaboration. Observation of electroweak single top-quark production. *Phys. Rev. Lett.*, 103:092002, Aug 2009. doi:10.1103/PhysRevLett.103.092002.

[68] D0 Collaboration. Observation of single top-quark production. *Phys. Rev. Lett.*, 103:092001, Aug 2009. doi:10.1103/PhysRevLett.103.092001.

[69] ATLAS Collaboration. Measurement of the top quark-pair production cross section with ATLAS in pp collisions at $\sqrt{s} = 7$ TeV. *Eur. Phys. J.*, C71:1577, 2011. doi:10.1140/epjc/s10052-011-1577-6.

[70] CMS Collaboration. First Measurement of the Cross Section for Top-Quark Pair Production in Proton-Proton Collisions at $\sqrt{s} = 7$ TeV. *Phys. Lett.*, B695:424–443, 2011. doi:10.1016/j.physletb.2010.11.058.

[71] D0 Collaboration. Model-independent measurement of t-channel single top quark production in $p\bar{p}$ collisions at $\sqrt{s} = 1.96$ TeV. *Phys. Lett.*, B705:313–319, 2011. doi:10.1016/j.physletb.2011.10.035.

[72] ATLAS Collaboration. Observation of t-Channel Single Top-Quark Production in pp Collisions at $\sqrt{s} = 7$ TeV with the ATLAS detector. ATLAS-CONF-2011-088, CERN, Geneva, 2011.

[73] ATLAS Collaboration. Evidence for the associated production of a W boson and a top quark in ATLAS at $\sqrt{s} = 7$ TeV. *Phys. Lett.*, B716:142–159, 2012. doi:10.1016/j.physletb.2012.08.011.

[74] CMS Collaboration. Single Top associated tW production at 8 TeV in the two lepton final state. CMS-PAS-TOP-12-040, CERN, Geneva, 2013.

[75] D0 Collaboration. Evidence for s-channel single top quark production in $p\bar{p}$ collisions at $\sqrt{s} = 1.96$ TeV. *Phys. Lett.*, B726:656–664, 2013. doi:10.1016/j.physletb.2013.09.048.

[76] S. L. Glashow, J. Iliopoulos, and L. Maiani. Weak Interactions with Lepton-Hadron Symmetry. *Phys. Rev.*, D2:1285–1292, 1970. doi:10.1103/PhysRevD.2.1285.

[77] N. Cabibbo. Unitary Symmetry and Leptonic Decays. *Phys. Rev. Lett.*, 10:531–533, Jun 1963. doi:10.1103/PhysRevLett.10.531.

[78] U. Amaldi, W. de Boer, and H. Fürstenau. Comparison of grand unified theories with electroweak and strong coupling constants measured at LEP. *Phys. Lett.*, B260(3–4):447–455, 1991. doi:10.1016/0370-2693(91)91641-8.

[79] M. Gonzalez-Garcia and M. Maltoni. Phenomenology with Massive Neutrinos. *Phys. Rept.*, 460:1–129, 2008. doi:10.1016/j.physrep.2007.12.004.

[80] L. Canetti, M. Drewes, and M. Shaposhnikov. Matter and Antimatter in the Universe. *New J. Phys.*, 14:095012, 2012. doi:10.1088/1367-2630/14/9/095012.

[81] W. de Blok, S. S. McGaugh, A. Bosma, and V. C. Rubin. Mass density profiles of LSB galaxies. *Astrophys. J.*, 552:L23–L26, 2001. doi:10.1086/320262.

[82] M. Kowalski, D. Rubin, G. Aldering, et al. Improved cosmological constraints from new, old, and combined supernova data sets. *Astrophys. J.*, 686(2):749, 2008. doi:10.1086/589937.

[83] D. Parkinson, S. Riemer-Sorensen, C. Blake, et al. The WiggleZ Dark Energy Survey: Final data release and cosmological results. *Phys. Rev.*, D86:103518, 2012. doi:10.1103/PhysRevD.86.103518.

[84] WMAP Collaboration. Nine-Year Wilkinson Microwave Anisotropy Probe (WMAP) Observations: Final Maps and Results. *Astrophys. J. Suppl.*, 208:20, 2013. doi:10.1088/0067-0049/208/2/20.

[85] Planck Collaboration. Planck 2013 results. XVI. Cosmological parameters. `arXiv:1303.5076 [astro-ph.CO]`, 2013.

[86] Supernova Cosmology Project Collaboration. Measurements of Omega and Lambda from 42 high redshift supernovae. *Astrophys. J.*, 517:565–586, 1999. doi:10.1086/307221.

[87] Supernova Search Team Collaboration. Observational evidence from supernovae for an accelerating universe and a cosmological constant. *Astron. J.*, 116: 1009–1038, 1998. doi:10.1086/300499.

[88] G. F. R. Ellis, R. Maartens, and M. A. H. MacCallum. *Relativistic Cosmology*. Cambridge University Press, Cambridge, UK, Mar 2012. ISBN 9780521381154.

[89] J. A. Aguilar-Saavedra and B. M. Nobre. Rare top decays $t \to c\gamma$, $t \to cg$ and CKM unitarity. *Phys. Lett.*, B553:251–260, 2003. doi:10.1016/S0370-2693(02)03230-6.

[90] F. del Aguila, J. A. Aguilar-Saavedra, and R. Miquel. Constraints on top couplings in models with exotic quarks. *Phys. Rev. Lett.*, 82:1628–1631, 1999. doi:10.1103/PhysRevLett.82.1628.

[91] J. A. Aguilar-Saavedra. Effects of mixing with quark singlets. *Phys. Rev.*, D67: 035003, 2003. doi:10.1103/PhysRevD.69.099901, 10.1103/PhysRevD.67.035003.

[92] J. L. Díaz-Cruz, R. Martínez, M. A. Pérez, and A. Rosado. Flavor-changing radiative decay of the t quark. *Phys. Rev.*, D41:891–894, Feb 1990. doi:10.1103/PhysRevD.41.891.

[93] A. Arhrib and W.-S. Hou. Flavor changing neutral currents involving heavy quarks with four generations. *JHEP*, 0607:009, 2006. doi:10.1088/1126-6708/2006/07/009.

[94] T. P. Cheng and M. Sher. Mass Matrix Ansatz and Flavor Nonconservation in Models with Multiple Higgs Doublets. *Phys. Rev.*, D35:3484, 1987. doi:10.1103/PhysRevD.35.3484.

[95] B. Grzadkowski, J. F. Gunion, and P. Krawczyk. Neutral current flavor changing decays for the Z boson and the top quark in two Higgs doublet models. *Phys. Lett.*, B268:106–111, 1991. doi:10.1016/0370-2693(91)90931-F.

[96] M. E. Luke and M. J. Savage. Flavor changing neutral currents in the Higgs sector and rare top decays. *Phys. Lett.*, B307:387–393, 1993. doi:10.1016/0370-2693(93)90238-D.

[97] D. Atwood, L. Reina, and A. Soni. Probing flavor changing top - charm - scalar interactions in e^+ e^- collisions. *Phys. Rev.*, D53:1199–1201, 1996. doi:10.1103/PhysRevD.53.1199.

[98] D. Atwood, L. Reina, and A. Soni. Phenomenology of two Higgs doublet models with flavor changing neutral currents. *Phys. Rev.*, D55:3156–3176, 1997. doi:10.1103/PhysRevD.55.3156.

[99] S. Bejar, J. Guasch, and J. Sola. Loop induced flavor changing neutral decays of the top quark in a general two-Higgs-doublet model. *Nucl. Phys.*, B600:21–38, 2001. doi:10.1016/S0550-3213(01)00044-X.

[100] C. S. Li, R. J. Oakes, and J. M. Yang. Rare decay of the top quark in the minimal supersymmetric model. *Phys. Rev.*, D49:293–298, 1994. doi:10.1103/PhysRevD.49.293. Erratum-ibid.D56:3156,1997.

[101] G. M. de Divitiis, R. Petronzio, and L. Silvestrini. Flavour changing top decays in supersymmetric extensions of the Standard Model. *Nucl. Phys.*, B504:45–60, 1997. doi:10.1016/S0550-3213(97)00476-8.

[102] J. L. Lopez, D. V. Nanopoulos, and R. Rangarajan. New supersymmetric contributions to $t \to cV$. *Phys. Rev.*, D56:3100–3106, 1997. doi:10.1103/PhysRevD.56.3100.

[103] J. Guasch and J. Sola. FCNC top quark decays: A door to SUSY physics in high luminosity colliders? *Nucl. Phys.*, B562:3–28, 1999. doi:10.1016/S0550-3213(99)00579-9.

[104] D. Delepine and S. Khalil. Top flavour violating decays in general supersymmetric models. *Phys. Lett.*, B599:62–74, 2004. doi:10.1016/j.physletb.2004.08.025.

[105] J. J. Liu, C. S. Li, L. L. Yang, and L. G. Jin. $t \to cV$ via SUSY FCNC couplings in the unconstrained MSSM. *Phys. Lett.*, B599:92–101, 2004. doi:10.1016/j.physletb.2004.07.062.

[106] J. J. Cao et al. SUSY-induced FCNC top-quark processes at the Large Hadron Collider. *Phys. Rev.*, D75:075021, 2007. doi:10.1103/PhysRevD.75.075021.

[107] J. M. Yang, B.-L. Young, and X. Zhang. Flavor-changing top quark decays in R-parity violating SUSY. *Phys. Rev.*, D58:055001, 1998. doi:10.1103/PhysRevD.58.055001.

[108] G. Eilam, A. Gemintern, T. Han, J. M. Yang, and X. Zhang. Top quark rare decay $t \to ch$ in R-parity-violating SUSY. *Phys. Lett.*, B510:227–235, 2001. doi:10.1016/S0370-2693(01)00598-6.

[109] G. Lu, F. Yin, X. Wang, and L. Wan. The rare top quark decays $t \to cV$ in the topcolor-assisted technicolor model. *Phys. Rev.*, D68:015002, 2003. doi:10.1103/PhysRevD.68.015002.

[110] F. Larios, R. Martínez, and M. A. Pérez. New physics effects in the flavor-changing neutral couplings of the top quark. *Int. J. Mod. Phys.*, A21:3473–3494, 2006. doi:10.1142/S0217751X06033039.

[111] J. A. Aguilar-Saavedra, R. Benbrik, S. Heinemeyer, and M. Pérez-Victoria. A handbook of vector-like quarks: mixing and single production. *Phys. Rev.*, D88: 094010, 2013. doi:10.1103/PhysRevD.88.094010.

[112] S. L. Glashow and S. Weinberg. Natural Conservation Laws for Neutral Currents. *Phys. Rev.*, D15:1958–1965, Apr 1977. doi:10.1103/PhysRevD.15.1958.

[113] J. Gunion, H. Haber, and G. Kane. *The Higgs Hunter's Guide*. Frontiers in physics. Basic Books, 2000. ISBN 9780786743186.

[114] G. Branco, P. Ferreira, L. Lavoura, et al. Theory and phenomenology of two-Higgs-doublet models. *Phys. Rept.*, 516:1–102, 2012. doi:10.1016/j.physrep.2012.02.002.

[115] M. Kuroda. Complete Lagrangian of MSSM. `arXiv:hep-ph/9902340`, 1999.

[116] R. E. Marshak. *Conceptual foundations of modern particle physics*. World Scientific, 1993. ISBN 9810211066.

[117] G. Couture, M. Frank, and H. König. Supersymmetric QCD flavor-changing top quark decay. *Phys. Rev.*, D56:4213–4218, Oct 1997. doi:10.1103/PhysRevD.56.4213.

[118] D. Chung, L. Everett, G. Kane, et al. The soft supersymmetry-breaking Lagrangian: Theory and applications. *Phys. Rep.*, 407(1–3):1–203, 2005. doi:10.1016/j.physrep.2004.08.032.

[119] L. Susskind. Dynamics of Spontaneous Symmetry Breaking in the Weinberg-Salam Theory. *Phys. Rev.*, D20:2619–2625, 1979. doi:10.1103/PhysRevD.20.2619.

[120] E. Eichten and K. D. Lane. Dynamical Breaking of Weak Interaction Symmetries. *Phys. Lett.*, B90:125–130, 1980. doi:10.1016/0370-2693(80)90065-9.

[121] C. T. Hill. Topcolor assisted technicolor. *Phys. Lett.*, B345:483–489, 1995. doi:10.1016/0370-2693(94)01660-5.

[122] K. D. Lane and E. Eichten. Natural topcolor assisted technicolor. *Phys. Lett.*, B352:382–387, 1995. doi:10.1016/0370-2693(95)00482-Z.

[123] C. Yue, G. Lu, G. Liu, and Q. Xu. Rare top decay $t \to cg$ in top-color assisted technicolor models. *Phys. Rev.*, D64:095004, Oct 2001. doi:10.1103/PhysRevD.64.095004.

[124] CDF Collaboration. Search for top-quark production via flavor-changing neutral currents in $W+1$ jet events at CDF. *Phys. Rev. Lett.*, 102:151801, 2009. doi:10.1103/PhysRevLett.102.151801.

[125] D0 Collaboration. Search for flavor changing neutral currents via quark-gluon couplings in single top quark production using 2.3 fb^{-1} of $p\bar{p}$ collisions. *Phys. Lett.*, B693:81–87, 2010. doi:10.1016/j.physletb.2010.08.011.

[126] ATLAS Collaboration. Search for FCNC single top-quark production at $\sqrt{s} = 7$ TeV with the ATLAS detector. *Phys. Lett.*, B712:351–369, 2012. doi:10.1016/j.physletb.2012.05.022.

[127] ALEPH Collaboration. Search for single top production in $\text{e}^+\,\text{e}^-$ collisions at $\sqrt{s}$ up to 209 GeV. *Phys. Lett.*, B543:173–182, 2002. doi:10.1016/S0370-2693(02)02307-9.

[128] DELPHI Collaboration. Search for single top production via FCNC at LEP at $\sqrt{s} = 189$ GeV - 208 GeV. *Phys. Lett.*, B590:21–34, 2004. doi:10.1016/j.physletb.2004.03.051.

[129] OPAL Collaboration. Search for single top quark production at LEP2. *Phys. Lett.*, B521:181–194, 2001. doi:10.1016/S0370-2693(01)01195-9.

[130] L3 Collaboration. Search for single top production at LEP. *Phys. Lett.*, B549: 290–300, 2002. doi:10.1016/S0370-2693(02)02933-7.

[131] DELPHI Collaboration, ALEPH Collaboration, L3 Collaboration, OPAL Collaboration, LEP Exotica Working Group. Search for single top production via flavour changing neutral currents: preliminary combined results of the LEP experiments. DELPHI-2001-119-CONF-542. CERN-DELPHI-2001-119-CONF-542. LEP-Exotica-WG-2001-01. ALEPH-2001-055. CERN-ALEPH-CONF-2001-035. L3-2706. OPAL-TN-698, CERN, Geneva, Jul 2001.

[132] H1 Collaboration. Search for Single Top Quark Production at HERA. *Phys. Lett.*, B678:450–458, 2009. doi:10.1016/j.physletb.2009.06.057.

[133] ZEUS Collaboration. Search for single top production in *ep* collisions at HERA. *Phys.Lett.*, B559:153–170, 2003. doi:10.1016/S0370-2693(03)00333-2.

[134] A. A. Ashimova and S. R. Slabospitsky. The Constraint on FCNC Coupling of the Top Quark with a Gluon from ep Collisions. *Phys. Lett.*, B668:282–285, 2008. doi:10.1016/j.physletb.2008.08.065.

[135] H1 Collaboration. Search for single top quark production in *ep* collisions at HERA. *Eur. Phys. J.*, C33:9–22, 2004. doi:10.1140/epjc/s2003-01588-2.

[136] CDF Collaboration. Search for flavor-changing neutral current decays of the top quark in $p\bar{p}$ collisions at $\sqrt{s} = 1.8$ TeV. *Phys. Rev. Lett.*, 80:2525–2530, 1998. doi:10.1103/PhysRevLett.80.2525.

[137] D0 Collaboration. Search for flavor changing neutral currents in decays of top quarks. *Phys. Lett.*, B701(3):313–320, 2011. doi:10.1016/j.physletb.2011.06.014.

[138] CMS Collaboration. Search for flavor changing neutral currents in top quark decays in pp collisions at 8 TeV. CMS-PAS-TOP-12-037, CERN, Geneva, 2013.

[139] X.-Q. Li, Y.-D. Yang, and X.-B. Yuan. Anomalous tqZ Coupling Effects in Rare B- and K-Meson Decays. *JHEP*, 1203:018, 2012. doi:10.1007/JHEP03(2012)018.

[140] BABAR Collaboration. The BABAR detector. *Nucl. Instrum. Meth.*, A479(1): 1–116, 2002. doi:10.1016/S0168-9002(01)02012-5.

[141] BELLE Collaboration. The Belle Detector. *Nucl. Instrum. Meth.*, A479:117–232, 2002. doi:10.1016/S0168-9002(01)02013-7.

[142] CDF Collaboration. The CDF-II detector: Technical Design Report. FERMILAB-DESIGN-1996-01, FERMILAB-PUB-96-390-E, FERMILAB, Batavia, IL, 1996.

[143] LHCb Collaboration. The LHCb Detector at the LHC. *JINST*, 3(08):S08005, 2008. doi:10.1088/1748-0221/3/08/S08005.

[144] H. Gong, Y.-D. Yang, and X.-B. Yuan. Constraints on anomalous tcZ coupling from $\bar{B} \to \bar{K}^* \mu^+ \mu^-$ and $B_s \to \mu^+ \mu^-$ decays. *JHEP*, 1305:062, 2013. doi:10.1007/JHEP05(2013)062.

[145] X.-Q. Li, Y.-D. Yang, and X.-B. Yuan. Anomalous $tq\gamma$ coupling effects in exclusive radiative B-meson decays. *JHEP*, 1108:075, 2011. doi:10.1007/JHEP08(2011)075.

[146] X. Yuan, Y. Hao, and Y. Yang. $B \to X_s \gamma$ constraints on the top quark anomalous $t \to c\gamma$ coupling. *Phys. Rev.*, D83:013004, 2011. doi:10.1103/PhysRevD.83.013004.

[147] W. Buchmüller and D. Wyler. Effective Lagrangian analysis of new interactions and flavour conservation. *Nucl. Phys.*, B268(3–4):621–653, 1986. doi:10.1016/0550-3213(86)90262-2.

[148] P. Ferreira and R. Santos. Strong flavor changing effective operator contributions to single top quark production. *Phys. Rev.*, D73:054025, 2006. doi:10.1103/PhysRevD.73.054025.

[149] R. Coimbra, A. Onofre, R. Santos, and M. Won. MEtop - a generator for single top production via FCNC interactions. *Eur. Phys. J.*, C72:2222, 2012. doi:10.1140/epjc/s10052-012-2222-8.

[150] J. J. Zhang, C. S. Li, J. Gao, et al. Next-to-leading order QCD corrections to the top quark decay via the Flavor-Changing Neutral-Current operators with mixing effects. *Phys. Rev.*, D82:073005, 2010. doi:10.1103/PhysRevD.82.073005.

[151] C. S. Li, R. J. Oakes, and T. C. Yuan. QCD corrections to $t \to W^+ + b$. *Phys. Rev.*, D43:3759–3762, Jun 1991. doi:10.1103/PhysRevD.43.3759.

[152] J. J. Liu, C. S. Li, L. L. Yang, and L. G. Jin. Next-to-leading order QCD corrections to the direct top quark production via model-independent FCNC couplings at hadron colliders. *Phys. Rev.*, D72:074018, 2005. doi:10.1103/PhysRevD.72.074018.

[153] J. Pumplin et al. New Generation of Parton Distributions with Uncertainties From Global QCD Analysis. *JHEP*, 0207:012, 2002. doi:10.1088/1126-6708/2002/07/012.

[154] P. M. Nadolsky et al. Implications of CTEQ global analysis for collider observables. *Phys. Rev.*, D78:013004, 2008. doi:10.1103/PhysRevD.78.013004.

[155] ATLAS Collaboration. The ATLAS Experiment at the CERN Large Hadron Collider. *JINST*, 3:S08003, 2008. doi:10.1088/1748-0221/3/08/S08003.

[156] CMS Collaboration. The CMS experiment at the CERN LHC. *JINST*, 3(08): S08004, 2008. doi:10.1088/1748-0221/3/08/S08004.

[157] ALICE Collaboration. The ALICE experiment at the CERN LHC. *JINST*, 3(08): S08002, 2008. doi:10.1088/1748-0221/3/08/S08002.

[158] O. S. Brüning, P. Collier, P. Lebrun, S. Myers R. Ostojic, J. Poole, and P. Proudlock (editors). *LHC Design Report*. CERN, Geneva, 2004. doi:10.5170/CERN-2004-003-V-1.

[159] E. Lyndon and B. Philip (editors). LHC Machine. *JINST*, 3(08):S08001, 2008. doi:10.1088/1748-0221/3/08/S08001.

[160] C. Lefèvre. The CERN accelerator complex. CERN-DI-0812015, Dec 2008. CERN Photolab.

[161] M. Lamont. Status of the LHC. *J. Phys. Conf.*, 455(1):012001, 2013. doi:10.1088/1742-6596/455/1/012001.

[162] ATLAS Collaboration. ATLAS detector and physics performance: Technical Design Report, 1. CERN-LHCC-99-014, ATLAS-TDR-014, CERN, Geneva, 1999.

[163] J. Pequenao. Computer generated image of the whole ATLAS detector. CERN-GE-0803012, Mar 2008. CERN Photolab.

[164] ATLAS Collaboration. Expected Performance of the ATLAS Experiment - Detector, Trigger and Physics. `arXiv:0901.0512 [hep-ex]` CERN-OPEN-2008-020, CERN, Geneva, 2009.

[165] J. Pequenao. Computer generated image of the ATLAS inner detector. CERN-GE-0803014, Mar 2008. CERN Photolab.

[166] ATLAS Collaboration. ATLAS magnet system: Technical design report. CERN-LHCC-97-018, CERN, Geneva, 1997.

[167] ATLAS Collaboration. ATLAS pixel detector: Technical design report. CERN-LHCC-98-013, CERN, Geneva, 1998.

[168] ATLAS Collaboration. ATLAS inner detector: Technical Design Report, 2. CERN-LHCC-97-017, CERN, Geneva, 1997.

[169] ATLAS Collaboration. ATLAS calorimeter performance: Technical Design Report. CERN-LHCC-96-040, CERN, Geneva, 1996.

[170] J. Pequenao. Computer Generated image of the ATLAS calorimeter. CERN-GE-0803015, Mar 2008. CERN Photolab.

[171] ATLAS Collaboration. ATLAS liquid-argon calorimeter: Technical Design Report. CERN-LHCC-96-041, CERN, Geneva, 1996.

[172] ATLAS Collaboration. ATLAS tile calorimeter: Technical Design Report. CERN-LHCC-96-042, CERN, Geneva, 1996.

[173] ATLAS Collaboration. ATLAS muon spectrometer: Technical Design Report. CERN-LHCC-97-022, CERN, Geneva, 1997.

[174] J. Pequenao. Computer generated image of the ATLAS Muons subsystem. CERN-GE-0803017, Mar 2008. CERN Photolab.

[175] ATLAS Collaboration. ATLAS high-level trigger, data-acquisition and controls: Technical Design Report. CERN-LHCC-2003-022, CERN, Geneva, 2003.

[176] ATLAS luminosity task force. Twiki page: ATLAS Luminosity Public Results, 2013. URL `https://twiki.cern.ch/twiki/bin/view/AtlasPublic/LuminosityPublicResults`. (visited on 15/11/2013).

[177] S. van der Meer. Calibration of the effective beam height in the ISR. CERN-ISR-PO-68-31. ISR-PO-68-31, CERN, Geneva, 1968.

[178] C. Rubbia. Measurement of the luminosity of p-$\bar{p}$ collider with a (generalized) Van der Meer Method. CERN-p$\bar{p}$-Note-38, CERN, Geneva, Nov 1977.

[179] ATLAS Collaboration. Improved luminosity determination in pp collisions at $\sqrt{s} =$ 7 TeV using the ATLAS detector at the LHC. *Eur. Phys. J.*, C73:2518, 2013. doi:10.1140/epjc/s10052-013-2518-3.

[180] ATLAS Collaboration. The ATLAS Simulation Infrastructure. *Eur. Phys. J. C*, 70:823–874, 2010. doi:10.1140/epjc/s10052-010-1429-9.

[181] T. Gleisberg, S. Höche, F. Krauss, et al. Event generation with SHERPA 1.1. *JHEP*, 0902:007, 2009. doi:10.1088/1126-6708/2009/02/007.

[182] R. P. Feynman. Very high-energy collisions of hadrons. *Phys. Rev. Lett.*, 23: 1415–1417, Dec 1969. doi:10.1103/PhysRevLett.23.1415.

[183] J. C. Collins, D. E. Soper, and G. F. Sterman. Factorization of Hard Processes in QCD. *Adv. Ser. Direct. High Energy Phys.*, 5:1–91, 1988. `arxiv:hep-ph/0409313`.

[184] R. Ellis, H. Georgi, M. Machacek, H. Politzer, and G. G. Ross. Perturbation theory and the parton model in QCD. *Nucl. Phys.*, B152(2):285–329, 1979. doi:10.1016/0550-3213(79)90105-6.

[185] H1 and ZEUS Collaboration. Combined Measurement and QCD Analysis of the Inclusive $e^{\pm}p$ Scattering Cross Sections at HERA. *JHEP*, 1001:109, 2010. doi:10.1007/JHEP01(2010)109.

[186] V. Gribov and L. Lipatov. Deep inelastic e-p scattering in perturbation theory. *Sov. J. Nucl. Phys.*, 15:438–450, 1972.

[187] G. Altarelli and G. Parisi. Asymptotic freedom in parton language. *Nucl. Phys.*, B126(2):298–318, 1977. doi:10.1016/0550-3213(77)90384-4.

[188] Y. L. Dokshitzer. Calculation of the Structure Functions for Deep Inelastic Scattering and e^+-e^- Annihilation by Perturbation Theory in Quantum Chromodynamics. *Sov. Phys. JETP*, 46:641–653, 1977.

[189] V. Sudakov. Vertex parts at very high-energies in quantum electrodynamics. *Sov. Phys. JETP*, 3:65–71, 1956.

[190] B. Andersson, G. Gustafson, G. Ingelman, and T. Sjöstrand. Parton fragmentation and string dynamics. *Phys. Rept.*, 97:31–145, 1983. doi:10.1016/0370-1573(83)90080-7.

[191] T. Sjöstrand. Jet fragmentation of multiparton configurations in a string framework. *Nucl. Phys.*, B248(2):469–502, 1984. doi:10.1016/0550-3213(84)90607-2.

[192] R. D. Field and S. Wolfram. A QCD model for e^+e^- annihilation. *Nucl. Phys.*, B213(1):65–84, 1983. doi:10.1016/0550-3213(83)90175-X.

[193] B. R. Webber. A QCD model for jet fragmentation including soft gluon interference. *Nucl. Phys.*, B238(3):492–528, 1984. doi:10.1016/0550-3213(84)90333-X.

[194] R. Field and R. P. Feynman. A parametrization of the properties of quark jets. *Nucl. Phys.*, B136(1):1–76, 1978. doi:10.1016/0550-3213(78)90015-9.

[195] P. Z. Skands. Tuning Monte Carlo Generators: The Perugia Tunes. *Phys. Rev.*, D82:074018, 2010. doi:10.1103/PhysRevD.82.074018.

[196] ATLAS Collaboration. ATLAS tunes of PYTHIA 6 and Pythia 8 for MC11. , CERN, Geneva, 2011. ATL-PHYS-PUB-2011-009.

[197] J. A. Aguilar-Saavedra. Single top quark production at LHC with anomalous Wtb couplings. *Nucl. Phys.*, B804:160–192, 2008. doi:10.1016/j.nuclphysb.2008.06.013.

[198] S. Slabospitsky and L. Sonnenschein. TopReX generator (version 3.25): Short manual. *Comput. Phys. Commun.*, 148:87–102, 2002. doi:10.1016/S0010-4655(02)00471-X.

[199] T. Sjöstrand, S. Mrenna, and P. Z. Skands. PYTHIA 6.4 Physics and Manual. *JHEP*, 05:026, 2006. doi:10.1088/1126-6708/2006/05/026.

[200] E. Boos et al. Method for simulating electroweak top-quark production events in the NLO approximation: Single Top event generator. *Phys. Atom. Nucl.*, 69:1317, 2006. doi:10.1134/S1063778806080084.

[201] J. Alwall, A. Ballestrero, P. Bartalini, et al. A Standard format for Les Houches event files. *Comput. Phys. Commun.*, 176:300–304, 2007. doi:10.1016/j.cpc.2006.11.010.

[202] J. Alwall, M. Herquet, F. Maltoni, O. Mattelaer, and T. Stelzer. MadGraph 5 : Going Beyond. *JHEP*, 1106:128, 2011. doi:10.1007/JHEP06(2011)128.

[203] M. L. Mangano, M. Moretti, F. Piccinini, R. Pittau, and A. D. Polosa. ALPGEN, a Generator for Hard Multiparton Processes in Hadronic Collisions. *JHEP*, 07: 001, 2003. doi:10.1088/1126-6708/2003/07/001.

[204] R. Hamberg, W. van Neerven, and T. Matsuura. A complete calculation of the order α_s^2 correction to the Drell-Yan k-factor. *Nucl. Phys.*, B359(2-3):343–405, 1991. doi:10.1016/0550-3213(91)90064-5.

[205] C. Anastasiou, L. J. Dixon, K. Melnikov, and F. Petriello. High precision QCD at hadron colliders: Electroweak gauge boson rapidity distributions at NNLO. *Phys. Rev.*, D69:094008, 2004. doi:10.1103/PhysRevD.69.094008.

[206] J. M. Campbell and R. Ellis. MCFM for the Tevatron and the LHC. *Nucl. Phys. Proc. Suppl.*, 205-206:10–15, 2010. doi:10.1016/j.nuclphysbps.2010.08.011.

[207] J. M. Campbell and R. K. Ellis. Next-to-leading order corrections to W+2 jet and Z+2 jet production at hadron colliders. *Phys. Rev.*, D65:113007, 2002. doi:10.1103/PhysRevD.65.113007.

[208] M. Alhroob. *Search for Flavour Changing Neutral Currents in Single Top-Quark Production at $\sqrt{s} = 7$ TeV with the ATLAS Detector*. PhD thesis, Bonn Univ., Jul 2012. CERN-THESIS-2012-293.

[209] F. A. Berends, H. Kuijf, B. Tausk, and W. Giele. On the Production of a W and Jets at Hadron Colliders. *Nucl. Phys.*, B357:32–64, 1991. doi:10.1016/0550-3213(91)90458-A.

[210] S. D. Ellis, R. Kleiss, and W. J. Stirling. W's, Z's and Jets. *Phys. Lett. B*, 154: 435, 1985. doi:10.1016/0370-2693(85)90425-3.

[211] S. Frixione, P. Nason and C. Oleari. Matching nlo qcd computations with parton shower simulations: the powheg method. *JHEP*, 0711:070, 2007. doi:10.1088/1126-6708/2007/11/070.

[212] B. P. Kersevan and E. Richter-Was. The Monte Carlo event generator AcerMC versions 2.0 to 3.8 with interfaces to PYTHIA 6.4, HERWIG 6.5 and ARIADNE 4.1. *Comp. Phys. Commun.*, 184(3):919 – 985, 2013. doi:http://dx.doi.org/10.1016/j.cpc.2012.10.032.

[213] G. Corcella et al. HERWIG 6.5: an Event Generator for Hadron Emission Reactions With Interfering Gluons (Including Supersymmetric Processes). *JHEP*, 01: 010, 2001. doi:10.1088/1126-6708/2001/01/010.

[214] J. M. Butterworth, J. R. Forshaw, and M. H. Seymour. Multiparton interactions in photoproduction at HERA. *Z. Phys.*, C72:637–646, 1996. doi:10.1007/s002880050286.

[215] S. Jadach, J. H. Kühn, and Z. Was. TAUOLA: A Library of Monte Carlo programs to simulate decays of polarized tau leptons. *Comput. Phys. Commun.*, 64:275–299, 1990. doi:10.1016/0010-4655(91)90038-M.

[216] J. Campbell and R. Ellis. Update on vector boson pair production at hadron colliders. *Phys. Rev.*, D60:113006, 1999. doi:10.1103/PhysRevD.60.113006.

[217] TOTEM Collaboration. Luminosity-Independent Measurement of the Proton-Proton Total Cross Section at $\sqrt{s} = 8$ TeV. *Phys. Rev. Lett.*, 111:012001, Jul 2013. doi:10.1103/PhysRevLett.111.012001.

[218] S. Agostinelli et al. GEANT4: A Simulation Toolkit. *Nucl. Instrum. Meth.*, A 506:250–303, 2003. doi:10.1016/S0168-9002(03)01368-8.

[219] T. Sjöstrand, S. Mrenna, and P. Z. Skands. A Brief Introduction to PYTHIA 8.1. *Comput. Phys. Commun.*, 178:852–867, 2008. doi:10.1016/j.cpc.2008.01.036.

[220] J. Boudreau and V. Tsulaia. The GeoModel Toolkit for Detector Description, In Proceedings of Computing in High Energy and Nuclear Physics 2004 (CHEP2004), Interlaken, Switzerland, September 27-October 1, 2004. 2005. doi:10.5170/CERN-2005-002. .

[221] ATLAS luminosity task force. Twiki page: General Production and Performance Public Results of the ATLAS Data Preparation Group, 2013. URL `https://twiki.cern.ch/twiki/bin/view/AtlasPublic/DataPrepGenPublicResults`. (visited on 10/12/2013).

[222] J. Pequenao and P. Schaffner. An computer generated image representing how ATLAS detects particles. CERN-EX-1301009, Jan 2013. CERN PhotoLab.

[223] B. Acharya, J. Adelman, S. Adomeit, et al. Object selection and calibration, background estimations and MC samples for the Winter 2013 Top Quark analyses with 2012 data. ATL-COM-PHYS-2013-088, CERN, Geneva, Jan 2013. Internal document.

[224] T. Cornelissen, M. Elsing, S. Fleischmann, et al. Concepts, Design and Implementation of the ATLAS New Tracking (NEWT). ATL-SOFT-PUB-2007-007, CERN, Geneva, Mar 2007.

[225] R. E. Kalman. A new approach to linear filtering and prediction problems. *Transactions of the ASME – Journal of Basic Engineering*, D82:35–45, 1960.

[226] D. Wicke (DELPHI Collaboration). A new algorithm for solving tracking ambiguities. DELPHI 98-163 PROG 236 TRACK 92, CERN, Geneva, Oct 1998.

[227] ATLAS Collaboration. EM Calorimeter Calibration and Performance, in: Expected performance of the ATLAS experiment, pp.43. `arXiv:0901.0512 [hep-ex]` CERN-OPEN-2008-020, CERN, Geneva, 2009.

[228] ATLAS Collaboration. Jets and missing transverse energy, in: Expected performance of the ATLAS experiment, pp.261. `arXiv:0901.0512 [hep-ex]` CERN-OPEN-2008-020, CERN, Geneva, 2009.

[229] W. Lampl, S. Laplace, D. Lelas, et al. Calorimeter Clustering Algorithms: Description and Performance. ATL-LARG-PUB-2008-002, CERN, Geneva, Apr 2008.

[230] ATLAS Collaboration. Performance of primary vertex reconstruction in proton-proton collisions at $\sqrt{s}$ =7 TeV in the ATLAS experiment. ATLAS-CONF-2010-069, CERN, Geneva, Jul 2010.

[231] ATLAS Collaboration. Performance of the ATLAS Inner Detector Track and Vertex Reconstruction in the High Pile-Up LHC Environment. ATLAS-CONF-2012-042, CERN, Geneva, Mar 2012.

[232] R. Fruhwirth, W. Waltenberger, and P. Vanlaer. Adaptive vertex fitting. *J. Phys.*, G34:N343, 2007. doi:10.1088/0954-3899/34/12/N01.

[233] ATLAS Collaboration. Expected electron performance in the ATLAS experiment. ATL-PHYS-PUB-2011-006, CERN, Geneva, Apr 2011.

[234] ATLAS Collaboration. Electron performance measurements with the ATLAS detector using the 2010 LHC proton-proton collision data. *Eur. Phys. J.*, C72:1909, 2012. doi:10.1140/epjc/s10052-012-1909-1.

[235] ATLAS Collaboration. Electron Efficiency Measurements for 2012 and 2011 Data, 2013. URL `https://atlas.web.cern.ch/Atlas/GROUPS/PHYSICS/EGAMMA/PublicPlots/20120611/ElectronEfficiency2012/ATL-COM-PHYS-2011-783/index.html`. (visited on 16/10/2013).

[236] ATLAS Collaboration. Calibrated $Z \to e^+e^-$ mass with 2011 data, 2011. URL `https://atlas.web.cern.ch/Atlas/GROUPS/PHYSICS/EGAMMA/PublicPlots/20110512/CalibratedZee/ATL-COM-PHYS-2011-1637/index.html`. (visited on 16/10/2013).

[237] ATLAS Collaboration. Performance of the ATLAS muon trigger in 2011. ATLAS-CONF-2012-099, CERN, Geneva, Jul 2012.

[238] ATLAS Collaboration. Muon Reconstruction and Identification, in: Expected performance of the ATLAS experiment, pp.161. `arXiv:0901.0512 [hep-ex]` CERN-OPEN-2008-020, CERN, Geneva, 2009.

[239] ATLAS Collaboration. Preliminary results on the muon reconstruction efficiency, momentum resolution, and momentum scale in ATLAS 2012 *pp* collision data. ATLAS-CONF-2013-088, CERN, Geneva, Aug 2013.

[240] K. Rehermann and B. Tweedie. Efficient Identification of Boosted Semileptonic Top Quarks at the LHC. *JHEP*, 1103:059, 2011. doi:10.1007/JHEP03(2011)059.

[241] M. Cacciari, G. P. Salam, and G. Soyez. The Anti-k_t jet clustering algorithm. *JHEP*, 0804:063, 2008. doi:10.1088/1126-6708/2008/04/063.

[242] M. Cacciari and G. P. Salam. Dispelling the N^3 myth for the k_t jet-finder. *Phys.Lett.*, B641:57–61, 2006. doi:10.1016/j.physletb.2006.08.037.

[243] ATLAS Collaboration. Jet energy measurement with the ATLAS detector in proton-proton collisions at $\sqrt{s} = 7$ TeV. *Eur. Phys. J.*, C73:2304, 2013. doi:10.1140/epjc/s10052-013-2304-2.

[244] ATLAS Collaboration. Data-Quality Requirements and Event Cleaning for Jets and Missing Transverse Energy Reconstruction with the ATLAS Detector in Proton-Proton Collisions at a Center-of-Mass Energy of $\sqrt{s} = 7$ TeV. , CERN, Geneva, Jul 2010. ATLAS-CONF-2010-038.

[245] ATLAS Collaboration. Selection of jets produced in proton-proton collisions with the ATLAS detector using 2011 data. ATLAS-CONF-2012-020, CERN, Geneva, Mar 2012.

[246] ATLAS Collaboration. Pile-up subtraction and suppression for jets in ATLAS. ATLAS-CONF-2013-083, CERN, Geneva, Aug 2013.

[247] ATLAS Collaboration. Jet energy resolution in proton-proton collisions at $\sqrt{s} = 7$ TeV recorded in 2010 with the ATLAS detector. *Eur. Phys. J.*, C73:2306, 2013. doi:10.1140/epjc/s10052-013-2306-0.

[248] ATLAS Collaboration. Jet energy scale and its systematic uncertainty in proton-proton collisions at $\sqrt{s} = 7$ TeV with ATLAS 2011 data. ATLAS-CONF-2013-004, CERN, Geneva, Jan 2013.

[249] ATLAS Collaboration. ATLAS Jets and Etmiss Combined Performance Group - Public Plots - Approved 2013 JER 2011, 2013. URL `https://twiki.cern.ch/twiki/bin/view/AtlasPublic/JetEtmissApproved2013Jer2011`. (visited on 20/10/2013).

[250] ATLAS Collaboration. Commissioning of the ATLAS high-performance b-tagging algorithms in the 7 TeV collision data. ATLAS-CONF-2011-102, CERN, Geneva, Jul 2011.

[251] ATLAS Collaboration. Measurement of the b-tag Efficiency in a Sample of Jets Containing Muons with $5\,\text{fb}^{-1}$ of Data from the ATLAS Detector. ATLAS-CONF-2012-043, CERN, Geneva, Mar 2012.

[252] ATLAS Collaboration. Measuring the b-tag efficiency in a top-pair sample with 4.7fb^{-1} of data from the ATLAS detector. ATLAS-CONF-2012-097, CERN, Geneva, Jul 2012.

[253] ATLAS Collaboration. Flavour Tagging Public Results – b-tag efficiency in 8 TeV data, 2013. URL `https://twiki.cern.ch/twiki/bin/view/AtlasPublic/FlavourTaggingPublicResultsCollisionData#Approved_Plots_for_8_TeV_Data`. (visited on 12/11/2013).

[254] ATLAS Collaboration. b-jet tagging calibration on c-jets containing D^{*+} mesons. ATLAS-CONF-2012-039, CERN, Geneva, 2012.

[255] ATLAS Collaboration. Measurement of the Mistag Rate with 5 fb^{-1} of Data Collected by the ATLAS Detector. ATLAS-CONF-2012-040, CERN, Geneva, 2012.

[256] ATLAS Collaboration. Performance of Missing Transverse Momentum Reconstruction in ATLAS studied in Proton-Proton Collisions recorded in 2012 at 8 TeV. ATLAS-CONF-2013-082, CERN, Geneva, Aug 2013.

[257] ATLAS Collaboration. Measurement of t-Channel Single Top-Quark Production in pp Collisions at $\sqrt{s} = 8$ TeV with the ATLAS detector. ATLAS-CONF-2012-132, CERN, Geneva, 2012.

[258] ATLAS Collaboration. Measurement of the t-channel single top-quark production cross section in pp collisions at $\sqrt{s} = 7$ TeV with the ATLAS detector. *Phys. Lett.*, B717:330–350, 2012. doi:10.1016/j.physletb.2012.09.031.

[259] ATLAS Collaboration. Measurement of the t-channel single top-quark and top-antiquark production cross-sections and their ratio in pp collisions at $\sqrt{s} = 7$ TeV. ATLAS-CONF-2012-056, CERN, Geneva, Jun 2012.

[260] M. Feindt. A Neural Bayesian Estimator for Conditional Probability Densities. `arXiv:physics/0402093 [physics.data-an]`, Feb 2004.

[261] M. Feindt and U. Kerzel. The NeuroBayes Neural Network Package. *Nucl. Instrum. Meth.*, A 559:190–194, 2006. doi:10.1016/j.nima.2005.11.166.

[262] D. J. MacKay. *Information theory, inference and learning algorithms*. Cambridge University Press, New York, NY, USA, 2002. ISBN 0521642981.

[263] D. Kriesel. A Brief Introduction to Neural Networks (version ZETA2-EN), 2007. URL `http://www.dkriesel.com/en/science/neural_networks`. (visited on 15/10/2013).

[264] D. J. C. MacKay. A Practical Bayesian Framework for Backpropagation Networks. *Neural Comput.*, 4(3):448–472, May 1992. doi:10.1162/neco.1992.4.3.448.

[265] ATLAS Collaboration. Light-quark and Gluon Jets: Calorimeter Response, Jet Energy Scale Systematics and Properties. ATLAS-CONF-2012-138, CERN, Geneva, Sep 2012.

[266] ATLAS Collaboration. In situ jet pseudorapidity intercalibration of the ATLAS detector using dijet events in $\sqrt{s} = 7$ TeV proton-proton 2011 data. ATLAS-CONF-2012-124, CERN, Geneva, Aug 2012.

[267] ATLAS Collaboration. Pile-up corrections for jets from proton-proton collisions at $\sqrt{s}$=7 TeV in ATLAS in 2011. ATLAS-CONF-2012-064, CERN, Geneva, Jul 2012.

[268] ATLAS Collaboration. Jet energy measurement and systematic uncertainties using tracks for jets and for b-quark jets produced in proton-proton collisions at $\sqrt{s} =$ 7 TeV in the ATLAS detector. ATLAS-CONF-2013-002, CERN, Geneva, Jan 2013.

[269] ATLAS Collaboration. ATLAS Jets and $E_{\mathrm{T}}^{\mathrm{miss}}$Combined Performance Group - Public Plots - Approved 2013 JES Uncertainty, 2013. URL `https://twiki.cern.ch/twiki/bin/view/AtlasPublic/JetEtmissApproved2013JESUncertainty`. (visited on 20/10/2013).

[270] ATLAS Collaboration. Performance of Missing Transverse Momentum Reconstruction in ATLAS with 2011 Proton-Proton Collisions at $\sqrt{s} = 7$ TeV. ATLAS-CONF-2012-101, CERN, Geneva, Jul 2012.

[271] R. D. Ball, V. Bertone, F. Cerutti, et al. Impact of heavy-quark masses on parton distributions and LHC phenomenology. *Nucl. Phys.*, B849:296–363, 2011. doi:10.1016/j.nuclphysb.2011.03.021.

[272] I. Bertram, G. Landsberg, J. Linnemann, R. Partridge M. Paterno, H.B. Prosper (DØ Collaboration). A Recipe for the construction of confidence limits. FERMILAB-TM-2104, FERMILAB, Batavia, IL, 2000.

[273] M. Bayes and M. Price. An Essay towards Solving a Problem in the Doctrine of Chances. By the Late Rev. Mr. Bayes, F. R. S. Communicated by Mr. Price, in a Letter to John Canton, A. M. F. R. S. *Phil. Trans.*, 53:370–418, 1763. doi:10.1098/rstl.1763.0053.

[274] R. Barlow. Asymmetric Errors. `arXiv:physics/0401042 [physics.data-an]`, Jan 2004.

[275] G. Cowan, K. Cranmer, E. Gross, and O. Vitells. Asymptotic formulae for likelihood-based tests of new physics. *Eur. Phys. J.*, C71:1554, 2011. doi:10.1140/epjc/s10052-011-1554-0.

[276] I. Asimov. *The complete stories*. Isaac Asimov. Doubleday, 1992. ISBN 9780385420785.

[277] G. Cowan, K. Cranmer, E. Gross, and O. Vitells. Asymptotic formulae for likelihood-based tests of new physics. *Eur. Phys. J.*, C71(2):1–19, 2011. doi:10.1140/epjc/s10052-011-1554-0.

[278] ATLAS Collaboration. Search for single top-quark production via FCNC in strong interaction in $\sqrt{s} = 8$ TeV ATLAS data. ATLAS-CONF-2013-063, CERN, Geneva, Jul 2013.

[279] S. Höche, F. Krauss, M. Schönherr, and F. Siegert. A critical appraisal of NLO+PS matching methods. *JHEP*, 1209:049, 2012. doi:10.1007/JHEP09(2012)049.

[280] ATLAS Collaboration. Letter of Intent for the Phase-II Upgrade of the ATLAS Experiment. CERN-LHCC-2012-022, LHCC-I-023, CERN, Geneva, Dec 2012.

[281] K. Nakamura et al. Review of particle physics. *J. Phys.*, G37:075021, 2010. doi:10.1088/0954-3899/37/7A/075021.

[282] F. Lackner, F. Savary, H. Prin, and A. Perin. An Improved Insulation System for the LHC Main 13 kA Interconnection Splices. CERN-ATS-2013-021, CERN, Geneva, Feb 2013.

[283] ATLAS Collaboration. ATLAS Insertable B-Layer Technical Design Report. CERN-LHCC-2010-013, ATLAS-TDR-019, CERN, Geneva, Sep 2010.

[284] ATLAS Collaboration. Studies for the development of the Inner Detector trigger algorithms at ATLAS. ATL-DAQ-PUB-2013-002, CERN, Geneva, Sep 2013.

[285] R. Garoby, H. Damerau, S. Gilardoni, et al. Status and Plans for the Upgrade of the LHC Injectors. CERN-ATS-2013-059, CERN, Geneva, May 2013.

[286] ATLAS Collaboration. Letter of Intent for the Phase-I Upgrade of the ATLAS Experiment. CERN-LHCC-2011-012. LHCC-I-020, CERN, Geneva, Nov 2011.

[287] ATLAS Collaboration. Expected pileup values at the HL-LHC. ATL-UPGRADE-PUB-2013-014, CERN, Geneva, Sep 2013.

[288] L. Rossi, O. Brüning, A. Ballarino, et al. High Luminosity Large Hadron Collider – A description for the European Strategy Preparatory Group. CERN-ATS-2012-236, CERN, Geneva, Aug 2012.

[289] ATLAS Collaboration. Physics at a High-Luminosity LHC with ATLAS (Update). ATL-PHYS-PUB-2012-004, CERN, Geneva, Oct 2012.

[290] ATLAS Collaboration. Performance assumptions based on full simulation for an upgraded ATLAS detector at a High-Luminosity LHC. ATL-PHYS-PUB-2013-009, CERN, Geneva, Sep 2013.

[291] C. Claeys and E. Simoen. *Radiation Effects in Advanced Semiconductor Materials and Devices*. Physics and Astronomy Online Library. Springer, 2002. ISBN 9783540433934.

[292] I. Dawson. Radiation background simulation and verification at the LHC: Examples from the ATLAS experiment and its upgrades, In Proceedings of the 21st International Workshop on Vertex Detectors (Vertex 2012) : Jeju, Korea, September 16-21, 2012. *PoS*, Vertex2012:015, 2013.

[293] P. S. Miyagawa and I. Dawson. Radiation background studies for the Phase II inner tracker upgrade. ATL-UPGRADE-PUB-2013-012, CERN, Geneva, Feb 2013.

[294] I. Dawson, P. Dervan, I. Mandic, and L. Nicolas. Fluence and dose measurements in the ATLAS inner detector and comparison with simulation. ATL-INDET-INT-2011-004, CERN, Geneva, May 2011.

[295] S. Burdin, I. Watson, M. Garcia-Sciveres, and N. Hartman. Study of Conical Layout for Upgrade Pixel Detector. ATL-UPGRADE-PUB-2013-003, CERN, Geneva, Feb 2013.

[296] A. Ludwig, B. Heinemann, and M. Garcia-Sciveres. Studies of Inner Detector Layouts with 5 Pixel layers for the Phase-II Upgrade. ATL-UPGRADE-PUB-2013-013, CERN, Geneva, Feb 2013.

[297] P. Delebecque, S. Elles, N. Geffroy, et al. Alpine Pixel Detector Layout. ATL-UPGRADE-PUB-2013-009, CERN, Geneva, Feb 2013.

[298] A. Clark, M. Elsing, N. Hessey, et al. Final Report: ATLAS Phase-2 Tracker Upgrade Layout Task Force. ATL-UPGRADE-PUB-2012-004, CERN, Geneva, Oct 2012.

[299] A. Affolder, J. Carrol, A. Greenall, and M. Wormald. Design and performance of serial powered single-sided modules within an integrated stave assembly for the ATLAS tracker barrel upgrade. *JINST*, 5:C12013, 2010. doi:10.1088/1748-0221/5/12/C12013.

[300] P. P. Allport, V. O'Shea, L. Wiik, et al. Progress with the single-sided module prototypes for the ATLAS tracker upgrade stave, In Proceedings of the 7th International "Hiroshima" Symposium on the Development and Application of Semiconductor Tracking Detectors, Int Conf Ctr, Hiroshima, Japan, Aug 29-Sep 01, 2009. *Nucl. Instrum. Meth.*, A 636(1, Supplement):S90–S96, 2011. doi:10.1016/j.nima.2010.04.091.

[301] F. Anghinolfi, M. F. Newcomer, and J. Kaplon. Draft ABC130 ASIC Specifications v4.3, Feb.5, 2013. , CERN, 2013. URL `http://indico.cern.ch/getFile.py/access?resId=0&materialId=0&confId=227566`. (visited on 05/02/2013).

[302] A. Clark, G. Barbier, F. Cadoux, et al. Development of a silicon-microstrip super module prototype for the high luminosity LHC, In Proceedings of the 8th International "Hiroshima" Symposium on the Development and Application of Semiconductor Tracking Detectors – Academia Sinica, Taipei, Taiwan, December 5-8, 2011. *Nucl. Instrum. Meth.*, A 699(0):97–101, 2013. doi:10.1016/j.nima.2012.04.016.

[303] S. Gonzalez-Sevilla, G. Barbier, F. Cadoux, et al. Electrical performance of a silicon micro-strip super-module prototype for the High-Luminosity LHC collider, In Proceedings of the 8th International "Hiroshima" Symposium on the Development and Application of Semiconductor Tracking Detectors – Academia Sinica, Taipei, Taiwan, December 5-8, 2011. *Nucl. Instrum. Meth.*, A 699(0):102–106, 2013. doi:10.1016/j.nima.2012.03.025.

[304] T. Affolder, F. Anghinolfi, A. Clark, et al. System Electronics for the ATLAS Upgraded Strip Detector. ATL-UPGRADE-PUB-2013-011, CERN, Geneva, Feb 2013.

[305] W. Dabrowski, F. Anghinolfi, C. M. Buttar, et al. Design and performance of the ABCD chip for the binary readout of silicon strip detectors in the ATLAS semiconductor tracker. *IEEE Trans. Nucl. Sci.*, 47(6, pt.1):1843, 2000. doi:10.1109/23.914457.

[306] M. Dentan, P. Abbon, P. Borgeaud, et al. Dmill, a mixed analog-digital radiation-hard bicmos technology for high energy physics electronics. In *Nuclear Science Symposium and Medical Imaging Conference Record, 1995., 1995 IEEE*, volume 2, pages 733–737 vol.2, 1995. doi:10.1109/NSSMIC.1995.510373.

[307] B. T. Huffman, A. R. Weidberg, T. Flick, and J. Ye. ITK optical links backup document. ATL-UPGRADE-PUB-2013-005, CERN, Geneva, Feb 2013.

[308] P. W. Phillips. ATLAS SCT power supply system, In Proceedings of the Topical Workshop on Electronics for Particle Physics, Prague, Czech Republic, 03-07 Sep 2007. 2007. doi:10.5170/CERN-2007-007.

[309] S. Díez. System Implications of the Different Powering Distributions for the ATLAS Upgrade Strips Tracker, In Proceedings of the 2nd International Conference on Technology and Instrumentation in Particle Physics (TIPP 2011), Chicago, IL, USA, June 8-14, 2011. *Phys. Proc.*, 37(0):960–969, 2012.

[310] A. Affolder, B. Allongue, G. Blanchot, et al. DC-DC converters with reduced mass for trackers at the HL-LHC. *JINST*, 6(11):C11035, 2011. doi:10.1088/1748-0221/6/11/C11035.

[311] M. F. Newcomer, M. Key-Charriere, F. Anghinolfi, et al. HCC Update - Blocks, Digital Design, Status. Talk at ATLAS Upgrade Week, CERN, Geneva, 4-8 Nov, 2013. , CERN, 2013. URL `http://indico.cern.ch/getFile.py/access?contribId=15&sessionId=15&resId=2&materialId=slides&confId=233534`. (internal document, visited on 05/11/2013).

[312] CERN PH department, ESE group. AMIS5MP daasheet rev. 1.3, Nov 2013. , CERN, 2013. URL `http://project-dcdc.web.cern.ch/project-dcdc/public/Documents/AMIS5Mod_DatasheetV1.3.pdf`. (visited on 06/11/2013).

[313] I. Gregor and A. Affolder. Electrical Design and Performance of Single- and Double-Sided Silicon Modules for the ATLAS Phase II Upgrade. ATL-UPGRADE-PUB-2012-005, CERN, Geneva, Dec 2012.

[314] J. Godlewski, G. Hallewell, N. Hessey, B. Verlaat, and G. Viehhauser. ATLAS upgrade tracker integration: Inner Tracker Cooling. Atu-sys-er-0017 ver1, CERN, 2012. URL `https://edms.cern.ch/document/1262223/1`. (visited on 17/01/2013).

[315] Y. Unno, T. Yamashita, S. Terada, et al. Evaluation of radiation damaged p-in-n and n-in-n silicon microstrip detectors. *IEEE Trans. Nucl. Sci.*, 46(6):1957–1963, 1999. doi:10.1109/23.819262.

[316] K.K. Hamamatsu Photonics, 1126-1 Ichino-cho, Hamamatsu-shi, Shizuoka 435-8558, Japan., 2013. URL `http://www.hamamatsu.com`.

[317] Y. Unno, A. Affolder, P. Allport, et al. Development of n-on-p silicon sensors for very high radiation environments, In Proceedings of the 7th International "Hiroshima" Symposium on the Development and Application of Semiconductor Tracking Detectors, Int Conf Ctr, Hiroshima, Japan, Aug 29-Sep 01, 2009. *Nucl. Instrum. Meth.*, A 636(1, Supplement):S24–S30, 2011. doi:10.1016/j.nima.2010.04.080.

[318] ATLAS SCT Collaboration. Technical Specification - Supply of Silicon Microstrip Sensors of ATLAS07 specification. , CERN, Geneva, 2007. URL `https://edms.cern.ch/file/888375/2/ATLAS07TechnicalSpecR4.6.pdf`. (visited on 14/11/2013).

[319] Cascade Microtech Inc. PA200 200 mm Semi-automatic Probe System, 2013. URL `http://www.cmicro.com/files/PA200-DS.pdf`. (visited on 05/11/2013).

[320] Keithley Instruments Inc. Series 2400 SourceMeter SMU Instruments - technical datasheet, 2013. URL `http://www.keithley.com/data?asset=372`. (visited on 20/12/2013).

[321] Keithley Instruments Inc. 6485 Picoammeter - technical datasheet, 2013. URL `http://www.keithley.com/data?asset=6199`. (visited on 20/12/2013).

[322] Agilent Technologies Inc. E4981A Capacitance Meter - technical datasheet, 2011. URL `http://cp.literature.agilent.com/litweb/pdf/5989-8963EN.pdf`. (visited on 20/12/2013).

[323] Agilent Technologies Inc. 4263B LCR Meter - technical datasheet, 2008. URL `http://cp.literature.agilent.com/litweb/pdf/5964-6181E.pdf`. (visited on 20/12/2013).

[324] J. Bohm, M. Mikestikova, A. Affolder, et al. Evaluation of the bulk and strip characteristics of large area n-in-p silicon sensors intended for a very high radiation environment, In Proceedings of 7th International "Hiroshima" Symposium on the Development and Application of Semiconductor Tracking Detectors, Int Conf Ctr, Hiroshima, Japan, Aug 29-Sep 01, 2009. *Nucl. Instrum. Meth.*, A 636 (1, Supplement):S104–S110, 2011. doi:10.1016/j.nima.2010.04.093.

[325] A. Chilingarov, D. Campbell, and G. Hughes. Interstrip capacitance stabilization at low humidity, In Proceedings of 13th International Workshop on Vertex Detectors (Vertex 2004) : Menaggio, Como, Italy, September 13-18, 2004. *Nucl. Instrum. Meth.*, A 560(1):118–121, 2006. doi:10.1016/j.nima.2005.11.198.

[326] Henkel AG & Co. KGaA. Hysol TRA-DUCT 2902 - technical datasheet, 2010. URL `https://tds.us.henkel.com//NA/UT/HNAUTTDS.nsf/web/8F6D7873703EA92C85257575004508BA/$File/TRA-DUCT%202902-EN.pdf`. (visited on 20/12/2013).

[327] LOT-QuantumDesign Ltd. Fuller Epolite FH-5313 - technical datasheet, 2011. URL `http://www.lot-qd.com/files/downloads/andover/en/epolite.pdf`. (visited on 20/12/2013).

[328] A.-L. Poley. ATLAS silicon detector upgrade: process optimisation and adhesive studies. Master's thesis, Humbold University of Berlin, Germany, Dec 2013.

[329] D. Nelson. HSIO Development Platform Users Guide - Version C02, Revision 1.1, Apr 2010. , SLAC National Accelerator Laboratory, 2010. URL `http://www.slac.stanford.edu/~djn/Atlas/hsio/HSIO%20Development%20Platform%20Users%20Guide_c02.pdf`. (visited on 06/12/2013).

[330] F. Anghinolfi. ABC-N ASIC specifications v1.3. , CERN, Oct 2008. URL `http://dpnc.unige.ch/atlas/upgrade/Upgrade/ABCN/abcn_V1.3.doc`. (visited on 16/02/2013).

[331] Y. Takubo, A. Clark, M. Endo, et al. Development of SiTCP based DAQ system of double-sided silicon strip super-module, In Proceedings of the 8th International "Hiroshima" Symposium on the Development and Application of Semiconductor Tracking Detectors – Academia Sinica, Taipei, Taiwan, December 5-8, 2011. *Nucl. Instrum. Meth.*, A 699(0):116–119, 2013. doi:10.1016/j.nima.2012.04.032.

[332] Barcelona Microelectronics Institute of the National Microelectronics Centre-CSIC, Campus UAB, Cerdanyola del Vallès, Barcelona, E-08193 Spain., 2013. URL `http://www.imb-cnm.csic.es`.

[333] S. Díez. Silicon strip prototypes for the Phase-II upgrade of the ATLAS tracker for the HL-LHC. `arXiv:1310.0098 [physics.ins-det]`, Sep 2013.

[334] P. W. Phillips. ATLAS strip tracker stavelets. *JINST*, 7(02):C02028, 2012. doi:10.1088/1748-0221/7/02/C02028.

List of Figures

List of Tables

Acknowledgements

The successful completion of this research work would not have been possible without the support and encouragement of many people I hereby want to express my sincere gratitude.

First of all I would like to thank my supervisor Ulrich Husemann for the opportunity to work on this thesis project and offering me such a warm welcome in his former research group. Although he lastly ended up at the competitor experiment, he always offered me his excellent support and advice in many scientific discussions and non-physics matters over the past years. Also many thanks go to Heiko Lacker for his advice and input to all kind of matters and for being second supervisor of this work, as well as to Hermann Kolanoski and Arno Straessner for refereeing this thesis. For the same reasons I want to take this opportunity to thank Ingo Bloch who practically took over the supervision of the hardware-related part of my work and whose friendly working atmosphere made the stays at DESY always as inspiring as amusing.

Certainly this work would not have been successful without the help of many of the collaborators within ATLAS or at CERN in general. I would like to thank in particular Dominic Hirschbühl and Muhammad Alhroob for their invaluable advice and answers to an uncountable number of questions and issues related to the data analysis, and to the many people within the ATLAS upgrade community for sharing all their knowledge and expertise and providing all the support since the earliest days of our hardware activities. I would also like to thank Carlos Garcia Argos, Liv Wiik and Todd Huffman for the many enjoyable and creative sessions in B180 at CERN. My sincere thanks also go to many other friends and colleagues at the DESY ATLAS group. Let it be Thorsten Kuhl for his unconditional availability for discussions or the (mis)calibration of coffee machines, Luz Gomez and Christoph Wasicki for the uncountable number of refreshing breaks, or Laura Rehnisch and Luise Poley for the many joyful hours of lab work and doing "real physics" at DESY. I'd also like to thank all guys from the HU-Berlin ATLAS group for all the recreational activity after work and at many GK block courses and meetings.

Last but certainly not least, I would like to thank my friends and family, many of whom I couldn't meet very often over the past year. Thanks a lot for all your support and understanding. In particular many thanks to Julia for who she is to me. There are many more who deserve to be mentioned here, and who I feel deeply indebted to. As well to all of them a big thank you!

Selbständigkeitserklärung

Ich erkläre, dass ich die vorliegende Arbeit selbständig und nur unter Verwendung der angegebenen Literatur und Hilfsmittel angefertigt habe.

Berlin, den 28.01.2014 Conrad Friedrich